Correlative Light Microscopy and FIB/SEM Tomography:

High-resolution 3D-analysis of single cells and tissues.

Dissertation der Fakultät für Biologie

der Ludwig-Maximilians-Universität München

Manja Luckner

München, 2018

Die vorliegende Doktorarbeit wurde im Zeitraum von November 2014 bis Juli 2018 an der Ludwig-Maximilians-Universität München und dem Deutschen Zentrum für Neurodegenerative Erkrankungen durchgeführt.

Erstgutachter: Prof. Dr. Gerhard Wanner
Zweitgutachter: PD. Dr. Martin Heß
Datum der Abgabe: 26.07.2018
Datum der mündlichen Prüfung: 01.10.2018

Eidesstattliche Erklärung

Ich versichere hiermit an Eides statt, dass die vorgelegte Dissertation von mir selbstständig und ohne unerlaubte Hilfe angefertigt wurde. Des Weiteren erkläre ich, dass ich nicht anderweitig ohne Erfolg versucht habe, eine Dissertation einzureichen oder mich der Doktorprüfung zu unterziehen. Die folgende Dissertation liegt weder ganz, noch in wesentlichen Teilen einer anderen Prüfungskommission vor.

_____

Manja Luckner

München, 20. Juli 2018

Statutory Declaration

I declare that I have authored this thesis independently, that I have not used other than the declared sources/resources. As well, I declare that, I have not submitted a dissertation without success and not passed the oral exam. The present dissertation (neither the entire dissertation nor parts) has not been presented to another examination board.

_____

Manja Luckner

Munich, 20. July 2018

Content

1 Abbreviations

2D/3D	two-dimensional/three-dimensional
AD	Alzheimer's diseases
ATUMtome	tape collecting ultramicrotome
BSE	backscattered electron(s)
CLEM	correlative light and electron microscopy
CLSM	confocal laser scanning microscopy
CPC	chromosomal passenger complex
DAB	diaminobenzidine
DIC	differential interference contrast
DNA	deoxyribonucleic acid
EDX	energy dispersive X-ray analysis/spectroscopy
EFTEM	energy-filtered transmission electron microscopy
EM	electron microscopy(ic)
ER	endoplasmic reticulum
ERGIC	ER-Golgi intermediate compartment
EsB	energy selective backscattered (electron)
FIB	focused ion beam
Fig.	Figure
FS	freeze-substitution
GB	gigabyte
GFP	green fluorescent protein
HPF	high-pressure freezing
IC	intermediate compartment
keV	kiloelectronvolt
kV	kilovolt
LM	light microscopy(ic)
MT	microtubule
NE	nuclear envelope
OCS	open canalicular system
OTO	osmium-thiocarbohydrazide-osmium
PALM	photoactivated localization microscopy
PE	primary electron(s)
ROI	region of interest
rOTO	reduced osmium-ferrocyanide-thiocarbohydrazide-osmium
SB	serial block-face
SE	secondary electron(s)
SEM	scanning electron microscopy(ic)
SIM	structured illumination microscopy
STEM	scanning transmission electron microscopy
STORM	stochastic optical reconstruction microscopy
TB	terabyte
TEM	transmission electron microscopy(ic)
VTC	vesicular tubular clusters

2 List of Publications

Publication I

From light microscopy to analytical SEM and FIB/SEM in biology: Fixed Coordinates, Flat Embedding, Absolute References.

Luckner, M., and Wanner, G. (2018a)

Microscopy and Microanalysis, doi: 10.1017/S1431927618015015 (in press)

Publication II

Structural stress responses and degradation of dictyosomes in algae analysed by TEM and FIB-SEM tomography.

Lütz-Meindl, U., **Luckner, M.**, Andosch, A., Wanner, G. (2016)

Journal of Microscopy, Vol. 263, Issue 2 2016, pp. 129–141 doi: 10.1111/jmi.12369

Publication III

Ionic stress induces fusion of mitochondria to 3-D networks: An electron tomography study.

Steiner, P., L**uckner, M**., Kerschbaum, H., Wanner, G., and Lütz-Meindl, U. (2018)

Journal of Structural Biology, 2018 Jul 2. pii: S1047-8477(18)30158-8; doi: 10.1016/j.jsb.2018.06.010

Publication IV

Migrating Platelets Are Mechano-scavengers that Collect and Bundle Bacteria.

Gaertner F, Ahmad Z, Rosenberger G, Fan S, Nicolai L, Busch B, Yavuz, **Luckner M**, Ishikawa-Ankerhold H, Hennel R, Benechet A, Lorenz M, Chandraratne S, Schubert I, Helmer S, Striednig B, Stark K, Janko M, Böttcher RT, Verschoor A, Leon C, Gachet C, Gudermann T, Mederos Y Schnitzler M, Pincus Z, Iannacone M, Haas R, Wanner G, Lauber K, Sixt M, Massberg S. (2017)

Cell 171, 1368–1382, 2017 doi: 10.1016/j.cell.2017.11.001

Publication V

Precise and economic FIB/SEM for CLEM: with 2 nm voxels through mitosis.

Luckner, M., and Wanner, G. (2018b)

Histochemistry and Cell Biology, doi: 10.1007/s00418-018-1681-x (in press)

Publication VI

Label-free 3D-CLEM using endogenous tissue landmarks.

Luckner, M*., Burgold, S*****., Filser, S*****., Scheungrab, M., Niyaz, Y., Hummel, E., Wanner, G., Herms, J. (2018)

iScience, doi: 10.1016/j.isci.2018.07.012 (in press)

*****Equal contribution

3 Declaration of contribution as a co-author

Publication I (Luckner and Wanner, 2018a)
Luckner, M., and Wanner, G. designed the experiments. **Luckner, M**., and Wanner, G. performed all experimental work presented in this publication. **Luckner, M.**, and Wanner, G. reconstructed the 3D models in Amira. **Luckner, M**., and Wanner, G. wrote the publication.

Publication II (Lütz-Meindl et al., 2016)
Lütz-Meindl, U., **Luckner, M.**, Andosch, A., Wanner, G. designed the experiments.
Lütz-Meindl, U. and Andosch, A. performed the cultivation of *Micrasterias* and *Nitella*, tstress induction, high-pressure freezing and TEM investigation**. Luckner, M.**, and Wanner, G. performed high-pressure freezing for FIB/SEM analysis. **Luckner, M.**, and Wanner, G. performed FIB/SEM microscopy. **Luckner, M.**, reconstructed the 3D models and created the supplementary movies. Lütz-Meindl, U., **Luckner, M**., Andosch, A., Wanner, G. wrote and corrected the publication.

Publication III (Steiner et al., 2018)
Lütz-Meindl, U. Steiner, P., designed the experiments, high-pressure freezing and TEM investigation. **Luckner, M**., and Wanner, G. performed FIB/SEM preparation, FIB/SEM microscopy and alignment of FIB/SEM stacks. Steiner, P., **Luckner, M.**, and Wanner G., performed Amira reconstruction. Lütz-Meindl, U., and Steiner wrote the publication. Wanner G. and Luckner M. corrected the publication.

Publication IV (Gaertner et al., 2017)
Gärtner F. designed the concept of the publication. **Luckner, M.**, and Wanner, G. designed the SEM and FIB/SEM experiments. General methodology, F.G., Z.A., G.R., S.F., L.N., A.B., M.I., B.B., M.M.y.S., **Luckner, M.**, G.W., M. Lorenz, and H.I.-A. **Luckner, M.**, and Wanner, G. developed a special embedding method for a correlative light and electron microscopy approach of migrating platelets. **Luckner, M.**, and Wanner, G. performed EM preparation, immuno-SEM and FIB/SEM microscopy. Gärtner F. performed the light microscopy part of the correlative workflow and migrating experiments.

Publication V (Luckner and Wanner, 2018b)
Luckner, M., and Wanner, G. designed the experiments. **Luckner, M**., and Wanner, G. performed all experimental work presented in this publication. **Luckner, M.**, and Wanner, G. reconstructed the 3D models in Amira. **Luckner, M.** created the movies of the supplementary data. **Luckner, M.**, and Wanner, G. wrote the publication.

We hereby confirm the above statements concerning publication I-V:

Manja Luckner | Prof. Dr. Gerhard Wanner

Publication VI (Luckner et al., 2018)
Luckner, M., Burgold, S., Wanner, G. and Herms, J. designed the experiments. Burgold, S., Filser, S., performed the surgeries and light microscopy. **Luckner, M.**, and Wanner, G. developed the flat embedding and performed the FIB/SEM microscopy. **Luckner, M.**, Scheungrab, M. and Burgold, S., performed the 3D reconstruction. **Luckner, M.** and Burgold, S. performed the 3D measurements. **Luckner, M.** created the supplemental movies. **Luckner, M**., Burgold, S., Filser, S. Wanner, G. and Herms, J wrote the publication. Hummel, E., corrected the manuscript.

We hereby confirm the above statements concerning publication VI:

Manja Luckner | Prof. Dr. Gerhard Wanner

Dr. Steffen Burgold | Dr. Severin Filser

4 Summary

A portfolio of technical improvements was developed for precise and economic correlative light and scanning electron microscopy and FIB/SEM serial block-face imaging, comprehending correlative investigations of single cells and large tissues sections. Customized coordinate systems for slides and cover slips were developed for thin and ultra-thin embedding for a wide range of biological specimens, ranging from prokaryotic (<1 µm) to eukaryotic cells (>10 µm). Immobilization of biological samples was examined with a variety of adhesives. For vibratome sections or biological specimens, which cannot be immobilized or being fragile, a filter system was developed for flat embedding. Ultra-thin embedding on laser marked slides or cover slips has proven to fulfill all demands for efficient, high resolution CLEM. As target cells or target regions can be re-located within minutes in SEM, without acrobatics and risky trimming, correlative investigations were reduced to a minimum of preparation steps, though reaching highest resolution. FIB/SEM milling procedure is facilitated and significantly accelerated as: i) milling a ramp becomes needless, ii) re-deposition of milled material does not occur and iii) charging effects are significantly reduced. Optimizing all technical parameters (choice of beam stable resins, prolonged polymerization, rOTO fixation/staining, short exposure times) FIB/SEM stacks with 2 nm iso-voxels can be achieved over thousand sections. In combination with the in-lens SE signal, with better resolution and a much better signal to noise ratio, exposure time of a single image can be reduced by 30-50% and with a modified contrast enhancement (rOTO) even by 70%. FIB/SEM, with its unsurpassed resolution in z-direction is the perfect bridge between high resolution LM, and TEM tomography. Several scientific questions involving CLEM could be addressed precisely and efficiently by and ultra-thin embedding in routine in an economic way. The feasibility was demonstrated by: i) 3D reconstruction of dictyosomes and mitochondria of stress induced *Micrasterias* ii) migration of human platelets on fibrin(ogen) coated slides to collect and bundle bacteria as innate immune response; iii) application of CLEM to different stages of mitosis in HeLa cells, including nuclear envelope breakdown and reconstitution; Golgi disassembly and reconstitution, formation of midzone and midbody and iv) *in vivo* 2-photon microscopy of dendrites of the somato-sensory cortex in mouse brain, combined with high-resolution FIB/SEM.

5 Zusammenfassung

Für präzise und ökonomische korrelative Licht- und Rasterelektronenmikroskopie sowie FIB/SEM Mikroskopie wurde ein Portfolio technischer Verbesserungen entwickelt, das korrelative Untersuchungen von Einzelzellen und größeren Gewebeschnitten umfasst. Objektträger und Deckgläser, mit speziellen Koordinatensystemen, wurden für eine dünne/ultradünne Einbettung, für eine Vielzahl biologischer Proben, von prokaryotischen (<1 µm) bis hin zu eukaryotischen Zellen (> 10 µm), entwickelt. Zahlreiche unterschiedliche Klebstoffe wurden für eine Eignung zur Immobilisierung von biologischen Objekten untersucht. Zur Flacheinbettung von Vibratom-Schnitten und biologischen Proben, die nicht immobilisiert werden können oder sehr fragil sind, wurde ein Filtersystem entwickelt. Die Einbettung in ultradünne Schichten auf lasermarkierten Objektträgern oder Deckgläsern erfüllt alle Anforderungen für korrelative licht- und elektronenmikroskopische Untersuchungen. Ausgewählte Zellen oder Regionen können innerhalb von Minuten im SEM re-lokalisiert werden, ohne riskantes Trimmen der Probe. Korrelative Untersuchungen werden dadurch auf ein Minimum von Präparationsschritten reduziert, ohne Beeinträchtigung der Hochauflösung. Der FIB/SEM-Schneidevorgang wird vereinfacht da: i) das Schneiden einer Rampe entfällt, ii) die Re-Deposition von abgetragenem Probenmaterial verhindert wird und iii) die Aufladungen deutlich verringert werden. Durch die Optimierung aller technischer Parameter (Auswahl strahl-stabiler Kunstharze, Verlängerung der Polymerisation-Zeiten; rOTO Fixierung/Kontrastierung, kurze Belichtungszeiten) konnten FIB/SEM-Bildstapel mit 2 nm Iso-Voxel, von tausend Serienbildern aufgenommen werden. Durch den Bildeinzug mit dem in-lens-SE-Signal, durch die höherer Auflösung und das bessere Signal-Rausch-Verhältnis, kann die Belichtungszeit eines Einzelbildes um 30-50% und mit modifizierter Kontrastverstärkung (rOTO) sogar um 70% reduziert werden. FIB/SEM stellt mit seiner unübertroffenen Auflösung in z-Richtung die ideale Brücke zwischen hochauflösender Lichtmikroskopie und TEM-Tomographie dar. Zahlreiche wissenschaftliche Fragen, die eine Korrelation zur Lichtmikroskopie benötigen, können durch dünne/ultradünne Einbettung präzise und effizient in Routine durchgeführt werden. Das Potenzial der Methode wurde an verschiedenen Untersuchungsobjekte gezeigt: i) 3D-Rekonstruktion von Dictyosomen und Mitochondrien stressinduzierter *Micrasterias* Zellen; ii) Migration von Human-Thrombozyten auf Fibrin(ogen) beschichteten Objektträgern, welche Bakterien in einer ersten Immunantwort aufsammeln; iii) die Anwendung von CLEM auf verschiedene Stadien der Mitose von HeLa-Zellen, einschließlich der Auflösung und des Wiederaufbaus der Kernhülle; Golgi-Zerfall und Rekonstitution, Bildung von *midzone* und *midbody* iv) *in vivo* 2-Photonenmikroskopie von Dendriten des somato-sensorischen Cortex im Mäusehirn kombiniert mit hochauflösender FIB/SEM Mikroskopie.

6 Introduction

6.1 From first Lenses to CLEM – Historical Aspects

The understanding of nature is limited by our own sensual perception. The primacy of our eyes is self-explanatory for the longing for optical devices that magnify, either for medical, astronomical and scientific reasons. A short journey through centuries should illustrate the evolution of light microscopy to modern correlative light and electron microscopy (CLEM). Here, the technical evolution from the first lenses, to microscopes, fixation of specimens, development of staining, documentation, starting with art-like drawings and venturous interpretation of results, is paralleled to the establishment of electron microscopy and finally correlative light and electron microscopic approaches (Fig. 1). Constant improvements of resolution, corrections of optical aberrations, development of better fixation, better knives, better staining and contrast enhancements, precision of documentation and finally interpretation of the data, is the same challenge today, admitted at a higher, much more sophisticated scientific level, but with the same spiritual/intellectual claim to increase cognition and to understand nature more profound. If not cited, many historical data are adopted from “A History of Life Sciences” of (Magner, 2002).

History of light microscopy

Da Vinci (1452-1519) recommended the use of lenses in viewing small objects (Levin, 2013). Perhaps the earliest recorded use of a magnifying instrument in a biological study may date to 1558: The Swiss biologist, Conrad Gesner (1516-1565) published studies on the structure of foraminifera, with detailed drawings of these protozoa (Gesner, 1551; Raven, 2010). In the 17th century Marcello Malpighi (1628-1694) was among the first, who used thin slices for light microscopic investigations of animal tissues (brain, liver, kidney, spleen, lungs and tongue) and plant tissues (Fig. 1 E). Robert Hooke’s (1635-1703) great discovery is the “cell” in 1665 (lat., *cella* = (little) room) when he examined a thin slice from a piece of dried cork (Fig. 1 C, D), published under the title *Micrographia* (Hooke, 1665). The Dutch microscopist, Anton van Leeuwenhoek (1632-1723) greatly improved the art of polishing lenses of short focal length, approaching 270-fold magnification, but he never built a compound microscope (Fig. 1 A, B).

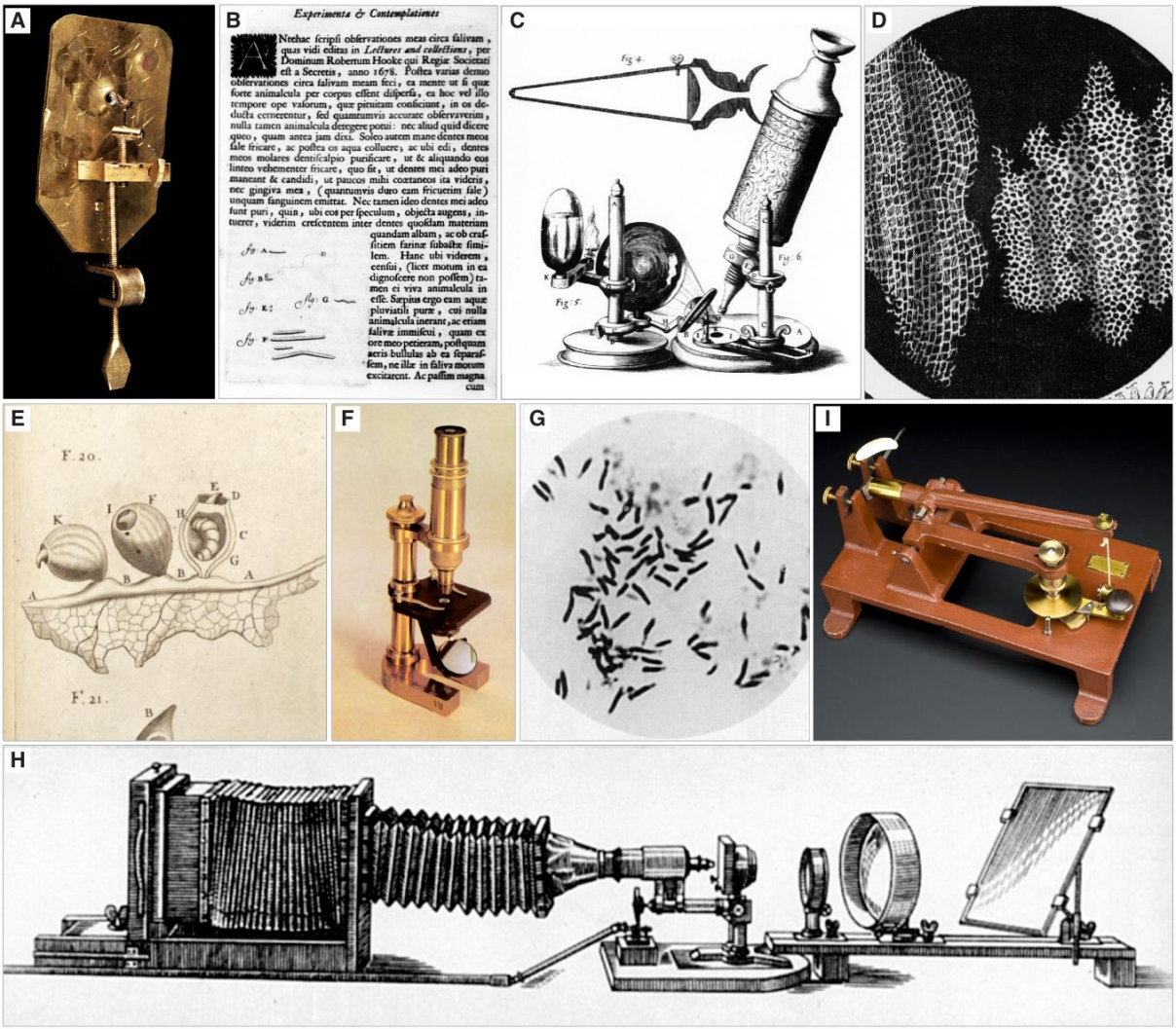

Fig. 1 Illustrated foray through the history of light microscopy. *Nearly all technical challenges from past are in principle relevant today: quality of lenses and resolution of microscopes, staining, microtomy and scientific documentation. Leeuwenhoek (1632-1723) used not a microscope* sensu stricto *but a high magnifying lens (**A**) with magnifications up to 270-fold, allowing him to describe bacteria for the first time (**B**). Hooke's used a composite microscope (**C**) and gave us the term "cell" in 1665 derived from observations of handmade sections of cork (**D**). Marcello Malpighi (1628-1694) was the first author, who made detailed drawings of individual organs of flowers (**E**). Robert Koch used a microscope with horseshoe stand and water immersion from Carl Zeiss 1882 (**F**) and after staining, he could observe* Mycobacterium tuberculosis *(**G**), the specific causative agent of tuberculosis, photographed with a bellows camera (**H**). An early technical accessory for light microscopy was the microtome. The rocking microtome was invented by Sir Horace Darwin (1851-1928), the son of Charles Darwin. The microtome was still available in the twentieth century (**I**; credit: Science Museum London).*

He was the first to observe free-living cells in water drops, described in 1675 (Gest, 2004). His sketches included numerous bacteria (*bacilli, cocci, spirilla*), protozoa, rotifers, and *Hydra* and he first described the sperm cells of humans, and various animals. The English plant micro-anatomist Nehemiah Grew (1641-1721) recognized the cellular nature of plant tissues much more precise as Malpighi (Grew, 1682). Due to the limited resolution of the microscopes in

17th-18th century, stagnation in scientific applications is recognized. Within the 19th century, there was a renaissance of light microscopy for amusement of the microcosm as a parlor game. A breakthrough in optics was given by the invention of achromatic double lenses as objectives and in combinations of several within one objective by Selligue (1784-1845) and Amici (1786-1863). However, a theory for construction of microscopes did not exist (Dippel, 1882). The usual way was testing and probing, which was necessary as the quality of glass was inconsistent. A milestone was set by Schleiden (1804-1881), when he determined that cells are the units of all tissues and that growth is bound to cell division. Theodor Schwann (1810-1882) adopted Schleidens theory to zoology, publishing 1839 "Mikroskopische Untersuchungen über die Übereinstimmung in der Struktur und dem Wachstum der Tiere und Pflanzen", which was the birth of cell biology (Schwann, 1839) and he introduced the term “metabolism” to describe the activities of the cells (Bignold et al., 2007).

Summarizing the limitations of light microscopy at the beginning: lenses could be manufactured only in small sizes due to the poor glass quality (mainly refraction anomalies, air bubbles, impurities), resulting in low resolution and insufficient brightness, as external illumination was not available. Biological objects have to be thin, that light can transmit, which was a challenge in this period, without disposable razor blades and microtomes. The contrast of cells and tissues is very weak (bacteria, brain, nerves etc.) and staining was not possible due to the lack of specific dyes.

The basic inventions for scientific research were made within the 19th century. Joseph Fraunhofer (1787-1826) was able to produce “*schlierenfreies Flint-Glas*” for correction of chromatic aberration. His knowledge about spectroscopy enabled him to determine the refractory index of glass and to use it for construction of objectives with higher resolution (Lommel, 1888). Ernst Abbe defined the term "*Numerische Apertur*" (numerical aperture) and therefore is credited for discovering the resolution limit of the light microscope. A less known invention of Abbe is the “*Abbesche Kondensor*” (= condenser), which concentrates and controls the light that passes through the specimen, prior to entering the objective. A precondition for producing thin section is an adequate fixation of tissues, to stop the metabolism and to harden the tissue for better sectioning properties. Standard fixations in the 19th century were mixtures of ethanol and acetic acid, harsh, but effective. Pol Bouin developed in 1897 a fixative based on picric acid, which hardens and conserves the tissues due to the strong acidity (Ortiz-Hidalgo, 1992). The preservation of cellular ultrastructure was not a topic in the 19th century. A major development in the world of histology originates from the dye production industry. A notable chemist was William Henry Perkin, who accidentally discovered at the age of 15, a dye called ‘*mauveine*’ (Hübner, 2006). This dye is still known as *toluidine blue,* which is still a basic and most efficient dye. Wilhelm Waldeyer used hematoxylin to stain nerve cells, in 1863. The next important step was the introduction of aniline-stains by Paul Ehrlich, described in his dissertation and perfected within the next decade (Ehrlich, 1878). After sectioning slices with razor knives, the first semi-automatic device for the preparation was invented by George Adams, Jr. (1750-1795) and further developed by Alexander Cummings

(1770). The device was hand operating, and the sample was held in a cylinder and sections were created from the top of the sample by using a hand crank. The son of Charles Darwin, Horace Darwin (1851-1928) invented the rocking microtome (Fig. 1 I), a new technology developed in 1885 (Cattermole and Wolfe, 1987). It is not surprising that with culmination of improvements of microscopes, dyes and accompanying techniques, an explosive development of discoveries took place in the second half of the 18th century leading to the modern cell theory.

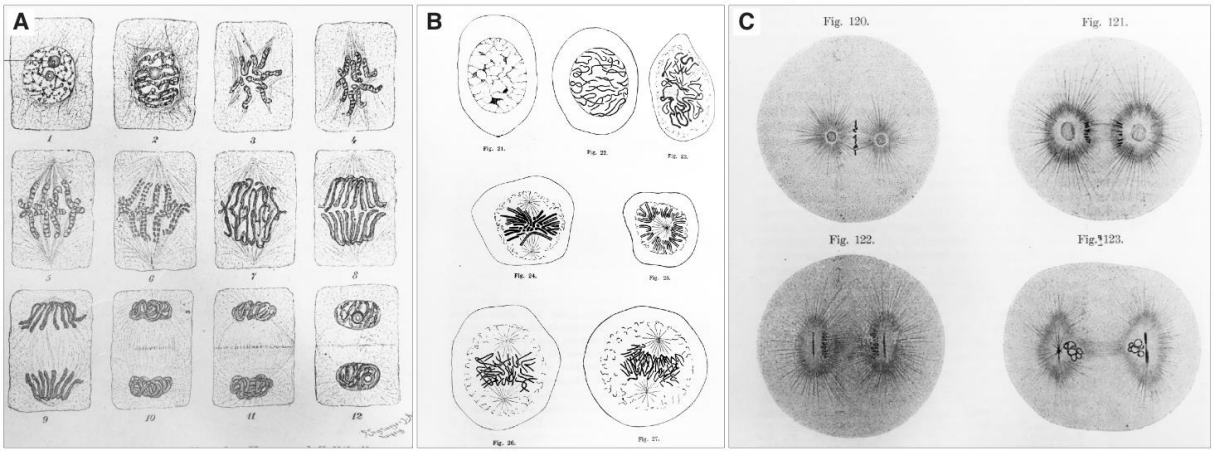

Figure 2: First observation of mitosis. *First description of mitosis in plant cell by Eduard Strasburger (1844-1912). From him originate the terms "cytoplasm" and "nucleoplasm" (**A**). (From:* Lehrbuch der Botanik von Dr. Eduard Strasburger; Gustav Fischer Jana, 1898*). Drawing from Walther Flemming (1843-1905) "*Mitose des Zellerns*" (mitosis of the nucleus) (**B**). From:* Allgemeine Biologie von Oscar Hertwig; Verlag Gustav Fischer, Jena 1906*. Early drawing from Boveri (1862-1915) of mitotic stages of sea urchin dated to 1901 (**C**). The centrosomes are very prominent compared to metaphase chromosomes. (From:* Allgemeine Biologie von Oscar Hertwig; Verlag Gustav Fischer, Jena 1906*).*

The cell theory was extended by Carl Wilhelm Nägeli (1817-1891), who showed in 1846, that plant cells arise from the division of pre-existing cells (Harris, 2000); he coined the term "*Zellmembran*" (cell membrane) which corresponds to the plant cell wall today. In 1855, Rudolf Virchow (1821-1902) confirmed the Nägeli's principle and stated the fundamental: "*omnis cellula e cellula*". Albert von Kolliker discovered in 1857 the mitochondria, called "sarcosomes". Gregor Mendel's revolution was the discovery of the principles of heredity in 1865. Anton Schneider described the chromosomes for the first time as "nuclear filaments" in 1873. Eduard Strasburger explained the mitosis in plant cells and introduced *"Zytoplasma*" (cytoplasm) and "*Nukleoplasma*" (nucleoplasm) (Fig. 2 A) and in the same year, Edouard van Beneden observed the centriole. Walther Flemming introduced the term "*Chromatin*" and described the mitosis in animal cells in 1879 (Fig. 2 B). Further investigations of Theodor Boveri lead to the structure of centrosomes in greater detail in 1888 (Fig. 2 C). At the end of the 19th century Otto Hertwig published a monograph "*Die Zelle und das Gewebe*", a general consideration of structure and function of cells (Hertwig, 1898). He created cytology as an important branch of

biology. The development of histology and cytology continued constantly within the 20th century. Although significant breakthroughs were given by the invention of phase contrast by Frits Zernike in 1932, the limitation of light microscopy defined by Abbe in 1876 made clear, that a real revolution was necessary:

„… *Nur glaube ich, daß diejenigen Werkzeuge, welche dereinst vielleicht unsere Sinne in der Erforschung der letzten Elemente der Körperwelt wirksamer als die heutige Mikroskopie unterstützen, mit diesem kaum etwas anderes als den Namen gemeinsam haben werden*." (Abbe, 1904)

History of Electron Microscopy

The evolution of LM from simple lenses to modern natural science, which lasted about 300 years, was repeated in three decades to establish electron microscopy (Fig. 3). The revolution came in the 1930s with the invention of the transmission electron microscope by Max Knoll and Ernst Ruska. And within two to three decades, all the obstacles during the development of light microscopy had to be mastered again with electron microscopy. Hans Walter Hugo Busch (1884-1973) gave the basis for electron optics by suggesting, that magnetic fields could be used to direct beams of electrons analogous to the way light is refracted by optical lenses, which was verified by E. Ruska in 1929 in his diploma thesis in the laboratory of M. Knoll with the title: "*Über eine elektrische Linse für Elektronenstrahlen* ". In 1931, M. Knoll and E. Ruska built the first transmission electron microscope with a rather poor magnification of 17:1 (Fig. 3 A). The basic innovation of magnetic lenses was the invention of the "*Polschuh*" (pole piece) by Ernst Ruska and Bodo von Borries in 1933, allowing a magnification of 12000:1, surpassing by far the magical border of light microscopy (Ruska, 1934). The achieved resolution was already 50 nm! With delay, the pioneer work of Louis de Broglie was recognized as being fundamental for electron microscopy: In his PhD thesis (1924) he postulated the wave nature of electrons and suggested that all matter has wave properties (Broglie, 1925). Like Abbe, the possibilities and limitations of electron microscopy could now be expressed as a physical equation.

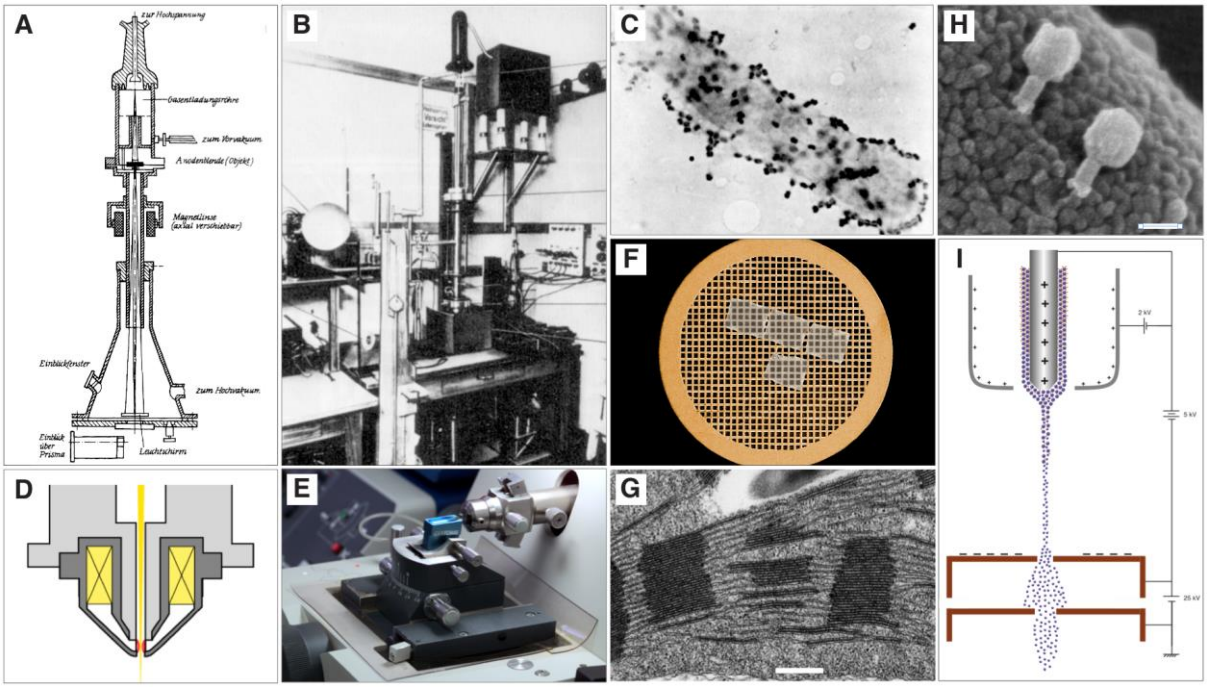

Fig. 3 Illustrated foray through the history of electron microscopy. *Ernst Ruska's design drawing for the first transmission electron microscope in 1929 (**A**). Manfred von Ardenne constructed the first functional SEM in 1937 (**B**). Helmut Ruska, the brother of Ernst Ruska, made the first TEM micrographs of phages on* E. coli *cells (**C**). Sophisticated improvement of the pole piece (objective lens) allowed high-resolutions for TEM and SEM (**D**). With modern ultramicrotomes and diamond knifes (**E**) ultrathin sections are cut and collected on copper grids (**F**), poststained with uranyl acetate and lead citrate resulting in very good contrast of cellular membranes e.g. thylakoid membranes of a tomato chloroplast (**G**; bar: 500 nm). Modern SEM reach 1 nm resolution at 1 kV, allowing imaging of T4 phages on* E. coli *(**H**; bar: 50 nm). Ion beam emitters are the centerpiece of FIB/SEM for milling of any material (**I;** © M. Luckner & G. Wanner).*

Fixation of tissues had to be improved, still used are classical receipts of Ferdinand Blum using formaldehyde (Blum, 1893), Keith Porter and F. Kallman using osmium tetroxide as tissue fixative in 1953 (Porter and Kallman, 1953) and David Sabatini introduced glutaraldehyde in 1963 as primary fixing agents (Sabatini et al., 1963). The combination of glutaraldehyde as pre-fixation step, followed by osmium fixation was a great methodological advance, as it preserves cytoplasmic structures (Ledbetter and Porter, 1963), a standard procedure till now. Hardening of tissues was replaced by embedding of fixed specimens into acrylic resin, introduced in 1949. The microtome had to be replaced by an ultramicrotome (Fig. 3 E). The metal knives used in microtomes were too dull to create slices thin enough. In 1950, Harrison Latta and J. Francis Hartmann discovered, that the edge of broken glass could be used to cut thin sections of specimens (Latta and Hartmann, 1950) and in 1954, Humberto Fernández-Morán Villalobos (1924-1999) invented a knife made of diamond for ultra-microtomy (Fernandez-Moran, 1954).

As electron microscopic images are monochrome, specimens are no longer *stained* but *contrasted*, which was and is a challenge since decades. Many protocols are listed in a gallery (honored today by a fulminant renaissance), starting from potassium-permanganate (Luft, 1956), followed by glutaraldehyde-osmiumtetroxide (Ledbetter and Porter, 1963), glutaraldehyde + osmiumtetroxide-potassium ferricyanide (Hepler, 1981), glutaraldehyde + osmium-thiocarbohydrazide-osmium impregnation (Friedman and Ellisman, 1981), or reduced osmium-ferrocyanide-thiocarbohydrazide (Willingham and Rutherford, 1984). The introduction of potassium permanganate, as a fixing agent by J. H. Luft (1956) and epoxy resins, as embedding material by Glauert et al., (1956) led to the visualization of the cell membrane, and finally, with improved fixation (glutaraldehyde/osmiumtetroxide) to a triple-layered structure, 7.5 nm thick consisting of two dense strata, each about 2.5 nm thick, bordering a light zone of about equal thickness (Stillwell, 2016). This triple-layered pattern was observed in all cells investigated. As soon as the unit membrane was discovered in the 1950s, a rapid development in cytology took place. As potassium permanganate oxidizes proteins, the ribosomes were not preserved. They were detected by G.E. Palade after fixation of tissues with Veronal-acetate buffered OsO_4 solutions as routine fixative in electron microscopy (Palade, 1952). Within the next two decades, a fascinating atlas of electron microscopy was available presenting any ultrastructural detail with stunning quality, even measured with today standard. The 70s were characterized by a rapid evolution of physiological techniques (sucrose gradients, cell fractioning, enzyme characterization) in rivalry to the rather slow proceeding electron microscopy pointed in “grind and find” countered by “seeing is believing”. To overcome the artifacts of chemical fixation, cryo-fixations were developed, leading to high-pressure freezing (HPF), already invented in 1961 by Hans Moor, but established as practical method in 1987 (Moor, 1987). Freeze substitution (FS) is required before embedding, which is still alchemistic, although frequently successful.

Stagnation

Despite constant evolution of EM techniques (e.g. histochemical reactions, immuno-labeling of proteins on ultrathin section), the great discrepancy between LM and EM could not be bridged during 1970 to 1980. The fascination of biology, visualized by true color, life-imaging LM in real time, slow motion of fast motion was confronted with static black and white micrographs, representing a snap-shot of a selected small area of a specimen fixed in a way, that artifacts had to be considered for any interpretation. Both methods could not provide 3D impressions of cells and tissues. Serial sectioning with ultrathin sections was restricted to very small volumes given by a few hundred sections with 70 nm thickness (Fig. 3 F) followed by time consuming 3D-reconstruction (copying TEM data to wallboard, followed by jigsawing and gluing) (Schötz et al., 1972). Summarizing, dynamic changes, visible in LM could not be easily correlated to EM data least of all in a 3D context.

Drifting Apart and Reunion in Steps

The revolution started in the 1980s with the introduction of confocal scanning light microscopy (CLSM) – an epochal sensation. However, CLSM could not show the structural origin of the

signals. The review of Giepmans about bridging fluorescence microscopy and electron microscopy brings it to the point:

"*Exaggeratedly stated, with fluorescence microscopy, you almost see nothing, i.e., only your fluorescent signal(s); with EM, you see everything, i.e., organelles, macromolecules and membranes. Bridging dynamic imaging in living cells and ultrastructural examination of proteins of interest opens a wide variety of possibilities to study protein localization, dynamics, activity and function at high spatiotemporal resolution inside cells*" (Giepmans, 2008).

Correlative light and electron microscopy (CLEM), as we understand it today, did not exist the first 50 years of electron microscopy (Boyde, 1991; Hayat, 1987). An excellent overview is presented by Schwarz and Humbel (2007). CLEM was proposed with the beginning of the EM era and was for the next two decades a sophisticated, often acrobatic, field of research limited to specialists. Enormous efforts were undertaken to enable or at least to facilitate a correlation. One of the main problems persisted: a large, hydrated, living tissue with 3D color information is processed to a small sample, embedded in resin, with imprecise orientation, which has to be trimmed to appropriate size. Still, these essential preparation steps impede a correlation between light and electron microscopy.

6.2 Volume Electron Microscopy

Five techniques are established for volume electron microscopy:

- TEM serial sectioning (Fig. 1A)
- (Cryo)-TEM tomography (Fig. 1 B)
- Array tomography (ATUMtome) (Fig. 4 C)
- Serial block-face sectioning (3View®) (Fig. 4 D)
- Focused ion beam scanning electron microscopy (FIB/SEM) (Fig. 4 E)

Confusion with "tomography"
Typically, in TEM/STEM/EFTEM the sample is tilted, projection images are acquired and then used to reconstruct a tomogram, using some mathematical method. This is referred to tomography, technically as c-tomography (c-computed as in CT scan). For SB/FIB/SEM the sample is being cut, in a sense, it is true tomography, but it is not used conventionally, since it creates confusion with EM tomography, mechanical cutting is not the principle of data acquisition. The FIB/SEM data set is not mathematically reconstructed, as it is a direct product of the milling process. Since, the term FIB-SEM tomography has already been used (as well as array-tomography) in numerous publications, even in the title, it seems to be accepted (e.g. (Beckwith et al., 2015; Cretoiu et al., 2015; Diblíková et al., 2018; Lütz-Meindl et al., 2015; Villinger et al., 2012; Wanner et al., 2013). The manufacturer of the Auriga Cross Beam Workstation (ZEISS) also uses the expression "FIB-SEM tomography" in their commercial

announcements. Therefore, it seems to be justified, that this term is used throughout the manuscript.

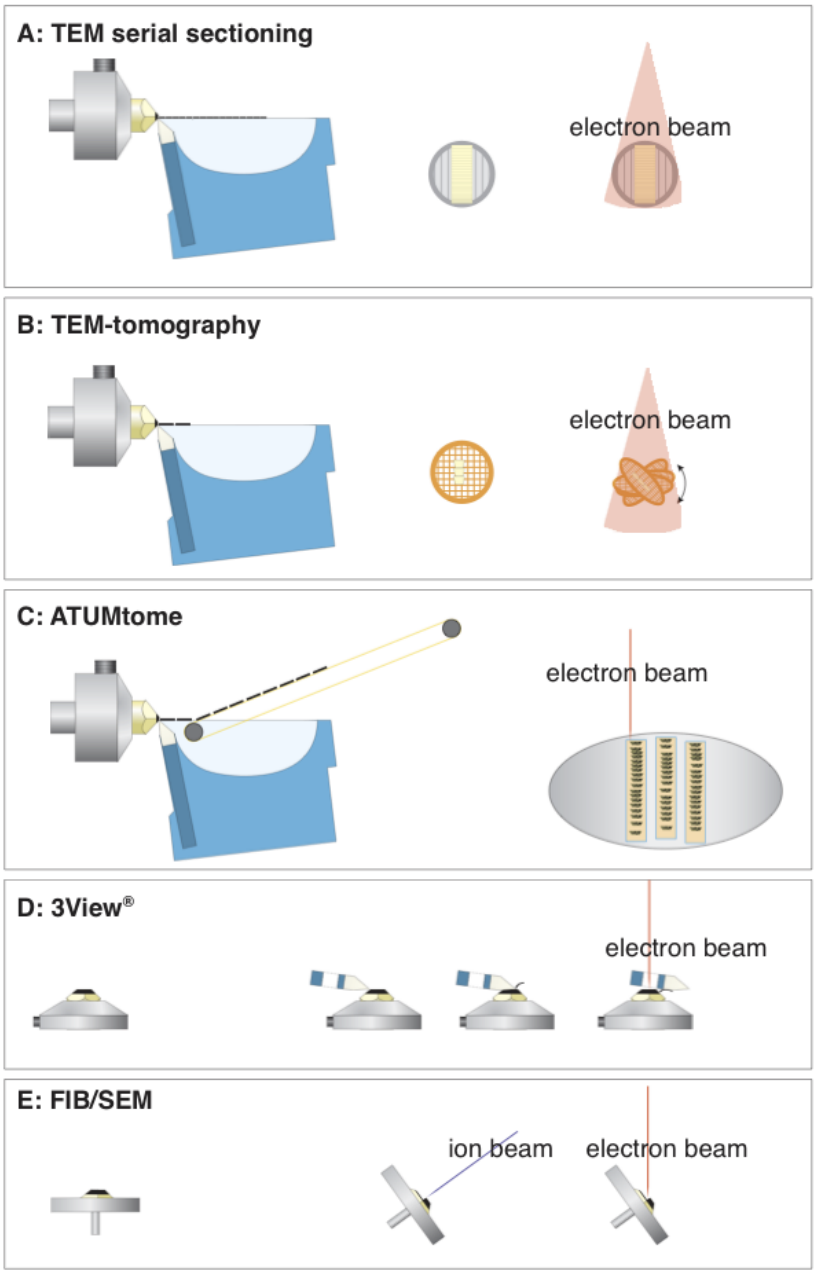

***Fig. 4 Comparison of volume EM techniques**.*
***A** For TEM serial sectioning, consecutive ultrathin sections are collected on grids and imaged separately with TEM.*
***B** For TEM-tomography, thin sections (0.3-1 µm) are cut with a diamond knife, collected onto a grid, which is tilted in TEM ± 70°. After registration and back-projection a tomogram is generated.*
***C** Serial sections are cut with a diamond knife, collected with an automated conveyor belt onto an adhesive tape (ATUMtome), mounted onto glass slides or silicon wafer and investigated with a SEM.*
***D** 3View®, the commercial version of the invention of W. Denk, manufactured by Gatan with a built-in ultramicrotome within the SEM. Serial sections are cut with a moving diamond knife and the block-face is imaged after every section.*
***E** FIB/SEM serial block-face milling is achieved by tilting a specimen in a SEM to 54°. An ion gun is placed in the SEM at the same angle, that sections can be milled orthogonal to the specimen surface. Block-face images are taken at an angle of 36° with a SEM, either backscattered electrons (BSE) or secondary electrons (SE) are detected. (© M. Luckner & G. Wanner).*

Cryo-TEM-tomography is the state of the art technique for structural preservation and resolution of sub-cellular structures, however, with severe limitations for investigations of larger volumes and the low signal-to-noise ratio of cryo-embedded specimens (Irobalieva et al.,

2016). At present, section thickness is limited to ~500 nm, with a macromolecular resolution of about 2 nm. The field of view is very small, in the range of 1-2 µm^2, due to the high magnification necessary for high-resolution tomograms and restricted depth of focus by tilting (Dubrovsky et al., 2015; Irobalieva et al., 2016). Array tomography is the state of the art version of the classical serial ultrathin sectioning for TEM, now adopted to SEM (Peddie and Collinson, 2014; Wacker et al., 2016; Wacker and Schroeder, 2013). Serial sections are cut with a diamond knife, collected with an automated conveyor belt onto an adhesive tape (ATUMtome), mounted onto glass slides or silicon wafer and investigated in a SEM using the BSE detector (Schalek et al., 2011) (Fig. 4 A). Combining array tomography with a multi-beam SEM technique (Zeiss; MultiSEM), gigantic image stacks in the range of hundreds of TB can be obtained within a rather short time with high-resolution (Eberle et al., 2015; Kemen et al., 2015). The disadvantages of ultrathin sectioning (fragmented ribbons, changing section thickness, precipitates, knife marks, section folds) persist and are even more critical, as e.g. compressions cannot be compensated by stretching. However, the sections can be re-investigated, and ROIs can be analyzed again or using other signals (e.g. EDX). The main advantage is that sections can be re-hydrated and fluorescent signals can be detected in the hydrated stage and the same antigenic epitope can be immuno-labeled with gold-labeled antibodies for visualization in SEM. An excellent overview is given by Heinz Schwarz a pioneer of CLEM (Schwarz and Humbel, 2007).

3View®, the commercial version of the invention of W. Denk (Denk and Horstmann, 2004a) manufactured by Gatan is a small ultramicrotome built into a SEM (Fig. 4 B). Serial sections are cut with a moving diamond knife and the block-face is imaged after every section. The advantage of 3View® is, that even from largest volumes (several mm^3) image stacks can be obtained (Denk and Horstmann, 2004a; Dohnalkova et al., 2010). 3View® investigations are limited by following facts: the section thickness of minimal 20 nm limits the resolution of the image-stack in z. In routine, section thicknesses of 30-60 nm are generally applicable for stable series. As the block-face is non-conductive, charging problems may be severe. An enhanced heavy metal impregnation by OTO or rOTO (Tapia et al., 2012; Deerinck et al., 2010; Hall et al., 2012; Mikula et al., 2012; Starborg et al., 2013) is therefore essential although not necessarily desired. The relatively high accelerating voltage of approx. 3 kV, which increases charging, cannot be reduced significantly because of the large working distance, necessary due to the built-in microtome.

FIB/SEM serial block-face milling is achieved by tilting a specimen in a SEM to approx. 54° (Fig. 4 C). A gallium ion gun is placed in the SEM at the same angle, that sections can be milled orthogonal to the specimen surface (Fig. 5). Block-face images are taken at an angle of 36° with SEM, either backscattered electrons (BSE) or secondary electrons (SE) are detected (Narayan and Subramaniam, 2015; Villinger et al., 2012). Two modes of image acquisition are possible: a section is ablated; the ion beam is blanked, and a block-face image is acquired. The advantage is, that correction of focus and astigmatism can be adjusted without interfering with the ion beam. If the image is acquired during the milling process, which is economic, if

long milling times are given (large areas and/or hard material), the ion beam influences the electron beam, which can be severe at higher ion currents (>1 nA). Therefore, low currents in the range of 100-500 pA have to be used. FIB/SEM is restricted in its block-face to approx. 200 µm in x and to a maximum of 100 µm in y (in practice to 50-70 µm due to curtaining effects in larger depths) (Karreman et al., 2016; Caroline Kizilyaprak et al., 2014; C. Kizilyaprak et al., 2014; Narayan and Subramaniam, 2015). Charging effects, limiting 3View®, can be neglected, if the entire specimen is carbon coated for conductivity. Charging by electron interaction is restricted to the milled area, which discharges to the conductive surface or bordering areas. Typically for array-tomography and 3View® the detection of the BSE signal is obtained with a chamber BSE detector.

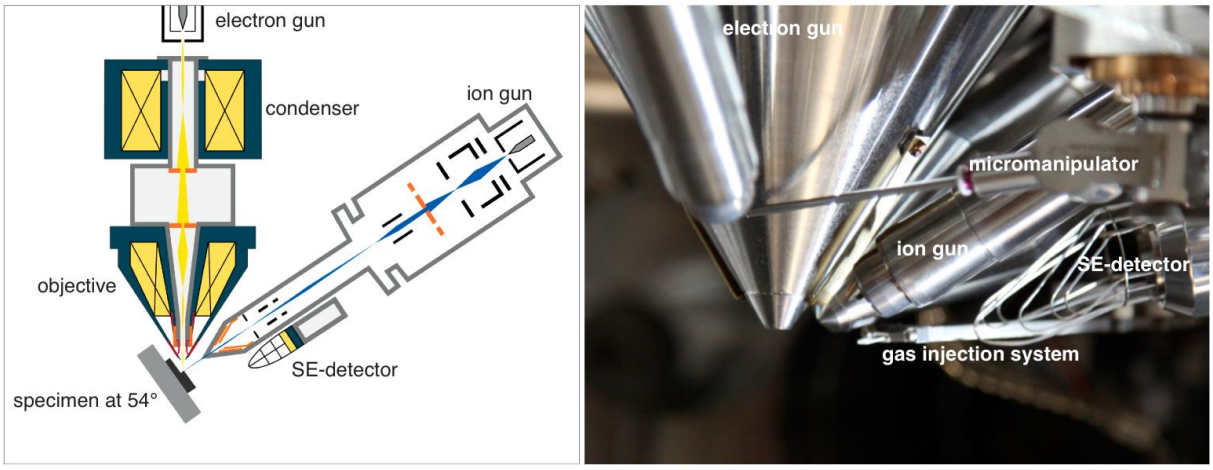

***Fig.5 Schematic drawing and insight of the Auriga FIB/SEM (Zeiss)**. An electron beam, emitted by the electron gun (= cathode), is focused both, by the condenser and the objective lens and scanned over the specimen surface (tilted to 54°). The ion gun produces a gallium ion beam, which is focused by electrostatic lenses and scans over the specimen surface at an angle of 90°. Both beams meet in the coincidence point. The ion beam mills layer by layer and the block-face is imaged either with the SE signal (collected by the chamber SE detector or the in-lens SE detector) or with the BSE signal (collected with the in-lens EsB detector). © M. Luckner & G. Wanner*

For FIB/SEM three different signals can be monitored: the SE-I with the in-lens SE detector (highest resolution, but highest sensitivity to potential contrast), the SE-II with the chamber SE detector and the BSE with either the chamber BSE detector (good resolution and good contrast) or the energy selective in-lens EsB detector (Zeiss patent) with a better resolution and the possibility of selecting back scattered electrons according to their energy, which dependents on their emerges depth (Fig. 6). Comparing the resolution of 3View®, array tomography and FIB/SEM-tomography, no significant differences in xy resolution (approx. 5 nm) are obvious. The differences in z-resolution are however striking: 3View® and array-tomography with 20 nm section thickness under best conditions, is surpassed by FIB/SEM-tomography by a factor of 10 (Boer et al., 2015; Karreman et al., 2016). As iso-voxel are

necessary for adequate high-resolution 3D representation in all spatial directions, FIB/SEM is the only technique allowing iso-voxels below 20 nm for large volumes.

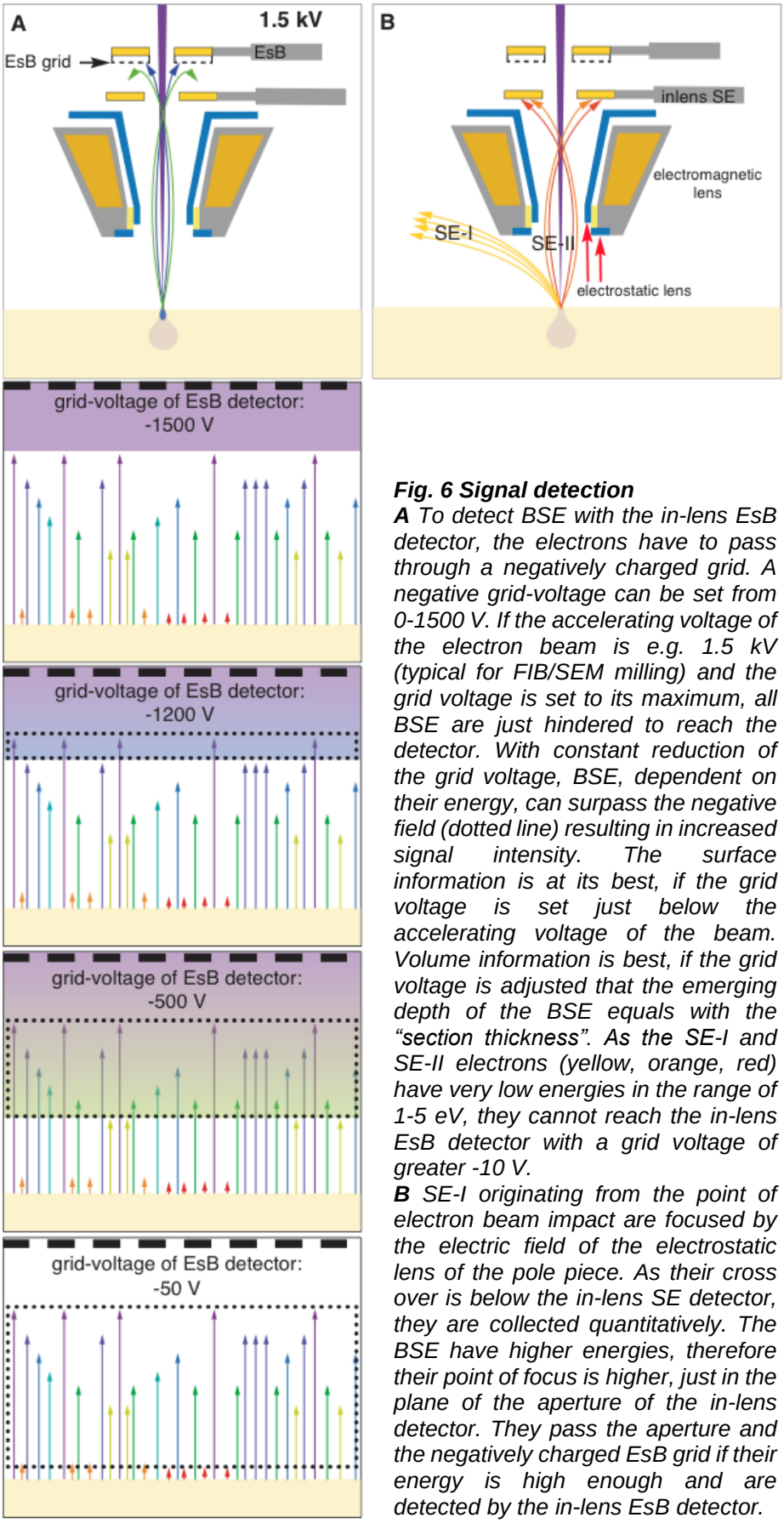

Fig. 6 Signal detection
A *To detect BSE with the in-lens EsB detector, the electrons have to pass through a negatively charged grid. A negative grid-voltage can be set from 0-1500 V. If the accelerating voltage of the electron beam is e.g. 1.5 kV (typical for FIB/SEM milling) and the grid voltage is set to its maximum, all BSE are just hindered to reach the detector. With constant reduction of the grid voltage, BSE, dependent on their energy, can surpass the negative field (dotted line) resulting in increased signal intensity. The surface information is at its best, if the grid voltage is set just below the accelerating voltage of the beam. Volume information is best, if the grid voltage is adjusted that the emerging depth of the BSE equals with the "section thickness". As the SE-I and SE-II electrons (yellow, orange, red) have very low energies in the range of 1-5 eV, they cannot reach the in-lens EsB detector with a grid voltage of greater -10 V.*
B *SE-I originating from the point of electron beam impact are focused by the electric field of the electrostatic lens of the pole piece. As their cross over is below the in-lens SE detector, they are collected quantitatively. The BSE have higher energies, therefore their point of focus is higher, just in the plane of the aperture of the in-lens detector. They pass the aperture and the negatively charged EsB grid if their energy is high enough and are detected by the in-lens EsB detector.*

6.3 CLEM with FIB/SEM at present

Ten years after FIB-SEM was recognized as a magic tool for 3D-EM in biology, these instruments are now accepted as very expensive, but highly complementary, necessary and efficient tool for CLEM (Beckwith et al., 2015; Karreman et al., 2016; Loussert Fonta and Humbel, 2015; Nixon et al., n.d.; Villinger et al., 2012; Xu et al., 2017) (Fig. 7). In daily routine, LSM data sets of entire cells can be recorded within few minutes, providing sufficient data for profound statistics, if desired. Corresponding ultrastructural information is not possible with TEM tomography at all, due to volume restrictions. 3View® and FIB/SEM would offer both, quantitative and high-resolution data sets of entire cells, which can be correlated to LM data but is still impeded by embedding cells/tissues in resin blocks and due to complicated and time-consuming re-location of target cells, insufficient for statistical investigation.

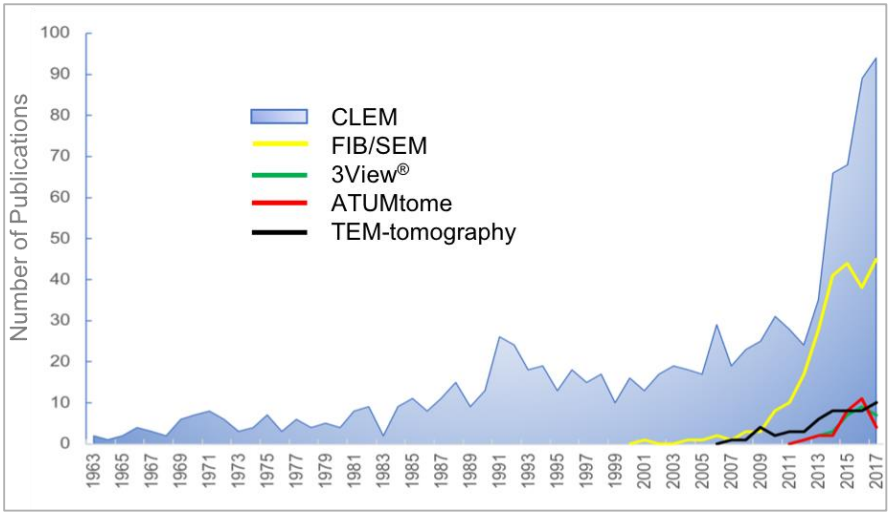

Fig.7 Number of publications/year related to CLEM. *Publications comprising CLEM according to different volume EM techniques. The statistic is based on buzzword-hits used in scientific search engines "PubMed" and "Google scholar".*

The standard procedure for FIB/SEM is a fixation of biological samples in fixative buffer, cutting small cubes with 1 mm edge length, post-fixation with osmium-tetroxide and embedding in epoxy resin. The embedding step severely hampers the CLEM workflow. The sample has to be trimmed with following demand: i) the orientation of the target region has to be parallel to the block-face and ii) the ROI must be as close as possible to the block-face. Approaching the target region in depth with an accuracy of few micrometer is complicated and risky, as an accidentally removal of the target happens quickly. The preparation becomes acrobatic and stressful if the sample is unique (transgenic mice monitored over month). Although landmarks facilitate re-localization, the different appearance of the sample before fixation (transparent) and e.g. after rOTO fixation (black cube) is an additional obstacle (Tapia et al., 2012; Deerinck et al., 2010; Hall et al., 2012; Mikula et al., 2012; Starborg et al., 2013).

CLEM could be more efficient by preparing biological samples appropriate for FIB/SEM right from the beginning. As it is crucial to define the coordinates of a target area for re-localization in SEM, a variety of slides with coordinates was developed and successively improved for different demands (Schroeder-Reiter et al., 2012). The aim was to embed cells on slides or cover slips within an ultra-thin resin layers i) for rapid and precise correlation to LM micrographs and ii) to allow FIB milling in any desired direction. Several modified protocols are available using thin embedding, but lack correlation to LM (Belu et al., 2016; Schieber et al., 2017) or involve delicate and critical preparation steps for CLEM (Booth et al., 2016; Lees et al., 2017; Murphy et al., 2011; Rennie et al., 2014; Santoro et al., 2017; Verkade, 2008). In a recent book chapter the technical possibilities for various embedding protocols (classical *en-bloc* embedding and thin-layer plastification) are presented for live cell imaging with volume scanning electron microscopy (Lucas et al., 2017). Ultra-thin embedding was adapted in our lab to a wide spectrum of biological specimens (from prokaryotes to tissues) and various fixation techniques. The thesis focused on technical improvements for CLEM with FIB/SEM and their application for cytological questions.

6.4 Biological Model Organisms for CLEM Application

Micrasterias denticulata

The unicellular freshwater alga *Micrasterias denticulata* is a cell biological plant model organism, which is genetically closely related to higher developed plants and shares common characteristics in many physiological and cell biological aspects. Not only their size of 200 µm, the bilateral symmetry of two semi-cells joined by an isthmus, where the nucleus is located, but also their highly conserved dictyosomes, which consist of 11 cisternae, are ideal features for light and electron microscopic observations. In the past, TEM and Immuno-TEM was used to study dictyosomal structure and function, cell wall formation and composition, cytoskeleton control of growth and morphogenesis as well as on ionic regulation and signal transduction (Lütz-Meindl, 2016). These investigations require life cell imaging, photosynthesis and respiration activities and TEM analysis to study the influence of metals like chromium, zinc, copper or cadmium, which have inhibiting effects in *Micrasterias* cell development and causes ultrastructural changes like involute dictyosomes (Volland et al., 2012). Environmental stress like heavy metal, high salinity or oxidative stress are questions related to environmental pollution and adaption, which can be answered only in a 3D context of complex organelle arrangements as ER/dictyosomes/vesicles. FIB/SEM showed that the dictyosomes are covered at both sides (cis and trans) by ER sheets, which almost encapsulate the dictyosomes (Wanner et al., 2013) forming an structural entity together with the vesicles formed from the cisternae and their derivatives. FIB/SEM should provide the 3D information for the complexity of both, general changes in morphology of ER and dictyosomes, organelle degradation and autophagy.

Human Platelets

Blood platelets are critical for hemostasis, thrombosis, and diverse roles during immune responses. Despite these versatile tasks in mammalian biology, their skills on a cellular level are deemed limited, mainly consisting in rolling, adhesion, and aggregate formation (Brass et al., 2005; Jackson, 2011). Adherent platelets use adhesion receptors to mechanically probe the adhesive substrate in their local microenvironment. When actomyosin-dependent traction forces overcome substrate resistance, platelets migrate and pile up the adhesive substrate together with any bound particulate material. They use this ability to act as cellular scavengers, scanning the vascular surface for potential invaders and collecting deposited bacteria (Gaertner et al., 2017). Microbe collection by migrating platelets boosts the activity of professional phagocytes, exacerbating inflammatory tissue injury in sepsis. This assigns platelets a central role in innate immune responses and identifies them as potential targets to dampen inflammatory tissue damage in clinical scenarios of severe systemic infection (Gaertner et al., 2017). Analysis of migrating platelets is an electron microscopic challenge. High resolution SEM at low kV is required to visualize the fibrin(ogen) coating of slides, allowing platelets to migrate. Immuno-gold labels can be correlated to fluorescence signals from fibrin(ogen) either by topographic and/or material contrast of high resolution SEM of critical point dried specimens or after ultra-thin embedding and FIB/SEM tomography. From 3D reconstructions based on FIB/SEM data sets it is expected to gain information whether and how fibrin(ogen) accumulates at the platelet surface and possibly within the open canalicular system (OCS) and if immuno-gold labels can be detected even within the cytoplasm (Gaertner et al., 2017).

HeLa cells

HeLa is the oldest and most common cell line used in scientific research in laboratories around the globe. Countless scientific fields like cancer research, infection studies, gene mapping, apoptosis and many more are addressed by their use. With the beginning of transmission electron microscopy HeLa cells were already in focus (Harford, 1957, 1956). Over more than 5 decades TEM investigations on HeLa covered almost any developmental topic. In the 1960s to 1970s outstanding micrographs document the quality of electron microscopy. Concerning mitosis, a bouquet of fascinating structural details presents a gigantic, but fragmentary mosaic. Almost any structural detail was presented in high quality, however due to the lack of 3D information, important structural changes during mitosis could not be adequately interpreted. With introduction of large volume EM techniques, the basis was given for investigation of whole HeLa cells (Murphy et al., 2011; Puhka et al., 2012; Booth et al., 2016; Nixon et al., 2017). Today, with high resolution LM, structural changes e.g. nuclear envelope breakdown and reconstitution can be visualized almost with ultrastructural quality (Lu et al., 2011). However, for Golgi disassembly and reconstitution, midzone formation, ER architecture, formation of endosomes/lipid bodies, especially if organelles are highly clustered, LM reaches its limitation due to the restricted resolution in z. HeLa is an ideal system to study the cell cycle with correlative LM and FIB/SEM and to verify the precision, efficacy and high-resolution obtained with flat embedded specimens. Staining of DNA allows the selection of target cells at any

mitotic stage, for addressing cytological questions still not answered in 3D. If FIB/SEM data acquisition is optimized, it is expected, that stacks with an iso-voxel size of 2 nm enable insight into HeLa cells at the resolution limit of FIB/SEM, unrivaled with any other large volume EM technique at present.

Dendritic spines of mouse brains

Mouse, as a model organism, is used to study human biology due to their genetical and physiological similarity. In neuroscience genetic manipulated mice models are used to explain neurodegenerative diseases. A mouse brain inherits more than 70 million neurons by an average mass of 0.4 g. Dendrites are branched extensions of neurons, which propagate electrochemical stimulations, *via* synapses, received from other neurons. Neurons have the ability to adjust their anatomy and function, termed plasticity. Synaptic plasticity is an important research fields in neurosciences, as such dynamics are linked to learn memory processes. Long-term *in vivo* 2-photon microscopy of dendrites and their spine plasticity offers fundamental information for Alzheimer's disease. Transgenic mice expressing green fluorescent protein (GFP-M line; (Feng et al., 2000), are an ideal tool for those investigations. This mouse line expresses a sparse GFP-labeling of single or few dendrites, which can be analyzed over month with 2-photon *in vivo* microscopy. For the investigation of dendrites and the plasticity of their spines in the clinical picture of Alzheimer's disease, cranial windows are implanted in one of the brain hemispheres in transgenic mice. This window provides direct optical access to the living mouse brain and allows the observation of labeled dendrites over several weeks using in vivo 2-photon microscopy. Dynamic processes - formation and elimination of dendritic spines - can be analyzed on the basis of the recorded 3D data sets. As with 2-photon microscopy exclusively fluorescence-labeled structures can be visualized, a correlation with high resolution EM data would help to understand spine dynamics in relation to associated structures on an ultrastructural level.

6.5 Aim of the Thesis

A. Technical aspects

- Development of slides and cover slips with a customized coordinate system.
- Immediate and precise correlation between LM and SEM.
- Immobilization of cells/tissues.
- Filter system for fixation and infiltration.
- Conservation of cell topography from LM to SEM by flat embedding.
- Adaption of the thickness of resin layers to any demand.
- Optimizing embedding in resins for better radiation stability (electron and ion-beam).
- Enabling direct access to the target cell (omitting a ramp).
- Reduction of the milling volume to its minimum, the cell volume.
- Optimizing contrast for faster acquisition of SEM-signals.

- Incorporating the slide as absolute reference for precise alignment of the FIB-stack.
- Implementing direct volume rendering for direct 3D visualization at high resolution.
- post-embedding coordinates by a stamp.

B. Cytological questions

- Change of dictyosomal and mitochondrial morphology in stress induced *Micrasterias.*
- Analysis of migrating human platelets on fibrin(ogen) coated slides, and their response to bacteria.
- Ultrastructural changes during mitosis in HeLa cells, including nuclear envelope bread down and reconstitution; Golgi disassembly and reconstitution, formation of spindle apparatus, central spindle, midzone and midbody.
- Spine dynamics of dendrites of mouse brain.

7 Discussion

7.1 Technical Improvements

7.1.1 Coordinate system as basis for CLEM

Correlative LM and FIB/SEM microscopy is often acrobatic and – compared to other techniques, very expensive from the electron microscopic part, which may be accepted, as a kind of pioneer spirit is still a motor, yet. But when statistical statements are requested, a state of the art technique has to become efficient and economical in daily routine. The correlation is challenging, as the coordinates of an oriented LM image stack have to be re-located within a volume of epoxy resin with a different orientation of the specimen. Fiducials, natural or artificial landmarks are necessary, which have to be correlated by fusion of two differently orientated spaces with different scaling and aberrations. Since few years, there is a strong attempt in creating digital coordinates to facilitate a correlation between light and electron microscopy, rather than having un-removable physical references. This approach is currently rising but often not applicable in daily routine. Typically, digital coordinates can be transferred from LM to SEM only if the manufacturer of both is the same, which is often not the case in interdisciplinary sciences. Simply correlating two planar micrographs, with a physical, well-defined coordinate system, which can be documented with high precision, independent of the physical signal production (light, electrons, X-rays), is the most efficient and safest way for correlative microcopy. The development of a variety of slides and coverslips labeled in different ways, to achieve suitable contrast in LM and SEM, customized to the actual scientific question was evaluated in the paper Luckner and Wanner (2018a).

The coverage of the labels can be varied widely according to the sizes and densities of sample investigated. For any purpose, there is a labeling allowing high resolution LM without any restrictions to optical requirements (bright field, phase contrast, DIC, epi-fluorescence) (Luckner and Wanner, 2018a). Once cells have been documented they can be controlled or tracked for e.g. structural changes during fixation, quality and uniformity of staining to optimizing further experiments (Luckner and Wanner, 2018a). Slides with coordinates are commercially available for correlative proposes. Ibidi GmbH offers a variety of gridded coverslips and bottom dishes as well as MatTek Corporation. Their products are expensive and only available in two different pattern densities. Kova International Inc. provides plastic gridded slides with a refractive index similar to glass, but nonresistant to acetone. Together with two companies, located in Bavaria, we developed customized slides and coverslips with fixed coordinates, available in any desired density and size (Luckner and Wanner, 2018a). The advantage of the labels is that they can be produced either engraved or elevated, which is important for thin-embedding procedures, where coordinates have to poke out of the resin layer. Further, the costs per labeled slide/coverslip are reduced by more than 50 % compared to commercial products.

7.1.2 Sample inherent reference points

Compared to single cells, which can be re-located easily, correlation of ROIs within a tissue is much more challenging. Coordinates of the supporting substrate can be hidden therefore internal/natural references are much more suitable. Natural landmarks compared to artificial fiducials omit the risk of losing references. However, they can only be used, if they unequivocally recognized in LM and SEM. For different tissues, reference points/landmarks can vary for plant or zoological material (Karreman et al., 2016). For plants, natural landmarks would be the calyptra and root hair for root tips, guard cells as rough references for leaves or crystals within the outer epidermal cell wall, detectable with light microscopes and at higher kV with the BSE-detector in SEM. Anatomical features as reference points of a zebra fish could be the yolk sac, notochord, melanocytes, muscles, endothelial cells, and blood vessels (Karreman et al., 2016). Another approach is the injection of fluorescent red blood cells to reveal vessel perfusion *in vivo*. This permits visualization of the living circulation and later identification of individual cells within semi-thin section of the embedded tissues, which were subsequently examined in the electron microscope (Beacham et al., 1976).

Natural landmarks are given for different organs like brain or liver sections. The references vary in number, density even in their presence at all (e.g. axons cannot serve as reference points in liver tissues). For every experiment the origin of the reference coordinates, either artificial implemented on the slide/coverslip or on a natural basis, has to be evaluated and adapted carefully for each scientific question. There will not be a ubiquitous labeling system, covering all scientific demands. However, a prerequisite that cells can be analyzed and selected with LM, and re-located in SEM, is a proper immobilization of the samples to a fixed coordinate system, visible in LM, SEM and FIB/SEM.

7.1.3 Immobilization of non-adherent cells

As from the broad spectrum of potential samples, adherent cells are only a minor sub-fraction; it was and is a challenge to immobilize biological objects permanently to slides/coverslips with fixed coordinates. Four different methods of immobilization of enzymes and cells are commonly used preferentially in biotechnology: i) adsorption; ii) encapsulation; iii) entrapment and iv) covalent bonding. As cells have to be immobilized as stable as possible, adsorption is not suitable as low energy bond as ionic interaction, hydrogen bond and van der Waal forces are involved. However, there are many protocols for cell adhesion for biomedical and biological applications with the aim of keeping their vitality (for review see: (Ahmad Khalili and Ahmad, 2015). Encapsulation and entrapment by hydrogels (for review see: (Jen et al., 1996), which can be used to study cell-cell interactions of 3D cell cultures in a native-like environment (Bodenberger et al., 2017) bares the risk of topographical changes (coating, masking) of the cells in SEM. The chemical mechanism for immobilization is preferentially a covalent bonding

between the cells and the support. As a poly-functional reagent, glutaraldehyde forms bindings between the glass and the amino groups of the cell surfaces, it is used for the drop cryo fixation, established in our lab e.g. for preparation of *Magnetobacterium bavaricum* (Jogler et al., 2011) and *Chlorochromatium aggregatum* (Wanner et al., 2008), which is very effective for small microorganism (0.5-3 µm), but loses stability if cells are too large and unfavorable in geometry with reduced contact area to the slide (e.g. spiral or spherical). Abundant chemical adhesives are described, each with different advantages and disadvantages. From a variety of adhesives investigated for immobilization, two of them peak out: Biobond with very good adhesive properties for prokaryotic and eukaryotic cells and cell aggregates (Luckner and Wanner, 2018a). As the adhesive is a coating in the nm range, the evenness of the slide is maintained, which is important for high resolution SEM e.g. of cells with flagella or filopodia. Cell-Tak™ is the strongest adhesive and therefore the first choice for large tissue sections (Luckner and Wanner, 2018a). As Cell-Tak™ is preferentially spread with a coverslip, the thickness cannot be controlled precisely, which limits its application in SEM for high-resolution topography of cell adherent structures. To reduce costs by application of the expensive Cell-Tak™ immobilization of hydrated soft-tissue, samples with transglutaminase, also known as “meat glue” for atomic force microscopy, is shown as simple and very cost-effective immobilization method (Sahai et al., 2016). As the specimens were used in hydrated state and the substrate was negatively charged polystyrene dish, it should be evaluated if transglutaminase is suitable for dehydration and infiltration of vibratome sections on glass slides as well. Although the chance for successful immobilization of any objects, estimated from our experiments, is only 50%, however, a flat embedding is still possible by alternative strategies. If live cell imaging can be relinquished or is not possible anyway (e.g. high-pressure freezing (HPF) of non-adherent cells), samples can be processed until infiltration with resin, spread onto slides with coordinates and embedded thin or ultra-thin. CLEM is still possible as surprisingly, even fluorescence, although much weaker, can still be detected for a variety of objects after HPF, FS and embedding, providing information e.g. for vitality (filamentous cyanobacteria) or stages of cell differentiation (heterocysts/vegetative cells) for a directed and economic milling. Recently a promising technique was presented utilizing surface-initiated photo-polymerization process; high-resolution pattering of mammalian cells has been achieved. A hydrogel glue with a thickness of nanometer are used to immobilize living cells on nano-electronic devices (Pandey et al., 2018).

7.1.4 Filter-system for conservative preparations

A successful immobilization of samples does not imply precise CLEM. Very large tissue sections may form folds during post-fixation and/or dehydration, which result in uneven thickness of the resin layer. In general, an uneven surface is not suitable for FIB-milling due to changes of focus plane of the ion beam, resulting in erratic milling properties. A filter system was developed to ensure flat tissue sections after dehydration and embedding (Luckner and

Wanner, 2018a). At first glance, CLEM seems to be excluded. However, tissue sections are either individual in size and shape or can be slightly trimmed for characteristic features, that the orientation is maintained. Light-microscopic investigations can be performed before using the filter system. If care is taken by placing the section after resin-infiltration top side up onto a slide or directly onto a SEM stub, a precise correlation is still given, as the topographic SEM image matches to the LM micrographs and a target region can be determined by triangulation of surface features/naturals landmarks, which are pertained after thin/ultra-thin embedding. Additionally, the filter-system is of great benefit if samples i) cannot be immobilized with any glue, ii) are available only in few individuals or iii) are fragile. Already in the 1970s, filter systems were used to process samples for scanning electron microcopy to prevent loss of cells and their aggregation by solvents (Kurtzman et al., 1974; Talens et al., 1973), which was demonstrated for yeasts, bacteria, actinomycetes and fragile vegetative spores of filamentous fungi and carried through all preparation steps including critical-point drying (Talens et al., 1973). These investigations only provided ultrastructural surface information of the samples. Recent studies published the potential of a membrane filter-system to concentrated rare samples like spermatozoa, pathogens or bacteria, as the fine structure of the membrane prevents damage and loss (Beniac et al., 2014; Golding et al., 2016; Nussdorfer et al., 2018). A disadvantage of their procedure is that various impurities, can cover the surface of the specimen, as they were just using one membrane instead of two, to cover the sample, compared to our procedure (Luckner and Wanner, 2018a). To date, no publications are available were membrane filter systems are used for CLEM, involving high-resolution LM and FIB/SEM. As its utility is proven for many demands, further improvements of the application are requested. It would be of great advantage if the filter would be transparent, solvent resistant and without auto fluorescent. Hence, samples could remain on the filter membrane during the whole CLEM procedure. Live cell imaging on filter membranes, with a subsequent preparation within a closed filter-system together with a thin-embedding (Luckner and Wanner, 2018a) would enable a convenient CLEM procedure of rare samples.

7.1.5 Flat embedding: efficient and economic FIB/SEM milling

The necessity and advantage of thin embedded samples became a topic within the last years, with the increasing demand of correlative LM with FIB/SEM in biosciences (Fig. 7). A few protocols are published for flat embedding in resins by draining, blotting, centrifugation with the primary aim to reduce the resin layer to its minimum (Caroline Kizilyaprak et al., 2014; Lucas et al., 2017; Schieber et al., 2017). It is a challenge to adjust the resin thickness for good milling properties and precise correlation. In a recent book chapter, the technical possibilities for various embedding protocols (classical *en bloc* embedding and thin-layer plastification) are comparatively presented for live cell imaging of adherent cells with volume scanning electron microscopy by using Ibidi µ-dish 500 or MatTek finder grid (Lucas et al., 2017). Minimal covering of the cells with resin was achieved by upright positioning of the cell substrate for

draining and polymerization starting at lower temperatures (Belu et al., 2016; Lucas et al., 2017). However, none of presented methods was suitable to really control the thickness to the scientific demands. For larger objects with sufficient height, flat embedding can be achieved successful, as variations in resin thickness do not severely impede FIB/SEM investigations. Adjustment of resin thickness becomes very critical if objects are rather small (microorganisms, platelets).

In practice, the aim is not the ultimate thin epoxy resin layer, rather to control its thickness, depending on the scientific question, type of sample, cell size and cell density. Thin embedding still shows the topography of the organisms, enabling localization of specific structures by their topography in SEM. This implicates that the target area gives sufficient topographic contrast to recognize previous selected areas. A main obstacle, that during spreading of thin resin layers, its viscosity rises significantly within seconds to few minutes, resulting in non-reproducible, local varying thicknesses. The removal of excessive resin by ethanol (Belu et al., 2016) is a good attempt, but bears the risk of uncontrolled reduction, which is critical, when prokaryotic cells should be embedded in a few µm thick resin layer. Keeping the slides in an acetone-saturated chamber, the fluidity of the resin is pertained, until an even spreading. By changing the parameters (surface properties of slides or coverslips, resin concentration, draining by gravity, centrifugation, exposure time) a suitable thickness of resin can be achieved for individual samples (Luckner and Wanner, 2018a). The quality of FIB/SEM milling does primarily depend on surface quality. If it is smooth, a block-face image of good quality can be achieved after adopting milling parameters properly. Rough surfaces, either by changing topography or material composition produce curtaining (Fig. 8).

Slightest curtaining is immediately recognized with in-lens SE-detector due to its extreme sensitivity to topographic changes (Xu et al., 2017). Using the BSE, curtaining may not be visible at the first glance, but if present, it artificially changes the contour of membranes (formation of step-like deviations), which severely influences resolution and the quality of volume rendering.

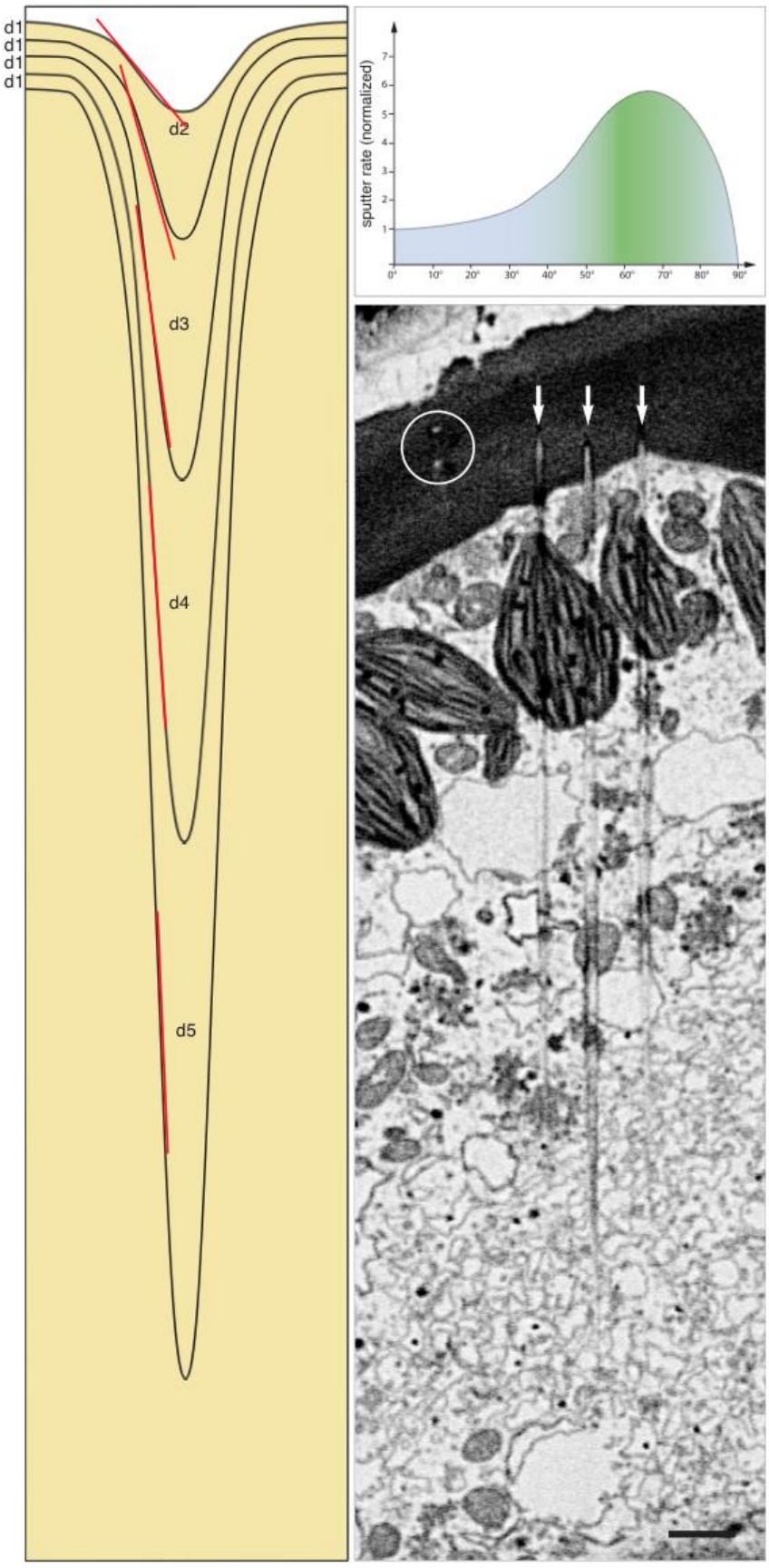

Fig. 8 Formation of curtaining at uneven surfaces.
A layer is ablated constantly, if the surface is completely smooth (d1) as milling conditions are the same at every point. At an indentation of the surface, the ion beam reaches the surface deeper and in a different angle. As the milling rate depends on the angle of the surface to the ion beam (curve), the ion beam mills faster within the indentation, as the wall shows higher inclination (red lines). With every milling step, the ablation is increased (d3-d5). Due to re-deposition effects, the indentation becomes narrower within the depth. As soon as the indentation is milled off, the striation disappears. The re-deposition fills part of the striation. Due to the high atomic number of gallium the striation appears bright in original or dark in inverted images. On a FIB/SEM micrograph of a cross section of Chara spec., striations (arrows) are visible over several slices, due to the uneven surface (little holes; circle). Scale bar: 1 µm. © M. Luckner & G. Wanner

The basic message is: the thicker the resin layer, the lesser the disturbance during milling. The thinner the resin layer, the more precise is the correlation to light microscopic images. In practice, the size of the cells restricts flat embedding: for small microorganism (diameter 500 nm), forming a monolayer, a resin layer of one micrometer may severely impede CLEM, as the cells are hidden within a continuous resin layer. For larger, single cells (diameter 20 µm), even few micrometer of epoxy layers may allow precise CLEM by freely defining the milling plane. If rather thick resin layers are necessary, elevated labels can be used for CLEM as they are still visible and re-localization is facilitated by triangulation.

Milling of flat embedded samples has enormous benefits compared to specimens embedded in a resin block. Milling cells within a resin block requires a ramp to get access to the target region. The size of the ramp depends on two parameters: i) the length, desired for a ROI in z and ii) the desired depth (in y), of the final block-face. For calculation of the minimal length to reach the desired depth, the depth is multiplied by 1.38 (tan 54°), implicating for a HeLa cell (diameter 20 µm in metaphase) a ramp of minimal 27.6 µm in z – which can be more than the length to be milled afterwards. Before milling, it is essential that, the width of the block-face is being calculated tolerant for compensation of re-deposition effects. Re-deposition occurs during milling of a block-face enclosed by the ramp. The gallium ions ablate layer by layer of the specimen in a sputter process. The gallium ions discharge to gallium and deposit with the epoxy debris near the block-face, which is typically at the bottom of the ramp and at both flanks (Fig. 9).

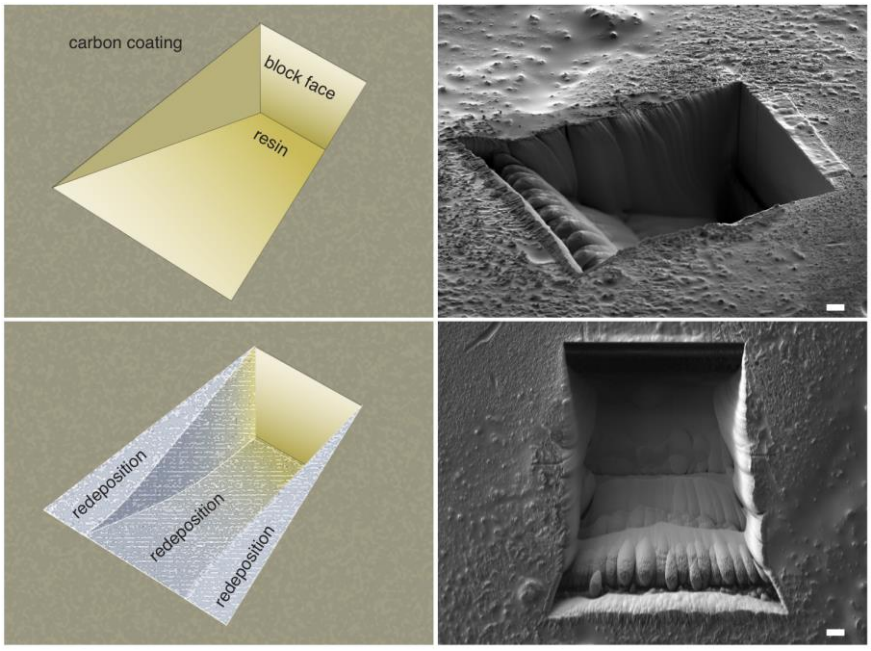

Fig. 9 Re-deposition. *For samples, embedded within a resin block, digging of a ramp is necessary to reach the block-face with the desired depth in y. During the milling process, gallium ions deposit as gallium atoms in a mixture with sputtered epoxy resin and sample components. The ramp is thereby narrowed from both sides and in depth (which makes a trapezoid design necessary). Scale bar: 10 µm (drawings: © M. Luckner & G. Wanner)*

The longer the target region in z, the broader the ramp has to be from the beginning. It has to be balanced between the desired length in z and an assessment factor. If it is too generous, it is wasting time and money, however, if it is calculated to tight, the broadness cannot be changed during the run, leading to severe lateral shadowing of the block-face images. As for flat embedded samples a ramp is needless, only the cell volume is milled without any re-deposition effects. Comparing the volumes, milled with FIB/SEM for conventional embedded HeLa cells with thin embedded cells, the volume is reduced by a factor of 10. As the target cell is constantly under visual control during milling, corrections, necessary by specimen drift, can be done on the fly. In addition, a FIB/SEM-run can be stopped, if heating of the gallium emitter is necessary, and continued without running the risk of narrowing the image field by re-deposition.

Summarizing the advantages of flat embedded samples: beside pecuniary aspects, important benefits are: i) saving time; ii) the possibility of setting the milling direction as precisely as desired for cross or longitudinal sectioning; iii) starting close to structural details documented before in LM, e.g. cellular inclusions, centrosomes or midbodies and iv) re-deposition does not occur for thin/ultra-thin embedding.

7.1.6 Post embedding labeling

Producing very thin resin layers is challenging. It occurs, that the manufactured coordinates are sometimes completely covered with resin, which impedes a re-localization within the SEM, of the ROIs previously monitored and selected by LM. A water-resistant stamp with customized coordinates can be printed on top of the polymerized sample. As a result of the thin embedding, light can still pass the sample, and both, the coordinates of the slide and the stamp, are visible in bright-flied. With that simple, but very powerful tool, a correlation between LM and SEM is guaranteed. Cell behaviors, like adhesion, migration, differentiation and proliferation can be affected by micro-environmental factors, as the topography of the substrate (Araujo et al., 2016; Baik et al., 2014; Kim et al., 2012; Recknor et al., 2004). Slides with coordinates, either engraved or elevated, can lead to undesired cellular behavior and bare the risk of falsifying or ruling out relevant results. The customized stamp (Luckner and Wanner, 2018a) is a suitable alternative, still enabling a correlation after thin embedding, as the stamp is visible in both, LM and SEM, due to the material contrast of the ink. Specific cells can be selected by their sizes, shapes, or contrast and immediately re-located in SEM to facilitate precise FIB/SEM milling, impossible with classical block embedding procedures. Recently, new protocols are available where the fluorescence signal is preserved after resin embedding (Bell et al., 2013; Peddie et al., 2014; Höhn et al., 2015). Combining these approaches with thin embedding including printed coordinates (stamp) (Luckner and Wanner, 2018a), would facilitate CLEM significantly. By omitting delicate preparation steps (removal of the substrate, sample trimming), correlative light and electron microscopic investigations become a method applicable in routine.

Additionally, the stamp can be used for statistical purposes. Simplified, it acts as a Thoma cell counting chamber to quantify ultrastructural details on nano-scale level.

7.1.7 Reaching the limits of FIB/SEM

Improvement of contrast

The classical staining of biological samples with osmiumtetroxide results in a fine contrast as osmium binds to the double bonds of fatty acids from the bio-membranes providing the images of a tripartite membrane, which is a dogma for EM but a point of discussion since the introduction of osmium as fixative and staining (Hayes et al., 1963). However, the contrast of bio-membranes of typical TEM micrographs is not a result of osmium alone but an enhancement of osmium contrast by post-staining with lead citrate (G. Wanner, personal communication). An *en bloc* staining of tissues is commonly used with uranyl acetate but not possible with lead citrate due to the formation of precipitates. A contrast enhancement is generally favored. TEM started within the 60s with permanganate fixation resulting in striking contrast of membranes seen as single black lines, without resolving their tripartite nature. With introduction of osmium-thiocarbohydrazide-osmium (OTO) described by (Seligman et al., 1966) and the ferrocyanide-reduced osmium method described by (Karnovsky, 1971) and (de Bruijn, 1973) the contrast of membranes was significantly improved with loss of resolution of the tripartite appearance. The methods were favored with morphometry coming up in the 70s for quantification of structural changes. With a digitizing tablet (wire technology, before computer area) micrographs had to be retraced with a stylus, and data (length, area, diameter, perimeter and form factor) were displayed on a calculator and documented by hand. The lack of resolution on the benefit of contrast was not a draw back for morphometry, however the images including the measurements could not be stored digitally. These extreme expensive early devices (15000 €) disappeared together with the application of OTO and rOTO for decades. With serial block-face imaging, there is a renaissance of these fixation/contrasting techniques. Although they are perfect for large volume investigations, the restriction becomes obvious when reaching resolution limits (pixel size below 5 nm). Due to the contrast enhancing effect, the discrimination between double membranes of mitochondria and plastids is still given but not the expected visualization of the tripartite bio-membrane (Fig. 10).

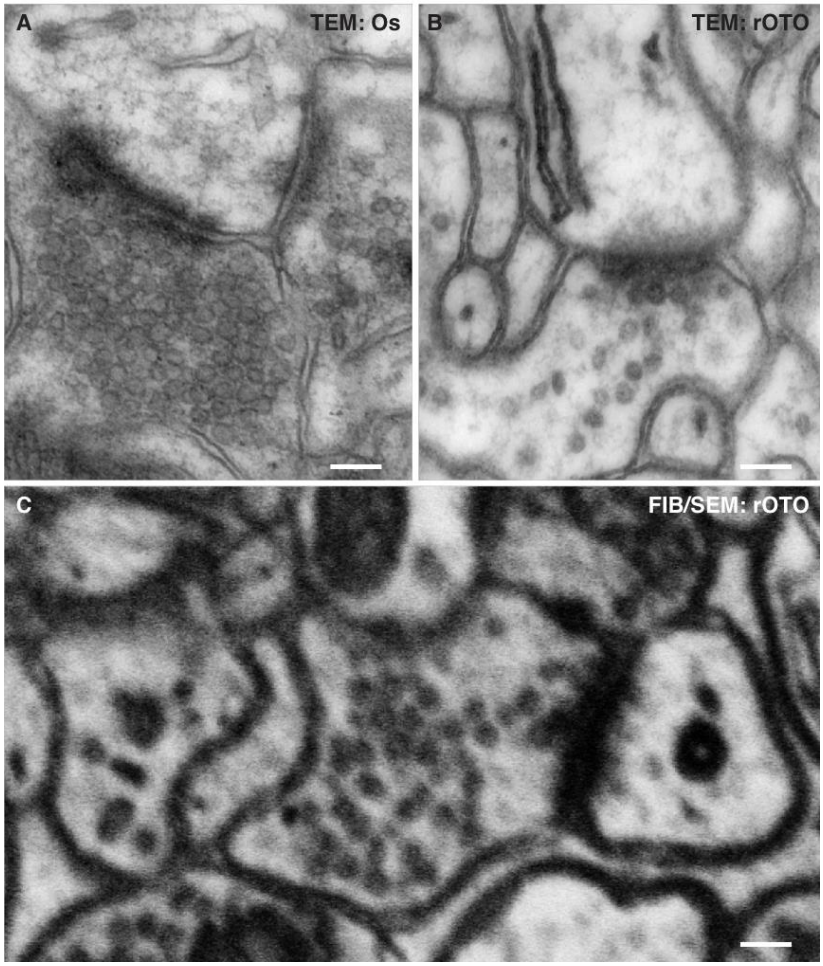

Fig. 10 Enhancement of contrast by rOTO. *TEM micrographs of ultra-thin sections of mouse brain, fixed either with glutaraldehyde and post-fixed with osmiumtetroxide (**A**) or with glutaraldehyde followed by rOTO (**B**). Due to the increased binding of osmium and some oxidation of cytoplasmic material, the contrast is much higher. FIB/SEM block-face image of mouse brain fixed with glutaraldehyde-rOTO (**C**). Although the resolution is lower compared to TEM, synaptic vesicles are clearly visible (EsB signal inverted). Scale bar: 100 nm*

One may argue that this is caused by the resolution limit of the SEM, but investigations of high-pressure frozen (HPF) and freeze substituted (FS) BON cells, could clearly resolve the unit membrane (Villinger et al., 2012). Two factors can explain the TEM like resolution: i) a more specific and thereby finer membrane contrast given by HPF/FS, compared to rOTO enhancement and ii) the use of the in-lens SE detector. The SE-I signal shows a much better signal to noise ratio compared to BSE and in addition a higher resolution as SE-I originate directly at the point of impact of the electron beam, whereas the BSE escape from the specimen, both from greater depth and larger radius around the spot, due to scattering effects (Fig. 11). As the SE-I have very low energy in the range of 1-3 eV (Reimer, 1998) compared to the BSE (approx. 0.5-1.5 keV), slightest charging disturbs image and curtaining is visible. There is still a discussion if HPF/FS after conventional pre-fixation or including glutaraldehyde in the freeze substitution cocktail gives much better results compared to conventional fixation alone (Meissner and Schwarz, 1990; Giddings, 2003; Bullen et al., 2014). It is known, that with cryo fixation, a view of tissue ultrastructure is closer to its natural state (Korogod et al., 2015), but at present, there are no studies published for CLEM with HPF fixed tissues, previously investigated with LM.

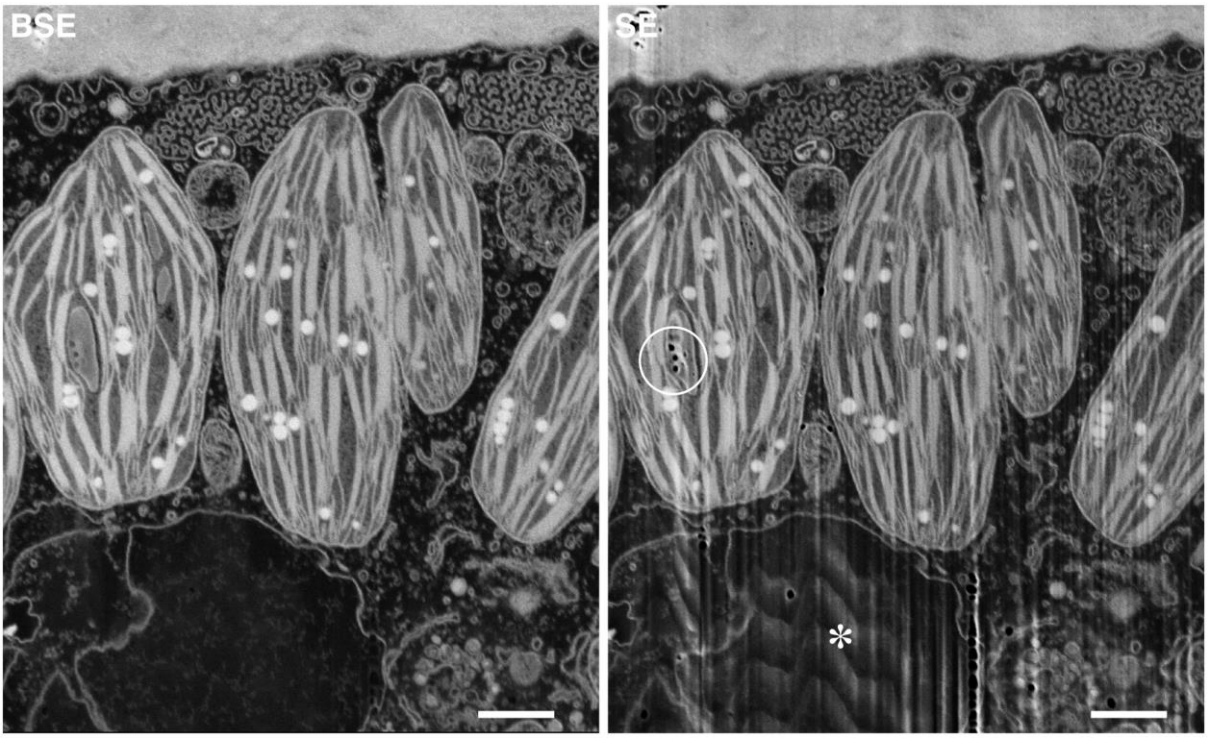

Fig. 11 Comparison of BSE and SE signal. *Block face image of* Chara spec*. at 1.5 kV (EsB grid voltage: -500 V) by simultaneous detection of the BSE (in-lens EsB detector) and SE (chamber SE detector). Due to a rather high milling current and a small milling depth, curtaining occurred. Although the EsB image (left) looks perfect, the in-lens SE image is dramatically disturbed by striations, little holes (circle) and in addition local charging (asterisk). Note: the charging effects influence only the in-lens SE-image. However, the striations are only visible in the in-lens SE-image, are artifacts and real, but not seen in the EsB-image.*

Importance of exposure time

The energy input of electrons during SEM was already described in detail from a physical point of view (Reimer, 1998). When applying physical formula to actual investigations, calculation can only be estimations, as important parameters of the specimen e.g. thermal conductivity of resin are not known and data from similar materials are used. Although the deviations will be minor, the heating of a resin by an electron beam (1.5 kV) at moderate magnifications should be neglected, as calculated in the range of only 0.5-1.5 °C (M. Wanner, personal communication). However, when pixel size reaches resolution limit, beam damage becomes obvious, which cannot be predicted by Reimer's formulas (Reimer, 1998). A resistive probe-based Scanning Thermal Microscope was implemented in an analysis chamber of a SEM. By means of this hybrid-system thermal device, specific characteristics are detectable. A measured temperature distribution on the sample surface, was shown to be in agreement with the calculated temperature distribution: temperature can be locally increased by up to 42 °C (Altes et al., 2002). Such an increase in temperature during FIB/SEM milling would heat the resin locally to almost 70 °C, a temperature where the resin becomes elastic. Although precise

measurements of temperature at the block-face and ROI are not possible at present, beam damage can reproducible be generated, when reducing the image frame either to a small size (5x5 µm) at constant dwell time for exposure or by increasing exposure time for a larger image frame (15x15 µm) (Luckner and Wanner; unpublished). A detailed investigation showed, that Hard Plus Resin-812 is more stable during exposition to ion beam (Kizilyaprak et al., 2015). After embedding specimens in Hard Plus Resin-812 instead of Epon-812 or Low Viscosity Spurr it became clear, that the stability of the resin is also increased for electron beam exposition. In practice, in our hands image pixel size of 2 nm iso-voxel can be achieved, where with Spurr only 4-5 nm iso-voxel could be reached for long series (unpublished data). An important aspect is not discussed in literature. Before beam damage becomes visible, a temperature below the melting point of a resin may be high enough to increase molecular vibration of the resin including the heavy metal clusters. If this would be true, a smearing of fine structural details can be expected, limiting resolution without visible beam damage. It might also help to reduce the sample temperature, which additionally affects the milling properties directly by changing the polymer stiffness, might substantially improve the resistance to radiation damage (Lamvik et al., 1991). The beam damage is discussed in detail for serial block-face sectioning by (Denk and Horstmann, 2004a). Compared with FIB/SEM the situation for 3View® concerning electron beam damage is much more unfavorable as the probe hits the block-face vertically. The energy is incorporated almost quantitatively into the resin. As the specimen in FIB/SEM is tilted to 54°, the electron beam angel strikes the block-face in an angle of 36°, which allows a better energy distribution (larger area). In addition, the kV applied for FIB/SEM is usually much lower (1.5 kV) compared to 3View® with 3 kV affecting a smaller volume due to the lower penetration depth of primary electrons (PE).

7.2 Cytological Investigations

7.2.1 Stress induced changes in morphology of dictyosomes and mitochondria in algae

Numerous investigations have focused on chloroplasts and mitochondria as main targets of different stressors in plant cells (Affenzeller et al., 2009a, 2009b, 2009b; Darehshouri and Lütz-Meindl, 2010; Demetriou et al., 2007; Lin et al., 2006; Logan, 2007; Reape and McCabe, 2008); there is a lack of information on the plant Golgi apparatus as stress sensor. TEM and Immuno-TEM was used to address the uptake and influence of chromium, which has inhibiting effects in *Micrasteria*s cell development and causes ultrastructural changes like involute dictyosomes (Volland et al., 2012). For a better understanding of ultrastructural changes (induction of autophagy) caused by the rapid production of reactive oxygen species (ROS), 3D information at an ultrastructural level is necessary. With the beginning of FIB/SEM investigations of interphase *Micrasterias* cells, new insights into the close spatial connection of the ER-Golgi machinery and the formation of multi-vesicular bodies were revealed (Wanner et al., 2013). ER strands, which are inconspicuous at single TEM micrographs, exhibit their dominant

structure by enwrapping dictyosomes and are even in contact with them, well known from mammalian cells, but not from higher plant cells (Lütz-Meindl, 2016; Mogelsvang et al., 2004). It became clear, that only FIB/SEM in combination with classical ultrathin sectioning and transmission electron microscopic analyses provide structural evidence for common stress responses of the large and highly stable dictyosomes in the algal model system *Micrasterias* (Lütz-Meindl et al., 2015). Metals such as manganese and lead induce stress, by starvation in 9 weeks of darkness or by inhibiting photosynthesis or glycolysis and by disturbing ionic homeostasis via KCl (Lütz-Meindl et al., 2015). A stress-induced degradation of dictyosomes was documented by disintegration of cisternae into single membrane balls, finally absorbed by the endoplasmic reticulum (Lütz-Meindl et al., 2015).

During reconstruction of large cellular volumes of *Micrasterias* it became obvious that the significant structural changes of the dictyosomes are accompanied by structural changes of mitochondria as well. Contrary to their illustration as ovoid structures since the first descriptions, based on TEM investigations, mitochondria are actually dynamic organelles that fuse and divide to form constantly changing tubular networks in most eukaryotic cells (Bereiter-Hahn and Vöth, 1994), first shown in plant cells based on the first 3D reconstruction of a single eukaryotic cell by (Schötz, 1972) and investigated during the vegetative life cycle by (Blank et al., 1980). They fuse to local mitochondrial networks in dependence on concentration and duration of exposure to ionic stress induced by addition of KCl, NaCl and $CoCl_2$. Fusion occurs either by formation of protuberances arising from the outer mitochondrial membrane, or by direct contact of the surface of elongated mitochondria. As mitochondria are autonomous organelles it is remarkable that obvious not the single mitochondrion is autonomous rather than the entire mitochondriome. The population is obviously stabilized under stress by forming larger entities (Steiner et al., 2018). As respiration is maintained during ionic stress and mitochondrial fusion, as well as formation of protuberances are reversible, it is interpreted that mitochondrial fusion is an ubiquitous process, helping the cells to cope with stress. This may occur by interconnecting the respiratory chains of the individual mitochondria and by enhancing the buffer capacity against stress induced ionic imbalance. As hypothesized, a branched mitochondrial network may allow ATP generation in oxygen-poor regions of a cell through electrical transmission of the mitochondrial membrane potential across the network (Skulachev, 2001). 3D reconstruction of large volumes of *Micrasterias* will offer structural information of mitochondrial fusion and a possible involvement of ER as tethering partner.

Micrasterias cells are capable of coping with environmental pollution to a considerable degree accomplished by a physiological flexibility as well as by the capability of performing autophagy, and of compartmentalizing pollutants in cell walls and vacuoles, respectively, by excreting them via constant mucilage production (for review see: (Lütz-Meindl, 2016). The molecular players that are involved in these processes as well as a possible regulation by signal molecules such as phytohormones, remains to be investigated. Further establishment of molecular tools and sequencing of essential regulators combined with employment of high

resolution 3-D microscopic techniques will enable the next steps for elucidating cell shape formation and for understanding intracellular stress response regulation. By its close relation to higher land plants *Micrasterias* may help in detecting plant specific cellular processes and pathways that would remain undiscovered when only using “classical” model system such as *Arabidopsis*.

Information from three-dimensional reconstructions as provided by FIB/SEM is absolutely required for a comprehensive understanding of the architecture of all cell organelles and their mutual interplay. FIB/SEM microscopy is a very time consuming and cost intense method, therefore a precise and efficient milling is indispensable. As the volume of the semi-cells of *Micrasterias* is dominated by their two chloroplasts and organelles like dictyosomes and mitochondria are only present within a rather small space along the chloroplast membrane and around the nucleus, it is important to know the exact orientation of the cells (Skaloud et al., 2011). With classical block embedding, a favored orientation is not given, as single *Micrasterias* cells are randomly distributed within the resin block. At that time, thin embedding of *Micrasterias* was not established. The small region where dictyosomes and mitochondria are located was only reached by chance. As the quality of high-pressure freezing, freeze-substitution, contrast and ultrastructural preservation is not guaranteed, cell by cell had to be milled, each with a rather large ramp, which was not straightforward, as a lot of samples had to be evaluated (Lütz-Meindl et al., 2015). At the end of the thesis, *Micrasterias* could by be embedded in thin resin layers for efficient milling routinely (Luckner and Wanner, 2018a). Post embedding CLEM was possible by printing a coordinate system onto the slide with a water-resistant stamp and severe ultrastructural distortions could be monitored already at LM level and appropriate cells could be selected and documented for oriented milling (Luckner and Wanner, 2018a).

7.2.2 Migrating human platelets as mechano-scavengers

Blood platelets are critical for hemostasis, thrombosis, and diverse roles during immune responses. Despite these versatile tasks in mammalian biology, their skills on a cellular level are deemed limited, mainly consisting in rolling, adhesion, and aggregate formation (Brass et al., 2005; Jackson, 2011). Adherent platelets use adhesion receptors to mechanically probe the adhesive substrate in their local microenvironment. When actomyosin-dependent traction forces overcome substrate resistance, platelets migrate and pile up the adhesive substrate together with any bound particulate material. They use this ability to act as cellular scavengers, scanning the vascular surface for potential invaders and collecting deposited bacteria (Gaertner et al., 2017). Microbe collection by migrating platelets boosts the activity of professional phagocytes, exacerbating inflammatory tissue injury in sepsis. This assigns platelets a central role in innate immune responses and identifies them as potential targets to dampen inflammatory tissue damage in clinical scenarios of severe systemic infection

(Gaertner et al., 2017). An autonomous migration of platelets was identified by live cell differential interference contrast, phase contrast and epi-fluorescence. The pseudonucleus of migrating platelets moved from the center to the rear and adopted a half moon shape (Gaertner et al., 2017). As fibrinogen is the physiological ligand of aIIbb3 integrin receptor at the platelet surface, we postulate its major role in migration (Nieswandt et al., 2002). Fibrinogen, a branched polymer, 45 nm in length and 4.5 nm in diameter (M = 340 kD), self assembles and forms fibrin fibers up to a length of 0.6-0.8 µm and 80-120 nm in diameter, thus termed as fibrin(ogen) (Zhmurov et al., 2016, 2011). The interaction of fibrin(ogen) with the platelet was unclear, whether there is an uptake or an accumulation at the surface of the platelets during migration. The resolution of suitable LM techniques, especially in z, is too weak to address the question of a fibrin(ogen) uptake. Previous studies demonstrated the power of FIB/SEM on procoagulant-activated platelets (Podoplelova et al., 2016). The complex and dynamic organization of “caps”, convex regions of platelets, was reconstructed in 3D and additionally immunogold-labeling of Annexin V, a blood coagulation factors, was predominantly detected at “cap”-like regions (Podoplelova et al., 2016). Analysis of migrating platelets on fibrin(ogen) coated slides was only possible in correlation with high-resolution SEM (topographical investigation) and FIB/SEM (ultrastructural 3D investigation). Visualization of macromolecules as fibrin on fibrin(ogen) coated slides/coverslips with SEM requires high resolution at low kV (Gaertner et al., 2017). As slides are electrically insulators, a conductive coating is necessary. However, even very thin (3-5 nm) layers of platinum (by sputtering) or carbon (by evaporation) limit or even prohibit visualization of fibrin and small gold labels used for immuno-SEM. The solution was a stable, conductive carbon coating of the slides beforehand, which does not impede the migration of platelets and the specimens could be investigated at very low kV (0.8-1.2 kV) with high resolution, allowing simultaneous visualization of the topography of the platelets with the chamber SE and in-lens SE detector together with the in-lens EsB signal to resolve gold colloids down to 5 nm (Gaertner et al., 2017).

Dynamic migrating processes were followed and investigated with live cell LM and subsequently fixed at a desired time point for correlative SEM and FIB/SEM microcopy to add ultrastructural information. Individual fibrinogen molecules could be visualized with high-resolution SEM of platelets growing on fibrin(ogen)-coated coverslips (Fig. 12). As already indicated by LM, fibrin(ogen) accumulates at the surface of the platelets, shown with high-resolution SEM of immuno-gold labeled fibrin of critical point dried samples (Gaertner et al., 2017). FIB/SEM of critical point dried specimens is the fastest preparation providing detailed information about the localization of the immuno-gold labeled fibrin(ogen). For CLEM with best ultrastructural preservations, platelets, migrating on fibrin(ogen) labeled slides and infected with fluorescent *E. coli* cells or latex beads were fixed and ultra-thin embedded (Gaertner et al., 2017).

Gold-labeled fibrin(ogen) localizes both, on the platelet surface and within an open canalicular system (OCS) (Fig. 12 D, E). Further, migrating platelets collect fibrinogen-trapped latex beads or E. coli cells (Gaertner et al., 2017) (Fig. 12 F-K). Earlier studies reveal the importance of

volume EM techniques and provide a detailed 3D view of the spatial membrane topology of the OCS and the 3D organization of granules within stimulated platelets (Eckly et al., 2016; van Nispen tot Pannerden et al., 2010). The OCS consists of small neck regions and multiple areas of membrane branching that serve to connect the platelet cell surface from one side to the other at multiple sites (van Nispen tot Pannerden et al., 2010). Although this study showed fascinating insights of platelets by TEM tomography and cryo-TEM tomography, of plunge frozen cells, a reconstruction of an entire platelet to visualize the whole OCS is missing (van Nispen tot Pannerden et al., 2010). To understand the dynamic of the OCS, live cell LM correlated to FIB/SEM data of thin embedded samples would be the favored method for high resolution CLEM of entire cells.

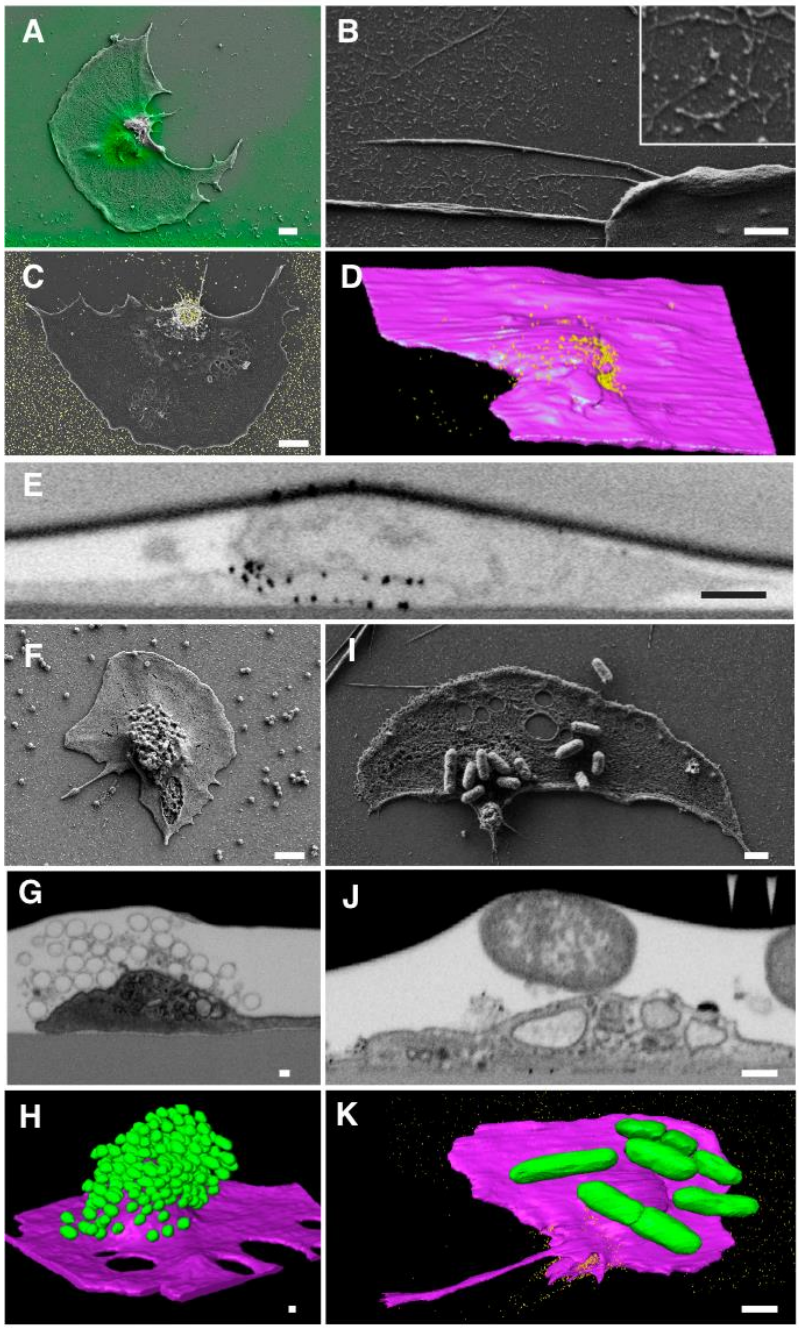

Fig. 12 Migrating Human platelets – a challenge for SEM and FIB/SEM*. Only if the slides are coated with carbon by evaporation, high-resolution SEM of platelets is possible without additional sputter coating for conductivity. Correlative LM/SEM microscopy of fluorescent labeled fibrin(ogen) coated slides with migrating platelets (**A**). High-resolution SEM reveals single fibrin fibers attached to the slide (**B**). Immuno-gold labeling of fibrin can be detected by high-resolution SEM (**C**; merged BSE and SE signals). 3D reconstruction of an ultra-thin embedded platelet, migrating on immuno-gold labeled fibrin(ogen) (**D**). Gold particles (10 nm) are present at the surface of the platelet and within an open canalicular system (OCS) (**E**). Platelets incubated with latex spheres (diameter 200 nm: **F**, **G** and **H**) or with pathogens (*E. coli*) (**I, J, K**) were reconstructed based on FIB/SEM data sets (**H, K**). The distribution of E. coli cells or latex beads can be analyzed with CPD samples (**F, I**) as well as after ultra-thin embedding to gain insights of the ultrastructure (**G, J**). Scale bars: A, B, F, C, I, J = 1 µm; E, G, H: 100 nm; F, J: 1 µm; K: 500 nm*

For CLEM, cell cultures are typically embedded on a slide/cover slip, which is removed after embedding e.g. by heat shock (Fermie et al., 2018). This procedure is not suitable for investigation of surface contacts as through removal of the slide the surface is not smooth but shows some undesired roughness. Application of the developed flat embedding (Luckner and Wanner, 2018a) maintained the overall appearance and orientation, offering a very precise retrieval and subsequent correlation of LM to SEM, FIB/SEM data. The fibrin(ogen) coated

glass slide is part of the platelet migrating experiment and has to remain in contact to the cells. Direct thin embedding on the slides it is of great benefit, as the coordinates and the orientation of the platelets is maintained.

Correlative microscopy with LM and FIB/SEM microscopy revealed platelet migration on fibrin(ogen), which enables the collection and bundling of bacteria to recruit and activate professional phagocytes. Both functions assign platelets a central role in innate immune responses and identify them as potential target to dampen inflammatory tissue damage in certain clinical scenarios (Gaertner et al., 2017).

7.2.3 Mitosis of HeLa

HeLa is an ideal system to study the cell cycle with correlative LM and FIB/SEM and to verify the precision, efficacy and high-resolution obtained with flat embedded specimens. Staining of DNA allows the selection of target cells at any mitotic stage and precise time series can be selected by fluorescence microscopy. Conventional confocal laser scanning microscopy enables investigations with resolutions down to 150x150x500 nm in routine or with STED and SIM down to 100 nm in xy and 250 nm in z (Betzig et al., 2006; Betzig and Trautman, 1992; Hell and Wichmann, 1994; Linde et al., 2011; Rust et al., 2006), further pushed to ~20 nm in xy and 50 nm in z by localization-based techniques, with STORM and PALM. FIB/SEM data stacks reach a pixel size of 2 nm iso-voxel, which equals to a resolution of about 5 nm in xyz under best conditions, not nearly reached in z with other block-face imaging approaches like 3View® or array tomography (minimal section thickness approx. 30 nm) (Denk and Horstmann, 2004b; Wacker and Schroeder, 2013).

Comparison of volume EM techniques for CLEM

An entire cell with a volume of 8000 µm^3 (20x20x20 µm) can be milled an imaged within 4.5 h if lower resolutions with a pixel size of 15x15x40 nm are sufficient (Luckner and Wanner, 2018). Increasing the resolution in z to 20 nm the data acquisition would take 8 h, with 10 nm 16 h. Highest resolution (2 nm iso-voxel) will be typically chosen for CLEM of smaller target volumes rather than entire cells. A centrosome including its environment can be imaged with FIB/SEM in 2-6 h, covering an image area of 6x4 µm and a depth of 2-6 µm. When comparing the advantages/disadvantages of the various volume-EM methods for 3D reconstruction, there is principally no competition between the methods, rather than a critical judgment, which advantages are balanced with the inherent limitations. TEM tomography, especially when using cryo-sections, is state of the art, concerning structural preservation and resolution (Wagner et al., 2017). For CLEM in combination with cryo-TEM tomography, acrobatic preparation would be necessary, when attempting to re-localize a target region within a cell. If adherent cells grow on sapphire discs for cryo-preparations, LM is possible before HPF, but without the possibility of cryo-sectioning. Cryo-fluorescence LM and cryo-TEM tomography is

only possible, for samples which can be prepared in very thin liquid layers on TEM grids (e.g. suspensions of viruses, phages, small prokaryotic cells) for plunge freezing (Hampton et al., 2017; Koning et al., 2014; Schorb and Briggs, 2014). Cryo-TEM of details of human cells requires cryo sectioning of pelleted, vitrified cells. Targeting centrosomes of cells e.g. just entering late anaphase, would be a frustrating challenge, as: i) only a minor fraction of cells will be in this state; ii) an ideal section plane is necessary to recognize the state and iii) the entire centrosome has to be located within the section of only a few hundred nm thicknesses. ATUMtome and 3View® are afflicted with the same difficulties: sections as thin as possible have to be produced in very long series. For 3View®, the situation is easier, as the block-face is imaged, and compressions or other distortions are not likely. However, variations of section thickness are not immediately evident. As the block-face is principally an electrical insulator, reduction of the electrical resistance by metallizing is absolutely necessary, given by rOTO or OTO fixations (Seligman et al., 1966; Aoki and Tavassoli, 1981; Friedman and Ellisman, 1981; Willingham and Rutherford, 1984). However, if areas of the tissues lack membranes (highly vacuolated plant tissue with intercellular spaces filled with resin) charging problems become severe. Serial sections produced with ATUMtome typically vary in thickness, which is evident by their interference color, are compressed, bear the risk of folds and are affected by knife artifacts. Being critical, long series can be achieved only at thicknesses of 60-70 nm, although 30 nm are possible (Hua et al., 2015). However once prepared properly for SEM, a variety of advantages are unique for ATUMtome: i) image series can be recorded automatically with overview and several details; ii) as the method is non-destructive, the ribbons can be stored for long time and re-imaged several times for additional information and control; iii) it is the only method available for both, correlative immuno-fluorescence and immuno-labeling in a 3D context; iv) the new generation of Zeiss MultiSEM allows data collection with gigantic efficiency by simultaneous acquisition of 91 images (Eberle et al., 2015; Marx, 2013), resulting in TB data sets which cannot be handled at present with standard PCs. The analytical capacity is the exceptional advantage of ATUMtome, however, both, 3View® and ATUMtome are far away from high isotropic resolution (20-60 nm iso-voxel). Only FIB/SEM allows iso-voxel in the range of 2-5 nm over long series (Luckner and Wanner, 2018b). Signal detection of FIB/SEM offers some additional advantages: i) with the in-lens EsB detector, the grid voltage can be adopted to the energy of the BSE desired, typical in a range of 800 V to 1.5 kV for optimal gathering BSE dependent on the milling rate. This assures that e.g. with a milling step of 2 nm only EsB are collected originating from 2 nm depth of the block-face. ii) The in-lens SE detector can be used for highest resolution as single signal or in combination with the EsB signal (Fig. 13). iv) As charging is not a major problem for adequately prepared specimens for FIB/SEM, fixations without rOTO or OTO and plant material can be investigated at high resolution when accepting longer exposure times.

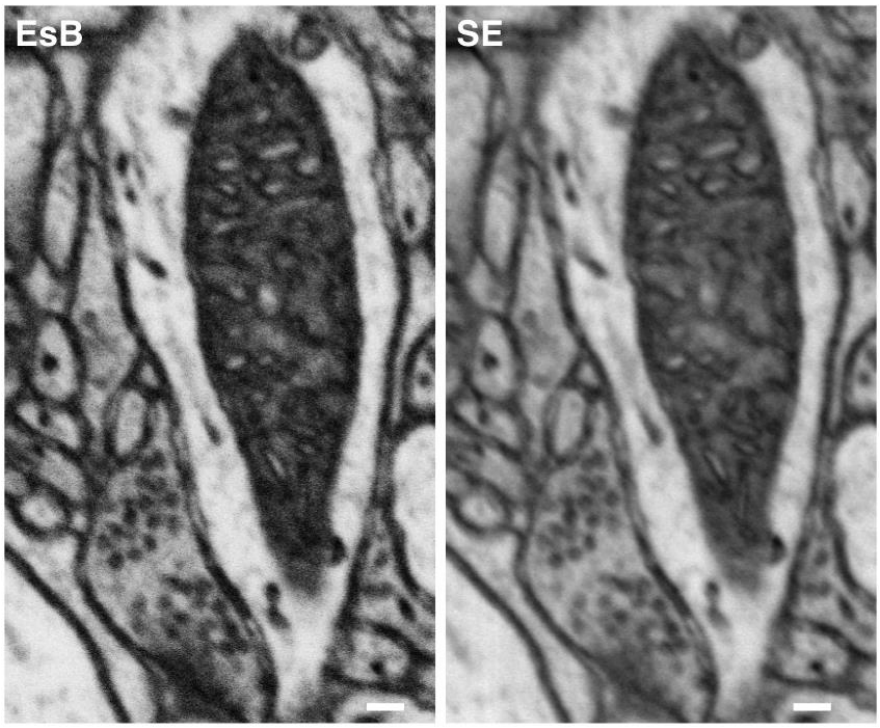

Fig. 13 Comparison of EsB and SE signal. *Detail of the FIB/SEM block-face, images of a mouse brain are taken at 1.5 kV (aperture: 60 µm; HC mode) with the in-lens EsB detector (grid voltage: -500 V) and simultaneous with the in-lens SE detector. The contrast of the EsB image is higher, however, the signal to noise ratio is better with the in-lens SE image. Scale bar: 100 nm*

3D visualization

Handling (storage and analysis) of large data sets, generated by volume EM is a general problem. A few years ago, already a 10 GB dataset would have been considered very large. Now, raw data sets can easily comprise several hundred terabytes during an overnight run (Zeiss MultiSEM). Considering that numerous data sets are required for a comprehensive study, and associated alignment and reconstruction files, even expand the amount of data; it becomes clear, that the data handling is no longer trivial. W. Denk estimated in 2013 that image capture of a whole mouse brain could yield 60 petabytes (petabyte = 10^{15} bytes = 1000 TB) of data (Marx, 2013), which was in 2016 already estimated with 1.5 exabyte (exabyte = 10^{18} bytes) and even 175 exabytes for a human brain (Mikula, 2016). Processing a FIB/SEM data set of 30 GB already takes a conventional workstation with 128 GB RAM to its limits.

To extract biologically relevant information from microscopic images, it is important to visualize the data in 3D (Ruthensteiner et al., 2010). Two-dimensional cross-sectional view of a 3D image stack is the most common method to observe 3D data sets. However, cross-sectional views are not able to visualize the 3D information of volumetric images. Most microscopic image analysis techniques can be categorized into three major classes, namely segmentation, registration, and annotation. Typically, substructures are discerned by a manual segmentation procedure followed by surface generation for each component using a standard software algorithm. Segmentation can be enormous time consuming. A FIB/SEM data set of a HeLa cell with 5 nm iso-voxel comprises 4000 sections. If only a few minutes are necessary to segment all ER strands of a single FIB/SEM slice, two months of mindless segmentation would be

needed. Despite the attractiveness and didactic excellence of reconstructed 3D models, manually segmentation is too time-consuming and charged with subjectivity. Although there are many successful attempts for software development with automatic recognition of cellular structures (Fua and Knott, 2015; Schlegel et al., 2017; Wanner et al., 2015), a commercial solution is not expected in near future. Visualizing the complete 3D information in a volumetric image, without subjective evaluation, requires the presentation of all individual voxels intensities, and the 3D spatial adjacency information of all voxels (Long et al., 2012). As voxels near the viewer will obscure far-away voxels, a selective exclusion (threshold) of non-important voxel intensity information is basis used in 3D volumetric image visualization (Long et al., 2012). Real-time volume rendering for large datasets is highly desirable to investigate EM image stacks, but often needs expensive, special hardware (i.e., high-throughput graphics card with large memory) and software (e.g. Amira). Striking 3D information is gained, by using the stereo-viewer with red-cyan anaglyph glasses. Due to the depth information, complex structures, which can be hardly interpreted by 2D presentation, offer their 3D architecture convincingly by interactive navigation (Luckner and Wanner, 2018b) (Fig. 14). As HeLa cells are densely packed with organelles of similar contrast, volume visualization is not trivial. The amount of volume, transparency, resolution, and threshold settings have to be balanced (Luckner and Wanner, 2018b). High contrast organelles (mitochondria, chromosomes) can be visualized throughout the entire cell, when increasing transparency and reducing resolution. If cellular structures are and irregular shaped and in addition densely packed (e.g. vesicle clouds, trans-Golgi-network, clusters of endosomes) an adequate 3D presentation is only possible in high-resolution mode (Amira *volren* setting), appropriate threshold and reduced number of sections used for 3D (e.g. 1 µm in z) (Luckner and Wanner, 2018b). But once adjusted for the ROI, convincing 3D information can be collected within a short time of dozens of similar ROIs (connection of ER to almost all lipid bodies and endosomes) (Luckner and Wanner, 2018b). However, due to the lack of color information of separate objects, distinction between structural elements with similar grey levels, contacting each other (e.g. ER-dictyosome) is not as convincing compared to segmentation. In practice, a combination of both, manual segmentation/reconstruction and volume rendering will enable a reliable 3D visualization (Luckner and Wanner, 2018b).

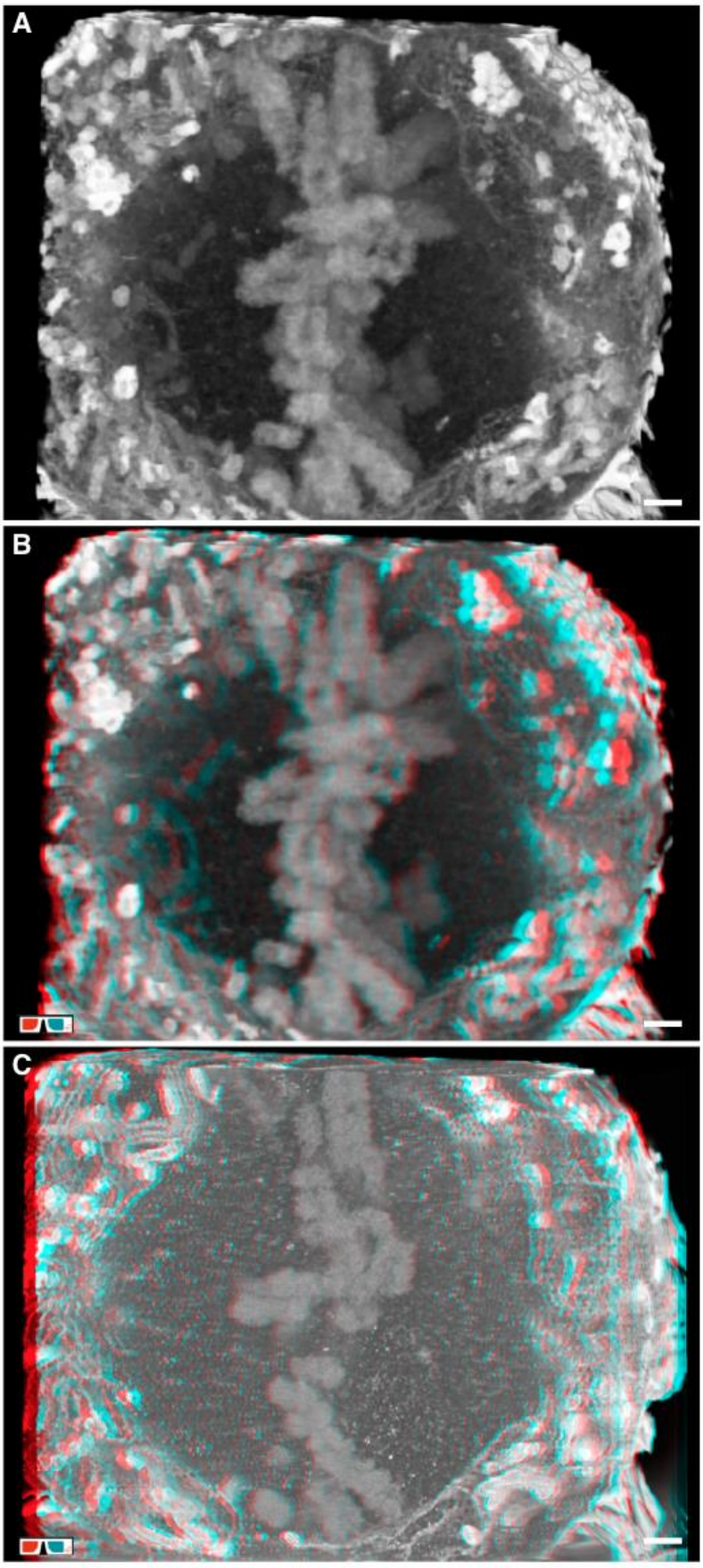

Fig. 14 3D visualization by volume rendering. *FIB/SEM images stack of a HeLa cell in metaphase with chromosomes arranged in a vertical plane, visualized with volume rendering. Comparison of 2D (**A**) and 3D (**B**; low resolution) presentation: the depth information is only given by displaying the micrographs in 3D. For high resolution (**C**), the transparency has to be reduced as well as the number of micrographs used for visualization. Examine an entire cell is achieved by adjusting all visualization parameters first (number of sections, threshold, brightness, contrast and transparency) and then shifting the segment through the cell. Scale bar: 1 µm*

Ultrastructural dynamics

Although mitosis in HeLa is described with classical TEM since decades with 2D images, 3D visualization is possible since a few years with serial block-face imaging (3View®; FIB/SEM) and gave impressing structural information of whole cells (Booth et al., 2016; Murphy et al., 2011; Nixon et al., 2017; Puhka et al., 2012). The potential of flat embedding for economic CLEM of mitotic stages and exploring in 3D topics of mitosis either not answered till now, or not be presented with a resolution possible with FIB/SEM:

- Nuclear envelope breakdown and reconstitution.
- Golgi ultrastructure, its degradation and reconstitution during mitosis.
- Lipid bodies are organelles integrated in a membrane carousel.
- Formation of midzone and midbody.

Metamorphosis of the Nuclear Envelope

Mitosis of HeLa is semi-open, which means that a large amount of the nuclear envelope (NE) is pertained during meta- and anaphase as ER sheets (Smoyer and Jaspersen, 2014). Its transition to ER and back to NE is documented by detailed LM investigations (Anderson and Hetzer, 2008; Lu et al., 2009). For 3D visualization of the NE transition both, segmentation and volume rendering had to be applied for getting insight into the mechanism. Volume rendering with FIB/SEM data at the resolution limit allows visualization of nuclear pore complexes in 3D, both from the cytoplasmic side as from the nuclear matrix with 2 nm iso-voxel. Due to this till now unreached resolution with FIB/SEM of nuclear pores, the first steps of NE breakdown were documented by loss of the NE complexes, but pertaining the nuclear pores (after transition) as fenestrations of the ER. The NE disappears as an integral structure; however, large areas of ER sheets derived from NE still outline the shape of the NE, as shown by live cell imaging (Anderson et al., 2009). The NE regions facing the centrosomes are completely dissolved, in accordance to CLEM data (Domart et al., 2012), allowing free access for attachment of the MT to the kinetochores. During reconstitution of the NE it is obviously an important strategy to neatly separate the chromosomes from cytoplasmic constituents which is achieved by compaction of the chromatin, reaching the maximum in late anaphase (Mora-Bermúdez et al., 2007) which facilitates attachment of ER sheets chromosomes, followed by enwrapping, as convincingly shown within the last decade by LM (Andrson et al., 2009; Anderson and Hetzer, 2008a; Lu et al., 2009). As the center of chromosome bulk is not covered evenly, due to uneven chromosome topography and reduced accessibility for ER sheets, nuclear tunnels through the nucleus form during telophase. They are typical for HeLa cells and persist absolutely until interphase, as shown for numerous organisms (Malhas et al., 2011). Reconstruction of nuclear tunnels is very time consuming with manual segmentation. However due to the high contrast of the nuclear envelope by rOTO fixation, they can be visualized by volume rendering within a few minutes in 3D.

Golgi

The Golgi ribbon is a general term implicating a linear arrangement of dictyosomes. During early prophase, the Golgi ribbon disintegrates to dictyosomes, cisternae and finally to vesicles

(Wang and Seemann, 2011). There are overwhelming CLSM investigations describing Golgi disassembly under various experimental conditions, but its compact structural organization and composition of stacks, cisternae, vesicles, MTs etc. impedes the high resolution, possible with state of the art LMs, by overlap of neighboring signals. 3D reconstructions are still rare, due to the late development of large volume reconstructions by block-face milling, especially in combination with cell-developmental aspects (Koga et al., 2017; Ladinsky et al., 1999; Marsh and Pavelka, 2013; Staehelin and Kang, 2008). FIB/SEM of flat embedded HeLa cells proved to be a very economic and efficient method for monitoring the Golgi during the cell cycle. First, the Golgi ribbon is not a ribbon rather than a basically cup shaped structure of interconnected dictyosomes with additional branches. In contrast to some assumptions explaining the Golgi disintegration as a sequential process disassemble into dictyosomes/stacks, further into cisternae and finally into vesicles (Ayala and Colanzi, 2016; Colanzi and Sütterlin, 2013) the 3D data suggest a simultaneous disintegration from the Golgi ribbon direct into vesicles. The possible contradiction to CLSM investigations, interpreting dictyosomes being separated, before they dissociate into single cisternae/vesicles (Wang and Seemann, 2011; Wei and Seemann, 2009), could be explained by the ultrastructural investigations, clearly showing that clouds of vesicles still outline the former stacks, suggesting the presence of intact dictyosomes. Golgi reassembly could be best studied with onset of telophase, as during anaphase-B neither dictyosomes nor cisternae are present. Volume rendering of restricted depth gives high-resolution 3D information of the interaction of ER in contact to endosomes and clouds of vesicles, obviously fusing/forming small, but typical dictyosomes, which connect to a patchwork, first being present as fragments proximal to the centrosome, as well as at the distal side of the nucleus, facing the midbody. When reaching resolution limit of FIB/SEM (2-4 nm voxel size) the quality of the data sets approaches fairly well to TEM tomography (Ferguson et al., 2017; Marsh and Pavelka, 2013; Ranftler et al., 2017; Staehelin and Kang, 2008).

Endomembrane System

For a long time, lipid bodies were not in focus of ultrastructural investigations. Their significance become obvious by investigation of approx. 35 HeLa cells studied in 3D in various stages of the cell cycle. They could be described as an organelle, abundantly present, and connected both, to the ER and to clouds of vesicles, possibly derived from Golgi. Although in plant cells the ontogeny and degradation of lipid bodies was already described in detail since the early 80th, as spherical organelles with an apolar matrix of triacylglycerols and half unit membrane as boundary to the cytoplasm (Wanner and Köst, 1984). Comparable models were not available for some decades for animal cells. A lack of motivation for lipid body investigations may be seen in a simple interpretation, that they are principally energy stores. The possible role of lipid bodies as a transient store for membrane components (Wanner and Köst, 1984) was probably not considered. The idea favors an economic metabolism of membrane lipids (e.g. lecithin) by simply replacing in few enzymatic steps the polar group by a fatty acid, to form triacylglycerol, the apolar matrix of lipid bodies, with minimal surface, but potentially providing an enormous amount of membranes, which can be readily reorganized on demand. Lipid bodies were long perceived as inert fat particles in animal systems and been largely ignored

by cell biologists. However, more recently, they are increasingly recognized as dynamic organelles that represent a frontier for cell biology (Farese and Walther, 2009). As for plants (Wanner et al., 1981) HeLa lipid bodies are typically connected to one or several strands of ER as shown both by 3D segmentation and volume rendering. Surprisingly, in close vicinity to lipid bodies, various types of endosomes are in luminal connection to the same strand of ER. As this is typical for the vast majority of lipid bodies and endosomes, they cannot be considered as independent compartments. The categorical separation of structural and functional cellular entities may be responsible for competing opinions – neither model is entirely concurrent with the dynamics of an interconnected system. A model is presented, illustrating the recycling of membrane components in a concert of ER, endosomes, and lipid bodies (defined as ERELB). Modern LM, involving *in vivo* imaging, complemented by high resolution FIB-SEM tomography could provide clarifying information at the nano-scale as discussed e.g. for the multitude of inter-organellar interactions involving lipid droplets (Gao and Goodman, 2015).

Essential Role of Clamps for Midzone Formation

The two sets of chromatids separate during mitotic anaphase, characterized by an organized central spindle midzone between in-between, consisting of a dense network of overlapping antiparallel microtubules (Mastronarde et al, 1993). The role of the spindle midzone is essential for the initiation and completion of cell cleavage and is the binding site for a number of proteins, which play a part in cytokinesis (Cao and Wang, 1996; Wheatley and Wang, 1996; Glotzer, 1997; Robinson and Spudich, 2000). Electron microscopy has already very early shown an amorphous electron-dense matrix centered on the zone of overlap of anaphase central spindle microtubules (Buck and Tisdale, 1962; Mclntosh and Landis, 1971). The midzone region of the anaphase spindle remains ill-defined with respect to morphology, constituents and function, although many antigens specific to the midzone region of the anaphase mitotic spindle have been reported (Kurasawa et al. 2004). A combination of manual segmentation and volume rendering gives new insight with high resolution to visualize the very early steps of midzone formation during anaphase-A. Although the time for mitosis is different for individual HeLa cells, ranging from 24 min to 90 min, anaphase-A is constantly very short in HeLa and typically only 2 min (Meraldi et al., 2004). Only CLEM with in combination with ultra-thin embedding enables to pick a sufficient number of the very rare cells in anaphase-A for high resolution FIB/SEM milling. Characteristic for early anaphase chromatids is an attachment of MT running from the central spindle through the chromosome aster to their flanks towards the sister chromatids. The formation of the midzone is characterized by two phases: i) initial step of clamp formation; ii) bundling of the MT by clamps, increasing in size and bundling more MTs, suggesting that midzone formation is mediated by microtubules (MT), passing the arms of separating chromatids thereby withdrawing chromatin from the telomere regions. Chromosomal passenger complexes (CPC) translocate in anaphase-B from the centromeres to the ends of the chromosomes (Carmena et al., 2012; Kurasawa et al., 2004). Accumulation of CPC and VTCs form clamps in the midzone. Electron dense clamps could be efficiently separated by semi-automatic threshold-based segmentation, due to their strong contrast of rOTO impregnation. The 3D reconstructions show clearly the contact of MTs and adhering putative

CPCs or ERGICs. Although many publications present EM images, where vesicles are seen in midzone area, there is no indication that they may play a role in midzone/clamp formation in anaphase. As it is likely that small vesicular-tubular structures are Golgi derivatives, intermediate compartments (IC) are the likely candidates representing the vesicles. This is supported by investigations of NRK cells, providing evidence that the permanent IC elements function as way stations during the COPI-dependent dispersal of Golgi components at prometa- and metaphase, indicating that they correspond to the previously described Golgi clusters (Marie et al., 2012). Although the IC elements maintain their clustering at the spindle poles during metaphase to telophase, they also associate with the central spindle, imaged with high-resolution CLSM. VTCs are omnipresent in the cytoplasm of HeLa cells. In mammalian cells, COPII vesicles are widely accepted to form VTCs, a more complex transport intermediate, by homotypic fusion (Hughes and Stephens, 2008). With increasing aggregation, the clamps reduce in length to ± 0.6 µm. In later stages they form a compact structure, the midbody. With onset of cytokinesis, densely packed MTs passing the midbody are still visible, ending as bundle in the daughter cells. Vesicles, vesicular-tubular clusters (VTCs) and tubular ER are located between the MT-bundles, till to the center of the midbody.

7.2.4 *In vivo* CLEM of spine plasticity

In neuroscience, there is an increasing demand to correlate dynamic *in vivo* fluorescence data with ultrastructural details. Two-photon microscopy is a well-established technique in the field of life sciences, especially neuroscience, providing the highest depth information for more than two decades (Denk et al., 1990). It is one of the few imaging methods that allows observation of suitable experimental animals over a period of weeks or even months. This method was successfully applied by several groups since the 1980th, to study mice brains with the ultimate goal of understanding the development of Alzheimer's disease (AD) (Kerr and Denk, 2008; Yang and Yuste, 2017). However, due to the limited resolution of 2-photon microscopy (lateral approx. 500 nm; 1-2 µm in the axial), morphological changes of dendrites, mitochondria, ER and Golgi apparatus, which play an essential role the pathogenesis of AD, cannot be addressed (Baloyannis, 2015).

For many years, electron microscopy has been successfully used, separate from light microscopy, for investigations of ultrastructural changes in neurodegenerative diseases brain tissues (Baloyannis et al., 1992; DeKosky and Scheff, 1990; Neuman et al., 2015; Baloyannis, 2015). Within the past 10 years several protocols were developed to correlate *in vivo* 2-photon microscopy with electron microscopic data, based either on DAB-conversion of GFP or near-infrared branding landmarks (NIRB) (Bishop et al., 2011; Grabenbauer, 2012; Karreman et al., 2016; Lees et al., 2017). Every few month, new protocols are published, but instead of facilitating acrobatic preparation procedures, the approaches getting more and more complex, involving additional applications, which do not facilitate CLEM in daily routine (Karreman et al.,

2016). CLEM will always be a challenge, because of completely different requirements of the samples for *in*/*ex vivo* LM and FIB/SEM microscopy, involving numerous preparation steps and physical modifications. Starting with a rather large sample (entire organism, tissue sections) hydrated, soft and e.g. transparent, which has to be cut into small pieces, becoming opaque after heavy metal impregnation, solid and brittle after dehydration, with loss of orientation.

Retrieval of a target dendrite and associated synapses with an approx. volume of 1 μm^3 within an entire mouse brain with approx. 10^{12} μm^3 is almost impossible without reference points. Simplified, it is like looking for an individual grain of sand within a sandbox. Recent research topics involve live cell observations into correlative workflows (Karreman et al., 2016; Maco et al., 2013). The feasibility of the living tissue-based correlative workflow using FIB/SEM technology was demonstrated by (Blazquez-Llorca et al., 2015).

Further improving and simplifying CLEM, as well as optimizing data acquisition provides now a stable technique, to address different correlative questions of life sciences. The workflow developed, is based on immobilized vibratome sections, and solely use of natural landmarks to re-locate target areas in FIB/SEM (Luckner et al., 2018). Any ultrastructural alterations (e.g. precipitations formed by DAB-conversions, mechanical distortion by NIRB marks) are avoided. Cutting and immobilizing 50 µm vibratome sections of the mouse brain enables in addition *ex vivo* confocal investigations of the previous *in vivo* imaged target region, immediately re-located by the characteristic blood vessel pattern. Mapping natural landmarks, either single or in combination (blood vessels, nuclei and axons), in close vicinity to the target, allow fast re-localization of the previously monitored dendrite, with a precision of few micrometer (Luckner et al., 2018). As blood vessels and nuclei are abundantly present in all animal tissues, this method can be applied for a variety of histological investigations (kidney, liver etc.). Vibratome sections are ideal for FIB-SEM investigations: due to their thickness of approx. 50 µm, they can be adequately fixed and milled by the ion-beam in their entire depth. As the brain sections are immobilized to a glass slide, their orientation does not change and a correlation only by superimposition of the LM-image with the SEM-image is directly given by ultra-thin embedding. Capitalizing the spectrum of SEM parameters, using different detectors and accelerating voltages, provides a topographic and material contrast visualizing blood vessels, nuclei and even myelinated axons of the upper surface for a precise correlation. With image pixel sizes down to 5 nm of serial FIB/SEM sections, detailed investigations of the tripartite synapse (spine, pre-synapse, astrocyte) are possible. FIB/SEM is the only method at present, to study fine astrocytic processes or spine necks with sizes down to 20 nm in 3D within large volumes. Several thousand consecutive sections of the same part of a dendrite, monitored over weeks by 2-photon microscopy, provide complementary ultrastructural information to dynamic *in vivo* data. The developed workflow of thin/ultra-thin embedded vibratome sections has proven for precise and economic CLEM in routine, reduced to a minimum of preparation steps, allowing highest resolution. It is now a promising tool for statistical relevant serial examination in routine for investigation of dynamics of neurodegenerative processes e.g. plaque disposal or

deposition of misfolded tau oligomers, a marker of AD, within synaptic components during Alzheimer's disease (Baloyannis, 2015).

8 Conclusion & Outlook

Correlative light and electron microscopy requests: i) high resolution; ii) precise correlation; iii) large volume analysis; iv) applicability in daily routine and v) being fast in acquisition and 3D analysis. TEM-tomography fulfills i) hardly ii) and not iii) and iv). Three further candidates are considered: array tomography (conservative, allowing post sectioning analytics), 3View® (cheapest, concerning acquisition of data sets and very suitable for largest volumes) and FIB/SEM (highest resolution in z; suitable for large volumes but very expensive). If primarily resolution is required, only FIB/SEM can bridge high resolution CLSM with TEM tomography. Large volumes can be investigated at high resolution, admitted beyond TEM tomography, but sufficient for a vast majority of cytological investigations. There is no competition between the four different techniques, only a comparison of which one is most suitable for given demand. If several mm^3 of tissue are needed for 3D reconstruction, 3View® will be the first, if not only choice. If re-investigations and immunofluorescence or post embedding immuno-labeling are necessary, only array-tomography can achieve these demands. If isotropic high-resolution is desired, only FIB/SEM can offer resolutions down to 2 nm iso-voxels.

For establishing FIB/SEM for CLEM as an economic routine method, four basic factors are a prerequisite: i) a coordinate system connected to the sample; ii) samples adherent to the slide/coverslip; iii) thin and ultra-thin embedding of the samples and, iv) an efficient 3D reconstruction. The coordinates on slides are appropriate for any investigation, from critical point dried samples to thin and ultra-thin embedding within epoxy resins, allowing precise correlation of adherent cells. Immobilization of non-adherent cells will be still a challenge. With thin- and ultra-thin embedding, FIB/SEM data acquisition is not limited in milling time (few seconds per section) rather than by the exposure time (in the range of 20-60 sec/image). Exposure time is defined basically by dwell time/per pixel and number of pixels/image. The total number of pixels is given by the desired field of view and the resolution being necessary. The only variable for resolution is the signal to noise ratio, which, however, is coupled, to the dwell time. The rOTO staining already provides a very strong membrane contrast, which cannot be further enhanced by modifying protocols without loss of ultra-structural resolution (artificial thickening of membranes). Increasing the dwell time e.g. by a factor of two, have two drawbacks: i) prolonged time of total FIB/SEM run (factor of two), resulting in higher costs (factor of two) and ii) higher risk of radiation damage by the imaging electron beam. There is a great expectation that new, more sensitive and efficient detectors, can improve the signal to noise ratio either by a constant dwell time or allow shorter exposure times for the same signal to noise ratio.

Exposure time is generally considered as a time factor and not in relation to stability of resins. Beam damage is not a problem at moderate resolutions (pixel size in x/y; 10-15 nm) but electron beam exposure dose increases squared, when the pixel size is halved. Decreasing from 10 nm to 2 nm voxel sizes, the dose is 25-fold and a visible electron beam damage can

be expected. For highest resolution, the resin stability is of utmost importance. The development of new, extreme beam-stable resins would be of great benefit.

With standard equipment, a FIB/SEM run needs a few hours to be stable enough for long data acquisition. If several days are needed for several thousand sections, these foreruns can be accepted. However, for economic high-resolution CLEM, this is too long. Instabilities during the first hours are supposed to derive primarily from the adaption of the sample to the temperature within the SEM, resulting in specimen drift (temperature adaption of the specimen + holder) and possibly specimen warming up due to energy uptake by electron and ion-beam. This is a complex physical situation, as specimen size is not constant, energy input depends on high voltage, ion-beam current, milling time and exposure time. Creating constant thermal conditions (Peltier cooling) in combination with online temperature registration could help to reduce instabilities.

Despite the attractiveness of manually segmented and reconstructed 3D models, it is too time consuming and charged with subjectivity, especially at high-resolution. Automatic feature recognition will not be available for a rapid analysis within the next years on standard computers. The best way at present is direct volume rendering, which proves to be a very efficient and objective tool. Its application could be facilitated by some software-based improvements e.g. automatic adaption of brightness and contrast, when changing volume rendering parameters (transparency, depth of volume) and by storing data direct from software (Amira) in a compatible format to examine the results interactively on other computer platforms, similar to interactive PDFs (Ruthensteiner et al., 2010; Ruthensteiner and Hess, 2008).

9 References

Abbe, E., 1904. Gesammelte Abhandlungen: Abhandlungen über d. Theorie d. Mikroskops. Mit 2 Taf. u, 29 Fig. u. 1 Portr. 1904. G. Fischer.

Affenzeller, M.J., Darehshouri, A., Andosch, A., Lütz, C., Lütz-Meindl, U., 2009a. Salt stress-induced cell death in the unicellular green alga Micrasterias denticulata. J. Exp. Bot. 60, 939–954. https://doi.org/10.1093/jxb/ern348

Affenzeller, M.J., Darehshouri, A., Andosch, A., Lütz, C., Lütz-Meindl, U., 2009b. PCD and autophagy in the unicellular green alga Micrasterias denticulata. Autophagy 5, 854–855.

Ahmad Khalili, A., Ahmad, M.R., 2015. A Review of Cell Adhesion Studies for Biomedical and Biological Applications. Int. J. Mol. Sci. 16, 18149–18184. https://doi.org/10.3390/ijms160818149

Altes, A., Joachimsthaler, I., Zimmermann, G., Heiderhoff, R., Balk, L.J., 2002. SEM/SThM-hybrid-system: a new tool for advanced thermal analysis of electronic devices, in: Proceedings of the 9th International Symposium on the Physical and Failure Analysis of Integrated Circuits (Cat. No.02TH8614). Presented at the Proceedings of the 9th International Symposium on the Physical and Failure Analysis of Integrated Circuits (Cat. No.02TH8614), pp. 196–200. https://doi.org/10.1109/IPFA.2002.1025657

Anderson, D.J., Hetzer, M.W., 2008. Shaping the endoplasmic reticulum into the nuclear envelope. J. Cell Sci. 121, 137–142. https://doi.org/10.1242/jcs.005777

Anderson, D.J., Vargas, J.D., Hsiao, J.P., Hetzer, M.W., 2009. Recruitment of functionally distinct membrane proteins to chromatin mediates nuclear envelope formation in vivo. J. Cell Biol. 186, 183–191. https://doi.org/10.1083/jcb.200901106

Aoki, M., Tavassoli, M., 1981. OTO method for preservation of actin filaments in electron microscopy. J. Histochem. Cytochem. Off. J. Histochem. Soc. 29, 682–683. https://doi.org/10.1177/29.5.6894766

Araujo, W.W.R., Teixeira, F.S., da Silva, G.N., Salvadori, D.M.F., Salvadori, M.C., Brown, I.G., 2016. Cell growth on 3D microstructured surfaces. Mater. Sci. Eng. C 63, 686–689. https://doi.org/10.1016/j.msec.2016.03.026

Ayala, I., Colanzi, A., 2016. Assays to Study the Fragmentation of the Golgi Complex During the G2-M Transition of the Cell Cycle. Methods Mol. Biol. Clifton NJ 1496, 173–185. https://doi.org/10.1007/978-1-4939-6463-5_14

Baik, K.Y., Park, S.Y., Namgung, S., Kim, D., Cho, D., Lee, M., Hong, S., 2014. Synthetic nanowire/nanotube-based solid substrates for controlled cell growth. Nano Converg. 1, 28. https://doi.org/10.1186/s40580-014-0028-0

Baloyannis, S.J., 2015. What has electron microscopy contributed to Alzheimer's research? Future Neurol. 10, 515–527. https://doi.org/10.2217/fnl.15.44

Baloyannis, S.J., Manolidis, S.L., Manolidis, L.S., 1992. The Acoustic Cortex in Alzheimer's Disease. Acta Otolaryngol. (Stockh.) 112, 1–13. https://doi.org/10.3109/00016489209137072

Beacham, W.S., Konishi, A., Hunt, C.C., 1976. Observations on the microcirculatory bed in rat mesocecum using differential interference contrast microscopy in vivo and electron microscopy. Am. J. Anat. 146, 385–425. https://doi.org/10.1002/aja.1001460404

Beckwith, M.S., Beckwith, K.S., Sikorski, P., Skogaker, N.T., Flo, T.H., Halaas, Ø., 2015. Seeing a Mycobacterium-Infected Cell in Nanoscale 3D: Correlative Imaging by Light Microscopy and FIB/SEM Tomography. PLoS ONE 10. https://doi.org/10.1371/journal.pone.0134644

Bell, K., Mitchell, S., Paultre, D., Posch, M., Oparka, K., 2013. Correlative Imaging of Fluorescent Proteins in Resin-Embedded Plant Material1. Plant Physiol. 161, 1595–1603. https://doi.org/10.1104/pp.112.212365

Belu, A., Schnitker, J., Bertazzo, S., Neumann, E., Mayer, D., Offenhäusser, A., Santoro, F., 2016. Ultra-thin resin embedding method for scanning electron microscopy of individual cells on high and low aspect ratio 3D nanostructures. J. Microsc. 263, 78–86. https://doi.org/10.1111/jmi.12378

Beniac, D.R., Siemens, C.G., Wright, C.J., Booth, T.F., 2014. A filtration based technique for simultaneous SEM and TEM sample preparation for the rapid detection of pathogens. Viruses 6, 3458–3471. https://doi.org/10.3390/v6093458

Bereiter-Hahn, J., Vöth, M., 1994. Dynamics of mitochondria in living cells: shape changes, dislocations, fusion, and fission of mitochondria. Microsc. Res. Tech. 27, 198–219. https://doi.org/10.1002/jemt.1070270303

Betzig, E., Patterson, G.H., Sougrat, R., Lindwasser, O.W., Olenych, S., Bonifacino, J.S., Davidson, M.W., Lippincott-Schwartz, J., Hess, H.F., 2006. Imaging intracellular fluorescent proteins at nanometer resolution. Science 313, 1642–1645. https://doi.org/10.1126/science.1127344

Betzig, E., Trautman, J.K., 1992. Near-field optics: microscopy, spectroscopy, and surface modification beyond the diffraction limit. Science 257, 189–195. https://doi.org/10.1126/science.257.5067.189

Bignold, L.P., Coghlan, B.L.D., Jersmann, H.P.A., 2007. David Paul von Hansemann: Contributions to Oncology: Context, Comments and Translations. Birkhäuser Basel.

Bishop, D., Nikić, I., Brinkoetter, M., Knecht, S., Potz, S., Kerschensteiner, M., Misgeld, T., 2011. Near-infrared branding efficiently correlates light and electron microscopy. Nat. Methods 8, 568–570. https://doi.org/10.1038/nmeth.1622

Blank, R., Hauptmann, E., Arnold, C.-G., 1980. Variability of Mitochondrial Population in Chlamydomonas reinhardii. Planta 150, 236–241.

Blazquez-Llorca, L., Hummel, E., Zimmerman, H., Zou, C., Burgold, S., Rietdorf, J., Herms, J., 2015. Correlation of two-photon in vivo imaging and FIB/SEM microscopy. J. Microsc. 259, 129–136. https://doi.org/10.1111/jmi.12231

Blum, 1893. Formol als Conservierungsflüssigkeit, 16th ed. Zool Anz.

Bodenberger, N., Kubiczek, D., Trösch, L., Gawanbacht, A., Wilhelm, S., Tielker, D., Rosenau, F., 2017. Lectin-mediated reversible immobilization of human cells into a glycosylated macroporous protein hydrogel as a cell culture matrix. Sci. Rep. 7, 6151. https://doi.org/10.1038/s41598-017-06240-w

Boer, P. de, Hoogenboom, J.P., Giepmans, B.N.G., 2015. Correlated light and electron microscopy: ultrastructure lights up! Nat. Methods 12, 503–513. https://doi.org/10.1038/nmeth.3400

Booth, D.G., Beckett, A.J., Molina, O., Samejima, I., Masumoto, H., Kouprina, N., Larionov, V., Prior, I.A., Earnshaw, W.C., 2016. 3D-CLEM Reveals that a Major Portion of Mitotic Chromosomes Is Not Chromatin. Mol. Cell 64, 790–802. https://doi.org/10.1016/j.molcel.2016.10.009

Boyde, A., 1991. Correlative microscopy in biology. Instrumentation and methods Edited by M. A. Hayat Academic Press, Orlando (1987) 432 pp + xiv $59 ISBN 0- 12-333922-7. Scanning 13, 200–200. https://doi.org/10.1002/sca.4950130206

Brass, L.F., Zhu, L., Stalker, T.J., 2005. Minding the gaps to promote thrombus growth and stability. J. Clin. Invest. 115, 3385–3392. https://doi.org/10.1172/JCI26869

Broglie, L.D., 1925. Recherches sur la théorie des Quanta. Ann. Phys. 10, 22–128. https://doi.org/10.1051/anphys/192510030022

Bullen, A., Taylor, R.R., Kachar, B., Moores, C., Fleck, R.A., Forge, A., 2014. Inner ear tissue preservation by rapid freezing: improving fixation by high-pressure freezing and hybrid methods. Hear. Res. 315, 49–60. https://doi.org/10.1016/j.heares.2014.06.006

Carmena, M., Wheelock, M., Funabiki, H., Earnshaw, W.C., 2012. The Chromosomal Passenger Complex (CPC): From Easy Rider to the Godfather of Mitosis. Nat. Rev. Mol. Cell Biol. 13, 789–803. https://doi.org/10.1038/nrm3474

Cattermole, M.J.G., Wolfe, A.F., 1987. Horace Darwin's shop: a history of the Cambridge Scientific Instrument Company, 1878 to 1968. A. Hilger.

Colanzi, A., Sütterlin, C., 2013. Signaling at the Golgi During Mitosis. Methods Cell Biol. 118, 383–400. https://doi.org/10.1016/B978-0-12-417164-0.00023-9

Cretoiu, D., Gherghiceanu, M., Hummel, E., Zimmermann, H., Simionescu, O., Popescu, L.M., 2015. FIB-SEM tomography of human skin telocytes and their extracellular vesicles. J. Cell. Mol. Med. 19, 714–722. https://doi.org/10.1111/jcmm.12578

Darehshouri, A., Lütz-Meindl, U., 2010. H2O2 localization in the green alga Micrasterias after salt and osmotic stress by TEM-coupled electron energy loss spectroscopy. Protoplasma 239, 49–56. https://doi.org/10.1007/s00709-009-0081-4

de Bruijn, W.C., 1973. Glycogen, its chemistry and morphologic appearance in the electron microscope: I. A modified OsO4 fixative which selectively contrasts glycogen. J. Ultrastruct. Res. 42, 29–50. https://doi.org/10.1016/S0022-5320(73)80004-8

Deerinck, T., Bushong, E., Lev-Ram, V., Shu, X., Tsien, R., Ellisman, M., 2010. Enhancing Serial Block-Face Scanning Electron Microscopy to Enable High Resolution 3-D Nanohistology of Cells and Tissues. Microsc. Microanal. 16, 1138–1139. https://doi.org/10.1017/S1431927610055170

DeKosky, S.T., Scheff, S.W., 1990. Synapse loss in frontal cortex biopsies in Alzheimer's disease: Correlation with cognitive severity. Ann. Neurol. 27, 457–464. https://doi.org/10.1002/ana.410270502

Demetriou, G., Neonaki, C., Navakoudis, E., Kotzabasis, K., 2007. Salt stress impact on the molecular structure and function of the photosynthetic apparatus—The protective role of polyamines. Biochim. Biophys. Acta BBA - Bioenerg. 1767, 272–280. https://doi.org/10.1016/j.bbabio.2007.02.020

Denk, W., Horstmann, H., 2004a. Serial block-face scanning electron microscopy to reconstruct three-dimensional tissue nanostructure. PLoS Biol. 2, e329. https://doi.org/10.1371/journal.pbio.0020329

Denk, W., Strickler, J.H., Webb, W.W., 1990. Two-photon laser scanning fluorescence microscopy. Science 248, 73–76.

Diblíková, P., Veselý, M., Sysel, P., Čapek, P., 2018. Reconstructing the microstructure of polyimide-silicalite mixed-matrix membranes and their particle connectivity using FIB-SEM tomography. J. Microsc. 269, 230–246. https://doi.org/10.1111/jmi.12618

Dippel, L., 1882. Das Mikroskop und seine Anwendung. Vieweg.

Dohnalkova, A., Kennedy, D., Mancuso, J., Marshall, M., Mainwaring, P., Fredrickson, J., 2010. High-Throughput 3D Visualization of Large Volumes at High Resolution by 3ViewTM. Microsc. Microanal. 16, 1870–1871. https://doi.org/10.1017/S1431927610058605

Domart, M.-C., Hobday, T.M.C., Peddie, C.J., Chung, G.H.C., Wang, A., Yeh, K., Jethwa, N., Zhang, Q., Wakelam, M.J.O., Woscholski, R., Byrne, R.D., Collinson, L.M., Poccia, D.L., Larijani, B., 2012. Acute manipulation of diacylglycerol reveals roles in nuclear envelope assembly & endoplasmic reticulum morphology. PloS One 7, e51150. https://doi.org/10.1371/journal.pone.0051150

Dubrovsky, A., Sorrentino, S., Harapin, J., Sapra, K.T., Medalia, O., 2015. Developments in cryo-electron tomography for in situ structural analysis. Arch. Biochem. Biophys., Electron Microscopy in Structural Biology 581, 78–85. https://doi.org/10.1016/j.abb.2015.04.006

Eberle, A., MIKULA, S., SCHALEK, R., LICHTMAN, J., TATE, M.K., ZEIDLER, D., 2015. High-resolution, high-throughput imaging with a multibeam scanning electron microscope. J. Microsc. 259, 114–120. https://doi.org/10.1111/jmi.12224

Eckly, A., Rinckel, J.-Y., Proamer, F., Ulas, N., Joshi, S., Whiteheart, S.W., Gachet, C., 2016. Respective contributions of single and compound granule fusion to secretion by activated platelets. Blood 128, 2538–2549. https://doi.org/10.1182/blood-2016-03-705681

Ehrlich, P., 1878. Beiträge zur Theorie und Praxis der histologischen Färbung. Test (Hrsg.), I. Teil: Die chemische Auffassung der Färbung. II. Teil: Die Anilinfarben in chemischer, technologischer und histologischer Beziehung Dissertation.

Farese, R.V., Walther, T.C., 2009. Lipid Droplets Finally Get a Little R-E-S-P-E-C-T. Cell 139, 855–860. https://doi.org/10.1016/j.cell.2009.11.005

Feng, G., Mellor, R.H., Bernstein, M., Keller-Peck, C., Nguyen, Q.T., Wallace, M., Nerbonne, J.M., Lichtman, J.W., Sanes, J.R., 2000. Imaging neuronal subsets in transgenic mice expressing multiple spectral variants of GFP. Neuron 28, 41–51.

Ferguson, S., Steyer, A.M., Mayhew, T.M., Schwab, Y., Lucocq, J.M., 2017. Quantifying Golgi structure using EM: combining volume-SEM and stereology for higher throughput. Histochem. Cell Biol. 147, 653–669. https://doi.org/10.1007/s00418-017-1564-6

Fermie, J., Liv, N., Ten Brink, C., van Donselaar, E.G., Müller, W.H., Schieber, N.L., Schwab, Y., Gerritsen, H.C., Klumperman, J., 2018. Single organelle dynamics linked to 3D structure by correlative live-cell - 3D electron microscopy. Traffic Cph. Den. https://doi.org/10.1111/tra.12557

Fernandez-Moran, 1954. Method of cutting substances.

Friedman, P.L., Ellisman, M.H., 1981. Enhanced visualization of peripheral nerve and sensory receptors in the scanning electron microscope using cryofracture and osmium-thiocarbohydrazide-osmium impregnation. J. Neurocytol. 10, 111–131.

Fua, P., Knott, G.W., 2015. Modeling brain circuitry over a wide range of scales. Front. Neuroanat. 9, 42. https://doi.org/10.3389/fnana.2015.00042

Gaertner, F., Ahmad, Z., Rosenberger, G., Fan, S., Nicolai, L., Busch, B., Yavuz, G., Luckner, M., Ishikawa-Ankerhold, H., Hennel, R., Benechet, A., Lorenz, M., Chandraratne, S., Schubert, I., Helmer, S., Striednig, B., Stark, K., Janko, M., Böttcher, R.T., Verschoor, A., Leon, C., Gachet, C., Gudermann, T., Schnitzler, M.M. y, Pincus, Z., Iannacone, M., Haas, R., Wanner, G., Lauber, K., Sixt, M., Massberg, S., 2017. Migrating Platelets Are Mechano-scavengers that Collect and Bundle Bacteria. Cell 171, 1368-1382.e23. https://doi.org/10.1016/j.cell.2017.11.001

Gao, Q., Goodman, J.M., 2015. The lipid droplet—a well-connected organelle. Front. Cell Dev. Biol. 3. https://doi.org/10.3389/fcell.2015.00049

Gesner, K., 1551. Conradi Gesneri... Historiae animalium lib. I de quadrupedibus viuiparis... apud Christ. Froschouerum.

Gest, H., 2004. The discovery of microorganisms by Robert Hooke and Antoni van Leeuwenhoek, Fellows of The Royal Society. Notes Rec. R. Soc. 58, 187–201. https://doi.org/10.1098/rsnr.2004.0055

Giddings, T.H., 2003. Freeze-substitution protocols for improved visualization of membranes in high-pressure frozen samples. J. Microsc. 212, 53–61.

Giepmans, B.N.G., 2008. Bridging fluorescence microscopy and electron microscopy. Histochem. Cell Biol. 130, 211–217. https://doi.org/10.1007/s00418-008-0460-5

Glauert, A.M., Glauert, R.H., Rogers, G.E., 1956. A new embedding medium for electron microscopy. Nature 178, 803.

Golding, C.G., Lamboo, L.L., Beniac, D.R., Booth, T.F., 2016. The scanning electron microscope in microbiology and diagnosis of infectious disease. Sci. Rep. 6, 26516. https://doi.org/10.1038/srep26516

Grabenbauer, M., 2012. Correlative light and electron microscopy of GFP. Methods Cell Biol. 111, 117–138. https://doi.org/10.1016/B978-0-12-416026-2.00007-8

Grew, N., 1682. The anatomy of plants : with an idea of a philosophical history of plants : and several other lectures read before the Royal Society / by Nehemiah Grew ... [London] : Printed by W. Rawlins, for the author,.

Hall, D.H., Hartwieg, E., Nguyen, K.C.Q., 2012. Modern electron microscopy methods for C. elegans. Methods Cell Biol. 107, 93–149. https://doi.org/10.1016/B978-0-12-394620-1.00004-7

Hampton, C.M., Strauss, J.D., Ke, Z., Dillard, R.S., Hammonds, J.E., Alonas, E., Desai, T.M., Marin, M., Storms, R.E., Leon, F., Melikyan, G.B., Santangelo, P.J., Spearman, P.W., Wright, E.R., 2017. Correlated fluorescence microscopy and cryo-electron tomography of virus-infected or transfected mammalian cells. Nat. Protoc. 12, 150–167. https://doi.org/10.1038/nprot.2016.168

Harford, C.G., 1957. ELECTRON MICROSCOPY OF HELA CELLS AFTER THE INGESTION OF COLLOIDAL GOLD. J. Cell Biol. 3, 749–756. https://doi.org/10.1083/jcb.3.5.749

Harford, C.G., 1956. ELECTRON MICROSCOPY OF HELA CELLS INFECTED WITH ADENOVIRUSES. J. Exp. Med. 104, 443–454. https://doi.org/10.1084/jem.104.3.443

Harris, H., 2000. The Birth of the Cell. Yale University Press.

Hayat, M.A., 1987. Correlative Microscopy In Biology - 1st Edition [WWW Document]. URL https://www.elsevier.com/books/correlative-microscopy-in-biology/hayat/978-0-12-333922-5 (accessed 5.9.18).

Hayes, T.L., Lindgren, F.T., Gofman, J.W., 1963. A QUANTITATIVE DETERMINATION OF THE OSMIUM TETROXIDE-LIPOPROTEIN INTERACTION. J. Cell Biol. 19, 251–255.

Hell, S.W., Wichmann, J., 1994. Breaking the diffraction resolution limit by stimulated emission: stimulated-emission-depletion fluorescence microscopy. Opt. Lett. 19, 780–782.

Hepler, P.K., 1981. The structure of the endoplasmic reticulum revealed by osmium tetroxide-potassium ferricyanide staining. Eur. J. Cell Biol. 26, 102–111.

Hertwig, O., 1898. Die Zelle und die Gewebe. Grundzüge der Allgemeinen Anatomie und Physiologie. Fischer, Jena,.

Höhn, K., FUCHS, J., FRÖBER, A., KIRMSE, R., GLASS, B., ANDERS-ÖSSWEIN, M., WALTHER, P., KRÄUSSLICH, H. -G., DIETRICH, C., 2015. Preservation of protein fluorescence in embedded human dendritic cells for targeted 3D light and electron microscopy. J. Microsc. 259, 121–128. https://doi.org/10.1111/jmi.12230

Hooke, R., 1665. *Micrographia*. Wikipedia.

Hua, Y., Laserstein, P., Helmstaedter, M., 2015. Large-volume en-bloc staining for electron microscopy-based connectomics. Nat. Commun. 6, 7923. https://doi.org/10.1038/ncomms8923

Hübner, K., 2006. 150 Jahre Mauvein. Chem. Unserer Zeit 40, 274–275. https://doi.org/10.1002/ciuz.200690054

Hughes, H., Stephens, D.J., 2008. Assembly, organization, and function of the COPII coat. Histochem. Cell Biol. 129, 129–151. https://doi.org/10.1007/s00418-007-0363-x

Irobalieva, R.N., Martins, B., Medalia, O., 2016. Cellular structural biology as revealed by cryo-electron tomography. J Cell Sci 129, 469–476. https://doi.org/10.1242/jcs.171967

Jackson, S.P., 2011. Arterial thrombosis—insidious, unpredictable and deadly. Nat. Med. 17, 1423–1436. https://doi.org/10.1038/nm.2515

Jen, A.C., Wake, M.C., Mikos, A.G., 1996. Review: Hydrogels for cell immobilization. Biotechnol. Bioeng. 50, 357–364. https://doi.org/10.1002/(SICI)1097-0290(19960520)50:4<357::AID-BIT2>3.0.CO;2-K

Jogler, C., Wanner, G., Kolinko, S., Niebler, M., Amann, R., Petersen, N., Kube, M., Reinhardt, R., Schüler, D., 2011. Conservation of proteobacterial magnetosome genes and structures in an uncultivated member of the deep-branching Nitrospira phylum. Proc. Natl. Acad. Sci. 108, 1134–1139. https://doi.org/10.1073/pnas.1012694108

Karnovsky, M.J., 1971. Use of ferrocyanide reduced osmium tetroxide in electron microscopy. Proc 14th Ann Meet Am SOLCell Biol, p. 146a.

Karreman, M.A., Hyenne, V., Schwab, Y., Goetz, J.G., 2016. Intravital Correlative Microscopy: Imaging Life at the Nanoscale. Trends Cell Biol. 26, 848–863. https://doi.org/10.1016/j.tcb.2016.07.003

Kemen, T., Garbowski, T., Zeidler, D., 2015. Multi-beam SEM technology for ultra-high throughput, in: Yoshioka, N. (Ed.), . p. 965807. https://doi.org/10.1117/12.2195705

Kerr, J.N.D., Denk, W., 2008. Imaging *in vivo*: watching the brain in action. Nat. Rev. Neurosci. 9, 195–205. https://doi.org/10.1038/nrn2338

Kim, D.-H., Provenzano, P.P., Smith, C.L., Levchenko, A., 2012. Matrix nanotopography as a regulator of cell function. J Cell Biol 197, 351–360. https://doi.org/10.1083/jcb.201108062

Kizilyaprak, Caroline, Bittermann, A.G., Daraspe, J., Humbel, B.M., 2014. FIB-SEM tomography in biology. Methods Mol. Biol. Clifton NJ 1117, 541–558. https://doi.org/10.1007/978-1-62703-776-1_24

Kizilyaprak, C., Daraspe, J., Humbel, B.M., 2014. Focused ion beam scanning electron microscopy in biology. J. Microsc. 254, 109–114. https://doi.org/10.1111/jmi.12127

Kizilyaprak, C., Longo, G., Daraspe, J., Humbel, B.M., 2015. Investigation of resins suitable for the preparation of biological sample for 3-D electron microscopy. J. Struct. Biol. 189, 135–146. https://doi.org/10.1016/j.jsb.2014.10.009

Koga, D., Ushiki, T., Watanabe, T., 2017. Novel scanning electron microscopy methods for analyzing the 3D structure of the Golgi apparatus. Anat. Sci. Int. 92, 37–49. https://doi.org/10.1007/s12565-016-0380-8

Koning, R.I., Celler, K., Willemse, J., Bos, E., van Wezel, G.P., Koster, A.J., 2014. Correlative Cryo-Fluorescence Light Microscopy and Cryo-Electron Tomography of Streptomyces, in: Methods in Cell Biology. Elsevier, pp. 217–239. https://doi.org/10.1016/B978-0-12-801075-4.00010-0

Korogod, N., Petersen, C.C., Knott, G.W., 2015. Ultrastructural analysis of adult mouse neocortex comparing aldehyde perfusion with cryo fixation. eLife 4, e05793. https://doi.org/10.7554/eLife.05793

Kurasawa, Y., Earnshaw, W.C., Mochizuki, Y., Dohmae, N., Todokoro, K., 2004. Essential roles of KIF4 and its binding partner PRC1 in organized central spindle midzone formation. EMBO J. 23, 3237–3248. https://doi.org/10.1038/sj.emboj.7600347

Kurtzman, C.P., Baker, F.L., Smiley, M.J., 1974. Specimen Holder to Critical-Point Dry Microorganisms for Scanning Electron Microscopy. Appl. Microbiol. 28, 708–712.

Ladinsky, M.S., Mastronarde, D.N., McIntosh, J.R., Howell, K.E., Staehelin, L.A., 1999. Golgi structure in three dimensions: functional insights from the normal rat kidney cell. J. Cell Biol. 144, 1135–1149.

Lamvik, M.K., Magid, A.D., Davilla, S.D., Córdova, L., 1991. Temperature directly affects the rate of irradiation-induced mass loss from phosphatidylcholine multilayers. Ultramicroscopy 35, 351–356.

Latta, H., Hartmann, J.F., 1950. Use of a Glass Edge in Thin Sectioning for Electron Microscopy. Proc. Soc. Exp. Biol. Med. 74, 436–439. https://doi.org/10.3181/00379727-74-17931

Ledbetter, M.C., Porter, K.R., 1963. A “MICROTUBULE” IN PLANT CELL FINE STRUCTURE. J. Cell Biol. 19, 239–250.

Lees, R.M., Peddie, C.J., Collinson, L.M., Ashby, M.C., Verkade, P., 2017. Correlative two-photon and serial block face scanning electron microscopy in neuronal tissue using 3D near-infrared branding maps. Methods Cell Biol. 140, 245–276. https://doi.org/10.1016/bs.mcb.2017.03.007

Levin, R.J., 2013. The Living Barrier: A Primer on Transfer across Biological Membranes. Butterworth-Heinemann.

Lin, J., Wang, Y., Wang, G., 2006. Salt stress-induced programmed cell death in tobacco protoplasts is mediated by reactive oxygen species and mitochondrial permeability transition pore status. J. Plant Physiol. 163, 731–739. https://doi.org/10.1016/j.jplph.2005.06.016

Linde, S. van de, Löschberger, A., Klein, T., Heidbreder, M., Wolter, S., Heilemann, M., Sauer, M., 2011. Direct stochastic optical reconstruction microscopy with standard fluorescent probes. Nat. Protoc. 6, 991–1009. https://doi.org/10.1038/nprot.2011.336

Logan, D.C., 2007. The mitochondrial compartment. J. Exp. Bot. 58, 1225–1243.

Lommel, E., 1888. The Nature of Light, with a General Account of Physical Optics. King.

Long, F., Zhou, J., Peng, H., 2012. Visualization and Analysis of 3D Microscopic Images. PLoS Comput. Biol. 8. https://doi.org/10.1371/journal.pcbi.1002519

Loussert Fonta, C., Humbel, B.M., 2015. Correlative microscopy. Arch. Biochem. Biophys., Electron Microscopy in Structural Biology 581, 98–110. https://doi.org/10.1016/j.abb.2015.05.017

Lu, L., Ladinsky, M.S., Kirchhausen, T., 2011. Formation of the postmitotic nuclear envelope from extended ER cisternae precedes nuclear pore assembly. J. Cell Biol. 194, 425–440. https://doi.org/10.1083/jcb.201012063

Lu, L., Ladinsky, M.S., Kirchhausen, T., 2009. Cisternal organization of the endoplasmic reticulum during mitosis. Mol. Biol. Cell 20, 3471–3480. https://doi.org/10.1091/mbc.E09-04-0327

Lucas, M.S., Günthert, M., Bittermann, A.G., de Marco, A., Wepf, R., 2017. Correlation of live-cell imaging with volume scanning electron microscopy. Methods Cell Biol. 140, 123–148. https://doi.org/10.1016/bs.mcb.2017.03.001

Luckner, M., Burgold, S., Filser, S., Scheungrab, M., Niyaz, Y., Hummel, E., Wanner, G., Herms, J., 2018. Label-free 3D-CLEM using endogenous tissue landmarks. iScience.

Luckner, M., Wanner, G., 2018. Precise and economic FIB/SEM for CLEM: with 2 nm voxels through mitosis. Histochem. Cell Biol. https://doi.org/10.1007/s00418-018-1681-x

Luckner, M., Wanner, G., 2018a. From light microscopy to analytical SEM and FIB/SEM in biology: Fixed Coordinates, Flat Embedding, Absolute References. Microsc. Microanal.

Luft, J.H., 1956. Permanganate; a new fixative for electron microscopy. J. Biophys. Biochem. Cytol. 2, 799–802.

Lütz-Meindl, U., 2016. Micrasterias as a Model System in Plant Cell Biology. Front. Plant Sci. 7. https://doi.org/10.3389/fpls.2016.00999

Lütz-Meindl, U., Luckner, M., Andosch, A., Wanner, G., 2016. Structural stress responses and degradation of dictyosomes in algae analysed by TEM and FIB-SEM tomography. J. Microsc. 263, 129–141. https://doi.org/10.1111/jmi.12369

Maco, B., Holtmaat, A., Cantoni, M., Kreshuk, A., Straehle, C.N., Hamprecht, F.A., Knott, G.W., 2013. Correlative in vivo 2 photon and focused ion beam scanning electron microscopy of cortical neurons. PloS One 8, e57405. https://doi.org/10.1371/journal.pone.0057405

Magner, L.N., 2002. A History of the Life Sciences, Revised and Expanded. CRC Press.

Malhas, A., Goulbourne, C., Vaux, D.J., 2011. The nucleoplasmic reticulum: form and function. Trends Cell Biol. 21, 362–373. https://doi.org/10.1016/j.tcb.2011.03.008

Marie, M., Dale, H.A., Kouprina, N., Saraste, J., 2012. Division of the intermediate compartment at the onset of mitosis provides a mechanism for Golgi inheritance. J. Cell Sci. 125, 5403–5416. https://doi.org/10.1242/jcs.108100

Marsh, B.J., Pavelka, M., 2013. Viewing Golgi structure and function from a different perspective--insights from electron tomography. Methods Cell Biol. 118, 259–279. https://doi.org/10.1016/B978-0-12-417164-0.00016-1

Marx, V., 2013. Neurobiology: Brain mapping in high resolution. Nature 503, 147–152. https://doi.org/10.1038/503147a

Meissner, D.H., Schwarz, H., 1990. Improved cryoprotection and freeze-substitution of embryonic quail retina: A tem study on ultrastructural preservation. J. Electron Microsc. Tech. 14, 348–356. https://doi.org/10.1002/jemt.1060140410

Mikula, S., 2016. Progress Towards Mammalian Whole-Brain Cellular Connectomics. Front. Neuroanat. 10. https://doi.org/10.3389/fnana.2016.00062

Mikula, S., Binding, J., Denk, W., 2012. Staining and embedding the whole mouse brain for electron microscopy. Nat. Methods 9, 1198–1201. https://doi.org/10.1038/nmeth.2213

Mogelsvang, S., Marsh, B.J., Ladinsky, M.S., Howell, K.E., 2004. Predicting function from structure: 3D structure studies of the mammalian Golgi complex. Traffic Cph. Den. 5, 338–345. https://doi.org/10.1111/j.1398-9219.2004.00186.x

Moor, H., 1987. Theory and Practice of High Pressure Freezing, in: Cryotechniques in Biological Electron Microscopy. Springer, Berlin, Heidelberg, pp. 175–191. https://doi.org/10.1007/978-3-642-72815-0_8

Mora-Bermúdez, F., Gerlich, D., Ellenberg, J., 2007. Maximal chromosome compaction occurs by axial shortening in anaphase and depends on Aurora kinase. Nat. Cell Biol. 9, 822–831. https://doi.org/10.1038/ncb1606

Murphy, G.E., Narayan, K., Lowekamp, B.C., Hartnell, L.M., Heymann, J.A.W., Fu, J., Subramaniam, S., 2011. Correlative 3D imaging of whole mammalian cells with light and electron microscopy. J. Struct. Biol. 176, 268–278. https://doi.org/10.1016/j.jsb.2011.08.013

Narayan, K., Subramaniam, S., 2015. Focused ion beams in biology. Nat. Methods 12, 1021–1031. https://doi.org/10.1038/nmeth.3623

Neuman, K.M., Molina-Campos, E., Musial, T.F., Price, A.L., Oh, K.-J., Wolke, M.L., Buss, E.W., Scheff, S.W., Mufson, E.J., Nicholson, D.A., 2015. Evidence for Alzheimer's disease-linked synapse loss and compensation in mouse and human hippocampal CA1 pyramidal neurons. Brain Struct. Funct. 220, 3143–3165. https://doi.org/10.1007/s00429-014-0848-z

Nieswandt, B., Schulte, V., Zywietz, A., Gratacap, M.-P., Offermanns, S., 2002. Costimulation of Gi- and G12/G13-mediated signaling pathways induces integrin alpha IIbbeta 3 activation in platelets. J. Biol. Chem. 277, 39493–39498. https://doi.org/10.1074/jbc.M207256200

Nixon, F.M., Gutiérrez-Caballero, C., Hood, F.E., Booth, D.G., Prior, I.A., Royle, S.J., n.d. The mesh is a network of microtubule connectors that stabilizes individual kinetochore fibers of the mitotic spindle. eLife 4. https://doi.org/10.7554/eLife.07635

Nixon, F.M., Honnor, T.R., Clarke, N.I., Starling, G.P., Beckett, A.J., Johansen, A.M., Brettschneider, J.A., Prior, I.A., Royle, S.J., 2017. Microtubule organization within mitotic spindles revealed by serial block face scanning electron microscopy and image analysis. J Cell Sci 130, 1845–1855. https://doi.org/10.1242/jcs.203877

Nussdorfer, P., Cilenšek, I., Zorn, B., Petrovič, D., 2018. Adapted methods for scanning electron microscopy (SEM) in assessment of human sperm morphology. Bosn. J. Basic Med. Sci. 18, 43–48. https://doi.org/10.17305/bjbms.2017.2173

Ortiz-Hidalgo, C., 1992. Pol André Bouin, MD (1870-1962). Bouin's fixative and other contributions to medicine. Arch. Pathol. Lab. Med. 116, 882–884.

Palade, G.E., 1952. A study of fixation for electron microscopy. J. Exp. Med. 95, 285–298.

Pandey, N., Hakamivala, A., Xu, C., Hariharan, P., Radionov, B., Huang, Z., Liao, J., Tang, L., Zimmern, P., Nguyen, K.T., Hong, Y., 2018. Biodegradable Nanoparticles Enhanced Adhesiveness of Mussel-Like Hydrogels at Tissue Interface. Adv. Healthc. Mater. 7, e1701069. https://doi.org/10.1002/adhm.201701069

Peddie, C.J., Blight, K., Wilson, E., Melia, C., Marrison, J., Carzaniga, R., Domart, M.-C., O'Toole, P., Larijani, B., Collinson, L.M., 2014. Correlative and integrated light and electron microscopy of in-resin GFP fluorescence, used to localise diacylglycerol in mammalian cells. Ultramicroscopy, SI: Correlative Microscopy 143, 3–14. https://doi.org/10.1016/j.ultramic.2014.02.001

Peddie, C.J., Collinson, L.M., 2014. Exploring the third dimension: volume electron microscopy comes of age. Micron Oxf. Engl. 1993 61, 9–19. https://doi.org/10.1016/j.micron.2014.01.009

Podoplelova, N.A., Sveshnikova, A.N., Kotova, Y.N., Eckly, A., Receveur, N., Nechipurenko, D.Y., Obydennyi, S.I., Kireev, I.I., Gachet, C., Ataullakhanov, F.I., Mangin, P.H., Panteleev, M.A., 2016. Coagulation factors bound to procoagulant platelets concentrate in cap structures to promote clotting. Blood 128, 1745–1755. https://doi.org/10.1182/blood-2016-02-696898

Porter, K.R., Kallman, F., 1953. The properties and effects of osmium tetroxide as a tissue fixative with special reference to its use for electron microscopy. Exp. Cell Res. 4, 127–141. https://doi.org/10.1016/0014-4827(53)90195-5

Puhka, M., Joensuu, M., Vihinen, H., Belevich, I., Jokitalo, E., 2012. Progressive sheet-to-tubule transformation is a general mechanism for endoplasmic reticulum partitioning in dividing mammalian cells. Mol. Biol. Cell 23, 2424–2432. https://doi.org/10.1091/mbc.E10-12-0950

Ranftler, C., Meisslitzer-Ruppitsch, C., Neumüller, J., Ellinger, A., Pavelka, M., 2017. Golgi apparatus dis- and reorganizations studied with the aid of 2-deoxy-d-glucose and visualized by 3D-electron tomography. Histochem. Cell Biol. 147, 415–438. https://doi.org/10.1007/s00418-016-1515-7

Raven, C.E., 2010. English Naturalists from Neckam to Ray: A Study of the Making of the Modern World. Cambridge University Press.

Reape, T.J., McCabe, P.F., 2008. Apoptotic-like programmed cell death in plants. New Phytol. 180, 13–26. https://doi.org/10.1111/j.1469-8137.2008.02549.x

Recknor, J.B.J.B., Recknor, J.C.J.C., Sakaguchi, D.S.D.S., Mallapragada, S.K.S.K., 2004. Oriented astroglial cell growth on micropatterned polystyrene substrates. Biomaterials 25, 2753–2767. https://doi.org/10.1016/j.biomaterials.2003.11.045

Reimer, L., 1998. Scanning Electron Microscopy: Physics of Image Formation and Microanalysis, 2nd ed, Springer Series in Optical Sciences. Springer-Verlag, Berlin Heidelberg.

Rennie, M.Y., Gahan, C.G., López, C.S., Thornburg, K.L., Rugonyi, S., 2014. 3D imaging of the early embryonic chicken heart with focused ion beam scanning electron microscopy. Microsc. Microanal. Off. J. Microsc. Soc. Am. Microbeam Anal. Soc. Microsc. Soc. Can. 20, 1111–1119. https://doi.org/10.1017/S1431927614000828

Ruska, E., 1934. Über ein magnetisches Objektiv für das Elektronenmikroskop. Vieweg, Braunschweig.

Rust, M.J., Bates, M., Zhuang, X., 2006. Sub-diffraction-limit imaging by stochastic optical reconstruction microscopy (STORM). Nat. Methods 3, 793–795. https://doi.org/10.1038/nmeth929

Ruthensteiner, B., Baeumler, N., Barnes, D.G., 2010. Interactive 3D volume rendering in biomedical publications. Micron 41, 886.e1-886.e17. https://doi.org/10.1016/j.micron.2010.03.010

Ruthensteiner, B., Hess, M., 2008. Embedding 3D models of biological specimens in PDF publications. Microsc. Res. Tech. 71, 778–786. https://doi.org/10.1002/jemt.20618

Sabatini, D.D., Bensch, K., Barrnett, R.J., 1963. Cytochemistry and electron microscopy. The preservation of cellular ultrastructure and enzymatic activity by aldehyde fixation. J. Cell Biol. 17, 19–58.

Sahai, S., Wilkerson, M., Zaske, A.M., Olson, S.D., Cox, C.S., Triolo, F., 2016. A cost-effective method to immobilize hydrated soft-tissue samples for atomic force microscopy. BioTechniques 61, 206–209. https://doi.org/10.2144/000114461

Santoro, F., Zhao, W., Joubert, L.-M., Duan, L., Schnitker, J., van de Burgt, Y., Lou, H.-Y., Liu, B., Salleo, A., Cui, L., Cui, Y., Cui, B., 2017. Revealing the Cell-Material Interface with Nanometer Resolution by Focused Ion Beam/Scanning Electron Microscopy. ACS Nano 11, 8320–8328. https://doi.org/10.1021/acsnano.7b03494

Schalek, R., Kasthuri, N., Hayworth, K., Berger, D., Tapia, J., Morgan, J., Turaga, S., Fagerholm, E., Seung, H., Lichtman, J., 2011. Development of High-Throughput, High-Resolution 3D Reconstruction of Large-Volume Biological Tissue Using Automated Tape Collection Ultramicrotomy and Scanning Electron Microscopy. Microsc. Microanal. 17, 966–967. https://doi.org/10.1017/S1431927611005708

Schieber, N.L., Machado, P., Markert, S.M., Stigloher, C., Schwab, Y., Steyer, A.M., 2017. Minimal resin embedding of multicellular specimens for targeted FIB-SEM imaging. Methods Cell Biol. 140, 69–83. https://doi.org/10.1016/bs.mcb.2017.03.005

Schlegel, P., Costa, M., Jefferis, G.S., 2017. Learning from connectomics on the fly. Curr. Opin. Insect Sci., Neuroscience * Pheromones 24, 96–105. https://doi.org/10.1016/j.cois.2017.09.011

Schorb, M., Briggs, J.A.G., 2014. Correlated cryo-fluorescence and cryo-electron microscopy with high spatial precision and improved sensitivity. Ultramicroscopy, SI: Correlative Microscopy 143, 24–32. https://doi.org/10.1016/j.ultramic.2013.10.015

Schötz, F., 1972. Dreidimensionale, maßstabgetreue Rekonstruktion einer grünen Flagellatenzelle nach Elektronenmikroskopie von Serienschnitten. Planta 102, 152–159.

Schötz, F., Bathelt, H., Arnold, C.-G., Schimmer, O., 1972. Die Architektur und Organisation der<Emphasis Type="Italic">Chlamydomonas</Emphasis>-Zelle. Protoplasma 75, 229–254. https://doi.org/10.1007/BF01279818

Schroeder-Reiter, E., Sanei, M., Houben, A., Wanner, G., 2012. Current SEM techniques for de- and re-construction of centromeres to determine 3D CENH3 distribution in barley mitotic chromosomes. J. Microsc. 246, 96–106. https://doi.org/10.1111/j.1365-2818.2011.03592.x

Schwann, T., 1839. Mikroskopische Untersuchungen über die Uebereinstimmung in der Struktur und dem Wachsthum der Thiere und Pflanzen. Sander.

Schwarz, H., Humbel, B.M., 2007. Correlative light and electron microscopy using immunolabeled resin sections. Methods Mol. Biol. Clifton NJ 369, 229–256. https://doi.org/10.1007/978-1-59745-294-6_12

Seligman, A.M., Wasserkrug, H.L., Hanker, J.S., 1966. A new staining method (OTO) for enhancing contrast of lipid--containing membranes and droplets in osmium tetroxide--fixed tissue with osmiophilic thiocarbohydrazide(TCH). J. Cell Biol. 30, 424–432.

Skaloud, P., Nemjová, K., Kulichová, J., Černá, K., Neustupa, J., 2011. A multilocus phylogeny of the desmid genus Micrasterias (Streptophyta): Evidence for the accelerated rate of morphological evolution in protists. Mol. Phylogenet. Evol. 61, 933–43. https://doi.org/10.1016/j.ympev.2011.08.018

Skulachev, V.P., 2001. Mitochondrial filaments and clusters as intracellular power-transmitting cables. Trends Biochem. Sci. 26, 23–29. https://doi.org/10.1016/S0968-0004(00)01735-7

Smoyer, C.J., Jaspersen, S.L., 2014. Breaking down the wall: the nuclear envelope during mitosis. Curr. Opin. Cell Biol. 26, 1–9. https://doi.org/10.1016/j.ceb.2013.08.002

Staehelin, L.A., Kang, B.-H., 2008. Nanoscale architecture of endoplasmic reticulum export sites and of Golgi membranes as determined by electron tomography. Plant Physiol. 147, 1454–1468. https://doi.org/10.1104/pp.108.120618

Starborg, T., Kalson, N.S., Lu, Y., Mironov, A., Cootes, T.F., Holmes, D.F., Kadler, K.E., 2013. Using transmission electron microscopy and 3View® to determine collagen fibril size and three-dimensional organization. Nat. Protoc. 8, 1433–1448. https://doi.org/10.1038/nprot.2013.086

Steiner, P., Luckner, M., Kerschbaum, H., Wanner, G., Lütz-Meindl, U., 2018. Ionic stress induces fusion of mitochondria to 3-D networks: an electron tomography study. J. Struct. Biol. https://doi.org/10.1016/j.jsb.2018.06.010

Stillwell, W., 2016. An Introduction to Biological Membranes: Composition, Structure and Function. Elsevier.

Talens, L.T., Miranda, M., Miller, M.W., 1973. Electron Micrography of Bud Formation in Metschnikowia krissii. J. Bacteriol. 114, 413–423.

Tapia, J.C., Kasthuri, N., Hayworth, K., Schalek, R., Lichtman, J.W., Smith, S.J., Buchanan, J., 2012. High contrast en bloc staining of neuronal tissue for field emission scanning electron microscopy. Nat. Protoc. 7, 193–206. https://doi.org/10.1038/nprot.2011.439

van Nispen tot Pannerden, H., de Haas, F., Geerts, W., Posthuma, G., van Dijk, S., Heijnen, H.F.G., 2010. The platelet interior revisited: electron tomography reveals tubular -granule subtypes. Blood 116, 1147–1156. https://doi.org/10.1182/blood-2010-02-268680

Verkade, P., 2008. Moving EM: the Rapid Transfer System as a new tool for correlative light and electron microscopy and high throughput for high-pressure freezing. J. Microsc. 230, 317–328. https://doi.org/10.1111/j.1365-2818.2008.01989.x

Villinger, C., Gregorius, H., Kranz, C., Höhn, K., Münzberg, C., von Wichert, G., Mizaikoff, B., Wanner, G., Walther, P., 2012. FIB/SEM tomography with TEM-like resolution for 3D imaging of high-pressure frozen cells. Histochem. Cell Biol. 138, 549–556. https://doi.org/10.1007/s00418-012-1020-6

Volland, S., Lütz, C., Michalke, B., Lütz-Meindl, U., 2012. Intracellular chromium localization and cell physiological response in the unicellular alga Micrasterias. Aquat. Toxicol. Amst. Neth. 109, 59–69. https://doi.org/10.1016/j.aquatox.2011.11.013

Wacker, I., Schroeder, R.R., 2013. Array tomography. J. Microsc. 252, 93–99. https://doi.org/10.1111/jmi.12087

Wacker, I., Spomer, W., Hofmann, A., Thaler, M., Hillmer, S., Gengenbach, U., Schröder, R.R., 2016. Hierarchical imaging: a new concept for targeted imaging of large volumes from cells to tissues. BMC Cell Biol. 17. https://doi.org/10.1186/s12860-016-0122-8

Wagner, J., Schaffer, M., Fernández-Busnadiego, R., 2017. Cryo-electron tomography—the cell biology that came in from the cold. FEBS Lett. 591, 2520–2533. https://doi.org/10.1002/1873-3468.12757

Wang, Y., Seemann, J., 2011. Golgi biogenesis. Cold Spring Harb. Perspect. Biol. 3, a005330. https://doi.org/10.1101/cshperspect.a005330

Wanner, A.A., Kirschmann, M.A., Genoud, C., 2015. Challenges of microtome-based serial block-face scanning electron microscopy in neuroscience. J. Microsc. 259, 137–142. https://doi.org/10.1111/jmi.12244

Wanner, G., Formanek, H., Theimer, R.R., 1981. The ontogeny of lipid bodies (spherosomes) in plant cells : Ultrastructural evidence. Planta 151, 109–123. https://doi.org/10.1007/BF00387812

Wanner, G., Köst, H.-P., 1984. «Membrane Storage» of the Red Alga Porphyridium cruentum During Nitrate- and Sulphate Starvation. Z. Für Pflanzenphysiol. 113, 251–262. https://doi.org/10.1016/S0044-328X(84)80006-9

Wanner, G., Schäfer, T., Lütz-Meindl, U., 2013. 3-D analysis of dictyosomes and multivesicular bodies in the green alga Micrasterias denticulata by FIB/SEM tomography. J. Struct. Biol. 184, 203–211. https://doi.org/10.1016/j.jsb.2013.10.003

Wanner, G., Vogl, K., Overmann, J., 2008. Ultrastructural Characterization of the Prokaryotic Symbiosis in “Chlorochromatium aggregatum.” J. Bacteriol. 190, 3721–3730. https://doi.org/10.1128/JB.00027-08

Wei, J.-H., Seemann, J., 2009. Mitotic division of the mammalian Golgi apparatus. Semin. Cell Dev. Biol. 20, 810–816. https://doi.org/10.1016/j.semcdb.2009.03.010

Willingham, M.C., Rutherford, A.V., 1984. The use of osmium-thiocarbohydrazide-osmium (OTO) and ferrocyanide-reduced osmium methods to enhance membrane contrast and preservation in cultured cells. J. Histochem. Cytochem. Off. J. Histochem. Soc. 32, 455–460. https://doi.org/10.1177/32.4.6323574

Xu, C.S., Hayworth, K.J., Lu, Z., Grob, P., Hassan, A.M., García-Cerdán, J.G., Niyogi, K.K., Nogales, E., Weinberg, R.J., Hess, H.F., 2017. Enhanced FIB-SEM systems for large-volume 3D imaging. eLife 6. https://doi.org/10.7554/eLife.25916

Yang, W., Yuste, R., 2017. In vivo imaging of neural activity. Nat. Methods 14, 349–359. https://doi.org/10.1038/nmeth.4230

Zhmurov, A., Brown, A.E.X., Litvinov, R.I., Dima, R.I., Weisel, J.W., Barsegov, V., 2011. Mechanism of Fibrin(ogen) Forced Unfolding. Structure 19, 1615–1624. https://doi.org/10.1016/j.str.2011.08.013

Zhmurov, A., Protopopova, A.D., Litvinov, R.I., Zhukov, P., Mukhitov, A.R., Weisel, J.W., Barsegov, V., 2016. Structural Basis of Interfacial Flexibility in Fibrin Oligomers. Structure 24, 1907–1917. https://doi.org/10.1016/j.str.2016.08.009

10 Appendices

10.1 Publication I

From light microscopy to analytical SEM and FIB/SEM in biology: Fixed Coordinates, Flat Embedding, Absolute References.

Manja Luckner & Gerhard Wanner (2018)

Microscopy and Microanalysis, 2018 July (in press)
doi: 10.1017/S1431927618015015

Abstract
A portfolio is presented documenting economic, high resolution correlative LM and SEM, and LM and focused ion beam scanning electron microscopy (FIB/SEM) in routine, comprising: i) the use of custom-labeled slides and coverslips for correlative light and electron microscopy (CLEM); ii) immobilization of cells and tissues onto slides; iii) development of a procedure to fix and embed tissues with a filter system; iv) embedding of cells in thin, or ultra-thin resin layers and v) the application of a stamp for post-embedding labeling.

Note
Accepted manuscript, PDF only. Full online edition to follow.

Microscopy and Microanalysis, page 1 of 19
doi:10.1017/S1431927618015015

Microscopy AND Microanalysis

Original Article

From Light Microscopy to Analytical Scanning Electron Microscopy (SEM) and Focused Ion Beam (FIB)/SEM in Biology: Fixed Coordinates, Flat Embedding, Absolute References

Manja Luckner and Gerhard Wanner

Department Biology I, Ultrastructural Research, Ludwig-Maximilians-University Munich, 82152 Planegg-Martinsried, Germany

Abstract

Correlative light and electron microscopy (CLEM) has been in use for several years, however it has remained a costly method with difficult sample preparation. Here, we report a series of technical improvements developed for precise and cost-effective correlative light and scanning electron microscopy (SEM) and focused ion beam (FIB)/SEM microscopy of single cells, as well as large tissue sections. Customized coordinate systems for both slides and coverslips were established for thin and ultra-thin embedding of a wide range of biological specimens. Immobilization of biological samples was examined with a variety of adhesives. For histological sections, a filter system for flat embedding was developed. We validated ultra-thin embedding on laser marked slides for efficient, high-resolution CLEM. Target cells can be re-located within minutes in SEM without protracted searching and correlative investigations were reduced to a minimum of preparation steps, while still reaching highest resolution. The FIB/SEM milling procedure is facilitated and significantly accelerated as: (i) milling a ramp becomes needless, (ii) significant re-deposition of milled material does not occur; and (iii) charging effects are markedly reduced. By optimizing all technical parameters FIB/SEM stacks with 2 nm iso-voxels were achieved over thousands of sections, in a wide range of biological samples.

Key words: CLEM, EDX, FIB-SEM, flat embedding, tomography

(Received 13 March 2018; revised 5 June 2018; accepted 16 July 2018)

Introduction

For three-dimensional (3D) ultrastructural investigations with electron microscopy (EM), five different techniques are typically used (Fig. 1). Each one of these techniques, however, has significant drawbacks: (i) classical transmission EM (TEM) serial sectioning, which is largely unsuitable for long series, has many drawbacks, such as compression of sections, uneven stretching, folds, knife marks, etc.; (ii) TEM-tomography, although achieving the highest resolution, is limited in section thickness (max. 1 μm); (iii) serial block face sectioning (3View®), a built-in ultramicrotome within a scanning electron microscopy (SEM), is suitable for large volumes but limited in section thickness (20 nm at best) and is hampered by charging; (iv) array tomography, which is non-destructive, but limited in *z*-resolution just as classical serial sectioning; and (v) focused ion beam (FIB)/SEM-tomography, which currently offers by far the highest resolution along the *z* axis with a "section thickness" down to 2 nm for long image series (for review see: Peddie & Collinson, 2014; Romero-Brey & Bartenschlager, 2015; Karreman et al., 2016; Xu et al., 2017). A period of 10 years after FIB/SEM was recognized as a revolutionary tool for 3D-EM in biology, these instruments are widely accepted as expensive, but highly complementary and efficient tools, which are indispensable for ultrastructural studies. However, the analytical potential of the instrument itself, the SEM, is still not fully exploited. Initially, a SEM was simply considered a surface imaging instrument. However, the use of different detectors and the variation of many SEM parameters offer enormous analytical capacities, well beyond surface imaging.

Three different signals can be routinely used for structural and analytical information, as described by Bozzola & Russell (1991). First, the secondary electrons (SE) give the characteristic topography of SEM images. Second, the backscattered electrons (BSE) provide a material contrast and due to their high energy and subsurface information. Third, X-ray detection can be harnessed to analyze the local atomic composition (Scala et al., 1985; Bozzola & Russell, 1991; Utke et al., 2012; Drobne, 2013). These signals can be monitored separately or in combination and are indispensable for SEM and to some extent required for FIB/SEM.

Despite utilizing multiple signals, a correlation of light microscopy (LM) and EM remains challenging. Reference points or fiducial markers are essential to facilitate a correlation, but a universal labeling does not exist, since the requirements vary widely for different experiments. Many years before they were commercially available, we developed slides (= point finder) with

Author for correspondence: Gerhard Wanner, Email: wanner@lrz.uni-muenchen.de
Cite this article: Luckner M and Wanner G (2018) From Light Microscopy to Analytical Scanning Electron Microscopy (SEM) and Focused Ion Beam (FIB)/SEM in Biology: Fixed Coordinates, Flat Embedding, Absolute References. *Microsc Microanal.* doi: 10.1017/S1431927618015015

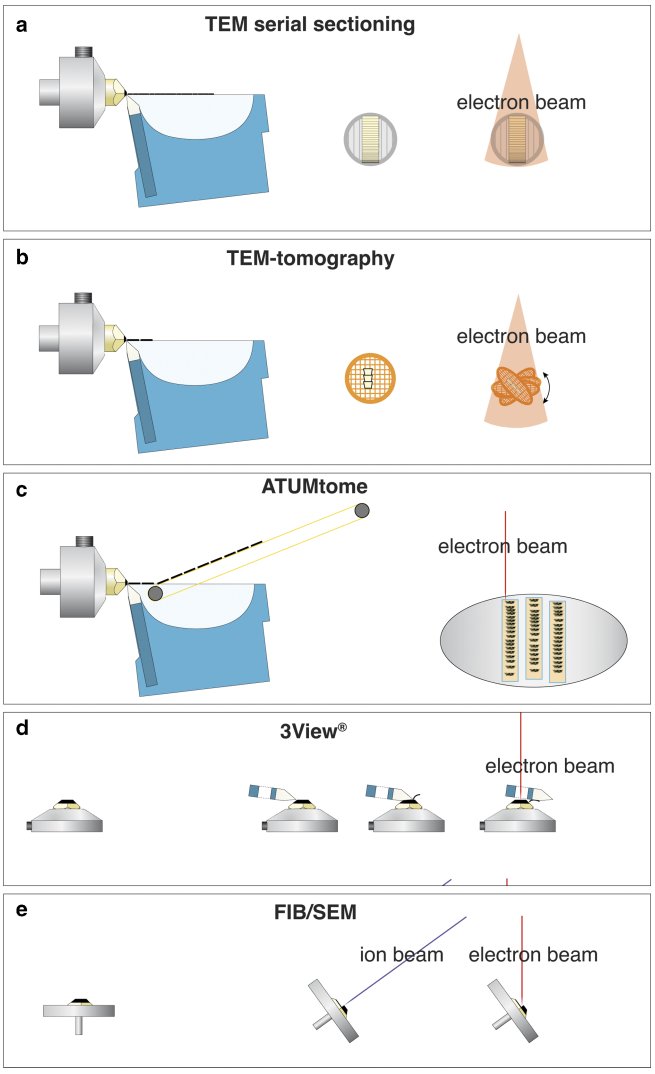

Figure 1. Comparison of volume electron microscopy techniques, for classical transmission EM (TEM) serial sectioning, consecutive ultrathin sections are collected on grids and imaged separately with TEM (**a**). For TEM-tomography thin sections (0.3–1 μm) are cut with a diamond knife, collected onto a grid, which is tilted relative to the TEM to 70°. After registration and back-projection, a tomogram is provided (**b**). For array-tomography serial sections are cut with a diamond knife, collected with an automated conveyor belt onto an adhesive tape (ATUMtome), mounted onto glass slides or silicon wafers and investigated with an scanning electron microscopy (SEM) (**c**). 3View®, the commercial version of the invention of W. Denk, manufactured by Gatan with a built-in ultramicrotome within the SEM. Serial sections are cut with a moving diamond knife and the block-face is imaged after every section (**d**). Focused ion beam (FIB)/SEM serial block-face milling is achieved by tilting a specimen in an SEM to 54°. An ion-gun is placed in the SEM at the same angle so that sections can be milled orthogonal to the specimen surface. Block-face images are taken at an angle of 36° with an SEM, and either backscattered electrons or secondary electrons are detected (**e**).

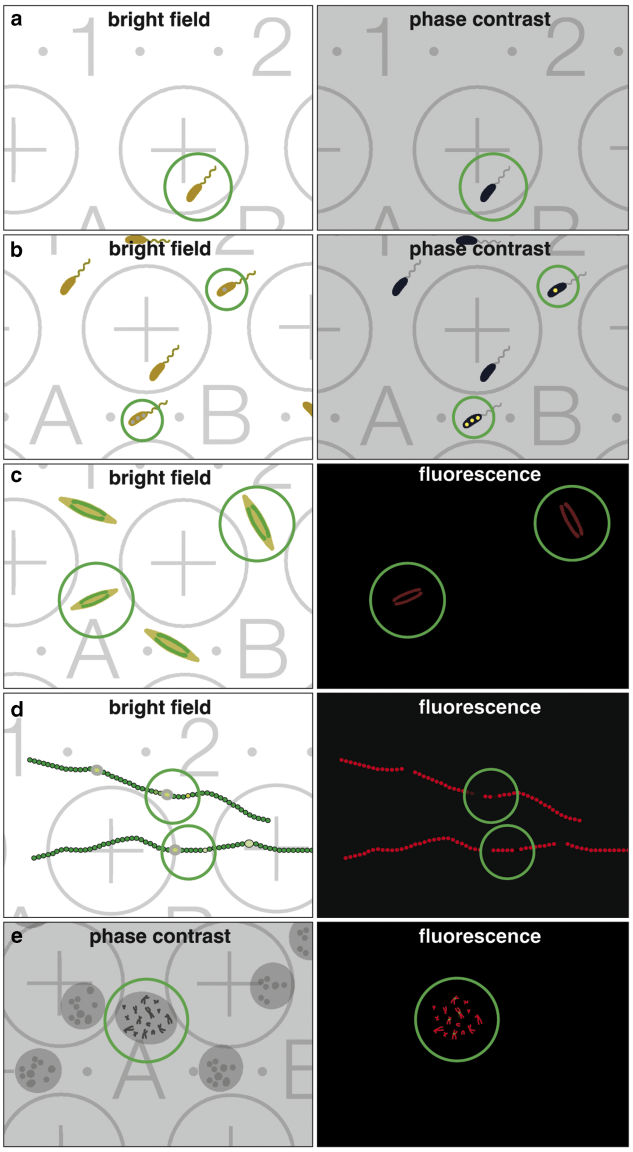

Figure 2. Benefit of a coordinate system for correlative light and electron microscopy. Examples of common investigations, which are either facilitated or made possible by correlative light microscopy (LM)/scanning electron microscopy (SEM). The classical claim, identifying rare objects in the LM with bright field or phase contrast (**a**; circle) and simply re-locating in SEM. Cells often produce inclusion bodies, not seen in the bright field but in phase contrast (**b**; circles), can be further analyzed in SEM. Vitality is an important criterion; cells (e.g. diatoms) with chloroplasts show autofluorescence in living state (**c**; circles). Non-fluorescent cells can be ignored for further investigation with SEM. For any image interpretation, oriented section planes of biological structures are essential; e.g. heterocysts of filamentous cyanobacteria can be investigated with LM, selected based on vitality of the vegetative cells (autofluorescence of chlorophyll) and presence of heterocysts, documented with the coordinates and re-located in SEM for either cross or longitudinal sections with focused ion beam (**d**; circles). Rare cytological targets, as specific labeled chromosomes, are investigated/selected with phase contrast and fluorescent signals to enable further SEM investigations (**e**; circle).

stable, solvent resistant coordinates by sintering transfer pictures (decalcomania; Wanner et al., 1993). Since the labeling was elevated, experiments such as chromosome spreads were impeded. With new laser technology, it was possible to produce engraved coordinate systems with much finer symbols. These slides were suitable for wider range of biological samples, including chromosome spreads, microorganisms, and proliferating cultured cells. Confocal laser scanning microscopy has broadened the spectrum allowing the production of labeled coverslips.

When correlative light and electron microscopy (CLEM) became fashionable, the scientific interest was primarily focused on improving LM resolution, aiming to image the smallest structures first in live mode, and afterwards complementing these images with ultrastructural information. Unfortunately, the term CLEM is usually associated with recent studies using state of the art high-resolution 3D-LM. However, many studies only require a rather simple correlation with low-resolution wide-field/fluorescence LM, which is illustrated for some examples (Fig. 2), highlighting the importance of coordinates facilitating CLEM, e.g. (i) finding rare cells growing in low density (Fig. 2a); (ii) finding

cells with inclusions (Fig. 2b); (iii) selecting vital cells of a population (Fig. 2c); (iv) registering heterocysts of filamentous cyanobacteria, either for cross or longitudinal FIB/SEM milling (Fig. 2d); or (v) selecting immunolabeled chromosomes in metaphase (Fig. 2e).

A critical requirement for CLEM is firmly maintaining the sample in position, thus maintaining the orientation from live imaging LM to SEM. As only a minor fraction of biological specimens are inherently adherent or sticky (e.g. adherent cell cultures), it is necessary to establish procedures to immobilize a wide range of biological objects, such as single cells, cell aggregates, tissues, or tissue sections. Sample adhesion has to be stable to withstand all changes of solutions, buffers, fixatives, and solvents both by plunging or centrifugation. Finally, a prerequisite for correlative microscopy consists of embedding specimens in very thin layers of epoxy resin for precise re-localization of regions of interest (ROIs). Depending on cell size, density, etc., it is desirable to control the thickness of the sample with regards to the requirements of the scientific question. The first attempts for flat embedding were achieved by draining the resin by gravity, centrifugation, or careful blotting (Kizilyaprak et al., 2014). In another study, animals infiltrated in 100% resin were removed from the resin droplet using toothpicks or pins, moved onto the substrate and drained with filter paper (Schieber et al., 2017). To significantly reduce the final resin layer, cells were infiltrated with 100% resin, then quickly rinsed with 100% ethanol to remove of excess resin (Belu et al., 2016). In a recent book chapter, the technical possibilities for various embedding protocols (classical *en bloc* embedding and thin-layer plastification) were compared for live cell imaging of adherent cells with volume SEM using Ibidi μ-dish 500 or MatTek finder grid dishes. Minimal resin covering of cells was achieved by upright positioning of the cell substrate for draining and with polymerization starting at lower temperatures (Lucas et al., 2017).

Our aim was to enable CLEM, by avoiding any hazardous or complicated manipulations, to evolve from an expensive method into a cost-effective technology suitable for a wide spectrum of biological samples. To this end, we focused on the following aims: (i) to design and produce slides and coverslips with a variety of customized coordinates for correlative LM and SEM and FIB/SEM of both critical point dried (CPD) and flat embedded samples; (ii) to establish a labeling technique for "post-embedding"; (iii) to evaluate strategies to immobilize cells and tissue sections; (iv) to develop a filter system for "flat embedding" of large, fragile or delicate specimens; and (v) to use thick epoxy sections for high-resolution LM, TEM, and FIB/SEM tomography. Each topic was validated for at least one scientific challenge.

Material and Methods

Manufacturing of Customized Coordinates

Elevated Labels for Slides and Cover Slips

Coordinates, which are elevated and added on top of the surface of the slides/cover slips, were made by Gaßner Glastechnik GmbH (Planegg, Germany) with transfer pictures (decalcomania), glued to the slide and sintered at high temperature (Point finder; Wanner et al., 1990, 1993). AG Lasergravuren (Weilheim, Germany) produced extremely dense and small labels with sintered titanium on cover slips.

Engraved Slides and Cover Slips

Laser engravings on slides or coverslips were produced by Laser Marking, (Fischen, Germany), Grüner Laser Products GmbH & Co. KG (Munich, Germany) and AG Lasergravuren (Weilheim, Germany), according to our desired coordinate systems template.

Water-Resistant Stamp

A water-resistant stamp with a coordinate system according to our design was manufactured by modico GmbH & Co KG (Fürstenfeldbruck, Germany).

Biological Material

Chromosomes were isolated, fixed with formaldehyde, and processed as described by Wanner & Schroeder-Reiter (2008) and Wanner et al. (2015). *M. bavaricum* (kindly provided by Prof. Dr. Dirk Schüler; University of Bayreuth) were fixed onto slides either by drop-cryo preparation (Wanner et al., 2008) or by high-pressure freezing as described by Jogler et al. (2011). *Anabaena catenula* (strain SAG 1403-1; EPSAG, Göttingen, Germany) was fixed with 2.5% glutaraldehyde in cacodylate buffer (2 mM NaCl; 2 mM $MgCl_2$; 75 mM cacodylate; pH 7,0) or high-pressure frozen and freeze substituted before immobilization onto slides. *Porphyridium purpureum* was purchased from EPSAG, fixed with 2.5% glutaraldehyde in cacodylate buffer (2 mM NaCl; 2 mM $MgCl_2$; 75 mM cacodylate; pH 7,0) and embedded into epoxy resin. *Tradescantia zebrina* was provided by the Botanical Garden (Munich, Germany) and fixed with 2.5% glutaraldehyde, 2 mM NaCl; 2 mM $MgCl_2$; 75 mM cacodylate; pH 7,0. HeLa Kyoto cells were kindly provided by Prof. Dr. Heinrich Leonhardt (LMU, Munich, Germany). Cells were cultured and grown on laser marked slides and fixed as described by Luckner & Wanner (2018). Human platelets were cultured and immunolabeled by Dr. Florian Gärtner (Klinikum, LMU) (Gaertner et al., 2017). Breast cancer cells (SKBR3) were kindly provided by Prof. Dr. Angelika Vollmar (LMU) and fixed the same way as HeLa cells. Mouse brain tissue was kindly provided by Prof. Dr. Jochen Herms (DZNE, Munich, Germany) fixed with 2.5% glutaraldehyde in cacodylate buffer and post-fixed as described below.

Coating of Slides with Adhesives

Poly-lysine (Merck, Darmstadt, Germany)

Laser marked slides/cover slips were coated with poly-lysine according to the manufacturer's instructions. Poly-lysine coated slides were used for drop/cryo-fixation of chromosomes (Martin et al., 1994; Wanner & Schroeder-Reiter, 2008; Wanner et al., 2015), fixation of *M. bavaricum* (Jogler et al., 2011) and *Chlorochromatium aggregatum* (Wanner et al., 2008).

Biobond (Science Service GmbH, Munich, Germany)

Slides were coated according to the manufacturer's instructions and stored for weeks. For a first test, a drop of sample (cyanobacteria, diatoms, green algae, filamentous algae, biofilm) was placed on a coated slide, covered with a cover slip, and gently pressed, resulting in a thin layer of cells and providing contact with the surface of the slide for sufficient adhesion (Fig. 3a). The coverslip was removed after a few minutes and the slide was gently agitated in the buffer, medium etc. and again covered by a cover slip.

Cell-Tak^{TM} (Corning^{TM}, New York, NY, USA)

Cell-Tak^{TM} a mussel protein (Waite & Tanzer, 1981) was used for adhesion of vibratome sections of mouse brain and histological sections with a thickness up to 100 μm. Cell-Tak^{TM} was applied to slides according to the manufacturer's instructions. The cells/tissues were placed on coated slides in the buffer, covered with a covered slip gently pressed for a proper contact of the tissue to the slide.

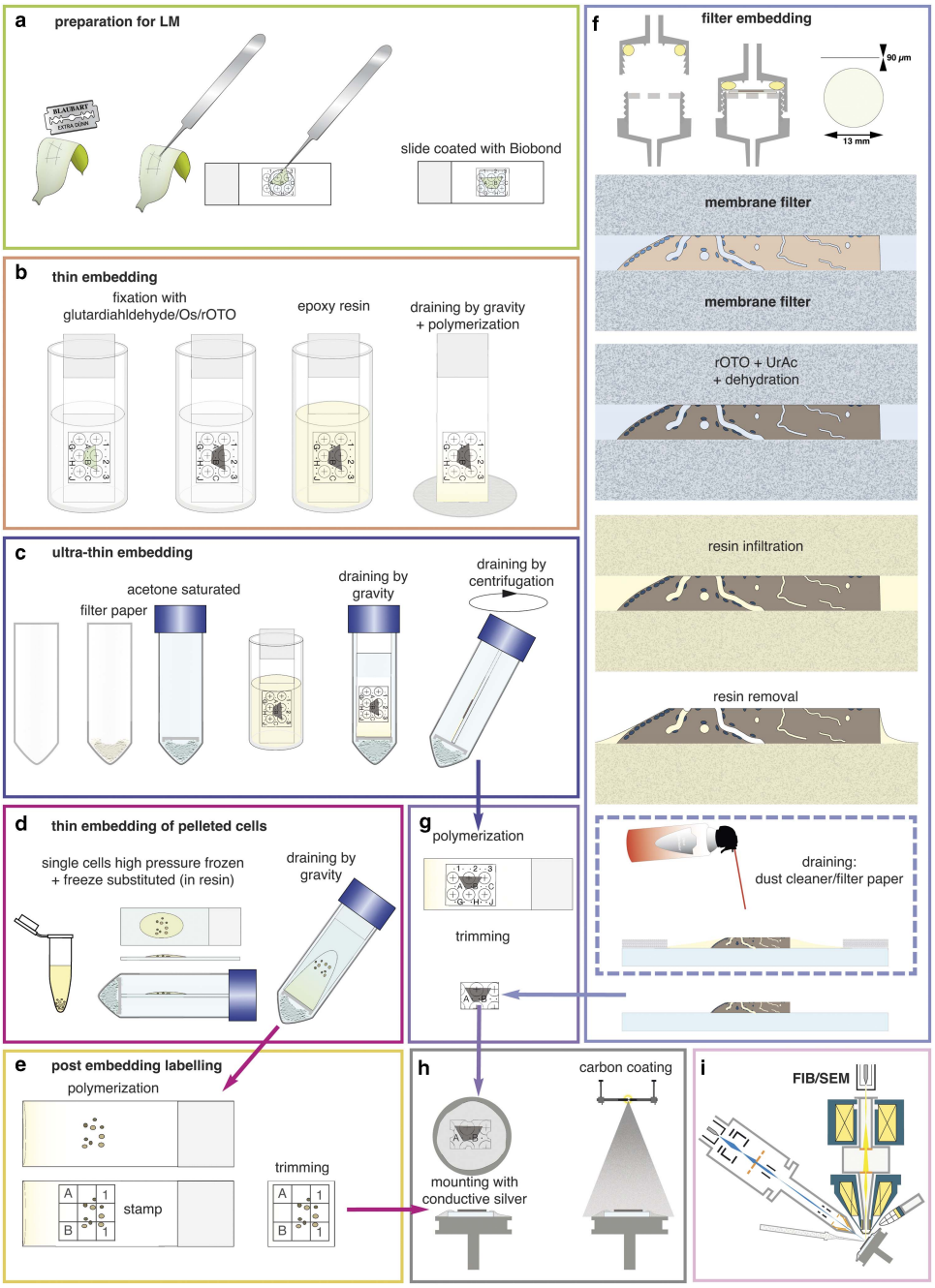

Figure 3. Preparations for flat embedding. If cells or tissues are either adherent or can be immobilized onto slides (**a**), fixation, post-fixation, dehydration, and infiltration with resin are carried out by submerging in cuvettes (**b**). Thin resin layers are achieved by draining (gravity) (**b**). For ultra-thin embedding, infiltrated slides are transferred into an acetone-saturated chamber for draining (gravity), which is optionally followed by centrifugation (**c**). Cells available only as resin infiltrated pellets (e.g. high pressure frozen) can be dropped onto slides and spread/drained in an acetone chamber (**d**). If resin layers obscure the coordinates of the slides, a stamp can be used for post-embedding labeling for correlative light and electron microscopy (**e**). Delicate biological samples can be infiltrated within a filter system (**f**): after light microscopy, samples are placed between acetone resistant filter membranes, sealed in a holder, processed until infiltration by flow through with a syringe. For thin embedding, samples are transferred to a glass slide (for additional LM after polymerization) before draining with filter paper or optional blowing with a dust cleaner for removal of excessive resin (**f**). For reduction of potential charging effects, specimens are trimmed to a proper size (**g**), mounted onto aluminum stubs with conductive silver by contacting the glass surface broadly. Specimens are coated with carbon by evaporation (**h**) and transferred to the focused ion beam (FIB)/scanning electron microscopy (SEM) (**i**).

Bondic® (VIKU UG, Munich, Germany)

Bondic® is a viscous adhesive polymerized by UV radiation. It is waterproof and heat resistant. A drop was spread over a slide with a coverslip. Pieces of biological material were placed in the buffer on the coated area, covered with a coverslip and exposed to UV light from the backside of the slide for a few seconds.

Immobilization and LM Procedure

Cells/tissues were immobilized with suitable adhesives previously described. Samples were sealed with a coverslip and Fixogum (Marabu GmbH & Co. KG, Tamm, Germany) in the buffer, to prevent drying during LM imaging. ROIs were marked on a template copy with the same coordinates as on the slides. For standard CLEM documentation of ROIs, two to three different

magnifications (objective: 5×, 10×, 40×) were sufficient for retrieval in SEM. Depending on specimen properties, bright field (BF), phase contrast (Ph), differential interference contrast (DIC), and epi-fluorescence or laser scanning microscopy (LSM) was used (Carl Zeiss, Oberkochen, Germany). Different areas were routinely documented, since (i) there can be a loss of few cells and/or damage during handling; (ii) some cells may show insufficient fixation quality or contrast in SEM among neighboring cells that are adequate in structure and contrast. LM can be repeated after thin embedding in epoxy resin, to monitor structural changes, control of contrast enhancement, and to check preservation of selected ROIs or to select new ones.

Post-Fixation by Submerging

Samples were processed, by submerging slides in buffers, fixatives, solvents, and resins, in standard staining cuvettes (Fig. 3b). The customized rOTO-protocol, was based on (Willingham & Rutherford, 1984), with 1% OsO_4 (Science Services, Munich, Germany) and 1% $K_4Fe(CN)_6$ (Merck) in cacodylate buffer for 30 min, washed three times in *aqua bidest.*, incubated with 1% thiocarbohydrazide (Merck) in *aqua bidest.* for 30 min, washed with *aqua bidest.* three times, followed by post-fixation with 1% OsO_4 in *aqua bidest.* for 30 min. The samples were rinsed three times with *aqua bidest.* and dehydrated in a graded series of acetone (10, 20, 40, 60, 80, 100%), with a 1% uranyl acetate (Science Services) step in 20% acetone for 30 min.

CPD

Dehydrated samples were CPD (Polaron, Montreal, Canada). After CPD, slides were either stored in a desiccator (to prevent hygroscopic water uptake and consequent ultrastructural changes) or in little transport boxes sealed with Parafilm (Merck).

Flat Embedding in Thin and Ultra-Thin Epoxy Layers

Immobilized cells and tissues were processed and embedded on a glass slide.

Thin Embedding

Immobilized cells/tissues were infiltrated with 1:1 Hard-Plus Resin-812 (Science Services) in acetone for 15 min, 2:1 for 30 min, 75–100% Hard-Plus Resin-812 for 30 min at RT. The excessive resin was removed by draining (Fig. 3b).

Ultra-Thin Embedding

Immobilized cells/tissues were infiltrated with 1:1 Hard-Plus Resin-812 in acetone for 15 min, 2:1 (resin in acetone) for 30 min and 75–100% Hard-Plus Resin-812 for 30 min. The slides were immediately placed in a falcon tube, saturated with acetone, allowing the excessive resin to drain into filter paper at the bottom of the falcon tube for 30 min. To prevent dilution of the resin, direct contact of the slides with the filter paper, soaked in acetone, was avoided by putting a spacer (e.g. polypropylene cap) in between. As the acetone cannot volatilize, the resin concentration is not increased during infiltration and maintains its high fluidity to drain quantitatively. In some cases, when necessary, an additional centrifugation step was added (2 min; 1000 rpm). All samples were polymerized at 60 °C for 72 h (Fig. 3c).

Protected SEM Preparation by Filter System

If tissues could not be immobilized, a filter system was used (Fig. 3f). Samples were placed, with a drop of buffer on hydrophilic, acetone-resistant 13 mm ipPore Track Etched Membranes (it4ip, Belgium), with a thickness of 12 μm, a pore size of 0.4 μm and a pore-density of $1 \times 10^8/cm^2$ to enable a sufficient flow rate by an appropriate stability. A second membrane is then placed to cover the tissue; subsequently the "membrane sandwich" is placed on top of the planar bottom part of the filter holder. The filter system is closed with the upper part of the holder, containing an O-ring (Fig. 3f). Care has to be taken that the O-ring is not contacting the "membrane sandwich" by screwing the plug. Reagents for post-fixation, dehydration, and resin infiltration were injected by 5 ml syringes (B. Braun Melsungen AG, Germany). Before polymerization, samples were transferred to slides. Draining and blotting of the excessive resin, with filter/lens paper or with a dust cleaner and monitored with a stereo lens (Fig. 3f), was effective in removing excessive resin until the samples appeared completely dry.

Thick Epoxy Sections

Classic TEM resin blocks were trimmed and sections with a thickness of 5–10 μm (depending on the cell size and density) were cut with a glass knife, then placed onto a drop of *aqua bidest.* on a laser-marked slide. If resins are brittle, the specimen can be heated with a blow dryer to ~50 °C to increase elasticity. While heating the slide to ~ 60–80 °C, the sections soften and stretch to their original size, which can be controlled while viewing with a stereo lens. Once the water droplet has evaporated, the sections stick to the slide.

Mounting and Conductive Coating

Coverslips were used in their entirety, whereas glass slides were scored with a diamond scriber (Ted Pella Inc., Redding, CA, USA) and a ruler and fractured into appropriately sized pieces, to reduce the surface area of the glass and consequently potential for charging during SEM investigations (Fig. 3g). If in-lens SE or in-lens energy selective backscattered electron (EsB) detectors were needed for highest resolution, the samples were cut to smaller pieces to allow short working distances (WD) in the range of 1–2 mm. Pieces were mounted with conductive silver colloid (Plano, Wetzlar, Germany) onto standard aluminum stubs (Plano) (Fig. 3g). Specimens were sputter coated with layers of a few nanometer (3–5 nm) of platinum (Balzers AG, Liechtenstein) for high-resolution SEM at low kV (Fig. 3g). For immuno-SEM and energy dispersive X-ray (EDX) analyses, specimens were carbon coated (3–5 nm) by evaporation (Cressington Scientific Instruments UK, Waterford, UK). If specimens were prepared for FIB/SEM-tomography, a carbon coating of 10–20 nm was used for both conductivity and protection, forming a glass-like, very stable conductive layer which is still transparent for higher energetic BSEs. For high-resolution SEM at low kV (0.8–1.8 kV), slides were carbon coated before cells/tissues were grown or immobilized, to enable conductivity without any coating (Table 1). The thickness of the glass slides (approx. 1 mm) or coverslips (precision coverslips: 0.17 mm) has no influence on SEM imaging if well grounded with silver colloid.

High-Resolution SEM

Samples were imaged with a Zeiss Auriga 40 FIB/SEM workstation operating under SmartSEM (Carl Zeiss Microscopy GmbH, Oberkochen, Germany). For re-localization and a rough

Table 1. Options for Coatings and Scanning Electron Microscopy (SEM) Operation.

	Pt-sputter Coating	Carbon Coating	Carbon Coated Slide	Pt-Deposition	kV	Detector
High-resolution SEM	3–5 nm				0.8–1	SE/in-lens SE
High res. immuno-SEM (10 nm gold)		3–5 nm	(+)		1–2 5–20	EsB QBSD
High res. immuno-SEM (5 nm gold)			+		1 5–20	EsB QBSD
SEM for depth information		3–5 nm			5–30	QBSD
SEM for element analysis		3–15 nm			1–30	EDX
CPD + FIB/SEM		3–15 nm		(0.5–1 μm)	1.5	EsB
Flat embedded + FIB/SEM		10–30 nm		(0.5–1 μm)	1.5	EsB

SE, secondary electrons; EsB, energy selective backscattered electron; QBSD, quadrant backscatter electron detector; EDX, energy dispersive X-ray; CPD, critical point dried; FIB, focused ion beam.

correlation of LM images with SEM micrographs, the WD has to be large (10 mm) and the kV high (5 kV) to ensure a sufficiently low magnification with acceptable low geometrical distortion. Although surface details are best monitored at 1 kV with the In-lens SE detector, correlation with LM micrographs sometimes need as much depth information as possible, gathered by the EsB detector (at 1–5 kV) or with the 4-quadrant backscatter electron detector (QBSD) at higher accelerating voltages (5–30 kV). Thin layers of resin then become transparent and laser marks are clearly visible. Using BSE signals, a larger aperture (60 μm) is necessary for a sufficient signal to noise ratio, which does not influence resolution at low and moderate kV. The high current mode (a feature of some Zeiss SEMs) is of benefit if the depth of focus is of importance: high current mode increases the active probe current by a stronger activation of the condenser lens. The resulting smaller angle of convergence increases the depth of field, which is important when imaging entire cells (with a height of 10–20 μm), which is not common with SEM in standard configuration.

High-Resolution FIB/SEM

Cells and tissues were milled and imaged with an Auriga 40 FIB/SEM workstation operating under SmartSEM or Atlas-3D (Fibics Incorporated, Ottawa, ON, Canada). Ion beam currents of 50 pA–10 nA (depending on the stability of the resin) were used. FIB/SEM milling started right in front of the target structure. Depending on the desired resolution image, voxel sizes between 2 nm and 10 nm in *x*/*y* were chosen. A milling rate that yield 2 nm slices allows the adjustment of the *z* resolution in 2 nm steps at any time during the FIB/SEM run. Due to metallic rOTO impregnation of the tissue, conduction with colloidal silver, carbon coating by evaporation, and an optional Pt-deposition upon the ROI, charging was completely avoided. As rOTO impregnation provides a strong material contrast, short exposure times down to 17 sec/image (3072 × 2048 pixel) could be achieved. The surface of the glass slide, as part of the image, serves as a reference for the *xz.* plane. For additional alignment in *yz*, reference lines were milled with a 50-pA beam next to the target region.

3D-Reconstruction

The resulting data sets were aligned using Amira™ (Thermo Fisher Scientific, Waltham, MA, USA), first automatically with the module "align slices" and corrected with the "shear" function. The quality of the alignment has to be verified by the references, the slide (*xz*) and the added reference lines (*yz*) and, if necessary, corrected manually. Image stacks were segmented and reconstructed in Amira™ (Thermo Fisher Scientific) and/or processed with a volume-rendering algorithm (*volren*) for direct visualization. 3D reconstructions/correlations were performed with Amira™.

Results

Linking Samples to Coordinates

We first tested several methods to label coordinates on glass slides and coverslips. All these labels were clearly visible in LM optical modes (bright field, DIC, phase contrast) as well as in SEM due to their topographic contrast (Fig. 4). The labels of the classic point finder (a sintered decalcomania with silk-screen printing), with a height of ~10–15 μm, yielded the strongest BSE signal, due to the lead content of the paint (Fig. 4a). Depending on the downstream applications, the composition of this paint can be modified if desired.

We found that laser engravings generated much finer lines. Upon closer inspection of fractured slides, the label appeared as a slight engraving outlined by an elevated border, deriving from either sintered TiO_2, a carbon compound, or both, which were used for focusing the laser and for the energy transfer (Figs. 4b–4e). In this regard, the term engraving is a bit misleading. For CLEM and FIB/SEM of a thin embedded specimen, elevated labels were required to poke out of the thin layer of resin (Figs. 4a, 4e). In general, when an inverted microscope was used for LSM, laser marked coverslips were preferable (Figs. 4d, 4e).

Although the fabrication of fine coordinates is limited in terms of line width and accuracy, the quality of the labeling is, in practice, of secondary importance. In fact, the unique edges of imperfect markings or engravings can be used to facilitate fast correlation. The "mesh size" of the labeling can be adjusted depending on the size of the samples, but in all cases, the coverage of the coordinates is below 15%. For samples already flat embedded on a slide or cover slip, or in situations where the labels were no longer visible due to the formation of a surface layer or hidden by epoxy resin, we used a water-resistant stamp to print a customized coordinate system on top of the specimen (Figs. 4 and 3f). After documentation and carbon coating for conductivity, the coordinates of the stamp were still visible in the SE-image by topographic and material contrast, which enabled a re-localization of the previously selected ROIs (Fig. 4f).

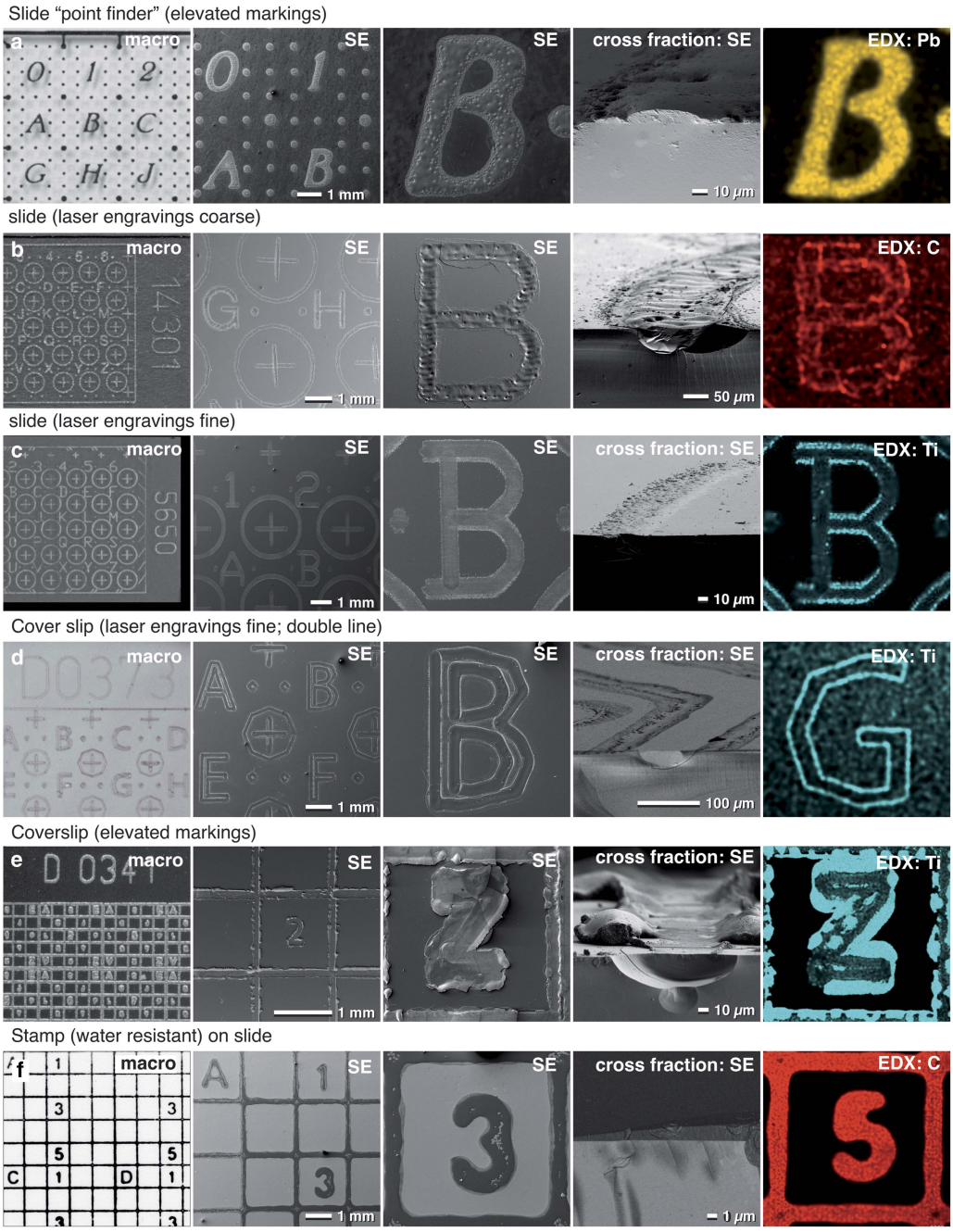

Figure 4. Properties of customized slides and cover slips. Macro images, light and scanning electron micrographs of slides and coverslips customized for correlative light microscopy (LM), high-resolution scanning electron microscopy (SEM) and focused ion beam (FIB)/SEM. Coordinates for slides and coverslips are either elevated (**a** and **e**), engraved (**b**) or a combination of both (**c**, **d**), suitable for different embedding properties (ultra-thin, medium-thin, thin). The coordinate system can be visualized with topography contrast and material contrast due to the sintered material. X-ray analysis can be used for visualizing of labels if they are hidden in the thin resin layer and/or for mapping of the elements characteristic for the labels (**a**). As titanium oxide mixed with organic carbon compounds is used to focus the laser (**b**–**e**), labels are visible based on their specific X-ray energies, which is beneficial for analytics or correlative light and electron microscopy (CLEM). If coordinates are printed with a stamp, the carbon-based ink is visible in black in LM, dark in SEM and gives a strong C signal with energy dispersive X-ray (EDX) (**f**).

Sample Immobilization

Proper immobilization is crucial to link the biological samples to the coordinate system of the substrate. This connection has to be rather strong to withstand the manipulations and buffers used during processing for SEM and FIB/SEM microscopy. Depending on the size, shape, and adhesive properties of the sample, a variety of “glues” can be applied for immobilization. For example, laser marked slides coated with poly-L-lysine, are routinely used for drop-cryo fixations of prokaryotic and eukaryotic microorganisms. Typically, these cells are abundant, so even the loss of a high percentage of cells is mostly inconsequential.

As a general rule, the larger the cells, the lower the yield of stably fixed cells remaining after sample preparation. As a result, stronger glues are required for such larger samples. In this regard, Biobond showed a rather strong adhesion to cells in addition to being easy to handle and moderate in price. Biobond was

successfully used to immobilize a wide range of mobile algae. In contrast, filamentous cyanobacteria forming slime sheets were initially improperly immobilized with Biobond. However, after choosing strains which do not form sheets, these cells were successfully immobilized.

Next, Cell-Tak™, derived from a mussel protein, is a very strong adhesive. Cell-Tak™ showed stronger adhesion properties than Biobond, which were beneficial for fixing larger tissue sections to slides. However, immobilizing thin or fragile tissue sections over their entire surface, without any folds, can be difficult. As soon as the tissue sections are in contact with the mussel protein, they will immediately adhere. If any folds occur due unevenly laying the tissue on the slide, the tissue cannot be flattened without disruption. As Cell-Tak™ has to be applied for each specimen individually, the adhesive layers vary in thickness and are not as thin and uniform compared with Biobond coating. This may be a disadvantage when investigating samples such as cellular protrusions, flagella, or cilia. These structures would be difficult to distinguish at higher magnification due to the uneven topography of the glue.

Bondic®, developed as an adhesive, can be used to immobilize samples in aqueous conditions. This adhesive is polymerized by radiating the contact area for a few seconds with UV light from the backside of the slide. It is an inexpensive and strong adhesive. However, the layers are rather thick and therefore only suitable for large and sturdy samples, such as those that can be handled with forceps.

For flat embedding of delicate and fragile tissues sections, we developed a customized filter system for tissue sections, which mechanically stabilizes the sample. To this end, the tissue sections are placed between two filter membranes and screwed in a filter holder, thereby ensuring that no significant forces perturb the geometry of the sections during the entire fixation and embedding process (Fig. 3f). In addition, only small amounts of post-fixation solutions are needed, due to the small volume of the holder. Importantly, large vibratome sections remain flat, even during dehydration, as they are mechanically stabilized, which is essential for FIB/SEM. Finally, excess resin is then removed, and samples are polymerized on laser marked slides (if coordinates are needed). A variety of samples are quite suitable for processing using the customized filter system:

- large histological sections;
- samples, which cannot be immobilized by adhesives;
- samples, which are very fragile; and
- samples, which have to remain flat during preparation/dehydration.

Choosing the Right Embedding

Depending on the scientific question, it is often desirable to control the thickness of the resin layer for flat embedding. In this regard, we demonstrate adjusting the embedding thickness with HeLa cells (Fig. 5). With the portfolio of procedures ranging from simply draining the resin, to centrifugation and infiltration in an acetone-saturated chamber, the thickness of the resin layer can be adapted from ultra-thin to thin embedding. These procedures were suitable for a broad spectrum of adherent or immobilized cells and tissues (Figs. 5b–5e). In general, a thin resin layer was advantageous for the stability of the FIB-SEM run (Fig. 5h). In contrast, ultra-thin embedding was preferable for CLEM of inner cellular features (e.g. centrosomes, kinetochore), which had to be re-localized with high precision in FIB/SEM (Figs. 5c, 5f). An efficient way of producing very thin layers of resin consists of embedding the specimens in 75–100% (resin/acetone). Since samples are infiltrated in a saturated acetone atmosphere (Fig. 3c), the resin concentration is not increased and maintains its high fluidity. After an appropriate time of infiltration, the excess resin/acetone mixture is drained either by gravity or centrifugation, resulting in an extremely thin resin layer after polymerization (Figs. 3c, 5a, 5c, 5f, 5i). Minor milling artifacts at the surface, which are the result of an extensively textured cellular surface, can be ignored, if the target area is located within the cell and if these artifacts do not influence the ROI itself (Fig. 5f). For correlative LM and SEM or FIB/SEM, ultra-thin to medium-thin embedding is beneficial, since SEM and LM images (DIC, bright field) were almost identical qualitatively and their correlation was very precise (Fig. 5a), comparable with CPD cells (compare: Fig. 5b with 5c), but with a substantial gain in resolution using the EsB signal, and visibly less curtaining during milling (Figs. 5f, 5g). If thin embedding is desired, the correlation is impeded because cells are partially hidden within resin droplets (Fig. 5h). Nevertheless, the identification of selected cells was still carried out by superimposing LM and SEM micrographs. For experiments relying on cellular surface information or looking at externalized vesicles such as exosomes, thin embedding is preferable (Fig. 5h). In all cases, regardless of the resin thickness, references (glass slide and reference lines) were clearly visible in each tomographic image (Fig. 5h).

X-ray analysis allows the estimation of resin thickness (before FIB/SEM) by increasing the kV until the silicon signal, derived from the glass slide becomes prominent (Figs. 5i, 5j). The X-ray signals of carbon, nitrogen, phosphorus, osmium, and uranium of ultra-thin and thin embedded HeLa cells at 25 kV correlated with the outlines of nearly all cells (SE image) present in the mapping area. By passing through the covering resin layer of thin embedded cells (in contrast to ultra-thin embedded cells), the primary electron beam loses a lot of energy and spreads in diameter, resulting in a blurry appearance of the cells (Fig. 5j).

Care must be taken during SEM and preparation for FIB-milling: thin resin layers on glass slides are sometimes very sensitive to the electron beam. Higher magnifications, used for focusing and correction of astigmatism, rapidly lead to the formation of "bubbles" in the resin, which look striking, but did not influence further milling. Low magnifications and using an appropriate kV are recommended for SEM and FIB adjustment. Once the FIB/SEM milling process has started, the energy input is concentrated onto the block face, and the risk of "bubbles" is negligible. For thin specimens (1–5 μm) a very low ion beam current (50 pA, as used for FIB imaging) is recommended.

Examples for Analytical SEM and FIB/SEM and Possibilities for CLEM

Chromosomes: Immuno-Labeling—from LM to FIB/SEM

The topography of isolated cell organelles or single cells can be investigated with high resolution, after application of a thin metal coating (3–5 nm platinum), using a short WD (1–2 mm) and with the in-lens SE detector at 0.8–1.2 kV. However, the platinum coating is incompatible with metal-based staining such as platinum blue for DNA or immuno-labeling with small gold colloids (5 nm). Even the thinnest platinum coating will prohibit detection of metal-based staining or gold-labels with the EsB-detector (Figs. 6a3, 6b4). Carbon coating can be used for conductive coating if higher currents are required, but with a dramatic loss of high-resolution topographic information gathered at 1 kV.

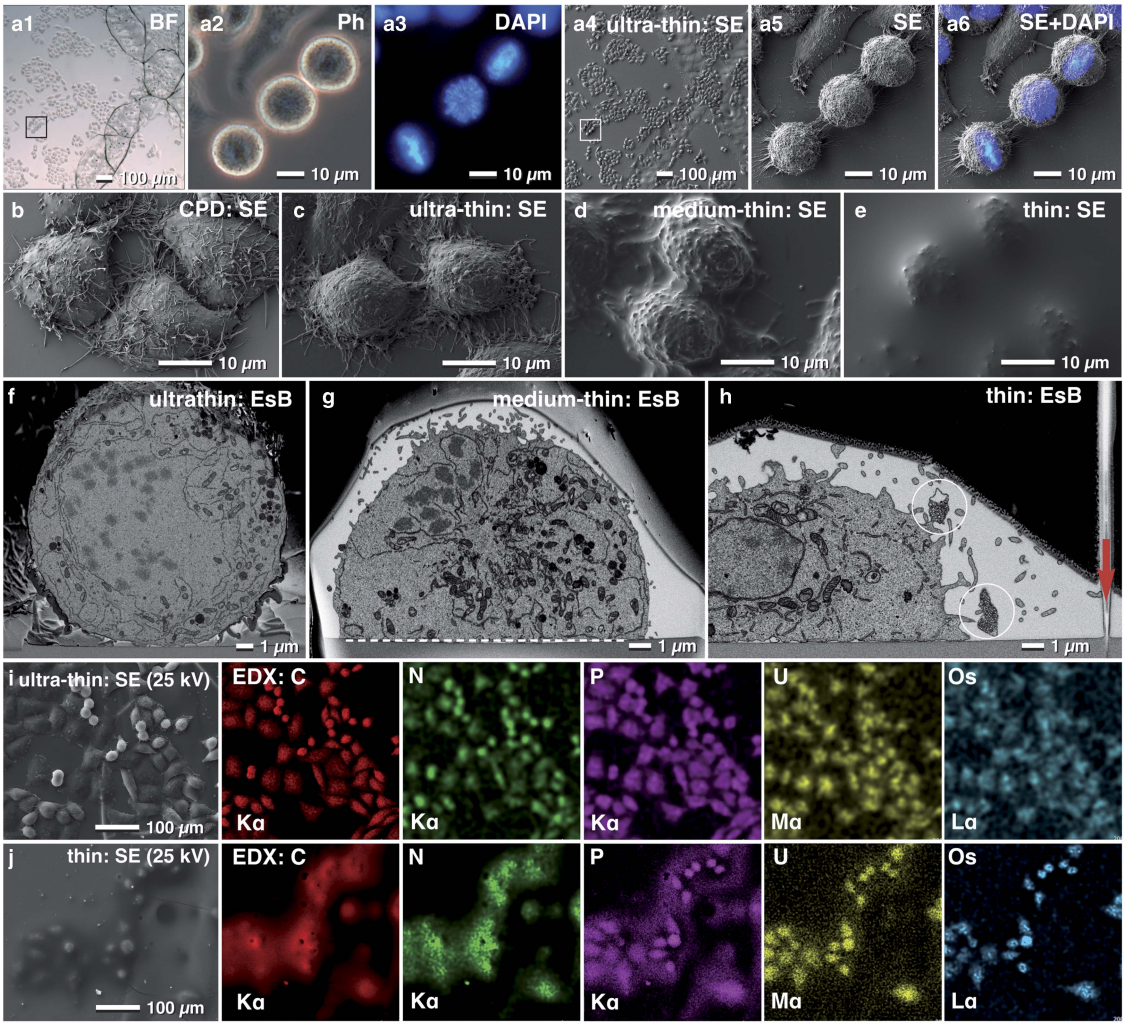

Figure 5. Re-localization after flat embedding. Light micrographs of HeLa cells grown on a laser-marked slide to the left to the letter X (**a1**). After 4′,6-Diamidin-2-phenylindol (DAPI) staining, metaphase cells were selected (**a2**, **a3**) and re-localized in SEM, already visible in the overview (**a4**, **a5**). DAPI and secondary electron (SE) image were superimposed to define a precise milling frame (**a6**). Scanning electron micrographs of critical point dried HeLa cells, compared with cells, embedded with different thick layers of resin. The topographic details of critical point dried cells (**c**) were preserved after ultra-thin embedding (**c**). Structural details like filopodia were clearly visible, whereas, after medium-thin embedding, they were obscured (**d**). Thin embedded cells, covered by a few microns of resin, could be still re-located and identified as small humps (**e**). Comparison of cross sections of HeLa cells embedded ultra-thin (**f**), medium-thin (**g**) and thin (**h**) in epoxy resin. The thicker the covering resin layer, the less topographic details of the cell surface were visible, however, the risk of curtaining is reduced by the smooth surface (**h**). The glass slide served as an absolute reference plane (xz) for alignment (**g**; dashed line). Lines, milled parallel to the regions of interest (ROI) into the slide in *xz* direction (**h**; arrow), served as a third reference plane for precise alignment of the image stack in three dimension. The X-ray signals were used for verification of resin thickness. The carbon signal of ultra-thin embedded cells, clearly visible at 25 kV (**i**), became blurred after thin embedding, due to the carbon portion of the covering resin (**j**). P, U and Os mapping of thin embedded cells revealed only a section of the cells appearing "in focus" as the higher energetic K-line of phosphorus, the M-line of uranium and the L-line of Os osmium were excited only from higher energetic electrons near the surface (Fig. 5j).

However, for a high-resolution analytical investigation of isolated biological structures such as chromosomes, carbon coating of the substrate (glass slides) before applying the sample is ideal since: (i) the problem of charging can be minimized and even eliminated, either at low kV or due to the conductive carbon layer; and (ii) the rather dark background in the BSE image enables high-resolution SE and high contrast BSE imaging at very low kV (0.8–1.5 kV).

Carbon-coated slides remain translucent after coating, therefore enabling LM to select ROIs beforehand. Since the re-localization of small biological structures such as mitotic chromosomes is not trivial, a linked reference coordinate system is critical. For example, the mitotic index for spelt is very low (2–15%), and therefore a previous selection in of ROIs in LM was essential (Fig. 6a1). FluoroNanogold^{TM}-labeled antibodies against alpha-tubulin were located at fibrillar bundles at the centromeric region of the mitotic chromosomes (Figs. 6a2, 6a3). Analytical investigations of metal impregnations at different depths of the sample were carried out by varying the negative grid voltage of the in-lens energy selective BSE detector for high resolution (Fig. 6).

To detect labeled structures located inside a biological structure, the kV must usually be increased. Typically, charging begins e.g. at 2–3 kV, but disappears at higher kV as the electrons penetrate the specimen and reach the conductive carbon layer. In this case, the system must be operated at two different accelerating voltages: 1 kV to image the surface topography and surface-located labels (in-lens SE detector, EsB detector) (Fig. 6a2, 6a3) and 10 kV for high-resolution imaging of labels in the interior of the sample (QBSD). Additionally, the low BSE-yield of carbon prevents interfering BSE signals from the substrate. To demonstrate this, holocentric chromosomes of *Luzula elegans* were stained with DAPI (for DNA) and with gold-labeled antibodies against a phosphorylated variant of Histone H2A

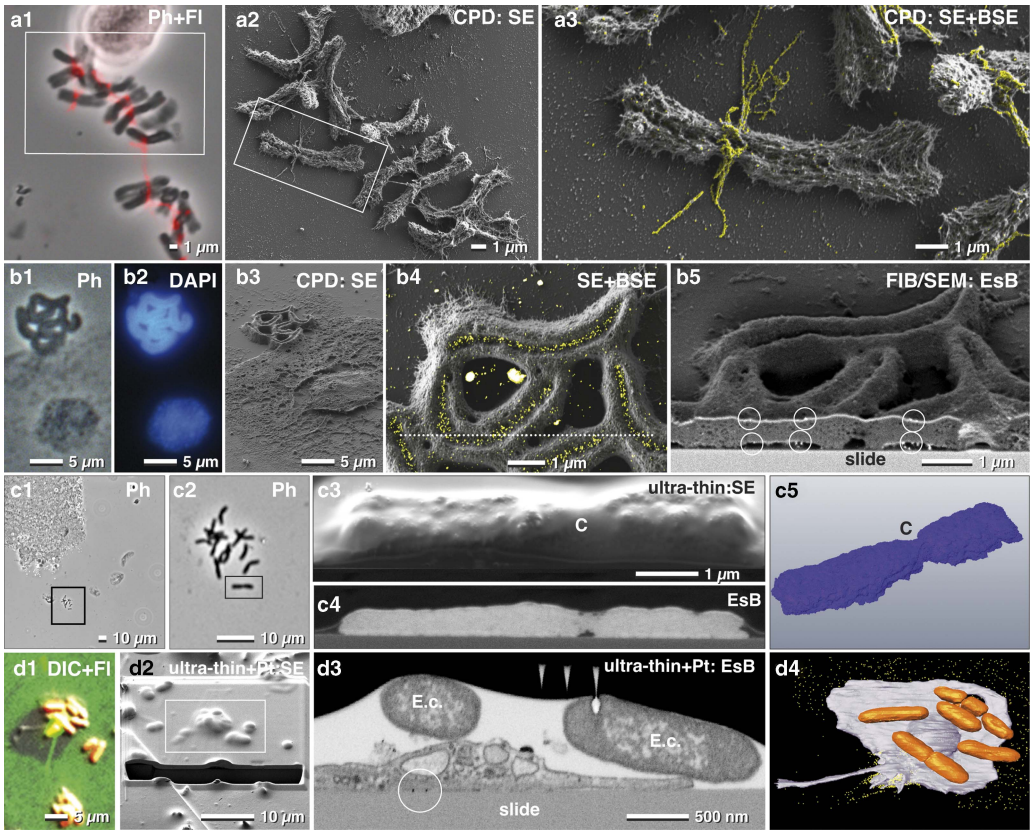

Figure 6. Correlative light and electron microscopy of isolated chromosomes. High-resolution correlative light microscopy, scanning electron microscopy and focused ion beam/SEM of specifically labeled spelt metaphase chromosomes, fixed onto carbon-coated slides. Chromosomes, immuno-labeled for α-tubulin, were selected with phase contrast combined with fluorescence (**a1**), re-located in SEM (**a2**) with secondary electrons (SE) and analyzed with both, SE- and backscattered electron (BSE)-signal for detection of FluoroNanogold™ labels enhanced with silver (yellow) located at bundles of tubulin attached to the centromere (**a3**; merging of SE-image with the colored BSE image). Holocentric chromosomes of *Luzula elegans* were visualized with phase contrast (**b1**), and fluorescence of DAPI (**b2**), re-located in SEM (**b3**). The gold-labeled antibodies against a centromere-specific phosphorylated histone (anti-Histone-H2A) were localized within the centromeric groove (**b4**; merged SE-image and BSE image). For verification of label distribution, the specimen was carbon coated before FIB/SEM milling. Gold-labeled antibodies were detected on both sides of the chromosomes, predominantly located at the surface (**b5**; framed area). Barley metaphase chromosomes were fixed onto slides (**c1**; **c2** = framed area of **c1**) stained for DNA distribution with platinum blue and embedded in the water-soluble resin Moviol (**c3**; SE-image) to prevent shrinkage during dehydration in ethanol/acetone. FIB/SEM tomography (**c4** = BSE) shows the global Pt (DNA) distribution in three dimension (**c5**). C = centromere. A migrating human platelet collecting fibrin-trapped *E. coli* (**d1**) (orange = tdTomato; green = fibrin-Alexa-488-10 nm-gold). SEM micrograph of the platelet of (**d1**) after thin embedding and platinum deposition (**d2**). FIB-SEM section shows *E. coli* accumulating at the surface of the platelets (**d3**). A 3D-rendered FIB-SEM stack of the same platelet (**d4**) demonstrates the accumulation of the *E. coli* (orange) via fibrin (immuno-gold labeled = yellow).

(for centromeres). These chromosomes were first visualized with phase contrast (Fig. 6b1), and with fluorescence microscopy (Fig. 6b2) and then re-located in SEM (Fig. 6b3). Gold-labeled antibodies (anti-Histone-H2A) were then visibly localized within the centromeric groove (Fig. 6b4). To verify the spatial distribution of the gold labels, the specimen was carbon coated before FIB/SEM milling, to avoid charging during milling. As a result, gold labels were clearly visible on both sides of the chromosomes (Fig. 6b5).

CPD samples of chromosomes can also be used to study DNA distribution with FIB/SEM. However, CPD may cause shrinkage and formation of cavities. To avoid dehydration artifacts, embedding in Moviol, a water-soluble resin, is beneficial, and offers a smooth block face which yields the highest resolution (Fig. 6c). The BSE signal of the Pt-stained chromosomes showed the global distribution of the DNA (Figs. 6c4, 6c5).

For correlative LM and FIB/SEM microscopy, samples are commonly embedded in a resin block together with the substrate. The substrate is then removed after polymerization by thermal shock, thereby leaving the cells in the resin. However, if the experiment involves examining how the cell contacts the substrate, for example, to analyze attachment or migrating activity, then the substrate cannot be removed. Therefore, in such cases, ultra-thin or thin embedding directly on the slide is required. With immuno-fluorescence microscopy, it was demonstrated that human platelets migrate and pile up on the adhesive substrate together with any bound particulate material. This occurs when actomyosin-dependent traction forces overcome substrate resistance (Gaertner et al., 2017) (Fig. 6d1). Once removed, fibrinogen is transported toward the center (pseudonucleus) of migrating platelets, remaining on the platelet surface, mainly within invaginations of the open canalicular system. After LM (Fig. 6d1) platelets were thin embedded, re-located in SEM and covered with two platinum protection layers by ion beam deposition (Fig. 6d2). Additionally, a carbon layer was implemented between these two layers for milling high contrast tracking lines for FIB/SEM microscopy using Atlas3D hard- and software. These tracking lines enabled correction of astigmatism and focus (*autostig and autofocus*) during the FIB/SEM run (Fig. 6d3). *Escherichia coli* cells were collected and accumulated at the pseudonucleus together with the fibrin(ogen)-forming bundles of several bacteria (Fig. 6d3). A 3D-rendered FIB-SEM stack of the platelets demonstrates the accumulation of the *E. coli* via fibrin (Fig. 6d4).

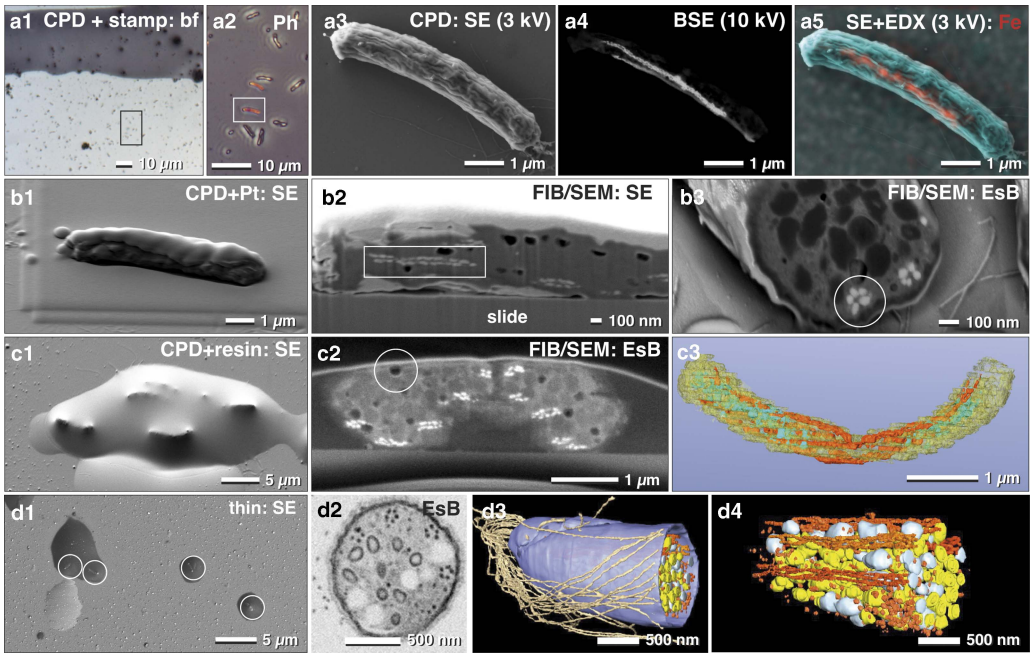

Figure 7. Correlative light and electron microscopy of immobilized and pelleted prokaryotic cells. Light and scanning electron micrographs of *Magnetobacterium bavaricum* cells, within a mixed-culture prepared for correlative light microscopy and focused ion beam (FIB)/scanning electron microscopy (SEM). A slide with critical point dried bacteria was labeled with a water-resistant stamp for reference coordinates (**a1**). A target cell of was documented by phase contrast (**a2**; framed area) and re-localized in SEM with secondary electrons (SE) at low kV (**a3**) and with backscattered electrons (BSE) at higher kV, for detection of the magnetosomes by material contrast (**a4**). Energy dispersive X-ray analysis mapping of iron distribution (L-line of Fe at 3 kV) was superimposed to the SE image, confirming the characteristic Fe component of magnetosomes (**a5**; red). After coating the cells with platinum by ion beam deposition (**b1**) and FIB/SEM milling, in both SE (**b2**) and BSE images (**b3**) the magnetosome chains were clearly visible by material contrast, longitudinally (**b2**; rectangle) or cross-sectioned (**b3**; circle). For better milling properties, critical point dried cells were flat embedded in epoxy resin (**c1**) and milled again with significantly better image quality (**c2**). Besides the magnetosome chains, storage granules (poly-β-hydroxy butyrate (PHB) and sulfur) were slightly distinguishable (**c2**). Embedded cells are still beam sensitive: little holes formed during milling, even at low ion-currents (**c2**; circle). A rough 3D visualization was achieved in a short time using the threshold tool (**c3**). Best results were obtained if a pellet of high pressure frozen and freeze substituted magnetobateria is spread and embedded on slides in small droplets of resin (**d1**) for FIB/SEM-tomography (**d2**). Several structural details were reconstructed with high resolution in 3D (**d3**; **d4**) such as the number and arrangement of the magnetosomes and their chains, storage granules (sulfur = yellow; PHB = white), cellular envelope (blue) and flagella (brown). EsB, energy selective backscattered electron.

Microorganisms: From fast Results To High Resolution

For non-adherent microorganisms, proper immobilization is a critical requirement for cost-effective FIB/SEM high-resolution experiments. In this regard, poly-L-lysine coated slides are widely known to provide adequate adhesion of prokaryotic cells. In order to demonstrate the potential and widespread applicability of fast, analytical investigations with FIB/SEM, we examined a mixed culture, containing magnetobacteria. While EDX in SEM is not commonly used in biology, it remains a very effective way to reveal for, example, metallic inclusions etc. Typically, only a minor fraction of *M. bavaricum* is found within an enriched mixed culture. Cells, immobilized by drop-cryo fixation, were CPD. ROIs containing magnetobacteria were then selected in LM by their characteristic size and shape (Figs. 7a1, 7a2). In order to retrieve the selected ROIs in SEM, we applied a stamp with a reference coordinate system on top of the CPD sample (Fig. 7a3). Chains of magnetosomes were then visualized by BSE at higher voltages (Fig. 7a4) and EDX mapping clearly confirmed and highlighted their iron content (Fig. 7a5). Together, these data allow statistical quantification of the number of magnetosome chains, their length, and their position.

There are, however, some limitations to using CPD specimens immobilized onto glass slides for EDX analysis, due to the strong signal from the glass (Si, O, and their numerous additional components). However, if beam damage is not a severe problem and if the elements have their energy lines in a suitable range, element analysis can be performed at low kV (1–3 kV) (Fig. 7a5).

We then obtained the three-dimensional distribution and architecture of single magnetosomes with FIB/SEM (Fig. 7b). CPD samples were post embedded with resin for higher resolution, compared with non-embedded samples (compare: Fig. 7b2 with 7c2). The cellular matrix was filled with epoxy resin, with resulted in a smoother block face. Since the topographic contrast of BSE is reduced, the signal to noise ratio of BSE is significantly improved (Fig. 7c2). We obtained the best ultra-structural preservation and resolution of structural details when magnetobacteria were high pressure frozen and freeze-substituted (as described by Jogler et al., 2011), then infiltrated in resin and spread on glass slides before polymerization (Fig. 7d1). Single cells, located in droplets of resin, still offer the possibility for post-embedding correlation with LM to identify target cells and enable directed (longitudinally or cross-sectioned) milling for efficient FIB/SEM microscopy (Fig. 7d2). Finally, structural details were reconstructed with high resolution in 3D, allowing for quantification of number and distribution of multiple cellular structures: single magnetosomes and chains, storage granules of sulfur and poly-β-hydroxybutyrate, as well as the cellular envelope and the bundle flagella (Figs. 7d3, 7d4).

Multicellular organisms: Targeted FIB/SEM

As discussed earlier, the larger the sample, the more elaborate is its immobilization, since different surface properties often require specific adhesives. Many multicellular cyanobacteria, such as *Anabaena,* produce specialized nitrogen-fixing heterocysts, which

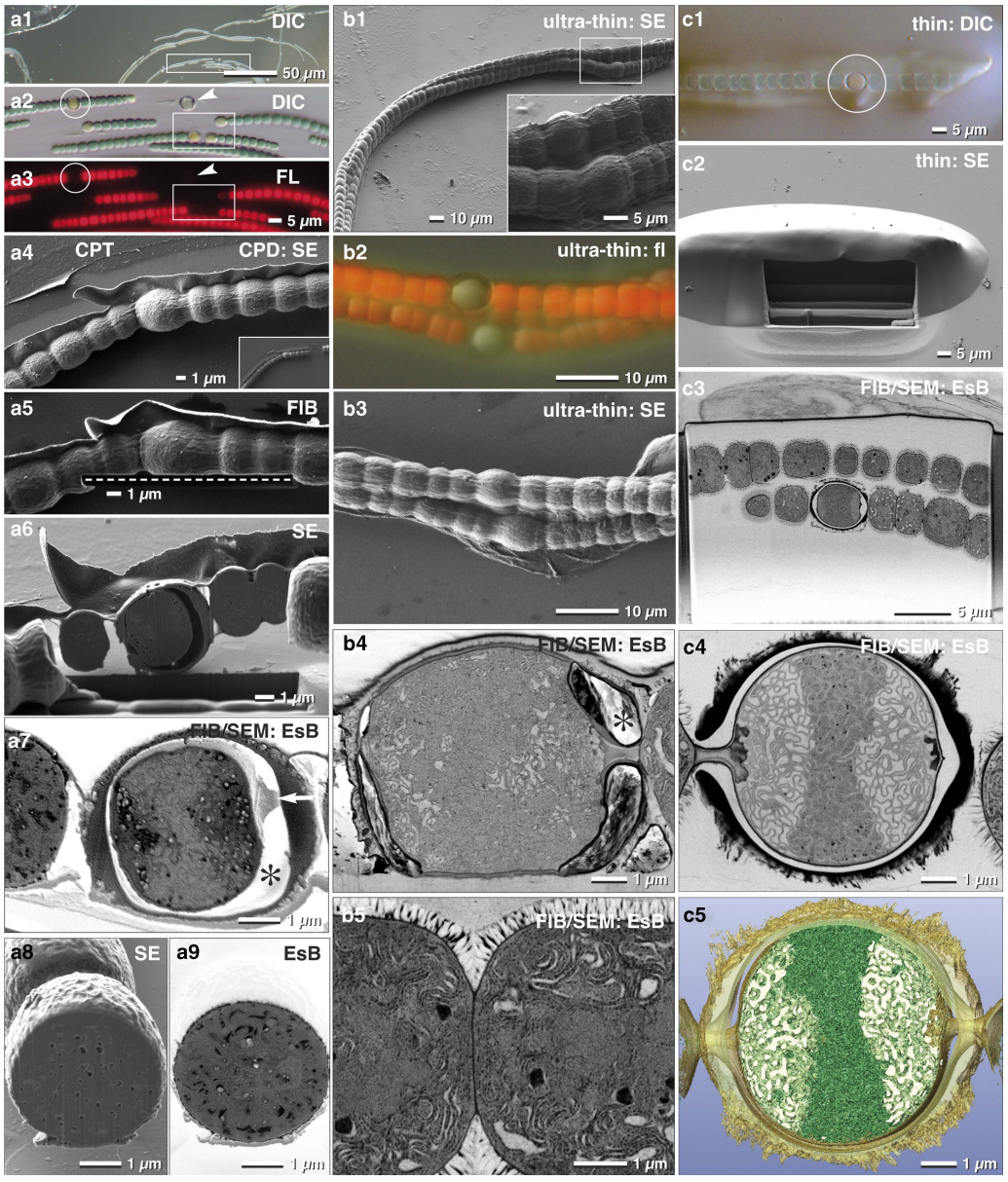

Figure 8. Comparison of critical point dried and embedded cells. Correlative light and electron microscopy (CLEM) of *Anabaena catenula* was facilitated by immobilization of filaments with Biobond. DIC (**a1**, **a2**) and fluorescence microscopy were used to demonstrate viability (**a3**) and re-localization in SEM (**a4**). Fine topographic details of vegetative cells and heterocysts were compared at low kV with high resolution (**a4**). Oriented focused ion beam(FIB)/scanning electron microscopy (SEM) milling of both cell types was easily achieved, as the desired milling plane could be defined with high precision in FIB mode (**a5**; dashed line). Heterocysts were stable for milling (**a6**); their connecting cytoplasmic strands to neighboring vegetative cells were clearly visible (**a7**; arrow), as well as a characteristic gap between the protoplast and the cell wall (**a7**; *) —possibly a shrinking artifact from dehydration. The cytoplasm exhibits some small holes, likely milling artifacts, best seen in SE images (**a8**), compared with the material contrast of metal impregnated cellular substructures, striking in the energy selective backscattered electron (EsB) image (**a9**). As high pressure frozen cells cannot be immobilized, they were infiltrated in resin, spread and ultra-thin embedded on laser marked slides (**b1**). Surprisingly, the autofluorescence of the vegetative cells was preserved (**b2**), although to a much weaker extent, and could be used for "post-embedding CLEM", control of viability and classifying the developmental stage of heterocysts (**b2**). The resolution of cell topography was only slightly reduced (**b3**). Hence, every filament and individual heterocyst was re-located immediately. The FIB/SEM images have excellent resolution of the elaborate thylakoid membranes of both, the heterocysts (**b4**) and the vegetative cells (**b5**), strikingly different in their arrangement. Due to the short infiltration time and the impeded diffusion by the protective cell wall, the gap between cytoplasm and cell wall was not filled with resin (**b4**;*). For optimal FIB/SEM tomography, high-pressure frozen (HPF) filaments were embedded in thicker layers of resin. Light microscopy and SEM were used to localize the heterocysts (**c1**; circle), along with the preserved autofluorescence of chlorophyll of vegetative cells (**c1**). After milling a short ramp, the heterocyst was reached (**c2**) and high-resolution FIB/SEM stacks were collected (**c3** and **c4**) and used for three-dimensional reconstruction (**c5**).

are organized in filaments. These filaments are characterized by a regulated developmental pattern of single heterocysts, separated by vegetative cells. We found that Biobond was sufficient for proper adhesion of *Anabaena* filaments to slides. With LM (DIC, fluorescence), we selected and documented different stages of the transition from vegetative cells to heterocysts, according to the coordinates of the slides (Fig. 8a1–8a3). ROIs were then easily retrieved since the appearance of the filaments was essentially identical in SEM when compared with LM micrographs (Fig. 8a4).

FIB/SEM acquisition of CPD processed samples started directly in front of the selected heterocyst, which allowed setting a precise milling direction (in this case, longitudinally) (Fig. 8a4). Since the sample is not embedded within an epoxy resin, milling a ramp to access the target region is unnecessary. Excavations between

membranes gave a strong topographical contrast (Fig. 8a5) at the expense of the BSE signal and consequentially resolution (Fig. 8a6). Of note, the large gap between the cell wall and the membrane of the heterocyst is at risk of charging. When comparing SE and BSE signals of vegetative cells, the block-face was visibly much smoother due to their dense, compact thylakoid system (Figs. 8a7, 8a8), even though, small holes still disturbed the image quality (Fig. 8a8).

Conveniently, the auto-fluorescence of *Anabaena* filaments was maintained after ultra-thin embedding and high-pressure freezing (Figs. 8b1, 8b2). This allows easy verification of the developmental status of heterocysts, and as a result, the quality of FIB/SEM was significantly improved (Figs. 8b4, 8b5). This improvement takes place even though the space between the cell wall and protoplast of the heterocysts remained empty (Fig. 8b4). We obtained the best results when thicker layers of resin were applied (Fig. 8c). A small ramp had to be milled in front of the target, however, it is clearly smaller compared with classic embedding protocols (Figs. 8c2, 8c3). As a result, single thylakoid membranes were clearly resolvable (Fig. 8c4), which then enabled striking 3D reconstructions, offering insights into the complex architecture down to 2 nm voxel sizes (Fig. 8c5).

Tissues: From LM to FIB/SEM

Immobilizing tissue sections to a slide stabilizes the sample during SEM preparation. This, in turn, keeps the sample flat and allows thin embedding directly on the substrate, without losing orientation. In our hands, tissues were adequately immobilized with Biobond or Cell-Tak™. To look further into this, we imaged a piece of *Tradescantia* epidermis, which inherited several stomata (Fig. 9a1). To determine the position of organelles such as nuclei or chloroplasts, we imaged the sample at higher magnification with different optical modes (DIC, fluorescence, Figs. 9a3, 9a4). Removal of excess resin is of primary importance. To this end, if tissues are tightly fixed (e.g. Cell-Tak™), a moderate centrifugation (500 rpm for 5 min) will remove most or all of the resin obscuring the surface. After polymerization, the SEM image was similar to the LM image (Fig. 9a2), which enabled an easy and fast correlation of these two images (Fig. 9a5). This demonstrates that the target area had sufficient topographic contrast to recognize the stomata over the entire epidermis (Fig. 9a2). This, in turn, allowed for precise and directed milling (longitudinal or cross-sectioned) with FIB (Figs. 9a6, 9a7) and subsequently 3D reconstruction (Fig. 9a8).

In neuroscience, FIB/SEM became an important tool for ultrastructural studies addressing connectomics of the entire brain. For example, vibratome sections of brain tissues are commonly used to study neuronal processes (Fig. 9b1). Slices can be rather large (>1 cm^2) or very fragile, which makes adequate immobilization onto slides particularly challenging.

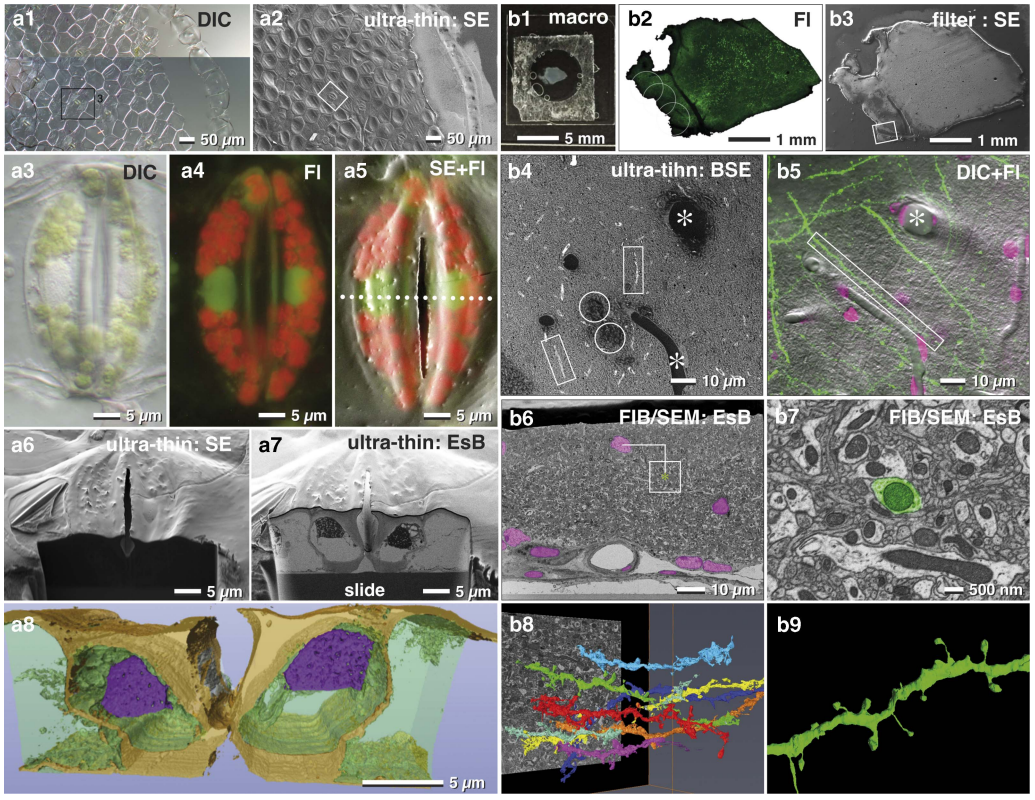

Figure 9. Correlative light and electron microscopy (CLEM) of thin embedded tissues. Light (LM) and scanning electron micrographs (SEM) of an isolated epidermis of *Tradescantia zebrina* used for correlative LM and focused ion beam (FIB)/SEM of oriented sectioning of stomata. The vital epidermis was immobilized to a laser marked slide with Bondic® (**a1**), fixed and ultra-thin embedded in epoxy resin for SEM (**a2**). After fixation stomata were imaged with DIC (**a3**; stomata of **a1**/**a2**) and fluorescence (**a4**). After flat embedding, the stomata were easily re-localized in SEM (**a2**; framed are corresponds to stomata labeled in a1). SEM and LM were superimposed to localize nuclei (**a5**). A ramp was milled with a higher ion-beam-energy (**a6**) until the target region was reached. With a lower ion beam current, serial block face images of the nuclei were acquired (**a7**) for tomographic 3D reconstruction (**a8**). Vibratome section of a mouse brain (**b1**) with GFP labeled dendrites (**b2**), processed with the filter system and flat embedded for FIB/SEM (**b3**). The target region (**b3**; framed are) was imaged at higher kV with backscattered electrons (BSE), for visualizing resin filled vessels (**b4**; *), nuclei (**b4**; circles) and axons (**b4**; rectangles), which was then correlated to LM of dendrites and nuclei (**b5**; merged images of DIC, GFP and DRAQ5). Nuclei and vessels visible in the key frames of FIB/SEM image stacks (**b6**) served for precise triangulation of the target dendrite (**b7**) and its three-dimensional reconstruction among neighboring dendrites (**b8** and b9).

In this regard, the filter system described earlier facilitates a gentle post-fixation, dehydration and infiltration of resin until the sections are in a stable condition (Fig. 3f). Superimposition of LM and SEM micrographs using the characteristic outline of the brain section was generally sufficient for a rough correlation (Figs. 9b2, 9b3). Natural markers like blood vessels and nuclei, detectable in both LM and SEM images, served as fiducial markers to re-locate ROIs within the SEM (Figs. 9b4, 9b5). The distinctive shapes and sizes of structures at the surface, or sectioned natural landmarks (e.g. blood vessels appear as channels or large holes, nuclei as dark dots), facilitated a subsequent superimposition of light and electron micrographs and to define the target area in x/y direction. The depth of the target dendrite within the tissue was determined by aligning block face images with the corresponding micrographs of the LSM stacks and triangulation of the respective landmarks (Fig. 9b6). A rough 3D reconstruction of potential target dendrites within the ROI (Fig. 9b8) revealed the selected dendrite by its unique spine arrangement (Figs. 9b7, 9b9).

Epoxy Sections for economic FIB/SEM

Several aspects favor the use of thick epoxy sections for FIB/SEM: (i) parts of biological specimens cannot be immobilized for various reasons and have to be embedded conventionally within resin blocks; (ii) an archive of samples already exists, which may be used for FIB/SEM years after initial preparation; (iii) samples were investigated with TEM and corresponding 3D stacks are desired of the same ROI. We found that resin sections mounted on laser marked slides was an elegant way for FIB/SEM milling of target structures embedded in resin blocks. The high potential and efficiency of thick sections was demonstrated for the red algae *Porphyridium purpureum* (Fig. 10a) and for SKBR3 breast cancer cells (Fig. 10b). ROIs were selected with bright field, DIC or phase contrast (Figs. 10b1, 10b3, 10b5). As sections are typically in the millimeter scale (feed size), the correlation was easily carried out by merging LM and SEM micrographs. At moderate kV (3–5 kV) *Porphyridium purpureum* were detected with the BSE signal (Fig. 10a4). Cells that overlapped in LM and SEM were located at the surface and already inter-sectioned. Cells visible in LM but

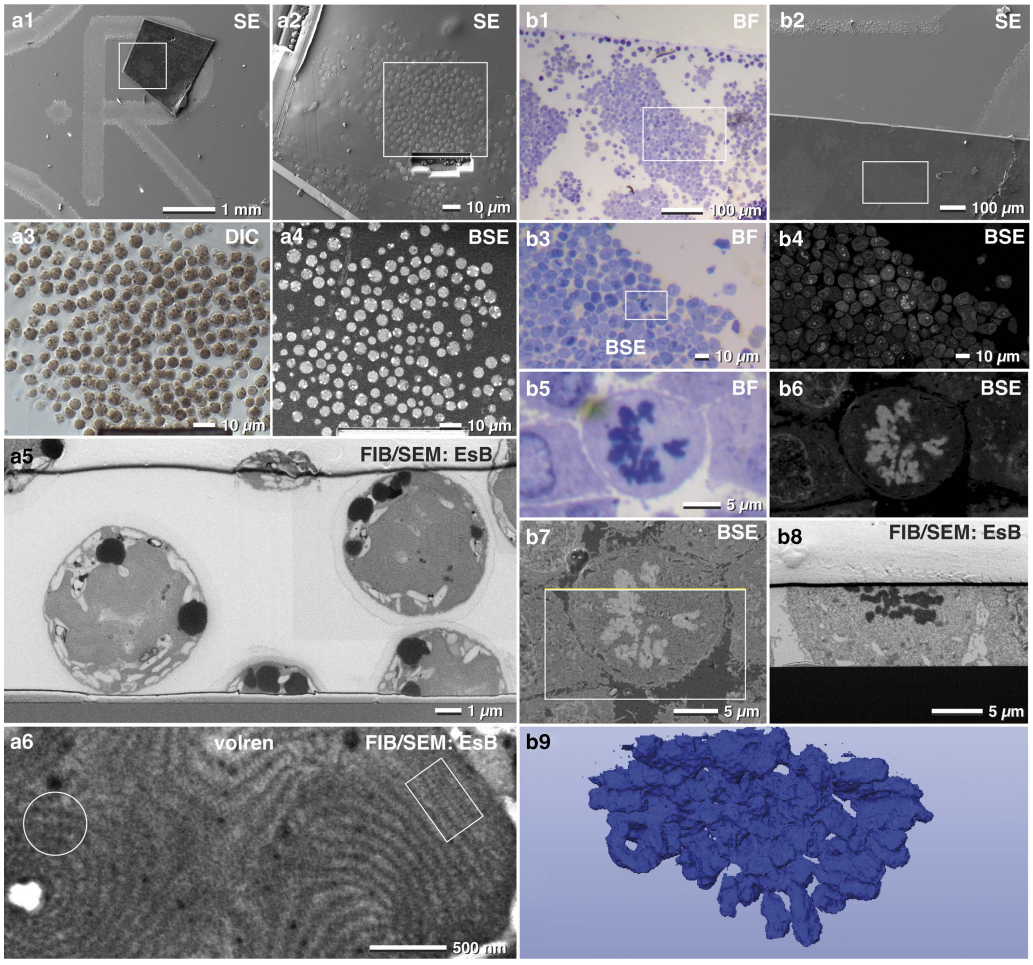

Figure 10. Advantages of thick resin sections for correlative light and electron microscopy. A 10-μm thick microtome section of a resin embedded culture of the red algae *Porphyridium purpureum* was immobilized to onto a laser marked slide (**a1**). The cells were visible in scanning electron microscopy (SEM) by topography (**a2**) and can be compared with light microscopy (LM) (**a3**). Target cells were selected by comparing LM (**a3**) and backscattered electrons (BSE) images (**a4**). After milling a short ramp, image stacks of cells were acquired (**a5**). High resolution confirmed the arrangement of phycobilisomes in side view (**a6**; rectangle) or front view (**a6**; circle). Light and scanning electron micrographs of SKBR3 breast cancer cells fixed as a pellet and processed for conventional transmission electron microscopy. Thick sections (10 μm) were mounted onto laser-marked slides and stained with toluidine blue (**b1**). The selected section were rapidly re-located in SEM (**b2**). At higher voltage, the material contrast of the SEM image (BSE signal) allowed precise localization of target cells in metaphase, imaged in LM (**b3**, **b5**) and SEM (**b4**, **b6**). After milling a short ramp, the target cell was milled (**b7**; rectangle). The yellow line marks the focused ion beam block face image of **b8**. A three-dimensional reconstruction of chromosomes was quickly achieved with the threshold tool (**b9**).

not in SEM were intact within the section (compare Fig. 10a3 with 10a4). We then selected intact cells and directly targeted them with FIB/SEM, omitting the need for a large trench to find whole cells by chance (Figs. 10a5; 11h). Stages of mitosis, infected cells, cells undergoing apoptosis etc. were found with different optical modes (BF, Ph, DIC) (Figs. 10b1–10b5). We selected a mitotic cancer cell, then milled and imaged it with FIB/SEM and finally reconstructed it in 3D (Fig. 10b). Ten-micron sections appeared a bit more sensitive to the ion beam. It is thus recommended to reduce the ion beam energy, which is not a problem as milling speed is generally much faster than imaging time. In addition, the use of a harder mixture of epoxy resin (EMS Hard-Plus Resin 812) is recommended.

Discussion

High-Resolution Analytical SEM for CLEM

Correlative LM combined with SEM and FIB-SEM is of fundamental importance to biomedical research. However, in order for this technique to evolve to a routinely used method, reproducible, efficient and cost-effective procedures need to be further developed. In this regard, compared with TEM, SEM has not reached the widespread use in bio-sciences that one might expect given its high resolution and potential. The potential of analytical high-resolution SEM techniques remains largely unexplored for many scientists starting out with FIB/SEM tomography. Published protocols may suggest that FIB/SEM milling is a stand-alone technique for correlative microscopy. However, we would argue that FIB/SEM milling is only one of the many facets of high-resolution SEM. Fully exhausting the benefits of all SEM capabilities is a prerequisite for efficient routine correlative microscopy. The right handling of WD, high voltage, the use and variation of different parameters (chamber SE, in-lens SE, in-lens EsB, QBSD, apertures, high-current mode) mean that SEM can be a versatile and powerful tool for a wide range of applications (Scala et al., 1985; Bozzola & Russell, 1991).

Correlation of light and EM as a method became substantially more elaborate with the introduction of serial block-face sectioning. Now, a 3D-LM data set with precise reference coordinates serves a basis (Lucas et al., 2012; Karreman et al., 2016; Cheng et al., 2017; Lees et al., 2017; Russell et al., 2017). For standard EM preparations, specimens have to be cut into small pieces, which is accompanied by a significant loss of the 3D-context. Even after oriented embedding, correlation can still be exquisitely difficult. The basic problem is that, in contrast to 2D, we are typically unable to correlate volumes without computing. Even our eyes do not see in 3D but rather interpret spaces by 2D

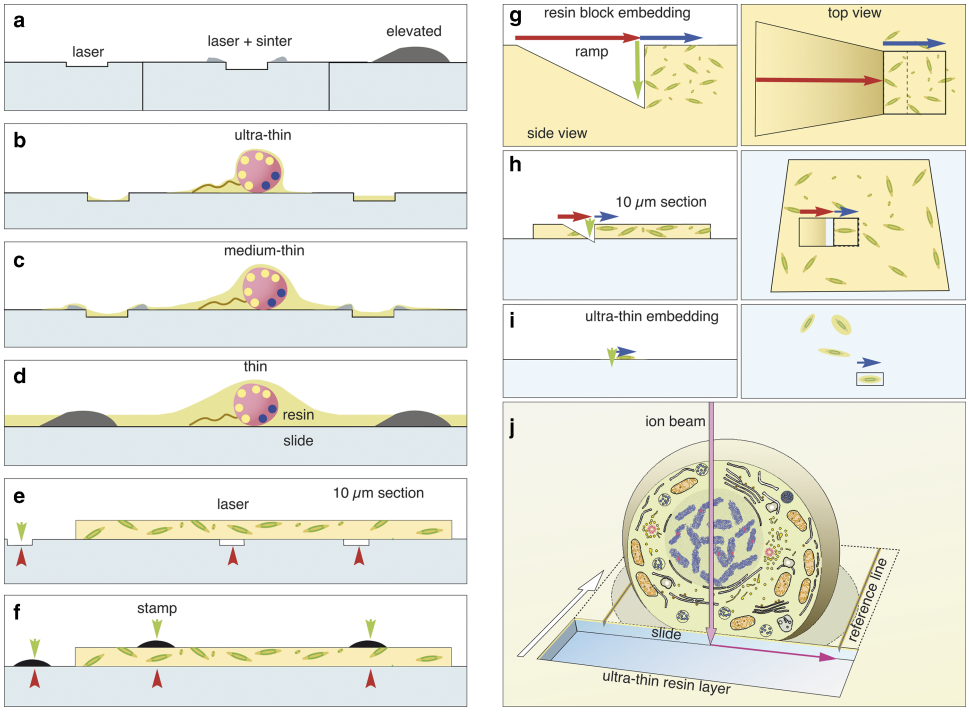

Figure 11. Choice of label type for correlative light and electron microscopy (CLEM). Fine customized labels can be produced with a laser (**a**). If TiO_2 is used for focusing the laser, a sintered relief outlines the labels. Elevated labels can be produced by silk-screen printing or sintering of transfer pictures (decalcomania). Depending on the desired thickness of the resin layer, the adequate labels are used for ultra-thin embedding (**b**), thin embedding (**c**), or thicker resin layers (**d**). Thick microtome sections (5–10 μm) can be mounted onto laser marked slides (**e**) or on standard slides and labeled with a stamp (**f**). Coordinates are always visible in light microscopy (red arrowheads) and in part in scanning electron microscopy (SEM) (green arrowheads) and can be used re-location directly or by triangulation. Advantage of flat samples for focused ion beam (FIB)/SEM If a single cell within a pellet (**g**) has to be reconstructed with FIB/SEM, a ramp must be milled (**g**; red arrow) to reach the desired depth (green arrow). As cells are randomly oriented, a large volume has to be sectioned (blue arrow) for an image stack to including a complete cell in the desired orientation (cross section, longitudinal section). The milling area (boxed area) has to be broader than the ROI due to re-deposition. Moderate magnifications have to be chosen to enhance the chance of catching a cell in the right orientation, thereby limiting resolution. When 10 μm resin sections are used for CLEM, the volume of the ramp is significantly reduced, and the surface of the slide can be used as a reference plane (*xy*) for alignment (**h**). If cells are embedded ultra-thin (**i**), the ramp is needless and only the actual size of the regions of interest (ROI) is milled (**i**; blue arrow, boxed area). The milling area can be precisely adjusted for each cell both in size and orientation. The magnification can be adapted, from the start of milling to the size of the target cell. If an ultra-thin embedded cell is used for FIB/SEM (**j**), the block face defines the first plane for the cubic volume of the image stack. The glass slide gives a second absolute reference plane (*xz*) for alignment. Lines, milled parallel to the ROI into the slide, serve as a third reference plane for precise alignment of the image stack in three dimension.

images on the retina. The simple postulate is: correlate in 2D and make the specimen suitable for it.

Which geometry of biological samples is desirable or restrictive for CLEM? The main limitation is in the FIB/SEM operation. The maximum milling depth is about 100 μm, but due to curtaining in at these depths, a more practical depth is around 50–60 μm. Specimens within that range are suitable for LM. Thus, if cells or tissues are naturally within this range (bacteria: few μm; HeLa cells: 20 μm; diatoms/algal cells 5–100 μm), then they simply have to be immobilized onto a slide. Depending on the sample, however, this can be quite challenging. If larger tissues are used (e.g. mouse brain with a volume of approx. 1 cm^3), the classic way of cutting small cubes with a feed size of 1 mm may result in an astronomic number of pieces (e.g. ~1000, each with the risk of severe damage), which should be fixed and embedded numerically. Cutting the same volume with a vibratome into 50–70 μm sections reduces the number of individual slices to 150–200. Compared with 1 mm^3 cubes, these slices have, due to their minor thickness, several advantages: (i) they are suitable for all LM modes (bright field, DIC, fluorescence, CLSM); (ii) fixation and contrast enhancement is faster and more consistent due to more permissive diffusion conditions; (iii) the entire slice can be investigated with SEM at high resolution; (iv) each ROI defined in LM can be re-localized by simple triangulation, as LM and SEM images match perfectly (Fig. 9b).

The Right Coordinate System

It is undisputed that a robust coordinate system is a solution for any correlative microscopy technique. This implies that instead of the structural details, the images of the coordinates in LM and SEM are initially correlated. This correlation is trivial, but only if the labels are clearly visible in both microscopy modalities (Fig. 5a). Today, complete solutions are commercially available and generally based on the same idea: selecting an ROI in LM, storing the coordinates, switching to SEM and recalling the coordinates (Liv et al., 2013; Brama et al., 2016; Schorb & Sieckmann, 2017). This is a valuable improvement if a set of instruments from the same manufacturer is used and trimming, mounting etc. does not alter the specimen. In practice, however, LM and SEM systems from different manufacturers, which do not intrinsically share a coordinate system, are often used for CLEM. To this end, inherent labels on the specimen are most beneficial for investigating the same specimen on different systems, for example when changing from LM instruments (LSM for fluorescence and DIC) to SEM or using micro-CT or X-ray microscopy. With different labeling methods covering a broad range of requirements for different applications, correlation with any microscope should be possible. Since the coordinate system is a 2D pattern, superimposition and only linear scaling or rotation is required—if at all. Finally, any image distortion is instantly recognized.

Immobilization and Flat Embedding

A prerequisite for any flat embedding of cells, cell aggregates, and tissues is their immobilization in a fixed position relative to the coordinate system. Immobilization of different biological objects, capable of withstanding the entire EM procedure, including exchanging fixatives, solutions, washing steps, and dehydration in ethanol or acetone, will always be challenging. From a variety of available adhesives, we found two that particularly stand out. First, Biobond had very good adhesive properties for prokaryotic cells, larger eukaryotic cells and cell aggregates (Fig. 8). Since the adhesive coating is in the nm range, the evenness of the slide is maintained, which is important for high-resolution SEM, e.g. of cells with flagella or filopodia. Second, Cell-Tak^{TM} is the strongest adhesive and therefore the best choice for larger tissue sections. As Cell-Tak^{TM} is preferentially spread with a coverslip, the thickness cannot be precisely controlled, which limits its application in SEM for high-resolution topography of cell adherent structures (Fig. 9a). Although the chance for successful immobilization of any objects is on 50%, flat embedding is still possible by alternative strategies. If live-cell imaging is dispensable or is not possible (e.g. high-pressure freezing of non-adherent cells), samples can be processed until infiltration with resin, spread onto slides with coordinates and embedded ultra-thin or thin (Figs. 3d, 7d, 8b, 8c). CLEM is still possible as fluorescence can surprisingly still be detected for a variety of objects, although much weaker, after HPF, FS, and embedding (Fig. 8b). This signal provides practical information e.g. about vitality (vegetative cells of *Anabaena catenula*) or stages of cell differentiation (heterocysts of *A. catenula*) for a directed and efficient milling (Fig. 8). It is generally attractive to embed samples into resins which maintain fluorescence such as Lowicryl (Kukulski et al., 2012). However, it must be determined experimentally whether this rather soft resin is stable enough for high-resolution FIB/SEM. If samples are (i) available only in few individuals; (ii) fragile; (iii) or have to be kept flat during fixation and dehydration (histological sections), the presented filter system is of great benefit (Fig. 3f).

CLEM is limited, but still possible for histological sections, as their characteristic shape and surface features are retained and can be examined after thin/ultra-thin embedding with LM and SEM (Fig. 9). The necessity and advantage of thin embedded samples became a topic of discussion within the last years, with the increasing demand of FIB/SEM in biosciences. A few protocols are published for flat embedding in resin by draining, blotting, centrifugation with the primary aim to reduce the resin layer to a minimum (Kizilyaprak et al., 2014; Lucas et al., 2017; Schieber et al., 2017). In practice, however, the aim is not an ultimately thin epoxy resin layer, but rather to control the thickness, depending on the samples and the scientific question. The main obstacle to this control is that the viscosity of resin rises significantly on the seconds to minutes timescale during spreading into thin layers, resulting in non-reproducible thickness. The removal of excessive resin by ethanol (Belu et al., 2016) is a good attempt but bears the risk of uncontrolled reduction, which is critical, when prokaryotic cells should be embedded in a resin layer of only a few microns thick. By keeping the slides in an acetone-saturated chamber (Fig. 3c), the fluidity of the resin is retained, until an even spreading is achieved. By changing the parameters (surface properties of slides or cover slips, resin concentration, draining by gravity, centrifugation, exposure time), a suitable thickness of resin can be achieved for individual samples after a few test runs. We illustrate the multiple possibilities for immobilization, fixation and thin embedding of various specimens for CLEM in a flow chart (Fig. 12).

Thick Sections for Bridging TEM-Tomography with FIB/SEM

When comparing TEM- and FIB/SEM tomography, the excellent TEM resolution in *xy* cannot be reached with SEM due to physical and geometrical considerations (Giannuzzi, 2004). Section

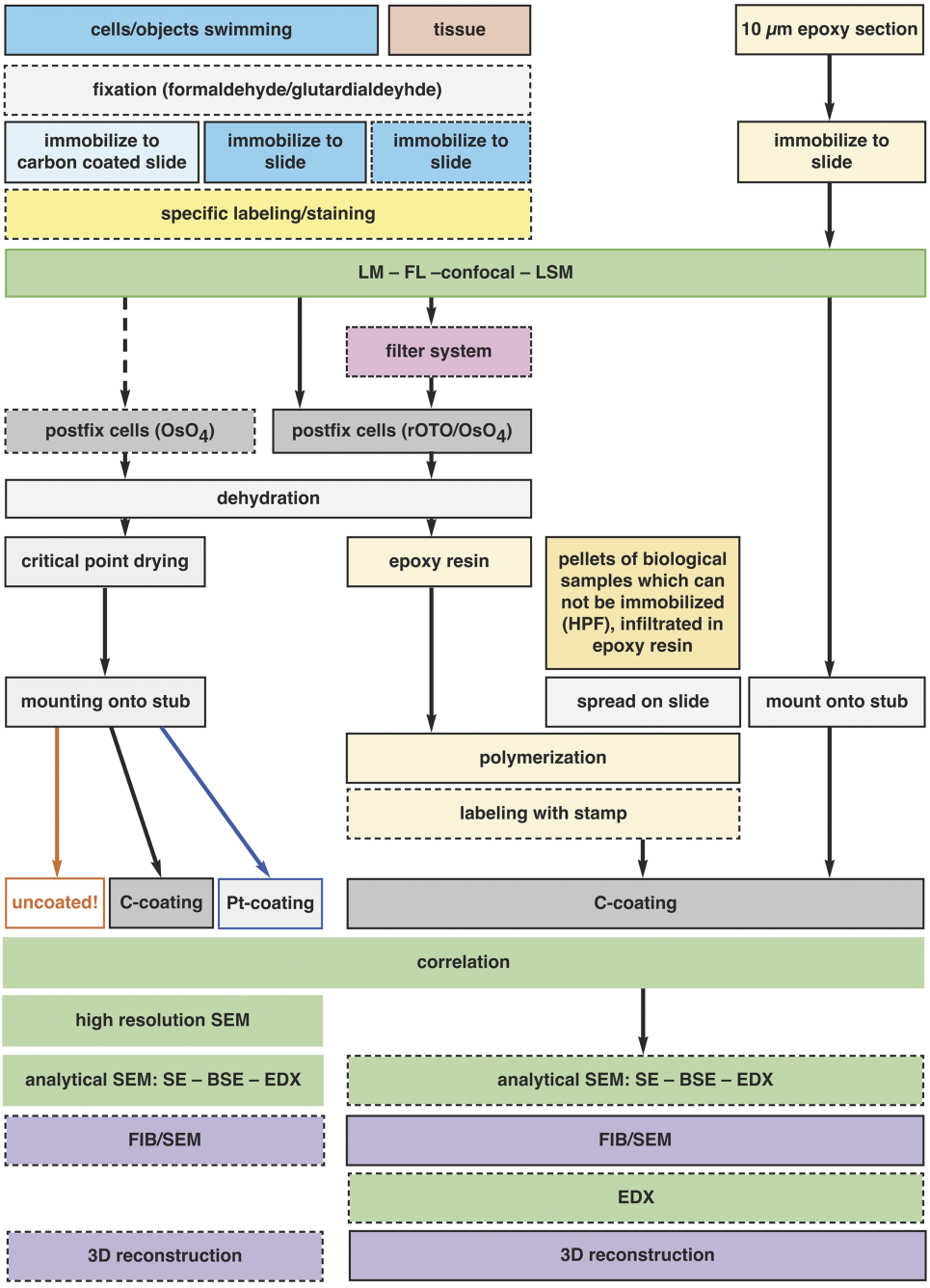

Figure 12. Preparation for correlative light and electron microscopy (CLEM). The flow chart illustrates the general schemes for the preparation of various specimens for flat embedding. The diagram includes all common specimen types from single cells to tissue sections, adherent cells, several immobilization procedures, and preparation of specimens which cannot be immobilized in principle (e.g. HPF frozen living cells), conservative fixation and embedding of fragile objects with a filter system and pre- and post-embedding CLEM. The possibilities of analytical investigations with the corresponding preparation or instrumental conditions are indicated.

thickness for TEM-tomography, however, is limited to ~200–1000 nm, ideal for prokaryotic cells and cellular structures as the endoplasmic reticulum, but not for the complex 3D architecture of entire eukaryotic cells (Ercius et al., 2015). TEM-tomography followed by FIB/SEM tomography is an attractive solution to combine the highest resolution with very large volume information. This works reliable if a 200–400 nm section from a resin block is used for TEM-tomography and the following 10 μm section is used for FIB/SEM of the same ROI, which can be repeated several times in cycles. Within a very large 3D volume (e.g. an entire cell), high-resolution 3D details can be implemented. The potential of thick serial sections for FIB/SEM is impressively demonstrated by Hayworth et al. (2015).

Defining Space

Three orthogonal planes define a cube, typically achieved by FIB/SEM milling, resulting in an image stack. After milling, the defined planes are not maintained due to specimen drift, image distortions etc. (Schaffer et al., 2007; Boergens & Denk, 2013; Šedivý & Jäger, 2017; Storm et al., 2017). Therefore, an alignment of each image stack is necessary, which requires absolute fiducial

markers for reference. The block face image represents the *xy* plane. If image stacks of resin blocks are automatically aligned (without references), the alignment is optimistically assumed to be correct, as it cannot be verified easily, except if substructures of known geometry (e.g. spheres) are present in abundance. The generation of references is not trivial for resin blocks. However, thin embedded samples provide the second reference plane in *xz* automatically, given by the surface of the slide/coverslip (Figs. 5f–5h; 11). The mandatory third reference plane can be easily produced, by milling parallel "lines", which represent *de facto* vertical planes through the resin, ending orthogonally in the glass slide (Figs. 5h; 11j). In fact, most FIB/SEM image stacks require drift correction, and thus reliable references are necessary.

Independent of the method used for alignment of a FIB/SEM stack (Kreshuk et al., 2011; Cardona et al., 2012; Saalfeld et al., 2012; Schindelin et al., 2012), the accuracy can be validated by the reference coordinates and adjusted manually, which is likely necessary for long series (Han et al., 2018). Without references, any changes in volume geometry cannot be recognized or corrected (Storm et al., 2017). There are promising examples of intelligent software which aim to learn each step of alignment by mimicking the human approach (Sommer & Gerlich, 2013; Kraus & Frey, 2016; Kan, 2017). These programs, however, require substantial computing power and are still far away from being routinely applicable to large data sets.

Cost-Effectiveness Considerations

If state of the art techniques is established as routine methods, cost-effectiveness becomes an important consideration. FIB/SEM will be always time-consuming, due to the enormous number of images for high-resolution tomography. Numerous scientific questions lead to results to some extent by chance, for instance when pellets of microorganisms are milled (Fig. 11g). In this regard, obtaining a longitudinal section through a heterocyst of cyanobacteria between vegetative cells, at the right stage and in the right orientation, is like winning the lottery. With flat embedded cyanobacteria filaments this can be achieved routinely with all controls, using different strains and culturing conditions (Fig. 8).

For questions involving eukaryotic cells or tissues, several efficiency aspects have to be considered. For example, for a HeLa cell in metaphase (spherical, with a diameter of 20 μm), a cube with a 20 μm feed size has to be milled. Then, by setting the section thicknesses to 10 nm, 2000 sections are needed. Under best conditions, with rOTO contrast enhancement (Seligman et al., 1966; Willingham & Rutherford, 1984) and using the in-lens SE-detector, the exposure time for an acceptable block face image can be around 15 s. This results in roughly an 8 h exposure time for the whole cell, thereby possible within a day. Classical glutaraldehyde/osmiumtetroxide (Palade, 1952) fixation, however, gives a much weaker contrast. If using the EsB detector, an exposure time of one minute or more is expected. Thus, the FIB/SEM experiment becomes a 2-day venture with at least one overnight session, bearing risks of the instability of the system, heating of the Ga-emitter and loss of information during the restart of the milling procedure. For a HeLa cell, milling time is much less than the exposure time. However, for cross sections of *C. elegans*, the milling time increases dramatically, especially when low ion currents (100–200 pA) have to be used. FIB/SEM investigations increase to several days or even weeks with costs of several thousand dollars per run.

The costs for FIB consumables (Ga-emitter, apertures, service costs) can be reduced to 50% simply by flat embedding due to omitting a ramp and reducing the volume to be milled exclusively to the ROI (compare: Fig. 11g with 11i). Beside economic aspects, an important benefit of flat embedded samples, compared with established procedures, is (i) saving time; (ii) the possibility of setting the milling frame as precisely as desired for cross or longitudinal section; and (iii) starting close to structural details documented before in LM, e.g. cellular inclusion, centrosomes etc.

Summary

We developed an easy and broadly applicable procedure, consisting of several technical improvements of relevant scientific investigations, including the whole range of simple correlative, high-resolution LM/SEM microscopy, with immuno-labeling, flat embedding for FIB/SEM and post-embedding investigations of specimens (Fig. 12). Since every sample has its own handling requirements and limitations, several adjustments based on sample properties and scientific question are offered (Fig. 12). Defining and maintaining coordinates of a target structure is the most important aspect for re-localization in SEM. With sample preparation, coordinate labeling, and with the right conductive coating, the analytical potential of the SEM with all detectable signals (SE, BSE, EDX) is of great advantage for correlative investigations.

Acknowledgments. The excellent technical assistance of Silvia Dobler, Jennifer Grünert, and Cornelia Niemann is gratefully acknowledged. The authors are much obliged to Joel Ryan for carefully revising the manuscript.

Conflict of interest. The authors declare that they have no conflict of interest.

References

Belu A, Schnitker J, Bertazzo S, Neumann E, Mayer D, Offenhäusser A and Santoro F (2016) Ultra-thin resin embedding method for scanning electron microscopy of individual cells on high and low aspect ratio 3D nanostructures. *J Microsc* **263**, 78–86.

Boergens KM and Denk W (2013) Controlling FIB-SBEM slice thickness by monitoring the transmitted ion beam. *J Microsc* **252**, 258–262.

Bozzola JJ and Russell LD (1991) *Electron Microscopy: Principles and Techniques for Biologists*. Boston, MA: Jones & Bartlett Publishers, Inc.

Brama E, Peddie CJ, Wilkes G, Gu Y, Collinson LM and Jones ML (2016) ultraLM and miniLM: Locator tools for smart tracking of fluorescent cells in correlative light and electron microscopy. Wellcome Open Res, 1. Available at https://www.ncbi.nlm.nih.gov/pmc/articles/PMC5234702/ (retrieved February 23, 2018).

Cardona A, Saalfeld S, Schindelin J, Arganda-Carreras I, Preibisch S, Longair M, Tomancak P, Hartenstein V and Douglas RJ (2012) TrakEM2 Software for Neural Circuit Reconstruction. *PLoS ONE* **7**, e38011.

Cheng D, Shami G, Morsch M, Huynh M, Trimby P and Braet F (2017) Chapter 11 – Relocation is the key to successful correlative fluorescence and scanning electron microscopy. In: *Methods in Cell Biology, vol. 140, Correlative Light and Electron Microscopy III*, Müller-Reichert T and Verkade P (Eds.), pp. 215–244. San Diego, CA: Academic Press.

Drobne D (2013) 3D Imaging of cells and tissues by focused ion beam/scanning electron microscopy (FIB/SEM). In: *Nanoimaging, Methods in Molecular Biology*, Sousa AA and Kruhlak MJ (Eds.), pp. 275–292. New York, NY: Humana Press.

Ercius P, Alaidi O, Rames MJ and Ren G (2015) Electron tomography: A three-dimensional analytic tool for hard and soft materials research. *Adv Mater* **27**, 5638–5663.

Gaertner F, Ahmad Z, Rosenberger G, Fan S, Nicolai L, Busch B, Yavuz G, Luckner M, Ishikawa-Ankerhold H, Hennel R, Benechet A, Lorenz M, Chandraratne S, Schubert I, Helmer S, Striednig B, Stark K, Janko M, Böttcher RT, Verschoor A, Leon C, Gachet C, Gudermann T, Schnitzler MY, Pincus Z, Iannacone M, Haas R, Wanner G, Lauber K, Sixt M and Massberg S (2017) Migrating platelets are mechano-scavengers that collect and bundle bacteria. *Cell* **171**, 1368–1382.e23.

Giannuzzi LA (2004) *Introduction to Focused Ion Beams: Instrumentation, Theory, Techniques and Practice*. New York, NY: Springer Science & Business Media.

Han R, Zhang F, Gao X and Murphy R (2018) A fast fiducial marker tracking model for fully automatic alignment in electron tomography. *Bioinformatics* **34**, 853–863.

Hayworth KJ, Xu CS, Lu Z, Knott GW, Fetter RD, Tapia JC, Lichtman JW and Hess HF (2015) Ultrastructurally-smooth thick partitioning and volume stitching for larger-scale connectomics. *Nat Methods* **12**, 319–322.

Jogler C, Wanner G, Kolinko S, Niebler M, Amann R, Petersen N, Kube M, Reinhardt R and Schüler D (2011) Conservation of proteobacterial magnetosome genes and structures in an uncultivated member of the deep-branching Nitrospira phylum. *Proc Natl Acad Sci USA* **108**, 1134–1139.

Kan A (2017) Machine learning applications in cell image analysis. *Immunol Cell Biol* **95**, 525–530.

Karreman MA, Hyenne V, Schwab Y and Goetz JG (2016) Intravital correlative microscopy: Imaging life at the nanoscale. *Trends Cell Biol* **26**, 848–863.

Kizilyaprak C, Bittermann AG, Daraspe J and Humbel BM (2014) FIB-SEM tomography in biology. *Methods Mol Biol* **1117**, 541–558.

Kraus OZ and Frey BJ (2016) Computer vision for high content screening. *Crit Rev Biochem Mol Biol* **51**, 102–109.

Kreshuk A, Straehle CN, Sommer C, Koethe U, Cantoni M, Knott G and Hamprecht FA (2011) Automated Detection and Segmentation of Synaptic Contacts in Nearly Isotropic Serial Electron Microscopy Images. *PLoS ONE* **6**, e24899.

Kukulski W, Schorb M, Welsch S, Picco A, Kaksonen M and Briggs JAG (2012) Precise, correlated fluorescence microscopy and electron tomography of lowicryl sections using fluorescent fiducial markers. *Methods Cell Biol* **111**, 235–257.

Lees RM, Peddie CJ, Collinson LM, Ashby MC and Verkade P (2017) Correlative two-photon and serial block face scanning electron microscopy in neuronal tissue using 3D near-infrared branding maps. *Methods Cell Biol* **140**, 245–276.

Liv N, Zonnevylle AC, Narvaez AC, Effting APJ, Voorneveld PW, Lucas MS, Hardwick JC, Wepf RA, Kruit P and Hoogenboom JP (2013) Simultaneous correlative scanning electron and high-NA fluorescence microscopy. *PLoS ONE* **8**, e55707.

Lucas MS, Günthert M, Bittermann AG, de Marco A and Wepf R (2017) Chapter 7 – Correlation of live-cell imaging with volume scanning electron microscopy. In: *Methods in Cell Biology, vol. 140, Correlative Light A Electron Microscopy III*, Müller-Reichert T and Verkade P (Eds.), pp. 123–148. San Diego, CA: Academic Press.

Lucas MS, Günthert M, Gasser P, Lucas F and Wepf R (2012) Bridging microscopes: 3D correlative light and scanning electron microscopy of complex biological structures. *Methods Cell Biol* **111**, 325–356.

Luckner M and Wanner G (2018) Precise and economic FIB/SEM for CLEM: With 2 nm voxels through mitosis. *Histochem Cell Biol* **150**, 1–22.

Martin R, Busch W, Herrmann RG and Wanner G (1994) Efficient preparation of plant chromosomes for high-resolution scanning electron microscopy. *Chromosome Res* **2**, 411–415.

Palade GE (1952) A study of fixation for electron microscopy. *J Exp Med* **95**, 285–298.

Peddie CJ and Collinson LM (2014) Exploring the third dimension: Volume electron microscopy comes of age. *Micron* 61, 9–19.

Romero-Brey I and Bartenschlager R (2015) Viral infection at high magnification: 3D electron microscopy methods to analyze the architecture of infected cells. *Viruses* **7**, 6316–6345.

Russell MRG, Lerner TR, Burden JJ, Nkwe DO, Pelchen-Matthews A, Domart M-C, Durgan J, Weston A, Jones ML, Peddie CJ, Carzaniga R, Florey O, Marsh M, Gutierrez MG and Collinson LM (2017) 3D correlative light and electron microscopy of cultured cells using serial blockface scanning electron microscopy. *J Cell Sci* **130**, 278–291.

Saalfeld S, Fetter R, Cardona A and Tomancak P (2012) Elastic volume reconstruction from series of ultra-thin microscopy sections. *Nat Methods* **9**, 717–720.

Scala C, Pasquinelli G, Martegani F and Laschi R (1985) Use of secondary electron detectors for compositional studies on embedded biological material. *Scan Electron Microsc* **Pt 4**, 1709–1718.

Schaffer M, Wagner J, Schaffer B, Schmied M and Mulders H (2007) Automated three-dimensional X-ray analysis using a dual-beam FIB. *Ultramicroscopy* **107**, 587–597.

Schieber NL, Machado P, Markert SM, Stigloher C, Schwab Y and Steyer AM (2017) Minimal resin embedding of multicellular specimens for targeted FIB-SEM imaging. *Methods Cell Biol* **140**, 69–83.

Schindelin J, Arganda-Carreras I, Frise E, Kaynig V, Longair M, Pietzsch T, Preibisch S, Rueden C, Saalfeld S, Schmid B, Tinevez J-Y, White DJ, Hartenstein V, Eliceiri K, Tomancak P and Cardona A (2012) Fiji: An open-source platform for biological-image analysis. *Nat Methods* **9**, 676–682.

Schorb M and Sieckmann F (2017) Matrix MAPS-an intuitive software to acquire, analyze, and annotate light microscopy data for CLEM. *Methods Cell Biol* **140**, 321–333.

Šedivý O and Jäger A (2017) On correction of translational misalignments between section planes in 3D EBSD. *J Microsc* **266**, 186–199.

Seligman AM, Wasserkrug HL and Hanker JS (1966) A new staining method (OTO) for enhancing contrast of lipid–containing membranes and droplets in osmium tetroxide–fixed tissue with osmiophilic thiocarbohydrazide (TCH). *J Cell Biol* **30**, 424–432.

Sommer C and Gerlich DW (2013) Machine learning in cell biology - teaching computers to recognize phenotypes. *J Cell Sci* **126**, 5529–5539.

Storm M, Beckmann F and Rau C (2017) Analytical registration of vertical image drifts in parallel beam tomographic data. *Opt Lett* **42**, 4982–4985.

Utke I, Moshkalev S and Russell P (2012) *Nanofabrication Using Focused Ion and Electron Beams: Principles and Applications*. Oxford, UK: Oxford University Press.

Waite JH and Tanzer ML (1981) Polyphenolic substance of mytilus edulis: Novel adhesive containing L-dopa and hydroxyproline. *Science* **212**, 1038–1040.

Wanner G, Gaβner G, Formanek H and Greiner G (1990) Plattenförmiger Objektträger für die Mikroskopie. Deutsches Patentamt, Gebrauchsmuster: G 89 14 0532.

Wanner G, Gaβner G, Formanek H and Greiner G (1993) Plattenförmiger Objektträger für die Rasterelektronenmikroskopie. Patentschrift: DE 39 02 348 C2, Deutsches Patentamt.

Wanner G and Schroeder-Reiter E (2008) Scanning electron microscopy of chromosomes. *Methods Cell Biol* **88**, 451–474.

Wanner G, Schroeder-Reiter E, Ma W, Houben A and Schubert V (2015) The ultrastructure of mono- and holocentric plant centromeres: An immunological investigation by structured illumination microscopy and scanning electron microscopy. *Chromosoma* **124**, 503–517.

Wanner G, Vogl K and Overmann J (2008) Ultrastructural Characterization of the Prokaryotic Symbiosis in "Chlorochromatium aggregatum". *J Bacteriol* **190**, 3721–3730.

Willingham MC and Rutherford AV (1984) The use of osmium-thiocarbohydrazide-osmium (OTO) and ferrocyanide-reduced osmium methods to enhance membrane contrast and preservation in cultured cells. *J Histochem Cytochem* **32**, 455–460.

Xu CS, Hayworth KJ, Lu Z, Grob P, Hassan AM, García-Cerdán JG, Niyogi KK, Nogales E, Weinberg RJ and Hess HF (2017) Enhanced FIB-SEM systems for large-volume 3D imaging. eLife 6. Available at https://elifesciences.org/articles/25916 (retrieved January 24, 2018).

10.2 Publication II

Structural stress responses and degradation of dictyosomes in algae analyzed by TEM and FIB-SEM tomography.

Ursula Lütz-Meindl, **Manja Luckner**, Ancuela Andosch & Gerhard Wanner (2016)

Journal of Microscopy, 2016 Aug;263(2):129-41
doi: 10.1111/jmi.12369

Summary
Stress-induced physiological deficiencies in cells are reflected in structural, morphological and functional reactions of organelles. Although numerous investigations have focused on chloroplasts and mitochondria as main targets of different stressors in plant cells, there is insufficient information on the plant Golgi apparatus as stress sensor. By using the advantages of field emission scanning electron microscopy tomography in combination with classical ultrathin sectioning and transmission electron microscopic analyses, we provide structural evidence for common stress responses of the large and highly stable dictyosomes in the algal model system *Micrasterias*. Stress was induced by different metals such as manganese and lead, by starvation in 9 weeks of darkness or by inhibiting photosynthesis or glycolysis and by disturbing ionic homeostasis via KCl. For the first time a stress-induced degradation pathway of dictyosomes is described that does not follow “classical” autophagy but occurs by disintegration of cisternae into single membrane balls that seem to be finally absorbed by the endoplasmic reticulum (ER). Comparison of the morphological features that accompany dictyosomal degradation in *Micrasterias* to similar reactions observed during the same stress application in *Nitella* indicates an ubiquitous degradation process at least in algae. As the algae investigated belong to the closest relatives of higher land plants these results may also be relevant for understanding dictyosomal stress and degradation responses in the latter phylogenetic group. In addition, this study shows that two-dimensional transmission electron microscopy is insufficient for elucidating complex processes such as organelle degradation, and that information from three-dimensional reconstructions as provided by field emission scanning electron microscopy tomography is absolutely required for a comprehensive understanding of the phenomenon.

Journal of Microscopy

Journal of Microscopy, Vol. 263, Issue 2 2016, pp. 129–141 doi: 10.1111/jmi.12369
Received 14 August 2015; accepted 25 November 2015

Structural stress responses and degradation of dictyosomes in algae analysed by TEM and FIB-SEM tomography

U. LÜTZ-MEINDL*, M. LUCKNER†, A. ANDOSCH* & G. WANNER†
*Plant Physiology Division, Cell Biology Department, University of Salzburg, Salzburg, Austria
†Ultrastructural Research, Faculty of Biology, Ludwig-Maximilians-University, Munich, Germany

Key words. Cadmium, dictyosomes, electron tomography, KCl, *Micrasterias*, *Nitella*.

Summary

Stress-induced physiological deficiencies in cells are reflected in structural, morphological and functional reactions of organelles. Although numerous investigations have focused on chloroplasts and mitochondria as main targets of different stressors in plant cells, there is insufficient information on the plant Golgi apparatus as stress sensor. By using the advantages of field emission scanning electron microscopy tomography in combination with classical ultrathin sectioning and transmission electron microscopic analyses, we provide structural evidence for common stress responses of the large and highly stable dictyosomes in the algal model system *Micrasterias*. Stress is induced by different metals such as manganese and lead, by starvation in 9 weeks of darkness or by inhibiting photosynthesis or glycolysis and by disturbing ionic homeostasis via KCl. For the first time a stress-induced degradation pathway of dictyosomes is described that does not follow "classical" autophagy but occurs by disintegration of cisternae into single membrane balls that seem to be finally absorbed by the endoplasmic reticulum (ER). Comparison of the morphological features that accompany dictyosomal degradation in *Micrasterias* to similar reactions observed during the same stress application in *Nitella* indicates an ubiquitous degradation process at least in algae. As the algae investigated belong to the closest relatives of higher land plants these results may also be relevant for understanding dictyosomal stress and degradation responses in the latter phylogenetic group. In addition, this study shows that two-dimensional transmission electron microscopy is insufficient for elucidating complex processes such as organelle degradation, and that information from three-dimensional reconstructions as provided by field emission scanning electron microscopy tomography is absolutely required for a comprehensive understanding of the phenomenon.

Correspondence to: Ursula Lütz-Meindl, Plant Physiology Division, Cell Biology Department, University of Salzburg, Hellbrunnerstrasse 34, A-5020 Salzburg, Austria. Tel: +43-662-8044-5555; fax: +43-662-8044-619; e-mail: ursula.meindl@sbg.ac.at

Introduction

Cellular stress reactions have been investigated intensively both in plant and animal cells. Among plant cell organelles, chloroplasts and mitochondria are regarded as main stress targets and their physiological reactions to stress are well known (Santos *et al.*, 2001; Lin *et al.*, 2006; Logan, 2006; Demetriou *et al.*, 2007; Reape & McCabe, 2008; Affenzeller *et al.*, 2009b; Darehshouri & Lütz-Meindl, 2010). Stress-induced physiological deficiencies of these organelles are reflected in structural alterations mostly determined by two-dimensional (2-D) transmission electron microscopic (TEM) analyses. Dilations of thylakoid membranes, decrease of grana stacks, increase or decrease of starch accumulation and formation of vacuolar structures are the most frequently reported structural stress reactions in the chloroplast (Hollosy, 2002; Holzinger & Lütz, 2006; Andosch *et al.*, 2012; Lütz *et al.*, 2015). Bloating of mitochondria and coinciding reduction of the number of abnormally elongated cristae is a typical structural hallmark of stress and/or programmed cell death (PCD) that can be found commonly both in plant (Gunawardena *et al.*, 2001; Kolb *et al.*, 2004; Scott & Logan, 2008) and animal cells (Muriel *et al.*, 2000; Klein *et al.*, 2011).

Among the endomembrane system organelles, the ER has been regarded as the main stress target and the term "ER stress" is well defined in the literature as a consequence of defective protein folding that may induce the expression of ER-located chaperones (Ron & Walter, 2007; Howell, 2013). Although changes in irregularly shaped ER cisternae are hard to determine by electron microscopy, there is increasing evidence from molecular studies that loss of proper shape and architectural integrity affects the stress response ability of the ER and thus survivability of cells (Chen & Brandizzi, 2013; Lai *et al.*, 2014; Stefano & Brandizzi, 2014).

Although dictyosomes are highly dynamic (Hawes, 2005) their steady-state structure reflects a balance between anterograde and retrograde transport from the ER through the dictyosomes (Staehelin & Moore, 1995; Faso *et al.*, 2009; Hwang & Robinson, 2009; Viotti *et al.*, 2010; Day *et al.*, 2013). This can be easily misdirected or blocked during any kind of stress

or experimental manipulation as shown in earlier studies by the fungal metabolite brefeldin A leading to dissociation of COPI proteins from dictyosomal membranes and to the formation of large dictyosome-ER hybrid stacks resulting from altered Golgi transport (Nebenführ *et al.*, 2002; Ritzenthaler *et al.*, 2002; Ito *et al.*, 2012) and/or to a reversible reduction in number of dictyosomes in favour of the ER (Salomon & Meindl, 1996; Satiat-Jeunemaitre *et al.*, 1996). More recently, molecular and structural aspects of dictyosomal deconstruction were elegantly demonstrated upon inhibition of ER-Golgi transport in a Sar1 GTPase mutant of *Nicotiana tabacum* (Hummel *et al.*, 2010; Osterrieder *et al.*, 2010) and have shown a tight functional interaction between the ER and Golgi apparatus (Chen *et al.*, 2011; Brandizzi & Barlowe, 2013; Stefano *et al.*, 2014). Besides this, numerous investigations analysing subcellular stress responses in plant cells have mentioned detrimental effects of dictyosomal morphology and structure as side effects (McManus *et al.*, 1998; Gunawardena *et al.*, 2001; Jiang *et al.*, 2009; Selga, 2013), however there is still no comprehensive view on the dictyosomes as stress-response system. Also, it is so far not known how dictyosomes are degraded under stress conditions. Recent studies on degradation of organelles by selective autophagy in plant cells (for review, see Michaeli & Galili, 2014) include results on ER, mitochondria, plastids and peroxisomes but not on dictyosomes. This lack of information on Golgi stress responses is at least in part due to a lack of appropriate model systems in which dictyosomal integrity, morphology and product formation in relation to the stage of the cell cycle is well known and any environmental induced stress reaction is easily detectable.

The alga *Micrasterias,* which belongs to the closest relatives of land plants (Wodniok *et al.*, 2011; Leliaert *et al.*, 2012) and has common ancestors with embryophytes, is an ideal model system for such investigations. The extraordinary cell shape of *Micrasterias* is highly sensitive to any environmental impact during its formation, which allows easy recognition when the cell is affected (Kiermayer, 1981; Meindl, 1993). The natural habitats of *Micrasterias* are small acid peat bog ponds that may be exposed to rapidly changing environmental conditions and entry of pollutants such as heavy metals via aerosols or water inflow. Both may cause stress to the algae and their organelles.

Corresponding to the considerable cell size of *Micrasterias*, its dictyosomes are large (2–3 μm) and have a constant number of 11 cisternae throughout the entire cell cycle. The different vesicle populations they produce have been well defined by immuno TEM investigations using antibodies against different cell wall matrix polysaccharides (Lütz-Meindl & Brosch-Salomon, 2000; Eder & Lütz-Meindl, 2008; Eder *et al.*, 2008). In contrast to most other nongrowing plant cells, intensive vesicle production is maintained throughout the entire life cycle of *Micrasterias*, as mucilage vesicles are pinched off continually (Oertel *et al.*, 2004). This facilitates identification of the impact of any environmental stress not only on dictyosomal structure but also on their function.

A recent study using focused ion beam milling and block face imaging by field emission scanning electron microscopy (FIB-SEM) provided the first information on dictyosomal morphology in high pressure frozen *Micrasterias* cells in three-dimensional (3-D) and showed that dictyosomes of *Micrasterias* are entirely enveloped by an ER sheath that is in close spatial contact to the dictyosomal cisternae, both at the *cis-* and the *trans-* side (Wanner *et al.*, 2013).

Numerous physiological investigations using inhibitors that targeted different steps of Golgi product processing as well as studies with different abiotic environmental stressors have given insight into structural and functional reactions of dictyosomes in *Micrasterias*. Disturbance of N-glycosylation by tunicamycin (Höftberger *et al.*, 1995) as well as inhibition of Ca^{2+}-ATPases by thapsigargin (Andosch *et al.*, 2012) or cyclopiazonic acid had drastic negative consequences on morphology of dictyosomes and secretion. Experimental release of nitric oxide by donors such as SNAP or SNP impaired dictyosomal structure and function in *Micrasterias* probably via inhibition of enzymes such as GAPDH (Lehner *et al.*, 2009). Oxidative stress by H_2O_2 resulted in a swelling of the cisternal rims accompanied by distinct dilatations of the first two or three *cis*-cisternae, combined with an overall reduction in dictyosomal cisternae (Darehshouri *et al.*, 2008). Salt stress evoked a complete inactivation of dictyosomes, structurally indicated by a loss of *cis-trans*-polarity and by collapsed cisternae (Affenzeller *et al.*, 2009a, b). Metals such as aluminium and copper reduced secretory activity and led to a complete decomposition of dictyosomes in the case of cadmium (Volland *et al.*, 2011, 2012, 2014; Andosch *et al.*, 2012).

The different interventions into dictyosomal integrity and function in *Micrasterias* resulted in a variety of drastic structural alterations that were difficult to interpret due to the limitations of 2-D TEM. In order to obtain a more comprehensive and more reliable insight into possible structural Golgi stress responses, we use FIB-SEM tomography and 3-D reconstruction of dictyosomes in this study in addition to TEM. Stress is induced by metals such as lead (Pb) and manganese (Mn), by energy deprivation (= "starvation") and by disturbance of the ionic balance via Cd and KCl. In this way and by comparison of our results to dictyosomal stress reactions in the charophycean alga *Nitella* sp. we intend to acquire an overview on the Golgi apparatus as stress sensor in algae and to show how dictyosomal degradation occurs under adverse conditions.

Material and methods

All chemicals were purchased from Roth (Karlsruhe, Germany) or Sigma-Aldrich (Vienna, Austria) unless stated differently.

Cultivation of Micrasterias and Nitella

Micrasterias denticulata (Streptophyta) was cultivated in a liquid Desmidiacean medium (Schlösser, 1982) in Erlenmeyer

flaks at constant temperature of 20°C and a light/dark regime of 14/10 h. Cells were subcultured every 4–5 weeks. To obtain defined interphase stages for untreated controls and for treatment with different stressors, developmental stages were collected and were allowed to grow in nutrient solution for 48 h prior to stress exposure.

Cultures of *Nitella sp.* (Charophyta) were purchased from Seerosen Wachter (Reichenbach, Germany) and were cultivated in rainwater in an open stone basin under natural environmental conditions.

Stress induction

Defined interphase cells of *M. denticulata* 48 h after mitosis were exposed to 3 mM $MnSO_4$ for 7 days, to 150 μM $CdSO_4$ for 4 h, or to 180, 200 or 300 mM KCl for 3 and 24 h, respectively, by replacing the nutrient solution by the chemicals in glass dishes. For lead incubation of *Micrasterias*, 5 μM $Pb(NO_3)_2$ was added to the culture medium for 21 days. In order to induce stress by energy deprivation (= 'starvation'), cells were either exposed to complete darkness for 9 weeks, or treated with the photosynthesis inhibitor 3-(3,4-dichlorophenyl)-1,1-dimethylurea (0.5 μM, 14 days) or exposed to the glycolysis inhibitor 2-deoxy-D-glucose (50 μM, 21 days), respectively. Corresponding to recent publications (Andosch et al., 2012), drug concentrations and time periods were chosen that evoke effects visible by light microscopy in *Micrasterias* cells without leading to necrosis. All electron microscopic investigations were accompanied by cell vitality assays of stressed cells (data not shown). All treated *Micrasterias* cells were kept under standard culture conditions during the experiments. As controls, interphase stages of the same age (48 h after mitosis) were kept in nutrient solution under the same conditions. For all experiments and concentrations a representative number of cells were taken.

Correspondingly, *Nitella sp. was* treated with 180 mM KCl for 3 h and vegetation points were carefully dissected and immediately transferred into 20% albumin in water and high-pressure frozen.

High-pressure freeze fixation for TEM and FIB-FESEM

Defined interphase cells of *M. denticulata* were high-pressure frozen and cryo-substituted according to standard methods adapted for *Micrasterias* (Meindl *et al.*, 1992; Aichinger & Lütz-Meindl, 2005). In brief, cells were wrapped in cotton fibres to obtain high cell numbers per sample holder and were frozen in a Leica EMPACT HPF device (Leica Microsystems, Vienna, Austria). Freeze substitution in 2% OsO_4 and 0.05% uranyl acetate in anhydrous acetone was done in a Leica EM AFS for 60 h at −80°C and 4 h at −30°C. Cells were embedded in epoxy resin (Agar low-viscosity resin; Agar Scientific, Essex, UK) and sectioned on a Leica UC7 ultramicrotome for TEM.

Nitella vegetation points were high-pressure frozen in a Leica EM HPM100 and cryo-substituted in a EM AFSM2 in the same way as *Micrasterias.*

Ultrathin sections were mounted on formvar-coated copper grids and investigated with a LEO 912 AB Omega TEM (Zeiss, Oberkochen, Germany) at 80 kV by means of zero-loss energy filtering (Lütz-Meindl & Aichinger, 2004). All samples for FIB-SEM were pre-viewed in TEM to determine fixation quality and for comparison of structure analyses.

FIB-FESEM tomography

Interphase cells of *M. denticulata* and vegetation points of *Nitella* sp., including both untreated controls, and cells exposed to 150 μM $CdSO_4$ for 4 h or to 180 mM KCl for 3 and 24 h respectively, were investigated by FIB-SEM tomography. After high-pressure freeze fixation and cryo-substitution, samples were rinsed with acetone, infiltrated and embedded in epoxy resin (see above). Embedded samples were mounted on aluminium stubs covered with a thin layer of polymerized epoxy resin. Blocks were trimmed with glass knives in a LKB Pyramitome with mesa technique in a way that vertical faces allowed lateral milling of the cells by the FIB. Tomographic datasets were obtained by the 'slice and view' technique using a Zeiss Auriga 40 crossbeam workstation (Carl Zeiss Microscopy, Oberkochen, Germany). For milling with the focused Ga-ion beam, the conditions were as follows: 0.5–1nA milling current of the Ga-emitter; with each step 5–10 nm of the epoxy resin was removed by milling with the FIB. SEM images were recorded with an aperture of 60 μm in the high-current mode at 1.5 kV of the in-lens EsB detector with the EsB grid set to −1000 V. Depending on the respective magnification, voxel size was in a range between 4 and 15 nm in x/y and 10–15 in z. Contrast of the images was inverted to conventional bright field (for methods, see also Wanner *et al.*, 2013).

Data processing and 3-D-reconstruction

Alignment of image stacks was done with the open source software ImageJ (http://rsbweb.nih.gov/ij/index.html) and Amira Software (VSG; Visualization Sciences Group, Hilsboro, U.S.A.). Segmentation and 3-D reconstructions were performed semi-automatically using Amira Software and were corrected manually.

Results

Dictyosomes of the model systems *Micrasterias* and *Nitella* differ considerably in size and architecture. Although dictyosomes of *Micrasterias* measure 2–3 μm in diameter and consist of a constant number of 11 cisternae, dictyosomes in *Nitella* are only 0.5–1 μm large and reveal a varying number of six to nine cisternae (Fig. 1). This leads to a completely different width-to-height ratio of dictyosomes in the two

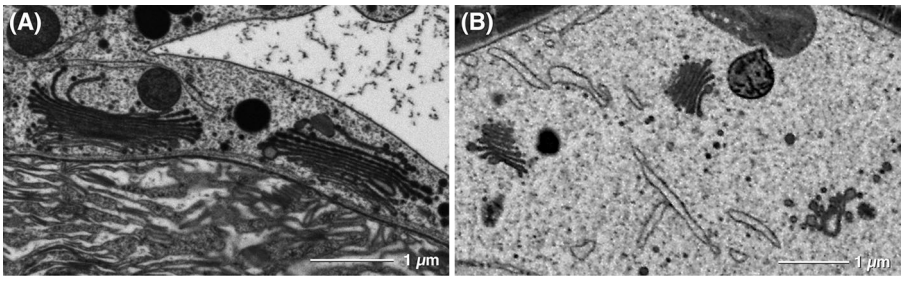

Fig. 1. Dictyosomes of untreated *Micrasterias* (A) and *Nitella* (B) cells. Scanning electron micrographs taken from FIB-SEM series.

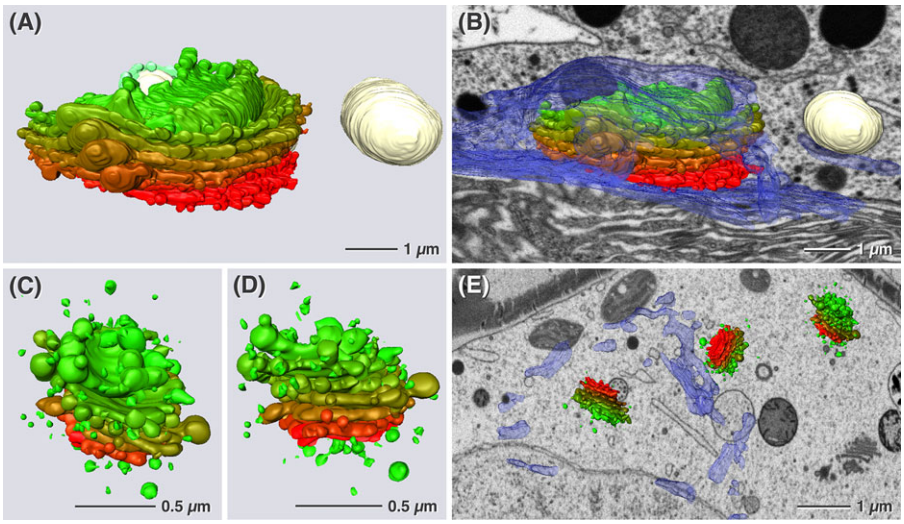

Fig. 2. Three-dimensional architecture of dictyosomes of untreated cells of *Micrasterias* (A,B) and *Nitella* (C–E). *Cis*-side indicated in red, *trans-side* in green. (A,C,D) without and (B,E) with ER (blue) and superimposed on EM micrographs. (B) Dictyosome of *Micrasterias* entirely enwrapped by ER, (E) distribution of dictyosomes and ER in *Nitella*. Mucilage vesicles in *Micrasterias* coloured in yellow.

algae. In both cells, *cis-trans*-polarity is present, yet it is structurally more clearly visible in *Micrasterias* by decreasing cisternal lumens from *cis to trans* (see also Kiermayer, 1970, 1981; Meindl, 1993). 3-D reconstruction obtained by FIB-SEM serial slicing and bloc face imaging show the different dimensions of the dictyosomes in the two algae (Figs. 2A–E). Dilations of the cisternal rims indicate vesicle formation in both instances (Figs. 2A,C,D). However, the ratio between vesicles and cisternae is different in a way that the number of vesicles at the *Nitella* dictyosome is much higher in relation to the cisternal surface than in *Micrasterias*. In *Nitella*, vesicles seem to be produced from all cisternae of the stack whereas vesicle budding in *Micrasterias* is limited to *middle* and *trans* cisternae (see also Meindl *et al.*, 1992). As clearly demonstrated in a recent study (Wanner *et al.*, 2013), dictyosomes in *Micrasterias* are entirely enwrapped by extensive ER cisternae both at their *cis*- and their *trans*-side (Fig. 2B). In *Nitella*, association between dictyosomes and ER is not close. ER cisternae are distributed randomly in the cytoplasm and are found only occasionally in spatial contact to dictyosomes (Fig. 2E).

Numerous studies using 2-D TEM analyses have reported on abiotic stress-induced adverse effects on dictyosomal structure in *Micrasterias* and have shown that product formation is affected (for details and references, see Introduction). In this study, we have extended these investigations to further metallic stressors such as Mn and Pb, and to stress by starvation induced by either 9 weeks darkness, inhibition of photosynthesis via 3-(3,4-dichlorophenyl)-1,1-dimethylurea or by inhibition of glycolysis by means of 2-deoxy-D-glucose, respectively. As demonstrated in Figs. 3A–E, dictyosomes during different moderate stress scenarios exhibit common structural reactions. They comprise curling of single cisternae or entire dictyosomes (Figs. 3A–D), reduction in cisternal number (Figs. 3A,E), loss in *cis-trans*-polarity (Figs. 3A,C,D) and decrease or inhibition of product formation indicated by a lack of vesicles still attached to the *trans*-cisternae or in close spatial vicinity to them (Figs. 3A,C,D,E). The degree to which these features are expressed refers to the magnitude of the threat (concentration or duration of exposure). Cisternae detached or partially detached from the dictyosomes indicating their degradation

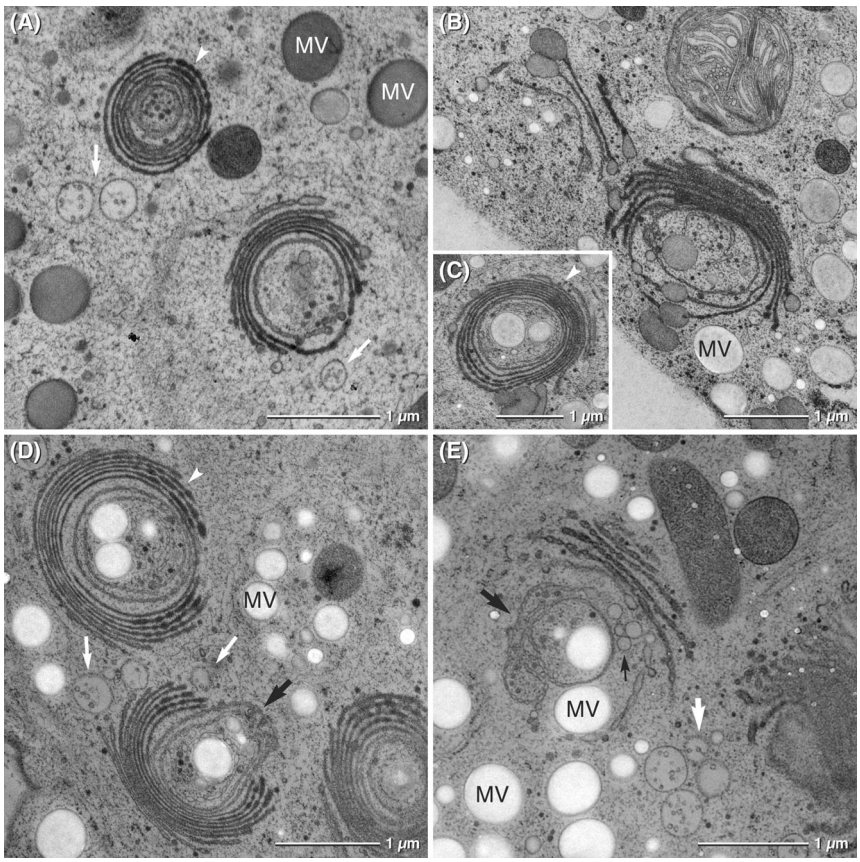

Fig. 3. Abnormal structure and morphology of dictyosomes in *Micrasterias* induced by different abiotic stressors (moderate stress). (A) 3 mM $MnSO_4$ for 7 days, (B,C) 5 μM $Pb(NO_3)_2$ for 21 days, (D) 9 weeks complete darkness and (E) 50 μM 2-deoxy-D-glucose for 21 days. White arrowheads point at dictyosomes without *cis-trans-* polarity, white arrows at multivesicular bodies, black arrow at partly (D) or completely detached (E) dictyosomal cisternae, small black arrow at ER. MV mucilage vesicles.

have been observed in cells exposed to complete darkness (Fig. 3D) and even more pronounced, after inhibition of photosynthesis by 3-(3,4-dichlorophenyl)-1,1-dimethylurea (data not shown) or after inhibition of glycolysis by 2-deoxy-D-glucose (Fig. 3E). In the latter case, dilated ER cisternae were frequently observed close to detached dictyosomal cisternae or to outermost *trans*-cisternae. During all stress scenarios an increased number of multivesicular bodies (MVB)s were found in the area of the dictyosomes (Figs. 3A,D,E) when compared to untreated controls.

When the ionic balance of the cells is disturbed as by exposure to Cd, structural and morphological Golgi reactions become more severe (see also Andosch *et al.*, 2012). Due to its ionic similarity, Cd displaces Ca^{2+} from different binding sites by using Ca-channels for entering the cells and thus disturbing Ca^{2+} homeostasis. In *Micrasterias,* this leads to cluster formation of dictyosomes and marked structural and morphological alterations of the dictyosomes (Figs. 4A,B) and ends up with their complete degradation. Cisternae become abnormally elongated and curl up both at the *cis-* and at the *trans*-side of the stacks (Figs. 4A,C). Numerous small vesicles representing degradation products accumulate between the cisternae. Again dilated ER cisternae are present at the *trans*-side of the dictyosomes. Finally, randomly distributed dictyosomal cisternae, frequently attached to larger compartments, are all that remain of the former dictyosomes (Fig. 4B).

3-D analyses by FIB-SEM tomography shows that the 'cisternal curls' observed by 2-D TEM investigations at both faces of dictyosomes are complete balls, forming compartments on their own (Figs. 4D,E). They represent detached or partially detached cisternae from the stack. Some middle cisternae of the former dictyosomes are still maintained, however their rims are abnormally lacerated and the entire stack is cup-shaped. The *trans*-ER, which has been described for the first time in untreated *Micrasterias* cells by FIB-SEM tomography as an expanded sheath covering the entire dictyosome (Wanner *et al.*, 2013) appears coiled up in Cd exposed cells to an abnormal structure (Supplementary videos S1 and S2).

As described in an earlier study (Affenzeller *et al.*, 2009b), the structural and morphological changes of dictyosomes become even more drastic when *Micrasterias* cells are exposed to KCl. In cells treated with 200–300 mM KCl for 3–24 h, the

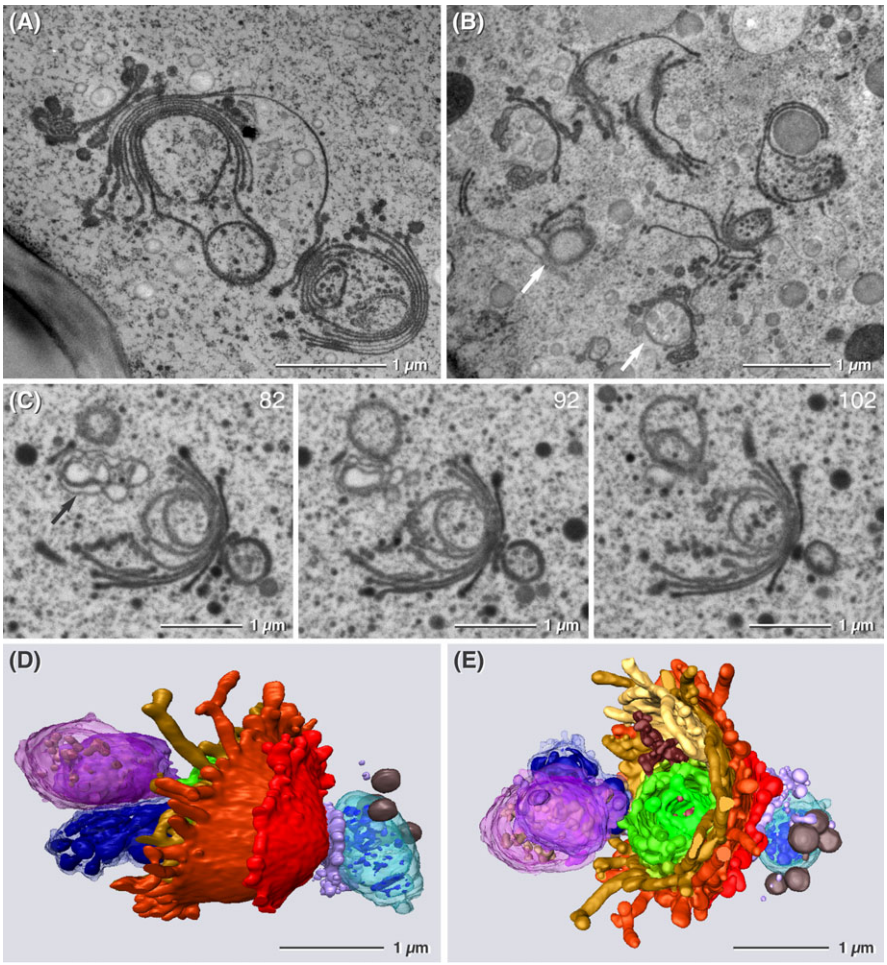

Fig. 4. Dictyosomes of *Micrasterias* after exposure to 150 μM CdSO4 for 4 h. (A,B) TEM micrographs, (A) cluster of dictyosomes with elongated partially detached cisternae, (B) remnants of dictyosomes attached to vacuolar compartments (= balls; white arrows) (C) images from FIB-SEM series, image number indicated, arrow marks ER at *trans*-side of abnormal dictyosome, (D,E) different views of corresponding 3-D reconstruction. Dictyosomal cisternae from *cis*- to *trans*-side: light blue to violet. Abnormal ER cisternae displayed in dark blue. Dictyosomal cisternae form balls both at *cis*- and *trans*-side of stack. Brownish vesicles at *cis*-side of dictyosome represent degradation products.

remaining dictyosomes completely lose their *cis-trans*-polarity and vesicles are no longer visible in their vicinity (Figs. 5A–C). The cisternae curl up and are always in contact with larger compartments that seem at least in part to derive from a *trans*-side located ER as indicated by ribosomes frequently found at the membranes (Figs. 5B,D). The more the dictyosomes are disintegrated the larger become these compartments (compare Figs. 5A to C). However, it is difficult to deduce from 2-D TEM micrographs in which way the observed compartments are structurally connected to the degrading dictyosomes. In our FIB-SEM investigations it becomes clear that the typical architecture of a dictyosome is completely lost during exposure of *Micrasterias* cells to KCl for 3 h (Figs. 6A–D). The former stacks consist of aggregations of single or spatially linked balls (= compartments) and are surrounded by numerous small vesicles representing degradation products. As is visible in the micrographs of the FIB-SEM series (Figs. 6A,B), the balls correspond to the former Golgi cisternae and may contain either cisternal remnants that are degraded to different degrees or have other cisternal balls incorporated in them. Up to three balls can be found in each other (see Figs. 6C,D and Supplementary video S3).

Figures 7A,B show that two different stages of dictyosomal degradation are frequently found in the cytoplasm of KCl treated *Micrasterias* cells: cisternal balls and reduced or partly degraded dictyosomes (= beginning ball formation). Both structures are in close spatial association to elongated ER cisternae that pervade the cytoplasm and increase in volume with decreasing dictyosomal disintegration. However, direct structural interactions have been found only between ER and membrane balls by our 3-D analyses (Fig. 7C). When zooming through a FIB-SEM series obtained by 10 nm slices (Supplementary video S4) it becomes obvious that the membranes of the cisternal balls are open towards the ER indicating

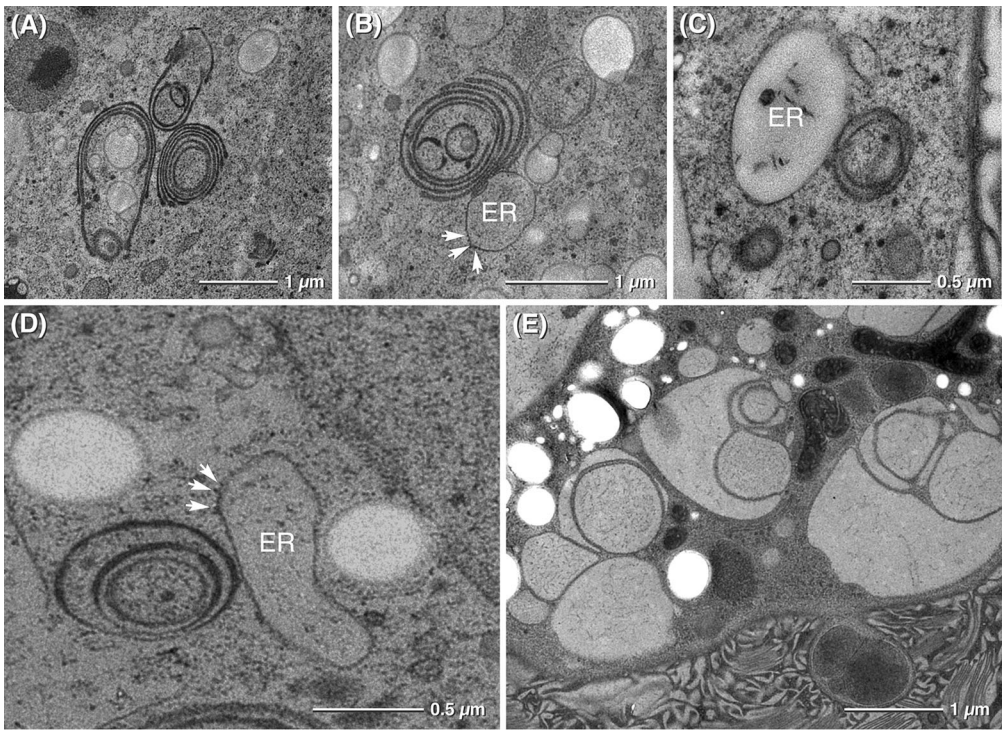

Fig. 5. TEM micrographs of different stages of degraded dictyosomes of *Micrasterias* after exposure to varying KCl concentrations (intense stress). (A,B) 300 mM KCl, 24 h, (C) 200 mM KCl, 3 h, (D) 300 mM KCl, 24 h and (E) 200 mM KCl, 24 h. (A–D) The size of the associated compartments increases with proceeding degradation of dictyosomes (= beginning ball formation). Ribosomes (indicated by arrows) at membranes of compartments in (B) and (D) suggest that they derive from ER. (E) Final stage of ball formation: compartments (= balls = former cisternae) enclose other compartments (remnants of dictyosomes = other balls).

that both compartments have already fused. Details of FIB-SEM series additionally show a number of spatial connections between cisternal balls and dictyosomal remnants (Figs. 7D,E) as well as between dictyosomal remnants and ER cisternae (Fig. 7F).

When the KCl treatment is prolonged to 24 h, dictyosomes are no longer visible in *Micrasterias* cells by TEM. Instead, the cells are filled with numerous vacuole-like compartments (= balls) that contain other balls or membranes of former dictyosomes (Fig. 5E).

Exposure of *Nitella* vegetation points to the same concentration of KCl as used for *Micrasterias* results in similar morphological and structural changes of the dictyosomes (Figs. 8A–C). Frequently, both at the *cis*- and the *trans*-side of the dictyosomes ball-shaped compartments appear (Fig. 8D). The dictyosomes, or some of their cisternae, are in contact with dilated ER cisternae (Figs. 8B,D). The volume of ER cisternae in the cytoplasm increases considerably (compare Figs. 2E to 9). Bending of *Nitella* dictyosomes occurs only occasionally. In KCl treated *Nitella* vegetation points not all dictyosomes show membrane ball formation during degradation. Occasionally another morphological aberration occurs which can be regarded as a moderate stress reaction. In this case dictyosomal cisternae disintegrate into an increasing number of smaller cisternae. Our 3-D reconstructions show that such dictyosomes are slightly bent both towards the *cis*- and the *trans*-side (Figs. 8E–G).

Discussion

Our study provides evidence for common structural, morphological and functional reactions of dictyosomes after a variety of different stress scenarios in the algal model system *Micrasterias* by using the advantages of serial slicing and FIB-SEM tomography in combination with classical ultrathin sectioning and TEM analyses. A stress-induced degradation pathway of dictyosomes is described that does not follow the "classical" autophagy concept (Bassham *et al.*, 2006; Avin-Wittenberg *et al.*, 2012; Klionsky *et al.*, 2012) but indicates disintegration of cisternae into single membrane balls. The close spatial association between the balls (= remnants of dictyosomal cisternae) and ER cisternae that increase in volume during Golgi degradation, may indicate that the cisternal balls are finally taken up into the ER. Comparison of the morphological features that accompany dictyosomal degradation in *Micrasterias* to structural dictyosomal reactions observed during the same stress application in *Nitella,* may point towards a ubiquitous degradation process, at least in algae.

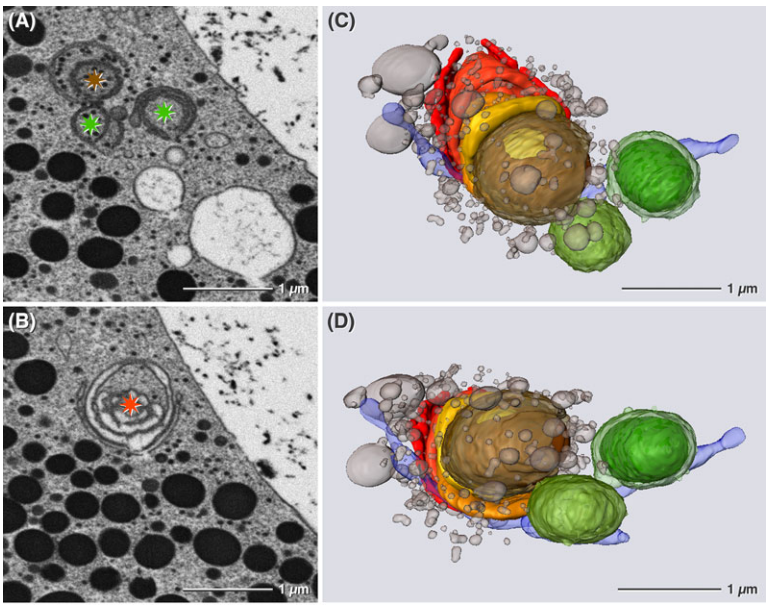

Fig. 6. Degraded dictyosomes of *Micrasterias* after exposure to 180 mM KCl for 3 h. (A,B) Micrographs of FIB-SEM series. Coloured asterisks at EM images indicate the corresponding 3-D structures. Red asterisk marks remnant of dictyosomes in which dictyosomal cisternae are still visible (= beginning ball formation), green and brown asterisks mark balls. (C,D) 3-D reconstruction from FIB-SEM series, different views. Degrading dictyosomal cisternae form single balls containing other compartments or dictyosomal remnants.

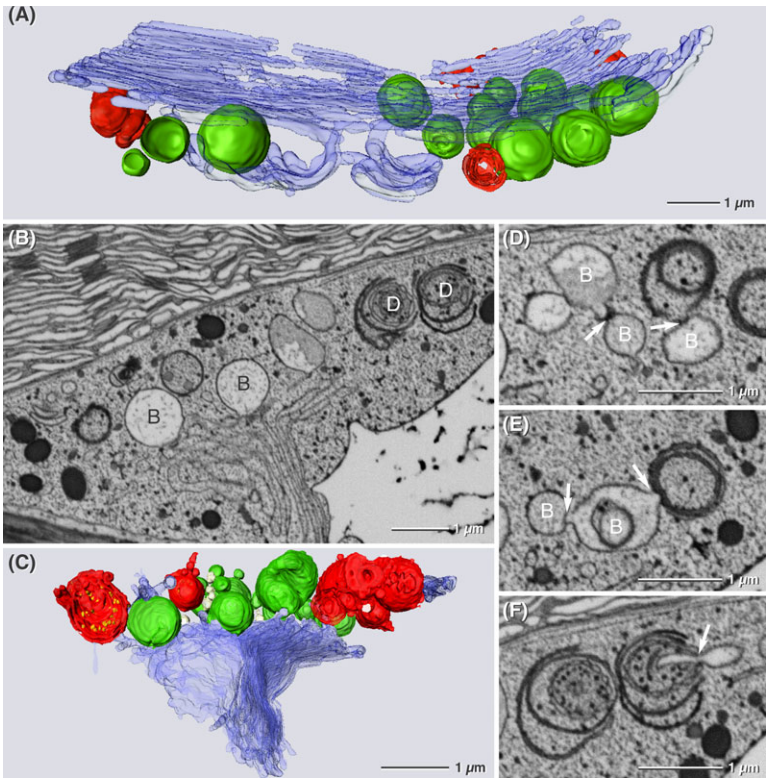

Fig. 7. Membrane connections between different stages of dictyosomal degradation in *Micrasterias* after exposure to 180 mM KCl for 3 h, visualized by 3-D reconstructions (A,C) and by micrographs of FIB-SEM series (B,D,E,F). (A) Distribution of membrane balls (green), dictyosomal remnants (red) and ER (blue). (B) Contacts between ER and membrane balls are visible. (C) Later stage of dictyosomal degradation. Membrane balls (green) are connected to ER cisternae (blue). (D,E) Membrane contacts between balls (arrows) and dictyosomal remnants. (F) ER cisternae (arrow) penetrating dictyosomal remnant. B, membrane balls; D, dictyosomal remnants.

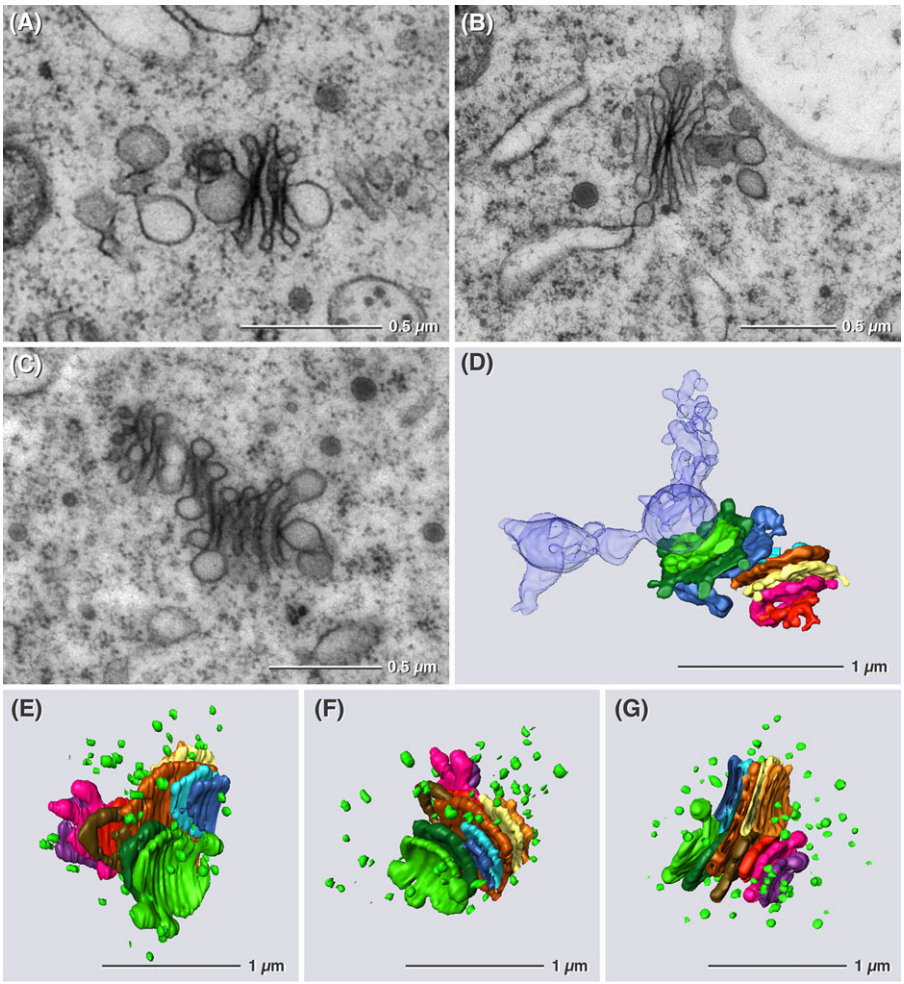

Fig. 8. *Nitella* dictyosomes after exposure to 180 mM KCl for 3 h in TEM (A–C) and 3-D reconstruction (D–G). Two different stress induced morphological changes can be observed. (A–D) Degrading dictyosome with ball shaped cisternae at *cis*- and *trans*-side. (B,D) ER cisternae in contact with degrading dictyosome. (E–G) Disintegration of dictyosome into increasing number of small cisternae, different views of dictyosome.

The results of our study have shown that moderate stress induced by metal solutions such as Pb nitrate or Mn sulphate, as well as energy deprivation by keeping *Micrasterias* cells in darkness or by either inhibiting photosynthesis or glycolysis induce similar structural reactions of the dictyosomes. Depending on the magnitude of the stress, they include curling of entire dictyosomes or single cisternae, reduction in cisternal number from 11 down to 2 to 6, loss in *cis-trans*-polarity and decrease or inhibition of product formation, indicated by reduction or lack of vesicles still attached to the *trans*-cisternae or found in their surroundings. Our results correspond well to structural Golgi stress reactions found upon a variety of different other stress situations in *Micrasterias* such as oxidative stress by H_2O_2 (Darehshouri *et al.*, 2008), increase in NO (Lehner *et al.*, 2009), exposure to different metals (Volland *et al.*, 2011, 2012, 2014) or to high UV-irradiation (Meindl & Lütz, 1996) and to the physiological stress reactions reported therein. This indicates that the Golgi apparatus in *Micrasterias* known as a stable, constant organelle in untreated controls (see Introduction) can be regarded as sensitive stress sensor. The characteristic structural and morphological changes that appear in TEM allow easy recognition when a cell has been exposed to stress. As the corresponding investigations are still missing we have no indications whether this is true for other plant cells as well. In mammalian cells it has already been recognized that Golgi structure is an important indicator for stress sensing and transduction of stress signals (Hicks & Machamer, 2005). The latter authors found that changes in structure and morphology of dictyosomes may reflect stress induced perturbation of cytoskeleton and trafficking, may indicate disturbance in lipid metabolism and distribution, and may reflect recruitment or release of specific regulating proteins.

When stress in *Micrasterias* becomes more severe as for example by disturbing the ionic balance of the cells by Cd or by KCl (this study and Affenzeller *et al.*, 2009b) degradation of dictyosomes is induced. Detachment of cisternae from the

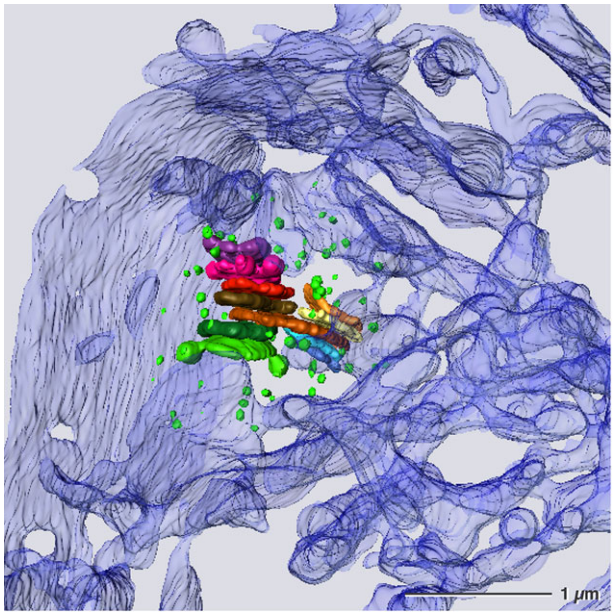

Fig. 9. Dictyosome of *Nitella* and ER distribution after exposure to 180 mM KCl for 3 h. 3-D reconstruction from FIB-SEM series. The ER is dramatically increased when compared to untreated control (Fig. 2E).

dictyosomes, also occasionally occurring during moderate stress e.g. by starvation, can be regarded as first indication for Golgi degradation. As clearly demonstrated in the 3-D reconstructions based on our FIB-SEM series, cisternae may become detached from both the *cis*- and the *trans*-side of the stack simultaneously and form individual balls (see schematic drawing in Fig. 10). Several cisternae (up to three) may contribute to the balls. The remaining middle cisternae of the stacks reveal distinctly lacerated rims and the presence of small vesicles surrounding the degrading dictyosomes indicate cisternal decomposition in addition to detachment of cisternae. Concomitantly with the structural disintegration of the dictyosomes, the arrangement of the ER and in particular the *trans*-side located ER changes as well. It loses its elongated shape and appears coiled up. It is frequently attached to the cisternal balls of the degrading dictyosomes. When Golgi degradation proceeds (see schematic drawing in Fig. 10) more and more cisternae form balls so that the dictyosomes end up in structures of five to six balls that may again include other cisternae. The degree to which the dictyosomes of a cell are degraded at a particular point of time after Cd or KCl treatment is different. Some cisternal balls appear empty in our 3-D analyses and some contain membrane structures that still resemble dictyosomal cisternae. The cisternal balls increase in size with proceeding degradation of dictyosomes and the *trans*-side located ER is reduced. This and the close contact of ER cisternae to the membranes of the balls indicate that the ER participates in the formation of cisternal balls and thus contributes to dictyosomal degradation. Finally the balls are seen in contact with large ER sheets that pervade the cytoplasm and increase in volume during stress. Our FIB-SEM series indicate that the balls are open towards the ER suggesting that they are absorbed by it. Our prior 2-D TEM studies suggested that autophagy of entire dictyosomes occurs particularly under KCl stress (Affenzeller *et al.*, 2009b); however, we could definitely find no evidence for a 'classical' autophagy process from

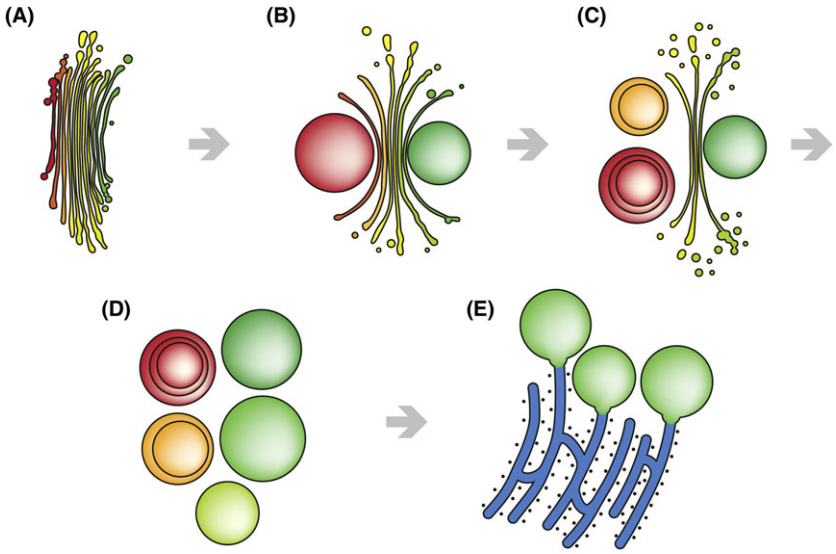

Fig. 10. Schematic drawing of dictyosomal degradation after intense stress in *Micrasterias*. *Cis*-side in red, *trans*-side in green. (A) Unaffected dictyosome with 11 cisternae. (B) Dicytosomal degradation has started, outermost *cis*- and *trans*-cisternae form balls, the number of "normal" cisternae is reduced. (C) Proceeding dictyosomal degradation. Cisternal balls incorporate other cisternal ball in them. The number of "normal" cisternae is further reduced; numerous small vesicles representing degradation products surround the dictyosome. (D) Normal dictyosomal architecture is completely lost. The former dictyosome consists only of cisternal balls with increased volume. (E) The cisternal balls fuse with long ER strands that have formed during stress.

analyses of our FIB-SEM series and the corresponding 3-D reconstructions. This shows that 3-D analysis is absolutely required for elucidating complex processes such as organelle degradation.

Comparison of dictyosome degradation in *Micrasterias* and *Nitella* after KCl stress indicates structural similarities. As in *Micrasterias,* many *Nitella* dictyosomes show ball-shaped cisternae both at their *cis*- and *trans*-side after KCl exposure and are frequently found in contact with dilated ER cisternae. Altogether, the volume of the ER in KCl stressed cells increases in the same way as in *Micrasterias*. The typical bending or curling of entire dictyosomes found after any kind of stress in *Micrasterias* cannot be observed in *Nitella*. This may be explained by the considerable difference of dictyosomal size and architecture in both algae. Bending of the huge *Micrasterias* dictyosomes during stress may be a result of intracellular dynamics and may help protect the sensitive *trans*-surface of dictyosomes from adverse conditions such as ionic imbalance. However, the small dictyosomes of *Nitella* revealing a complete different width to height architecture as those of *Micrasterias* are probably not able to bend.

In summary our 3-D structural investigations show for the first time that algal dictyosomes are not degraded as whole organelles inside of autophagosomes or other lytic compartments, but are disintegrated into several cisternal balls which are finally transformed into ER cisternae. This indicates that the Golgi apparatus and the ER essentially consist of the same type of membranes and can be regarded as a functional unit as already proposed from various other structural and molecular data (Staehelin & Moore, 1995; Hawes, 2005; Faso *et al.*, 2009; Viotti *et al.*, 2010; Chen *et al.*, 2011; Brandizzi & Barlowe, 2013; Day *et al.*, 2013; Stefano *et al.*, 2014 and others). Our observation that both membranes contribute to the formation of cisternal balls during Golgi degradation additionally corroborates this view. Further immuno electron microscopic, molecular biological and physiological investigations will be required to obtain a more comprehensive insight into the plant Golgi apparatus as a stress sensor and into stress-induced degradation pathways of dictyosomes.

Acknowledgements

The authors thank Silvia Dobler for excellent technical assistance and Jenny Grünert, Tillman Schäfer and Martin Niedermeier for their engagement in the manual segmentation for the 3-D reconstructions. The authors thank Viola Schwarz for preparing the schematic drawing and also thank Pia Anwander, Elisabeth Bayer, Viola Schwarz and Nicole Naumann for kindly providing TEM micrographs from their Master theses [Figs. 3a (Anwander), b, c, (Bayer), d (Schwarz), e (Naumann)]. The financial support by the Austrian Science Fund (project 21035-B16 to U.L.-M.) as a basis for this investigation is also acknowledged.

References

Affenzeller, M.J., Darehshouri, A., Andosch, A., Lütz, C. & Lütz-Meindl, U. (2009a) PCD and autophagy in the unicellular green alga *Micrasterias denticulata*. *Autophagy*, **5**, 854–855.

Affenzeller, M.J., Darehshouri, A., Andosch, A., Lütz, C. & Lütz-Meindl, U. (2009b) Salt stress-induced cell death in the unicellular green alga *Micrasterias denticulata*. *J. Exp. Bot.* **60**, 939–954.

Aichinger, N. & Lütz-Meindl, U. (2005) Organelle interactions and possible degradation pathways visualized in high-pressure frozen algal cells. *J. Microsc.* **219**, 86–94.

Andosch, A., Affenzeller, M.J., Lütz, C. & Lütz-Meindl, U. (2012) A freshwater green alga under cadmium stress: ameliorating calcium effects on ultrastructure and photosynthesis in the unicellular model *Micrasterias*. *J. Plant Physiol.* **169**, 1489–1500.

Andosch, A., Höftberger, M., Lütz, C. & Lütz-Meindl, U. (2015) Subcellular sequestration and impact of heavy metals on the ultrastructure and physiology of the multicellular freshwater alga *Desmidium swartzii*. *Int. J. Mol. Sci.* **16**, 10389–10410.

Avin-Wittenberg, T., Honig, A. & Galili, G. (2012) Variations on a theme: plant autophagy in comparison to yeast and mammals. *Protoplasma* **249**, 285–299.

Bassham, D. C., Laporte, M., Marty, F., Moriyasu, Y., Ohsumi, Y., Olsen, L.J. & Yoshimoto, K. (2006) Autophagy in development and stress responses of plants. *Autophagy*, **2**, 2–11.

Brandizzi, F. & Barlowe, C. (2013) Organization of the ER-Golgi interface for membrane traffic control. *Nat. Rev. Mol. Cell Biol.* **14**, 382–392.

Chen, J., Stefano, G., Brandizzi, F. & Zheng, H. (2011) *Arabidopsis* RHD3 mediates the generation of the tubular ER network and is required for Golgi distribution and motility in plant cells. *J. Cell Sci.* **124**, 2241–2252.

Chen, Y. & Brandizzi, F. (2013) IRE1: ER stress sensor and cell fate executor. *Trends Cell Biol.* **23**, 547–555.

Darehshouri, A., Affenzeller, M. & Lütz-Meindl, U. (2008) Cell death upon H_2O_2 induction in the unicellular green alga *Micrasterias*. *Plant Biol.* **10**, 732–745.

Darehshouri, A. & Lütz-Meindl, U. (2010) H_2O_2 localization in the green alga *Micrasterias* after salt and osmotic stress by TEM-coupled electron energy loss spectroscopy. *Protoplasma* **239**, 49–56.

Day, K.J., Staehelin, L.A. & Glick, B.S. (2013) A three-stage model of Golgi structure and function. *Histochem. Cell Biol.* **140**, 239–249.

Demetriou, G., Neonaki, C., Navakoudis, E. & Kotzabasis, K. (2007) Salt stress impact on the molecular structure and function of the photosynthetic apparatus—the protective role of polyamines. *Biochim. Biophys. Acta* **1767**, 272–280.

Eder, M. & Lütz-Meindl, U. (2008) Pectin-like carbohydrates in the green alga *Micrasterias* characterized by cytochemical analysis and energy filtering TEM. *J. Microsc.* **231**, 201–214.

Eder, M., Tenhaken, R., Driouich, A. & Lütz-Meindl, U. (2008) Occurrence and characterization of arabinogalactan-like proteins and hemicelluloses in *Micrasterias* (Streptophyta). *J. Phycol.* **44**, 1221–1234.

Faso, C., Boulaflous, A. & Brandizzi, F. (2009) The plant Golgi apparatus: Last 10 years of answered and open questions. *FEBS Lett.* **583**, 3752–3757.

Gunawardena, A.H., Pearce, D.M., Jackson, M.B., Hawes, C.R. & Evans, D.E. (2001) Characterisation of programmed cell death during aerenchyma formation induced by ethylene or hypoxia in roots of maize (*Zea mays* L.). *Planta*, **212**, 205–214.

Hawes, C. (2005) Cell biology of the plant Golgi apparatus. *New Phytol.* **165**, 29–44.

Hicks, S.W. & Machamer, C.E. (2005) Golgi structure in stress sensing and apoptosis. *Biochim. Biophys. Acta* **1744**, 406–414.

Höftberger, M., Url, T. & Meindl, U. (1995) The ionophore nigericin prevents the stopping mechanism of the microtubule-dependent nuclear migration in desmids. *Cryptogamic Bot.* **5**, 5–13.

Hollosy, F. (2002) Effects of ultraviolet radiation on plant cells. *Micron* **33**, 179–197.

Holzinger, A. & Lütz, C. (2006) Algae and UV irradiation: effects on ultrastructure and related metabolic functions. *Micron* **37**, 190–207.

Howell, S.H. (2013) Endoplasmic reticulum stress responses in plants. *Annu. Rev. Plant Biol.* **64**, 477–499.

Hummel, E., Osterrieder, A., Robinson, D.G. & Hawes, C. (2010) Inhibition of Golgi function causes plastid starch accumulation. *J. Exp. Bot.* **61**, 2603–2614.

Hwang, I. & Robinson, D.G. (2009) Transport vesicle formation in plant cells. *Cur. Opin. Plant Biol.* **12**, 660–669.

Ito, Y., Uemura, T., Shoda, K., Fujimoto, M., Ueda, T. & Nakano, A. (2012) *cis*-Golgi proteins accumulate near the ER exit sites and act as the scaffold for Golgi regeneration after brefeldin A treatment in tobacco BY-2 cells. *Mol. Biol. Cell* **23**, 3203–3214.

Jiang, W.S., Liu, D.H. & Xu, P. (2009) Cd-induced system of defence in the garlic root meristematic cells. *Biol. Plant.* **53**, 369–372.

Kiermayer, O. (1970) Elektronenmikroskopische Untersuchungen zum Problem der Cytomorphogenese von *Micrasterias denticulat* Bréb. *Protoplasma* **69**, 97–132.

Kiermayer, O. (1981) Cytoplasmic basis of morphogenesis in *Micrasterias*. *Cytomorphogenesis in Plants* (ed. by O. Kiermayer). Springer, Vienna 147–189.

Klein, B., Worndl, K., Lütz-Meindl, U. & Kerschbaum, H.H. (2011) Perturbation of intracellular K+ homeostasis with valinomycin promotes cell death by mitochondrial swelling and autophagic processes. *Apoptosis* **16**, 1101–1117.

Klionsky, D.J., Abdalla, F.C., Abeliovich, H., *et al.* (2012) Guidelines for the use and interpretation of assays for monitoring autophagy. *Autophagy* **8**, 445–544.

Kolb, R.M., Dolder, H. & Cortelazzo, A.L. (2004) Effects of anoxia on root ultrastructure of four neotropical trees. *Protoplasma* **224**, 99–105.

Lai, Y.S., Stefano, G. & Brandizzi, F. (2014) ER stress signaling requires RHD3, a functionally conserved ER-shaping GTPase. *J. Cell Sci.* **127**, 3227–3232.

Lehner, C., Kerschbaum, H.H. & Lütz-Meindl, U. (2009) Nitric oxide suppresses growth and development in the unicellular green alga *Micrasterias denticulata*. *J. Plant Physiol.* **166**, 117–127.

Leliaert, F., Smith, D.R., Moreau, H., Herron, M.D., Verbruggen, H., Delwiche, C.F. & De Clerck, O. (2012) Phylogeny and molecular evolution of the green algae. *Crit. Rev. Plant Sci.* **31**, 1–46.

Lin, J., Wang, Y. & Wang, G. (2006) Salt stress-induced programmed cell death in tobacco protoplasts is mediated by reactive oxygen species and mitochondrial permeability transition pore status. *J. Plant Physiol.* **163**, 731–739.

Logan, D.C. (2006) The mitochondrial compartment. *J. Exp. Bot.* **57**, 1225–1243.

Lütz-Meindl, U. & Aichinger, N. (2004) Use of energy-filtering transmission electron microscopy for routine ultrastructural analysis of high-pressure-frozen or chemically fixed plant cells. *Protoplasma* **223**, 155–162.

Lütz-Meindl, U. & Brosch-Salomon, S. (2000) Cell wall secretion in the green alga *Micrasterias*. *J. Microsc.* **198**, 208–217.

Lütz, C., Di Piazza, L., Fredersdorf, J. & Bischof, K. (2015) The effect of ultraviolet radiation on cellular ultrastructure and photosystem II quantum yield of *Alaria esculenta* (L.) Greville from Spitsbergen (Norway). *Polar Biol.* doi:10.1007/s00300-015-1659-2.

McManus, M.T., Thompson, D.S., Merriman, C., Lyne, L. & Osborne, D.J. (1998) Transdifferentiation of mature cortical cells to functional abscission cells in bean. *Plant Physiol.* **116**, 891–899.

Meindl, U. (1993) *Micrasterias* cells as a model system for research on morphogenesis. *Microbiol. Rev.* **57**, 415–433.

Meindl, U., Lancelle, S. & Hepler, P. (1992) Vesicle production and fusion during lobe formation in *Micrasterias* visualized by high-pressure freeze fixation. *Protoplasma*, **170**, 104–114.

Meindl, U. & Lütz, C. (1996) Effects of UV irradiation on cell development and ultrastructure of the green alga *Micrasterias*. *J. Photochem. Photobiol. B-Biol.* **36**, 285–292.

Michaeli, S. & Galili, G. (2014) Degradation of organelles or specific organelle components via selective autophagy in plant cells. *Int. J. Mol. Sci.* **15**, 7624–7638.

Muriel, M.P., Lambeng, N., Darios, F., Michel, P.P., Hirsch, E.C., Agid, Y. & Ruberg, M. (2000) Mitochondrial free calcium levels (Rhod-2 fluorescence) and ultrastructural alterations in neuronally differentiated PC12 cells during ceramide-dependent cell death. *J. Comp. Neurol.* **426**, 297–315.

Nebenführ, A., Ritzenthaler, C. & Robinson, D.G. (2002) Brefeldin A: deciphering an enigmatic inhibitor of secretion. *Plant Physiol.* **130**, 1102–1108.

Oertel, A., Aichinger, N., Hochreiter, R., Thalhamer, J. & Lütz-Meindl, U. (2004) Analysis of mucilage secretion and excretion in *Micrasterias* (Chlorophyta) by means of immunoelectron microscopy and digital time lapse video microscopy. *J. Phycol.* **40**, 711–720.

Osterrieder, A., Hummel, E., Carvalho, C.M. & Hawes, C. (2010) Golgi membrane dynamics after induction of a dominant-negative mutant Sar1 GTPase in tobacco. *J. Exp. Bot.* **61**, 405–422.

Reape, T.J. & McCabe, P.F. (2008) Apoptotic-like programmed cell death in plants. *New Phytol.* **180**, 13–26.

Ritzenthaler, C., Nebenführ, A., Movafeghi, A., Stussi-Garaud, C., Behnia, L., Pimpl, P., Staehelin, L.A. & Robinson, D.G. (2002) Reevaluation of the effects of brefeldin A on plant cells using tobacco Bright Yellow 2 cells expressing Golgi-targeted green fluorescent protein and COPI antisera. *Plant Cell*, **14**, 237–261.

Ron, D. & Walter, P. (2007) Signal integration in the endoplasmic reticulum unfolded protein response. *Nat. Rev. Mol. Cell Biol.* **8**, 519–529.

Salomon, S. & Meindl, U. (1996) Brefeldin A induces reversible dissociation of the Golgi apparatus in the green alga *Micrasterias*. *Protoplasma*, **194**, 231–242.

Santos, C.L., Campos, A., Azevedo, H. & Caldeira, G. (2001) In situ and in vitro senescence induced by KCl stress: nutritional imbalance, lipid peroxidation and antioxidant metabolism. *J. Exp. Bot.* **52**, 351–360.

Satiat-Jeunemaitre, B., Cole, L., Bourett, T., Howard, R. & Hawes, C. (1996) Brefeldin A effects in plant and fungal cells: something new about vesicle trafficking? *J. Microsc.* **181**, 162–177.

Schlösser, U.G. (1982) Sammlungen von Algenkulturen. *Ber. Deutsch. Bot. Ges.* **95**, 181–276.

Scott, I. & Logan, D.C. (2008) Mitochondrial morphology transition is an early indicator of subsequent cell death in *Arabidopsis*. *New Phytol.* **177**, 90–101.

Selga, T. (2013) Changes of the secretory system of leaf epidermal and mesophyll cells during stress and programmed cell death. *Acta Universitatis Latviensis*, **662**, 51–58.

Staehelin, L.A. & Moore, I. (1995) The plant Golgi apparatus: structure, functional organization and trafficking mechanisms. *Annu. Rev. Plant Physiol. Plant Mol. Biol.* **46**, 261–288.

Stefano, G. & Brandizzi, F. (2014) Unique and conserved features of the plant ER-shaping GTPase RHD3. *Cell Logist*, **4**, e28217.

Stefano, G., Hawes, C. & Brandizzi, F. (2014) ER—the key to the highway. *Curr. Opin. Plant Biol.* **22**, 30–38.

Viotti, C., Bubeck, J. & Stierhof, Y.D. (2010) Endocytic and secretory traffic in *Arabidopsis* merge in the *trans*-Golgi network/early endosome, an independent and highly dynamic organelle. *Plant Cell*, **22**, 1344–1357.

Volland, S., Andosch, A., Milla, M., Stöger, B., Lütz, C. & Lütz-Meindl, U. (2011) Intracellular metal compartmentalization in the green algal model system *Micrasterias denticulata* (Streptophyta) measured by transmission electron microscopy-coupled electron energy loss spectroscopy. *J. Phycol.* **47**, 565–579.

Volland, S., Bayer, E., Baumgartner, V., Andosch, A., Lütz, C., Sima, E. & Lütz-Meindl, U. (2014) Rescue of heavy metal effects on cell physiology of the algal model system *Micrasterias* by divalent ions. *J. Plant Physiol.* **171**, 154–163.

Volland, S., Lütz, C., Michalke, B. & Lütz-Meindl, U. (2012) Intracellular chromium localization and cell physiological response in the unicellular alga *Micrasterias*. *Aquat. Toxicol.* **109**, 59–69.

Wanner, G., Schaefer, T. & Lütz-Meindl, U. (2013) 3-D analysis of dictyosomes and multivesicular bodies in the green alga *Micrasterias denticulata* by FIB/SEM tomography. *J. Struct. Biol.* **184**, 203–211.

Wodniok, S., Brinkmann, H., Glöckner, G., Heidel, A.J., Philippe, H., Melkonian, M. & Becker, B. (2011) Origin of land plants: do conjugating green algae hold the key? *BMC Evol. Biol.* **11**, 104–114.

Supporting Information

Additional Supporting information may be found in the online version of this article at the publisher's website:

Video S1. Movie through FIB-SEM series of the abnormal dictyosome of *Micrasterias denticulata* depicted in Figs. 4C–E.
Video S2. 3-D visualization of the dictyosome of *Micrasterias denticulata* depicted in Figs. 4C–E.
Video S3. 3-D reconstruction of degraded dictyosomes into cisternal balls after treatment with 180 mm KCl for 3 h.
Video S4. Movie through FIB-SEM series of cytoplasmic area of *Micrasterias denticulata* after treatment with 180 mm KCl for 3 h.

10.3 Publication III

Ionic stress induces fusion of mitochondria to 3-D networks: An electron tomography study.

Philip Steiner, **Manja Luckner**, Hubert Kerschbaum, Gerhard Wanner, Ursula Lütz-Meindl (2018)

Journal of Structural Biology, 2018 Jul 2. pii: S1047-8477(18)30158-8
doi: 10.1016/j.jsb.2018.06.010

Abstract
Mitochondria are central organelles for energy supply of cells and play an important role in maintenance of ionic balance. Consequently mitochondria are highly sensitive to any kind of stress to which they mainly response by disturbance of respiration, ROS production and release of cytochrome c into the cytoplasm. Many of the physiological and molecular stress reactions of mitochondria are well known, yet there is a lack of information on corresponding stress induced structural changes. 3-D visualization of high-pressure frozen cells by FIB-SEM tomography and TEM tomography as used for the present investigation provide an excellent tool for studying structure related mitochondrial stress reactions. In the present study it is shown that mitochondria in the unicellular freshwater algal model system Micrasterias as well as in the closely related aquatic higher plant Lemna fuse to local networks as consequence of exposure ionic stress induced by addition of KCl, NaCl and CoCl2. In dependence on concentration and duration of the treatment, fusion of mitochondria occurs either by formation of protuberances arising from the outer mitochondrial membrane, or by direct contact of the surface of elongated mitochondria. As our results show that respiration is maintained in both model systems during ionic stress and mitochondrial fusion, as well as formation of protuberances are reversible, we assume that mitochondrial fusion is a ubiquitous process that may help the cells to cope with stress. This may occur by interconnecting the respiratory chains of the individual mitochondria and by enhancing the buffer capacity against stress induced ionic imbalance.

Journal of Structural Biology xxx (xxxx) xxx–xxx

Contents lists available at ScienceDirect

Journal of Structural Biology

journal homepage: www.elsevier.com/locate/yjsbi

Ionic stress induces fusion of mitochondria to 3-D networks: An electron tomography study

Philip Steiner[a], Manja Luckner[b], Hubert Kerschbaum[a], Gerhard Wanner[b], Ursula Lütz-Meindl[a,*]

[a] Department of Biosciences, University of Salzburg, Hellbrunnerstraße 34, A-5020 Salzburg, Austria
[b] Ultrastructural Research, Faculty of Biology, Ludwig-Maximilians-University, Munich, Großhadernerstr. 2-4, D-82152 Planegg-Martinsried, Germany

ARTICLE INFO

Keywords:
FIB-SEM tomography
TEM-tomography
Algae
Mitochondria
Micrasterias denticulata
Salt stress

ABSTRACT

Mitochondria are central organelles for energy supply of cells and play an important role in maintenance of ionic balance. Consequently mitochondria are highly sensitive to any kind of stress to which they mainly response by disturbance of respiration, ROS production and release of cytochrome *c* into the cytoplasm. Many of the physiological and molecular stress reactions of mitochondria are well known, yet there is a lack of information on corresponding stress induced structural changes. 3-D visualization of high-pressure frozen cells by FIB-SEM tomography and TEM tomography as used for the present investigation provide an excellent tool for studying structure related mitochondrial stress reactions. In the present study it is shown that mitochondria in the unicellular fresh-water algal model system *Micrasterias* as well as in the closely related aquatic higher plant *Lemna* fuse to local networks as a consequence of exposure to ionic stress induced by addition of KCl, NaCl and $CoCl_2$. In dependence on concentration and duration of the treatment, fusion of mitochondria occurs either by formation of protuberances arising from the outer mitochondrial membrane, or by direct contact of the surface of elongated mitochondria. As our results show that respiration is maintained in both model systems during ionic stress and mitochondrial fusion, as well as formation of protuberances are reversible, we assume that mitochondrial fusion is a ubiquitous process that may help the cells to cope with stress. This may occur by interconnecting the respiratory chains of the individual mitochondria and by enhancing the buffer capacity against stress induced ionic imbalance.

1. Introduction

Mitochondria are fundamental organelles in animal and plant cells for energy supply by synthesis of ATP via oxidative and are thus highly sensitive to impact of stress, disease or ageing (Choi et al., 2014; Curley et al., 2014; Gallage and Gil, 2016; Hafiz Che-Othman et al., 2017; Nunnari and Suomalainen, 2012; Vartapetian et al., 2003; Wiley et al., 2016). They are highly dynamic discrete organelles in plant cell that are able to move along cytoskeleton elements, to fuse with each other and to change their shape (Arimura et al., 2004; Logan, 2006; Logan, 2010). In plant cells molecular and physiological reactions of mitochondria to stress are well known and essentially comprise increase or decrease of respiration, ROS production as well as release of cytochrome *c* into the cytoplasm (Colombatti et al., 2014; Martinez-Fabregas et al., 2013; Tiwari et al., 2002; Virolainen et al., 2002, and others). The latter processes are central in intracellular signaling and known to induce programmed cell death (PCD) both in plant and animal cells (Krishnamurthy, 2000; Logan and Murphy, 2017; Zhan et al., 2014).

Several molecular players that are involved in mitochondrial shaping as well as in fusion or fission processes have been identified (Cogliati et al., 2016; El Zawily et al., 2014; Hales and Fuller, 1997; Logan et al., 2003; Sesaki and Jensen, 1999) which has provided valuable information on the regulation of these physiologically important processes. However, in most studies information on mitochondrial morphology has been obtained by light- or fluorescent microscopic techniques which can only provide an overall view due to limit in spatial resolution. Detailed depiction of mitochondrial structure and shape alterations such as fusion, changes in cristae or membrane constrictions are only possible at high resolution of electron microscopy and require 3-D analysis. In the present study we employ two different methods of electron tomography for analyzing pronounced shape aberrations of mitochondria during ionic stress in the algal model system *Micrasterias* after cryo-preparation.

The freshwater alga *Micrasterias denticulata* (Zygnematophyceae; Charophyta) which is closely related to higher land plants (Leliaert et al., 2012; Wodniok et al., 2011) and has been used as a cell biological model system since many years (for summary see Lütz-Meindl, 2016; Meindl, 1993) is highly appropriate for such investigations as,

* Corresponding author.
E-mail address: ursula.meindl@sbg.ac.at (U. Lütz-Meindl).

https://doi.org/10.1016/j.jsb.2018.06.010
Received 12 February 2018; Received in revised form 27 June 2018; Accepted 30 June 2018

corresponding to its considerable cell size, it possesses large, distinct organelles that are well defined throughout the cell cycle. Recent studies by FIB-SEM tomography (Lütz-Meindl et al., 2016; Wanner et al., 2013) have provided insight into stress induced sub-structural alterations of dictyosomes and on dictyosomal degradation in *Micrasterias*. 2-D standard TEM methods after cryo-preparation have provided evidence that high salinity induces the formation of pronounced protuberances of the outer mitochondrial membrane as well as mitochondrial elongation (Affenzeller et al., 2009a). Moreover in this, and in many other plant and animal cells, bloating of mitochondria combined with reduced but elongated cristae is regarded as a characteristic hallmark for PCD (Zhan et al., 2014).

Other organelles such as chloroplasts (Santos et al., 2001), dictyosomes (Lütz-Meindl et al., 2016; Wanner et al., 2013) and endoplasmic reticulum (ER; (Faso et al., 2009)) clearly reveal structural stress hallmarks as well. Stress induced inhibition of photosynthesis is frequently linked to structural disorganization of the chloroplast such as dilations of thylakoid membranes (Niewiadomska et al., 2011; Pottosin and Shabala, 2016), formation of vacuolar structures (Lütz et al., 2016) and redistribution of starch accumulation and grana stacks (Holzinger and Lütz, 2006). Depending on the stress mode, dictyosomes may react with a reduction in number or volume of cisternae both reflecting a disturbed material flow (Donohoe et al., 2013). In the alga *Micrasterias*, dictyosomes for example are degraded during stress by formation of cisternal balls which are finally taken up into the ER (Lütz-Meindl et al., 2016).

Naturally, the freshwater green alga *Micrasterias* inhabits peat bogs with low pH, which may be exposed to extreme environmental conditions like high UV-radiation, fluctuation of temperature and different anthropogenic pollutions such as pesticides, high salinity or heavy metals. Metal stress (Cu, Zn, Al, Cd, Cr, Fe, Pb) for example, causes alterations in photosynthesis, morphogenesis, respiration and ultrastructure of *Micrasterias* (Andosch et al., 2012; Volland et al., 2011). Analytical TEM has provided evidence that metals are differently sequestered in compartments such as vacuoles or the cell wall but can be also taken up into organelles like chloroplasts or different vesicle populations (Volland et al., 2011; Zheng et al., 2012). Different classes of phytochelatins have been identified in Cd treated *Micrasterias* samples by mass spectrometry and are obviously involved in stress diminishment (Volland et al., 2013). To avoid cell damage, the alga has developed different strategies to cope with different stress scenarios and to maintain viable functions such as photosynthesis and respiration.

Particularly, salt stress represents a considerable thread to algae like *Micrasterias* as due to their low concentrated surroundings in clean freshwater (peat bogs). The cells do only face minor traces of salt such as KCl or NaCl in their natural habitats. Entry of salt into the cells thus causes severe intracellular disturbances such as degradation of dictyosomes, increase in ROS production, autophagy and finally PCD (Affenzeller et al., 2009a; Affenzeller et al., 2009b). The pronounced protuberances that were visualized by standard 2-D TEM in KCl stressed *Micrasterias* cells seem to indicate an influence on the respiratory system, which however was rebutted by the finding that oxygen consumption was maintained or only slightly reduced under these adverse conditions (Affenzeller et al., 2009a). This led us to the conclusion that the structural alterations of mitochondria during ionic stress are somehow related to the fact that they are able to maintain their respiration, despite severe stress impact. To prove this working hypothesis the present study is aimed to analyze the structural mitochondrial alterations in detail, to correlate them to the intensity of the stress and to find out whether different ionic stressors cause the same reactions and to investigate what happens when mitochondrial deformations are experimentally prevented during stress.

Structural aberrations of mitochondria have been reported in the literature during stress or disease in plant and animal cells (Choi et al., 2014; Vartapetian et al., 2003). For example protuberances of the outer mitochondrial membrane were observed in transgenic mouse brain as consequence of Alzheimer's disease (Choi et al., 2014) and non-invasive radiofrequency induced elongation of mitochondria of pancreatic cancer cells and altered the outer mitochondrial membrane (Curley et al., 2014). By means of 3-D electron microscopy a recent study (Song et al., 2017) in the model system *Paramecium bursaria* showed that a membrane-associated mitochondrial network is involved in symbiotic interactions with *Zoochlorella*. In higher plants such as *Cucurbita pepo* (Vartapetian et al., 2003), mitochondria elongate and form aggregations due to anaerobic stress.

In order to obtain comprehensive insight into salt-stressed alterations of mitochondria in the model system *Micrasterias* and to link structural alterations to physiological function, two different methods of electron tomography have been used for the present investigations. FIB-SEM tomography which allows observation of large volumes of the cytoplasm was employed for investigating mitochondrial shape and distribution, TEM tomography providing high resolution of structural details was used for depicting fusion processes and membrane alterations. Although electron tomography is an important tool for studying the relation between function and structure (Asano et al., 2016), particularly in plants only few studies have used this method so far. For example the relationship of ER and Golgi apparatus in plants and the corresponding membrane trafficking (Day et al., 2013; Donohoe et al., 2006; Donohoe et al., 2013; Kang and Staehelin, 2008; Kang et al., 2011), as well as arrangement of thylakoid membranes of an unicellular cyanobacterium (Liberton et al., 2011) and chromosome centromere structure (Schroeder-Reiter et al., 2012), have been investigated by electron tomographic imaging so far. 3-D reconstructions of mitochondria have been used for studying functionality and ultrastructure of mitochondria during different nutritional stress-conditions such as iron (Fe) deficiency in leaves of *Cucumis sativus* L. (Vigani et al., 2015). The study revealed that number and volume of mitochondrial cristae is altered due to Fe shortage. Parallel to these 3-D structural alterations, the respiratory chain was operating at a lower rate compared to control cells.

It is the aim of the present study to correlate alterations of mitochondrial structure and morphology in *Micrasterias* to its physiological functions in stress response during different ionic stress scenarios. In order to prove their general validity the results are compared to those obtained in the aquatic higher plant *Lemna* sp. under the same stress conditions. This is particularly interesting as *Lemna* (Araceae) is closely related to *Micrasterias* from an evolutionary point of view (see Leliaert et al., 2012). It is also an aquatic plant but is adapted to completely different environmental conditions and can thus cope with environmental pollution much better than *Micrasterias* (see citations below). Moreover it has been used as a model system since many years (see e.g. Appenroth et al., 2015) and numerous highly important results on its physiological reactions to different stress conditions, and also to high salinity have been collected over the years (Basile et al., 2015; Dalla Vecchia et al., 2005; Fodorpataki et al., 2015; Oukarroum et al., 2015; Sikorski et al., 2013; Sree et al., 2015, and many others). By comparing stress induced structural reactions of mitochondria in these two organisms, by recovery experiments, measurements of respiration and photosynthetic oxygen production as well as by employment of the K channel inhibitor bumetanide, we aim to prove the hypothesis, that formation of mitochondrial networks represents a survival strategy of plant cells during ionic stress impact.

2. Material and methods

All chemicals were purchased from Sigma-Aldrich (Vienna, Austria) or Roth (Karlsruhe, Germany) unless stated differently.

2.1. Cultivation of Micrasterias denticulata and Lemna sp

Micrasterias denticulata Breb. was cultivated in Erlenmeyer flasks in 30 ml Desmidiacean medium (Schlösser, 1982) at 20 °C and a

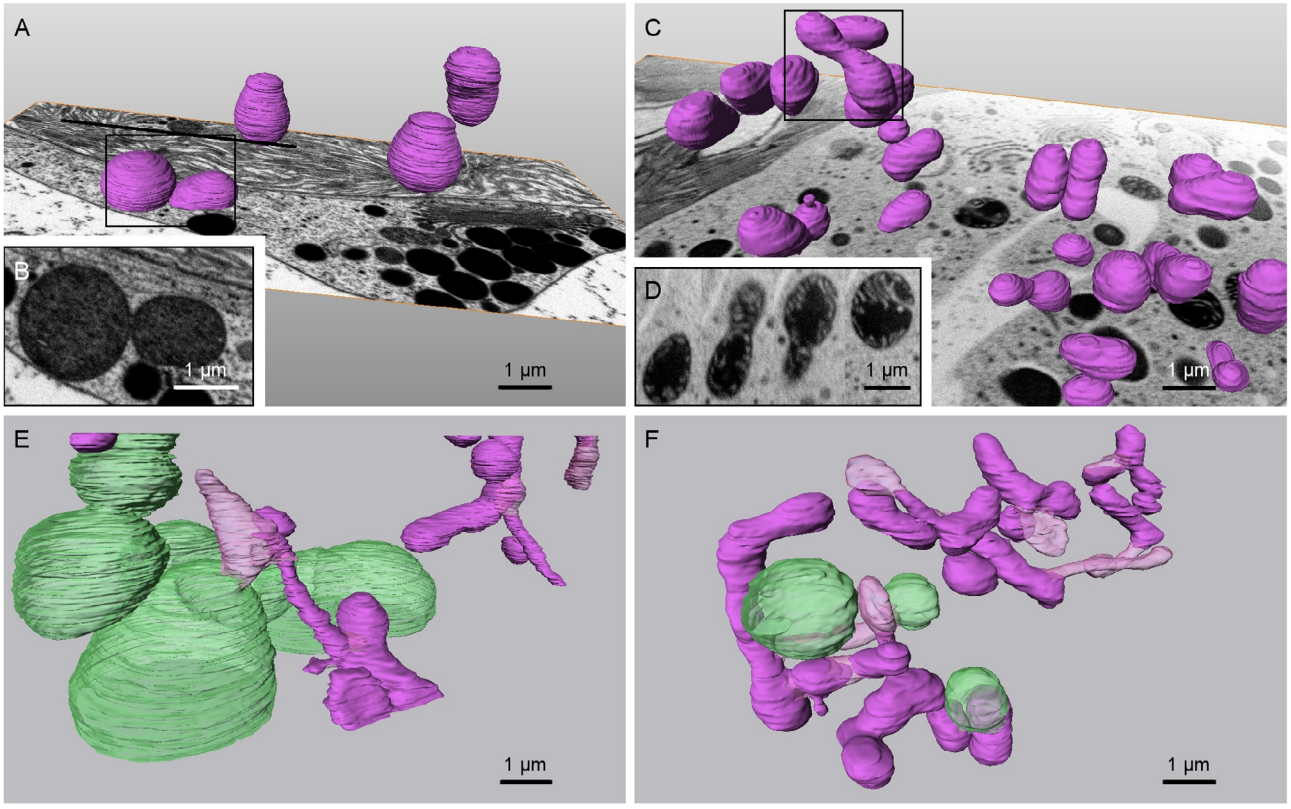

Fig. 1. 3-D visualization of mitochondria (purple) from FIB-SEM tomograms of *Micrasterias denticulata.* (A) Untreated control cell; solitary mitochondria round to oval. (B) Image from FIB-SEM series (see inlet), showing two adjacent mitochondria that are not fused. (C) Elongated, partially fused (inset) mitochondria of 150 mM KCl (3 h) treated cell, (D) 4 consecutive images of FIB-SEM series demonstrating fused mitochondria in inlet of C. (E, F) Mitochondria in 180 mM KCl (3 h) treated cells fused to elaborate networks. Mitochondria are partially connected to membrane balls (=degenerated dictyosomes; green); protuberances of the outer mitochondrial membrane in transparent purple.

light–dark cycle of 14–10 h. Desmidiacean medium consists of 100 mg KNO_3, 10 mg $(NH_4)_2$ HPO_4, 10 mg $MgSO_4$ $7H_2O$, 10 ml of saturated $CaSO_4$, 5 ml trace element stock solution ($ZnSO_4$ $7H_2O$, $MnSO_4$ $4H_2O$, H_3BO_3, $Co(NO_3)_2$ $6H_2O$, Na_2MoO_4 $2H_2O$, $CuSO_4$ $5H_2O$, $FeSO_4$ $7H_2O$, EDTA (Titriplex III Merck)) and 30 ml soil extract solved in 2 L distilled water. The culture medium does not contain KCl, NaCl or $CoCl_2$. In order to obtain defined interphase cells for the KCl treatment, developmental stages were collected and were allowed to grow in nutrient solution for 48 h under standard culture conditions before the exposure to KCl started. *Micrasterias* cells were subcultered every 3–4 weeks.

The aquatic freshwater plant *Lemna* sp. was also cultivated in Erlenmeyer flasks in 50 ml of Hoagland's Medium (Cowgill and Milazzo, 1989) under axenic conditions. The cultures were stored in incubators at a temperature of 20 °C and a light–dark cycle of 12–12 h. *Lemna* was subcultered every 5–6 weeks by transferring two single plants into a new Erlenmeyer flask of Hoagland's medium.

2.2. KCl treatment

Defined interphase cells (see above) of *Micrasterias denticulata* were treated with 120, 150 and 180 mM KCl for 3 h (Affenzeller et al., 2009a) in glass dishes by substituting the nutrient medium by the respective solution. *Lemna* sp. was treated with 150 mM KCl for 5 days by transferring two plants each into the respective solution.

2.3. Recovery

Cells treated with 150 mM KCl for 3 h, as well as untreated control cells of *Micrasterias*, were re-transferred into Desmidiaceaen medium for 24 h, respectively 48 h recovery and investigated by light microscopy and TEM.

2.4. Bumetanide treatment

In order to determine how the mitochondrial protuberances are formed, *Micrasterias* cells were exposed to the NKCC (Na-K-Cl_2-cotransporter) blocker bumetanide that inhibits water channels as well (Hamann et al., 2010). Interphase cells of *Micrasterias denticulata* were treated with 100 µM bumetanide, 1 h and were transferred into 150 mM KCl for 3 h, thereafter. In parallel, cells were treated with a mixture of 10 µM bumetanide and 150 mM KCl for 3 h. Untreated cells and 100 µM bumetanide, 1 h cells were used as controls. After fixation (see above), cells were observed in TEM.

2.5. NaCl and $CoCl_2$ exposure

For comparison to KCl effects, ionic stress was induced by NaCl and $CoCl_2$ as well. Interphase cells of *Micrasterias denticulata* were treated with 180 mM NaCl (3 h, 24 h) and 30 µM $CoCl_2$ (2 weeks), respectively. Treated cells and controls were investigated in TEM.

2.6. Measurement of photosynthetic oxygen production and respiration

Oxygen measurements of KCl treated *Micrasterias* cells, *Lemna* plants and untreated controls were performed by polarographic oxygen determination (Hansatech, King's Lynn, England) during 6 light and dark cycles in order to obtain insight into their respiratory and photosynthetic efficiency during exposure to elevated KCl concentrations. The temperature in the surrounding medium was 20 °C at an illumination of approximately 200 µmol photons $m^{-2}s^{-1}$. Cell cultures of

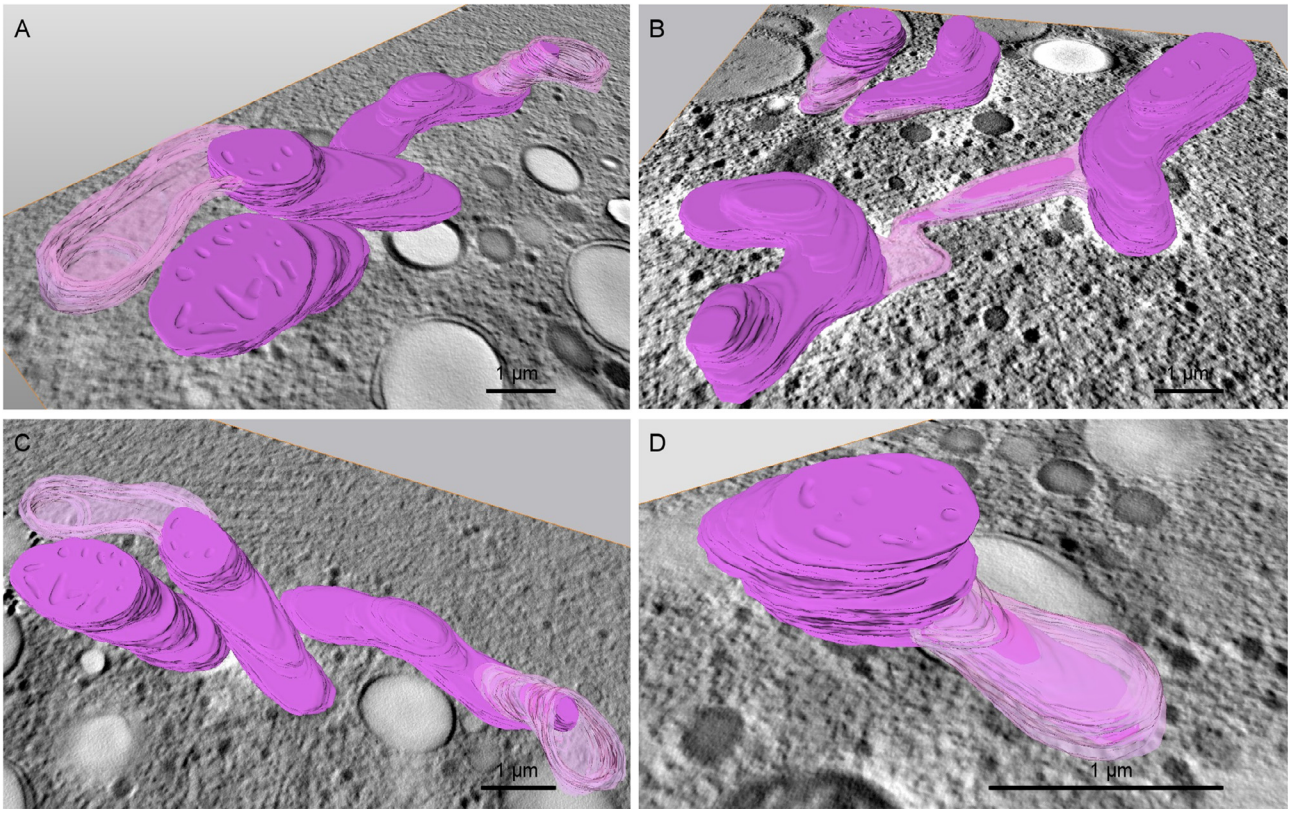

Fig. 2. Reconstructions of mitochondria from TEM tomograms of 180 mM KCl (3 h) treated *Micrasterias* cells (A-D). Reconstructions of mitochondria (purple) in different angles superimposed on TEM micrographs. (A, C, D) Mitochondrial protuberances (transparent purple) are formed by outer mitochondrial membrane. (B) Mitochondria are fused via protuberances.

Micrasterias denticulata (approximately 2000 cells/ml) were treated with 150 mM KCl for 3 and 24 h, respectively. O_2 measurements of *Micrasterias denticulata* were performed according to earlier experiments (Lütz et al., 1997; Weiss et al., 1999). For *Lemna*, leaves were treated with DMF (dimethylformamide) for chlorophyll extraction. O_2 measurements of *Lemna* were performed according to Porra et al. (1989).

2.7. Preparation for TEM and FIB-SEM

Untreated control cells and *Micrasterias* cells treated as described above were transferred into the sample holder of the high-pressure freezer attached to cotton fibers (for details see Meindl et al., 1992). The sample holders were filled up with yeast suspension, to guarantee pressure transfer. High-pressure freezing of both *Micrasterias* and *Lemna* was done in a Leica EMPACT HPF device (Leica Microsystems, Vienna, Austria) with a cooling rate of at least 12.270 K/s and a pressure of 2040 bar.

Leaf samples of *Lemna* were punched out in the exact diameter of the sample holder of the high pressure freezer. Again, the holders were topped with yeast suspension.

The substitution medium contained 2 % OsO_4 and 0.05 % uranyl acetate in anhydrous acetone. Cryo-substitution was performed in a Leica EM AFS with the following cycles: 60 h at −80 °C and 4 h at −30 °C. After cryo-substitution, the samples were embedded in epoxy resin (Agar Scientific, Essex, UK). Sectioning for TEM and TEM-tomography was done in a Leica UC7 ultramicrotome.

Ultrathin sections were collected on Formvar coated copper grids. For standard TEM, square meshed grids and 60–70 nm sections were used. For TEM tomography, 120–180 nm sections were mounted on parallel meshed grids.

2.8. TEM and TEM tomography

TEM analysis and TEM tomography were carried out in a LEO 912 AB TEM with in column Omega energy filter (Zeiss, Oberkochen, Germany). For standard TEM imaging the TEM was operated at an acceleration voltage of 80 kV, for electron tomography at 120 kV. Images were taken by a Tröndle TRS Sharp Eye bottom mount 2 K CCD camera (Tröndle, Moorenweis, Germany) and were always filtered at zero energy loss imaging mode.

For TEM tomography, Formvar coated grids with 120 nm to 180 nm sections were incubated in 2 µl of 15 nm colloidal gold particles (BBI Solutions, Cardiff, UK) on both grid sides in order to facilitate the subsequent alignment processes. Up to 3 serial sections were join-aligned for reconstruction. The samples were automatically tilted from −70° to +70° with 1° increment. For acquisition and calibration, iTEM (Olympus Soft Imaging Solutions GmbH, Münster, Germany) Software was employed. For the tilting series of the TEM tomography, images were first stack aligned in iTEM a several times. Tiff files were converted via ImageJ to st-files for the actual alignment and reconstruction (WBP) with IMOD (Mastronarde, Boulder, University of Colorado, USA). Segmentation was done manually by Thermo Scientific™ Amira™ Software.

2.9. FIB/SEM tomography

Sample preparation for FIB/SEM tomography was implemented as explained above until the embedding step in epoxy resin. For further use, aluminum stubs were coated with a thin layer of polymerized epoxy resin within small plastic tubes. The blocks were trimmed with a LKB Pyramitome (mesa technique) to enable lateral milling via FIB (Ga-ion beam). For conductivity the specimens were coated with approx. 15 nm carbon by evaporation. “Slice and view” technique was applied

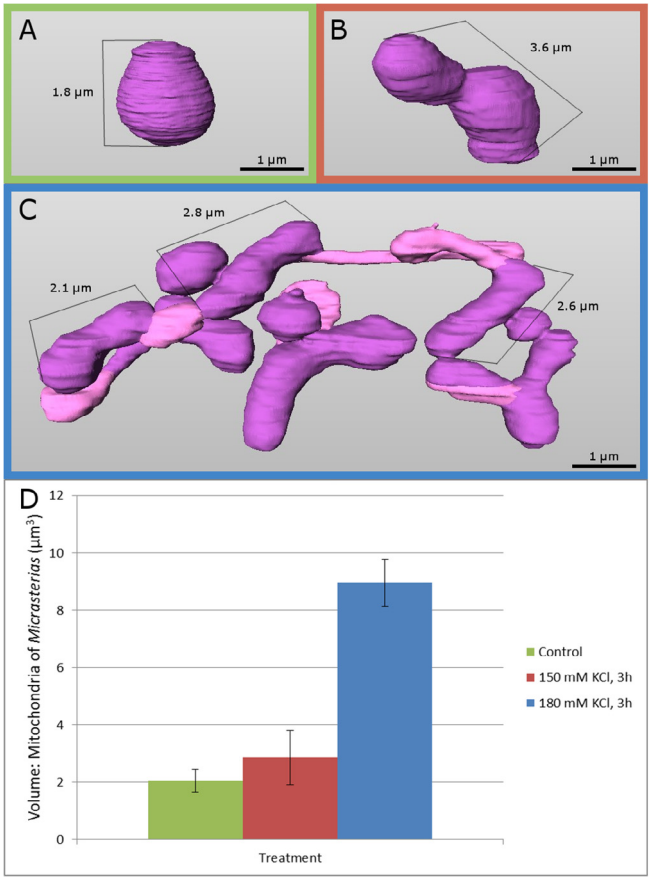

Fig. 3. Statistical analysis of mitochondrial volume and length measurement from FIB-SEM tomograms in *Micrasterias denticulata*. (A) Comparison of mitochondrial volumes of controls and of cells treated with different KCl concentrations (with standard deviation; see Section 2). (B) Mitochondrion of untreated control cell. (C) Mitochondrion of 150 mM KCl, 3 h treated cell. (D) Mitochondrial network of 180 mM KCl, 3 h treated cell.

with a Zeiss Auriga 40 crossbeam workstation (Carl Zeiss Microscopy, Oberkochen, Germany) to obtain tomographic datasets. FIB milling was performed with 0.5–1nA milling current of the Ga-emitter. The "slice thickness" was chosen between 5 nm and 10 nm. Micrographs of the block faces were taken at 1.5 kV with the back scattered electron signal of the in-lens EsB detector with an aperture of 60 µm in the high-current mode (for methods see Lütz-Meindl et al., 2016; Wanner et al., 2013).

For each experimental approach, at least 4 cells were investigated via TEM and FIB-SEM.

The alignment (semi-automatically) of the FIB/SEM image stacks, as well as segmentation (manually) was done with Amira™ Software (Visualized Sciences Group, Hilsboro, USA).

2.10. Statistics

In order to obtain statistical evaluation of the 3-D data, volumes of mitochondria were calculated in controls and after treatment with different KCl concentrations in *Micrasterias* using the "material statistics" tool of Amira™ Software. Due to the high technical and financial expenses of FIB-SEM imaging the sample number had to be limited to 2 samples, respectively mitochondrial networks per treatment.

3. Results

3.1. Mitochondria in KCl-stressed Micrasterias cells fuse to elaborate networks

Corresponding to the considerable cell size, with a diameter up to 200 µm, mitochondria of *Micrasterias denticulata* are large (1–2 µm in diameter) and exceed the size of higher plant organelles. Organelle morphology is well defined and both, their structure and distribution under normal culture conditions is well known from numerous 2-D TEM and light microscopic investigations (for summary see Lütz-Meindl, 2016; Meindl, 1993). 3-D visualization by FIB-SEM tomography of untreated control cells of *Micrasterias* reveals round to slightly oval shaped mitochondria, with an average diameter of 1.5 µm. Mitochondria in untreated control interphase cells are solitary dispersed and randomly scattered within the cell (Fig. 1 A). This finding corroborates earlier light microscopic and 2-D TEM observations (Lütz-Meindl, 2016; Meindl, 1993). Neither aggregations, nor fusions (Fig. 1 B) between individual mitochondria have been observed by TEM imaging, TEM-tomography or by FIB-SEM tomography in controls.

Concentrations up to 100 mM KCl did not induce structural alterations in mitochondria of *Micrasterias*. In a concentration range between 120 mM and 180 mM KCl for 3 h, salt stress evoked distinct structural alterations of shape and distribution of mitochondria when compared to untreated controls (Fig. 3 A; for 2D-TEM images see Affenzeller et al., 2009a). 120 mM and 150 mM KCl treatment resulted in extreme elongations of mitochondria, which exceeded multiple times the length of untreated control mitochondria of *Micrasterias* (Fig. 3 B; Fig. 4 B; Table 1). With increasing concentration mitochondrial matrix appeared electron dense and condensed, indicating shrinkage. Our 3-D visualization from FIB-SEM tomography show that at 150 mM KCl, mitochondria have already started fusing (Fig. 1 C, D). The most striking structural alterations of mitochondria are pronounced elongations and formation of protuberances that interconnect mitochondria to local networks as occurring at 180 mM KCl (Fig. 1 E, F; Fig. 2 A-D; Fig. 3 C). Numerous networks that are obviously formed by fusion of several mitochondria are found inside these cells, yet there is no indication that the single networks are connected to each other. As visualized by TEM tomography fusion of mitochondria takes place by formation of protuberances of the outer mitochondrial membrane (Fig. 2 A-D). Fig. 1 (E, F) shows that mitochondria in KCl (180 mM) stressed cells may also be structurally connected to membrane balls resulting from dictyosome degradation during salt stress (Lütz-Meindl et al., 2016). Statistical analyses show that the volume of mitochondria increases from 2.1 µm^3 (control) to 2.9 µm^3 (at 150 mM KCl) and to 9 µm^3 at the highest concentration of 180 mM KCl in average (Fig. 3 D).

3.2. Mitochondria regain their solitary distribution and morphology during recovery from KCl treatment

In order to find out whether mitochondrial fusion via protuberances is reversible, recovery experiments were performed. The KCl solution was replaced by Desmidiaceaen medium and the cells were allowed to recover for 24 h or 48 h, respectively. After 24 h of recovery (Fig. 4 D), mitochondria reveal only slight alterations and are in maximum only double the size when compared to untreated control mitochondria. Such minor elongations have been occasionally observed even in untreated control cells of *Micrasterias*. Neither fusions, nor protuberances of the outer mitochondrial membrane as during KCl treatment (Fig. 4 B, C) were observed after 24 h of recovery in TEM. Overall, only few mitochondria reveal structural alterations, yet dictyosomes appeared in different stages of degeneration (see Lütz-Meindl, 2016). After 48 h recovery (Fig. 4 E), both, mitochondria and dictyosomes of *Micrasterias denticulata* have the same structure and size as in untreated control cells (Fig. 4 A). These results show that KCl induced fusion of mitochondria is completely reversible when the cells are re-transferred into nutrient

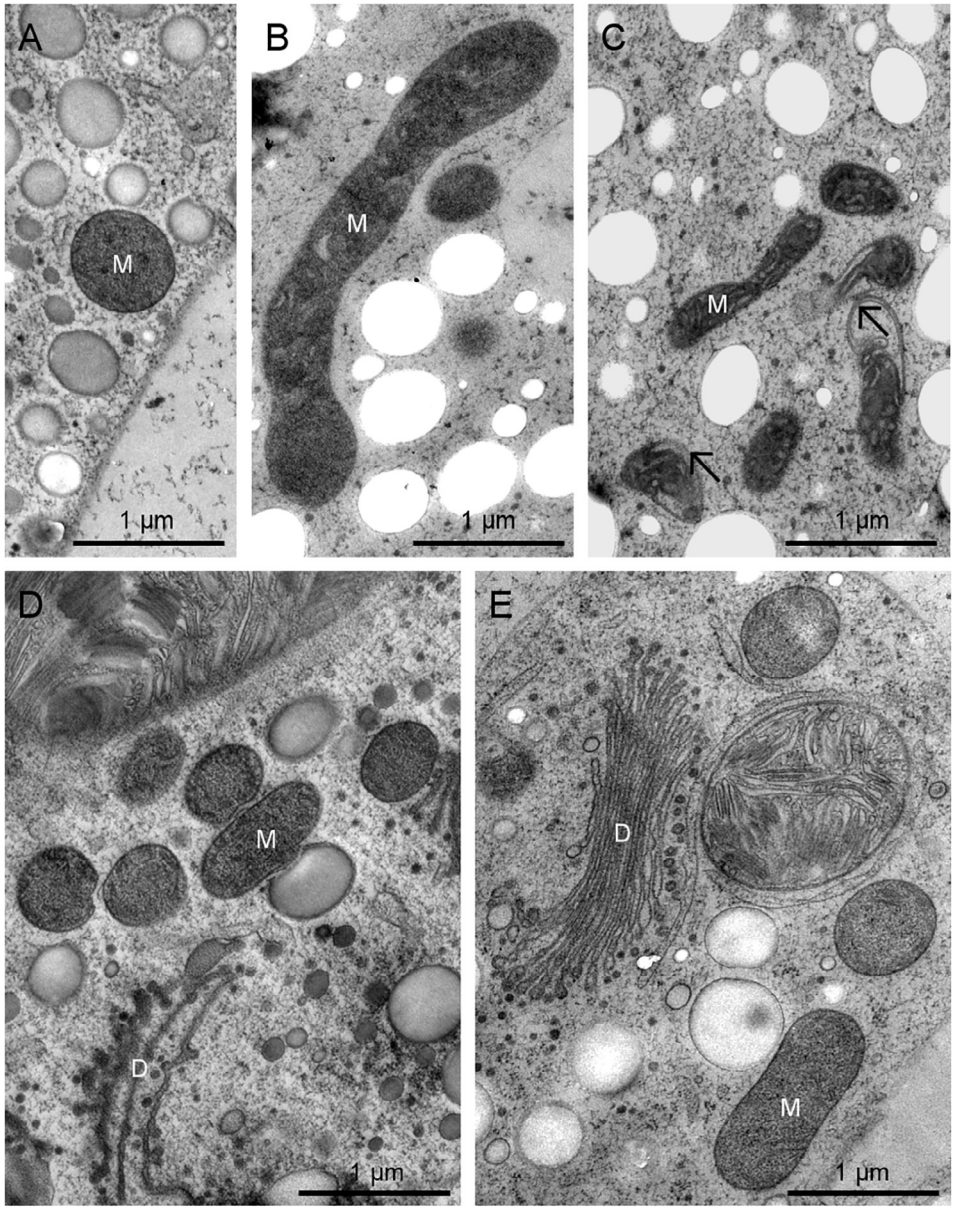

Fig. 4. TEM micrographs of mitochondria of *Micrasterias* before and during recovery from 150 mM KCl (3 h) treatment. (A) Solitary mitochondrion (M) in untreated control cell. (B) Extremely elongated mitochondrion in *Micrasterias* cell treated with 120 mM KCl (3 h). (C) KCl stressed cell (150 mM, 3 h); mitochondria in network with elongated electron dense, condensed matrix, protuberances of outer membrane (arrows) visible. (D) 24 h recovery from 150 mM (3 h) KCl stress; cluster of mitochondria still visible, no protuberances, D degenerated dictyosome. (E) 48 h recovery from 150 mM (3 h) KCl stress; solitary mitochondria like in controls; (D). Dictyosome (D) recovered.

solution.

3.3. The K-channel inhibitor bumetanide prevents formation of mitochondrial protuberances

In order to clarify whether formation of mitochondrial protuberances that leads to fusion is due to a swelling process induced by disturbance of the ionic balance, KCl exposed *Micrasterias* cells were treated with the NKCC transporter inhibitor, bumetanide (for methodological details see Section 2). In *Micrasterias* cells that were treated with 100 µM bumetanide (1 h) prior to 150 mM KCl (3 h) exposure, mitochondria do form clusters but do not fuse to local mitochondrial networks, as described in exclusively KCl treated *Micrasterias* cells. Protuberances of the outer mitochondrial membrane were not found (Fig. 5 A). Similar effects were observed by coincident treatment with 10 µM bumetanide + 150 mM KCl (3 h) of *Micrasterias* (Fig. 5 B). Also, in this case protuberances of the mitochondrial membrane did not exist and the structure of mitochondria was similar to that of cells treated with 100 µM bumetanide alone (Fig. 5 C) which were slightly swollen when compared to untreated control cells of *Micrasterias* (Fig. 5 D).

3.4. Other ionic stressors such as NaCl and $CoCl_2$ do also induce aggregation of mitochondria

Other ionic stressors such as NaCl and $CoCl_2$ have similar effects on mitochondria of *Micrasterias* as KCl as observed by TEM (Fig. 6 A-D). Aggregations of mitochondria, as well as protuberances of the outer mitochondrial membrane (Fig. 6 A, see arrows) were observed in 30 µM $CoCl_2$, 2 weeks (Fig. 6 A), 180 mM NaCl, 3 h (Fig. 6 B) and 180 mM NaCl, 24 h (Fig. 6 C) treated cells of *Micrasterias*, indicating that stress induced fusion of mitochondria takes place in the same way as after KCl exposure.

3.5. KCl induces fusion of mitochondria also in the aquatic higher plant Lemna

The freshwater duckweed *Lemna* shows similar sub-structural effects after KCl treatment as KCl stressed *Micrasterias* cells. Whereas mitochondria of untreated control *Lemna* leaves appear solitarily dispersed in the cytoplasm (Fig. 7 E, F), mitochondrial elongations in *Lemna* as well as fusion between mitochondria, to form large networks, are even more pronounced than in the alga *Micrasterias*. However,

Table 1
Different treatments of *Micrasterias* and *Lemna* and resulting structural alterations in 2-D (by TEM) and 3-D (by FIB-SEM and TEM tomography) in comparison to controls.

Treatment	Mitochondria in 2-D	Mitochondria in 3-D
Micrasterias control	round, slightly oval shaped	spherical, bean-shaped
Micrasterias 120 mM KCl, 3 h	elongation	elongation, fusion
Micrasterias 150 mM KCl, 3 h	single protuberances of outer membrane, elongation, aggregation	elongation, fusion to local networks
Micrasterias 180 mM KCl, 3 h	protuberances of outer membrane, elongation, aggregation	fusion to local networks via protuberances of outer membrane, linked to membrane balls, elongation
Micrasterias 180 mM NaCl, 3 h, 24 h	protuberances of outer membrane, elongation, aggregation	–
Micrasterias 30 µM $CoCl_2$, 2 weeks	protuberances of outer membrane, elongation, aggregation	–
Micrasterias 100 µM bumetanide, 1 h - > 150 mM KCl, 3 h	no protuberances, no elongation, mitochondria slightly swollen	–
Micrasterias 10 µM bumetanide + 150 mM KCl, 3 h	no protuberances, no elongation, mitochondria slightly swollen	–
Micrasterias 100 µM bumetanide, 1 h	no protuberances, no elongation, mitochondria slightly swollen	–
Lemna control	round, slightly oval shaped	spherical, bean-shaped
Lemna 150 mM KCl, 5 d	elongation, aggregation	elongation, fusion to local networks
Lemna 180 mM KCl, 5d	slight protuberances of outer membrane, elongation, aggregation	slight protuberances of outer membrane, elongation, fusion to local networks, linked to ER

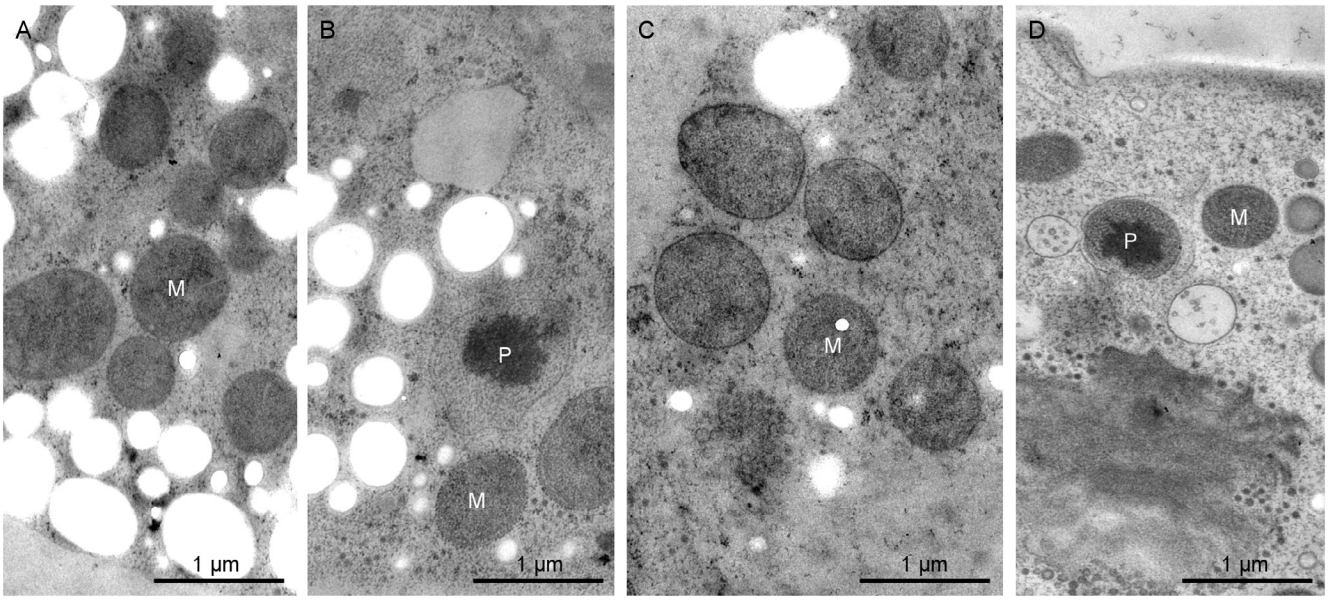

Fig. 5. Effects of K-channel inhibitor bumetanide on mitochondria of *Micrasterias* in TEM. (A) 100 µM bumetanide (1 h) prior to 150 mM KCl (3 h) cluster of mitochondria, no protuberances visible, mitochondria swollen in comparison to controls (D). (B) Coincident treatment with 10 µM bumetanide + 150 mM KCl (3 h), single mitochondria, no protuberances. (C) 100 µM bumetanide (1 h) alone. Swollen mitochondria, no protuberances (D) Untreated control cell of *Micrasterias*; M: mitochondria, P: peroxisome.

protuberances of the outer mitochondrial membrane appear only rarely and it seems that mitochondria of *Lemna* frequently fuse by direct contact with each other. Mitochondrial networks are frequently found in close spatial contact to ER cisternae in *Lemna* (Fig. 7 A-D).

3.6. Photosynthetic O_2 production and O_2 consumption (dark respiration) is maintained in Micrasterias and Lemna during salt stress

O_2 production (photosynthesis) and O_2 consumption (respiration) was measured by polarographic oxygen determination during KCl stress. Both apparent photosynthesis and dark respiration of *Micrasterias* increase during 3 h treatment with 150 mM KCl and decrease after 24 h KCl exposure when compared to untreated controls (Fig. 8 A). Photosynthesis of *Lemna* sp. increases after 5 d treatment with 150 mM KCl, while respiration drops down to approximately 75% in comparison to control cells. After 9 d of salt-stress respiration decreases to approximately 10% while photosynthesis is slightly higher than in untreated control cells (Fig. 8 B). O_2 measurements of *Lemna* after 9 d of KCl treatment have shown, that the stressed plants reacts slower to light and dark cycles than untreated controls.

4. Discussion

The present study shows that mitochondria both, in the unicellular alga *Micrasterias* and in the aquatic higher plant *Lemna* fuse to numerous local networks under ionic stress conditions experimentally induced by application of unphysiological high concentrations of KCl, NaCl and $CoCl_2$ (Fig. 9 A-F) . By means of 2-D TEM as well as TEM- and FIB-SEM tomography it is shown that mitochondrial fusions are frequently formed by formation of protuberances of the outer mitochondrial membrane in *Micrasterias* but may also occur by direct contact of adjacent mitochondria like in *Lemna*. In both organisms cells are able to

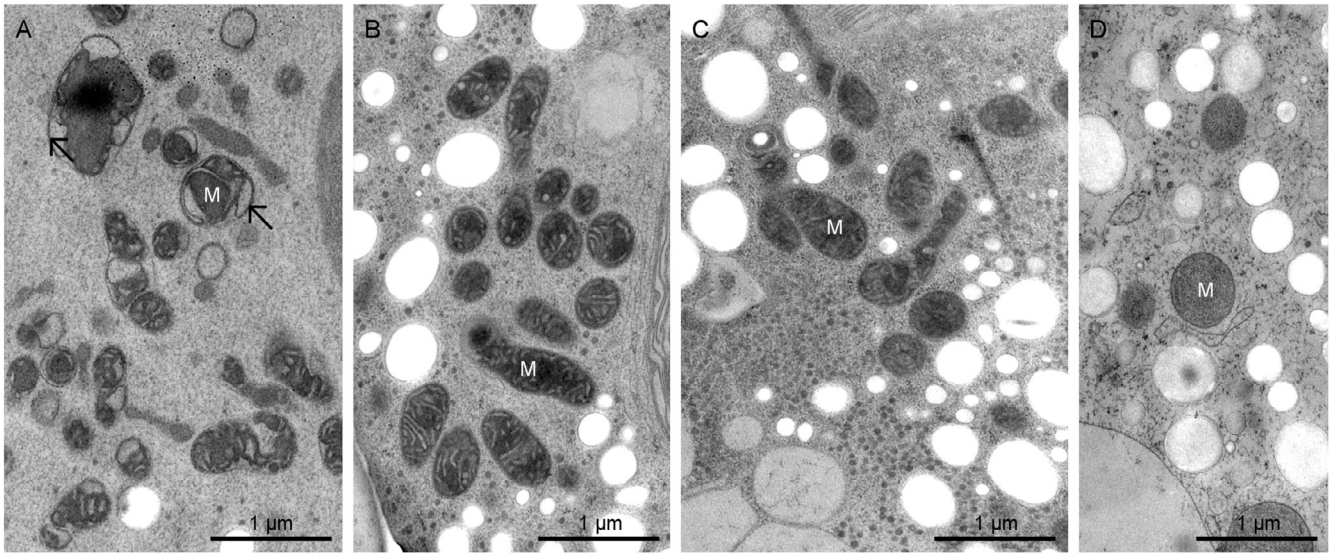

Fig. 6. Mitochondria in $CoCl_2$ and NaCl treated *Micrasterias* cells. (A) 30 µM $CoCl_2$ (2 weeks) induces membrane protuberances of mitochondria (arrows) and mitochondrial clusters. TEM micrograph kindly provided by Lothar Götz. (B) 180 mM NaCl (3 h) and (C) 180 mM NaCl (24 h); mitochondrial clusters are formed and mitochondrial matrix condenses in a similar way as during KCl treatment (compare Fig. 4 C). (D) Mitochondria in untreated control.

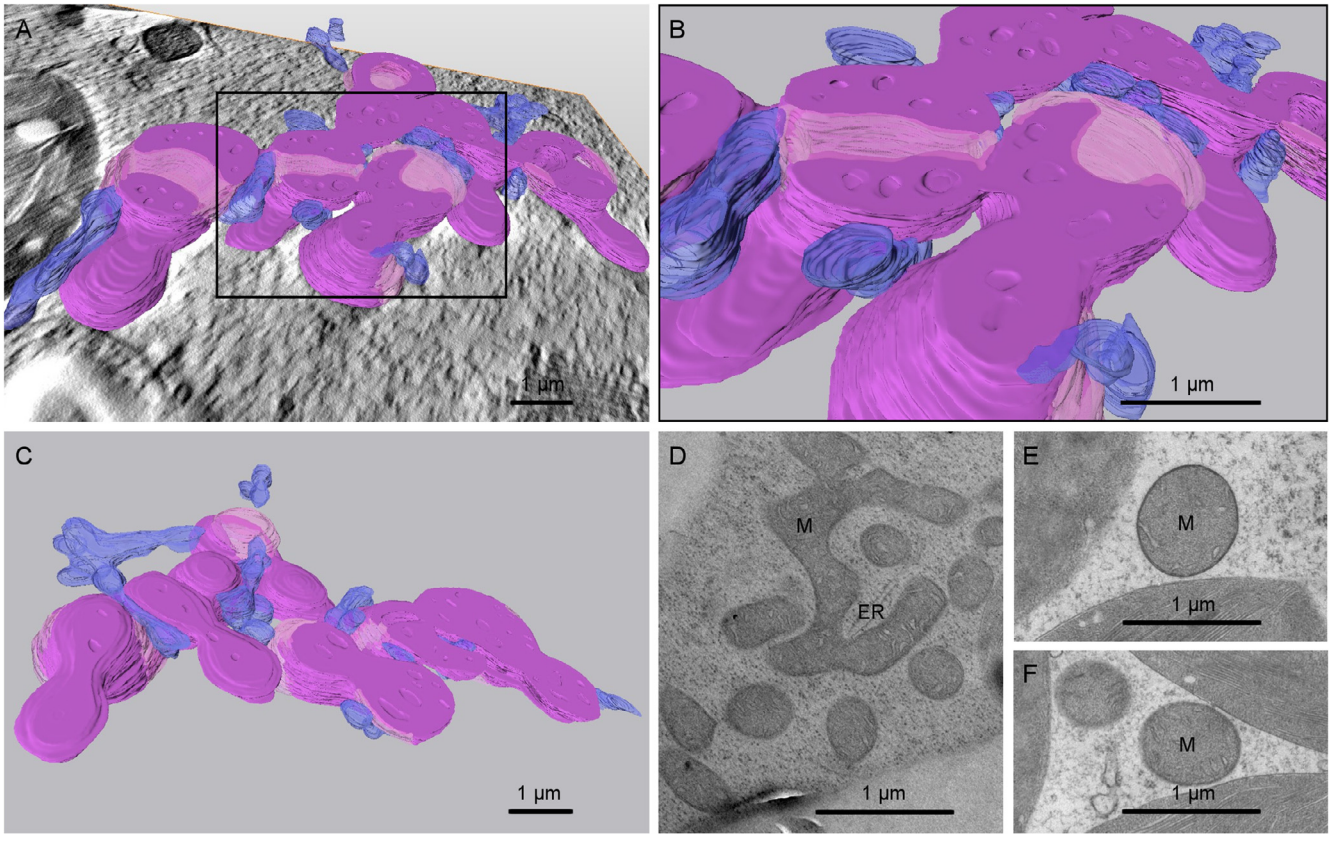

Fig. 7. Reconstruction of mitochondrial networks in *Lemna* leaves from TEM tomogram (A-C) and TEM micrographs (D-F) of mitochondria and ER of 150 mM KCl (5 days) treated (A-D) and untreated *Lemna* control (E, F). Mitochondria (purple) form networks by direct fusion or via protuberances (transparent purple). Mitochondrial networks are closely associated with ER cisternae (blue).

maintain their respiratory activity during mitochondrial network formation in a similar way as controls. This allows the conclusion that formation of mitochondrial networks in which the single organelles are fused to each other, represents an effective mode for the cell to cope with stress. All structural alterations of mitochondria observed during stress exposure, such as fusion, aggregation, elongation and formation of protuberance of the outer mitochondrial membrane are reversible upon stress relief.

Formation of mitochondrial aggregations or fusion of mitochondria have been reported in algal cells (Scholz and Westermann, 2013; Song et al., 2017), higher plants (Arimura et al., 2004; Hales and Fuller, 1997; Logan, 2010; Vartapetian et al., 2003), and animal cells (Choi et al., 2014) by means of different techniques, sometimes but not always in relation to stress. It is generally believed that mitochondrial

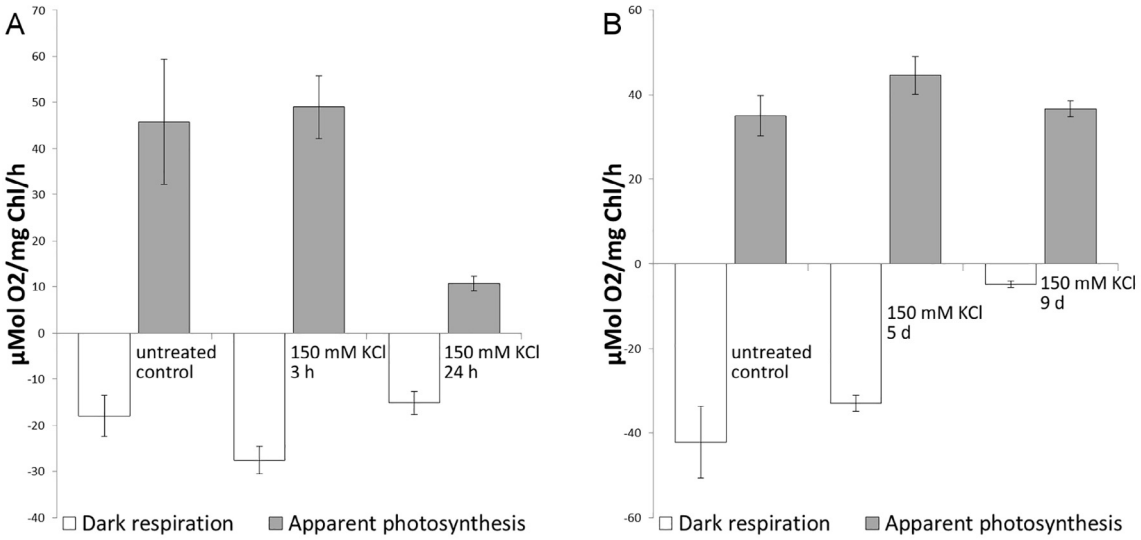

Fig. 8. Photosynthetic oxygen production (apparent photosynthesis) and dark respiration of (A) *Micrasterias* and (B) *Lemna*. In both organisms respiration is still efficient after 3 h exposure when mitochondrial fusions occur.

fusion is important for maintenance of respiratory capacity, for allowing mitochondrial DNA complementation and recombination as well as for dissipation and exchange of metabolic constituents (Logan, 2010; Scholz and Westermann, 2013). Cytoskeleton driven transient fusions of mitochondria as reported from live cell imaging, are assumed to be the basis for control of mitochondrial "health" (Logan, 2010). The way in which alterations of mitochondrial morphology are expressed depends both, on the stressor and on the organism. Mitochondria of transgenic AD (Alzheimer's disease) mice form protuberances of the outer mitochondrial membrane (Choi et al., 2014), similar to KCl treated mitochondria of *Micrasterias*, but neither fission nor fusion of mitochondria were reported. In Las-infected (autotransporter protein of *Candidatus* Liberibacter asiaticus) periwinkle plant, mitochondria fuse to aggregates but no protuberances have been reported (Hao et al., 2013).

Our electron tomography study shows that mitochondrial networks of *Micrasterias* are formed via protuberances of the outer mitochondrial membrane whereas in the closely related higher aquatic plant *Lemna* fusion occurs preferentially by direct membrane contact of adjacent mitochondria. Only rarely protuberances of the outer mitochondrial membrane were observed in *Lemna*. In *Micrasterias* the formation of mitochondrial protuberances depends on the KCl concentration and seems to result from a membrane surplus as consequence of shrinkage of the mitochondrial matrix due to the ionic imbalance (see below). At higher concentrations (150 mM and above) mitochondria of *Micrasterias* fuse primarily via protuberances of the outer mitochondrial membrane, whereas lower concentrations lead to elongation of mitochondria and results in direct mitochondrial fusion without protuberances, similar to the observations in KCl treated *Lemna*. We thus assume that mitochondrial elongation, approach and fusion via direct membrane contact represent a basic stress response in both organisms. Formation of protuberances of the outer mitochondrial membrane does not seem to be essential for this process but may facilitate and may accelerate the fusion process. Additionally it may prevent rupture of the outer mitochondrial membrane which may initialize cell death (Matic et al., 2017; Ruffoli et al., 2015; Szklarczyk et al., 2014). The observed mitochondrial transition from ovoid to elongated shape in our experiments, both in *Micrasterias* and in *Lemna* may represent an adaptive response that may have two beneficial consequences. (1) It prevents salt stress-induced rupture of the outer membrane and, accordingly, it guarantees survival of cells. (2) An increase in matrix volume also may increase respiratory chain activity and ATP production (for review see Kaasik et al., 2007). Thus, elongation of mitochondria may promote maintenance of physiological mitochondrial processes, like respiration (see Fig. 8). Despite their different natural environment *Micrasterias* and *Lemna* mitochondria exist in two discrete phenotypes - a spheroid phenotype in "normal" conditions and an elongated one in hyperosmotic conditions. Both phenotypes are adaptive responses to the environment and increase the likelihood of survival.

That salt stress signaling pathways are directly connected to mitochondrial metabolism is excellently shown in a recent publication on higher plants (Hafiz Che-Othman et al., 2017) indicating that mainly two biochemical processes are affected. These are the TCA cycle and the transport of metabolites across the inner mitochondrial membrane (Ivanova et al., 2016). The mitochondrial K^+ cycle has been tightly associated with cytoprotective consequences in animal as well as in plant cells (for review see Garlid and Paucek, 2003; Laskowski et al., 2016). It consists of an K^+ influx into the mitochondrial matrix across K^+ channels, located in the inner mitochondrial membrane and is accompanied by flux of water across aquaporins causing swelling of the mitochondrial matrix. In the plasma membrane, K^+ as well as water flux can be handled by single transporter, NKCC, which is sensitive to bumetanide at least in astrocyte mitochondria (Kintner et al., 2007).

In the present study, we found that bumetanide pretreatment suppresses protuberance formation in stressed *Micrasterias* cells. We thus suggest that protuberances are formed by the outer mitochondrial membrane as a consequence of mitochondrial matrix shrinkage, indicated by the electron dense, condensed appearance of the mitochondrial matrix in our TEM analysis. Bumetanide pretreated *Micrasterias* cells show swollen mitochondria, which do not contain a surplus outer mitochondrial membrane. If *Micrasterias* mitochondria contain NKCC transporters, our finding indicate that in mitochondria this transporter mediates an efflux of ions as well as of water in stressed cells. Consequently, the matrix shrinks and the surplus of outer mitochondria membrane forms protuberances.

In *Micrasterias*, mitochondria within local networks are partially linked to membrane balls that are remnants of degenerated dictyosomes, as determined recently by FIB-SEM tomography in *Micrasterias* (Lütz-Meindl et al., 2016). We assume that these structural connections between mitochondria and membrane balls are functional in stabilizing mitochondrial networks. Such connections between mitochondria and other membranous compartments have not been observed so far neither in control cells nor in *Micrasterias* cells under stress. In *Lemna* where protuberances of the outer mitochondrial membrane were less

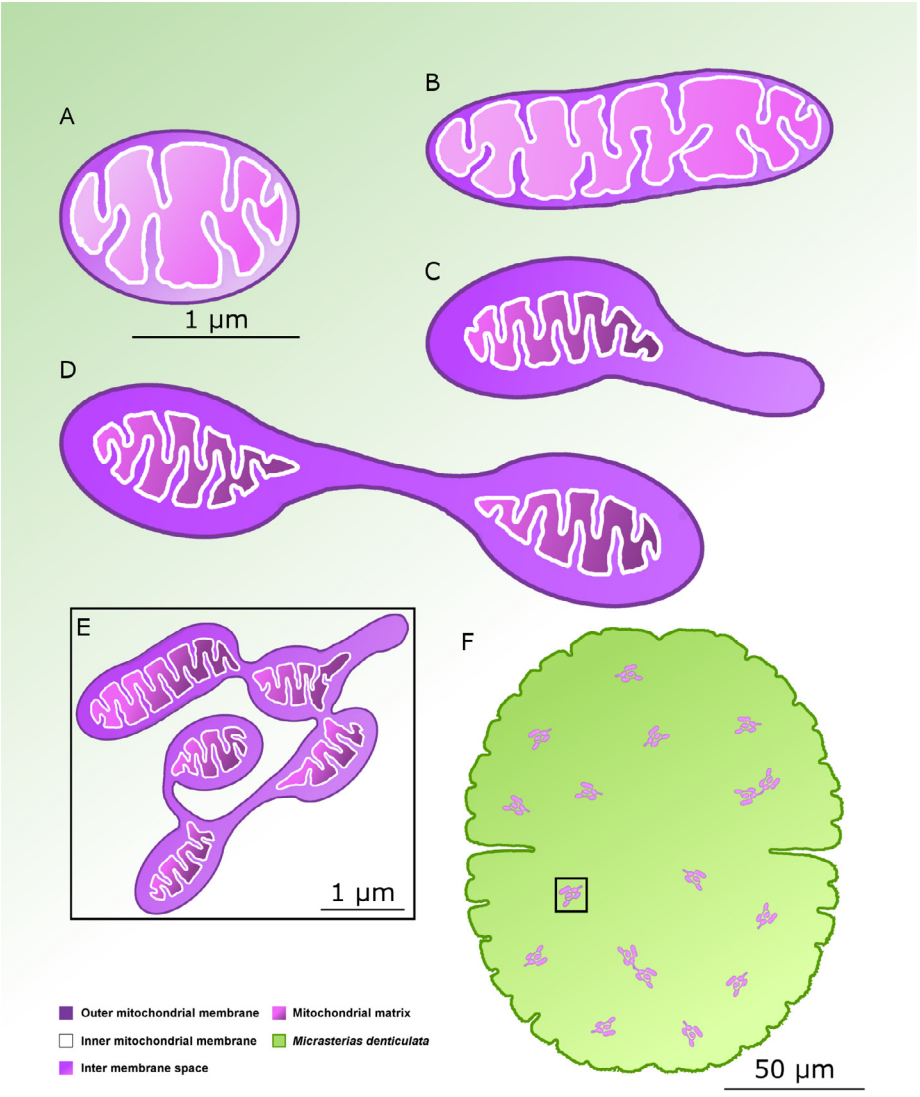

Fig. 9. Schematic drawing of mitochondrial structure responses to ionic stress in *Micrasterias* (B-F): Mitochondria fuse to local networks with increasing concentration of stressor (B- > E). (A) Untreated mitochondrion. (B) Elongated mitochondrion after low concentration of stressor. (C) Protuberance of outer mitochondrial membrane during high concentration of stressor. Inner membrane and mitochondrial matrix slightly condensed. (D) Fusion of two mitochondria via prolonged mitochondrial protuberances. (E) Local network formed by fusion of mitochondria. (F) Solitary dispersed local networks of mitochondria in *Micrasterias*.

pronounced, mitochondrial networks were always enwrapped by ER cisternae which may as well act in their stabilization. Also in other higher plant cells ER is enveloping the tight fusion parts of mitochondria and the cytoskeleton is supporting the mitochondria-mitochondria contact (Logan, 2010) and may thus stabilize the mitochondrial fusion and networking process. The tight mitochondrial-ER relationship may enable Ca^{2+} signaling between the two organelles and may thus be important for maintenance of an active physiological status and thus for survival (Pizzo and Pozzan, 2007). A similar additional function in ionic exchange might be attributed to the structural connections between mitochondria and membrane balls in *Micrasterias* (see above). ER-mitochondria contacts were also reported in neurodegenerative disease such Parkinson, Alzheimer's disease or dementia (Krols et al., 2016; Vannuvel et al., 2013). In yeast and mammalian cells, molecular re- and interactions between ER and mitochondria are well known for fusion as well as for fission/fragmentation of mitochondria (de Brito and Scorrano, 2010; Phillips and Voeltz, 2016).

Our study shows that mitochondrial fusion and formation of protuberances of the outer mitochondrial membrane are not only induced by elevated levels of KCl. Other ionic stressors such as NaCl or $CoCl_2$ induce the same process and even non-ionic stressors such as different diseases result in similar mitochondrial alterations (Choi et al., 2014; Curley et al., 2014).

Within a particular concentration range and duration of treatment, the respiratory potential was maintained during KCl treatment in *Micrasterias* and *Lemna* when compared to controls. When concentrations were increased and the exposure time was prolonged, photosynthesis and particularly respiration decreased until the organisms were no longer viable (see this study and also Affenzeller et al., 2009a). This indicates that formation of mitochondrial fusion seems to contribute to maintain the respiratory activity, possibly by interconnecting the respiratory chains of the individual mitochondria and by enhancing the buffer capacity against ionic imbalance induced by the stressors. Analytical electron microscopy such as electron energy loss spectroscopy (EELS) or X-ray analyses (EDX) could be helpful for getting insight into details of salt stress induced changes in intracellular ionic distribution in future investigations.

In summary this study provides evidence that mitochondria of plant

cells fuse to local networks under different stress conditions which may be either formed via membrane protuberances or by direct fusion of mitochondria. As similar processes have been reported in plant and animal cells during stress and disease we assume that network formation of mitochondria can be regarded as a ubiquitous stress response. Fusion of mitochondria to large networks may help the organism to cope with the stress situation, by maintaining one of the most important vital functions, namely respiration.

Acknowledgment

The authors wish to thank Silvia Dobler for expert technical assistance in FIB-SEM sample preparation and Ancuela Andosch for excellent technical assistance in different physiological and electron microscopic experiments as well as for her help in preparing this manuscript. The expertise of Cornelius Lütz in oxygen measurements and in the interpretation of the respective data is highly appreciated. We are also thankful to Stefanie Volland for helpful suggestions concerning TEM tomography and to Lothar Götz for providing a TEM micrograph (Fig. 6 A) from his Master thesis. Financial support by the Stiftungs- und Förderungsgesellschaft der Universität Salzburg as well as by the Austrian Science Fund (P30139-B32) is acknowledged. The first author of this paper is associated to the PLUS Doctoral College “Interdisciplinary Stress Research” of the University of Salzburg.

Appendix A. Supplementary data

Supplementary data associated with this article can be found, in the online version, at http://dx.doi.org/10.1016/j.jsb.2018.06.010.

References

Affenzeller, M.J., Darehshouri, A., Andosch, A., Lütz, C., Lütz-Meindl, U., 2009a. Salt stress-induced cell death in the unicellular green alga *Micrasterias denticulata*. J. Exp. Bot. 60, 939–954.

Affenzeller, M.J., Darehshouri, A., Andosch, A., Lütz, C., Lütz-Meindl, U., 2009b. PCD and autophagy in the unicellular green alga *Micrasterias denticulata*. Autophagy 5, 854–855.

Andosch, A., Affenzeller, M.J., Lütz, C., Lütz-Meindl, U., 2012. A freshwater green alga under cadmium stress: ameliorating calcium effects on ultrastructure and photosynthesis in the unicellular model *Micrasterias*. J. Plant Physiol. 169, 1489–1500.

Appenroth, K.J., Sree, K.S., Fakhoorian, T., Lam, E., 2015. Resurgence of duckweed research and applications: report from the 3rd international duckweed conference. Plant Mol. Biol. 89, 647–654.

Arimura, S., Yamamoto, J., Aida, G.P., Nakazono, M., Tsutsumi, N., 2004. Frequent fusion and fission of plant mitochondria with unequal nucleoid distribution. Proc. Natl. Acad. Sci. USA 101, 7805–7808.

Asano, S., Engel, B.D., Baumeister, W., 2016. In situ cryo-electron tomography: a post-reductionist approach to structural biology. J. Mol. Biol. 428, 332–343.

Basile, A., Sorbo, S., Cardi, M., Lentini, M., Castiglia, D., Cianciullo, P., Conte, B., Loppi, S., Esposito, S., 2015. Effects of heavy metals on ultrastructure and Hsp70 induction in *Lemna minor* L. exposed to water along the Sarno river, Italy. Ecotoxicol. Environ. Saf. 114, 93–101.

Choi, K.J., Kim, M.J., Je, A.R., Jun, S., Lee, C., Lee, E., Jo, M., Huh, Y.H., Kweon, H.S., 2014. Three-dimensional analysis of abnormal ultrastructural alteration in mitochondria of hippocampus of APP/PSEN1 transgenic mouse. J. Biosci. 39, 97–105.

Cogliati, S., Enriquez, J.A., Scorrano, L., 2016. Mitochondrial cristae: where beauty meets functionality. Trends Biochem. Sci. 41, 261–273.

Colombatti, F., Gonzalez, D.H., Welchen, E., 2014. Plant mitochondria under pathogen attack: a sigh of relief or a last breath? Mitochondrion 19 Pt B, 238-244.

Cowgill, U.M., Milazzo, D.P., 1989. The culturing and testing of two species of duckweed. Aquat. Toxicol. Hazard. Assess. 12, 379–391.

Curley, S.A., Palalon, F., Sanders, K.E., Koshkina, N.V., 2014. The effects of non-invasive radiofrequency treatment and hyperthermia on malignant and nonmalignant cells. Int. J. Environ. Res. Public Health 11, 9142–9153.

Dalla Vecchia, F., La Rocca, N., Moro, I., De Faveri, S., Andreoli, C., Rascio, N., 2005. Morphogenetic, ultrastructural and physiological damages suffered by submerged leaves of *Elodea canadensis* exposed to cadmium. Plant Sci. 168, 329–338.

Day, K.J., Staehelin, L.A., Glick, B.S., 2013. A three-stage model of golgi structure and function. Histochem. Cell Biol. 140, 239–249.

de Brito, O.M., Scorrano, L., 2010. An intimate liaison: spatial organization of the endoplasmic reticulum-mitochondria relationship. EMBO J. 29, 2715–2723.

Donohoe, B.S., Mogelsvang, S., Staehelin, L.A., 2006. Electron tomography of ER, golgi and related membrane systems. Methods 39, 154–162.

Donohoe, B.S., Kang, B.H., Gerl, M.J., Gergely, Z.R., McMichael, C.M., Bednarek, S.Y., Staehelin, L.A., 2013. Cis-golgi cisternal assembly and biosynthetic activation occur sequentially in plants and algae. Traffic 14, 551–567.

El Zawily, A.M., Schwarzlander, M., Finkemeier, I., Johnston, I.G., Benamar, A., Cao, Y., Gissot, C., Meyer, A.J., Wilson, K., Datla, R., Macherel, D., Jones, N.S., Logan, D.C., 2014. FRIENDLY regulates mitochondrial distribution, fusion, and quality control in *Arabidopsis*. Plant Physiol. 166, 808–828.

Faso, C., Chen, Y.N., Tamura, K., Held, M., Zemelis, S., Marti, L., Saravanan, R., Hummel, E., Kung, L., Miller, E., Hawes, C., Brandizzi, F., 2009. A missense mutation in the *Arabidopsis* COPII coat protein Sec24A induces the formation of clusters of the endoplasmic reticulum and golgi apparatus. Plant Cell 21, 3655–3671.

Fodorpataki, L., Barna, S., Holinka, B., 2015. Differential responses of components of the antioxidant defense system to high salinity stress in the lesser duckweed (*Lemna minor* L.). Studia Universitatis Babes-Bolyai. Biologia 60, 39–55.

Gallage, S., Gil, J., 2016. Mitochondrial dysfunction meets senescence. Trends Biochem. Sci. 41, 207–209.

Garlid, K.D., Paucek, P., 2003. Mitochondrial potassium transport: the K^+ cycle. Biochim. Biophys. Acta 1606, 23–41.

Hafiz Che-Othman, M., Harvey Millar, A., Taylor, N.L., 2017. Connecting salt stress signalling pathways with salinity induced changes in mitochondrial metabolic processes in C3 plants. Plant Cell Environ.

Hales, K.G., Fuller, M.T., 1997. Developmentally regulated mitochondrial fusion mediated by a conserved, novel, predicted GTPase. Cell 90, 121–129.

Hamann, S., Herrera-Perez, J.J., Zeuthen, T., Alvarez-Leefmans, F.J., 2010. Cotransport of water by the Na^+-K^+-$2Cl^-$ cotransporter NKCC1 in mammalian epithelial cells. J. Physiol. 588, 4089–4101.

Hao, G., Boyle, M., Zhou, L., Duan, Y., 2013. The intracellular citrus huanglongbing bacterium, ‘*Candidatus Liberibacter asiaticus*’ encodes two novel autotransporters. PLoS One 8, e68921.

Holzinger, A., Lütz, C., 2006. Algae and UV irradiation: effects on ultrastructure and related metabolic functions. Micron. 37, 190–207.

Ivanova, T.V., Maiorova, O.V., Orlova, Y.V., Kuznetsova, E.I., Khalilova, L.A., Myasoedov, N.A., Balnokin, Y.V., Tsydendambaev, V.D., 2016. Cell ultrastructure and fatty acid composition of lipids in vegetative organs of *Chenopodium album* L. under salt stress conditions. Russ. J. Plant Physiol. 63, 763–775.

Kaasik, A., Safiulina, D., Zharkovsky, A., Veksler, V., 2007. Regulation of mitochondrial matrix volume. Am. J. Physiol. Cell. Physiol. 292, C157–163.

Kang, B.H., Staehelin, L.A., 2008. ER-to-golgi transport by COPII vesicles in *Arabidopsis* involves a ribosome-excluding scaffold that is transferred with the vesicles to the golgi matrix. Protoplasm. 234, 51–64.

Kang, B.H., Nielsen, E., Preuss, M.L., Mastronarde, D., Staehelin, L.A., 2011. Electron tomography of RabA4b- and PI-4Kbeta1-labeled trans golgi network compartments in *Arabidopsis*. Traffic 12, 313–329.

Kintner, D.B., Luo, J., Gerdts, J., Ballard, A.J., Shull, G.E., Sun, D., 2007. Role of Na^+-K^+-Cl^- cotransport and Na^+/Ca^{2+} exchange in mitochondrial dysfunction in astrocytes following in vitro ischemia. Am. J. Physiol. Cell Physiol. 292, C1113–1122.

Krishnamurthy, K.V., 2000. The programme of cell death in plants and animals - A comparison. Curr. Sci. 79 1603–1603.

Krols, M., van Isterdael, G., Asselbergh, B., Kremer, A., Lippens, S., Timmerman, V., Janssens, S., 2016. Mitochondria-associated membranes as hubs for neurodegeneration. Acta Neuropathol. 131, 505–523.

Laskowski, M., Augustynek, B., Kulawiak, B., Koprowski, P., Bednarczyk, P., Jarmuszkiewicz, W., Szewczyk, A., 2016. What do we not know about mitochondrial potassium channels? Biochim. Biophys. Acta Bioenergetics 1857, 1247–1257.

Leliaert, F., Smith, D.R., Moreau, H., Herron, M.D., Verbruggen, H., Delwiche, C.F., De Clerck, O., 2012. Phylogeny and molecular evolution of the green algae. Crit. Rev. Plant Sci. 31, 1–46.

Liberton, M., Austin 2nd, J.R., Berg, R.H., Pakrasi, H.B., 2011. Insights into the complex 3-D architecture of thylakoid membranes in unicellular cyanobacterium *Cyanothece sp.* ATCC 51142. Plant Signal Behav. 6, 566–569.

Logan, A., Murphy, M.P., 2017. Using chemical biology to assess and modulate mitochondria: progress and challenges. Interface Focus 7.

Logan, D.C., 2006. Plant mitochondrial dynamics. Biochim. Biophys. Acta Mol. Cell Res. 1763, 430–441.

Logan, D.C., 2010. Mitochondrial fusion, division and positioning in plants. Biochem. Soc. Trans. 38, 789–795.

Logan, D.C., Scott, I., Tobin, A.K., 2003. The genetic control of plant mitochondrial morphology and dynamics. Plant J. 36, 500–509.

Lütz-Meindl, U., 2016. *Micrasterias* as a model system in plant cell biology. Front. Plant Sci. 7, 999.

Lütz-Meindl, U., Luckner, M., Andosch, A., Wanner, G., 2016. Structural stress responses and degradation of dictyosomes in algae analysed by TEM and FIB-SEM tomography. J. Microsc. 263, 129–141.

Lütz, C., Seidlitz, H.K., Meindl, U., 1997. Physiological and structural changes in the chloroplast of the green alga *Micrasterias denticulata* induced by UV-B simulation. Plant Ecol. 128, 54–64.

Lütz, C., Di Piazza, L., Fredersdorf, J., Bischof, K., 2016. The effect of ultraviolet radiation on cellular ultrastructure and photosystem II quantum yield of *Alaria esculenta* (L.) Greville from Spitsbergen (Norway). Polar Biol. 39, 1957–1966.

Martinez-Fabregas, J., Diaz-Moreno, I., Gonzalez-Arzola, K., Janocha, S., Navarro, J.A., Hervas, M., Bernhardt, R., Diaz-Quintana, A., De la Rosa, M.A., 2013. New *Arabidopsis thaliana* cytochrome c partners: a look into the elusive role of cytochrome c in programmed cell death in plants. Mol. Cell Proteomics 12, 3666–3676.

Matic, I., Strobbe, D., Di Guglielmo, F., Campanella, M., 2017. Molecular biology digest of cell mitophagy. Int. Rev. Cell Mol. Biol. 332, 233–258.

Meindl, U., 1993. *Micrasterias* cells as a model system for research on morphogenesis. Microbiol. Rev. 57, 415–433.

Meindl, U., Lancelle, S., Hepler, P.K., 1992. Vesicle production and fusion during lobe

formation in *Micrasterias* visualized by high-pressure freeze fixation. Protoplasma 170, 104–114.
Niewiadomska, E., Bilger, W., Gruca, M., Mulisch, M., Miszalski, Z., Krupinska, K., 2011. CAM-related changes in chloroplastic metabolism of *Mesembryanthemum crystallinum* L. Planta 233, 275–285.
Nunnari, J., Suomalainen, A., 2012. Mitochondria: in sickness and in health. Cell 148, 1145–1159.
Oukarroum, A., Bussotti, F., Goltsev, V., Kalaji, H.M., 2015. Correlation between reactive oxygen species production and photochemistry of photosystems I and II in *Lemna gibba* L. plants under salt stress. Environ. Exp. Bot. 109, 80–88.
Phillips, M.J., Voeltz, G.K., 2016. Structure and function of ER membrane contact sites with other organelles. Nat. Rev. Mol. Cell Biol. 17, 69–82.
Pizzo, P., Pozzan, T., 2007. Mitochondria-endoplasmic reticulum choreography: structure and signaling dynamics. Trends Cell Biol. 17, 511–517.
Porra, R.J., Thompson, W.A., Kriedemann, P.E., 1989. Determination of accurate extinction coefficients and simultaneous-equations for assaying chlorophyll-a and chlorophyll-b extracted with 4 different solvents - Verification of the concentration of chlorophyll standards by atomic-absorption spectroscopy. Biochim. Biophys. Acta 975, 384–394.
Pottosin, I., Shabala, S., 2016. Transport across chloroplast membranes: optimizing photosynthesis for adverse environmental conditions. Mol. Plant 9, 356–370.
Ruffoli, R., Bartalucci, A., Frati, A., Fornai, F., 2015. Ultrastructural studies of ALS mitochondria connect altered function and permeability with defects of mitophagy and mitochondriogenesis. Front. Cell Neurosci. 9.
Santos, C.L.V., Campos, A., Azevedo, H., Caldeira, G., 2001. In situ and in vitro senescence induced by KCl stress: nutritional imbalance, lipid peroxidation and antioxidant metabolism. J. Exp. Bot. 52, 351–360.
Schlösser, U.G., 1982. Sammlungen von Algenkulturen. Berichte der deutschen botanischen Gesellschaft 95, 181–276.
Scholz, D., Westermann, B., 2013. Mitochondrial fusion in *Chlamydomonas reinhardtii* zygotes. Eur. J. Cell Biol. 92, 80–86.
Schroeder-Reiter, E., Sanei, M., Houben, A., Wanner, G., 2012. Current SEM techniques for de- and re-construction of centromeres to determine 3D CENH3 distribution in barley mitotic chromosomes. J. Microsc. 246, 96–106.
Sesaki, H., Jensen, R.E., 1999. Division versus fusion: Dnm1p and Fzo1p antagonistically regulate mitochondrial shape. J. Cell Biol. 147, 699–706.
Sikorski, L., Piotrowicz-Cieslak, A.I., Adomas, B., 2013. Phytotoxicity of sodium chloride towards common duckweed (*Lemna minor* L.) and yellow lupin (*Lupinus luteus* L.). Arch. Environm. Prot. 39, 117–128.
Song, C., Murata, K., Suzaki, T., 2017. Intracellular symbiosis of algae with possible involvement of mitochondrial dynamics. Sci. Rep. 7, 1221.
Sree, K.S., Adelmann, K., Garcia, C., Lam, E., Appenroth, K.J., 2015. Natural variance in salt tolerance and induction of starch accumulation in duckweeds. Planta 241, 1395–1404.
Szklarczyk, R., Nooteboom, M., Osiewacz, H.D., 2014. Control of mitochondrial integrity in ageing and disease. Philos. T. R Soc. B 369.
Tiwari, B.S., Belenghi, B., Levine, A., 2002. Oxidative stress increased respiration and generation of reactive oxygen species, resulting in ATP depletion, opening of mitochondrial permeability transition, and programmed cell death. Plant Physiol. 128, 1271–1281.
Vannuvel, K., Renard, P., Raes, M., Arnould, T., 2013. Functional and morphological impact of ER stress on mitochondria. J. Cell Physiol. 228, 1802–1818.
Vartapetian, B.B., Andreeva, I.N., Generozova, I.P., Polyakova, L.I., Maslova, I.P., Dolgikh, Y.I., Stepanova, A.Y., 2003. Functional electron microscopy in studies of plant response and adaptation to anaerobic stress. Ann. Bot. 91, 155–172.
Vigani, G., Faoro, F., Ferretti, A.M., Cantele, F., Maffi, D., Marelli, M., Maver, M., Murgia, I., Zocchi, G., 2015. Three-dimensional reconstruction, by TEM tomography, of the ultrastructural modifications occurring in *Cucumis sativus* L. mitochondria under Fe deficiency. PLoS One 10, e0129141.
Virolainen, E., Blokhina, O., Fagerstedt, K., 2002. Ca^{2+}-induced high amplitude swelling and cytochrome c release from wheat (*Triticum aestivum* L.) mitochondria under anoxic stress. Ann. Bot. 90, 509–516.
Volland, S., Schaumloffel, D., Dobritzsch, D., Krauss, G.J., Lütz-Meindl, U., 2013. Identification of phytochelatins in the cadmium-stressed conjugating green alga *Micrasterias denticulata*. Chemosphere 91, 448–454.
Volland, S., Andosch, A., Milla, M., Stoger, B., Lütz, C., Lütz-Meindl, U., 2011. Intracellular metal compartmentalization in the green algal model system *Micrasterias denticulata* (Streptophyta) measured by transmission electron microscopy-coupled electron energy loss spectroscopy. J. Phycol. 47, 565–579.
Wanner, G., Schafer, T., Lütz-Meindl, U., 2013. 3-D analysis of dictyosomes and multivesicular bodies in the green alga *Micrasterias denticulata* by FIB/SEM tomography. J. Struct. Biol. 184, 203–211.
Weiss, D., Lütz, C., Lütz-Meindl, U., 1999. Photosynthesis and heat response of the green alga *Micrasterias denticulata* (Desmidiaceae). Zeitschrift für Naturforschung 54c, 508–516.
Wiley, C.D., Velarde, M.C., Lecot, P., Liu, S., Sarnoski, E.A., Freund, A., Shirakawa, K., Lim, H.W., Davis, S.S., Ramanathan, A., Gerencser, A.A., Verdin, E., Campisi, J., 2016. Mitochondrial dysfunction induces senescence with a distinct secretory phenotype. Cell Metab. 23, 303–314.
Wodniok, S., Brinkmann, H., Glockner, G., Heidel, A.J., Philippe, H., Melkonian, M., Becker, B., 2011. Origin of land plants: Do conjugating green algae hold the key? BMC Evol. Biol. 11.
Zhan, J., Li, W., He, H.Y., Li, C.Z., He, L.F., 2014. Mitochondrial alterations during Al-induced PCD in peanut root tips. Plant Physiol. Biochem. 75, 105–113.
Zheng, L.J., Peer, T., Seybold, V., Lütz-Meindl, U., 2012. Pb-induced ultrastructural alterations and subcellular localization of Pb in two species of *Lespedeza* by TEM-coupled electron energy loss spectroscopy. Environ. Exp. Bot. 77, 196–206.

10.4 Publication IV

Migrating Platelets Are Mechano-scavengers that Collect and Bundle Bacteria.

Florian Gaertner, Zerkah Ahmad, Gerhild Rosenberger, Shuxia Fan, Leo Nicolai, Benjamin Busch, Gökce Yavuz, **Manja Luckner**, Hellen Ishikawa-Ankerhold, Roman Hennel, Alexandre Benechet, Michael Lorenz, Sue Chandraratne, Irene Schubert, Sebastian Helmer, Bianca Striednig, Konstantin Stark, Marek Janko, Ralph T. Böttcher, Admar Verschoor, Catherine Leon, Christian Gachet, Thomas Gudermann, Michael Mederos y Schnitzler, Zachary Pincus, Matteo Iannacone, Rainer Haas, Gerhard Wanner, Kirsten Lauber, Michael Sixt, and Steffen Massberg (2017)

Cell, 2017 Nov 30;171(6):1368-1382.e23.
doi: 10.1016/j.cell.2017.11.001

Summary
Blood platelets are critical for hemostasis and thrombosis and play diverse roles during immune responses. Despite these versatile tasks in mammalian biology, their skills on a cellular level are deemed limited, mainly consisting in rolling, adhesion, and aggregate formation. Here, we identify an unappreciated asset of platelets and show that adherent platelets use adhesion receptors to mechanically probe the adhesive substrate in their local microenvironment. When actomyosin-dependent traction forces overcome substrate resistance, platelets migrate and pile up the adhesive substrate together with any bound particulate material. They use this ability to act as cellular scavengers, scanning the vascular surface for potential invaders and collecting deposited bacteria. Microbe collection by migrating platelets boosts the activity of professional phagocytes, exacerbating inflammatory tissue injury in sepsis. This assigns platelets a central role in innate immune responses and identifies them as potential targets to dampen inflammatory tissue damage in clinical scenarios of severe systemic infection.

Article

Cell

Migrating Platelets Are Mechano-scavengers that Collect and Bundle Bacteria

Graphical Abstract

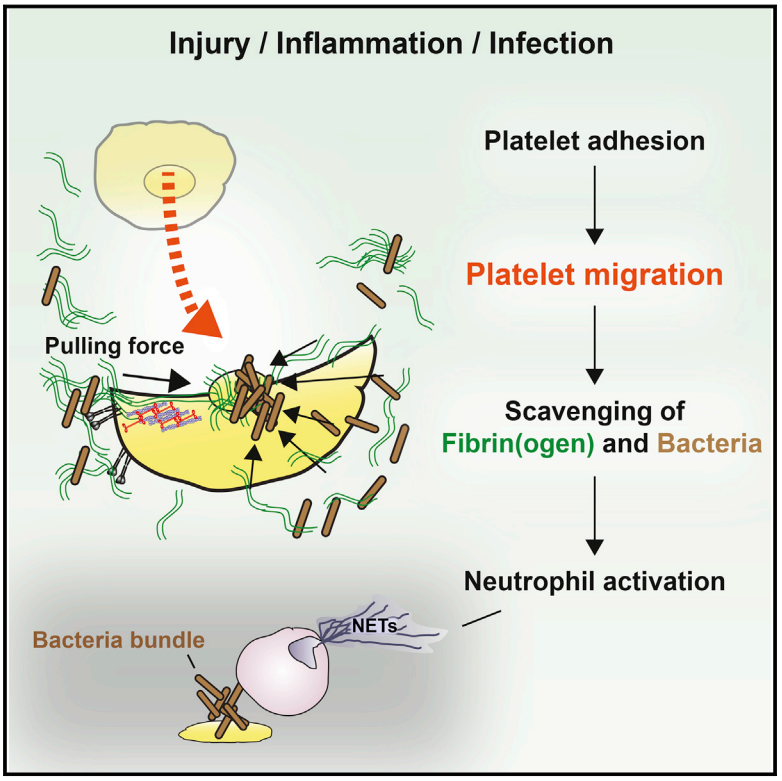

Highlights

- Platelets migrate at sites of vascular injury and inflammation
- Platelets use mechanical force to scavenge substrate-bound particulate material
- Migrating platelets use this ability to collect and bundle bacteria
- Collection and bundling of bacteria facilitates neutrophil activation in sepsis

Authors

Florian Gaertner, Zerkah Ahmad, Gerhild Rosenberger, ..., Kirsten Lauber, Michael Sixt, Steffen Massberg

Correspondence

f.gaertner@med.uni-muenchen.de (F.G.), steffen.massberg@med.uni-muenchen.de (S.M.)

In Brief

In addition to their role in thrombosis and hemostasis, platelets can also migrate to sites of infection to help trap bacteria and clear the vascular surface.

Gaertner et al., 2017, Cell *171*, 1368–1382
November 30, 2017
https://doi.org/10.1016/j.cell.2017.11.001

CellPress

Cell

Article

Migrating Platelets Are Mechano-scavengers that Collect and Bundle Bacteria

Florian Gaertner,[1,13,15,*] Zerkah Ahmad,[1] Gerhild Rosenberger,[1] Shuxia Fan,[1] Leo Nicolai,[1] Benjamin Busch,[3] Gökce Yavuz,[1] Manja Luckner,[2] Hellen Ishikawa-Ankerhold,[1] Roman Hennel,[5] Alexandre Benechet,[4] Michael Lorenz,[1] Sue Chandraratne,[1] Irene Schubert,[1] Sebastian Helmer,[1] Bianca Striednig,[1] Konstantin Stark,[1,13] Marek Janko,[6] Ralph T. Böttcher,[7,13] Admar Verschoor,[8] Catherine Leon,[9] Christian Gachet,[9] Thomas Gudermann,[10,13] Michael Mederos y Schnitzler,[10,13] Zachary Pincus,[11] Matteo Iannacone,[4] Rainer Haas,[3,14] Gerhard Wanner,[2] Kirsten Lauber,[5] Michael Sixt,[12] and Steffen Massberg[1,13,*]

[1]Medizinische Klinik und Poliklinik I, Ludwig-Maximilians-Universität, 81377 Munich, Germany
[2]Ultrastructural Research, Department Biology I, Biozentrum, Ludwig-Maximillians-Universität, 82152 Martinsried, Germany
[3]Chair of Medical Microbiology and Hospital Epidemiology, Max von Pettenkofer Institute, Faculty of Medicine, LMU, 80336 Munich, Germany
[4]Division of Immunology, Transplantation and Infectious Diseases, Experimental Imaging Center, IRCCS San Raffaele Scientific Institute, Vita-Salute San Raffaele University, 20132 Milan, Italy
[5]Department of Radiation Oncology, University Hospital, LMU Munich, 81377 Munich, Germany
[6]Department of Materials Science, Technische Universität, 64287 Darmstadt, Germany
[7]Max-Planck Institute of Biochemistry, 82152 Martinsried, Germany
[8]Institute for Systemic Inflammation Research, Universität zu Lübeck, 23538 Lübeck, Germany
[9]UMR S949, Inserm, Université de Strasbourgh, Etablissement Français du Sang-Alsace, 67065 Strasbourg, France
[10]Walther-Straub-Institut für Pharmakologie und Toxikologie, Ludwig-Maximilians-Universität, 80336 Munich, Germany
[11]Department of Developmental Biology and Department of Genetics, Washington University, St. Louis, St. Louis, MO 63110, USA
[12]Institute of Science and Technology (IST) Austria, 3400 Klosterneuburg, Austria
[13]Deutsches Zentrum für Herz-Kreislaufforschung (DZHK), 13347 Berlin, Germany
[14]German Center for Infection Research (DZIF), Munich Site, 80336 Munich, Germany
[15]Lead Contact
*Correspondence: f.gaertner@med.uni-muenchen.de (F.G.), steffen.massberg@med.uni-muenchen.de (S.M.)
https://doi.org/10.1016/j.cell.2017.11.001

SUMMARY

Blood platelets are critical for hemostasis and thrombosis and play diverse roles during immune responses. Despite these versatile tasks in mammalian biology, their skills on a cellular level are deemed limited, mainly consisting in rolling, adhesion, and aggregate formation. Here, we identify an unappreciated asset of platelets and show that adherent platelets use adhesion receptors to mechanically probe the adhesive substrate in their local microenvironment. When actomyosin-dependent traction forces overcome substrate resistance, platelets migrate and pile up the adhesive substrate together with any bound particulate material. They use this ability to act as cellular scavengers, scanning the vascular surface for potential invaders and collecting deposited bacteria. Microbe collection by migrating platelets boosts the activity of professional phagocytes, exacerbating inflammatory tissue injury in sepsis. This assigns platelets a central role in innate immune responses and identifies them as potential targets to dampen inflammatory tissue damage in clinical scenarios of severe systemic infection.

INTRODUCTION

Approximately 750 billion platelets circulate in human blood, constantly scanning the vasculature for damage of the endothelial surface. Upon encountering endothelial injury or inflammation, platelets are immediately recruited in a well-characterized cascade of events, including initial platelet tethering and rolling, followed by platelet activation, adhesion, and spreading, eventually leading to fibrin(ogen)-dependent aggregation and subsequent thrombus retraction (Jackson, 2011; Brass et al., 2005). Once recruited from the blood stream, platelets are considered sessile, attaching firmly and spreading on whatever subendothelial matrix or plasma protein they first encounter. This is consistent with the view that anucleate platelets, unlike most other blood cells, are unable to migrate.

Cell migration is critically involved in many physiological and pathological processes, including embryonic development, tumor metastasis, and immune responses. Cell migration on adhesive surfaces involves repetitive cycles of four major sequential steps: (1) extension of a protrusion (leading edge); (2) adhesion to a substrate; (3) contraction of the cytoplasm; and (4) release from contact sites (Lauffenburger and Horwitz, 1996). These cycles both require and maintain morphological polarization, often characterized by a steering leading edge lamellipodium and a trailing cell body. Quantitative morphometric analyses revealed that leading edge morphology mainly depends on actin polymerization coupled to cell matrix

adhesion assembly, whereas the trailing edge of a migrating cell is largely shaped by myosin-IIa-mediated contraction and adhesion disassembly (Barnhart et al., 2011; Yam et al., 2007). Both processes have to be tightly coordinated to generate traction force and forward movement; their balance determines overall cell shape and speed (Gupton and Waterman-Storer, 2006). Even though platelets are considered to be stationary cells once recruited from the circulation, they possess all molecular assets required for cell migration (Bettex-Galland and Luescher, 1959). Correspondingly, earlier studies proposed that platelets have the capacity to undergo locomotion (Lowenhaupt et al., 1973; Feng et al., 1998; Pitchford et al., 2008; Kraemer et al., 2010). However, the existence of active platelet migration has not been established on a cell biological level. In particular, whether autonomous platelet migration occurs in a physiological context *in vivo* and serves a biological function has not been demonstrated.

Whereas platelets are classically recognized for their major role in hemostasis and thrombosis (Jackson, 2011), they also evolved a large variety of non-hemostatic, mainly immunologic functions (Semple et al., 2011; Yeaman, 2014). Platelets are among the first cells recruited to sites of inflammation and infection and play an essential role in initiating intravascular immune responses (Wong et al., 2013). Accordingly, platelets coordinate the recruitment of a variety of immune cells and instruct them with their effector programs (Sreeramkumar et al., 2014; Guidotti et al., 2015). Platelets also have the ability to directly fight pathogens by releasing anti-microbial mediators and/or physically trapping and encapsulating invaders, thus preventing dissemination with the blood flow (Yeaman, 2014; Wong et al., 2013). Importantly, most of these platelet effector functions require the formation of tight platelet-pathogen interactions. To fully understand how platelets execute their immunologic functions, it is therefore essential to develop a better picture of how these interactions are regulated on a cell biological level. Here, we identify platelet migration as an autonomous platelet function and show that migration of single platelets enables them to collect and bundle bacteria and to boost neutrophil activation.

RESULTS

In Vivo Tracing of Single Platelets at Sites of Vascular Injury and Inflammation Reveals Unidentified Patterns of Motility

To study the fate of individual platelets at sites of vascular injury and inflammation, we generated a multicolor platelet reporter mouse (Figures S1A and S1B) by crossing *PF4-Cre* and *R26R-Confetti* mice, which permitted us to track individual platelets with unique single-cell contrast using intra-vital two-photon (2P-IVM) microscopy in a needle- and a laser-injury model (Figures 1A, 1B, and S1C). Using single-cell resolution analysis, we observed a fraction of adherent platelets in the periphery of the injury (Figure S1D), which remained motile and rearranged its position independent of the collective retraction within the thrombus, suggesting autonomous motility (Figures 1C and S1E; Movie S1). The mean velocity of these platelets was significantly lower and migration paths were less straight compared to platelet rolling and retraction (Figures 1C–1H and S1F). The directionality was independent of blood flow, and platelets were able to migrate against the blood stream, indicating an active process rather than passive translocation (Figure 1E). Platelet migration is independent of clot retraction (Auger and Watson, 2008; Ono et al., 2008), because tracks of migrating platelets were not directed toward the centroid of injury (Figures 1D and 1F). Platelet motility was also not influenced by migrating leukocytes (Sreeramkumar et al., 2014), because it was not affected when we depleted leukocytes prior to experiments (Figures S1G and S1H).

Spreading Platelets Are Motile and Have a Polarized Shape

To address the mechanistic basis of platelet migration, we mimicked the physiological microenvironment of vascular injury and inflammation *in vitro* by adding mouse or human-platelet-rich plasma (PRP) to coverslips precoated with subendothelial fibrillar collagen and plasma (Figure S2A). Platelets that encountered immobilized collagen fibers immediately started to spread and recruited additional platelets from the supernatant, forming immotile micro-aggregates. In contrast, spreading platelets that did not contact collagen fibers rearranged their morphology and became motile (Figure S2A). Initiation of motility was associated with a characteristic change in platelet morphology (Figure 2A). Spreading platelets showed a fried-egg-like shape with high circularity (aspect ratio $\approx$1). Platelets then polarized by protruding one side of the lamellipodium and simultaneously retracting the opposite side. During this process, the pseudonucleus moved from the center to the rear of the platelet. At the same time, the now-migrating platelet adopted a half moon shape reminiscent of highly motile fish keratocytes (Keren et al., 2008), resulting in an increase of the aspect ratio to approximately 2 (Figure 2B; Movie S2). We found this to be the characteristic phenotype of persistently migrating platelets (Figures 2B and S2B). Migration and shape changes were resistant to shearing flow at arterial velocities, and platelets were able to migrate against flow direction, further indicating a cell-autonomous, active process (Figure S2C).

In most eukaryotic cells, shape change and maintenance are active cellular processes requiring assembly and disassembly of actin filaments (Pollard and Cooper, 2009). Consequently, when we inhibited actin polymerization, platelets immediately stopped migrating followed by a loss of polarization and a decrease in the projected platelet area (Figures 2C, 2D, and S2D; Movie S2). Loss of platelet polarization mainly resulted from loss of leading edge lamellipodia, indicating that migration depends on branched lamellipodial actin networks. Indeed, inhibition of actin branching abrogated platelet migration (Figure 2E). Hence, platelet locomotion is an active process initiated by a cascade of morphological changes that depend on branched lamellipodial actin networks.

Migration on Plasma Proteins Requires Platelet Activation and Depends on $\alpha_{IIb}\beta_3$ Integrin Ligation and Substrate Adhesiveness

Interestingly, platelet migration was only observed when platelets were not in direct contact with collagen fibers (Figure S2A). Besides mediating platelet adhesion, collagen is known to

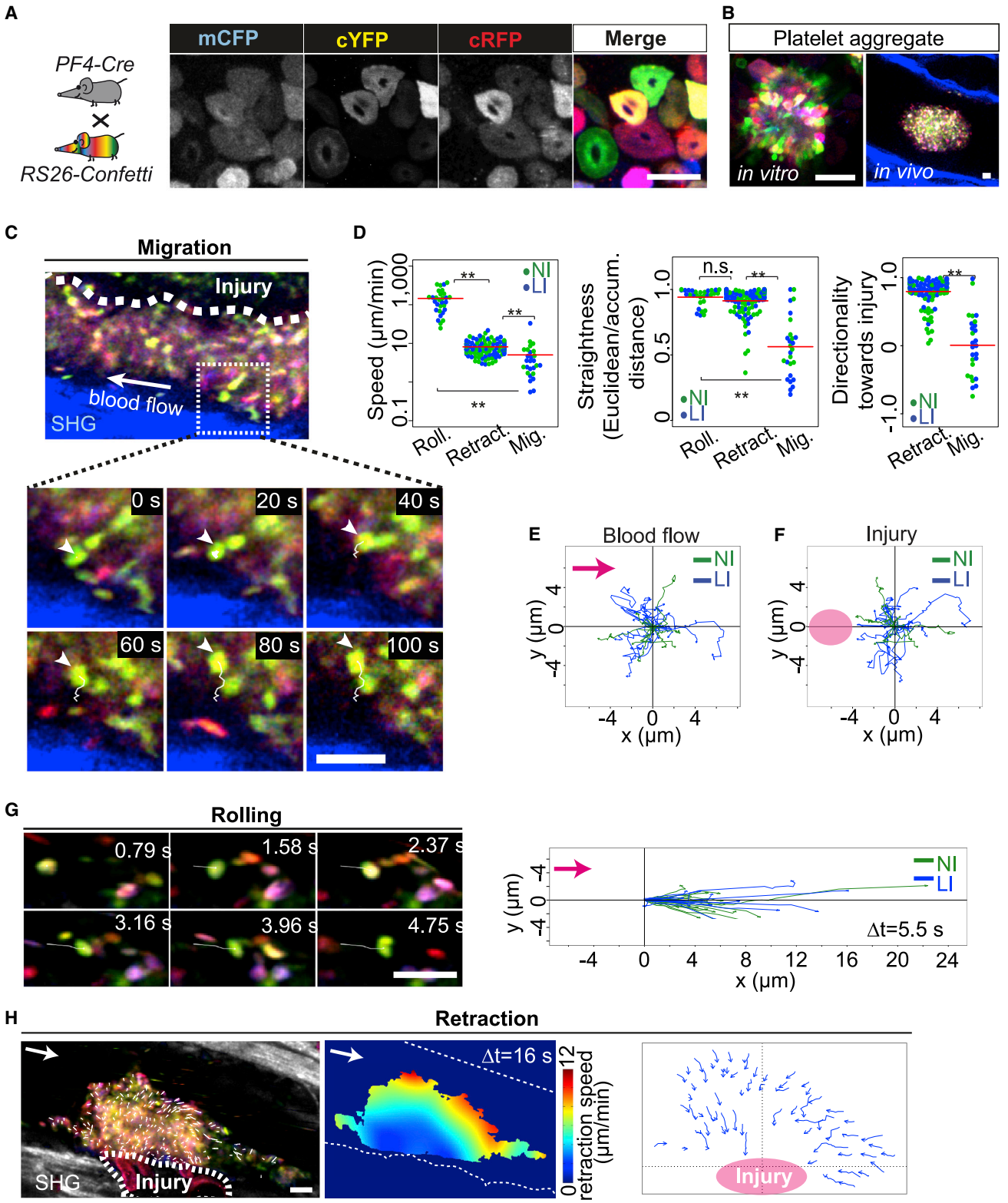

Figure 1. Platelets Migrate *In Vivo*

(A) Confocal sections of spreading *PF4-Cre/R26R-Confetti* platelets.

(B) Platelet aggregates formed *in vitro* (confocal microscopy) and *in vivo* (2P-IVM).

(legend continued on next page)

trigger the release of secondary platelet mediators. Hence, we hypothesized that migration of platelets requires paracrine priming through soluble mediators released by platelets interacting with collagen. To test this, we examined platelet migration on collagen-free coverslips in the presence of supernatant from either collagen-activated or resting platelets (see STAR Methods). Supernatant from collagen-activated platelets, but not from resting platelets, promoted platelet migration (Figure S3A). Pretreatment with indomethacin and apyrase to inhibit paracrine signaling via TXA2 and ADP, the two major agonists released by collagen-activated platelets, significantly attenuated the effect of platelet supernatant on migration (Figures S3A and S3B). On the other hand, ADP and U46619 induced platelet migration in the absence of supernatant from collagen-activated platelets (Figure 3A; Movie S3). This suggests that platelet activation by the soluble mediators ADP and TXA2 is both sufficient and required to trigger and maintain platelet migration.

Leukocytes use integrin-mediated adhesion when migrating over vascular surfaces (Nourshargh et al., 2010). Platelets also carry several integrin receptors, including αIIbβ3 integrin, which promotes platelet spreading upon activation by agonists, such as ADP and TXA2 (Nieswandt et al., 2002). We found activated αIIbβ3 integrin distributed in clusters along the lamellipodium during migration (Figure 3B). When we incubated migrating platelets in the presence of soluble linear H-Arg-Gly-Asp-Ser-OH (RGDS) peptides, which block RGD binding to β integrins, the number of spreading, lamellipodium-forming platelets was significantly reduced with a decrease in both mean platelet area and aspect ratio (Figures S3C and S3D). At the same time, platelet migration was virtually abolished (Figure S3D). The few platelets that still managed to migrate in the presence of RGDS did so only for short durations (Figure S3D). To address whether αIIbβ3 integrin directly mediates migration or rather supports migration indirectly by inducing platelet spreading, we allowed human platelets to first spread and migrate before adding C7E3-Fab, the β3 integrin-specific blocking Fab fragment. Upon C7E3-Fab exposure, platelets immediately stopped migrating while initially maintaining their spread morphology (Figures 3C and 3D). In contrast, specific inhibition of αvβ3 (LM609), the second platelet integrin comprising the β3 subunit, had no effect on either spreading or migration (Figure S3E). αIIb integrin-deficient mouse platelets and human platelets from a patient with Glanzmann thrombasthenia expressing defective αIIbβ3 integrin, adhered to immobilized plasma by developing filopodia rather than the usual lamellipodia. Consequently, these platelets neither showed spreading nor migration (Figures S3F and S3G). In contrast, platelets from mice lacking β1 integrins or GPIbα, the two other major platelet adhesion receptors, spread and migrated normally (Figure S3F). This identifies a critical and direct involvement of αIIbβ3 integrin in the process of platelet migration.

Because fibrinogen is the physiological ligand of αIIbβ3 integrin and was highly enriched in the 15-nm-thick layer of immobilized blood plasma (Figure S3H), we addressed whether fibrinogen is sufficient to promote platelet migration. Fibrinogen alone induced robust spreading, but not migration of platelets (Figure S3I), indicating the requirement for additional plasma components. Indeed, migration was reconstituted when we added serum to purified fibrinogen (Figure 3E). In terms of platelet morphology, the increase in migration was paralleled by an increase in platelet polarization (aspect ratio) and in membrane ruffles at the leading edge (measured by the normalized curvature; Figure 3F; Movie S3). By systematic analysis of serum fractions in terms of their impact on both platelet migration and morphology (Figure S3J), we identified albumin and calcium as the two additional serum components required for characteristic platelet shape change and migration on fibrinogen (Figures 3G, 3H, and S3K–S3Q). Whereas immobilized albumin likely lowers substrate adhesiveness of fibrinogen (Figure S3R; Park et al., 1991) and thus induces membrane ruffling (Borm et al., 2005; affecting normalized curvature; Figures S3L, S3O, and S3Q), the presence of free calcium is required for platelet polarization (affecting aspect ratio; Figure 3H; Movie S3). Consequently, at physiological conditions (in the presence of calcium-rich serum), migration and shape of activated platelets was ultimately determined by the adhesiveness of the substrate (Figures 3I and S3S–S3U).

Extracellular Calcium Mediates the Switch from Spreading to Migration by Myosin-IIa-Dependent Trailing Edge Formation

Intracellular calcium levels play a fundamental role in the control of platelet function (Varga-Szabo et al., 2009) and the polarization of migrating cells (Brundage et al., 1991). We therefore tested whether extracellular calcium supports migration by controlling intracellular calcium oscillations. In calcium-free buffer, spreading platelets remained sessile while showing only minimal intracellular calcium oscillations. In contrast, amplitudes increased 8-fold in the presence of extracellular calcium and platelets became polarized and started to migrate (Figure 4A; Movie S4). Depletion of intracellular calcium by BAPTA-AM significantly reduced platelet migration without affecting platelet spreading (Figure 4B; Movie S4). Elevation of intracellular calcium has been shown to control migration through activation of myosin IIa, generating contractile forces necessary for rear retraction and adhesion release (Lee et al., 1999). We found activated myosin IIa mainly localized at the trailing edge of migrating platelets (Figure 4C). The activity of myosin IIa depends on

(C) Needle injury of ear microcirculation. Arrowheads, migrating platelet; white lines, migration paths.
(D) Speed and straightness (Euclidean distance/accumulated distance) of rolling, retracting, and migrating platelets. Directionality = forward migration index (FMI). Each dot represents a single platelet. Rolling: n = 30 pooled from 4 mice; retraction: n = 115 pooled from 2 mice; migrating: n = 27 pooled from 11 mice. Red bars, mean; Kruskal-Wallis/Wilcox; **p < 0.01; LI, laser injury (blue); NI, needle injury (green); n.s., not significant; SHG, second harmonic generation.
(E and F) Directionality plots of migrating platelets (pink circle, injury, E; pink arrow, blood flow, F).
(G) Platelet rolling *in vivo* following needle injury (2P-IVM; pink arrow, blood flow).
(H) Clot retraction *in vivo* following laser injury (2P-IVM). Vector maps are overlaid (white arrows); heatmaps show retraction speed.
The scale bars represent 10 μm. See also Figure S1 and Movie S1.

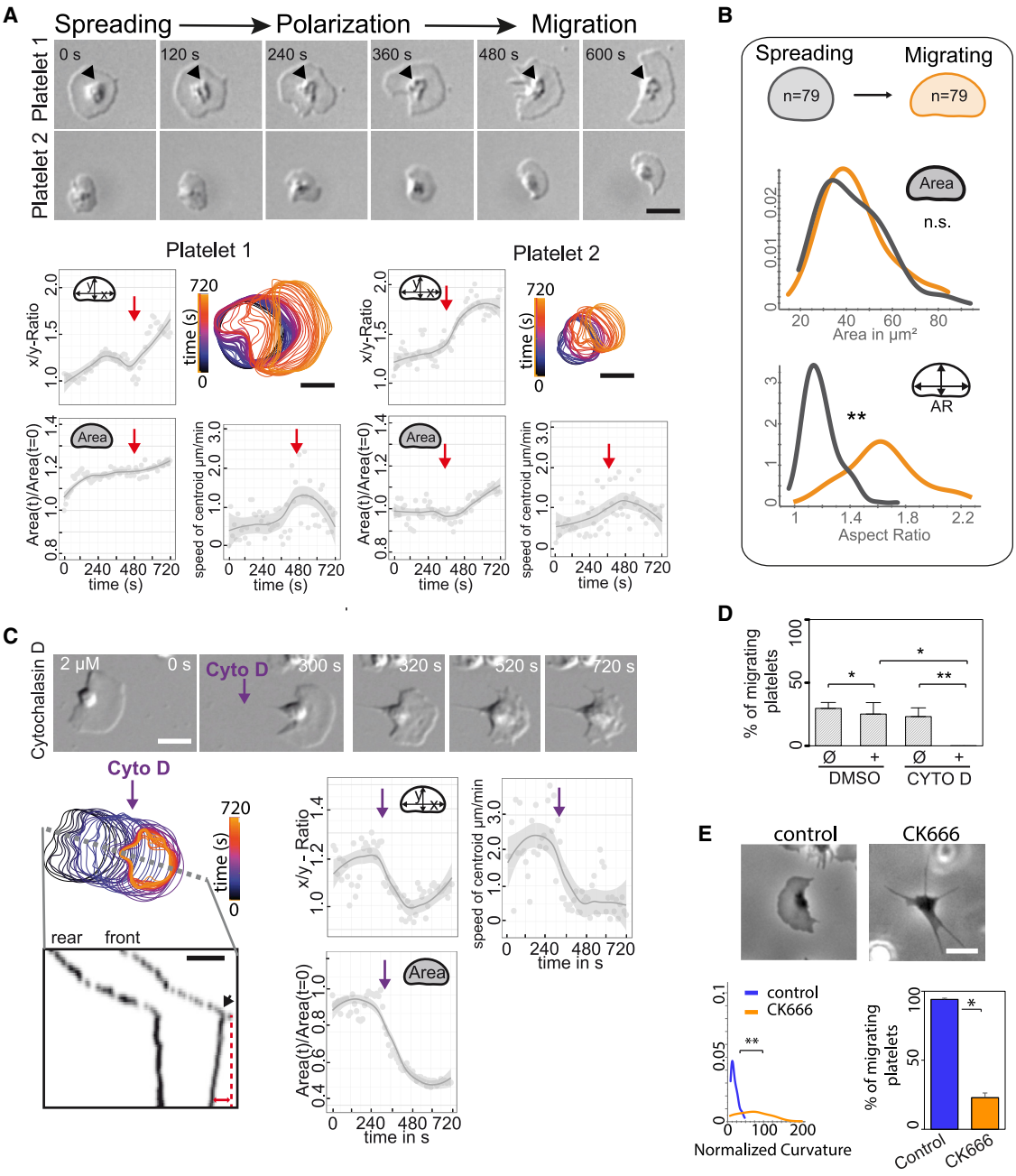

Figure 2. Platelets Actively Migrate by Adopting a Characteristic Shape

(A) (Upper) Initiation of migration. During polarization, the pseudonucleus (arrowheads) is relocated to the trailing edge. (Lower) Color-coded time sequence of platelet outlines is shown. Rear retraction is faster than front protrusion, resulting in an increased aspect ratio. Morphological parameters (aspect ratio [width/height] and area) and centroid velocity were continuously recorded.

(B) Polarized, migrating platelets and spreading, non-migrating platelets have a distinct shape. Smooth density histograms displaying area and aspect ratio (x axis) as a density function (y axis) are shown; Wilcox test; $^{**}p < 0.01$.

(C) Platelet migration depends on actin polymerization. (Upper) Differential interference contrast (DIC) time series before and after cytochalasin D treatment. (Lower left) Color-coded platelet outlines (time) and corresponding kymograph show immediate stop of platelet migration (arrow) and subsequent shrinkage of the lamellipodium. (Lower right) Tracing of aspect ratio, area, and centroid velocity over time is shown.

(D) Quantification of platelet migration before and after CytoD treatment. n = 5 experiments; mean ± SEM; paired t test. The scale bars represent 5 µm.

(E) Phase contrast micrographs from platelets treated with CK666 (50 µM) and control (CK689; 50 µM). Membrane roughness measured by the normalized curvature of platelet contours is shown (CK666: n = 67; CK689: n = 53; smooth density histograms displaying normalized curvature [x axis] as a density function [y axis]; percentage of migrating platelets was quantified; n = 5 experiments; mean ± SEM); Student's t test; $^{*}p < 0.05$; $^{**}p < 0.01$.

See also Figure S2 and Movie S2.

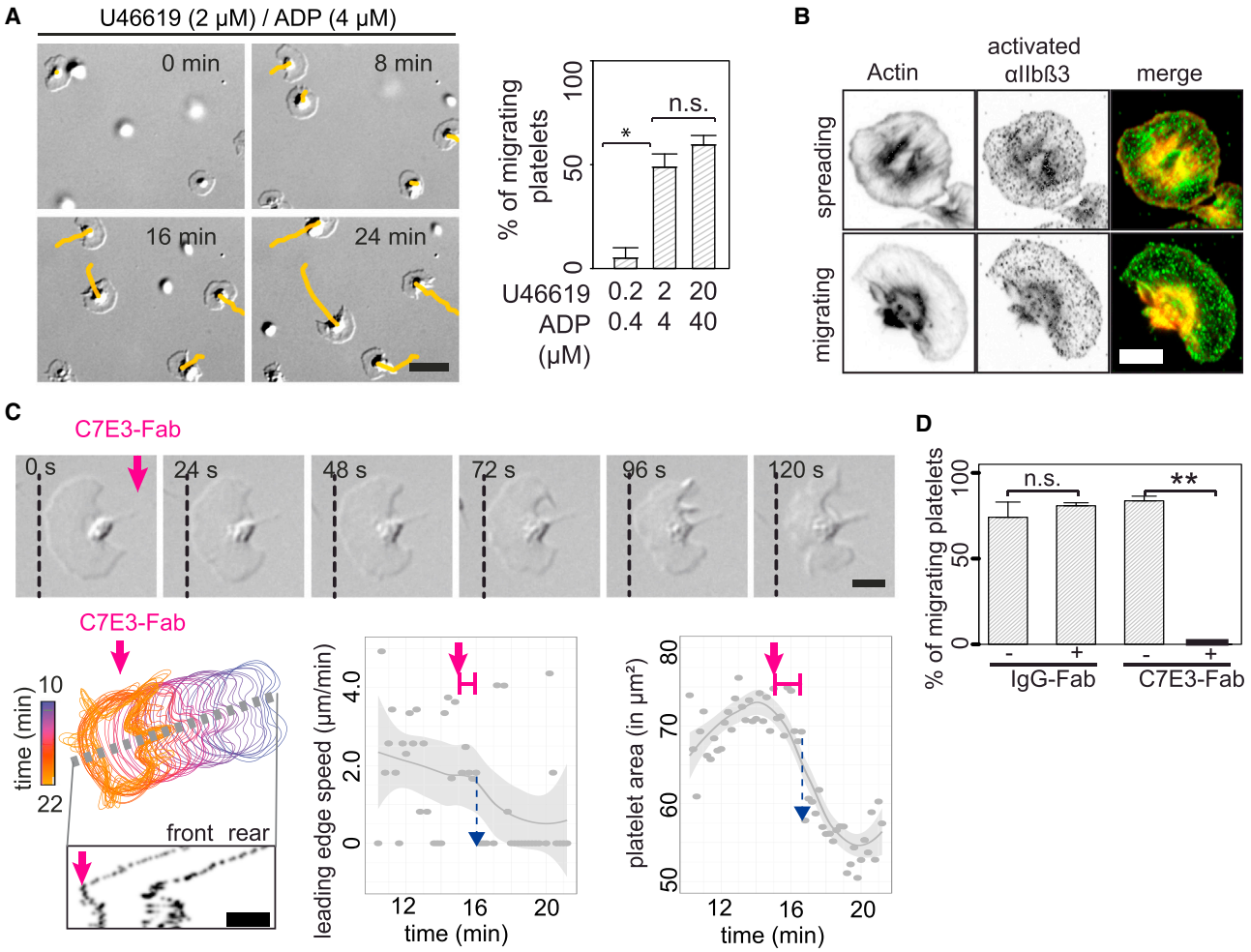

(legend on next page)

myosin light chain phosphorylation (pMLC) and is regulated by calcium-dependent myosin light chain kinase (MLCK) (Yang and Huang, 2005). Platelet pMLC levels were significantly higher in the presence of calcium compared to a calcium-free microenvironment or after intracellular calcium depletion (Figure 4D). Inhibition of myosin-IIa-mediated contraction with blebbistatin had no impact on platelet spreading but dose dependently prevented migration (Figure 4E; Movie S5). Population-based morphology analysis revealed significantly increased aspect ratios of blebbistatin-treated platelets, suggesting that platelets still polarize (Figure 4F). Correspondingly, single-cell analysis showed that blebbistatin-treated platelets become elongated but are unable to move their trailing edge (Figures 4G and S4A). Platelets from *PF4-Cre+/MYH9*$^{fl/fl}$ mice that have a severe reduction in myosin expression in the megakaryocytic lineage (Léon et al., 2007) revealed a similar migration defect both *in vitro* and *in vivo* (Figures 4H–4J and S4B; Movie S5). Thus, myosin-IIa-dependent platelet contractility generates traction forces that overcome the adhesive forces of the substratum, eventually leading to autonomous locomotion (Figure S4C).

Migrating Platelets Act as Mechano-scavengers

We were interested whether the mechanical forces generated by myosin contractions contribute to adhesion release by disruption of cytoskeletal-to-integrin or of integrin-to-substrate bonds or rather by removal of the integrin-bound substrate. Immunofluorescent tracking of actin and αIIbβ3 integrin revealed that only a minor fraction of cytoskeleton components and/or integrins are ripped off the rear of migrating platelets (Figure S5A). In contrast, migrating platelets efficiently removed fibrinogen from the surface, a process depending on αIIbβ3 integrin ligation and actomyosin contraction (Figures 5A–5E, S5B, and S5C; Movie S6). Covalently bound fibrinogen remained attached to the surface, confirming that removal is mechanical and does not involve proteolysis (Figure 5F). Once removed, fibrinogen is transported toward the center (pseudonucleus) of migrating platelets remaining on the platelet surface, mainly within invaginations of the open canalicular system (OCS) (Figures 5G and S5D; Movie S6). Because fibrinogen forms insoluble fibrin polymers at sites of vascular injury and inflammation *in vivo* (Prasad et al., 2015), we performed platelet migration assays in the presence of immobilized fibrin strands. Platelets efficiently migrated on and removed and accumulated large fibrin fibers, indicating that both migration and migration-dependent ligand removal is not restricted to soluble fibrinogen molecules (Figures S5E–S5G; Movie S6). Indeed, migrating platelets even collected larger-sized latex particles bound to the fibrin(ogen) matrix (Figures 5H and 5I; Movie S6). Thus, migrating platelets act as mechanosensors that probe the mechanical resistance of their local microenvironment. The high contraction and adhesive forces generated by individual platelets (Lam et al., 2011) couple migration to efficient mechanical scavenging of bound objects (Figures 5H–5J).

Migrating Platelets Bind and Collect Bacteria

Platelets are among the first cells recruited to sites of tissue injury. Besides their crucial role in forming blood clots and preventing severe bleeding, platelet activation within injured and inflamed tissues also provides a first line of defense against potential pathogenic invaders (Yeaman, 2014). We thus hypothesized that the scavenging function of single migrating platelets may boost the ability of platelets to fight infection. Because platelets possess bactericidal and phagocytic-like activities (Yeaman, 2014; White, 2005), we examined their ability to migrate and collect fibrin-bound bacteria using live-cell microscopy. Similar to the latex particles, different species of bacteria (*Escherichia coli*, *Staphylococcus aureus*, and *Listeria monocytogenes*) were readily collected and accumulated at the pseudonucleus together with fibrin(ogen)-forming bundles of more than 3 bacteria (>20 μm^2; Figures 6A–6C and S6A–S6C; Movie S7). Platelet-bound bacterial bundles were more resistant to shear stress, accomplishing efficient bacterial trapping (Figure 6D). MYH9-deficient platelets were significantly less effective in collecting, bundling, and containing fibrin-bound bacteria due to their inability to migrate (Figures 6D, 6E, S6C, and S6D).

Next, we infected mice systemically with *Escherichia coli* (*E. coli*) to address whether platelets also form bacterial bundles *in vivo*. *E. coli* sepsis causes fibrin formation in various organs, including the liver (Massberg et al., 2010) and triggers the recruitment of bacteria and individual platelets to the hepatic microcirculation (McDonald et al., 2012; Figures S7A–S7C). Recruited platelets remained motile *in vivo* and migrated several microns independent of leukocytes (Figures 7A, 7B, S7D, and S7E; Movie S7). Autonomously migrating platelets were significantly slower than platelets bound to leukocytes, reaching migration speeds comparable to those found *in vitro* and at sites of vascular injuries

Figure 3. Platelet Migration on Plasma Proteins Requires Platelet Activation and Depends on $\alpha_{IIb}\beta_3$ Integrin Ligation and Substrate Adhesiveness

(A) DIC time series of migrating platelets in the presence of ADP and TXA2 (left); n = 4 experiments; error bars, SEM; ANOVA/Tukey honestly significant difference (HSD).

(B) Confocal sections of spreading and migrating human platelets. Actin (phalloidin, red) and activated αIIbβ3 (PAC1, green).

(C) (Upper) DIC time series. After treatment with C7E3-Fab (15 min), platelets immediately stopped migrating (black dashed line) and only started to shrink with a lag time of ≈60 s. (Lower) Platelet outline is shown (color code: time). The kymograph highlights the immediate stop of migration after treatment (pink arrow), whereas leading edge shrinkage followed with a temporal delay. Measurements of leading edge speed and platelet area further revealed this temporal delay of lamellipodium shrinkage as indicated by the width of the pink bar.

(D) Percentage of migration before and after treatment; n = 3 experiments; mean ± SEM; paired t test.

(E and G) Migration quantified for indicated treatments (in the presence of 150 μg/mL fibrinogen). Platelets were pooled from n = 4 (E) or n = 3 (G) experiments; mean ± SEM; ANOVA/Tukey HSD.

(F and H) Platelet shapes and density histograms are shown for different concentrations of serum (F) and calcium (H). Kruskal-Wallis/Wilcox.

(I) Migration quantified for indicated fibrinogen concentrations (in the presence of 1,500 μg/mL serum); n = 4 experiments; mean ± SEM; ANOVA/Tukey HSD.

*$p < 0.05$; **$p < 0.01$. See also Figure S3 and Movie S3.

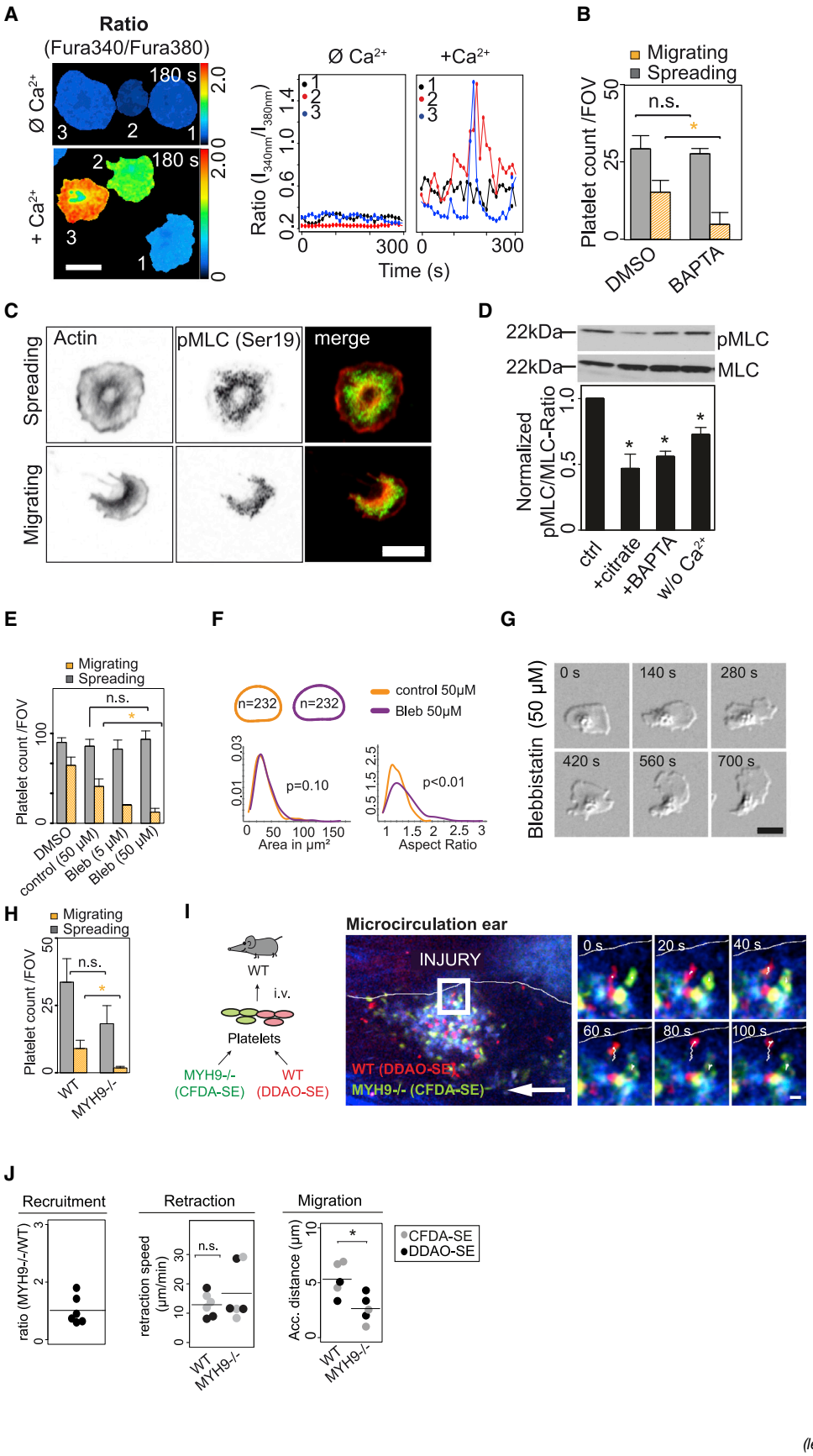

(legend on next page)

in vivo (Figures 1F, 2, and 7B). Importantly, motile platelets interacted with *E. coli* bound to the luminal aspect of sinusoids, resembling the collecting behavior observed *in vitro* (Figures 7A and 7C; Movie S7). Next, we analyzed platelet-bacteria interactions in *PF4-Cre+/MYH9$^{fl/fl}$* mice showing impaired platelet migration. Four hours after infection, platelet recruitment to the liver was not significantly altered in *PF4-Cre+/MYH9$^{fl/fl}$* compared to control mice. Hence, the previously reported mild reduction in the capacity to activate integrins in *MYH9*-deficient mice has no impact on platelet adhesion to infected liver sinusoids (Léon et al., 2007; Figures 7D and S7F). Correspondingly, hepatic platelet adhesion was also unaffected by loss of integrin αIIb (Figure S7G). Similar amounts of bacteria were recruited to the liver in wild-type, *PF4-Cre+/MYH9$^{fl/fl}$*, or *αIIb*-deficient mice and bound to platelets with or without defect in migration (Figures 7D, S6D, and S7G). However, the fraction of large *E. coli* bundles (>20 μm^2) associated with platelets was significantly reduced in mice with defective platelet migration (*PF4-Cre+/MYH9$^{fl/fl}$* and *αIIb*-null mice) compared to controls (Figures 7D, S7F, and S7G). We excluded reduced blood platelet counts as a reason for defective platelet bundling in *PF4-Cre+/MYH9$^{fl/fl}$* mice (Léon et al., 2007; Figure S7I). Together, this shows that migrating platelets also collect and bundle bacteria *in vivo*. This is not restricted to *E. coli*, because we obtained similar results with a clinically important methicillin-resistant *Staphylococcus aureus* (MRSA) isolate (USA 300; Figures 7E, S7H, and S7I).

We then evaluated whether bundling by migrating platelets facilitates bacterial killing. Whereas activated platelets can directly kill MRSA in the absence of immune cells, their bactericidal activity depends on platelet secretion (Ali et al., 2017), but not platelet migration or the formation of bundles (Figure S7J). Rather than promoting direct killing, microbe collection by migrating platelets boosts the activity of professional phagocytes. By time-lapse microscopy, we observed *in vitro* that migrating polymorphonuclear neutrophils (PMNs) slow down, arrest (Figure S7K; Movie S7), and engage in phagocytosis (Figure S7L; Movie S7) once they encounter bacterial bundles formed by migrating platelets. During this process, PMNs reveal increased intracellular calcium oscillations (Figure S7M; Movie S7). They also release neutrophil extracellular traps (NETs) (Figure S7N), reflecting PMN activation at sites of platelet-bacteria bundles. Inhibition of platelet migration and bacterial bundling by genetically removing MYH9 diminishes the formation of NETs (Figure S7N). We further show *in vivo* that bundling of bacteria by migrating platelets also promotes activation of PMNs upon infection with MRSA. PMNs interact with platelet-bacteria bundles, form multicellular Ly6Gpve aggregates, and release NETs in hepatic microvessels of MRSA-infected mice (Figure S7O). Aggregate formation and NETosis are significantly reduced in *PF4-Cre+/MYH9$^{fl/fl}$* mice, indicating that collection and bundling of bacteria by migrating platelets supports these processes (Figures 7F–7H, S7P, and S7Q). MRSA survives intracellularly upon phagocytosis and triggers neutrophil-induced cytolysis, leading to a dramatic and often deadly increase in neutrophil-driven inflammation (Greenlee-Wacker et al., 2015). Consistent with the hepatotoxic effect of NETs (Kolaczkowska et al., 2015), abrogation of platelet migration not only reduced neutrophil activation and NETosis but also attenuated liver damage, whereas clearance of MRSA from the liver was not affected (Figures 7I, 7J, and S7R). Consequently, *PF4-Cre+/MYH9$^{fl/fl}$* mice yielding defective platelet migration and collection of bacteria derived protection in the early course of lethal MRSA sepsis (Figures 7K and S7S).

DISCUSSION

Previous studies reported that platelets recruited to vascular injuries (Lowenhaupt et al., 1973) or sites of inflammation can change their position (Pitchford et al., 2008; Kraemer et al., 2010). However, direct *in vivo* evidence of autonomous platelet locomotion was lacking and fundamental questions regarding the underlying mechanisms remained unaddressed. This has resulted in a general skepticism as to whether true autonomous migration of platelets exists in the mammalian organism.

Non-mammalian vertebrates, including birds, have nucleated thrombocytes (Belamarich et al., 1966). However, this property has not been conserved during the evolution of specialized mammalian platelets, which are released as cytoplasmic fragments from megakaryocytes and no longer possess a nucleus. Consequently, the ability of mammalian platelets to migrate is linked to the fundamental question of whether cells can migrate despite the absence of a nucleus. The nucleus is important for *de novo* transcription, and its removal has originally been associated with impaired motility in amoebae (Clark, 1942). Meanwhile, however, experimentally derived enucleated cytoplasmic fragments of protozoan and metazoan cells have been shown to migrate without considerable impairment, indicating that the essential machinery driving locomotion is positioned within the

Figure 4. Extracellular Calcium Mediates the Switch from Spreading to Migration by Myosin-IIa-Dependent Trailing Edge Formation

(A) Fura ratios (340 nm/380 nm) of platelets in the presence (200 μM) or absence of extracellular calcium.

(B) Spreading and migration of BAPTA-AM (10 μM) pre-treated platelets; n = 3 experiments; mean ± SEM; ANOVA/Tukey HSD.

(C) Immunofluorescence of phalloidin-rhodamine (red) and anti-pMLC (green). Migrating, pMLC relocates to the trailing edge; spreading, concentric distribution of actin and pMLC. The scale bar represents 5 μm.

(D) Reduced pMLC (Ser19) after depletion of intracellular calcium or removal from the extracellular space; n = 3 experiments; mean ± SEM; Student's t test.

(E) Spreading and migration after Blebbistatin treatment; control, inactive enantiomer (50 μM); n = 5 experiments; mean ± SEM; ANOVA/Tukey HSD.

(F) Shape analysis. Data are pooled from n = 5 experiments; Kruskal-Wallis/Wilcox.

(G) DIC time series of a Blebbistatin-treated platelet. Note the functional dissociation of front and back resulting in platelet elongation.

(H) Spreading and migration of wild-type (WT) (*PF4-Cre−/MYH9$^{fl/fl}$*) and MYH9−/− (*PF4-Cre+/MYH9$^{fl/fl}$*) platelets; n = 5 mice; mean ± SEM; ANOVA/Tukey HSD.

(I) 2P-IVM of WT and MYH9−/− platelets competitively transfused into *PF4-Cre/R26R-Confetti* mice. White arrows, blood flow; white lines, migration paths.

(J) WT and MYH9−/− platelets were equally recruited to injuries (MYH9/WT ratio). Clot retraction was unaffected and independent of the staining procedure. Mean accumulated distances of motile platelets are shown; migration was independent of platelet labeling (see Figure S4B); n = 5 mice; bar, mean; paired t test. *p < 0.05; **p < 0.01; scale bars, 5 μm. Also see Figure S4 and Movies S4 and S5.

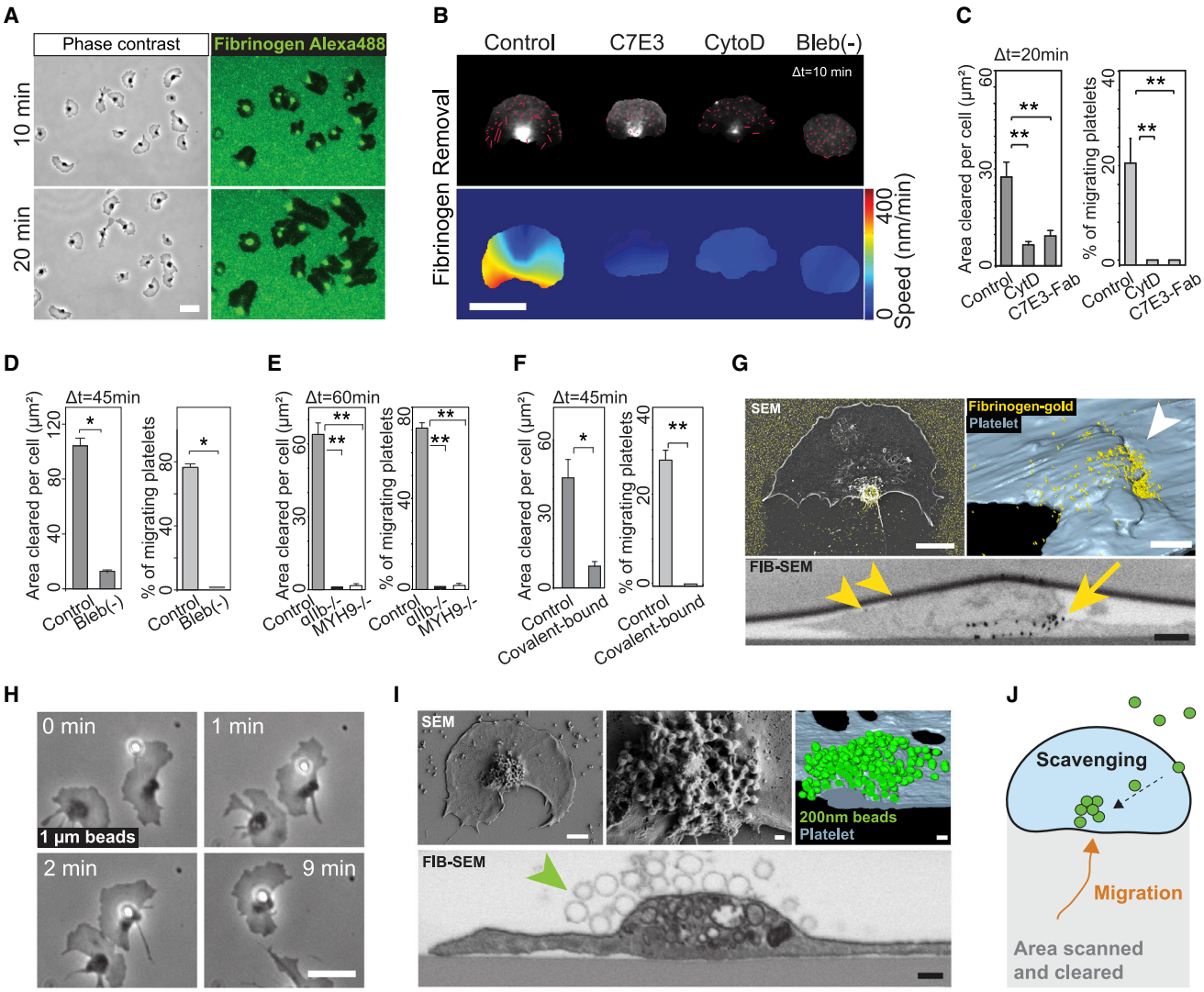

Figure 5. Migrating Platelets Probe and Clear Their Microenvironment

(A) Phase contrast/epifluorescence time series showing removal of fibrinogen (Alexa 488 labeled) during migration.

(B) Centripetal fibrinogen removal mainly occurs at the rear and is blocked by inhibition of αIIbβ3 integrins (C7E3; 10 μg/mL; n = 5), actin (cytochalasin D; 2 μM; n = 5), and myosin IIa (Bleb(−); 50 μM; n = 3).

(C–F) Percentage of migrating platelets and area of fibrinogen removed per platelet were quantified. (C and D) Inhibitor-treated human platelets are shown (n = 3–5). (E) *PF4-Cre+/MYH9*$^{fl/fl}$, *αIIb*−/−, and control (*bl6*) mice are shown (n = 3 mice). (F) Human platelets migrating on covalently bound fibrinogen are shown (n = 4 experiments); Δt, recording time; mean ± SEM; ANOVA/Tukey HSD/Student's t test. *p < 0.05; **p < 0.01; scale bar, 5 μm.

(G) (Upper left) SEM of platelets migrating on 10-nm-gold-labeled fibrinogen; scale bar, 2 μm. (Upper right) 3D reconstruction of a platelet-pseudonucleus (arrowhead) is shown; scale bar, 500 nm. (Lower) Longitudinal section (FIB-SEM) of the same platelet is shown. Gold-labeled fibrinogen (arrowheads) is localized on the platelet surface and within the open canalicular system (OCS) (arrow); scale bar, 100 nm.

(H) Platelet-scavenging fibrinogen-bound beads (1 μm); scale bar, 5 μm.

(I) (Upper left) Migrating platelets collect fibrinogen-trapped latex beads (200 nm; SEM); scale bars, 2 μm/200 nm. (Upper right and lower panel) FIB-SEM is shown: beads accumulate on the platelet surface (arrowhead); scale bar, 200 nm.

(J) Migrating platelets scavenge their microenvironment.

Also see Figure S5 and Movie S6.

cytoplasm and does not necessarily depend on a nucleus (Euteneuer and Schliwa, 1984). Therefore, in theory, the platelet as a terminally differentiated anucleate cell fragment containing all contractile elements necessary for locomotion should also be able to migrate (Bettex-Galland and Luescher, 1959). Indeed, we show here persistent migration of single platelets *in vitro* and *in vivo*, providing direct evidence for anucleate cell migration under physiological conditions in mammals, a phenomenon of potential relevance beyond platelet biology (Yount et al., 2007; Yipp et al., 2012). Previous studies showed that platelet motility

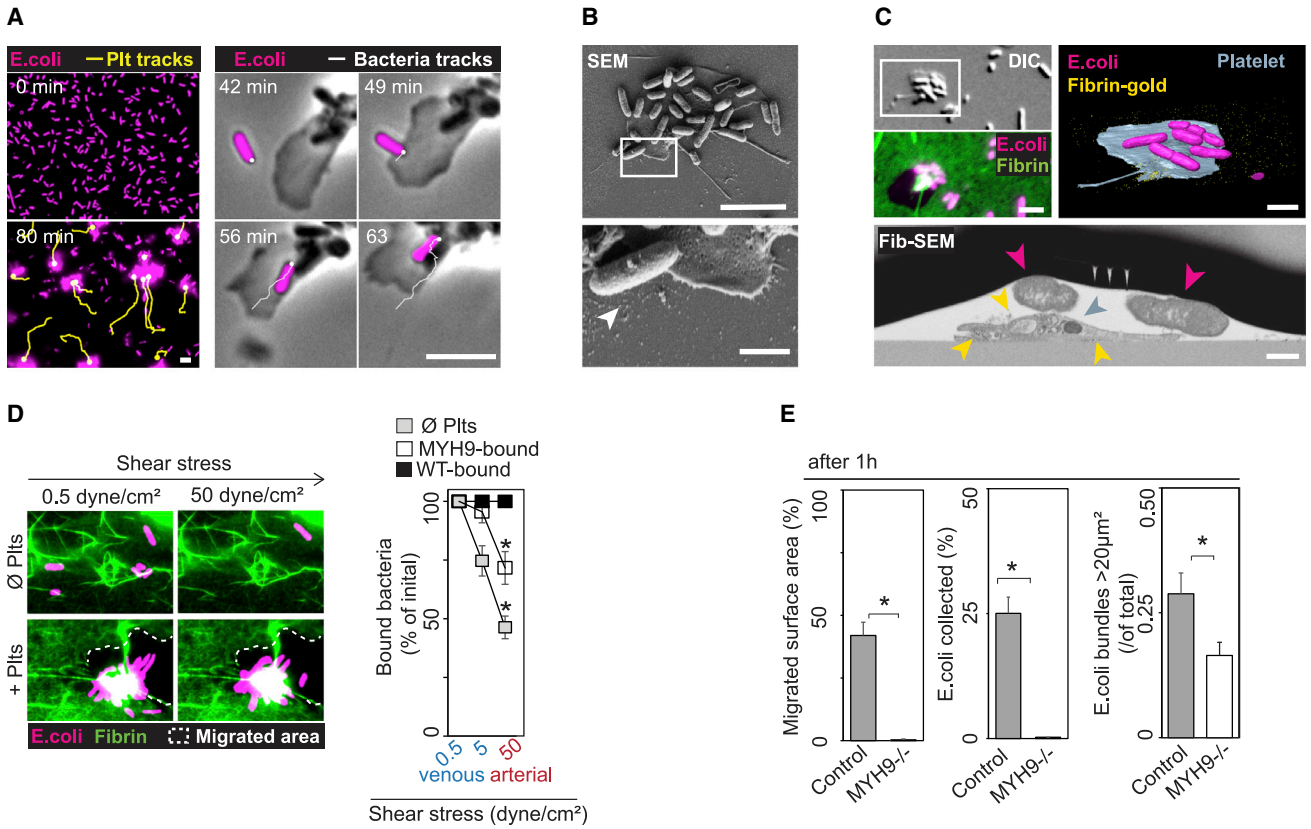

Figure 6. Migrating Platelets Collect and Bundle Bacteria

(A) Epifluorescence micrographs of *E. coli* (tdTomato) before (0 min) and after (80 min) platelet migration (yellow tracks). (Right) Platelet collecting *E. coli* is shown (highlighted in magenta). The scale bar represents 5 μm.

(B) SEM of *E. coli* accumulating on the platelet surface. (Lower) Fibrin-trapped bacteria (arrowhead) collected by a migrating platelet at higher magnification are shown. The scale bars represent 5 μm/1 μm.

(C) (Upper left) DIC and epifluorescence of a platelet collecting fibrin-trapped *E. coli* (magenta, tdTomato; green, fibrin-Alexa-488-10 nm-gold); scale bar, 5 μm. (Right) 3D-rendered FIB-SEM stack of the same platelet is shown; scale bar, 1 μm. (Lower) Longitudinal FIB-SEM section is shown. *E. coli* (pink arrowheads) accumulate at the platelet (blue arrowhead) surface; gold-labeled fibrin (yellow arrowheads) is localized on the platelet surface and within the OCS; scale bar, 500 nm.

(D) Bacterial bundles are protected from shear stress (venous: 0.5 and 5 dyne/cm^2; arterial: 50 dyne/cm^2; for details, see STAR Methods); n = 6 experiments; mean ± SEM; Kruskal-Wallis/Wilcox; *p < 0.05; scale bar, 5 μm.

(E) Quantification of platelet migration, fraction of *E. coli* collected, and fraction of *E. coli* bundles >20 μm^2. n = 3 mice; mean ± SEM; Wilcox test; *p < 0.05. Also see Figure S6 and Movie S7.

requires intracellular calcium as well as actin polymerization, suggesting an active process (Schmidt et al., 2011, 2012; Kraemer et al., 2010). However, the biomechanical principles underlying platelet migration still remain elusive. Initiation of forward locomotion on 2D surfaces requires the transduction of myosin-generated forces at adhesive sites, thus facilitating their release (Lauffenburger and Horwitz, 1996). Consequently, conditions where traction forces are dominated by adhesive forces render platelets immobile. As such, most studies analyzing platelet spreading and adhesion were performed on highly adhesive substrates, likely impeding migration. The correlation of adhesiveness and migration has systematically been studied in different cell types (Palecek et al., 1997; Gupton and Waterman-Storer, 2006), including cytoplasmic fragments (Grębecka et al., 1997), but not in platelets. Here, we systematically analyzed platelet shape change and locomotion on immobilized blood plasma components. Our study shows that the balanced co-adsorption of pro-adhesive fibrinogen and anti-adhesive albumin (Park et al., 1991) determines the ability of the substratum to initiate and maintain polarization and integrin-dependent locomotion of spread platelets.

We identified platelet migration as an active cell-autonomous and physiological process at sites of vascular injury and thrombosis *in vivo* that is resistant to arterial shear forces. Whereas platelet migration as a slow process is unlikely to contribute to rapid thrombus formation, our data suggest a role during thrombus reorganization and consolidation where the ability to migrate may allow platelets to reposition within the lesion while at the same time reorganizing the fibrin(ogen) network (Lam et al., 2011). Our data illustrate that platelet aggregates are no longer to be considered static but rather represent dynamic structures constantly reorganizing due to platelet motility.

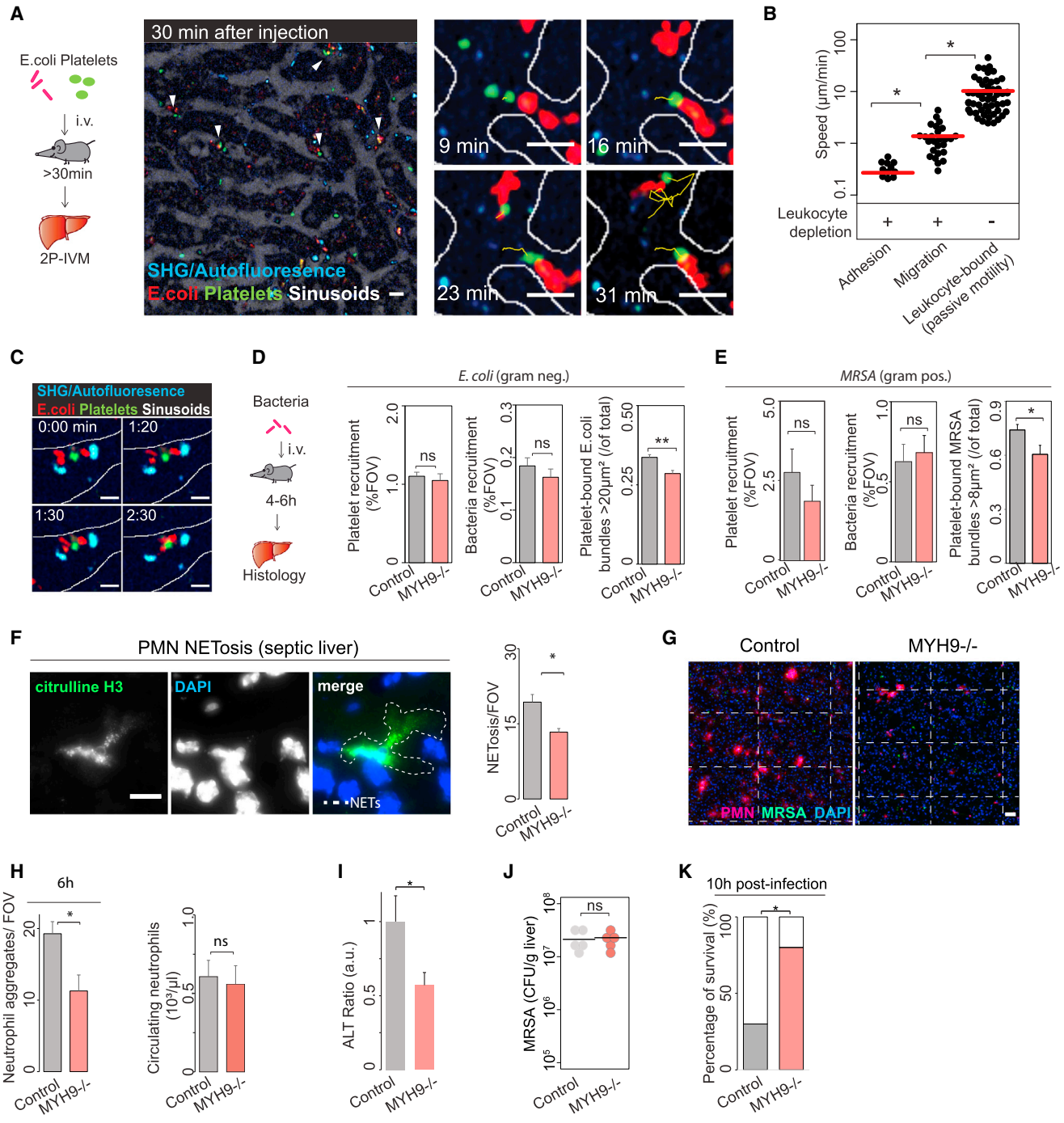

Figure 7. Platelets Migrate at Sites of Infection *In Vivo*

(A) 2P-IVM of platelets (*PF4-Cre/RSzgreen*) and *E. coli* (tdTomato) in liver sinusoids. (Left) Overview image is shown; liver sinusoids were reconstructed from tissue autofluorescence; (right) time series of migrating platelets. The scale bars represent 10 µm.

(B) Autonomous platelet migration is distinct from passive leukocyte-mediated motility. Migration/adhesion was quantified in leukocyte-deficient animals (depletion; anti-Ly6G/C clone: RB6-8C5). Leukocyte-dependent passive platelet motility was quantified in leukocyte-proficient animals (also see Figure S7E). Adhesion: n = 14 (pooled from 2 mice); migration: n = 26 (pooled from 2 mice); leukocyte bound: n = 53 (pooled from 3 mice); red bars, mean; Kruskal-Wallis/ Wilcox; *p < 0.05.

(C) Platelets interact with and bundle *E. coli in vivo*. The scale bar represents 5 µm.

(D) Platelet and bacteria recruitment and fraction of *E. coli* bundles >20 μm^2 colocalizing with platelets were quantified in liver sections of septic leukocyte-proficient mice (also see Figure S7H); n = 6 mice (*PF4-Cre+/MYH9$^{fl/fl}$*-BM chimeras); mean ± SEM; Student's t test; *p < 0.05.

(legend continued on next page)

Platelets are specialized sentinels of the circulation equipped with a plethora of receptors allowing to respond and stick to almost any surface foreign to human blood, including many pathogens. When spreading over small particles like fibrin fibers, latex beads, or bacteria, platelets can fully cover these objects and secure them within invaginations of their OCS, a continuous invagination of the outer plasma membrane (White, 2005). The observation that the distended portions of the OCS, which contain engulfed objects, are not phagocytic vacuoles led to propose a "covercyte," rather than a "phagocyte" function of platelets (White, 2005). Here, we show that migrating platelets use actomyosin-dependent forces to mechanically probe their microenvironment. If an encountered object does not resist these pulling forces, it is translocated toward the center of the migrating platelet, remaining attached to the platelet surface or the OCS. In the case of pathogens, this leads to the formation of stable bacterial packages at the platelet surface secured by the large actomyosin forces of individual platelets. Interestingly, platelet-bound bacterial bundles resemble the structural organization of typical platelet-dependent bacterial biofilms, as found in many infectious diseases, such as infective endocarditis (Jung et al., 2012). Intravascular immunity in invertebrates like Limulus horseshoe crabs is largely established by migrating hemocytes that share common features with mammalian platelets (Levin, 1988). Consequently, it is tempting to speculate that platelets, the first cells sealing vascular lesions in mammals, may have retained their ability to migrate and to collect pathogens from these ancient amoebocytes, thereby establishing the first line of host defense. Our data therefore provide a mechanism supporting and further explaining the previously proposed covercyte function of platelets that was not fully understood at the cell biology level.

The liver microcirculation provides a unique vascular platform, orchestrating several innate immune mechanisms acting together to combat blood-borne infections (Jenne and Kubes, 2013). The dense network of Kupffer cells lining liver sinusoids both efficiently captures bacteria from the circulation while at the same time providing adhesion signals to recruit circulating platelets (Wong et al., 2013). We now show that platelets adherent to the liver vasculature actively migrate to scan their microenvironment for bacteria, accumulating these pathogens on their surface. At the same time, platelets provide an "adhesion platform" for neutrophils (Sreeramkumar et al., 2014), which interact and phagocytose platelet-bound bacteria bundles. This leads to robust neutrophil activation and release of NETs. Boosted neutrophil activation by migrating platelets is detrimental in case of infection with MRSA, a pathogen that survives intracellularly upon phagocytosis and leads to a dramatic and often deadly increase in neutrophil-driven inflammation (Greenlee-Wacker et al., 2015). Abrogation of platelet migration reduces neutrophil activation and NETosis and attenuates tissue damage.

Together, evolution provided circulating blood platelets not only to prevent blood loss after injury but also as an efficient defense line to constantly scan the vascular system for potential invaders. Once platelets are recruited to sites of bacterial infection, they start to migrate, which enables the collection and bundling of bacteria and to recruit and activate professional phagocytes. The orchestration of these two functions assigns platelets a central role in innate immune responses and identifies them as potential target to dampen inflammatory tissue damage in certain clinical scenarios.

STAR★METHODS

Detailed methods are provided in the online version of this paper and include the following:

- KEY RESOURCES TABLE
- CONTACT FOR REAGENT AND RESOURCE SHARING
- EXPERIMENTAL MODEL AND SUBJECT DETAILS
  - Mouse strains
  - Human blood donors
  - Bacterial strains
  - Culture of primary murine polymorphonuclear leukocytes (PMNs)
- METHOD DETAILS
  - Inhibitors and blocking antibodies
  - 2P-IVM of vascular injury and bone marrow megakaryocytes
  - 2P-IVM of liver microcirculation
  - Systemic infection with E.coli
  - Systemic infection with Staph. aureus (MRSA USA300)
  - Adoptive Transfer
  - Confocal imaging of platelets and megakaryocytes
  - Isolation and staining of human and murine platelets
  - Plasma and serum preparation
  - Preparation of platelet supernatants
  - Functionalization of coverslips and migration assay
  - Characterization of plasma coated surfaces
  - Time-lapse video microscopy
  - Flow chamber assay
  - Bacterial trapping experiment under flow
  - Platelet phagocytosis assay
  - Platelet tracking protocol

(E) Platelet and bacteria recruitment and fraction of *MRSA* bundles >8 μm^2 colocalizing with platelets were quantified in liver sections of septic leukocyte-proficient mice (also see Figure S7I); n = 9/10 liver sections from 5 mice; mean ± SEM; Student's t test; *p < 0.05.
(F) NETosis was quantified in liver sections of septic mice (n = 3); mean ± SEM; Wilcox test; *p < 0.05. The scale bar represents 10 μm.
(G) Mosaic scans (each containing 3x3 stitched regions of interest (ROIs); dashed line indicates stitching of liver sections show PMN forming aggregates. Scale bar=50 μm. See also Figure S7P.
(H) Reduced PMN aggregate formation in *PF4-Cre+/MYH9$^{fl/fl}$* mice (n = 6); mean ± SEM; Wilcox test; *p < 0.05. *PF4-Cre+/MYH9$^{fl/fl}$* mice have normal circulating neutrophils counts. Control: n = 15 mice; MYH9−/−: n = 30 mice; mean ± SEM; Wilcox test.
(I) Alanine aminotransferase (ALT) plasma levels are normalized to control. n = 4 mice; mean ± SEM; paired t test; *p < 0.05.
(J) Colony-forming units (CFUs) of MRSA were measured in homogenized livers of septic mice (n = 5) 6 hr after infection; mean ± SEM; Wilcox test.
(K) *PF4-Cre+/MYH9$^{fl/fl}$* are protected in the early course of lethal MRSA sepsis (n = 10 mice); mean ± SEM; log rank test; *p < 0.05.
Also see Figure S7 and Movie S7.

- Shape analysis
- Immunofluorescence of migrating platelets
- Fura-2 imaging of migrating platelets
- pMLC western blot
- Correlative electron microscopy (SEM/FIB-SEM)
- Bacterial viability
- Neutrophil migration, phagocytosis, calcium imaging and NETosis

● QUANTIFICATION AND STATISTICAL ANALYSES

SUPPLEMENTAL INFORMATION

Supplemental Information includes seven figures and seven movies and can be found with this article online at https://doi.org/10.1016/j.cell.2017.11.001.

AUTHOR CONTRIBUTIONS

Conceptualization, F.G.; Methodology, F.G., Z.A., G.R., S.F., L.N., A.B., M.I., B.B., M.M.y.S., M. Luckner, G.W., M. Lorenz, and H.I.-A.; Investigation, F.G., Z.A., G.R., S.F., L.N., G.Y., A.B., B.B., B.S., H.I.-A., M.M.y.S., S.C., I.S., S.H., R. Hennel, K.L., M. Luckner, G.W., M. Lorenz, M.J., R.T.B., and K.S.; Software, Z.P.; Resources, C.L., C.G., Z.P., R. Haas, A.V., T.G., and M.S.; Formal Analysis, F.G., L.N., and B.B.; Writing – Original Draft, F.G. and S.M.; Writing – Editing, all authors; Visualization, F.G.; Supervision, F.G. and S.M.; Project Administration, F.G.; Funding Acquisition, F.G. and S.M.

ACKNOWLEDGMENTS

We thank Christin Lehmann, Anja Titova, Nicole Blount, and Cornelia Niemann for excellent technical assistance. We thank Reinhard Fässler, Barbara Walzog, Eva Kiermaier, and Joachim Pilcher for helpful discussions. This study was supported by the DFG SFB 914 (S.M. [B02 and Z01], K.S. [B02], R.T.B. [A05], A.V. [B04], and R. Haas [B05]), the DFG SFB 1123 (S.M. [B06]), the DFG FOR 2033 (S.M. and F.G.), the German Centre for Cardiovascular Research (DZHK) (MHA 1.4VD [S.M.]), FP7 program (project 260309, PRESTIGE [S.M.]), FöFoLe project 947 (F.G.), the Friedrich-Baur-Stiftung project 41/16 (F.G.), Marie Skłodowska Curie Individual Fellowship (EU project 747687, LamelliActin [F.G.]).

Received: March 23, 2017
Revised: August 27, 2017
Accepted: October 30, 2017
Published: November 30, 2017

REFERENCES

Ali, R.A., Wuescher, L.M., Dona, K.R., and Worth, R.G. (2017). Platelets mediate host defense against Staphylococcus aureus through direct bactericidal activity and by enhancing macrophage activities. J. Immunol. *198*, 344–351.

Auger, J.M., and Watson, S.P. (2008). Dynamic tyrosine kinase-regulated signaling and actin polymerisation mediate aggregate stability under shear. Arterioscler. Thromb. Vasc. Biol. *28*, 1499–1504.

Barnhart, E.L., Lee, K.-C., Keren, K., Mogilner, A., and Theriot, J.A. (2011). An adhesion-dependent switch between mechanisms that determine motile cell shape. PLoS Biol. *9*, e1001059.

Belamarich, F.A., Fusari, M.H., Shepro, D., and Kien, M. (1966). In vitro studies of aggregation of non-mammalian thrombocytes. Nature *212*, 1579–1580.

Benechet, A.P., Ganzer, L., and Iannacone, M. (2017). Intravital microscopy analysis of hepatic T cell dynamics. Methods Mol. Biol. *1514*, 49–61.

Bettex-Galland, M., and Luescher, E.F. (1959). Extraction of an actomyosin-like protein from human thrombocytes. Nature *184* (*Suppl 5*), 276–277.

Borm, B., Requardt, R.P., Herzog, V., and Kirfel, G. (2005). Membrane ruffles in cell migration: indicators of inefficient lamellipodia adhesion and compartments of actin filament reorganization. Exp. Cell Res. *302*, 83–95.

Boulaftali, Y., Hess, P.R., Getz, T.M., Cholka, A., Stolla, M., Mackman, N., Owens, A.P., 3rd, Ware, J., Kahn, M.L., and Bergmeier, W. (2013). Platelet ITAM signaling is critical for vascular integrity in inflammation. J. Clin. Invest. *123*, 908–916.

Brass, L.F., Zhu, L., and Stalker, T.J. (2005). Minding the gaps to promote thrombus growth and stability. J. Clin. Invest. *115*, 3385–3392.

Brundage, R.A., Fogarty, K.E., Tuft, R.A., and Fay, F.S. (1991). Calcium gradients underlying polarization and chemotaxis of eosinophils. Science *254*, 703–706.

Clark, A.M. (1942). Some effects of removing the nucleus from amoeba. Aust. J. Exp. Biol. Med. Sci. *20*, 241–247.

Clark, S.R., Ma, A.C., Tavener, S.A., McDonald, B., Goodarzi, Z., Kelly, M.M., Patel, K.D., Chakrabarti, S., McAvoy, E., Sinclair, G.D., et al. (2007). Platelet TLR4 activates neutrophil extracellular traps to ensnare bacteria in septic blood. Nat. Med. *13*, 463–469.

Coller, B.S. (1985). A new murine monoclonal antibody reports an activation-dependent change in the conformation and/or microenvironment of the platelet glycoprotein IIb/IIIa complex. J. Clin. Invest. *76*, 101–108.

Daley, J.M., Thomay, A.A., Connolly, M.D., Reichner, J.S., and Albina, J.E. (2008). Use of Ly6G-specific monoclonal antibody to deplete neutrophils in mice. J. Leukoc. Biol. *83*, 64–70.

Emambokus, N.R., and Frampton, J. (2003). The glycoprotein IIb molecule is expressed on early murine hematopoietic progenitors and regulates their numbers in sites of hematopoiesis. Immunity *19*, 33–45.

Euteneuer, U., and Schliwa, M. (1984). Persistent, directional motility of cells and cytoplasmic fragments in the absence of microtubules. Nature *310*, 58–61.

Feng, D., Nagy, J.A., Pyne, K., Dvorak, H.F., and Dvorak, A.M. (1998). Platelets exit venules by a transcellular pathway at sites of F-met peptide-induced acute inflammation in guinea pigs. Int. Arch. Allergy Immunol. *116*, 188–195.

Grębecka, L., Pomorski, P., and Łopatowska, A. (1997). Adhesion to the substratum improves the motility of *Amoeba proteus* in the absence of a cell nucleus. Protoplasma *197*, 174–181.

Greenlee-Wacker, M., DeLeo, F.R., and Nauseef, W.M. (2015). How methicillin-resistant Staphylococcus aureus evade neutrophil killing. Curr. Opin. Hematol. *22*, 30–35.

Guidotti, L.G., Inverso, D., Sironi, L., Di Lucia, P., Fioravanti, J., Ganzer, L., Fiocchi, A., Vacca, M., Aiolfi, R., Sammicheli, S., et al. (2015). Immunosurveillance of the liver by intravascular effector CD8(+) T cells. Cell *161*, 486–500.

Gupton, S.L., and Waterman-Storer, C.M. (2006). Spatiotemporal feedback between actomyosin and focal-adhesion systems optimizes rapid cell migration. Cell *125*, 1361–1374.

Jackson, S.P. (2011). Arterial thrombosis–insidious, unpredictable and deadly. Nat. Med. *17*, 1423–1436.

Jenne, C.N., and Kubes, P. (2013). Immune surveillance by the liver. Nat. Immunol. *14*, 996–1006.

Jung, C.-J., Yeh, C.-Y., Shun, C.-T., Hsu, R.-B., Cheng, H.-W., Lin, C.-S., and Chia, J.-S. (2012). Platelets enhance biofilm formation and resistance of endocarditis-inducing streptococci on the injured heart valve. J. Infect. Dis. *205*, 1066–1075.

Kanaji, T., Russell, S., and Ware, J. (2002). Amelioration of the macrothrombocytopenia associated with the murine Bernard-Soulier syndrome. Blood *100*, 2102–2107.

Kardash, E., Bandemer, J., and Raz, E. (2011). Imaging protein activity in live embryos using fluorescence resonance energy transfer biosensors. Nat. Protoc. *6*, 1835–1846.

Keren, K., Pincus, Z., Allen, G.M., Barnhart, E.L., Marriott, G., Mogilner, A., and Theriot, J.A. (2008). Mechanism of shape determination in motile cells. Nature *453*, 475–480.

Kolaczkowska, E., Jenne, C.N., Surewaard, B.G., Thanabalasuriar, A., Lee, W.Y., Sanz, M.J., Mowen, K., Opdenakker, G., and Kubes, P. (2015). Molecular

mechanisms of NET formation and degradation revealed by intravital imaging in the liver vasculature. Nat. Commun. *6*, 6673.

Kraemer, B.F., Borst, O., Gehring, E.-M., Schoenberger, T., Urban, B., Ninci, E., Seizer, P., Schmidt, C., Bigalke, B., Koch, M., et al. (2010). PI3 kinase-dependent stimulation of platelet migration by stromal cell-derived factor 1 (SDF-1). J. Mol. Med. (Berl.) *88*, 1277–1288.

Lam, W.A., Chaudhuri, O., Crow, A., Webster, K.D., Li, T.-D., Kita, A., Huang, J., and Fletcher, D.A. (2011). Mechanics and contraction dynamics of single platelets and implications for clot stiffening. Nat. Mater. *10*, 61–66.

Lauffenburger, D.A., and Horwitz, A.F. (1996). Cell migration: a physically integrated molecular process. Cell *84*, 359–369.

Lee, J., Ishihara, A., Oxford, G., Johnson, B., and Jacobson, K. (1999). Regulation of cell movement is mediated by stretch-activated calcium channels. Nature *400*, 382–386.

Léon, C., Eckly, A., Hechler, B., Aleil, B., Freund, M., Ravanat, C., Jourdain, M., Nonne, C., Weber, J., Tiedt, R., et al. (2007). Megakaryocyte-restricted MYH9 inactivation dramatically affects hemostasis while preserving platelet aggregation and secretion. Blood *110*, 3183–3191.

Levin, J. (1988). The horseshoe crab: a model for gram-negative sepsis in marine organisms and humans. Prog. Clin. Biol. Res. *272*, 3–15.

Lowenhaupt, R.W., Miller, M.A., and Glueck, H.I. (1973). Platelet migration and chemotaxis demonstrated in vitro. Thromb. Res. *3*, 477–487.

Massberg, S., Grahl, L., von Bruehl, M.-L., Manukyan, D., Pfeiler, S., Goosmann, C., Brinkmann, V., Lorenz, M., Bidzhekov, K., Khandagale, A.B., et al. (2010). Reciprocal coupling of coagulation and innate immunity via neutrophil serine proteases. Nat. Med. *16*, 887–896.

Mazharian, A., Ghevaert, C., Zhang, L., Massberg, S., and Watson, S.P. (2011). Dasatinib enhances megakaryocyte differentiation but inhibits platelet formation. Blood *117*, 5198–5206.

McDonald, B., Urrutia, R., Yipp, B.G., Jenne, C.N., and Kubes, P. (2012). Intravascular neutrophil extracellular traps capture bacteria from the bloodstream during sepsis. Cell Host Microbe *12*, 324–333.

Meijering, E., Dzyubachyk, O., and Smal, I. (2012). Methods for cell and particle tracking. Methods Enzymol. *504*, 183–200.

Mendoza, M.C., Besson, S., and Danuser, G. (2012). Quantitative fluorescent speckle microscopy (QFSM) to measure actin dynamics. Curr. Protoc. Cytom. *Chapter 2*, Unit2.18.

Nieswandt, B., Schulte, V., Zywietz, A., Gratacap, M.-P., and Offermanns, S. (2002). Costimulation of Gi- and G12/G13-mediated signaling pathways induces integrin alpha IIbbeta 3 activation in platelets. J. Biol. Chem. *277*, 39493–39498.

Nourshargh, S., Hordijk, P.L., and Sixt, M. (2010). Breaching multiple barriers: leukocyte motility through venular walls and the interstitium. Nat. Rev. Mol. Cell Biol. *11*, 366–378.

Ono, A., Westein, E., Hsiao, S., Nesbitt, W.S., Hamilton, J.R., Schoenwaelder, S.M., and Jackson, S.P. (2008). Identification of a fibrin-independent platelet contractile mechanism regulating primary hemostasis and thrombus growth. Blood *112*, 90–99.

Palecek, S.P., Loftus, J.C., Ginsberg, M.H., Lauffenburger, D.A., and Horwitz, A.F. (1997). Integrin-ligand binding properties govern cell migration speed through cell-substratum adhesiveness. Nature *385*, 537–540.

Park, K., Mao, F.W., and Park, H. (1991). The minimum surface fibrinogen concentration necessary for platelet activation on dimethyldichlorosilane-coated glass. J. Biomed. Mater. Res. *25*, 407–420.

Pincus, Z., and Theriot, J.A. (2007). Comparison of quantitative methods for cell-shape analysis. J. Microsc. *227*, 140–156.

Pitchford, S.C., Momi, S., Baglioni, S., Casali, L., Giannini, S., Rossi, R., Page, C.P., and Gresele, P. (2008). Allergen induces the migration of platelets to lung tissue in allergic asthma. Am. J. Respir. Crit. Care Med. *177*, 604–612.

Pollard, T.D., and Cooper, J.A. (2009). Actin, a central player in cell shape and movement. Science *326*, 1208–1212.

Prasad, J.M., Gorkun, O.V., Raghu, H., Thornton, S., Mullins, E.S., Palumbo, J.S., Ko, Y.-P., Höök, M., David, T., Coughlin, S.R., et al. (2015). Mice expressing a mutant form of fibrinogen that cannot support fibrin formation exhibit compromised antimicrobial host defense. Blood *126*, 2047–2058.

R Core Team (2014). R: A language and environment for statistical computing (R Foundation for Statistical Computing).

Schindelin, J., Arganda-Carreras, I., Frise, E., Kaynig, V., Longair, M., Pietzsch, T., Preibisch, S., Rueden, C., Saalfeld, S., Schmid, B., et al. (2012). Fiji: an open-source platform for biological-image analysis. Nat. Methods *9*, 676–682.

Schmidt, E.-M., Münzer, P., Borst, O., Kraemer, B.F., Schmid, E., Urban, B., Lindemann, S., Ruth, P., Gawaz, M., and Lang, F. (2011). Ion channels in the regulation of platelet migration. Biochem. Biophys. Res. Commun. *415*, 54–60.

Schmidt, E.-M., Kraemer, B.F., Borst, O., Münzer, P., Schönberger, T., Schmidt, C., Leibrock, C., Towhid, S.T., Seizer, P., Kuhl, D., et al. (2012). SGK1 sensitivity of platelet migration. Cell. Physiol. Biochem. *30*, 259–268.

Semple, J.W., Italiano, J.E., Jr., and Freedman, J. (2011). Platelets and the immune continuum. Nat. Rev. Immunol. *11*, 264–274.

Snippert, H.J., van der Flier, L.G., Sato, T., van Es, J.H., van den Born, M., Kroon-Veenboer, C., Barker, N., Klein, A.M., van Rheenen, J., Simons, B.D., and Clevers, H. (2010). Intestinal crypt homeostasis results from neutral competition between symmetrically dividing Lgr5 stem cells. Cell *143*, 134–144.

Sreeramkumar, V., Adrover, J.M., Ballesteros, I., Cuartero, M.I., Rossaint, J., Bilbao, I., Nácher, M., Pitaval, C., Radovanovic, I., Fukui, Y., et al. (2014). Neutrophils scan for activated platelets to initiate inflammation. Science *346*, 1234–1238.

Stalker, T.J., Traxler, E.A., Wu, J., Wannemacher, K.M., Cermignano, S.L., Voronov, R., Diamond, S.L., and Brass, L.F. (2013). Hierarchical organization in the hemostatic response and its relationship to the platelet-signaling network. Blood *121*, 1875–1885.

Thévenaz, P., Ruttimann, U.E., and Unser, M. (1998). A pyramid approach to subpixel registration based on intensity. IEEE Trans. Image Process. *7*, 27–41.

Tsai, F.-C., and Meyer, T. (2012). Ca2+ pulses control local cycles of lamellipodia retraction and adhesion along the front of migrating cells. Curr. Biol. *22*, 837–842.

Turbill, P., Beugeling, T., and Poot, A.A. (1996). Proteins involved in the Vroman effect during exposure of human blood plasma to glass and polyethylene. Biomaterials *17*, 1279–1287.

Varga-Szabo, D., Braun, A., and Nieswandt, B. (2009). Calcium signaling in platelets. J. Thromb. Haemost. *7*, 1057–1066.

Wanner, G., Schäfer, T., and Lütz-Meindl, U. (2013). 3-D analysis of dictyosomes and multivesicular bodies in the green alga Micrasterias denticulata by FIB/SEM tomography. J. Struct. Biol. *184*, 203–211.

White, J.G. (2005). Platelets are covercytes, not phagocytes: uptake of bacteria involves channels of the open canalicular system. Platelets *16*, 121–131.

Wong, C.H.Y., Jenne, C.N., Petri, B., Chrobok, N.L., and Kubes, P. (2013). Nucleation of platelets with blood-borne pathogens on Kupffer cells precedes other innate immunity and contributes to bacterial clearance. Nat. Immunol. *14*, 785–792.

Yam, P.T., Wilson, C.A., Ji, L., Hebert, B., Barnhart, E.L., Dye, N.A., Wiseman, P.W., Danuser, G., and Theriot, J.A. (2007). Actin-myosin network reorganization breaks symmetry at the cell rear to spontaneously initiate polarized cell motility. J. Cell Biol. *178*, 1207–1221.

Yang, S., and Huang, X.-Y. (2005). Ca2+ influx through L-type Ca2+ channels controls the trailing tail contraction in growth factor-induced fibroblast cell migration. J. Biol. Chem. *280*, 27130–27137.

Yeaman, M.R. (2014). Platelets: at the nexus of antimicrobial defence. Nat. Rev. Microbiol. *12*, 426–437.

Yipp, B.G., Petri, B., Salina, D., Jenne, C.N., Scott, B.N.V., Zbytnuik, L.D., Pittman, K., Asaduzzaman, M., Wu, K., Meijndert, H.C., et al. (2012). Infection-induced NETosis is a dynamic process involving neutrophil multitasking in vivo. Nat. Med. *18*, 1386–1393.

Yount, G., Taft, R.J., Luu, T., Rachlin, K., Moore, D., and Zhang, W. (2007). Independent motile microplast formation correlates with glioma cell invasiveness. J. Neurooncol. *81*, 113–121.

STAR★METHODS

KEY RESOURCES TABLE

REAGENT or RESOURCE	SOURCE	IDENTIFIER
Antibodies		
Mouse anti-Integrin αVβ3 Antibody (clone LM609)	Merck Millipore	Cat#MAB1976; RRID: AB_2296419
Rat anti-Ly6G/C (clone RB6-8C5)	eBioscience	RRID: AB_467730
Rat anti-CD45 (clone 30-F11)	eBioscience	RRID: AB_467251
Rat anti-CD42b (clone Xia.B)	Emfret	Cat#M043-0
Goat anti-*E. coli* serotype O/K polyclonal	Thermo Fisher Scientific	RRID: AB_1074273
Sheep anti-Human Fibrinogen polyclonal	BioRad	Cat#4440-8004; RRID: AB_620402
Rabbit anti-Staphylococcus aureus antibody polyclonal	Abcam	Cat#ab20920; RRID: AB_445913
Rabbit anti-Fibrinogen polyclonal	Abcam	Cat#ab34269; RRID: AB_732367
Rabbit anti-Von Willebrand Factor polyclonal	Abcam	Cat#ab6994; RRID: AB_305689
Rabbit anti-Fibronectin polyclonal	Abcam	Cat#ab2413; RRID: AB_2262874
Mouse anti-CD41 (clone HIP8)	Abcam	Cat#ab15021; RRID: AB_301581
Mouse anti-CD41-FITC (clone PAC1)	BD	Cat#340507; RRID: AB_2230769
Rabbit anti-Myosin Light Chain (phosphor S20) polyclonal	Abcam	Cat#ab2480; RRID: AB_303094
Rabbit anti-Myosin Light Chain 2 (D18E2)	Cell Signaling Technology	Cat#8505
Anti-rabbit IgG, HRP-linked Antibody	Cell Signaling Technology	Cat#7074
Mouse anti-human IL-4R	R&D	Cat#MAB230
Mouse anti-human IL-4R-PE	R&D	Cat#FAB230P
Rat anti-mouse Ly6G (clone 1A8)	Biolegend	RRID: AB_1186104
Rabbit anti-mouseHistone H3 (citrulline R2 + R8 + R17)	Abcam	Cat#ab5103; RRID: AB_304752
Bacterial and Virus Strains		
Methicillin-resistant Staphyloccocus aureus (MRSA) (strain USA 300)	Max von Pettenkofer-Institut München	N/A
E.coli (strain DH12)	Dr. Engelmann; Massberg et al., 2010	N/A
Listeria monocytogenes (strain 10403S)	Dr. Verschoor	N/A
Biological Samples		
Human blood	Healthy voluntary donors	N/A
Chemicals, Peptides, and Recombinant Proteins		
C7E3-Fab (Reopro)	Lilly	CAS: 143653-53-6
Cytochalasin D	Sigma	CAS: 22144-77-0
(-)Blebbistatin	Cayman Chemical	CAS: 856925-71-8
BAPTA-AM	Invitrogen	Cat#B6769
Prostaglandin I_2 sodium salt	Abcam	CAS: 61849-14-7
Thrombin from bovine plasma	Sigma	CAS: 9002-04-4
Lepirudin	Schering	CAS: 120993-53-5
PPACK	Enzo	CAS: 71142-71-7
Equine collagen fibrils (type I)	Chrono Log	Cat#385
Apyrase	New England Biolabs	Cat#M0398L
Indomethacin	Sigma	CAS: 53-86-1
ADP	Sigma	CAS: 58-64-0
U46619	Tocris Biosience	CAS: 56985-40-1

(*Continued on next page*)

Continued

REAGENT or RESOURCE	SOURCE	IDENTIFIER
Fibrinogen from human plasma	Sigma	CAS: 9001-32-5
Fibrinogen From Human Plasma, Alexa Fluor 488 Conjugate	Thermo Fisher Scientific	Cat#F13191
Hexamethyldisilazane	Sigma	CAS: 999-97-3
Recombinant human albumin	Sigma	CAS: 70024-90-7
Casein	Sigma	Cat#C7078
Alexa Fluor 488 Streptavidin, 10 nm colloidal gold conjugate	Thermo Fisher Scientific	Cat#A32361
FluoSpheres NeutrAvidin-Labeled Microspheres, 0.2 μm	Thermo Fisher Scientific	Cat#F8774
Fura-2, AM	Thermo Fisher Scientific	Cat#F1221
pHrodo Red *S. aureus* Bioparticles Conjugate for Phagocytosis	Thermo Fisher Scientific	Cat#A10010
SYTOX Green Nucleic Acid Stain	Thermo Fisher Scientific	Cat#S7020
CK666	Sigma	CAS: 442633-00-3
5(6)-Carboxyfluorescein diacetate *N*-succinimidyl ester	Sigma	CAS: 150347-59-4
Critical Commercial Assays		
EZ-LinkSulfo-NHS-SS-Biotin kit	Thermo Fisher Scientific	Cat#21331
LIVE/DEAD *Bac*Light Bacterial Viability Kit	Thermo Fisher Scientific	Cat#L7007
Alanine Aminotransferase (ALT or SGPT) Activity Colorimetric/Fluorometric Assay Kit	Biovision	Cat#K752
Experimental Models: Organisms/Strains		
Mouse: *PF4*-Cre	The Jackson Laboratory	JAX: 008535
Mouse: *R26R-Confetti*	The Jackson Laboratory	JAX: 013731
Mouse: *Ai6(RCL-ZsGreen)*	The Jackson Laboratory	JAX: 007906
Mouse: *MYH9fl/fl*	Dr. Gachet; Léon et al., 2007	N/A
Mouse: *αIIb−/−*	Dr. Frampton; Emambokus and Frampton, 2003	N/A
Mouse: *GPIb-Il4R*	Dr. Ware; Kanaji et al., 2002	N/A
Mouse: *PC-G5-tdT*	The Jackson Laboratory	JAX: 024477
Software and Algorithms		
FIJI	Schindelin et al., 2012	https://fiji.sc/
MTrackJ	Meijering et al., 2012	https://imagescience.org/meijering/software/mtrackj/
Celltool	Pincus and Theriot, 2007	http://zplab.wustl.edu/celltool/
Manual Tracking	Fabrice Cordelieres, Institut Curie, Orsay (France)	https://imagej.nih.gov/ij/plugins/track/track.html
StackReg	Thévenaz et al., 1998	http://bigwww.epfl.ch/thevenaz/stackreg/
Imaris	Bitplane	http://www.bitplane.com/imaris/imaris
R	R Core Team, 2014	https://www.r-project.org/
SPSS Statistics 22	IBM	https://www.ibm.com/analytics/de/de/technology/spss/

CONTACT FOR REAGENT AND RESOURCE SHARING

Further information and requests for resources and reagents should be directed to and will be fulfilled by the Lead Contact, Florian Gaertner (F.Gaertner@med.uni-muenchen.de).

EXPERIMENTAL MODEL AND SUBJECT DETAILS

Mouse strains

PF4-Cre, R26R-Confetti, PC-G5-tdT-mice and *C57BL/6*-mice were purchased from The Jackson Laboratory and maintained and cross-bred at our animal facility. *PF4-Cre/Ai6(RCL-ZsGreen)*-mice were bred at IRCCS San Raffaele Scientific Institute. *PF4-Cre/MYH9*$^{fl/fl}$-mice were a gift of Dr. Gachet (Léon et al., 2007). *αIIb−/−* mice were a gift of Dr. Frampton (Emambokus and Frampton, 2003). *GPIb-hIl4R*-mice were a gift of Dr. Ware (Kanaji et al., 2002). All strains were backcrossed to and maintained on C57BL/6-background. If not otherwise stated, animals of same sex and age were randomly assigned to experimental groups. For sepsis experiments, knockout and control animals were paired according to age, sex and weight. All procedures performed on mice were approved by the local legislation on protection of animals (Regierung von Oberbayern, Munich).

Human blood donors

Human blood was drawn from male and female healthy voluntary donors at the age of 25-40 after informed consent was obtained from all subjects. Both genders were equally represented in all our analyses. Migration assays performed in this study did not reveal gender-specific differences (data not shown). Blood from a patient with type I Glanzmann thrombasthenia was collected after approval from the ethical review board (LMU Munich) and written informed consent.

Bacterial strains

Methicillin-resistant Staphyloccocus aureus (MRSA)

MRSA (strain USA300) was cultured in brain heart infusion (BHI, Bacto™ Brain Heart Infusion (Porcine), BD) medium at 37°C with 180 rpm shaking. The CFU (colony forming units) per milliliter (ml) was determined for OD_{600} = 0.1 with $2*10^8$ CFU/ml. For infection experiments *S. aureus* USA300 was inoculated in BHI medium (37°C, 180 rpm) overnight. The overnight culture was diluted in BHI to OD_{600} = 0.1 and further incubated at 37°C with 180 rpm for 1.5 h. Subsequently, OD_{600} was measured and adjusted to OD_{600} = 1.25 which equals $5*10^8$ CFU/200 μl. Bacteria were washed once with 0.9% Sodium chloride solution (Braun) and kept on ice until injection.

E. coli

E.coli (strain DH12) was cultured in LB-broth medium (LB Broth (Luria lowsalt) Powdermicrobialgrowth medium, Sigma Aldrich, Steinheim) medium at 37°C with 260 rpm shaking. The CFU (colony forming units) per milliliter (ml) was determined for OD_{600} = 1.0 with $2,8*10^8$ CFU/ml. For infection experiments *E.coli* from a frozen stock was inoculated in LB-broth medium with 1 mM IPTG (1:100 IPTG, Isopropyl β-D-1-thiogalactopyranoside; Sigma Aldrich Chemie, Steinheim) and 100μM Ampicillin (1:1000 Ampicillinsodiumsalt, Sigma Aldrich Chemie, Steinheim) (37°C, 260 rpm) overnight. A starter culture of the saturated overnight culture was prepared the next morning in a 1:1000 dilution with LB-broth medium (1:1000), 1 mM IPTG (1:100) and 100μM Ampicillin (1:1000) and further incubated at 37°C with 250rpm for 2.5 h to allow growth to early log phase. Subsequently, OD_{600} (reading of 0,3-0,4) was measured and the needed volume adjusted to OD_{600} = 1.0 which equals $2,8*10^8$CFU/ml to get an injection volume of 100μl per animal with a concentration of $3,2*10^8$CFU. Bacteria were washed twice with 0.9% Sodium chloride solution (Braun) and kept on ice until injection.

Listeria monocytogenes (LM)

LM WT strain 10403S were grown to exponential phase at 37°C in BHI broth, washed, resuspended in PBS. LM was fluorescently labeled by incubation for 30 min at 37°C with 5mM CSFE (carboxyfluorescein diacetate succinimidyl ester; Sigma). Bacteria were heat-inactivated at 70°C for 2 hr.

Culture of primary murine polymorphonuclear leukocytes (PMNs)

Mice *(C57Bl6)* were anesthetized by isoflurane and sacrificed by neck dislocation. Bone marrow (BM) cells were flushed from femurs and tibias (ice cold PBS), centrifuged (300 g, 4°C for 5 min) and resuspended in 1 mL PBS. 1 mL of BM cell suspension was laid on a three-layer Percoll (Sigma) gradient (72% (3 ml) / 64% (3 ml) / 52% (3 ml)) and centrifuged at 1000 g for 30 min with the brake switched off to avoid mixing of the three layers. PMNs were harvested from the 64% / 72% interface, washed in PBS and cultured overnight in VLE- RPMI 1640 medium (Biochrom) supplemented with 10% FBS and 100 U/ml penicllin and 100ug/ml streptomycin.

METHOD DETAILS

Inhibitors and blocking antibodies

αIIbβ3 inhibition: C7E3-Fab (Reopro, Lilly) (10 μg/ml), a blocking β3-specific Fab-fragment (Coller, 1985). αvβ3 inhibition: LM609 (blocking antibody; Merck Millipore) (30μg/ml). Inhibition of actin polymerization: Cytochalasin D (Sigma) (2 μM) Myosin IIa inhibition: Blebbistatin(-) (Cayman Chemical) (5 μM or 50 μM); Blebbistatin(+) (Cayman Chemical) was used as negative control. Extracellular calcium depletion: 100 mM citrate. Intracellular calcium depletion: BAPTA-AM (10 μM) (Molecular Probes), Inhibition of Arp2/3: CK666 (50μM) (Sigma).

2P-IVM of vascular injury and bone marrow megakaryocytes

Mice were anaesthetized by intraperitoneal injection of a solution of midazolame (5 mg/kg body weight; Ratiopharm), medetomidine (0.5 mg/kg body weight; Pfizer), and fentanyl (0.05 mg/kg body weight; CuraMed Pharma GmbH). Mice were placed in a lateral position to allow careful immobilization of the ear-pinnae (ventral side up) to a custom-built imaging platform using 30G needles, as previously reported. A 3 mm x 3 mm piece of dermis was carefully removed to expose small subcutaneous veins. Two injury models were used to subsequently induce vascular injury. We either mechanically injured the vessel wall with a 30G needle or disrupted the vascular integrity by focusing a high power laser-beam of our two-photon microscope onto the vessel wall. Both injury models, triggered the exposure of subendothelial collagen as well as the accumulation of fibrin(ogen) at the site of injury (Figure S1C) and are established models to study hemostasis (Stalker et al., 2013). To exclude passive platelet movement imitated by migrating leukocytes, we depleted leukocytes by i.p. injection of anti-Ly6G/C (150 μg/mouse 24 h and 4 h prior to injury; clone RB6-8C5, eBioscience) and anti-CD45 (100 μg/mouse 24 h prior to injury; clone 30-F11, eBioscience) (Daley et al., 2008). Depletion efficiency was locally controlled by injection of fluorescently labeled (PE) anti-CD45 (eBioscience) and anti-Ly6G/C (clone RB6-8C5; eBioscience) following the experiment, and white blood cells were counted, using an automated cell counter (ABX Micros ES60, Horiba Medical) (Figures S1G and S1H). Images were acquired using a Trimscope II multi-photon imaging platform (LaVision Biotech) on an upright Olympus stand, enclosed in a custom-built incubator maintaining 37°C. Images were acquired using a Plan-Apochromat 20x/1.0 NA objective (Carl Zeiss Microscopy) with saline as immersion medium. Fluorescent signals were collected using 4 external/non-descanned photomultipliers (PMTs). For imaging of *Confetti* fluorescence the following filter combination was used: mCFP was collected with a 480/40 nm bandwidth and 520 nm longpass filter cYFP with a 535/30 nm bandwith and the same 520 nm longpass filter and cRFP with a 605/70 nm band- width and 560 nm longpass filter. Fluorescence excitation was provided by a Chameleon Ti:Sapphire laser (Coherent) tuned to 910 nm for simultaneous excitation of cYFP, cRFP and mCFP and generation of collagen second harmonic signal. 800 nm excitation wavelength was used for imaging of CFDA-SE, DDAO-SE, Alexa488 and Alexa546 and PE using the same laser. Z stacks were recorded with 2μm step-size and time series were captured with 1 frame every 5 s, unless otherwise specified. To visualize megakaryocytes in *PF4-Cre/R26R-Confetti*-mice we performed 2P-IVM of the mouse calvarian bone marrow. To get access to the frontoparietal skull, the scalp of an anesthetized mouse is incised in the midline. A plastic ring is inserted in the incision to spread the skin and to allow application of sterile physiologic saline solution to prevent drying of the tissue. During these procedures the animal's head is immobilized in a customized plexiglas stage equipped with a stereotactic holder. Imaging is performed using the multi-photon imaging platform as described above.

2P-IVM of liver microcirculation

Anesthetized mice (*C57/Bl6*) received tdTomato labeled *E.coli (DH12)* (3.2×10^8 CFU suspended in 200 μL saline) via the tail vein and platelets isolated from a *PF4-Cre/Ai6(RCL-ZsGreen)* donor mouse were transfused immediately prior to surgery. Platelet-leukocyte binding was enhanced by i.v. injection of 25 μg LPS /mouse (Clark et al., 2007). In some experiments leukocytes were fluorescently labeled using anti-Ly6G/C-FITC antibody (15μg/mouse; clone RB6-8C5, eBioscience). Where indicated in the figure legends, leukocyte depletion was performed as previously described by i.p. injection of anti-Ly6G/C (200 μg/mouse 24h prior to injury; clone RB6-8C5, eBioscience)). Surgical procedures were performed as previously described (Benechet et al., 2017). Briefly, after opening the skin with a midline incision and detaching peritoneal adherences, midline and left subcostal incisions were made in the peritoneum through a high-temperature cautery. The falciform ligament was resected and mice were placed in a left lateral position with the left liver lobe gently exteriorized onto a glass coverslip attached to a custom-made imaging platform. The liver was covered with plastic wrap, the incision was packed with moist gauze, and the imaging platform was sealed to prevent dehydration. Images were acquired with a LaVision BioTec TriMScope II coupled to a Nikon Ti-U inverted microscope enclosed in a custom-built environmental chamber (Life Imaging Services) that was maintained at 37-38°C with heated air. Continuous body temperature monitoring through a rectal probe was performed to ensure that a narrow range of 37–38°C was maintained at all times. Fluorescence excitation was provided by two tunable fs-pulsed Ti:Sa lasers (680–1080 nm, Ultra II, Coherent). The setup includes four photomultiplier tubes (3 Hamamatsu H7422-40 GaAsP High Sensitivity PMTs and 1 Hamamatsu H7422-50 GaAsP High Sensitivity red-extended PMT) and a high working distance water-immersion 20x objective (NA = 1.0, Zeiss). Images were acquired every 10 s for up to 4 h. Images sequences were processed using FIJI (Schindelin et al., 2012). X-Y Image drift was corrected using the StackReg plugin (Thévenaz et al., 1998). Gaussian filtering was used to reduce image noise. Migrating cells were tracked manually using the ''Manual Tracking'' or the ''MTrackJ'' plugin in FIJI (Meijering et al., 2012). Architecture of sinusoids was reconstructed from the smoothed auto-fluorescence signal of the liver (median filtered z-protection of the imaging sequence).

Systemic infection with E.coli

Bone marrow (BM) chimeras were generated by injection of isolated bone marrow from *PF4-Cre+/MYH9$^{fl/fl}$* - or *PF4-Cre-/MYH9$^{fl/fl}$-mice* into sublethally (900 rad) irradiated 8 weeks old recipient mice (sex: female; *C57Bl6*). Mice were used 24 weeks after reconstitution. Systemic infection with fluorescently labeled *E.coli (DH12)* (tdTomato) were performed as previously described (Massberg et al., 2010). Briefly, *E.coli* at an amount of 3.2×10^8 CFU (suspended in 200 μL saline) was injected into the tail vein of mice (BM-Chimeras). 4 h after infection mice were sacrificed and livers were explanted, embedded in

OCT and snap frozen in liquid nitrogen. Livers were cut with a cryotome into sections of 5μm thickness. Specimens were fixed with 4% formalin for 4 min, washed in PBS and stained for platelets (anti-CD42b, clone Xia.B, Emfret), E.coli (*E. coli* serotypes O + K Antibody, ThermoFisher) and/or fibrin(ogen) (4440-8004F, Bio-rad). Mosaic micrographs of liver sections were acquired using a Zeiss Axio Imager M2 epifluorescent microscope with a Plan Apochromat 40x/0.75 air objective and an AxioCam MRm camera (Carl Zeiss Microscopy). Images were analyzed using Imaris software (Bitplane).

Systemic infection with Staph. aureus (MRSA USA300)

Mice were intravenously injected with $2*10^8$ CFU of *S. aureus* USA300. Mice were sacrificed after 6h of infection.

CFU-Assay

Mice (*PF4-Cre+/MYH9$^{fl/fl}$* (age: 12-14 weeks, sex: 2 females and 3 males) or *PF4-Cre-/MYH9$^{fl/fl}$* (age: 12-14 weeks, sex: 2 females and 3 males) were sacrificed and organs were harvested and placed in phosphate buffered saline (DPBS, Dulbecco GIBCO) at 4°C until further processing. Organs were homogenized using a QIAGEN TissueLyser^{TM} with an oscillation of 50/s for 10 min. Serial dilutions were made in BHI and plated on MRSA II (Oxoid, ThermoFischer Scientific) and LB plates. Plates were incubated for 20 h at 37°C. Colonies were counted and CFU per gram organ was calculated.

Histology

Mice (*PF4-Cre+/MYH9$^{fl/fl}$* (age: 12-17 weeks, sex: 4 females and 8 males) or *PF4-Cre-/MYH9$^{fl/fl}$* (age: 12-17 weeks, sex: 8 females and 4 males) were sacrificed and livers were explanted, processed as described above and immuno-stained: Platelets (anti-CD42b, clone Xia.B, Emfret), S. aureus (ab20920, Abcam) and fibrin(ogen) (4440-8004F, Bio-rad), Neutrophiles (anti-LY6G, Clone:1A8, Biolegend), NETs (anti-citrulline Histone 3; Abcam). Images were acquired using a Zeiss Axio Imager M2 epifluorescent microscope with a Plan Apochromat 40x/0.75 air objective and an AxioCam MRm camera (Carl Zeiss Microscopy) or a LSM 880 confocal microscope with Airyscan module from Carl Zeiss, with Plan-Apochromat 20x/0.8 air objective (Carl Zeiss Microscopy). The channels were acquired using the laser lines 633, 561, 488 and 405 nm with the respective filters settings BP 420-480/LP 605, BP 495-550/LP 570, BP 495-550/LP 570 and BP 420-480/BP 495-550, on the Airyscan module in super-resolution mode. Platelet-MRSA colocalizations and size-distributions were analyzed using Imaris software (Bitplane). Neutrophil infiltration was manually analyzed by blinded investigators. Neutrophil infiltrates were classified as LY6-G-positive aggregates with a minimum of three cells. Platelet-depleted *C57Bl6*-mice (Figure S7D) (depletion group: age: 9 weeks, sex: 3 females and 3 males; isotype control group: age: 9 weeks, sex: 3 females and 3 males) were generated by i.v. injection of anti-GPIbα antibodies (2μg/g mouse; R300, Emfret). Mice were infected 12 h after treatment.

Plasma isolation

Mice (*PF4-Cre+/MYH9$^{fl/fl}$* (age: 12-14 weeks, sex: 2 females and 3 males) and *PF4-Cre-/MYH9$^{fl/fl}$* (age: 12-14 weeks, sex: 2 females and 3 males) were sacrificed and blood was drawn intracadially. Plasma was isolated from citrated whole blood by centrifugation at 1500 g for 15 min at 4°C and subsequently snap frozen in liquid nitrogen. Samples were stored at −80°C.

Plasma ALT activity

Serum levels of the liver enzyme ALT were determined with the alanine aminotransferase (ALT) activity fluorimetric assay kit from Biovision (Milpitas, CA, USA) according to the manufacturer's protocol. All necessary biochemical components were provided in the assay kit. Briefly, 5 μL blood serum was used to analyze the transformation of α-ketoglutarate with alanine to glutamate and pyruvate. The pyruvate is further converted, resulting in fluorescence (Ex/Em = 535/587 nm). The fluorescence was monitored on a Synergy Mx microplate reader (BioTek, Bad Friedrichshall, Germany) every 2 min for 2 h and ALT activity calculation was performed using measurements in the linear range of the standard curve.

Survival experiments

Mice (*PF4-Cre+/MYH9$^{fl/fl}$* (age: 17-40 weeks; sex: 10 females and 1 male) or *PF4-Cre-/MYH9$^{fl/fl}$* (age: 17-40 weeks; sex: 9 females and 2 males) were intravenously injected with $2*10^8$ CFU of *S. aureus* USA300. Infected mice were continuously monitored for a maximum of 24h (all mice died within the observation time).

Adoptive Transfer

Adoptive transfer of *WT (C57/Bl6)* and *MYH9*-deficient platelets into thrombocytopenic *GPIb;hIL4R–Tg* recipient mice (mice receiving *WT* plts: age: 10 weeks, sex: 2 males and 1 female; mice receiving *MYH9−/−* plts: age: 10 weeks, sex: 2 males and 1 female) was performed as previously described (Boulaftali et al., 2013) with small modifications:

A, Platelet depletion

Thrombocytopenia was induced in *GPIb;hIL4R–Tg* mice by i.v. injection of antibodies against hIL-4R (MAB230, R&D, 5 μg/g body weight; 12 h and 3h before transfusion).

B, Platelet transfusion

Washed platelets were isolated as described below. Platelets from several donor mice were pooled, and the platelet count was adjusted to 5×10^8 platelets/200 μl. Recipient mice were injected with 200 μL washed platelets.

C, Flow cytometry

For determination of endogenous and transfused platelet counts, diluted whole blood was stained with anti-hIL-4R-PE (FAB230P, R&D), and fraction of hILR4 positive platelets was assessed by flow cytometry (LSRFortessa; BD Biosciences).

Confocal imaging of platelets and megakaryocytes

Isolated washed platelets were incubated on fibrinogen coated coverslips (100 μg/ml) in the presence of 0.1 U/ml bovine Thrombin for 20 min at 37°C and subsequently imaged without prior fixation. Motility assays of confetti aggregates were performed using the migration assay as described below with adapted platelet concentrations ($50x10^3/\mu l$). Megakaryocytes (MKs) were isolated as previously described (Mazharian et al., 2011). Briefly, BM cells were flushed from femurs and cultured in serum-supplemented StemPro medium (2.6%) with 2mM l-glutamine, penicillin/streptomycin, and 20 ng/mL of murine stem cell factor at 37°C under 5% CO_2 for 2 days. Cells were then cultured for a further 4 days in the presence of 20 ng/mL of stem cell factor and 50 ng/mL of TPO. Mature MKs were enriched using a 1.5%/3% BSA gradient under gravity (1*g*) for 45 minutes at room temperature. MKs were allowed to spread on fibrinogen-coated coverslips (100 μg/ml) for 6 h at 37°C and imaged without prior fixation. Images were captured on an inverted Zeiss LSM 780 confocal microscope using a Plan-Apochromat 100x/1.46 oil-immersion objective (Carl Zeiss Microscopy).

Isolation and staining of human and murine platelets

Human blood was drawn from the cubital into a syringe containing 1/7 volume of Acid-Citrate-Dextrose (39 mM citric acid, 75 mM sodium citrate, 135 mM dextrose; ACD). Blood from a patient with type I Glanzmann thrombasthenia was collected after approval from the ethical review board and written informed consent. Whole blood was diluted 1:1 with modified Tyrode's buffer (137 mM NaCl, 2.8 mM KCl, 12 mM NaHCO3, 5.5 mM glucose, 10mM HEPES, pH = 6.5) and centrifuged with 70 g for 30 min at RT with the break switched off. The supernatant contains the platelet rich plasma (PRP), either used for experiments or transferred into a second tube to prepare washed platelets. Platelets were washed by further diluting PRP (1:3) with PGI2 (0.1 μg/ml, Abcam) - containing, modified Tyrode's buffer (pH = 6.5) followed by centrifugation with 1250 g for 10 min at RT. The pellet was then carefully re-suspended in modified Tyrode's buffer (pH = 7,4) and platelets were counted with an automated cell counter (ABX Micros ES60, Horiba Medical). Mouse blood was drawn intracardially from anesthetized (isoflurane (DeltaSelect), fentanyl i.p. (0.05 mg/kg body weight; CuraMed Pharma)) mice and processed as described for human platelets. For some experiments platelets were stained with either 4.5 μM CFDA-SE (Carboxyfluorescein diacetate succinimidyl ester, Molecular Probes) or 4.5 μM DDAO-SE (CellTrace Far Red, Molecular Probes) for 30 min at room temperature, followed by additional washing with modified Tyrode's buffer (pH = 6.5).

Plasma and serum preparation

Platelet poor plasma (PPP) was isolated from human or mouse anti-coagulated whole blood (ACD 1:7) and diluted in modified Tyrode's buffer (pH = 7.4) (1:1); followed by centrifugation with 1750 g for 10 min at RT. PPP from the supernatant was either used for experiments or further processed to generate serum. PPP was incubated with bovine thrombin (1 U/ml, Sigma) for 30 min at RT to initiate coagulation. Fibrin was removed from the solution by centrifugation (2000 g, 15 min, RT) and thrombin activity was blocked by adding 2U/ml Lepirudin (Refludan, Schering) and 40 μM PPACK (D- Phenylalanyl-prolyl-arginyl Chloromethyl Ketone, Enzo Life Science). To determine the protein concentration of serum, Bradford assays were performed (Quick Start Bradford Protein Assay, Bio-Rad) using bovine serum albumin (BSA) as protein standard. In some experiments, serum was further processed. To heat-denature serum proteins, samples were incubated at 37°C, 50°C, 70°C and 90°C (Thermomixer, Eppendorf) for 30 min and cooled down to RT prior to the experiment. To fractionate serum by size and to remove low molecular components, dialysis was performed against PBS using dialysis cassettes of 2 kDa molecular weight cut-off (Slide-A-Lyzer Dialysis Cassettes, Thermo Scientific).

Preparation of platelet supernatants

Supernatants of collagen-activated platelets were generated from PRP pre-incubated with 10 μg/ml fibrillar collagen (Chrono-Log) for 20 min at 37°C. Some preparations were performed in the presence of 2 U/ml apyrase (New England Biolabs) and 10 μM indomethacin (Sigma) or vehicle (Succinate buffer or Ethanol). Activated platelets were removed by centrifugation at 9000 g for 10 min and PPP containing the platelet releasate was used for experiments.

Functionalization of coverslips and migration assay

Plasma-coated coverslips

A plastic ring was glued to a coverslips (Desag 263 low alkaline glass, Bioptechs) to build a custom made migration chamber. The chamber was filled with modified Tyrode's buffer (pH = 7.4) supplemented with isolated plasma (1:1) and platelet activators (4 μM ADP (Sigma) / 2 μM U46619 (Tocris Bioscience)). Within 5 min at RT the coverslips were coated with a homogeneous protein layer (Turbill et al., 1996) as verified by AFM and immunostainings (see Figures S3H and S3I). Finally, PRP was added to reach a final concentration of $10x10^6$ platelets/ml. In some experiments, coating with fibrillar collagen (fCol) and plasma was performed by incubating coverslips with 200μg/ml fCol (Chrono-log) in plasma/thyrodes 7.4 (1:1) for 2 h at RT before adding PRP.

Serum/Fibrinogen-coated coverslips

A plastic ring was glued to coverslips (Desag 263 low alkaline glass, Bioptechs) to build a custom-made migration chamber. The chamber was filled with modified Tyrode's buffer (pH = 7.4) supplemented with isolated serum (concentrations as indicated), fibrinogen (concentrations as indicated) and platelet activators (4 μM ADP (Sigma) / 2 μM U46619 (Tocris Bioscience)). Washed platelets were added to reach a final concentration of $10x10^6$ platelets/ml.

HSA/Fibrinogen-coated coverslips

Coverslips (No. 1.5, D263T, Nexterion) were acid washed (20% HNO_3) for 1 hour at RT and thoroughly rinsed in ddH2O for another hour. Freshly cleaned coverslips were air-dried and silaned with hexamethyldisilazane (HMDS, Sigma) by spin-coating at 80 rps for 30 s. A plastic ring was glued to the pretreated coverslips to build a custom made migration chamber. Migration buffer containing modified Tyrode's buffer (pH = 7.4) was supplemented with adhesive proteins (fibrinogen (Sigma) or fibrinogen-Alexa488(−10 nm-gold) (Invitrogen)) and anti-adhesive proteins (rHSA (Sigma) or Casein (Sigma) or Ovalbumin (Sigma)), platelet activators (ADP (Sigma) / U46619 (Tocris Bioscience)) and divalent cations (calcium) at the concentrations indicated. If not otherwise stated the following concentrations were used: rHSA (1500 μg/ml) or casein (30μg/ml); fibrinogen (150 μg/ml), calcium (200 μM), ADP (4 μM), U46619 (2 μM). Washed platelets were added to the migration buffer to reach a final concentration of $10x10^6$ platelets/ml.

HSA/Fibrin(ogen)-Alexa488-coated coverslips

Coverslips were silaned as described above. To improve imaging quality, plastic channels (sticky slides, Ibidi) were used instead of plastic rings to build the migration chamber. Fibrinogen-Alexa488 coating: Channels were incubated with modified Tyrodes (pH 7.4) supplemented with 40 μg/ml Fibrinogen-Alexa488 (Invitrogen) and 2 mg/ml rHSA (Sigma) for 15 min at RT. Fibrin-Alexa488 coating: Channels were incubated with modified Tyrodes (pH 7.4) supplemented with 300 μg/ml Fibrinogen (Sigma) (1:10 spiked with Fibrinogen Alexa488 (Invitrogen)), 12 mg/ml rHSA (Sigma), 2U/ml bovine Thrombin (Sigma), 1 mM Calcium for 15 min at RT. After coating, slides were washed with PBS and washed platelets ($10x10^6$/ml) in modified Tyrodes buffer (pH 7.4) supplemented with plasma, anti-adhesive proteins, platelet activators, and divalent cations (see above) were added.

Immobilization of beads

Fibrinogen was biotinylated using the EZ-LinkSulfo-NHS-SS-Biotin kit (Thermo Fisher). HSA/Fibrinogen-coated slides were prepared as described above. Neutravidin-conjungated-200 nm (or 1 μm)-beads (FluoSpheres, Molecular Probes) were immobilized on biotinylated-Fibrinogen monolayers via the biotin-neutravidin bond.

Immobilization of bacteria

Bacteria (*E.coli or L. monocytogenes or MRSA USA300 or inactivated Staph. aureus*) were incubated on fibrin-coated slides (see above) for 30-60min h at 37°C. Slides were washed with Thyrodes buffer (pH 7.4) to remove non-adherent bacteria. Washed platelets ($10x10^6$/ml) in modified Tyrodes buffer (pH 7.4) supplemented with plasma, anti-adhesive proteins, platelet activators, and divalent cations (see above) were added.

In all experimental settings, platelet spreading and migration were subsequently observed using time-lapse video microscopy.

Characterization of plasma coated surfaces

Atomic force microscope (AFM) measurements were performed on a NanoWizard-II (JPK Instruments) AFM in ambient conditions. The AFM was operated in tapping mode, to minimize abrasion of the molecule layer by the AFM tip. Silicon cantilevers (BS Tap 300, Budget Sensors) with typical spring constants of 40 N/m and nominal resonance frequencies of 300 kHz were used. The nominal tip radius was smaller than 10 nm. The images were analyzed using SPIP (SPIP 4.5.2, Image Metrology).

Immunostainigs of fixed plasma coated coverslips were performed using the following primary antibodies (anti-fibrinogen (ab34269, Abcam), anti-vWF (ab6994, Abcam), anti-fibronectin (ab2413, Abcam)). Slides were incubated with antibodies for 1 h at RT, washed with PBS and stained with Alexa 488 labeled secondary antibodies (Molecular Probes) for another hour.

Time-lapse video microscopy

Differential interference contrast (DIC), Phase Contrast and Epifluorescence movies (1frame/12 s) were recorded on an automated inverted IX83 Olympus microscope with an UPlan 40x/1.0 or UPLSAPO-PH 100x/1.4 oil-immersion objective (Olympus) and a cooled CCD camera (XM10, Olympus). The microscope was equipped with a stage incubator (37°C, humidified, Tokai Hit).

Flow chamber assay

To observe platelet migration under flow conditions plasma-coated (see above) circular glass coverslips (40mm, Bioptechs) were placed into a parallel plate flow chamber (FCS2, Bioptechs) and incubated with migration buffer and PRP ($10x10^6$ platelets/ml). Once platelets were fully spread the flow-chamber was perfused with pre-warmed migration buffer (37°C; shear rate: 1300/s) using a recirculating air pressure pump (Ibidi) and migration was observed by time-lapse microscopy.

Bacterial trapping experiment under flow

E.coli were seeded on fibrin (Alexa488-labeled)-coated coverslips in the presence or absence of platelets for 1 hour at 37°C (see above). Microfluidic channels were then assembled (ibidi sticky slides $VI^{0.4}$ (ibidi)), connected to a syringe pump and placed on an inverted microscope (IX83, Olympus) with a heated stage. Channels were perfused with modified Tyrode's buffer (see above, 37°C) at 0.5 dyne/cm^2 to remove non-adhering bacteria. After 1 min Tyrode's buffer was perfused at 5 dyne/cm^2 for 5 min and subsequently at 50 dyne/cm^2 for 30 s. Images were taken after each perfusion step. Number and size of trapped bacteria was quantified manually using FIJI software (Schindelin et al., 2012). Bacteria were extracted from phase-contrast images and pseudo-colored in magenta.

Platelet phagocytosis assay

Human Fibrinogen (Sigma) was biotinylated with cleavable Sulfo-NHS-SS-Biotin using the EZ-LinkSulfo-NHS-SS-Biotin kit purchased from Thermo Fisher. Coverslips were then coated with Fibrinogen-Biotin and platelet migration experiments were performed as described above. Fibrinogen-Biotin removed from the surface and accumulated at the migrating platelet was traced by fluorescent labeling using Streptavidin-Alexa488 (SA488) (Invitrogen). Taking advantage of the cleavable SS-Biotin bond we designed 3 sets of experiments to determine the site of Fibrinogen accumulation (intracellular versus extracellular) (also see Figure S5D). I. Platelets were incubated with SA488 without further treatment; II. SS-Biotin was cleaved using TCEP (Tris-(2-carboxyethyl)-phosphin) (Sigma) prior to SA488 incubation; III. Platelets were permeabilized with Saponin and SS-Biotin was cleaved using TCEP prior to SA488 incubation. Mean fluorescence intensities (Alexa488) of platelet pseudonuclei were recorded for each condition. Fibrinogen localization (extracellular versus intracellular) was determined by comparing the relative loss of fluorescence in all conditions (also see Figure S5D).

Platelet tracking protocol

Spreading platelets (migrating and non-migrating) were counted manually and tracked using the ''Manual Tracking'' or the ''MTrackJ'' plugin in FIJI (Schindelin et al., 2012, Meijering et al., 2012). The fraction of migrating platelets was calculated by dividing the number of migrating platelets by the total number of spreading (migrating and non-migrating) platelets. The pseudonucleus of a migrating platelet served as a morphological landmark for tracking. Platelets moving a distance $\geq$ 1 platelet diameter were classified as migrating. In some experiments, the straightness of migration was calculated by dividing the Euclidean distance of migration by the accumulated distance of migration. The directionality toward a vessel injury was quantified by the forward migration index (FMI), defined by the ratio of the fractional displacement along the line connecting starting point of migration and injury and the total accumulated distance of migration; maximal directionality = 1; minimal directionality = -1. The duration of platelet migration is plotted in respect to the initial starting-point within the observation time and duration $_{\text{effective}}$ / duration $_{\text{max}}$ defines the ratio of the effective duration of migration or spreading and the maximum duration possible in respect to the initial starting-point. For representation of *in vivo* migration tracks the starting points were normalized to zero and plotted in respect to the direction of blood flow or the localization of the vessel injury. Heatmaps illustrating retraction speed and fibrinogen removal were generated using QFSM software (Mendoza et al., 2012).

Shape analysis

We performed an unbiased, systematic analysis of platelet shapes to analyze the morphological variations of migrating and non-migrating platelets without pre-selecting particular shape measurements (e.g., area or cell-diameter). Platelet shapes were represented as polygonal outlines and principal component analysis (PCA) was performed to extract principal modes of shape variation along which to measure each platelet. Platelet shapes from DIC movies were manually masked and converted into binary images using FIJI (Schindelin et al., 2012). Polygonal outlines were extracted from masks and sampled at evenly spaced 200 points. To ensure that all polygons were orientated equally, an algorithm based on Procrustes analysis was used to rotate and translate the polygons until corresponding points were optimally aligned. Next, we used the pseudonucleus as a characteristic landmark defining the rear of a migrating platelet. The pseudonuclei were manually marked in FIJI and extracted to another set of binary images. This additional landmark was also used in the Procrustes procedure and improved the alignment. Finally, the alignment was manually verified. Aligned contours were further analyzed by principle component analysis. The principle components, scaled by the standard deviation of the analyzed population for each mode of shape were depicted. To explore whether the classified shape modes allow the discrimination of functionally distinct platelet subpopulations (e.g., migrating versus non- migrating), platelet polygons were arrayed in a scatterplot. Finally, the following cellular characteristics were measured based on shape modes detected by PCA: (1) Area in μm^2 (mode 1) and (2) Aspect Ratio = long axis/short axis (mode 2). In some experiments polygon curvature was measured as an approximation of membrane roughness. The average of the absolute values of the point wise curvature of the contour is computed over a specified range, and multiplied by the contour length over the same range. Absolute values must be used because otherwise positive and negative curvatures would cancel out; the sum is multiplied by the arc length to make the measurement scale-invariant. All algorithms are implemented in the ''Celltool'' software package (Pincus and Theriot, 2007). To analyze the spatio-temporal coordination of leading-edge protrusion and trailing edge retraction kymographs were extracted along the central axis of migrating platelets.

Immunofluorescence of migrating platelets

Polarized, migrating or spread, non-migrating platelets were fixed at 37°C in 1% paraformaldehyde for 10 min. Platelets were washed three times with PBS and incubated with 2% Glycin (Roth) for 5 min, followed by incubation with 0.2% Triton X-100 (Fluka) and 3% bovine serum albumin (Roth), to permeabilize the cells and to block unspecific binding, respectively. For αIIbβ3 staining, platelets were incubated for 1 h at RT with primary antibodies (1:50, clone HIP8, Abcam) followed by 1 h at RT with secondary antibodies (goat anti-mouse IgG Alexa488, 1:200, A11001, Molecular Probes). Activated αIIbβ3 was stained in live cells during migration for 20min (PAC1-FITC, 1 μg/ml, BD) followed by incubation for 1 h at RT with secondary antibodies (rabbit anti-FITC Alexa488, 1:200, A11090, Molecular Probes). Filamentous actin was stained by Rhodamin-Phalloidin (1:40, Molecular Probes).

Images were captured on a Zeiss LSM 780 confocal microscope using a Plan-Apochromat 100x/1,46 Oil DIC objective (Carl Zeiss Imaging).

Fura-2 imaging of migrating platelets

Platelets were loaded with 5 μM Fura-2/AM (Invitrogen) at 37°C, 25 min before imaging. Fura-2 images were taken on an inverted iMIC2 (FEI) stand equipped with a climate chamber (37°C, humidified) (ibidi) and using an UplanSApo 60x/1.35 oil-immersion objective (Olympus). 340 nm and 380 nm filters were used for the excitation of Ca^{2+}-bound Fura-2 and Ca^{2+}-free Fura-2, respectively and emission at 510 nm was captured with an EMCCD camera (iXon 897, Andor), gain = 120. Time-lapse movies were recorded with a frame rate of 1/30 s. Image processing was performed as previous published by using FIJI (Kardash et al., 2011, Tsai and Meyer, 2012). Briefly, mask images to separate platelets and the background were created by manually drawing the platelet contour in the bright field image. Background subtraction was performed using the "rolling ball" algorithm. To determine intracellular Ca^{2+} oscillations, the ratio images (Ca^{2+}-bound/Ca^{2+}-free) were created by dividing the images generated using 340 nm over 380 nm excitation of Fura-2.

pMLC western blot

Washed human platelets, suspended in migration buffers were activated in the presence or absence of 100 mM citrate. In some experiments platelets were pretreated with BAPTA-AM. After the indicated time points, platelet suspensions were centrifugated at 1900xg for 8 min at RT in a microcentrifuge. Obtained platelet pellets were homogenized in RIPA buffer containing protease and phosphatase inhibitor cocktails (Thermo Fisher Scientific). Equal amounts of total protein (50μg) were subjected to western blot analysis. The signal from the phosphorylated Myosin Light Chain (anti-pMLC; 1:1000, Abcam) was normalized for that of total Myosin Light chain using an antibody against Myosin Light Chain (1:1000, Cell Signaling Technology). Immunoreactive protein bands were detected using horseradish peroxidase-labeled secondary antibodies (1:2000, Cell Signaling Technology) and enhanced chemiluminescence western blotting detection reagents (Perkin Elmer).

Correlative electron microscopy (SEM/FIB-SEM)

SEM/FIB-SEM was performed as previously described (Wanner et al., 2013). Briefly, platelets were embedded in epoxy resin on laser-marked coverslips. Platelets selected for light microscopy were relocated in the SEM. Tomographic datasets were obtained by the 'slice and view' technique using a Zeiss Auriga 40 crossbeam workstation (Carl Zeiss Microscopy, Oberkochen, Germany). For milling with the focused Ga-ion beam, the conditions were as follows: 0.5–1 nA milling current of the Ga-emitter; with each step 10–15nm of the epoxy resin was removed by milling with the FIB. SEM images were recorded with an aperture of 60 μm in the high current mode at 1.5 kV of the in-lens EsB detector with the EsB grid set to −1000 V. Depending on the respective magnification, voxel size was in a range between 3.5 and 5 nm in x/y and 10–15 in z. Contrast of the images was inverted to conventional bright field.

Bacterial viability

Platelets were incubated with MRSA for 90 min at 37°C as described above and bacterial viability was subsequently determined using the LIVE/DEAD BacLight Bacterial Viability Kit from Thermo Fisher Scientific. Ethanol-treated bacteria (70% for 10 min) were used as positive control, untreated bacteria were used as negative control. Briefly, slides were stained with propidium iodide (PI) and Syto 9 for 15 min at 37°C. While PI enters only dead cells with compromised membranes (Excitation/Emission: 536/617), Syto 9 enters all cells (Excitation/Emission: 485/498). Fluorescent images were recorded on an automated inverted IX83 Olympus microscope with an UPlan 40x/1.0 or UPLSAPO-PH 100x/1.4 oil-immersion objective (Olympus) and a cooled CCD camera (XM10, Olympus). The microscope was equipped with a stage incubator (37°C, humidified, Tokai Hit). Live and dead bacteria were counted using the "Find Maxima" function in FIJI (Schindelin et al., 2012).

Neutrophil migration, phagocytosis, calcium imaging and NETosis

Platelets were incubated together with MRSA or pHrodo Red S. aureus Bioparticles Conjugate for Phagocytosis (Thermo Fisher Scientific) on fibrin-coated substrates (see above) to allow migration and bundle formation (90 min at 37°C; also see above). Neutrophils ($1x10^6$) were then added in RPMI media (RPMI 1640 with 1% FBS and 10mM HEPES) and live cell imaging was performed to track migration of neutrophils and to measure their interaction with platelet-bound bacterial bundles. Phagocytosis was visualized by the increased fluorescence intensity of pHRodo within phagolysosomes using epifluorescence microscopy according to the manufacturer's protocol. Neutrophils isolated from *LysM-Cre/PC-G5-tdT* (JAX#024477) calcium-reporter-mice were used to measure intracellular calcium oscillations during interaction with platelet-bacteria bundles. Neutrophils from these mice express the calcium indicator variant, GCaMP5G (GFP) and tdTomato. tdTomato signal was used to normalize the intracellular calcium signal (GFP).

NETosis was visualized by staining neutrophils after 90 min of incubation with platelet-bacteria-bundles with SYTOX Green Nucleic Acid Stain (1 μM, Thermo Fisher Scientific) to label extracellular DNA. Cells were counterstained with Hoechst 33342 (Thermo Fisher Scientific) and the fraction of neutrophils undergoing NETosis was measured as fraction of SytoxGreen positive cells.

QUANTIFICATION AND STATISTICAL ANALYSES

Statistical parameters, including the exact value of replicates (“n”) for individual experiments can be found within the figure legends. t tests and analysis of variance (ANOVA) were performed after data were confirmed to fulfill the criteria of normal distribution (Kolmogorov-Smirnov-test), otherwise Kruskal–Wallis- or wilcox-rank-sum-tests were applied. If overall ANOVA or Kruskal–Wallis-tests were significant, we performed a post hoc test (Tukey-HSD for ANOVA and wilcox-rank-sum post hoc test for Kruskal Wallis, respectively). In matched-sample experiments, the paired t test was used. Survival was analyzed using the log rank test. A p value of < 0.05 was considered statistically significant. Analyses were performed with R (http://www.r-project.org/; R Core Team, 2014) or IBM SPSS Statistics 22.

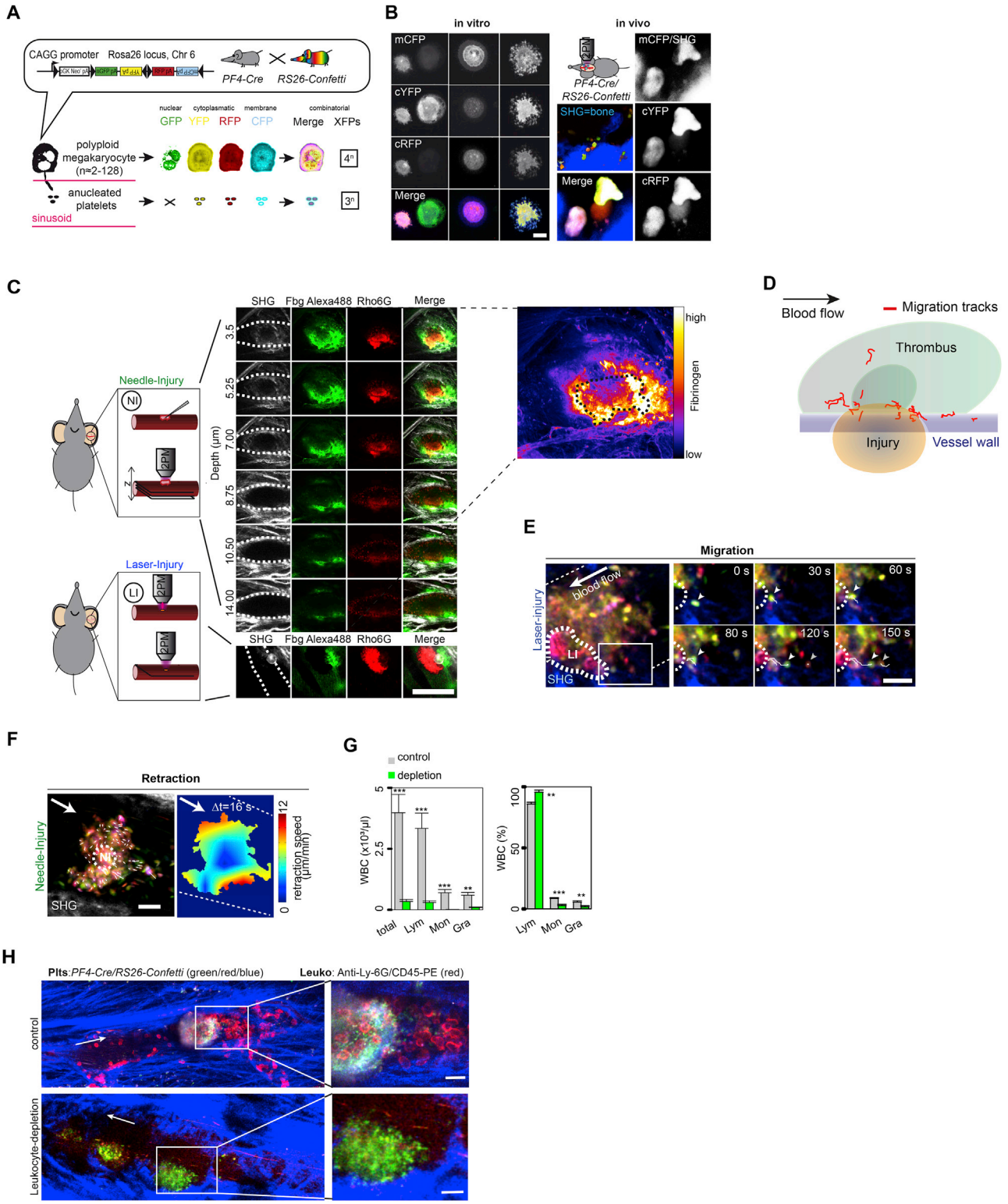

Figure S1. Imaging of Single Platelets at Vascular Injuries *In Vivo*, Related to Figure 1

(A) Principle of multicolor labeling of megakaryocytes and platelets using the *PF4-Cre/R26R-Confetti* mouse model. After Cre-mediated recombination the *R26R-Confetti*-Reporter stochastically drives expression of one out of the four fluorescent proteins mCFP, nGFP, cYFP or cRFP (Snippert et al., 2010). Mature

(legend continued on next page)

megakaryocytes, the direct platelet precursor cells, are highly polyploid, thus expressing more than one *R26R-Confetti*-transgene. Consequently, Cre-recombination results in combinatorial expression of multiple fluorescent proteins. Color diversity is retained on the platelet level.
(B) Confocal sections of megakaryocytes isolated from *PF4-Cre/R26R-Confetti* mice (left). 2P-IVM of the calvarian bone of *PF4-Cre/R26R-Confetti* mice (right). Note that our imaging setup (also see STAR Methods) does not allow detection of GFP-positive nuclei. SHG = Second Harmonic Generation. Scale bar, 20 μm.
(C) Models of microvascular injury and inflammation of the mouse ear. Needle injuries were performed using a 30G needle and a z-scan of the vessel surface shows the localized injury. Laser injuries were induced by focusing the laser-beam of the 2-photon microscope on the vessel wall (dashed lines indicate the vessel wall). Note the destroyed collagen architecture (Second Harmonic Generation = SHG) and the accumulation of fibrin(ogen) at the site of injury in both models (Fibrinogen labeled with Alexa488 dye). Fibrin(ogen) is non-uniformly distributed at the site of injury with a maximum at the center of the lesion, as highlighted by the color-coded intensity of Alexa488-labeled fibrinogen (magnified at the right). The black dashed line outlines a platelet-rich thrombus. Note the high density of platelets. Scale bars, 50 μm.
(D) Migration tracks of individual platelets were manually aligned, scaled and depicted in respect to the site of injury and the thrombus. Please note the preferential location at the outer border of the injury and the thrombus.
(E) Migrating platelets after laser-injury are highlighted by arrow-heads and migration paths are indicated as white lines.
(F) Clot retraction following needle-injury *in vivo* (2P-IVM). Vector maps are overlaid (white arrows); heatmaps show retraction speed. Dashed white line highlights the injury.
(G) Leukocytes were depleted prior to experiments to exclude leukocyte dependent platelet motility. Depletion of circulating white blood cells by i.p. injection of anti-CD45 (clone 30F11) and anti-Ly6G/C (clone RB6-8C5). control: n = 10; depletion: n = 13; p values < 0.05 indicate significance; mean ± SEM; wilcox-test.
(H) Local depletion efficiency at the site of injury was verified after each experiment by i.v. injection of fluorescently labeled CD45/LY6G/C antibodies. Scale bar, 10 μm.

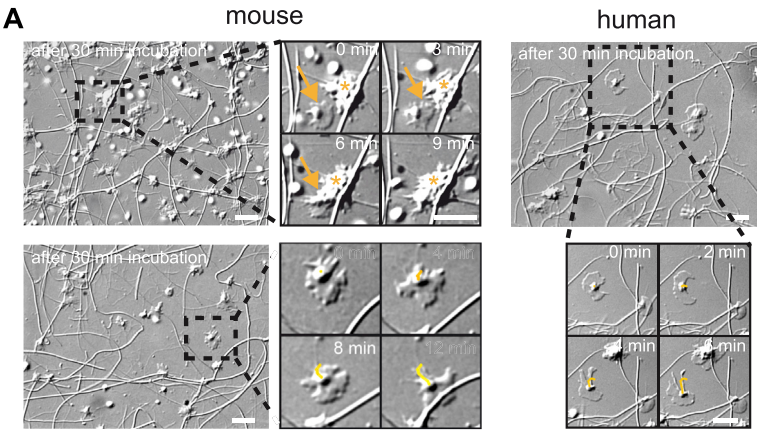

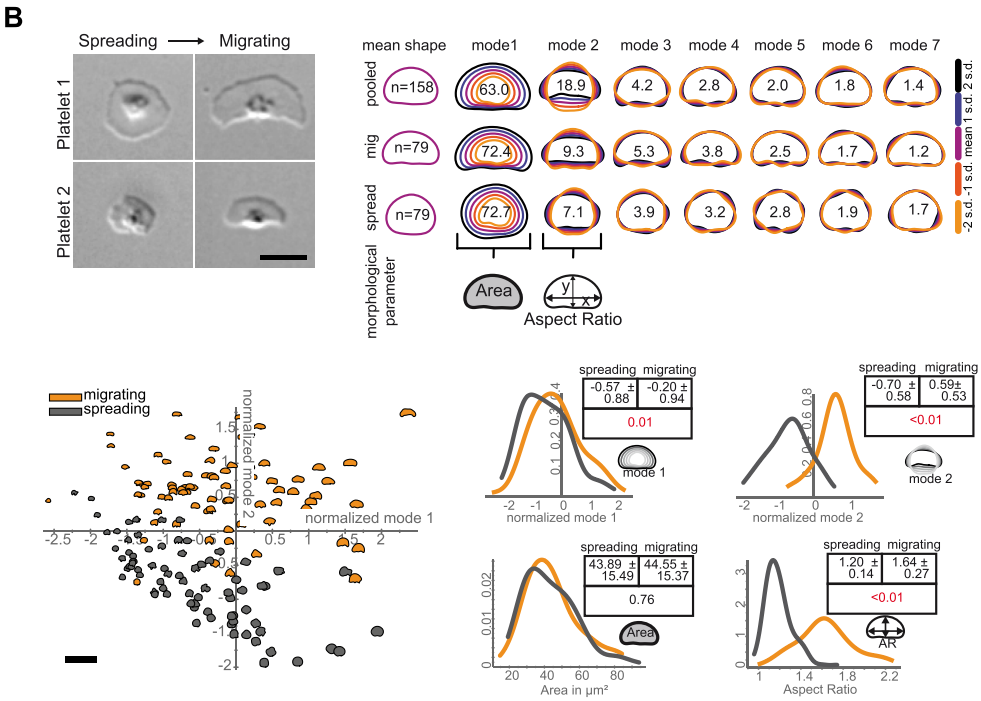

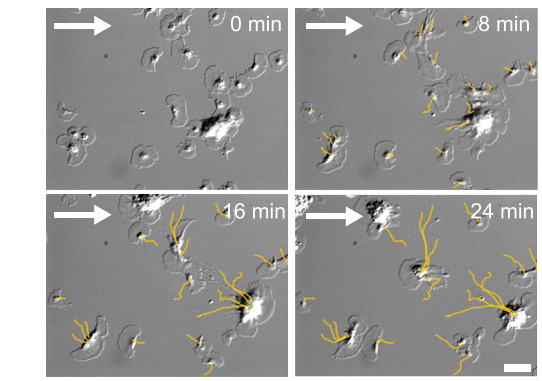

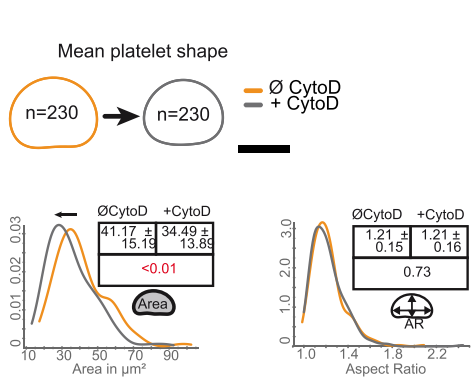

(legend on next page)

Figure S2. Platelets Actively Migrate by Adopting a Characteristic Shape, Related to Figure 2

(A) Platelets polarize and migrate on adsorbed plasma proteins in the presence of collagen fibers. Platelets spreading on plasma proteins and fibrillar collagen after 30 min of incubation were visualized by DIC time lapse microscopy. Motile platelets (arrowhead) were either incorporated into a micro- aggregate (*) (upper left) or stuck to collagen fibers (lower left). Migration was observed in mouse (left) and human (right) platelets. Scale bar, 10 μm.

(B) Polarized, migrating platelets were quantitatively discriminated from spreading, non-migrating platelets by shape. Upper left: representative DIC micrographs of platelets before and after polarization. Upper right: The mean shape and the principal modes of shape variability are shown for the spreading, non-migrating, the polarized, migrating and the pooled platelet population; the number of analyzed platelets is indicated for each group. The mean and the first and second standard deviation (SD) is shown for each shape mode of each platelet population. The contribution of each shape mode to the total shape variation within the population is indicated in %. Each shape mode is assigned to a characteristic morphological parameter: area, aspect-ratio. Scale bar, 5 μm. Lower left: Scatterplots arraying spreading, non-migrating and polarized, migrating platelets by SD-normalized shape mode 1 and 2. Scale bar, 25 μm. Lower right: Smooth density histograms displaying shape modes, area and aspect ratio (x axis) as a density function (y axis). Note, the similar population-shift of mode 2 and aspect ratio. The table shows mean ± SD; p values < 0.05 (red) indicate significance; paired t test.

(C) Platelet migration is resistant to arterial shear rates (1300/s). White arrow indicates flow direction.

(D) Left: the mean platelet shapes are shown for treatment with Cytochalasin D (2 μM) and vehicle; scale bar, 5 μm. μRight: smooth density histograms displaying area and aspect ratio before and after Cytochalasin D treatment; the table shows mean ± SD; p values < 0.05 (red) indicate significance; platelets were pooled from n = 5 experiments; paired Wilcox test.

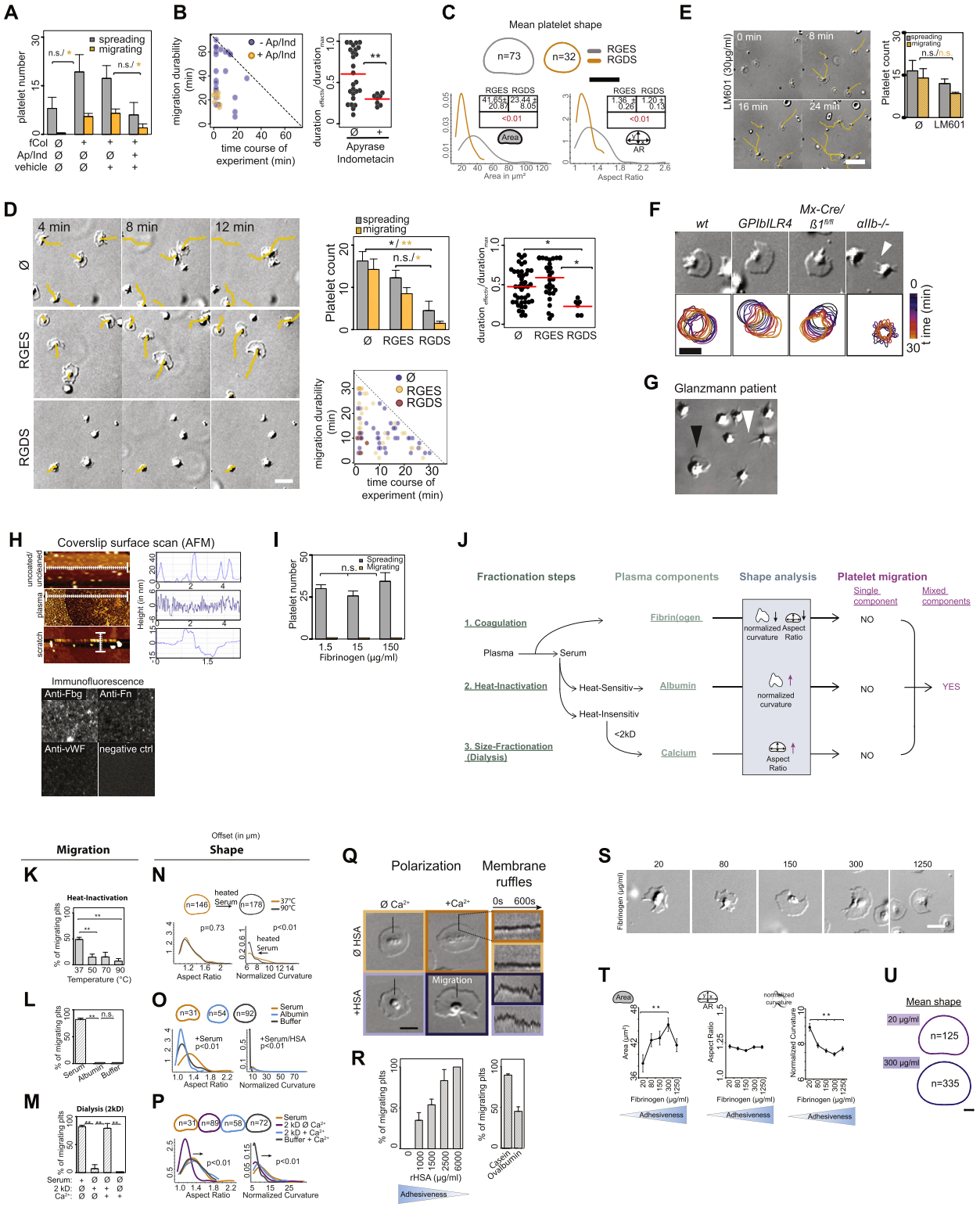

Figure S3. Platelet Migration on Plasma Proteins Requires Platelet Activation and Depends on $\alpha_{IIb}\beta_3$ Integrin Ligation and Substrate Adhesiveness, Related to Figure 3

(A and B) Paracrine ADP and TXA2 release facilitates platelet locomotion. (A) Migration and spreading was quantified for platelets incubated in conditioned plasma supernatants from platelets activated with fibrillar collagen (+/− fCol) (10 µg/ml) in the presence of Apyrase (2 U/ml) and Indomethacin (10 µM)

(legend continued on next page)

(+/− Ap/Ind). n = 4 experiments; error bars, SEM; Student's t test. (B) Duration of single platelet migration was plotted in respect to the initial starting-point within the observation time of 60 min and the ratio of the effective duration ($duration_{effective}$) and maximum duration possible in respect to the starting point ($duration_{max}$) is shown. Red bars indicate mean; platelets were pooled from n = 4 experiments; Student's t test. (C–G) Platelet migration depends on αIIbβ3 integrin ligation. (C) Human platelets were treated with 200 μM RGDS (inhibitory peptide) or 200 μM RGES (non-inhibitory control). The mean shapes are shown for the indicated groups and the measured platelet numbers are depicted. Scale bar, 5 μm. Smooth density histograms displaying area, aspect ratio and normalized curvature (x axis) as a density function (y axis). The table shows mean ± SD; p values < 0.05 (red) indicate significance; Student's t test.

(D) Platelet migration and spreading was quantified. n = 4 experiments; error bars, SEM; ANOVA/TukeyHSD; scale bar, 10 μm. Duration of single platelet migration was plotted in respect to the initial startingpoint within the observation time of 65 min and the ratio of the effective duration ($duration_{effective}$) and maximum duration possible in respect to the starting-point ($duration_{max}$) is shown. Platelets were pooled from n = 4 experiments; red bars indicate mean; Kruskal-Wallis/Wilcox.

(E) Time series of platelets migrating in the presence of αvβ3 integrin blocking antibody (LM609, 30μg/ml). Quantification of platelet spreading and migration did not reveal a significant difference compared to the control group. n = 16 platelets pooled from 2 experiments; mean; n.s. = not significant ($p \geq 0.05$); Student's t test; scale bars, 5 μm.

(F) Representative DIC micrographs and corresponding color-coded time series of migrating platelets isolated from mice with mutated adhesion receptors. αIIb-deficient platelets did not spread on immobilized plasma and only formed short filopodia (white arrow head). Scale bar, 5 μm.

(G) Platelets isolated from a patient with Glanzmann thrombasthenia were seeded on plasma protein coated coverslips. Platelets did not migrate and only a small fraction formed unstable lamellipodia (black arrow head) and extended short filopodia (white arrow head). H-Q: Platelet migration depends on substrate adhesiveness and calcium.

(H) Surface topography of an uncoated and a plasma-coated coverslip was measured by atomic force microscopy (AFM). Note that after cleaning and coating, slides are covered by a homogeneous protein layer (≈15 nm) with only small height variations of (≈6 nm), while larger irregularities (≈50 nm; most likely representing dust) were removed. (I) The presence of immobilized, adhesive platelet-binding plasma proteins was confirmed by immunostainings for Fibrinogen (Fbg), Fibronectin (Fn) and von Willebrandt Factor (vWF).

(J) Schematic summary of our fractionation protocol showing the relationship of plasma components, platelet shape and migration.

(K–M) Platelet migration was quantified for the indicated treatments. Platelets were pooled from n = 4 (D) or n = 3 (E,F) experiments; mean ± SEM; ANOVA/TukeyHSD.

(N–P) Corresponding mean platelet shapes and density histograms of aspect ratio and normalized curvature are shown. Kruskal-Wallis/wilcox.

(Q) Representative DIC micrographs and related kymographs. Note the increased aspect ratio in the presence of calcium and the higher membrane roughness in the presence of albumin.

(R) Anti-adhesive proteins trigger platelet migration. rHSA (recombinant human serum albumin); Casein (200 μg/ml); Ovalbumin (10 mg/ml); n = 3.

(S) DIC micrographs of platelets migrating on various concentrations of Fibrinogen (scale bar, 5 μm).

(T) Quantification of platelet morphology on various concentrations of Fibrinogen (20: n = 125; 80: n = 239; 150: n = 340; 300: n = 335; 1250: n = 250; mean ± SEM; Kruskal-Wallis-Test/ pairwise wilcox; ** = $p < 0.01$). (U) Mean platelet contours (scale bar, 1 μm).

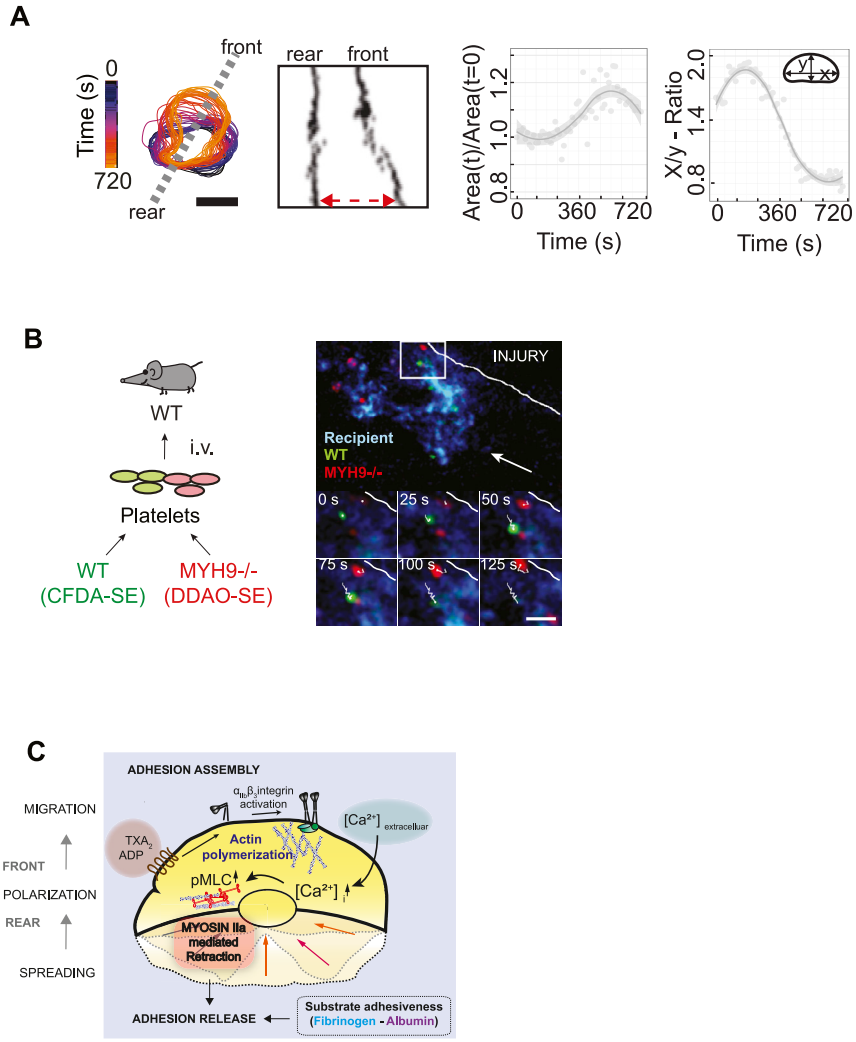

Figure S4. Extracellular Calcium Mediates the Switch from Spreading to Migration by Myosin-IIa-Dependent Trailing Edge Formation, Related to Figure 4

(A) Platelet outlines (from Figure 4G) and the corresponding kymograph reveal the functional dissociation of front and back resulting in platelet elongation (red arrows). X/y-Ratio and area was measured over time. Scale bars, 5 μm.

(B) Washed platelets from *PF4-Cre-/MYH*$^{fl/fl}$- and *PF4-Cre+/MYH9*$^{fl/fl}$ mice were stained with CFDA-SE or DDAO-SE, respectively and competitively transfused into *PF4-Cre/R26R-Confetti* mice. White arrows indicate blood flow. White lines indicate migration paths. Scale bar, 10 μm.

(C) Platelet migration requires a characteristic front-rear polarity. Actin-mediated protrusions and integrin-dependent adhesions are formed at the leading edge. A calcium-mediated increase in myosin IIa-dependent contractile forces then initiates retraction and adhesion release at the platelet rear resulting in forward locomotion.

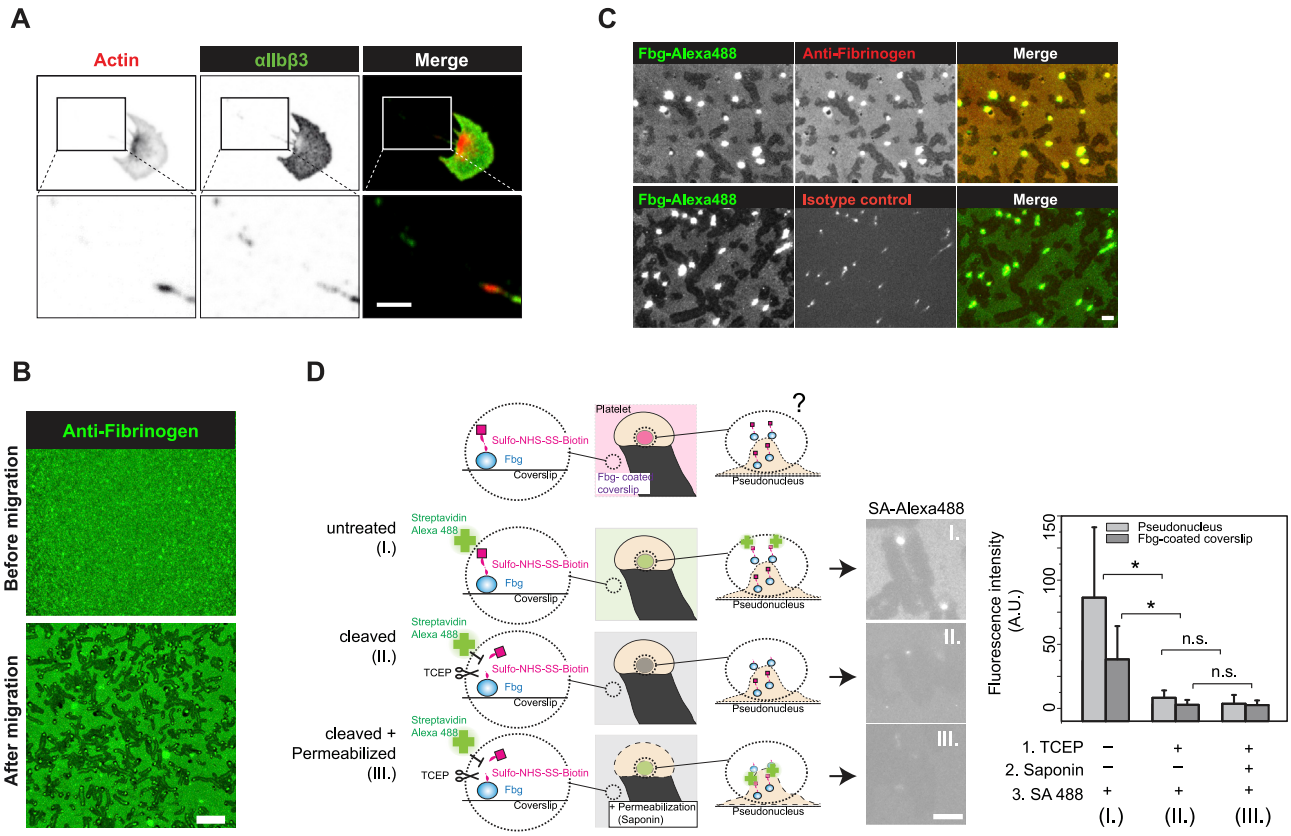

(legend on next page)

Figure S5. Platelet Migration Is Coupled to Fibrin(ogen) Removal, Related to Figure 5

(A–D) Adhesions to the substrate are released by substrate removal. (A) Immunostainings of actin (Phalloidin) and αIIbβ3 (clone: Hip8) show that only a minor fraction of cytoskeleton/integrin is released from platelets during migration. Scale bar, 5 μm. (B) Immunostaining of fibrinogen before and after platelet migration shows the removal of fibrinogen. Scale bar, 50 μm. (C) Fibrinogen-Alexa488 (40 μg/ml) is a reliable fluorescent reporter for fibrinogen removal (also see Figure 5A). Immunostainings of fibrinogen were negative in areas of fibrinogen-Alexa488 removal. Scale bar, 5 μm. (D) Biotinylation of fibrinogen shows that the major fraction of fibrinogen accumulated at the pseudonucleus is deposited on the platelet surface (also see Figure 5G). Left: cartoon showing the experimental design (also see STAR Methods). Right: Cleavage of Sulfo-NHS-SS-biotin from fibrinogen after migration shows a significant reduction of Streptavidin (SA)-Alexa488 intensities (II.). No increase in fluorescence-intensity was measured when platelets were permeabilized (III.) before the incubation with SA-Alexa488, indicating that the major fraction removed biotinylated-fibrinogen remained on the platelet surface and is not endocytosed. TCEP = Tris(2-carboxyethyl)phosphine. n = 4 experiments; mean ± SEM; ** = $p < 0.01$; Kruskal-Wallis/wilcox; scale bar, 10 μm.

(E–G) Platelets migrate on fibrin. (E) Time-lapse sequence of a platelet migrating on fibrin. Phase-contrast and epifluorescence micrographs (fibrin-Alexa488 generated from 840μg/ml fibrinogen; see STAR Methods) are shown for the indicated time-points. Scale bar, 10 μm. Right: Percentage of migrating platelets and area of fibrin removed per platelet was quantified (control, cytoD, C7E3-Fab: n = 5; Bleb: n = 3). Δt = recording time; mean ± SEM; ANOVA/Tukey-HSD/Student's t test. * = $p < 0.05$; ** = $p < 0.01$ (F) Upper left: DIC and epifluorescence micrographs of a platelet migrating on Alexa488-10 nm-gold-labeled fibrin. Scale bar, 10 μm. Upper right: 3D-reconstruction from a FIB-SEM stack showing the same platelet. Fibrin (green), fibrin-bound gold (yellow) accumulate at the pseudonucleus of the migrating platelet (arrow); scale bar, 500 nm. Lower: FIB-SEM section of the pseudonucleus showing fibrin (green arrowhead) and fibrin-bound gold (yellow arrowhead) accumulating on the surface of the platelet; scale bar, 500 nm. (G) Left: DIC and epifluorescence micrograph of a platelet migrating on Alexa488-labeled fibrin. Scale bar, 10 μm. Right: The same platelet is shown at higher resolution by scanning electron microscopy. Platelets remove the fine meshwork as well as larger strands while migrating over fibrin (arrowheads). Scale bars, 10 μm and 1 μm.

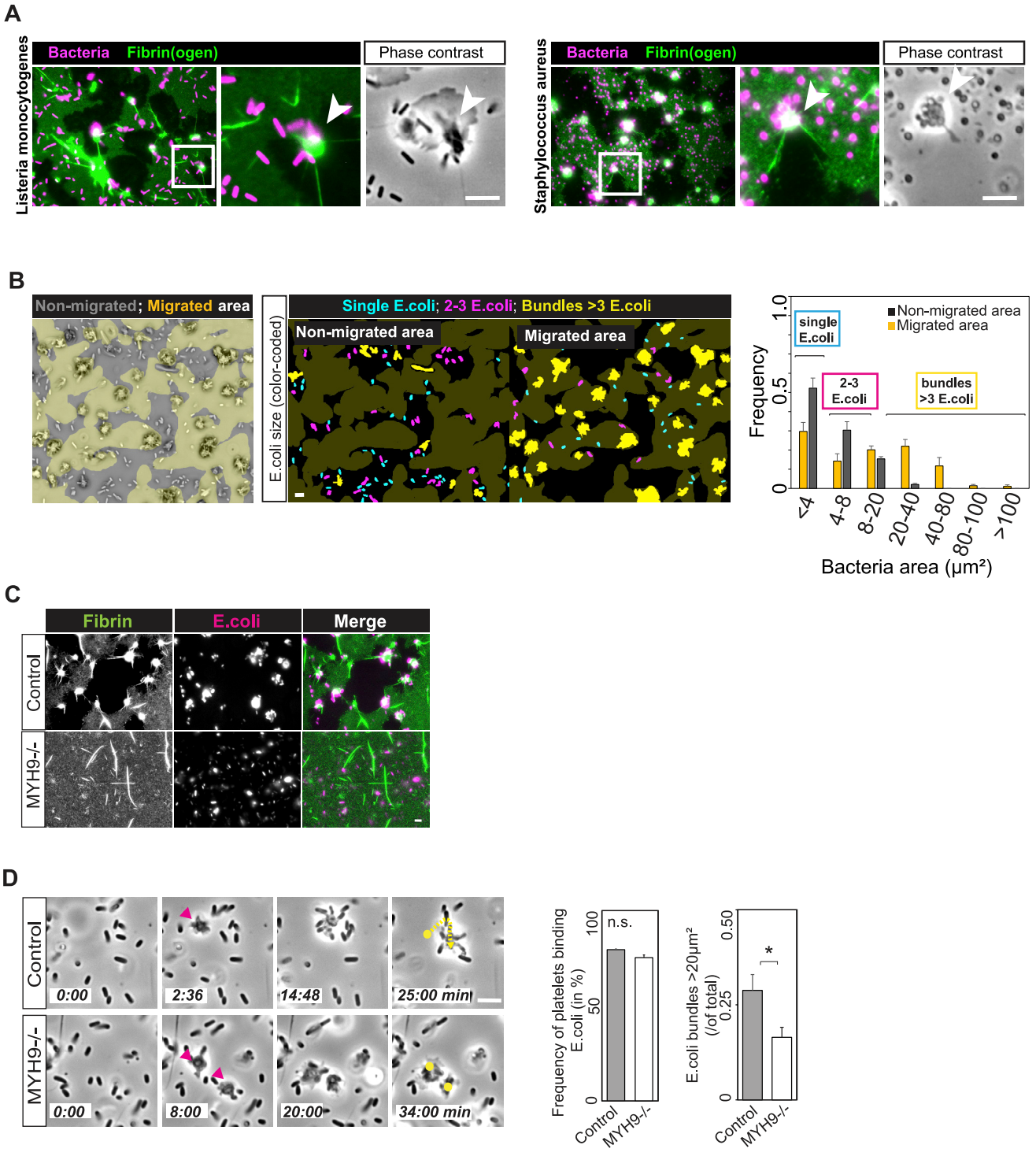

Figure S6. Migrating Platelets Collect and Bundle Fibrin-Trapped Bacteria, Related to Figure 6

(A) Migrating platelets collect gram-positive bacteria (inactivated Listeria monocytogenes and inactivated Staphylococcus aureus): Phase-contrast and epi-fluorescence micrographs show bacteria (magenta) and Alexa488-labeled fibrin (green). Bacteria accumulate at the pseudonucleus (arrowhead).

(B) Left: Platelets were migrating on a fibrin-Alexa488-coated and *E.coli*-colonized coverslip. The total area was segmented into migrated (yellow) and non-migrated (gray) fractions based on the remaining fluorescent signal (fibrin-Alexa488). *E.coli* aggregates were measured by size and a color-coded overlay is shown for the migrated and non-migrated areas. Aggregates with more than 3 *E.coli* are indicated as bundles (yellow). Right: Histogram showing the size distribution (area in μm^2) of *E.coli* aggregates for migrated and non-migrated areas. Bundles > 3 *E.coli* have a size larger than ~20 μm^2.

(legend continued on next page)

(C) Migration facilitates collection and accumulation of *E.coli* by platelets. Epifluoresence micrographs of fibrin (green) and *E.coli* (magenta) after 1 h of platelet-migration (control, *PF4-Cre/MYH9*$^{fl/fl}$); mean ± SEM.

(D) Time series of platelets (pink arrow heads) spreading on fibrin-coated coverslips grown with *E.coli.* Notably, both migrating (control) and non-migrating (*PF4-Cre/MYH9*$^{fl/fl}$) platelets can bind *E.coli*. However, migrating platelets are more efficient in interacting with bacteria as they cover a larger territory due to motility (indicated by yellow dashed line). As a consequence, migrating platelets bind larger numbers of *E.coli* as indicated by the more efficient formation of bacterial bundles (also see Figure 6E), n = 3, mean ± SEM, wilcox-test, * = $p < 0.05$. Scale bars, 5 μm.

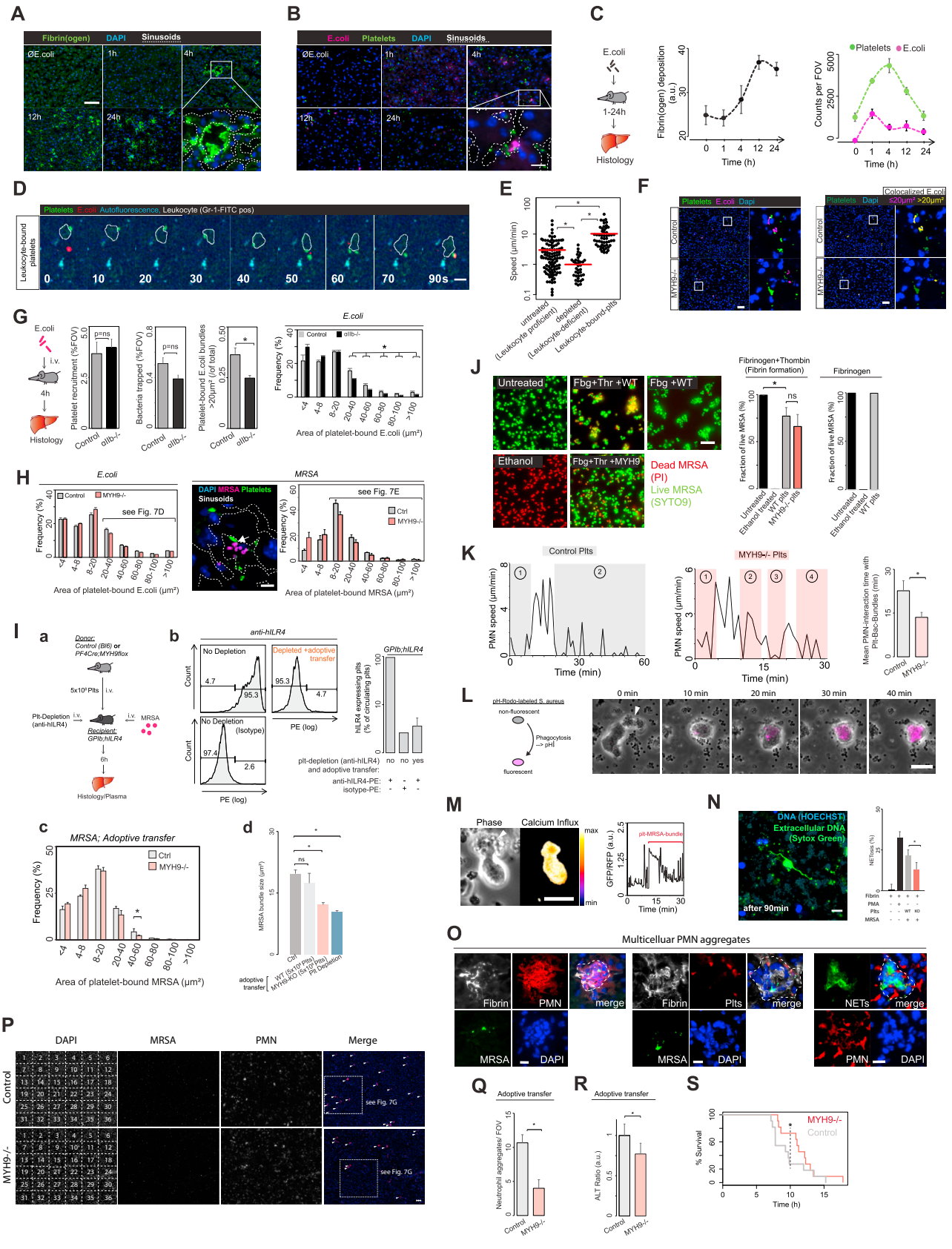

(legend on next page)

Figure S7. Migrating Platelets Bundle Bacteria *In Vivo* and Boost Neutrophil Activation, Related to Figure 7

(A and B) Epifluorescence micrographs (cropped from mosaic scans with stitched adjacent tiles) show liver sections of systemic (i.v.) *E.coli*-infected mice at the indicated time points after infection. (A) green = fibrin(ogen); blue = DAPI; dashed line indicates sinusoids. (B) magenta = *E.coli*; green = platelets; blue = DAPI; dashed line indicates sinusoids. Scale bar, 50 μm.

(C) Quantitative analysis of A, and B, (n = 4). Platelet recruitment to the liver is highest at 4h after infection.

(D) 2P-IVM time series of a leukocyte (Gr1-FITC labeled; white outline) carrying a bound platelet (green) liver when migrating within liver sinusoids after *E.coli* infection; scale bar, 10 μm.

(E) Autonomous platelet migration in liver sinusoids is distinct from passive leukocyte-mediated motility. Platelets bound to leukocytes (Gr1-FITC-labeled) move with the average speeds of migrating leukocytes (~10 μm/min) (Sreeramkumar et al., 2014), while active autonomous platelet migration in the absence of leukocytes (depletion) is significantly slower (~1 μm/min) (see Figure 7B). Consequently, mean platelet speeds are lower in leukocyte-deficient animals that lack passive leukocyte-mediated platelet motility. Untreated (leukocyte proficient): n = 104 (pooled from 3 experiments), depleted (leukocyte deficient; anti-Ly6G/C (200 μg/mouse 24h prior to injury; clone RB6-8C5)): n = 40 (pooled from 2 experiments), Leukocyte-bound: n = 53 (pooled from 3 experiments); platelet-leukocyte binding was enhanced by i.v. injection of LPS (25 μg/mouse) (Clark et al., 2007); red bars, mean; Kruskal-Wallis/wilcox; * = $p < 0.05$.

(F) left: Representative micrographs of liver cryo-sections (cropped from mosaic scans with stitched adjacent tiles) 4 h after infection with *E.coli*. Platelets (anti-CD42b; green) and *E.coli* (anti-*E.coli* O- and K-antigen; magenta) were tresholded based on fluorescence intensities and pseudo-colored for illustration. Scale bar, 50 μm. right: Data obtained on the left was further analyzed using Imaris software (Bitplane) to retrieve *E.coli* colocalizing with platelets. Liver cryo-sections (from left,) highlighting *E.coli* colocalizing with platelets (*E.coli* $\leq$ 20 μm^2 = magenta; *E.coli* > 20 μm^2 = yellow); platelets = dark-green; DAPI = blue; scale bar, 50 μm; (also see Figure 7D).

(G) Platelet and bacteria recruitment to liver sinusoids of $\alpha IIb-/-$ mice is comparable to controls while platelet-bacterial-bundling is reduced. n = 4; mean ± SEM; wilcox-test; * = $p < 0.05$.

(H) Histograms showing size distribution of platelet-bound bacteria. Size cut-offs used for quantification (see Figures 7D and 7E) are indicated by brackets. Confocal image shows a platelet bundling *MRSA (methicillin resistant Staphylococcus aureus)* within the liver sinusoids. Scale bar, 5 μm.

(I) a, Control or MYH9−/− platelets were transfused into platelet-depleted *GPIb;hILR4 mice* and sepsis experiments were performed. b, Efficiency of platelet depletion and transfusion was controlled for each mouse using flow cytometry (mean ± SD). c, Histograms showing size distribution of platelet-bound bacteria. Transfused control platelets formed significantly more larger-sized MRSA-bundles compared to MYH9−/− platelets; n = 3, mean ± SEM, wilcox-test, * = $p < 0.05$. d, Transfusion of control, but not of MYH9-deficient platelets corrected defective bacterial bundling after platelet depletion. Ctrl: n = 6; WT/MYH9-KO/Depletion: n = 3, mean ± SEM, wilcox-test, * = $p < 0.05$.

(J) Viability of MRSA was measured using the LIVE/DEAD BacLight Bacterial Viability Kit (red: dead bacteria (PI); green: live bacteria (Syto 9), see STAR Methods). In the presence of thrombin, platelets were able to partly kill MRSA = (Ali et al., 2017) = (Ali et al., 2017). However, killing was independent of their ability to migrate and to form bacteria bundles. n = 3, mean ± SEM, wilcox-test, * = $p < 0.05$.

(K) Interaction time of migrating PMN with platelet-bound bacteria was measured for MYH9−/− and control platelets. Each number indicates a platelet-PMN-bacteria interaction. Also see Movie S7. WT: n = 29; MYH9−/−: n = 21, mean ± SEM, wilcox-test, * = $p < 0.05$.

(L) PMN phagocytose bacteria-bundles as indicated by the increase of fluorescence of pH-rodo-labeled S. aureus. Also see Movie S7. Scale Bar, 10 μm.

(M) PMN (from calcium reporter mice: *LysM-Cre/PC-G5-tdT*) show increased intracellular calcium oscillations when encountering platelet-bound bacterial bundles. Also see Movie S7. Scale Bar, 10 μm.

(N) PMN undergo NETosis when encountering platelet-bound bacteria bundles. Increase over negative control (fibrin only) is shown. n = 3, mean ± SEM, paired t test, * = $p < 0.05$. Scale Bar, 10 μm.

(O) PMN form multicellular aggregates within livers of MRSA infected mice. Representative micrographs showing the presence of Fibrin strands (anti-Fbg), PMN (anti-Ly6G), Plts (anti-GPIb), MRSA (anti-S.aureus) and NETs (anti-citrulline H3) within PMN aggregates. Scale Bar, 10 μm. (P) Large stitched mosaic scans (containing 6x6 adjacent ROIs) giving an overview of liver sections of MRSA infected mice. Arrow heads indicate packed Ly6G-pve PMN aggregates (>= 3 nuclei). Dashed line indicates cropped region shown in Figure 7G. Scale bar,100 μm.

(Q and R) Platelet depleted *GPIb;hILR4*-mice transfused with MYH9−/− platelets show less PMN aggregates within the liver and have reduced ALT plasma levels compared to WT-transfused animals. n = 3, mean ± SEM, paired t test, * = $p < 0.05$.

(S) Survival curve of *PF4-Cre+/MYH9$^{fl/fl}$* and *Control* mice receiving a lethal dose of MRSA (i.v.). n = 10; log rank test;, * = $p < 0.05$.

10.5 Publication V

Precise and economic FIB/SEM for CLEM: with 2 nm voxels through mitosis.

Manja Luckner & Gerhard Wanner (2018)

Histochemistry and Cell Biology, 2018 May 23 (in press)
doi: 10.1007/s00418-018-1681-x

Abstract
A portfolio is presented documenting economic, high resolution correlative focused ion beam scanning electron microscopy (FIB/SEM) in routine, comprising: i) the use of custom-labeled slides and coverslips, ii) embedding of cells in thin, or ultra-thin resin layers for correlative light and electron microscopy (CLEM) and iii) the claim to reach the highest resolution possible with FIB/SEM in xyz. A very small region of interest (ROI) defined in light microscope (LM), can be re-located quickly and precisely in SEM. As proof of principle, HeLa cells were investigated in 3D context at all stages of the cell cycle, documenting as yet unexplored ultrastructural changes during mitosis: nuclear envelope breakdown and reassembly, Golgi degradation and reconstitution and the formation of spindle apparatus, midzone and midbody.

Histochemistry and Cell Biology
https://doi.org/10.1007/s00418-018-1681-x

ORIGINAL PAPER

Precise and economic FIB/SEM for CLEM: with 2 nm voxels through mitosis

Manja Luckner[1] · **Gerhard Wanner**[1]

Accepted: 16 May 2018

Abstract

A portfolio is presented documenting economic, high-resolution correlative focused ion beam scanning electron microscopy (FIB/SEM) in routine, comprising: (i) the use of custom-labeled slides and coverslips, (ii) embedding of cells in thin, or ultra-thin resin layers for correlative light and electron microscopy (CLEM) and (iii) the claim to reach the highest resolution possible with FIB/SEM in xyz. Regions of interest (ROIs) defined in light microscope (LM), can be relocated quickly and precisely in SEM. As proof of principle, HeLa cells were investigated in 3D context at all stages of the cell cycle, documenting ultrastructural changes during mitosis: nuclear envelope breakdown and reassembly, Golgi degradation and reconstitution and the formation of the midzone and midbody.

Keywords FIB/SEM · Golgi · Midzone · Mitosis · Nuclear Envelope

Introduction

Four ultrastructural techniques are established for 3D-reconstruction of biological specimens: (i) cryo-TEM tomography highest resolution, but limited in section thickness (approx. 500 nm); (ii) serial block face sectioning (3View®; large volumes; limited resolution and charging problems; (iii) array tomography (non-destructive; limited resolution in z); and (iv) focused ion beam scanning electron microscopy (FIB/SEM) tomography (larger volumes and highest resolution in z). There is no doubt, that cryo-TEM tomography is the state of the art technique for structural preservation and resolution of sub-cellular structures, however, with severe limitations, when investigating larger volumes in 3D. At present, section thickness is 500 nm at maximum, with a macromolecular resolution of about 3 nm. Comparing resolutions of 3View®, array tomography and FIB/SEM-tomography, there are no significant differences in xy (approx. 5 nm), but only possible after metal impregnation. The differences in resolution in z direction are, however, striking: 3View® and array tomography with 20 nm section thickness under best conditions, surpassed by FIB/SEM-tomography by a factor of 10 (Xu et al. 2017). As iso-voxels are necessary for adequate high-resolution 3D-representation in all spatial directions, FIB/SEM is the only technique allowing iso-voxels below 5 nm for large volumes. In daily routine, LSM data sets of entire cells can be recorded within few minutes, providing data for profound statistics, if desired. Corresponding ultrastructural information is not possible with TEM tomography at all, due to volume restrictions. FIB/SEM would offer both, quantitative and high-resolution data sets of entire cells, which can be correlated to LM data. CLEM is still impeded by embedding cells/tissues in resin blocks, due to complicated and time-consuming relocation of target cells, insufficient for statistical investigation.

CLEM could be more efficient by preparing biological samples appropriate for FIB/SEM right from the beginning. As it is crucial to define the coordinates of a target area for re-localization in SEM we developed a variety of slides with coordinates, successively improved for different demands (Schroeder-Reiter et al. 2012). Our aim was to embed cells on slides or cover slips within an ultra-thin resin layer (i) for rapid and precise correlation to LM micrographs and (ii) to allow FIB-milling in any desired direction. Several modified protocols are available using thin embedding, but lack

Electronic supplementary material The online version of this article (https://doi.org/10.1007/s00418-018-1681-x) contains supplementary material, which is available to authorized users.

✉ Gerhard Wanner
wanner@lrz.uni-muenchen.de

[1] Department Biology I, Ultrastructural Research, , Ludwig-Maximilians-University Munich, 82152 Planegg-Martinsried, Germany

Published online: 23 May 2018

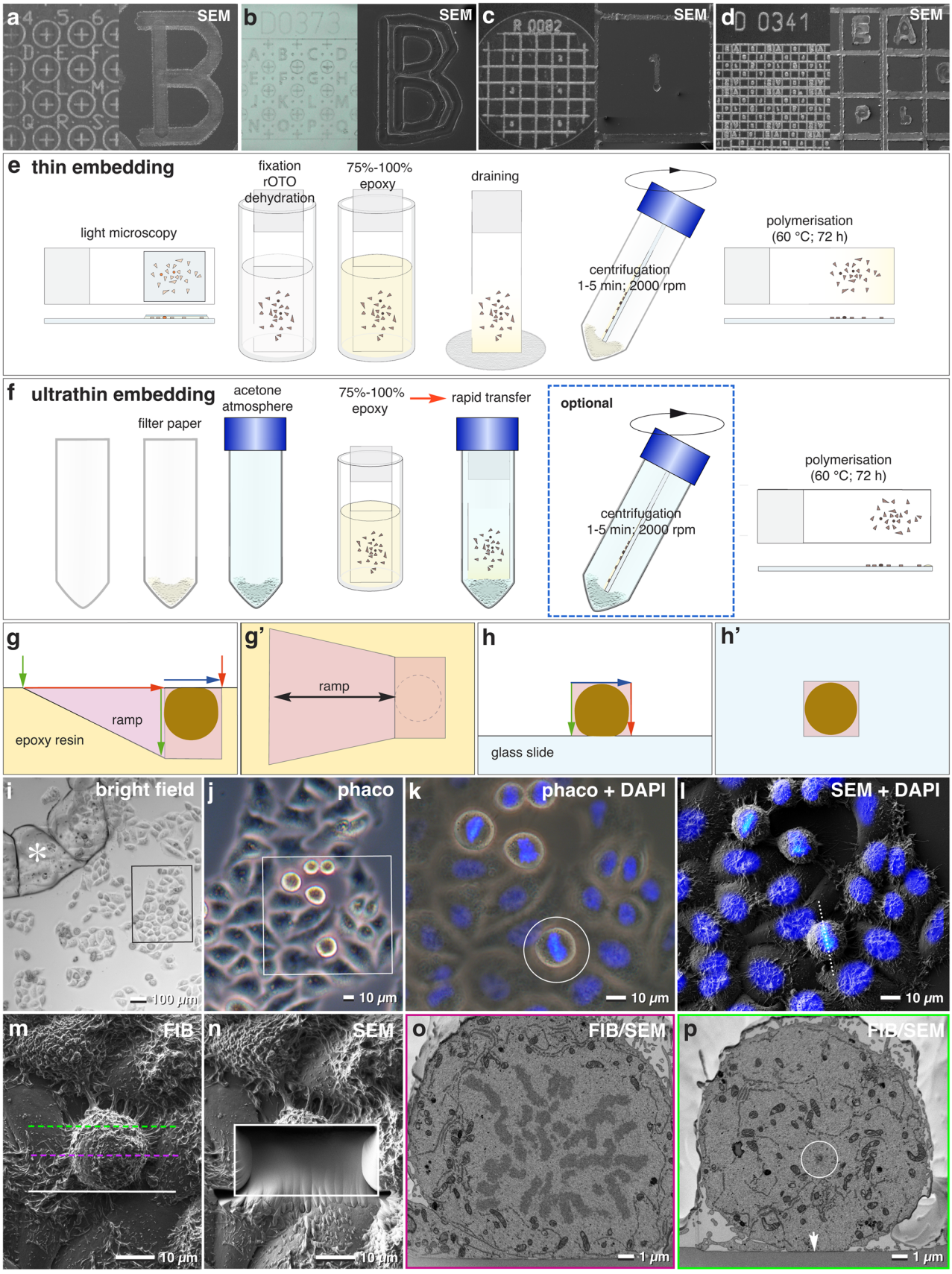
a
SEM
b
SEM
c
SEM
d
SEM
e thin embedding
light microscopy
fixation
rOTO
dehydration
75%-100%
epoxy
draining
centrifugation
1-5 min; 2000 rpm
polymerisation
(60 °C; 72 h)
f ultrathin embedding
acetone
atmosphere
filter paper
75%-100%
epoxy
rapid transfer
optional
centrifugation
1-5 min; 2000 rpm
polymerisation
(60 °C; 72 h)
g
ramp
epoxy resin
g'
ramp
h
glass slide
h'
i
bright field
100 µm
j
phaco
10 µm
k
phaco + DAPI
10 µm
l
SEM + DAPI
10 µm
m
FIB
10 µm
n
SEM
10 µm
o
FIB/SEM
1 µm
p
FIB/SEM
1 µm

◂**Fig. 1** Ultra-Thin Embedding of Cells: Precise and Economic CLEM. **a–d** Close-up photographs of laser marked slides and coverslips with different coordinates and label properties and corresponding SEM micrographs. Labels are seen as indentations in SEM, best suitable for ultra-thin embedding (**a, b**). For thin embedding, raised labels are of advantage for better visualization in SEM (**c, d**). **e, f** Workflow for thin (**e**) and ultra-thin (**f**) embedding. For thin embedding, a simple draining of epoxy resin in concentrations from 75 to 100% can be adequate for larger cells/objects. After centrifugation, the epoxy layer is significantly reduced, but a slight gradient in thickness at the lower part of the slide is typical (e). For ultra-thin embedding, a filter paper, saturated with acetone, is inserted at the bottom of a Falcon® tube to provide an acetone atmosphere, which prohibits increase of resin viscosity, occurring within seconds to few minutes. Simple draining in an upright position results in a very thin resin layer. After centrifugation, the resin layer is extremely thin, surface details of cells appear to be uncovered (**f**). **g, h** Comparison of FIB/SEM milling of a conventionally embedded cell within a resin block, which requires a deep ramp (**g** = side view; **g'** = top view) or ultra-thin embedded on a laser marked slide (**h**). As a deep ramp is needless, milling and block face imaging can start directly at the cell (**h** = side view; h' = top view). The volume that has to be milled (pink) for an entire data set of a cell is reduced to 10% (**h, h'**). i Bright field light micrograph of HeLa cells, grown on slide with laser marks (asterisk) serving as coordinates to retrieve target cells in the SEM (framed area). Scale bar 100 µm. **j** Phase contrast micrograph of the target region from (**i**). Dividing cells are spherical and appear bright (framed area). Scale bar 10 µm. **k** Merged DAPI fluorescence and phase contrast micrographs (framed area of **j**) shows mitotic stages and a target cell (circle) with upright orientation of the metaphase plate. Scale bar 10 µm. **l** Merged SEM and DAPI micrographs of the target area. After ultra-thin embedding in epoxy resin, the target cell is precisely relocated. The axis of the metaphase plate is in upright position (dotted line). Scale bar 10 µm. **m** SEM micrograph of the target cell (FIB image), oriented for FIB/SEM milling parallel to the metaphase plate. White line = starting position for milling; magenta line = position of metaphase plate; green line = expected position of the distal centrosome. Scale bar 10 µm. **n** SEM micrograph of the target area shown in (**m**) after FIB/SEM milling (framed area). Image acquisition started direct in front of the cell and stopped just after reaching the desired depth. Scale bar 10 µm. **o, p** Selected SEM micrographs from the FIB/SEM-tomogram (magenta and green dotted line in (**m**), illustrating the position of the images shown in (**o**) and (**p**). 1100 micrographs cover the entire metaphase plate including the centrosomes (circle). Arrow indicates the reference line (slide) for precise alignment. Scale bar 1 µm

correlation to LM (Belu et al. 2016; Schieber et al. 2017) or involve delicate and critical preparation steps for CLEM (Verkade 2008; Murphy et al. 2011; Rennie et al. 2014; Booth et al. 2016; Lees et al. 2017; Santoro et al. 2017). In a recent book chapter the technical possibilities for various embedding protocols (classical *en bloc* embedding and thin-layer plastification) are presented for live cell imaging with volume scanning electron microscopy (Lucas et al. 2017). Ultra-thin embedding was adapted in our lab to a wide spectrum of biological specimens (from prokaryotes to tissues) and various fixation techniques. Technical improvements for precise and economic CLEM focused on following aspects:

- Conservation of cell topography from LM to SEM.
- Adaption of the thickness of the resin layer to any demand.
- Immediate and precise correlation between LM and SEM.
- Enabling direct access to the target cell to omit a ramp.
- Reduction of the entire milling volume to its minimum, the cell volume.
- Incorporating the slide as an absolute reference for precise alignment of the FIB-stack.
- Including volume rendering for direct 3D visualization at high-resolution.

Mouse C2C12 myoblast cells, stable expressing a fusion of GFP to DNA methyltransferase 1 (GFP-Dnmt1), visible in late S-phase as many looped or toroidal spots (Leonhardt et al. 1992; Schneider et al. 2013), were used for determination of precision of CLEM in a sub-micrometer range. HeLa cells were investigated in detail for ultrastructural changes during the cell cycle to illustrate the enormous potential of this technique, providing new 3D insights in metamorphosis of the Golgi, nuclear envelope breakdown and reconstitution, formation of the midzone and midbody, based on high-resolution 3D FIB/SEM data sets. The economy of FIB/SEM was improved by optimizing all technical parameters to achieve a voxel-size of $2 \times 2 \times 2$ nm over hundreds of sections.

Materials and methods

Cell culture

HeLa Kyoto and mouse C2C12 myoblast cells were kindly provided by Prof. Dr. Heinrich Leonhardt. Cells were cultured in DMEM (Thermo Fisher Scientific) + 10% FBS (GIBCO) and Gentamicin (5 µg/ml) (Thermo Fisher Scientific). Laser marked slides or coverslips (Fig. 1a–d) were placed in a dish and cells were grown in an incubator at 37 °C, 5% CO_2 in a water vapor saturated atmosphere, until an appropriate density on the slides was reached (30–50%).

LM of HeLa cells and mouse C2C12 myoblast cells

Slides/coverslips were rinsed with PBS (Thermo Fisher Scientific) and immediately fixed with 2.5% glutardialdehyde (Science Services GmbH, München) in 75 mM cacodylate (Sigma–Aldrich), 75 mM NaCl, 2 mM $MgCl_2$ for 30 min, followed by 3 washing steps in cacodylate buffer. Cells were stained with DAPI, sealed with a coverslip and Fixogum (Marabu GmbH & Co. KG, Tamm, Germany) to prevent drying during LM investigation. ROIs were marked on a template, with the same coordinates (Fig. 1a–d). For documentation 2–3 different magnifications (Objective: 5x,

10x, 40x) were sufficient to retrieve ROIs in SEM. Depending on specimen properties, bright field, phase contrast, DIC were used. Different areas were documented, as (i) there can be a loss of few cells and/or damage during handling; (ii) some cells may show insufficient fixation quality or contrast in SEM among neighboring cell, adequate in structure and contrast. For correlative CLSM of mouse C2C12 myoblast cells, overview images were acquired in "tile scan" mode with a LSM 780 with a Plan-Apochromat 40x/1.3 oil DIC M27 objective (Zeiss, Germany) to select cells in the desired stage, identified by the characteristic signal of GFP-Dnmt1. Emission of green fluorescent protein (GFP) and DAPI was collected using standard filter sets for GFP (486–564 nm) and DAPI (403–473 nm). Confocal z-stacks ($113.27 \times 113.27 \times 15.86$ µm) were recorded with an image pixel size of 78 nm in xy and 260 nm in z.

EM preparation

After removal of Fixogum and cover slip, cells were post-fixed (customized rOTO-protocol) with 1% OsO_4 and 1% $K_4Fe(CN)_6$ in cacodylate buffer for 30 min, washed 3 times in ddH_2O, incubated with 1% thiocarbohydrazide in ddH_2O for 30 min, washed with ddH_2O 3 times, followed by post-fixation with 1% OsO_4 in ddH_2O for 30 min. The samples were rinsed 3 times with ddH_2O and dehydrated in a graded series of acetone (10%, 20%, 40%, 60%, 80%, 100%), containing a 1% uranyl acetate step in 20% acetone for 30 min, infiltrated and embedded on the glass slide (Fig. 1e, f).

Thin embedding

Cell were infiltrated with 1:1 Hard-Plus Resin-812 in acetone for 15 min, 2:1 for 30 min, 75–100% Hard-Plus Resin-812 for 30 min at RT. Excessive resin was removed by centrifugation (2 min; 1000 rpm) (Fig. 1e).

Ultra-thin embedding

Cells were infiltrated with 1:1 Hard-Plus Resin-812 in acetone for 15 min, 2:1 (resin/acetone) for 30 min and 3:1 (resin/acetone) for 30 min. A filter paper, completely soaked with acetone, was placed at bottom of a Falcon® tube to provide an acetone saturated atmosphere. A polypropylene cap was placed on top of the filter paper to avoid direct contact with the slide. The slide was placed upright into the Falcon® tube, allowing the excessive resin to drain into filter paper at the bottom of the Falcon® tube for 10–30 min. If necessary, an additional centrifugation can be added (2 min, 1000 rpm) (Fig. 1f).

The samples were polymerized for 72 h at 60 °C. The size of the glass slides was reduced to appropriate size by fracturing with aid of a diamond pen. The specimens were mounted on an aluminum stubs with colloidal silver.

Conductive coating

Platinum is the metal coating commonly used for scanning electron microscopy (SEM). Due to its high back-scattered electron (BSE) yield, platinum coating prohibits material contrast of sub-surface structures. Carbon coating allows both, high-resolution BSE and topographic secondary electron (SE) images, despite the lower SE-yield of carbon—which is in practice compensated—as for BSE/energy selective back-scattered electron (EsB) imaging, larger apertures (60 µm) and high current mode are preferentially used. A carbon coating of 15 nm thickness for FIB/SEM-tomography is preferred to any sputter coating with heavy metals for the following reasons: metal grains deposited by sputtering, separate under prolonged exposition to the electron beam and lead to charging. The high yield of SE favored by heavy metal coating, images the upper few nm of the surface. The surface of the specimen itself is only part of the information needed for correlation to LM micrographs. Together with the subsurface information of the BSE signal, a very precise correlation of LM data sets is given.

High-resolution SEM

The most important SEM parameters should be picked out to illustrate the potential for CLEM. For the first step, simple correlation of size and shape of a specimen in LM and SEM, working distance has to be large (10 mm) and kV high (5 kV) to ensure a sufficient low magnification with acceptable low geometrical distortion in SEM. Although surface details are best monitored at 1 kV with the inlens SE detector, correlation with LM micrographs needs as much as possible depth information. This information is gathered by the EsB detector (1–5 kV) or at higher kV (5–30 kV) with the 4-quadrant back-scattered electron detector (QBSD) detector. Thin layers of resin become transparent and laser marks are clearly visible. When using BSE signals, a larger aperture is necessary for a sufficient signal to noise ratio, which does not influence resolution a low and moderate kV. The high current mode is of benefit if the depth of focus is of importance: high current mode increases the active probe current by a stronger activation of the condenser lens. The resulting smaller angle of convergence increases the depth of field. LM and SEM images perfectly match after merging. Only minor corrections, as rotation and some linear scaling are sufficient for a fast and precise correlation.

High-resolution FIB/SEM

HeLa and mouse C2C12 myoblast cells were imaged in an Auriga 40 FIB/SEM workstation operating under SmartSEM® (Carl Zeiss Microscopy GmbH, Oberkochen, Germany) or Atlas 3D (Fibics incorporated, Ottawa, Canada). FIB/SEM milling was started right in front of the cell. Ion beam currents (dependent on the stability of the resin) of 50 pA to 10 nA were used. Due to ultra-thin embedding, milling of a trench is needless and direct excess to the target structure is given (compare Fig. 1g, h, m, n). Dependent on the desired resolution, image pixel sizes between 2 nm and 10 nm in x/y were chosen. Milling rate was set to 2 nm, which allows the adjustment of the z-resolution in 2 nm steps at any time during the FIB/SEM run. Due to metallic rOTO impregnation of the tissue, carbon coating, conducting with colloidal silver and, if necessary, Pt-deposition upon the ROI, charging was completely avoided. The rOTO impregnation provides a strong material contrast; therefore, shorter exposure times down to 17 s/image (3072 × 2048 pixel) could be achieved.

3D-reconstruction

The datasets were aligned using Amira™ (Thermo Fisher Scientific, USA) with the module *align slices*. The image stacks, either from CLSM or FIB/SEM were segmented and reconstructed in Amira™ or processed with an direct volume rendering algorithm (volren) for immediate visualization. For correlative microscopy of Dnmt1, landmarks, as characteristic surface details of the nucleus, were used as reference points to correlate CLSM and FIB/SEM data sets. With the *Landmark Surface Wrap* option, the "DAPI nucleus" was adapted to the "FIB/SEM nucleus" by aligning the previous set reference points and further optimized by manual transformations.

Results

Locating target cells in routine

Changes in the 3D ultrastructure of HeLa cells were studied in the context of developmental and/or functional aspects. The entire EM preparation of cells was performed on customized laser marked coverslips/slides to track the position from LM through SEM investigation (Fig. 1). Several coverslips/slides with different coordinate systems varying in size and type, either engraved or elevated by a sinter process (Fig. 1a–d) were produced for either thin- or ultra-thin embedding (Fig. 1e, f). After ultra-thin embedding, the appearance of the cells remains unaltered from LM to SEM, enabling a fast retrieval of target cells (Fig. 1i–l). The thickness of epoxy layers can be adjusted using 75–100% epoxy/acetone mixtures as final concentrations (Fig. 1e, f) and adapted by draining and centrifugation or by an acetone saturated chamber and an optional centrifugation step (Fig. 1f). Excellent structural preservation enables easy recognition and relocation of HeLa cells in LM and SEM (Fig. 1i–l). Merging light micrographs with SEM micrographs, the target cells fit perfectly (Fig. 1l). If thin resin layers obscure laser markings, increasing the accelerating voltage (3–5 kV) enhances the overall material contrast. For smooth cell surfaces, ultra-thin epoxy layers are optimal. If the cell surface is extremely structured, a thin embedding is advantageous to avoid curtaining and therefore slides with elevated coordinates, which poke out and are not covered by the epoxy resin, are favored (Fig. 1d).

Economic FIB-SEM milling

FIB/SEM milling of a target cell is very efficient, as the cells remain on the substrate and thin embedding enables a fast re-localization of selected ROIs (Fig. 1m, n). Cells, classical embedded in a resin block, a ramp has to be milled, to get access to the target ROI (Fig. 1g, g'). With ultra-thin embedding, a ramp is needless, and only the actual volume of the ROI is ablated without redeposition effects (compare Fig. 1g with h). The required ablation volume for a single cell within a resin block is ten times larger, compared to cells after ultra-thin embedding (Fig. 1g, h). The position and orientation of sub-cellular structures in top view (e.g., metaphase plate) can be determined quickly with precision in the micrometer range (Fig. 1k–m). With ion beam currents of 2–5 nA, an HeLa cell can be milled to its center within 5–20 min. An image stack of a centrosomal region with several hundred micrographs can be recorded with 2 nm iso-voxels within a few hours (Fig. S1; Movie S1).

Fast imaging and precise alignment

During FIB-milling, the cross section of the glass slide serves as absolute reference for precise alignment (Fig. 1h, o, p). Demonstrating the necessity of a reference for immaculate alignment, an image stack including the glass slide as base line (Fig. S2a) was cropped (Fig. S2b), aligned separately and compared in yz view, illustrating striking differences in shape and position of cellular structures, especially if they are elaborate and filigree as e.g. ER (Fig. S2a', S2b'). For FIB/SEM, the signal of the in-lens EsB detector is standard. Approaching the resolution limit, applying the inlens SE signal has several advantages: better resolution, better signal to noise ratio and much shorter exposure times (Villinger et al. 2012). With an increased heavy metal impregnation (rOTO), high-resolution images (3072 × 2048 pixel) can

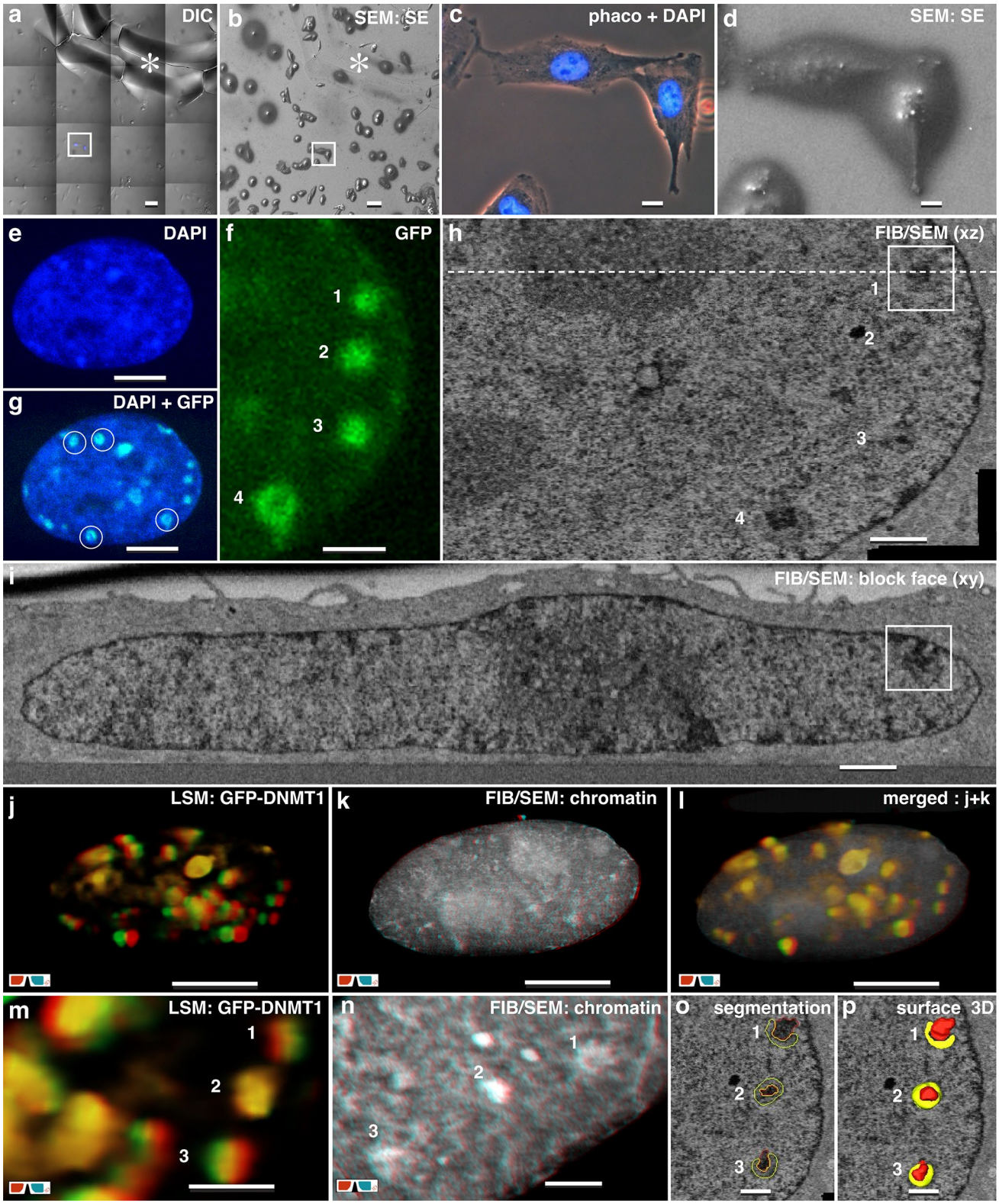

be taken within 17–23 s, compared to the EsB signal with 30–50 s (Fig. 1o, p). However, finest curtaining is immediately visible in the inlens SE image (not shown).

CLEM of Dnmt1 In mouse C2C12 myoblast cells

The precision of the CLEM workflow is demonstrated by localization of the DNA methyltransferase 1 (Dnmt1) during

◂**Fig. 2** CLEM of Dnmt1 in mouse C2C12 myoblast Cells. **a** Light micrograph (DIC) of mouse C2C12 myoblast cells, stable expressing GFP-Dnm1, grown on a laser marked coverslip and counter stained with DAPI, imaged in tile scan mode. Scale bar 100 µm. **b** Scanning electron micrograph of the target area from **a**. The coordinates of the coverslip allow precise re-localization in SEM, as they are visible after thin embedding (asterisk). Scale bar 100 µm. **c** Light micrograph of target cell (phase contrast) merged with DAPI signal. Scale bar 10 µm. **d** Scanning electron micrograph of the target cell (SE image). Scale bar 10 µm. **e**–**g** Maximum intensity projection of confocal image stacks of DAPI (**e**) GFP-Dnmt1 (**f**) and merged (**g**) of the target cell from (**c, d**). Scale bar in **e** and **g** 10 µm; in **f** 5 µm. **h** FIB/SEM micrograph of the target cell in top view (xz). The section plane shows 4 chromocenters with same arrangement as GFP-signals from (**f**). The dotted line marks the position of the block face image presented in (**i**). Scale bar 1 µm. **i** FIB/SEM micrograph of the target cell in front view (xy). The section plane shows the region of the chromocenter 1 (frame). Scale bar 1 µm. **j**–**l** 3D visualization by volume rendering of GFP-Dnmt1 signal (**j**) FIB/SEM nucleus (**k**) and correlation of both volumes (**l**). Scale bar 5 µm. **m**–**n** Detail of 3 prominent GFP spots in 3D (**m**) and corresponding to their ultrastructure, based on the FIB/SEM volume **n**. Scale bar in m 1 µm; in n 500 nm. **o**–**q** FIB/SEM micrograph of 3 chromocenters, characterized by an electron dense core surrounded by a less electron dense hem, identified and segmented based on their electron density (**o**) reconstructed in 3D (**p**) and merged with the GFP signal (**q**) demonstrating the co-localization. Scale bar in **o** and **p** 500 nm

late S-phase in mouse C2C12 myoblast cells. Dnmt1 is enriched in replication foci at chromocenters, when DNA of peri-centromeric heterochromatin (pHC) is replicated (Schneider et al. 2013). From target cells, grown on labeled slides, confocal z-stacks were recorded. Cells can be easily relocalized after thin embedding by the coordinates and similar appearance in phase contrast and SEM (Fig. 2a–d). The data set from FIB/SEM-tomography was examined in xz-view to facilitate direct comparison to CLSM optical sections (Fig. 2e–h). The GFP-Dnmt1 signal (Fig. 2g, f) correlates with characteristic ultrastructural details: electron dense regions of heterochromatin, surrounded by a less electron dense hem, distributed within the nuclear matrix (Fig. 2h). In multi-planar mode (Amira™), the ROI can be visualized in any desired direction with high-resolution (Fig. 2i, h). 3D reconstructions of the confocal image-stacks were correlated to the FIB/SEM volume to localize and identify the ultrastructure of Dnmt1. As the LM and FIB/SEM data sets are different, both, in resolution and orientation of the axis of their stacks, their surfaces had to be aligned. Due to the lower resolution, the LM reconstruction was adapted to the high-resolution FIB/SEM data. The volume of the nucleus (based on the DAPI signal) was scaled to the 3D coordinates of the nuclear envelope derived from FIB/SEM-tomography (Fig. 2j–n). Two different modes for visualization can be used: volume rendering (based on threshold of grey levels), which is very objective but limited, if very large volumes have to be visualized, as resolution decreases with depth (Fig. 2n). Manual segmentation is time consuming, often subjective, but with the advantage of separating and visualization of several different structural details (Fig. 2o, p). 3D FIB/SEM reconstructions reveal the electron dense regions as a core, sheathed in a less electron dense structure, either completely or in part enwrapping the core (Fig. 2o, p). Dnmt1 rather corresponds to the hem, than the core. GFP-Dnmt1 signals can be generally assigned to similar organization of the chromatin varying from 0.7 µm to 1.5 µm in diameter.

Ultrastructural changes during mitosis

Shuttling between nuclear envelope (NE) and ER

3D reconstructions of interphase nuclei reveal their varying shapes, including invaginations and nuclear tunnels. Nuclear pores (NP) are discernible as ring structures (± 120 nm in diameter), homogeneously distributed (Fig. 3a, a', a''). Examining image stacks through the NE, the outer nuclear ring complex with its subunits is visible first (Fig. 3a'), followed by a circular opening in the NE and the inner nuclear ring complex (Fig. 3a''). In prophase, the NE opens at several positions toward both centrosomes, giving access to microtubules (MTs) to enter the nucleus (Fig. 3b, b'). NPs lose their ring complex, either in part or complete and their diameter is variable (Fig. 3b'). Concurrently, the NE becomes fenestrated and the distribution of the (former) NPs becomes inhomogeneous (Fig. 3b'). During metaphase, the NE is transformed into an ER-cage encompassing the chromosomes (Fig. 3c, c', a). 3D reconstruction shows a fenestrated ER-cage, open at two ends toward the centrosomes (Fig. 3c). The fenestration of the NE is best illustrated by volume rendering (*volren*) (Fig. 3c'). NPs were not detected within the ER-cage. With mitotic progression, the cage stretches, but continues to encompass the chromosomes (Fig. 3c). In anaphase, the chromosomes form a disc-shaped mass with a rim region, a proximal side facing the spindle pole and a distal side facing the cell interior (Fig. 3d). With anaphase progression, a striking contact of ER-sheets with the surface of the chromosome mass at the rim is observed (Fig. 3d, e, g, h; Movie S2). In transition from fenestrated ER to a reassembled NE, smaller openings (diameter: ±125 nm) are locally concentrated. NPs with nuclear pore complexes (NPCs) become visible in anaphase when ER-sheets are encompassing the chromosomes (Fig. 3h'). In anaphase-B, the NE outlines the chromosome shapes of the daughter nuclei (Fig. 3e, e', h, h'). Interruptions in ER-sheets between neighboring chromosomes indicate the origin of nuclear tunnels (Fig. 3h, h'). In telophase, the NE is completely reconstituted with randomly distributed NPs. Nuclear invaginations and tunnels are visible, varying in number (up to 5 or even more) (Fig. 3f, f', i, i'). Within the nuclear

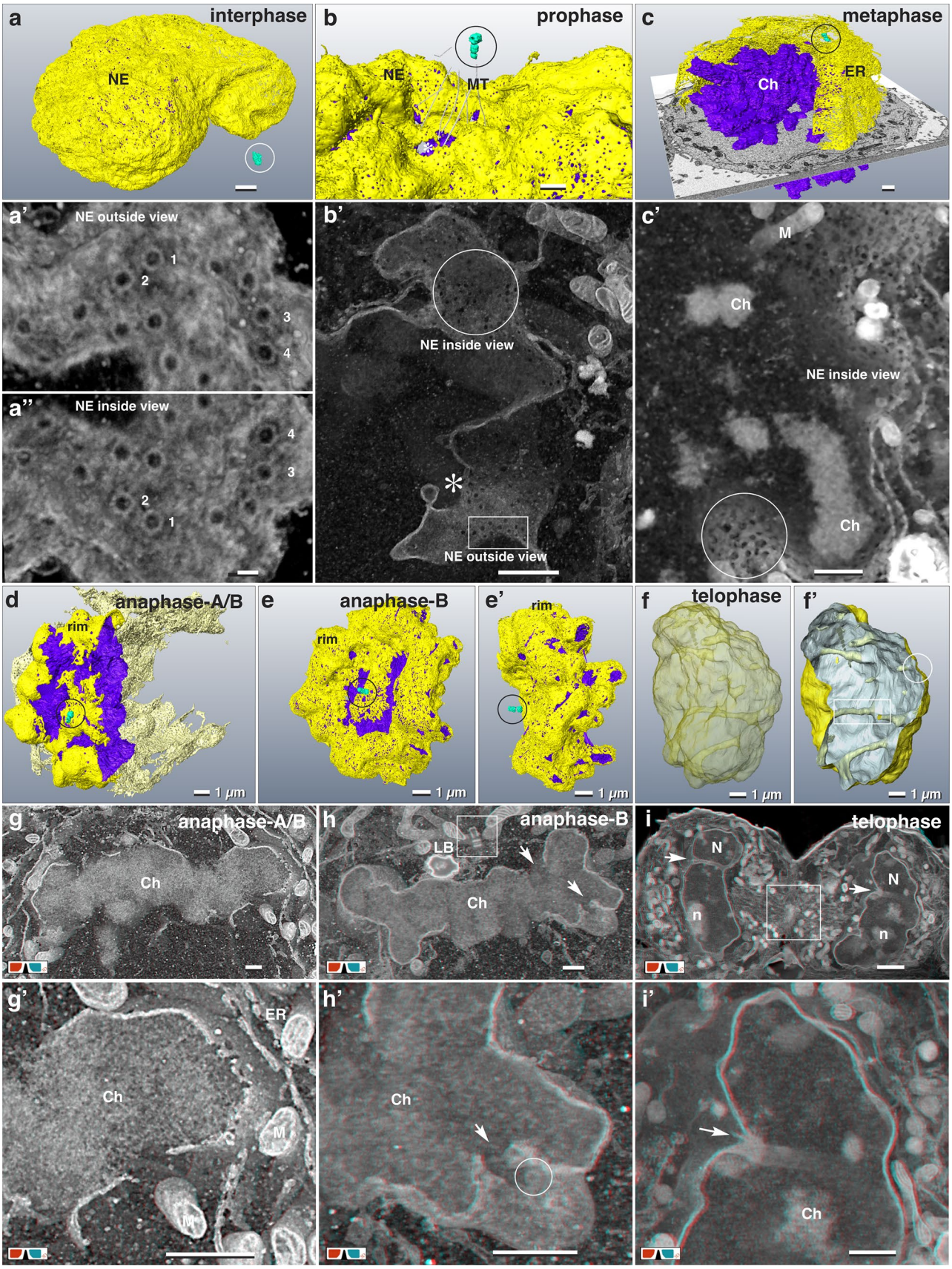
a
interphase
NE
b
prophase
NE
MT
c
metaphase
Ch
ER
a'
NE outside view
1
2
3
4
a''
NE inside view
4
3
2
1
b'
NE inside view
*
NE outside view
c'
M
Ch
NE inside view
Ch
d
anaphase-A/B
rim
1 μm
e
anaphase-B
rim
1 μm
e'
rim
1 μm
f
telophase
1 μm
f'
1 μm
g
anaphase-A/B
Ch
h
anaphase-B
LB
Ch
i
telophase
N
n
N
n
g'
ER
Ch
M
M
h'
Ch
i'
Ch

◂**Fig. 3** Nuclear envelope breakdown and reconstitution. **a–c** 3D-reconstruction (**a–c**) and volume rendering (**a'–c'**) of the nuclear envelope (NE; yellow) and chromatin (Ch; purple) of HeLa cells in inter- (**a**), pro- (**b**) and metaphase (**c**) with their centrosomes (turquoise). **a, a', a''** The nuclear pores are evenly distributed across the NE in interphase (**a**). Volume rendering of the NE, in view from the cytoplasmic side (**a'**) and from the nuclear matrix (**a''**). High-resolution (2 nm iso-voxel) of the outer and corresponding inner nuclear pore complexes with their subunits (1–4). Scale bar in **a** 1 µm; in **a'** and **a''** 100 nm. **b** NE in prophase with several openings (asterisk), towards the centrosome. MTs start to enter the NE. Scale bar 1 µm. **b'** With onset of NE degradation in prophase, the NE opens, facing the centrosome (asterisk). The regularly arranged NPs (rectangle) with their NPCs disappear, leaving holes of irregular sizes and shapes (circle) unevenly distributed over the NE. Scale bar 500 nm. **c** The metaphase NE transforms to a fenestrated ER-cage surrounding the condensed chromosomes (Ch), open at the poles, where the centrioles (circle) are located. Scale bar 1 µm. **c'** Volume rendering of a metaphase cell illustrates the fenestrated ER-cage without NPCs (circle), surrounding the condensed chromosomes (Ch). Typically, some mitochondria (M) enter the (former) nuclear matrix. Scale bar 1 µm. **d** 3D-reconstruction of the NE in anaphase. ER-sheets (yellow) encompass the chromosomes (purple) starting at the rim and the proximal side of the chromosome mass. The ER cage (derived from NE breakdown) is still preserved (light yellow). See Movie S2. Scale bar 1 µm. **e** During anaphase-B, ER-sheets creeping over the condensed chromatin, tightly covering the chromosome arms, still presenting their typical anaphase shape (**e'**). Scale bar 1 µm. **f, f'** 3D-reconstruction of a telophase NE with several nuclear invaginations (circle) and tunnels (rectangle). Scale bar 1 µm. **g, g'** Anaglyph images of anaphase-A/B from (**d**) show the discontinuous covering of the chromatin (facing the centrosome) by ER-sheets. NE formation at the chromatin, distal to the centrosome, is retarded. **g'** Higher magnification form (**g**), an ER-sheet in transition from fenestrated ER to attachment to the chromatin, forming the NE. Scale bar 1 µm. **h, h'** Anaglyph images of anaphase-B (from **e**) demonstrating the formation of nuclear tunnels by attachment of ER-sheets and tubular ER between neighboring chromosome arms (arrows). Typically, lipid bodies (LB) and mitochondria are located within the region of the spindle apparatus. Square: centrioles; circle: nuclear pore with typical pore complex. Scale bar 1 µm. **i, i'** Anaglyph images of telophase from (**f**). Nuclei (N) of telophase cells, with almost decondensed chromosomes and formation of nucleoli (**n**). Daughter cells are still connected via midbody (framed area). Typically, several nuclear tunnels and invaginations are present in telophase (arrows). Scale bar 1 µm

tunnels, strands of ER and bundles of MTs are frequently present.

Formation of midzone and midbody

With high-resolution FIB/SEM, kinetochores (KC), characterized by their tripartite appearance, are documented on ±40 consecutive longitudinal sections (Fig. 4b–b'' and Fig. S3). Their diameters vary between 200–450 nm (Fig. 4b–d). Distal to the chromatin, a larger disk is located (outer KC), followed by a diffuse layer, adjacent to a second, slightly smaller disc (inner KC) attached to or embedded in the chromatin (Fig. 4b, c). Due to the high-resolution in xyz (2 nm iso-voxel) individual MTs, discerned as two parallel lines in longitudinal sections with a diameter of approx. 25 nm, can be tracked over several sections (Fig. 4b, b', b'' and Fig. S3). During anaphase, MTs of the central spindle are attached in parallel to the flanks of the chromosome arms (Fig. 4d). With onset of anaphase, long electron dense strands (0.5-2 µm) are observed, either located halfway between the separating chromatids or emanating from the telomeric regions of the chromosomes (Fig. 4d–f), always attached to microtubules (Fig. 4d–g). Structurally, they are similar to chromatin (Fig. 4d, e). With progression to anaphase-B the midzone is formed: single, electron dense, spindle like structures (Fig. 5a) or aggregates, which we designate as "clamps" (Fig. 5b–d), with a length of up to 2 µm, are arranged in a plane (= midzone) (Fig. 5b–e; Movie S2). Single spindles bundle 2–4 MTs (Fig. 5a); larger clamps bundle up to 25 MTs (Fig. 5–e). With increasing aggregation, the clamps reduce in length to ±0.6 µm (compare Fig. 5a, d). In later stages they form a compact structure, the midbody (Fig. 5f, g; Fig. S4b). With onset of cytokinesis, densely packed MTs passing the midbody are still visible (Fig. 5f, g; Fig. S4a), ending as bundles in the daughter cells (Fig. 5f, g). Vesicles, vesicular–tubular clusters (VTCs) and tubular ER are located between the MT-bundles, till to the center of the midbody (Fig. 5f, g). A compact midbody can be already formed, even though the envelope of the telophase nuclei has not been reconstituted for each nucleus separately. In this case nuclear bridges are crossing the midbody (Fig. S4). From telophase to cytokinesis the daughter cells move apart, while forming elongated tubular structures (Fig. S4b, S4c), connected to the midbody, which remains in its position. Cytokinesis is characterized by separation of the midbody from the daughter cells (abscission). The tubules exhibit a segmentation by membrane adhering substructures (Fig. S4c), forming sort of short helices similar to structures, described as cortical filaments in the constriction zone of HeLa cells with TEM-tomography (Guizetti et al. 2011; Fededa and Gerlich 2012) and with soft X-ray cryo-tomography (Sherman et al. 2016).

The Golgi ribbon is not a ribbon

In interphase, large dictyosomes are present with distinct cis- and trans-sites, 3-(5) cisternae and abundant peripheral vesicles (Fig. 6a). Dictyosomes cluster at one side of the nucleus in the vicinity of the centrosome forming a network of approx. 30 two-dimensionally interconnected stacks (0.75-3 µm in diameter) (Fig. 6b). The Golgi-network is generally cup-shaped but can form a complex 3D architecture (Fig. 6b; Movie S3). In all interphase cells, some single dictyosomes were randomly distributed. Bundles of actin are present in interphase and all stages of mitosis (Fig. S6). Characteristic is their package of numerous thin electron dense fibrils (Fig. S5), the thinnest with diameters of 6–8 nm. Locally, groups of rather flat electron dense vesicles, aligned in a row, are frequently observed in contact to

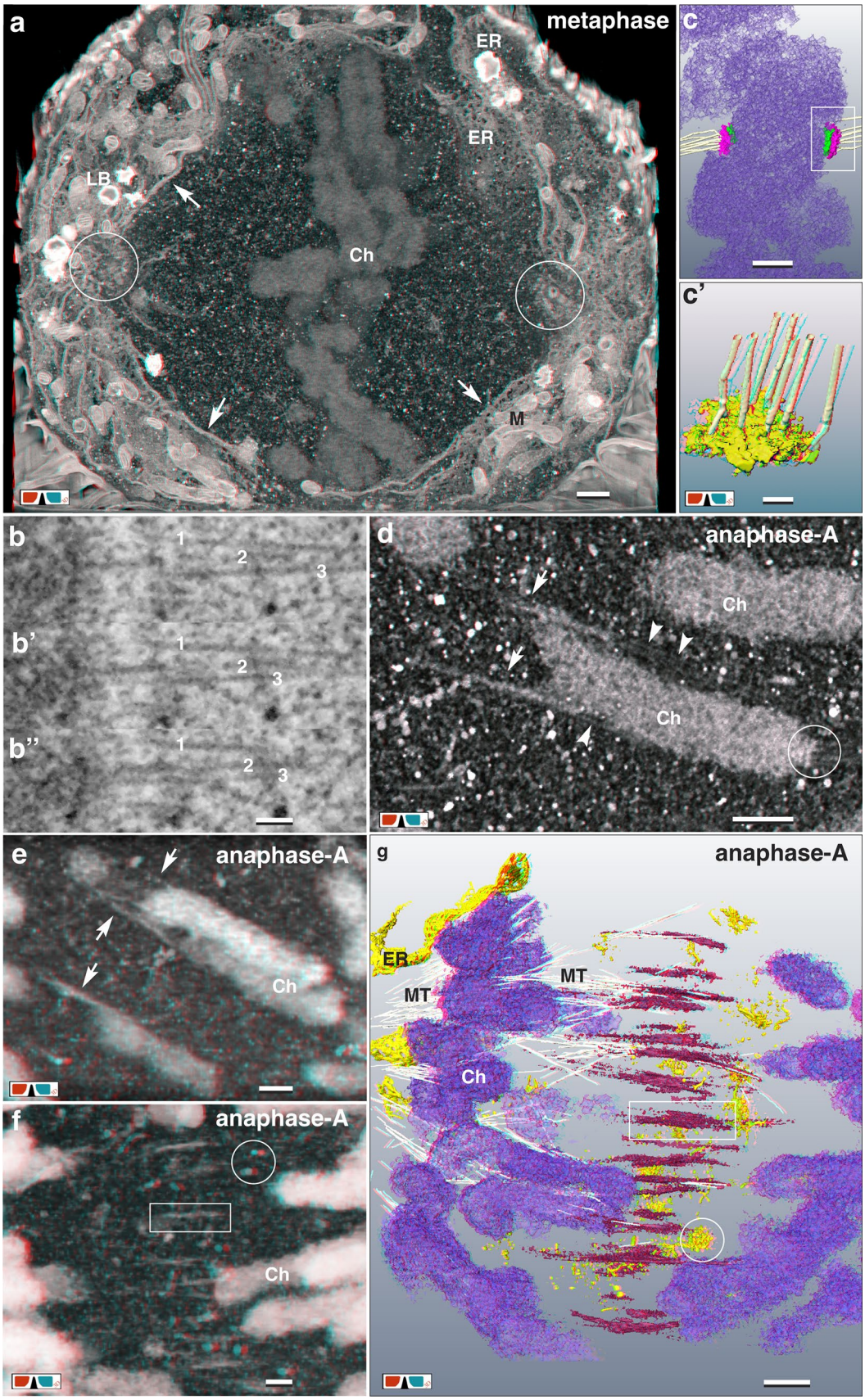
a
metaphase
ER
ER
LB
Ch
M
c
c'
b
1
2
3
b'
1
2
3
b''
1
2
3
d
anaphase-A
Ch
Ch
e
anaphase-A
Ch
f
anaphase-A
Ch
g
anaphase-A
ER
MT
MT
Ch

◂**Fig. 4** From meta- to anaphase: kinetochores and midzone formation. **a** Chromosomes (Ch) of a metaphase plate surrounded by a fenestrated ER-cage (arrows). Several layers of ER-sheets at the spindle poles are in contact to the centrosomes (circles), probably acting as an anchor. Scale bar 1 µm. **b, b', b''** Due to an ablation rate of only 6 nm/section, single MTs, attached to the kinetochore are visible on several consecutive FIB/SEM micrographs. Scale bar 100 nm. **c, c'** 3D-reconstruction of sister kinetochores with their disc-like structure of the larger outer kinetochore (pink) and the smaller inner kinetochore (green). 6–7 MT are attached to the kinetochore. **c'** = detail of **c**. Scale bar in **c** 500 nm; in **c'** 100 nm. **d** Anaglyph image of microtubules (arrowheads) passing the chromosomes flanks, acting as central spindle MTs. Electron dense strands (arrows) seem to be pulled out from the ends of the chromosomes by MTs. Circle marks the kinetochore. Scale bar 500 nm. **e** Anaglyph image of strands of chromatin (arrows), in contact to MTs, emanate laterally from the chromosome arms in anaphase-A. Scale bar 500 nm. **f** Anaglyph image (volume rendering at low resolution for high depth information) of clamp-like structures are arranged midway between the dividing chromosomes (rectangle) in anaphase-A. Characteristic for the midzone is the presence of numerous, electron dense single or aggregated vesicular–tubular clusters (circle). Scale bar 500 nm. **g** Anaglyph image of 3D-reconstruction of chromosomes and midzone in anaphase-A. Clamps (red) are up to 2 µm long and bundle MTs (for clarity only a few are labeled). Halfway between the separating chromosomes (purple), they are arranged in a plane. Numerous vesicular-tubular clusters (circle) are located within the midzone. Scale bar 1 µm

actin-bundles (Fig. S5b, b'). Sickle-shaped ribbons of actin follow the contour of the Golgi (Fig. 6b; Fig. S5c, c', d, d') and numerous microtubules and/or microfilaments interlace the space between the interconnected dictyosomes (Fig. 6a, b). Clouds of vesicles fill the space between the Golgi stacks. Primary endosomes, late endosomes and strands of tubular ER are densely packed (either by attachment or interconnected), within the cloud of dictyosomal vesicles, that a discrimination in 2D is hardly possible (Fig. 6c; Fig. S5c, c'). During prophase, the connections between the dictyosomes and the stacks of disc-shaped cisternae are lost and the entire Golgi disintegrates into clouds of vesicles (Fig. 6d; Fig. S6a, a'), still retaining the 3D organization of the Golgi in interphase (Fig. 6i; compare with Fig. 6b). The vesicle clouds remain in contact to both endoplasmic reticulum (ER) and numerous endosomes (Fig. 6d; Fig. S6a). Strands of actin are randomly distributed between the clouds of vesicles (Fig. S6a, a'). Compared to interphase, the amount of MTs interlacing the Golgi is reduced significantly (Fig. S6a). Volume rendering of 100–150 nm thick layers reveals the vesicles as vesicular–tubular clusters (VTC), or ER-Golgi intermediate compartments (ERGICs) (Fig. 6d, e; Fig. S5a). In prometaphase, the disintegration of the Golgi progresses by a reduction of the volume (not number) of the vesicle clouds (Fig. 6e). In metaphase, only a minor fraction of dictyosomal stacks was still present, lacking the typical parallel cisternae (Fig. 6j; Fig. S6b). In anaphase only very few rudimentary dictyosomal stacks were present, scattered in the cytoplasm (Fig. 6k; Fig. S6c); MTs were not observed in their vicinity. In telophase, dictyosomes reappear (Fig. 6–h), the major fraction reassembling in proximity to the centrosome or opposite of the nucleus near the midbody (Fig. 6l). They were not inter-connected, ranging from rudimentary (Fig. 6f, g; Fig. S6d) to mature dictyosomes, with their typical cis- and trans-site (Fig. 6h). After dictyosomal reassembly, VTCs are present at the cis-sites (Fig. 6h). MTs and bundles of actin are visible again, crossing the dictyosomes (Fig. S6d). From telophase to interphase, increased aggregation of dictyosomes forms the characteristic architecture of the Golgi again.

Interconnected system: ER, endosomes and lipid bodies

The ER forms an extensive network, which consists of sheets and tubules (Fig. 3g, h, a and Fig. S7a). Independent of the stage of the cell cycle, fenestrated sheets are predominantly found in the cell periphery (Fig. 4a). In interphase, tubular ER typically interlaces the bulk of cell organelles located at one side of the nucleus. From pro-meta- to anaphase, ER is typically cap-shaped with approx. 3 parallel layers at both poles (Fig. 4a), significantly reduced from anaphase to telophase to one (if any) polar ER-sheet beneath the plasma membrane. Numerous small VTCs are always distributed within the cytoplasm (Fig. S7b–d). Although variable in size and shape, 3D reconstruction reveals a basic "monomer" structure: short strands of extremely thin, straight or forked tubules, terminated by small vesicles (Fig. S7b–d). Larger aggregates form spider-like discs (Fig. S7c, d). In interphase, although present in large numbers, VTCs are difficult to detect, as they are cryptic between the cell organelles.

Lipid bodies (LB) are prominent structures in all stages of the cell cycle. The number of LBs per cell varies from 30 up to 120. They have a maximal diameter of 1 µm, are irregularly shaped with an uneven electron dense cortex, a middle layer and an inner core (Fig. 7a–d). Nearly all LBs exhibit multiple connections to the ER (Fig. 7a–d) and are in close vicinity to endosomes and dictyosomes (Fig. 7a), implicating a functional relation. Characteristic for a fraction of LBs are electron dense, knob-like protuberances at their surface (Fig. 7d) and an accumulation of small granules or vesicles close to their cortex (Fig. 7c, d').

Endosomes are abundant (100–250 per cell) in all stages of the cell cycle in HeLa cells (Fig. 7a, e, f). All endosomes are almost spherical, with a diameter ranging between 0.5 and 1.2 µm (Fig. 7a, f). Typically, they are connected to the lumen of the ER (Figs. 6f, 7f) and in contact to dictyosomes (Fig. 6f). Three major types of endosomes can be categorized: (i) primary endosomes = cup-shaped ER, partially filled with vesicles and VTCs connected to their ER-derived membrane (Fig. 7e, e'); (ii) late endosomes = enclosed

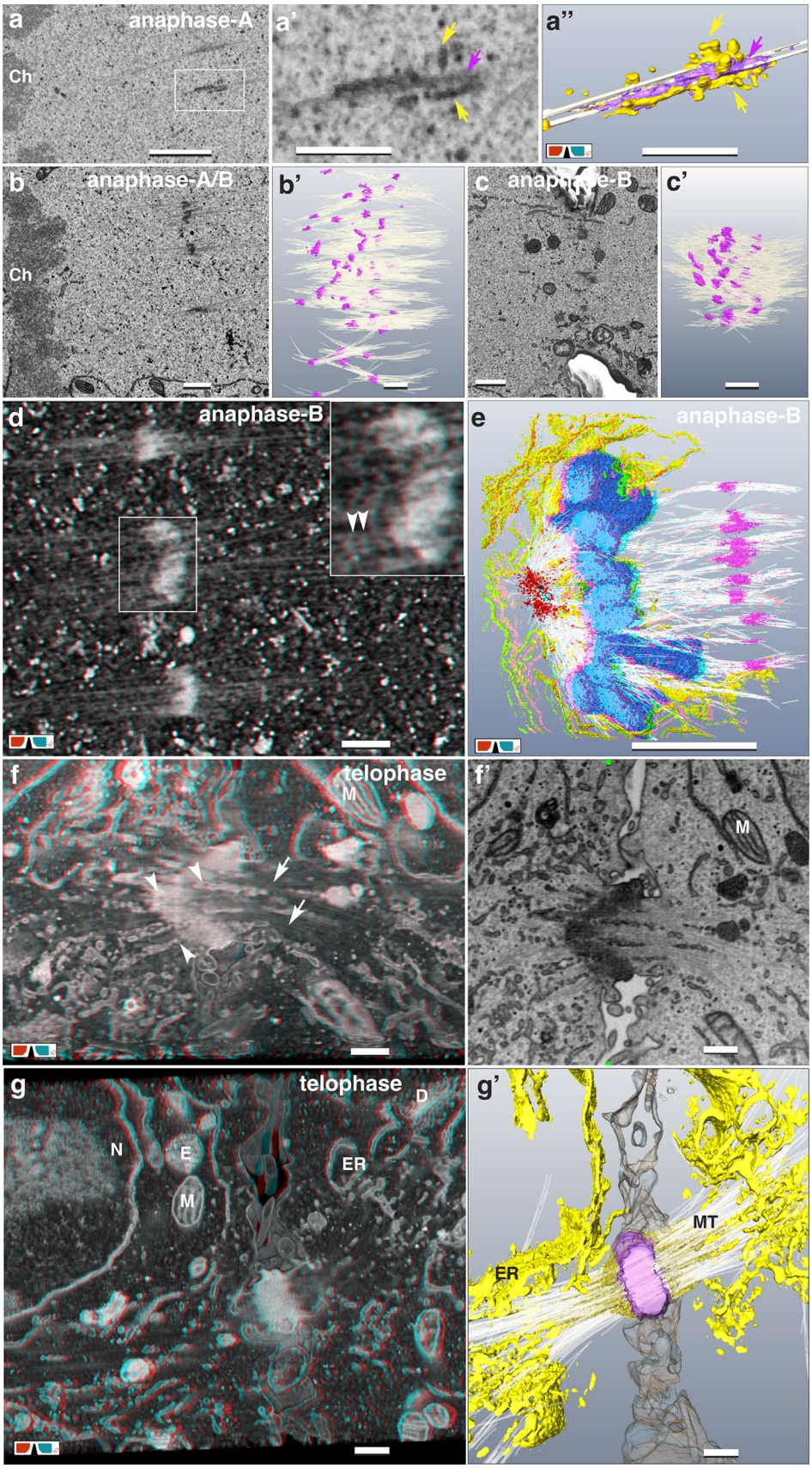

Fig. 5 From Midzone to Midbody. **a, a', a''** Clamps are built up of single spindle like units (**a**), which bundle 2–3 MTs (**a', a''**). At higher magnification, two different zones can be distinguished (**a', a''**): a matrix (pink), bundling MTs and attached VTCs (yellow). Scale bar in **a** 1 µm; **a'** and **a''** 500 nm. **b, b'** With anaphase progression, clamps become more electron dense, begin to cluster and bundle several MTs. Scale bar 1 µm. **c, c'** Clamps in anaphase-B increase in size, simultaneously decreasing in number, by intertwining. Scale bar 1 µm. **d** Anaglyph image of clamps of the midzone in anaphase, discernible as electron dense structures, which are formed by aggregation of several spindle units, bundling numerous MTs. Inset: Next to the clamps, electron dense granular structures, interconnect single MTs (arrowheads). Scale bar 500 nm. **e** Anaglyph image of 3D-reconstruction of a midzone in anaphase-B. Clamps (pink) aggregate, bundling numerous MTs. Nuclear envelope reconstitution starts by attachment of ER-sheets and tubular ER (yellow), to the condensed chromosomes (blue). Scale bar 5 µm. **f, f'** Anaglyph image of midbody in early stage of its formation during telophase. Bundles of MTs permeate the midbody (arrows); tubules and vesicles fuse with the midbody (arrowheads). Scale bar 500 nm. **g, g'** With progression of cytokinesis, the midbody (pink), visible as compact electron dense structure, is located between dividing daughter cells. Microtubules are still present, passing through the midbody and ending diffuse in each daughter cell. (D = dictyosomes; E = endosomes; ER = endoplasmic reticulum; M = mitochondrion; N = nucleus). Scale bar 500 nm

endosomes including collapsed membranes or vesicles (Fig. 7f, f'); (iii) endosomes with a homogenous, rather electron dense matrix, representing endo-lysosomes (Fig. S6a, a').

Discussion

Metamorphosis of the nuclear envelope

For HeLa cells there are detailed LM investigations on the transition from NE to ER and back to NE (Anderson and Hetzer 2008; Lu et al. 2009). Although the NE disappears as an integral structure in metaphase, large areas of ER-sheets, derived from NE, still outline the shape of the NE (Figs. 3c, 4a) as shown by live cell imaging (Anderson et al. 2009). The NE perforates at the regions facing the centrosomes (Figs. 3b, 4a) in accordance to CLEM data (Domart et al. 2012), allowing MTs access for attachment to kinetochores (Fig. 3b). It is obviously an important strategy of the NE/ER-cage to neatly separate the chromosomes from cytoplasmic constituents during mitosis. Maximum compaction of the chromatin is reached in late anaphase (Mora-Bermúdez et al. 2007), necessary for wrapping of the chromosomes by ER-sheets (Fig. 3d, e, g–h; Movie S2) as shown by LM (Anderson and Hetzer 2008; Anderson et al. 2009; Lu et al. 2009). The center of chromosome bulk is not covered completely due to the uneven chromosome topography and reduced accessibility for ER-sheets (Fig. 3d, e, g, h; Movie S2), resulting in formation of tunnels through the nucleus in telophase, that persist absolutely until interphase (Fig. 3f, i), as shown for numerous organisms (for review see: Malhas et al. 2011).

Essential role of clamps for midzone formation

The paradigm that chromosome segregation is mandatory dependent on MT attached to kinetochores has to be attenuated by observations of kinetochore-independent segregation in *C. elegans*: lateral microtubule–chromosome associations, established during pro-metaphase, remain intact during anaphase to facilitate separation (Muscat et al. 2015). Attachment of MTs to chromosome arms is also typical for HeLa cells, as shown during anaphase (Fig. 4d). Spindle-MTs are attached to the flanks of chromosomes and characteristic electron dense strands, emanating from their telomeric regions (Fig. 4–g). According to structural criteria (electron density, granularity) these strands are simply interpreted as chromatin. DAPI staining may be too weak in intensity to visualize these thin strands within an entire nucleus in presence of condensed bulk chromatin. Further experiments with state of the art super-resolution LM and staining with the most sensitive fluorescent dyes e.g. YOYO-1 could provide specific information already at the LM level during anaphase-A (Pyle and Chen 2017; Rocha et al. 2017). These strands are withdrawn from the chromosomes, which could be explained by pulling forces from the MT-movement. As they are apparently involved in formation of the later midzone, it is hard to believe that a substantial amount of chromatin is spent to build a rather solid structure (midbody), needed for cell fission. An explanation could be, that the translocation of chromosomal passenger complexes (CPC), from the centromeric region along the chromosome arms, is mediated by MTs attached to chromatin, due to their increased microtubule binding affinity (Hümmer and Mayer 2009) (Fig. 8). As chromatin condenses further during anaphase (Mora-Bermúdez et al. 2007), the protuberances are obviously retracted into the chromatin bulk.

Clamp-like structures were already published since the 60th with high quality TEM micrographs, either just named "fibrillar substances" (Buck and Tisdale 1962), "midbody" (Robbins et al. 1968), "CENP-E cross-links" of the interzonal microtubules (Yao et al. 1997), or as an accumulation of dynamin, shown by immuno labeling (Thompson et al. 2002). The characteristic shape of the clamps, 0.5–2 µm long strands, and their orientation in a plane between separating chromosomes (midzone) (Figs. 4f–g, 5a–e; Movie S2), match in size and spindle shape with LM localization of PRC1, MKLP1, KIF4 and CPCs (comprising Aurora B, INCENP, borealin and survivin), as shown by Kurasawa et al. (2004) and presented in detail by publications from the Earnshaw group (for review see: Carmena et al. 2012) (Fig. 8). PRC1 is responsible for cross-linking of overlapping antiparallel microtubules (Schuldt 2010). We, therefore, conclude, according to published data, that the electron dense matrix of the clamps (Fig. 5a) mainly represents microtubule-associated proteins (PRC1), microtubule-based motor proteins (KIF4) and chromosomal passenger complexes (Aurora B, INCENP, borealin and survivin), which bundle and stabilize antiparallel microtubules, thereby forming the midzone (Carmena et al. 2012). 3D-reconstructions reveal that VTCs are attached to the microtubule bundling matrix of the clamps (Fig. 5a), described as "midbody vesicular complexes" in 1969, based on TEM micrographs (Robbins and Jentzsch 1969). The observed clusters of small membranous vesicles located close to the clamps, were assumed to provide a morphological basis for spindle elongation (Robbins and Jentzsch 1969). As it is likely that small vesicular–tubular structures are Golgi derivatives, intermediate compartments (IC) are candidates, representing the vesicles aggregates. This is supported by investigations of NRK cells, providing evidence that the permanent IC elements function as way stations during dispersal of Golgi components at prometa- and metaphase, indicating that they correspond to

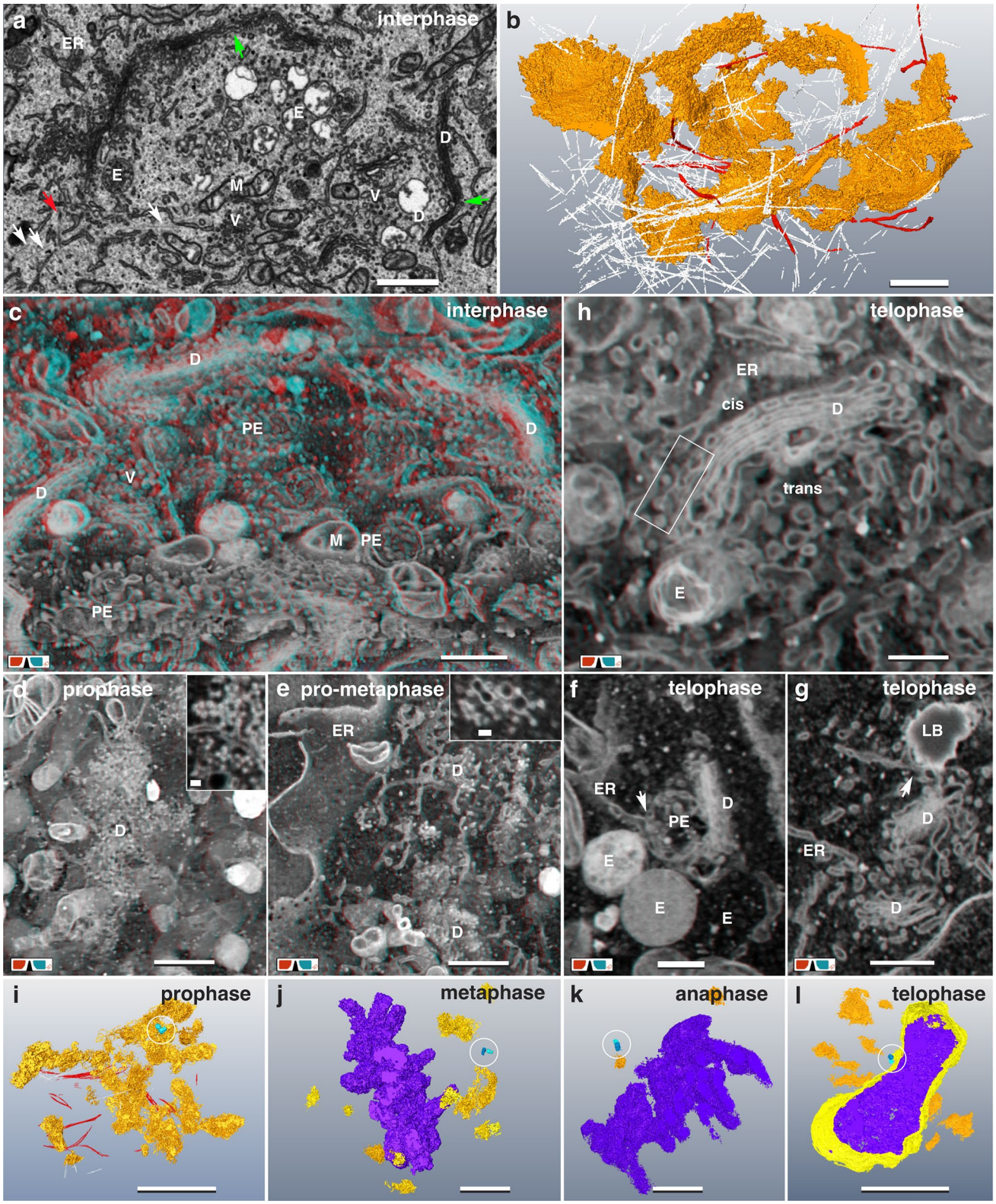

the Golgi clusters (Marie et al. 2012). Although the IC elements maintain their clustering at the spindle poles during metaphase to telophase, they also associate with the central spindle, imaged with high-resolution CLSM (Marie et al. 2012). As division of plant cells is much different compared to animal cells, especially concerning centrosomes and midbody, there is a fascinating conformance, shown by detailed ultrastructural investigation with electron tomography of

◂**Fig. 6** Golgi disintegration and reassembling. **a** SEM micrograph of an interphase Golgi apparatus. Single dictyosomes (D) are interconnected by shared single cisternae (green arrows). Abundant Golgi vesicles (V), primary endosomes (PE) and mitochondria (M) are located in between. MT (white arrows) and actin filaments (red arrow) interlace the Golgi. Scale bar 1 µm. **a'** 3D-reconstruction of the interphase Golgi apparatus (of **a**) illustrates its 3D architecture. White lines representing a fraction of MTs, which interlace the Golgi-network. Actin fibers (red), circumjacent the cup-shaped Golgi. See Movie S3. Scale bar 1 µm. **c** Anaglyph image of the Golgi-network in interphase, revealing its three-dimensional architecture by interconnected dictyosomes (D). Several endosomes (E), vesicles (V) and mitochondria (M) are present in between. Scale bar 1 µm. **d** Golgi in early prophase, disintegrating synchronous into stacks and clouds of vesicles and vesicular–tubular clusters. High-resolution reveals that ERGICs (inset) represent the major fraction of the cloud, rather than single vesicles. Scale bar 1 µm; inset 100 nm. **e** Disintegrating Golgi in pro-metaphase: only rudimental dictyosomes (D), formed of vesicular–tubular clusters are present (inset). Scale bar 1 µm; inset 100 nm. **f, g** The Golgi reassembles in telophase. Single, separated dictyosomes form stacks of few cisternae. Typically, they are in direct contact to ER, primary endosome (PE) (**f**) and lipid bodies (**g**). Both, endosomes and lipid bodies have at least one or several connections to the ER. Scale bar 500 nm. **h** Anaglyph image of a dictyosome formed in telophase. Single dictyosomes (D) with characteristic cis- and trans-site are in contact to ER, lipid bodies and endosomes. ERGICs (framed area) are typically observed at the cis-site. Scale bar 1 µm. **i–l** Representative 3D-reconstructions of the entire Golgi apparatus (orange), chromatin (purple) and centrosomes (blue, encircled) at different mitotic stages. Scale bars 5 µm. **i** With onset of prophase the Golgi disintegrates rapidly into single dictyosomes, which collapse synchronous into clouds of vesicles and vesicular-tubular clusters. **j** After Golgi disassembly, several small, rudimentary dictyosomes and/or vesicle clusters are present in metaphase. **k** Only few rudimentary dictyosomes and vesicle clusters are still present in anaphase. **l** In telophase, groups of typical dictyosomes, sometimes interconnected, are visible in close proximity to the centrosome (circle) and on the opposite side of the nucleus

meristem cells of *Arabidopsis*, preserved by high-pressure freezing (Seguí-Simarro et al. 2004). The phragmoplast, a homologous structure to the midzone/midbody is formed by accumulation of a vesicle cloud followed by tubulo-vesicular network (TVN) (Seguí-Simarro et al. 2004). Correlative high-resolution CLSM in combination with FIB/SEM could provide important structural information for elucidating the first steps of midzone formation.

Golgi transition

The Golgi has been studied extensively in structure and function (Sütterlin and Colanzi 2010; Wang and Seemann 2011; Yadav and Linstedt 2011; Gosavi and Gleeson 2017; Wei and Seemann 2017). 3D-EM techniques made data available for the Golgi of plants (Staehelin and Kang 2008) and mammals (Ladinsky et al. 1999; Marsh and Pavelka 2013; Koga et al. 2017). Telophase is most instructive to understand the metamorphosis of the Golgi. The first stacks reappear, distributed in the cytoplasm close to endosomes and lipid bodies, and in contact to ER (Fig. 6f, g). As small clouds of vesicles accompany the first dictyosomes, still reduced in cisternae, their reconstitution from vesicles is likely. Different models exist for Golgi dis- and reassembly during cell division: (i) upon disassembly, Golgi vesicles are completely integrated into the ER, and with onset of telophase, reassemble out of the ER (Zaal et al. 1999; Altan-Bonnet et al. 2006); (ii) ER and the Golgi are considered as independent compartments: the Golgi-network disintegrates into COPI vesicles that are distributed via MTs, and reassembles from these vesicles after mitosis (Jesch and Linstedt 1998; Jokitalo et al. 2001; Seemann et al. 2002; Axelsson and Warren 2004). Within the last two decades it became evident, that the Golgi (beside the centrosome) acts as a microtubule organization center (MTOC) (Chabin-Brion et al. 2001; Nakamura et al. 2012; Zhu and Kaverina 2013; Rios 2014; Sanders and Kaverina 2015; Nishita et al. 2017). Earlier studies have shown that the Golgi reassembly dependents on the actin and microtubule cytoskeleton and their associated molecular motors, which are responsible for transport of vesicular carriers (Brownhill et al. 2009; Tang and Wang 2013), supported by the presented 3D-reconstructions (Fig. 6b; S5; Movie S3).

Membrane carousel: ER, Golgi, endosomes and lipid bodies

For single-copy cellular elements (chromosomes, centrosomes), a duplication before cell division is essential (Birky 1983). Autonomic mitochondria have to be separated to equip both daughter cells with an adequate population (Birky 1983). All cell constituents present in large numbers or can be synthesized de novo, can be divided in parts of their population (Birky 1983; Lucocq et al. 1987; Lucocq and Warren 1987). The Golgi, predominant in interphase, disintegrates rapidly with onset of pro-metaphase into clouds of vesicles (Fig. 6d, e). In contrast, ER, endosomes and lipid bodies are present all the time during mitosis (Fig. 7). All types of endosomes and endo-lysosomal compartments are directly interconnected with ER (Fig. 7f), forming a common network as shown by light and electron microscopy in Cos-7 cells (Friedman et al. 2013), neurons (Wu et al. 2017) or recently in HeLa cells, were contact sides to early endosomes and late endo-lysosomal compartments are identified with CLEM by (Fermie et al. 2018). There may be principally two different pathways for endosome turnover, summarized by (Huotari and Helenius 2011). A "recycling" pathway characterized by uptake of exogenous material via early endosomes, defined initially as the compartment that first receives incoming cargo and fluid (Helenius et al. 1983) and a cytosolic "degradation" pathway, involving early endosomes, late endosome and lysosomes (for review see: Huotari and Helenius 2011). It is implicated, that the

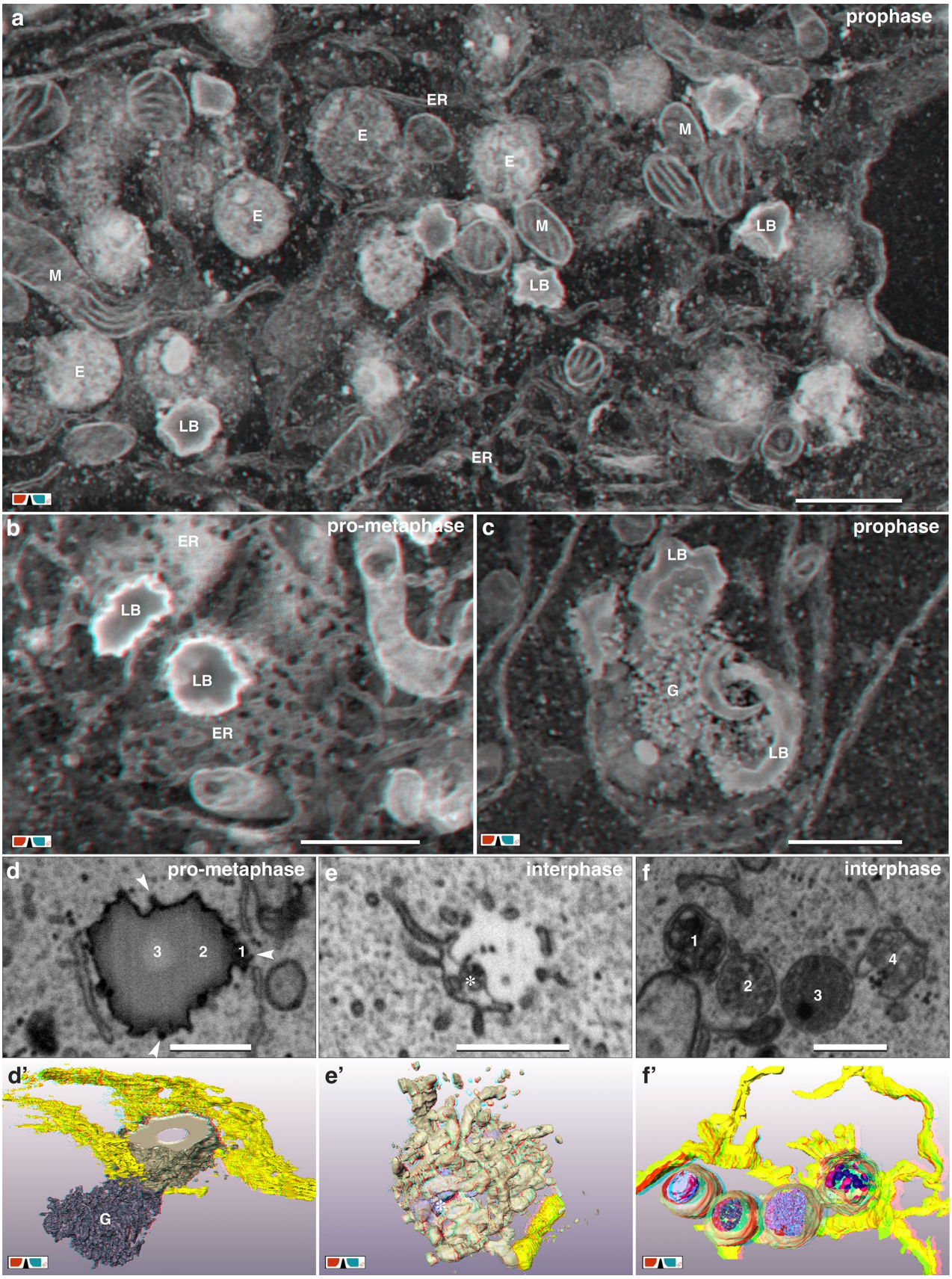
a
prophase
ER
E
E
M
E
E
M
LB
M
LB
E
LB
ER
b
pro-metaphase
ER
LB
LB
ER
c
prophase
LB
G
LB
d
pro-metaphase
3
2
1
e
interphase
f
interphase
1
2
3
4
d'
G
e'
f'

◂**Fig. 7** Interconnected system: ER, endosomes and lipid bodies. **a** During all stages of mitosis, endosomes (E), Lipid bodies (LB) and Mitochondria (M) are in compact vicinity to each other and interconnected by ER. (Anaglyph image) Scale bar 1 µm. **b** Lipid bodies, characterized by their electron dense cortex, are circumjacent and in contact with ER-sheets. (Anaglyph image) Scale bar 1 µm. **c** Formation of lipid bodies. Cup-shaped LBs are surrounded by electron dense granular structures (G), which seem to fuse with the cortex of the LBs. (Anaglyph image) Scale bar 1 µm. **d/d'** Lipid body (LB; grey), in contact with ER. The LB consists of 3 zones: an electron dense "rough" cortex (1), a less electron dense middle layer (2) and an electron translucent core (3). A cloud of electron dense granules (G) is in direct contact with the LB (d'). Numerous, single granules are in contact with the LB surface (d; arrowheads). Scale bar 500 nm. **e/e'** Primary endosome, which is connected to the lumen of the ER (yellow). Vesicles and small tubules start to form an open, hollow sphere, including vesicles and membranous structures (asterisks). Scale bar 500 nm. **f/f'** Different types of endosomes, connected to the same strand of ER, containing membranous structures (1), small vesicles (2; 4) or a mixture of vesicles, granules and electron dense inclusions (3). Scale bar 500 nm

recycling pathway provides the early endosomes, necessary for the degradation pathway. Based on 3D-data we conclude that early endosomes (sensu stricto) are not necessary for an endosome carousel: formation of cup-shaped ER and accumulation/fusion with (dictyosomal) vesicles resulting in a characteristic structure, here defined as "primary endosome" (PE), which is transformed during maturation, further incorporation of vesicles and degradation of vesicle membranes to late endosomes and possibly lysosomes. It is difficult to discriminate between endosomes and lysosomes, as their transition is very dynamic, contradictory to a strict functional separation (Fermie et al. 2018). LAMP-1 is referred as an specific marker for lysosomes (Gowrishankar et al. 2015); however, a recent correlative light and electron microscopy study showed, that LAMP-1-GFP not only correlates with lysosomes, but with all types of endosomes and endo-lysosomal compartments, verified by FIB/SEM microscopy (Fermie et al. 2018). Identifying lysosomes by fluorescence microscopy, using LAMP-1-GFP, may therefore lead to incorrect interpretations concerning lysosomes.

The role of lipid bodies (lipid droplets) has been less clear, as there is only limited ultrastructural information available (Beller et al. 2008; Farese and Walther 2009; Soni et al. 2009; Gao and Goodman 2015). Lipid bodies were long perceived as inert fat particles in animal systems and been largely ignored by cell biologists (Farese and Walther 2009). Interest in the organelle's cell biology has exponentially increased over the last decade due to the link between LBs and prevalent human diseases (for review see Pol et al. 2014). Typically, LBs are spherical, have a half-unit membrane (Yatsu and Jacks 1972; Martin and Parton 2005), a homogeneous matrix and are formed at the ER in animals (Martin and Parton 2005; Thiam and Beller 2017) and in plant cells at the ER or plastid membranes/envelope (Wanner et al. 1981). ER-sheets enwrapping the LBs is characteristic for both, plants, animals e.g. HeLa cells (Soni et al. 2009), fibroblasts (Martin and Parton 2005), U937 cells (Wan et al. 2007) and Huh7 cells (Fujimoto and Parton 2011). For HeLa cells the contact between LB and ER was quantified, showing that ER-lipid body and ER-endolysosome association is characteristic, deduced from single ultra-thin sections and confirmed with 3D reconstruction with TEM-tomography (Zhao et al. 2017). Typical for LBs is the electron dense cortex, enhanced in contrast by fixation with ferrocyanide-reduced osmium/thiocarbohydrazide/osmium (=rOTO) also shown for HeLa cells by Zhao et al., (2017) and for human mast cells, however, fixed with 2% glutardialdehyde and 1% osmium tetroxide only (Dichlberger et al. 2011). The lipid body cortex is always in contact with ER (Fig. 7a–d) and frequently accompanied by vesicles (Fig. 7c, d). The striking accumulation of Golgi vesicles in prophase, paralleled by vesicle clouds, which are in contact to lipid bodies (Fig. 7a–d), is interpreted as interplay of dictyosomal derivatives with lipid body formation.

The attempt of quantifying lipid bodies for volumetric and for balancing with Golgi membrane and ER volume (provided by the segmentation data), was impeded by the fact, that their number per cell varies widely. Even in dividing cells (telophase), one daughter cell can contain much more lipid bodies compared to the other. When calculating the volume of a Golgi (approx. 36 stacks, each with 3 cisternae) and transforming the membrane area into vesicles (size: 40–80 nm), 360.000 vesicles would be formed. However, compressing the vesicles to the volume of their membrane lipids, the resulting lipid volume would be only 1 μm^3, fitting into 5 lipid bodies, which is only a minor fraction of those observed (approx. 80/per cell). If the membrane volume of the Golgi disappears rapidly *via* vesicles into the ERELB, significant ultrastructural changes cannot be expected, particularly since the numbers of LBs and endosomes per cell vary widely.

Our data strongly support a formation of endosomes by aggregation of vesicles presumably of dictyosomal origin with direct involvement of ER, forming at least for some time, a luminal connection. As the ER strands are wound around the endosomes like an "umbilical cord", the luminal connection between ER and endosome matrix will be rarely seen convincingly in ultra-thin sections with TEM. As ER is intimately connected with other organelles, shown by 3D reconstruction (Fig. 7) we postulate that ER, LBs and endosomes play an essential role in membrane turnover of HeLa cells. According to the 3D data, the ER-endosome-lipid body system, here defined as "ERELB", forms a permanently maintained system, playing the leading role for the turnover of the endomembrane system, discussed since decades in numerous variants based on LM and EM studies (e.g., English and Voeltz 2013; Klumperman and Raposo

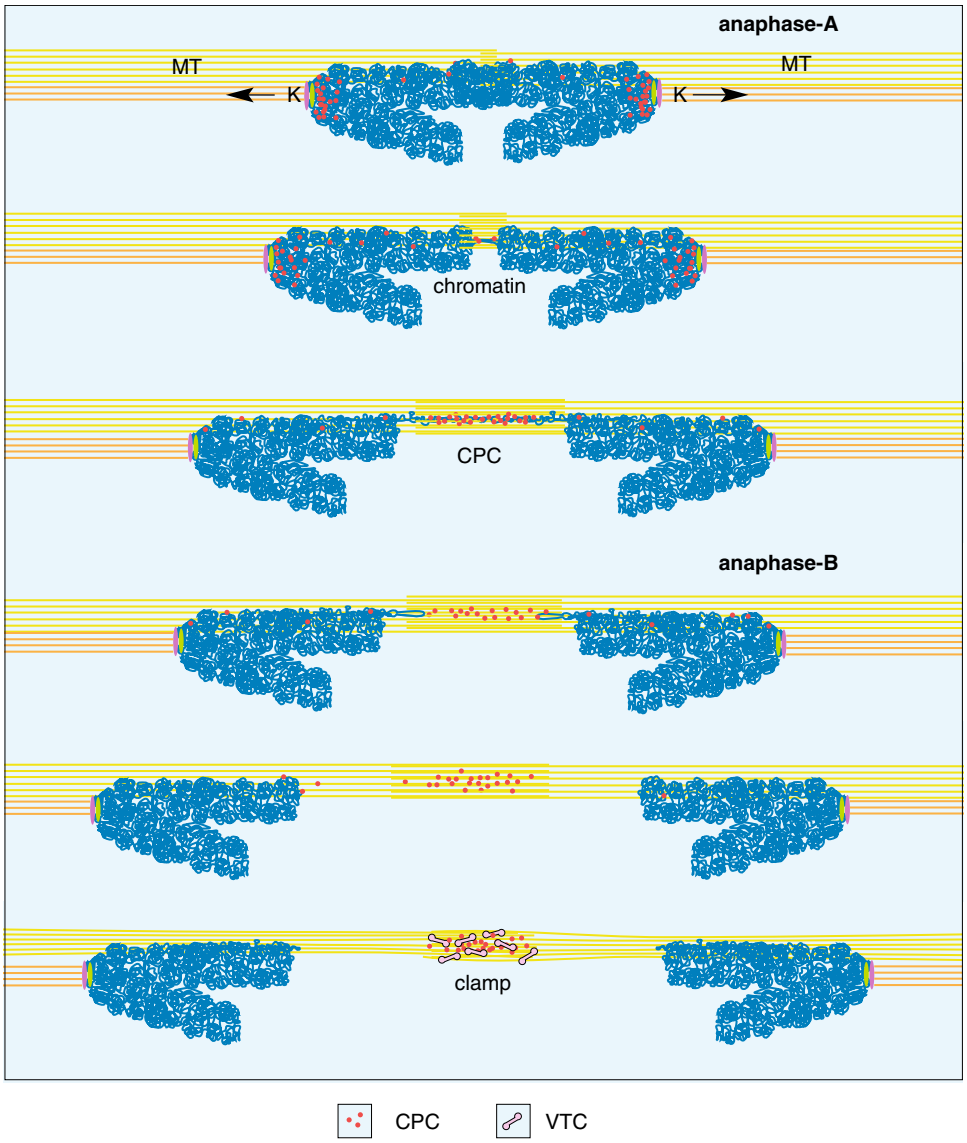

Fig. 8 Midzone formation. Midzone formation is mediated by microtubules (MT), passing the arms of separating chromatids and withdrawing chromatin from the telomere regions. Chromosomal passenger complexes (CPC) such as Aurora B, INCENP, borealin and survivin, translocate in anaphase-A from the centromeres to the ends of the chromosomes. Accumulation of CPCs in the midzone is initiated, where antiparallel microtubules overlap. With attachment of VTCs to accumulated CPCs, clamps are formed. Simultaneously, with anaphase progression chromatin strands relocate to their chromosomes, which are pulled to the centrosomes by microtubules, attached to kinetochore (K), whereas clamps remain in the midzone

2014; Wu et al. 2017). The ERELB-system explains an essential membrane circulation involving: (i) Golgi disintegration and reconstitution; (ii) vesicle/membrane turnover mediated by endosomes; (iii) storage of membrane lipids by LBs (Fig. 9). From the 3D data presented, it is clear that ER, dictyosomes, endosomes and lipid bodies cannot be considered as independent compartments. The categorical separation of structural and functional cellular entities may be responsible for competing opinions; neither model is entirely concurrent with the dynamics of an interconnected system. Whether dictyosomes derive from ER, endosomes and lipid bodies or in a concert of all three partners of the ERELB is still an open question (Fig. 9).

Capabilities of FIB/SEM

Within the last two decades TEM tomography established as the state of art technique for high-resolution 3D-imaging of resin embedded or cryo-samples. The parameters limiting 3D investigations are section thickness (approx. 300–500 nm) and the small field of view (approx. 5×5 µm). For large volumes, especially in combination with 3D LM, three candidates have to be compared: array tomography, 3View® and FIB/SEM. There is no competition between the different techniques, only a decision, which one is most suitable for the scientific question. If several mm^3 of tissues are needed for 3D-reconstructions, 3View® will be the first, if not only choice. If re-investigations of sections are necessary, only array tomography can achieve this demand. FIB/SEM, with its unsurpassed z-resolution, is recommended for bridging high-resolution

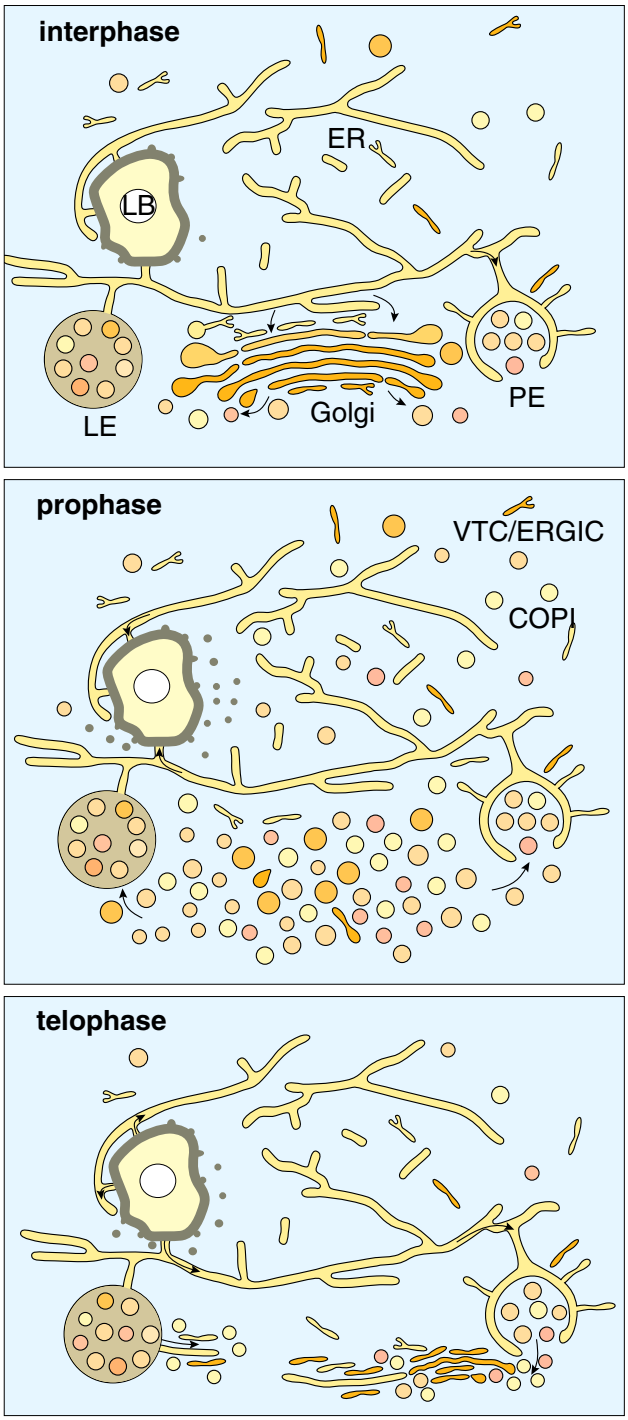

Fig. 9 Membrane traffic—the ERELB-network. Elaborate network ▶ of ER, endosomes, lipid bodies, Golgi and their mutual relation. All partners are permanently connected *via* endoplasmic reticulum (ER) in interphase, either by fusion with the ER membrane, typical for primary endosomes (PE), which originate from cup-shaped ER-segments, fusing with dictyosomal vesicles or late endosomes (LE), still connected to ER. The lipid bodies are connected by fusion of the outer leaflet of the ER membrane with the half unit membrane of the lipid body. A direct flow of membrane components (arrows) between the compartments is given. During prophase of mitosis the disintegration of the Golgi into vesicles (COPI) or ICs/VTCs/ERGICs and their integration into the ER, primary or late endosomes is achieved by a membrane circulation involving: (i) recycling and distribution by endosomes and (ii) storage of membrane lipids by lipid bodies (LB). During telophase, the Golgi is reassembled in interplay of all partners of the ERELB by reverse flow of membrane components, indicated by arrows

LM with TEM tomography. Many cytological questions can be addressed with correlative light microscopy combined with FIB/SEM-tomography of ultra-thin embedded cells in an efficient way.

Summarizing aspects

Ultra-thin embedding of cells on labeled slides has proven to fulfill all demands for CLEM:

- Thickness of the resin layer can be adapted, as desired, to any specimen by use of an acetone-saturated chamber.
- Immediate and precise correlation between LM and SEM is given.
- Milling plane can be set with high precision.
- Direct access to the target cell makes a ramp needless.
- Milling volume is restricted to the cell volume without any redeposition effects.
- Topography of the target cell is visible during the entire run, allowing immediate corrections on the fly.
- Slides serve as an absolute reference necessary for precise alignment of the FIB-stack.

Acknowledgements We thank Prof. Dr. Heinrich Leonhardt for kindly providing HeLa cells and mouse C2C12 GFP-Dnmt1 myoblast cells; Dr. Andrea Rottach for important suggestions; Dr. Hartmann Harz and Andreas Maiser for their LM expertise and Katharina Brandstetter for cultivation of HeLa cells. The excellent technical assistance of Cornelia Niemann and support of Maximilian Scheungrab with 3D-reconstruction is gratefully acknowledged. The authors are much obliged to Dr. Elizabeth Schroeder-Reiter for carefully revising the manuscript.

Compliance with ethical standards

Conflict of interest The authors declare that they have no conflict of interest.

References

Altan-Bonnet N, Sougrat R, Liu W, Snapp EL, Ward T, Lippincott-Schwartz J (2006) Golgi inheritance in mammalian cells is mediated through endoplasmic reticulum export activities. Mol Biol Cell 17:990–1005. https://doi.org/10.1091/mbc.E05-02-0155

Anderson DJ, Hetzer MW (2008) Shaping the endoplasmic reticulum into the nuclear envelope. J Cell Sci 121:137–142. https://doi.org/10.1242/jcs.005777

Anderson DJ, Vargas JD, Hsiao JP, Hetzer MW (2009) Recruitment of functionally distinct membrane proteins to chromatin mediates nuclear envelope formation in vivo. J Cell Biol 186:183–191. https://doi.org/10.1083/jcb.200901106

Axelsson MAB, Warren G (2004) Rapid, endoplasmic reticulum-independent diffusion of the mitotic Golgi haze. Mol Biol Cell 15:1843–1852. https://doi.org/10.1091/mbc.E03-07-0459

Beller M, Sztalryd C, Southall N, Bell M, Jäckle H, Auld DS, Oliver B (2008) COPI complex is a regulator of lipid homeostasis. PLoS Biol 6:e292. https://doi.org/10.1371/journal.pbio.0060292

Belu A, Schnitker J, Bertazzo S, Neumann E, Mayer D, Offenhäusser A, Santoro F (2016) Ultra-thin resin embedding method for scanning electron microscopy of individual cells on high and low aspect ratio 3D nanostructures. J Microsc 263:78–86. https://doi.org/10.1111/jmi.12378

Birky CW (1983) The partitioning of cytoplasmic organelles at cell division. Int Rev Cytol Suppl 15:49–89

Booth DG, Beckett AJ, Molina O, Samejima I, Masumoto H, Kouprina N, Larionov V, Prior IA, Earnshaw WC, 2016. 3D-CLEM Reveals that a Major Portion of Mitotic Chromosomes Is Not Chromatin. Mol Cell 64, 790–802. https://doi.org/10.1016/j.molcel.2016.10.009

Brownhill K, Wood L, Allan V (2009) Molecular motors and the Golgi complex: staying put and moving through. Semin Cell Dev Biol 20:784–792. https://doi.org/10.1016/j.semcdb.2009.03.019

Buck RC, Tisdale JM (1962) AN ELECTRON MICROSCOPIC STUDY OF THE DEVELOPMENT OF THE CLEAVAGE FURROW IN MAMMALIAN CELLS. J Cell Biol 13:117–125

Carmena M, Wheelock M, Funabiki H, Earnshaw WC (2012) The Chromosomal Passenger Complex (CPC): From Easy Rider to the Godfather of Mitosis. Nat Rev Mol Cell Biol 13:789–803. https://doi.org/10.1038/nrm3474

Chabin-Brion K, Marceiller J, Perez F, Settegrana C, Drechou A, Durand G, Poüs C (2001) The Golgi complex is a microtubule-organizing organelle. Mol Biol Cell 12:2047–2060

Dichlberger A, Schlager S, Lappalainen J, Käkelä R, Hattula K, Butcher SJ, Schneider WJ, Kovanen PT (2011) Lipid body formation during maturation of human mast cells. J Lipid Res 52:2198–2208. https://doi.org/10.1194/jlr.M019737

Domart M-C, Hobday TMC, Peddie CJ, Chung GHC, Wang A, Yeh K, Jethwa N, Zhang Q, Wakelam MJO, Woscholski R, Byrne RD, Collinson LM, Poccia DL, Larijani B (2012) Acute manipulation of diacylglycerol reveals roles in nuclear envelope assembly & endoplasmic reticulum morphology. PloS One 7:e51150. https://doi.org/10.1371/journal.pone.0051150

English AR, Voeltz GK (2013) Endoplasmic reticulum structure and interconnections with other organelles. Cold Spring Harb Perspect Biol 5:a013227. https://doi.org/10.1101/cshperspect.a013227

Farese RV, Walther TC, 2009. Lipid Droplets Finally Get a Little R-E-S-P-E-C-T. Cell 139, 855–860. https://doi.org/10.1016/j.cell.2009.11.005

Fededa JP, Gerlich DW (2012) Molecular control of animal cell cytokinesis. Nat Cell Biol 14:440. https://doi.org/10.1038/ncb2482

Fermie J, Liv N, Brink T, van Donselaar C, Müller EG, Schieber WH, Schwab NL, Gerritsen Y, Klumperman HC, J., 2018. Single organelle dynamics linked to 3D structure by correlative live-cell – 3D electron microscopy. Traffic Cph. Den. https://doi.org/10.1111/tra.12557

Friedman JR, Dibenedetto JR, West M, Rowland AA, Voeltz GK (2013) Endoplasmic reticulum-endosome contact increases as endosomes traffic and mature. Mol Biol Cell 24:1030–1040. https://doi.org/10.1091/mbc.E12-10-0733

Fujimoto T, Parton RG, 2011. Not Just Fat: The Structure and Function of the Lipid Droplet. Cold Spring Harb Perspect Biol 3. https://doi.org/10.1101/cshperspect.a004838

Gao Q, Goodman JM, 2015. The lipid droplet—a well-connected organelle. Front Cell Dev Biol 3. https://doi.org/10.3389/fcell.2015.00049

Gosavi P, Gleeson PA, 2017. The Function of the Golgi Ribbon Structure - An Enduring Mystery Unfolds! BioEssays News Rev. Mol Cell Dev Biol 39. https://doi.org/10.1002/bies.201700063

Gowrishankar S, Yuan P, Wu Y, Schrag M, Paradise S, Grutzendler J, De Camilli P, Ferguson SM, 2015. Massive accumulation of luminal protease-deficient axonal lysosomes at Alzheimer's disease amyloid plaques. Proc. Natl. Acad. Sci. U. S. A. 112, E3699–E3708. https://doi.org/10.1073/pnas.1510329112

Guizetti J, Schermelleh L, Mäntler J, Maar S, Poser I, Leonhardt H, Müller-Reichert T, Gerlich DW (2011) Cortical Constriction During Abscission Involves Helices of ESCRT-III–Dependent Filaments. Science 331:1616–1620. https://doi.org/10.1126/science.1201847

Helenius A, Mellman I, Wall D, Hubbard A (1983) Endosomes Trends Biochem Sci 8:245–250. https://doi.org/10.1016/0968-0004(83)90350-X

Hümmer S, Mayer TU (2009) Cdk1 Negatively Regulates Midzone Localization of the Mitotic Kinesin Mklp2 and the Chromosomal Passenger Complex. Curr Biol 19:607–612. https://doi.org/10.1016/j.cub.2009.02.046

Huotari J, Helenius A (2011) Endosome maturation. EMBO J 30:3481–3500. https://doi.org/10.1038/emboj.2011.286

Jesch SA, Linstedt AD (1998) The Golgi and endoplasmic reticulum remain independent during mitosis in HeLa cells. Mol Biol Cell 9:623–635

Jokitalo E, Cabrera-Poch N, Warren G, Shima DT (2001) Golgi clusters and vesicles mediate mitotic inheritance independently of the endoplasmic reticulum. J Cell Biol 154:317–330

Klumperman J, Raposo G (2014) The complex ultrastructure of the endolysosomal system. Cold Spring Harb Perspect Biol 6:a016857. https://doi.org/10.1101/cshperspect.a016857

Koga D, Ushiki T, Watanabe T (2017) Novel scanning electron microscopy methods for analyzing the 3D structure of the Golgi apparatus. Anat Sci Int 92:37–49. https://doi.org/10.1007/s12565-016-0380-8

Kurasawa Y, Earnshaw WC, Mochizuki Y, Dohmae N, Todokoro K (2004) Essential roles of KIF4 and its binding partner PRC1 in organized central spindle midzone formation. EMBO J 23:3237–3248. https://doi.org/10.1038/sj.emboj.7600347

Ladinsky MS, Mastronarde DN, McIntosh JR, Howell KE, Staehelin LA (1999) Golgi structure in three dimensions: functional insights from the normal rat kidney cell. J Cell Biol 144:1135–1149

Lees RM, Peddie CJ, Collinson LM, Ashby MC, Verkade P (2017) Correlative two-photon and serial block face scanning electron microscopy in neuronal tissue using 3D near-infrared branding maps. Methods Cell Biol 140:245–276. https://doi.org/10.1016/bs.mcb.2017.03.007

Leonhardt H, Page AW, Weier HU, Bestor TH (1992) A targeting sequence directs DNA methyltransferase to sites of DNA replication in mammalian nuclei. Cell 71:865–873

Lu L, Ladinsky MS, Kirchhausen T (2009) Cisternal organization of the endoplasmic reticulum during mitosis. Mol Biol Cell 20:3471–3480. https://doi.org/10.1091/mbc.E09-04-0327

Lucas MS, Günthert M, Bittermann AG, de Marco A, Wepf R (2017) Correlation of live-cell imaging with volume scanning electron microscopy. Methods Cell Biol 140:123–148. https://doi.org/10.1016/bs.mcb.2017.03.001

Lucocq JM, Warren G (1987) Fragmentation and partitioning of the Golgi apparatus during mitosis in HeLa cells. EMBO J 6:3239–3246

Lucocq JM, Pryde JG, Berger EG, Warren G (1987) A mitotic form of the Golgi apparatus in HeLa cells. J Cell Biol 104:865–874

Malhas A, Goulbourne C, Vaux DJ (2011) The nucleoplasmic reticulum: form and function. Trends Cell Biol 21:362–373. https://doi.org/10.1016/j.tcb.2011.03.008

Marie M, Dale HA, Kouprina N, Saraste J (2012) Division of the intermediate compartment at the onset of mitosis provides a mechanism for Golgi inheritance. J Cell Sci 125:5403–5416. https://doi.org/10.1242/jcs.108100

Marsh BJ, Pavelka M (2013) Viewing Golgi structure and function from a different perspective–insights from electron tomography. Methods Cell Biol 118:259–279. https://doi.org/10.1016/B978-0-12-417164-0.00016-1

Martin S, Parton RG (2005) Caveolin, cholesterol, and lipid bodies. Semin Cell Dev Biol 16:163–174. https://doi.org/10.1016/j.semcdb.2005.01.007

Mora-Bermúdez F, Gerlich D, Ellenberg J (2007) Maximal chromosome compaction occurs by axial shortening in anaphase and depends on Aurora kinase. Nat Cell Biol 9:822–831. https://doi.org/10.1038/ncb1606

Murphy GE, Narayan K, Lowekamp BC, Hartnell LM, Heymann JAW, Fu J, Subramaniam S (2011) Correlative 3D imaging of whole mammalian cells with light and electron microscopy. J Struct Biol 176:268–278. https://doi.org/10.1016/j.jsb.2011.08.013

Muscat CC, Torre-Santiago KM, Tran MV, Powers JA, Wignall SM (2015) Kinetochore-independent chromosome segregation driven by lateral microtubule bundles. eLife 4:e06462. https://doi.org/10.7554/eLife.06462

Nakamura N, Wei J-H, Seemann J (2012) Modular organization of the mammalian Golgi apparatus. Curr Opin Cell Biol 24:467–474. https://doi.org/10.1016/j.ceb.2012.05.009

Nishita M, Satake T, Minami Y, Suzuki A (2017) Regulatory mechanisms and cellular functions of non-centrosomal microtubules. J Biochem (Tokyo) 162:1–10. https://doi.org/10.1093/jb/mvx018

Pol A, Gross SP, Parton RG (2014) Biogenesis of the multifunctional lipid droplet: Lipids, proteins, and sites. J Cell Biol 204:635–646. https://doi.org/10.1083/jcb.201311051

Pyle JR, Chen J (2017) Photobleaching of YOYO-1 in super-resolution single DNA fluorescence imaging. Beilstein J Nanotechnol 8:2296–2306. https://doi.org/10.3762/bjnano.8.229

Rennie MY, Gahan CG, López CS, Thornburg KL, Rugonyi S (2014) 3D imaging of the early embryonic chicken heart with focused ion beam scanning electron microscopy. Microsc Microanal Off J Microsc Soc Am Microbeam Anal Soc Microsc Soc Can 20:1111–1119. https://doi.org/10.1017/S1431927614000828

Rios RM, 2014. The centrosome-Golgi apparatus nexus. Philos Trans R Soc Lond B Biol Sci 369. https://doi.org/10.1098/rstb.2013.0462

Robbins E, Jentzsch G (1969) ULTRASTRUCTURAL CHANGES IN THE MITOTIC APPARATUS AT THE METAPHASE-TO-ANAPHASE TRANSITION. J Cell Biol 40:678–691

Robbins E, Jentzsch G, Micali A (1968) THE CENTRIOLE CYCLE IN SYNCHRONIZED HELA CELLS. J Cell Biol 36:329–339

Rocha LC, Jankowska M, Fuchs J, Mittelmann A, Techio VH, Houben A (2017) Decondensation of chromosomal 45S rDNA sites in Lolium and Festuca genotypes does not result in karyotype instability. Protoplasma 254:285–292. https://doi.org/10.1007/s00709-016-0942-6

Sanders AAWM., Kaverina I (2015) Nucleation and Dynamics of Golgi-derived Microtubules. Front Neurosci 9:431. https://doi.org/10.3389/fnins.2015.00431

Santoro F, Zhao W, Joubert L-M, Duan L, Schnitker J, van de Burgt Y, Lou H-Y, Liu B, Salleo A, Cui L, Cui Y, Cui B (2017) Revealing the Cell-Material Interface with Nanometer Resolution by Focused Ion Beam/Scanning Electron Microscopy. ACS Nano 11:8320–8328. https://doi.org/10.1021/acsnano.7b03494

Schieber NL, Machado P, Markert SM, Stigloher C, Schwab Y, Steyer AM (2017) Minimal resin embedding of multicellular specimens for targeted FIB-SEM imaging. Methods Cell Biol 140:69–83. https://doi.org/10.1016/bs.mcb.2017.03.005

Schneider K, Fuchs C, Dobay A, Rottach A, Qin W, Wolf P, Álvarez-Castro JM, Nalaskowski MM, Kremmer E, Schmid V, Leonhardt H, Schermelleh L (2013) Dissection of cell cycle–dependent dynamics of Dnmt1 by FRAP and diffusion-coupled modeling. Nucleic Acids Res 41:4860–4876. https://doi.org/10.1093/nar/gkt191

Schroeder-Reiter E, Sanei M, Houben A, Wanner G (2012) Current SEM techniques for de- and re-construction of centromeres to determine 3D CENH3 distribution in barley mitotic chromosomes. J Microsc 246:96–106. https://doi.org/10.1111/j.1365-2818.2011.03592.x

Schuldt A (2010) Cytoskeleton: Midzone microtubule management [WWW Document]. Nat Rev Mol Cell Biol https://doi. https://doi.org/10.1038/nrm2965

Seemann J, Pypaert M, Taguchi T, Malsam J, Warren G (2002) Partitioning of the matrix fraction of the Golgi apparatus during mitosis in animal cells. Science 295:848–851. https://doi.org/10.1126/science.1068064

Seguí-Simarro JM, Austin JR, White EA, Staehelin LA (2004) Electron Tomographic Analysis of Somatic Cell Plate Formation in Meristematic Cells of Arabidopsis Preserved by High-Pressure Freezing. Plant Cell 16:836–856. https://doi.org/10.1105/tpc.017749

Sherman S, Kirchenbuechler D, Nachmias D, Tamir A, Werner S, Elbaum M, Elia N (2016) Resolving new ultrastructural features of cytokinetic abscission with soft-X-ray cryo-tomography. Sci Rep 6:27629. https://doi.org/10.1038/srep27629

Soni KG, Mardones GA, Sougrat R, Smirnova E, Jackson CL, Bonifacino JS (2009) Coatomer-dependent protein delivery to lipid droplets. J Cell Sci 122:1834–1841. https://doi.org/10.1242/jcs.045849

Staehelin LA, Kang B-H (2008) Nanoscale architecture of endoplasmic reticulum export sites and of Golgi membranes as determined by electron tomography. Plant Physiol 147:1454–1468. https://doi.org/10.1104/pp.108.120618

Sütterlin C, Colanzi A (2010) The Golgi and the centrosome: building a functional partnership. J Cell Biol 188:621–628. https://doi.org/10.1083/jcb.200910001

Tang D, Wang Y (2013) Cell cycle regulation of Golgi membrane dynamics. Trends Cell Biol 23:296–304. https://doi.org/10.1016/j.tcb.2013.01.008

Thiam AR, Beller M (2017) The why, when and how of lipid droplet diversity. J Cell Sci 130:315–324. https://doi.org/10.1242/jcs.192021

Thompson HM, Skop AR, Euteneuer U, Meyer BJ, McNiven MA (2002) The Large GTPase Dynamin Associates with the Spindle Midzone and Is Required for Cytokinesis. Curr Biol CB 12:2111–2117

Verkade P (2008) Moving EM: the Rapid Transfer System as a new tool for correlative light and electron microscopy and high throughput for high-pressure freezing. J Microsc 230:317–328. https://doi.org/10.1111/j.1365-2818.2008.01989.x

Villinger C, Gregorius H, Kranz C, Höhn K, Münzberg C, von Wichert G, Mizaikoff B, Wanner G, Walther P (2012) FIB/SEM

tomography with TEM-like resolution for 3D imaging of high-pressure frozen cells. Histochem Cell Biol 138:549–556. https://doi.org/10.1007/s00418-012-1020-6

Wan H-C, Melo RCN, Jin Z, Dvorak AM, Weller PF (2007) Roles and origins of leukocyte lipid bodies: proteomic and ultrastructural studies. FASEB J Off Publ Fed Am Soc Exp Biol 21:167–178. https://doi.org/10.1096/fj.06-6711com

Wang Y, Seemann J, 2011. Golgi biogenesis. Cold Spring Harb. Perspect. Biol. 3, a005330. https://doi.org/10.1101/cshperspect.a005330

Wanner G, Formanek H, Theimer RR (1981) The ontogeny of lipid bodies (spherosomes) in plant cells: Ultrastructural evidence. Planta 151:109–123. https://doi.org/10.1007/BF00387812

Wei J-H, Seemann J (2017) Golgi ribbon disassembly during mitosis, differentiation and disease progression. Curr Opin Cell Biol 47:43–51. https://doi.org/10.1016/j.ceb.2017.03.008

Wu Y, Whiteus C, Xu CS, Hayworth KJ, Weinberg RJ, Hess HF, Camilli PD, 2017. Contacts between the endoplasmic reticulum and other membranes in neurons. Proc. Natl. Acad. Sci. 114, E4859–E4867. https://doi.org/10.1073/pnas.1701078114

Xu CS, Hayworth KJ, Lu Z, Grob P, Hassan AM, García-Cerdán JG, Niyogi KK, Nogales E, Weinberg RJ, Hess HF, 2017. Enhanced FIB-SEM systems for large-volume 3D imaging. eLife 6. https://doi.org/10.7554/eLife.25916

Yadav S, Linstedt AD, 2011. Golgi positioning. Cold Spring Harb Perspect Biol 3. https://doi.org/10.1101/cshperspect.a005322

Yao X, Anderson KL, Cleveland DW (1997) The microtubule-dependent motor centromere-associated protein E (CENP-E) is an integral component of kinetochore corona fibers that link centromeres to spindle microtubules. J Cell Biol 139:435–447

Yatsu LY, Jacks TJ (1972) Spherosome membranes: half unit-membranes. Plant Physiol 49:937–943

Zaal KJ, Smith CL, Polishchuk RS, Altan N, Cole NB, Ellenberg J, Hirschberg K, Presley JF, Roberts TH, Siggia E, Phair RD, Lippincott-Schwartz J (1999) Golgi membranes are absorbed into and reemerge from the ER during mitosis. Cell 99:589–601

Zhao YG, Chen Y, Miao G, Zhao H, Qu W, Li D, Wang Z, Liu N, Li L, Chen S, Liu P, Feng D, Zhang H (2017) The ER-Localized Transmembrane Protein EPG-3/VMP1 Regulates SERCA Activity to Control ER-Isolation Membrane Contacts for Autophagosome Formation. Mol Cell 67:974–989.e6. https://doi.org/10.1016/j.molcel.2017.08.005

Zhu X, Kaverina I (2013) Golgi as an MTOC: making microtubules for its own good. Histochem Cell Biol 140:361–367. https://doi.org/10.1007/s00418-013-1119-4

Supplementary Material

Precise and economic FIB/SEM for CLEM: with 2 nm voxels through mitosis

Manja Luckner & Gerhard Wanner

https://link-springer-com.emedien.ub.uni-muenchen.de/article/10.1007%2Fs00418-018-1681-x#SupplementaryMaterial

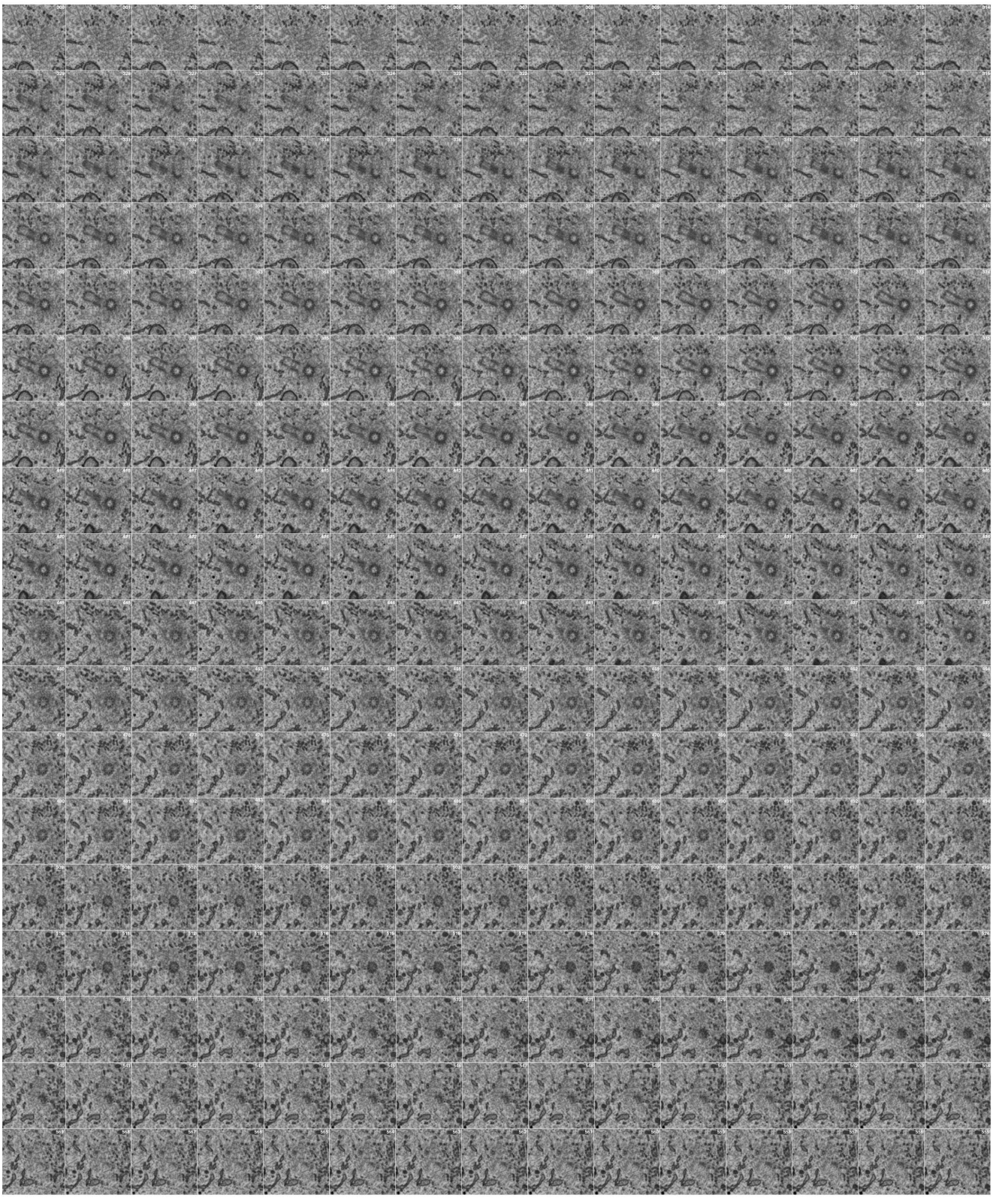

Fig. S1
High Resolution FIB/SEM at its Limit.
270 consecutive block face FIB/SEM micrographs (out of a series of 720 sections) through a centrosome of a HeLa cell in metaphase, sectioned with a voxel size of 2x2x2 nm illustrating the high resolution in z and stability that can be achieved with FIB/SEM. Scale bar 500 nm.

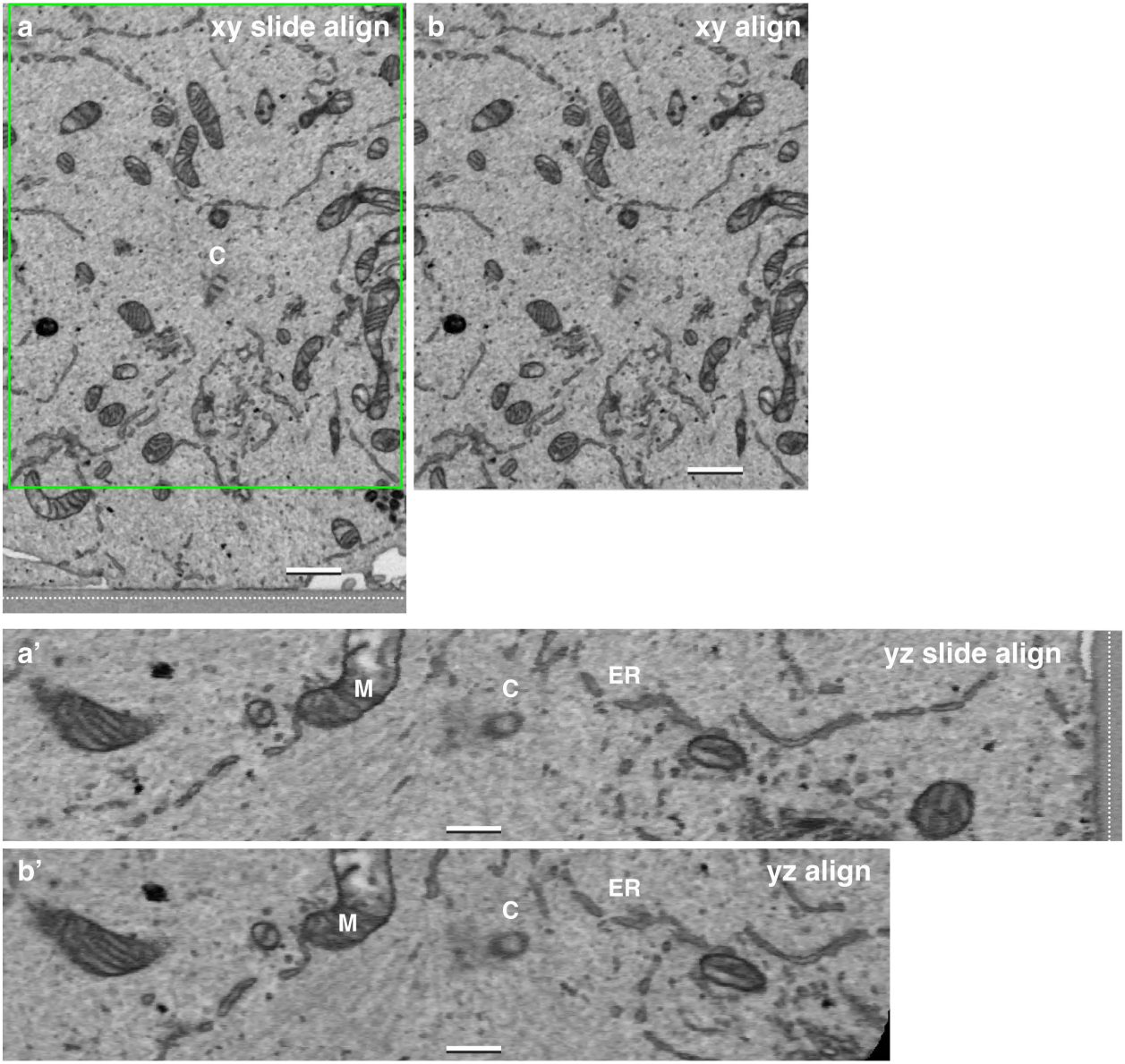

Fig. S2
Alignments of FIB/SEM stack with absolute reference.

a Image stack (xy view) with slide as reference (dotted line). Scale bar 1 μm.

b Image stack (xy view) cropped, without reference (b; = framed area of a). Scale bar 1 μm.

a' Alignment with shear function and manually fine correction (straight line of the slide surface in yz). Scale bar 500 nm.

b' Alignment using only the cellular area. In side view (yz) the mitochondria (M) and endoplasmic reticulum (ER) show striking differences in shape and position (a', b'). Scale bar 500 nm.

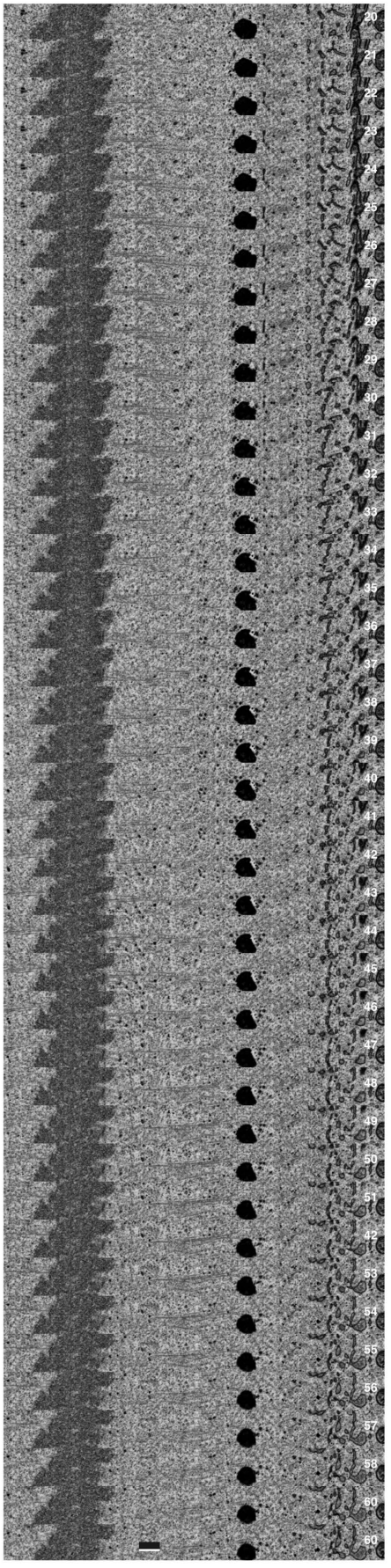

Fig. S3
FIB/SEM tomography of a kinetochore.

40 consecutive block face FIB/SEM micrographs through a centromeric region of a HeLa cell in metaphase, sectioned with a voxel size of 3.5x3.5x6 nm. Individual microtubules can be followed over several sections, proving the quality of thin milling. Scale bar 500 nm.

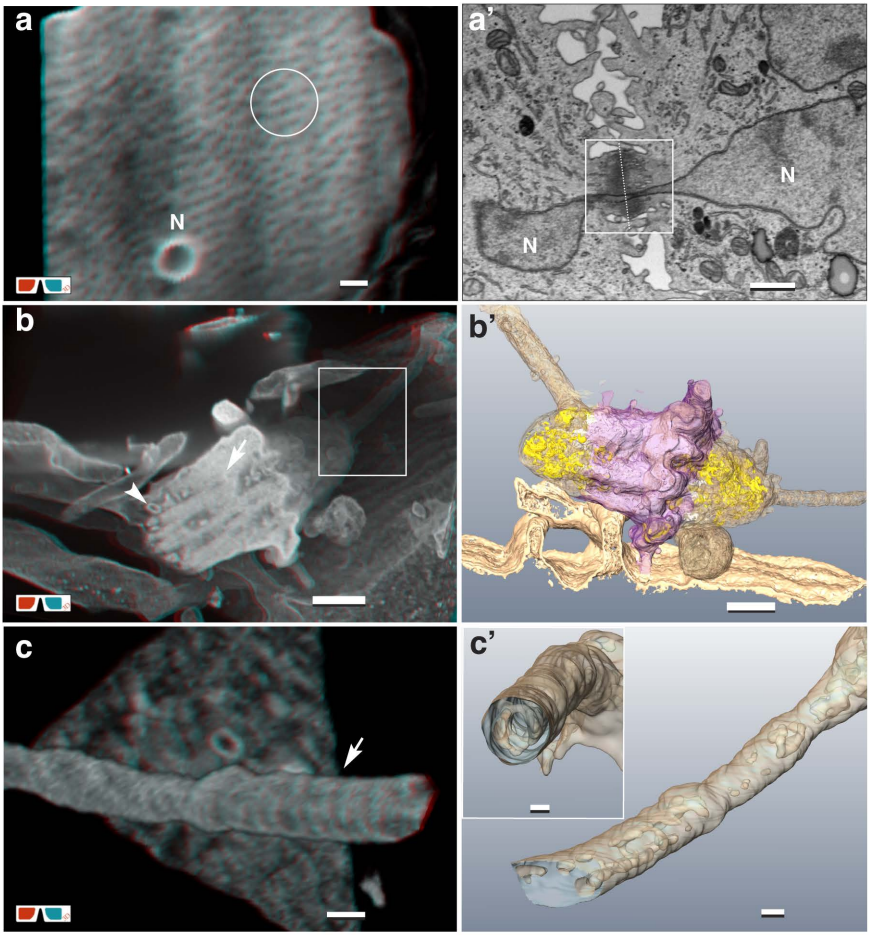

Fig. S4
FIB/SEM tomography of midbody.

a High-resolution volume rendering of a midbody in cross section exhibits an electron dense matrix with numerous MTs (circle) and a nucleus bridge (N) in cross section. Scale bar 1 μm. a' Longitudinal section of the midbody in (a). The NE of the dividing cells has not been reconstituted for each nucleus (N) separately, therefore crossing the midbody (rectangle). Dotted line represents position of section plane in (a). Scale bar 1 μm.

b Intersected midbody, just before abscission and its corresponding 3D reconstruction (b'), still containing MTs (arrow; violet) and vesicular-tubular structures (arrow heads; yellow). At both sides of the midbody, constrictions are visible as small plasma membrane tubes, representing the sites of abscission (framed area). Scale bar 500 nm.

c Detail of the site of abscission. Anaglyph images and the corresponding 3D-reconstruction (c') reveal a partial helical structure, attached to the wall of the tube. Scale bar 100 nm.

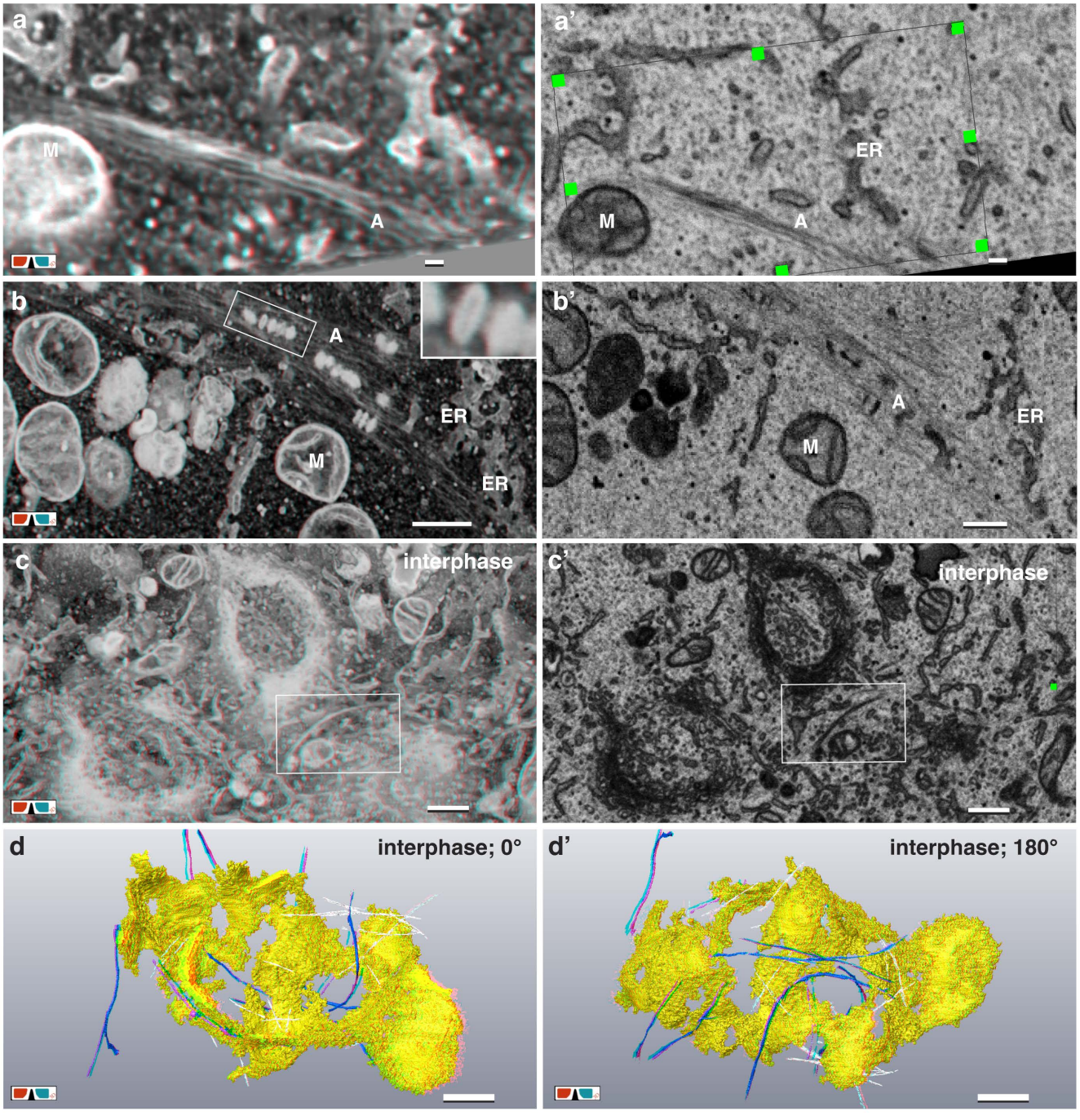

Fig. S5
Actin bundles with associated vesicles.

Actin forms bundles of electron dense fibrils with different degrees of compaction (a, a'). Scale bar 100 nm. Locally, groups of rather flat electron dense vesicles, typically aligned in a row are in contact to actin-bundles (b; framed area; inset). Scale bar 500 nm. Several sickle shaped strands of actin are associated with the Golgi apparatus, visualized with volume rendering (c) and after 3D reconstruction (d/d': actin = blue; microtubules = white). Scale bar in c 500 nm; d and d' 1 μm.

Supplementary Material
Movie S1.mp4

Supplementary Material
Movie S2.mp4

Supplementary Material
Movie S3.mp4

https://link-springer-com.emedien.ub.uni-muenchen.de/article/10.1007%2Fs00418-018-1681-x#SupplementaryMaterial

10.6 Publication VI

Label-free 3D-CLEM using endogenous tissue landmarks**.**

Manja Luckner, Steffen Burgold, Severin Filser, Maximilian Scheungrab, Yilmaz Niyaz, Eric Hummel, Gerhard Wanner & Jochen Herms (2018)

iScience, 2018 July (in press)
doi: 10.1016/j.isci.2018.07.012

Abstract
Emerging 3D correlative light and electron microscopy (CLEM) approaches enable studying neuronal structure-function relations at unprecedented depth and precision. However, established protocols for the correlation of light and electron micrographs rely on the introduction of artificial fiducial markers, such as polymer beads or near-infrared branding, which might obscure or even damage the structure under investigation. Here, we report an efficient, general applicable "flat embedding" preparation, enabling high-precision overlay of light and electron micrographs, using exclusively endogenous landmarks in the brain: blood vessels, nuclei and myelinated axons. Furthermore, we demonstrate feasibility of the workflow by combining in vivo 2-photon microscopy and high-resolution FIB/SEM microscopy to dissect the role of astrocytic coverage in the persistence of dendritic spines.

Note
Accepted manuscript, PDF only. Full online edition to follow.

iScience

CellPress

Article

Label-free 3D-CLEM Using Endogenous Tissue Landmarks

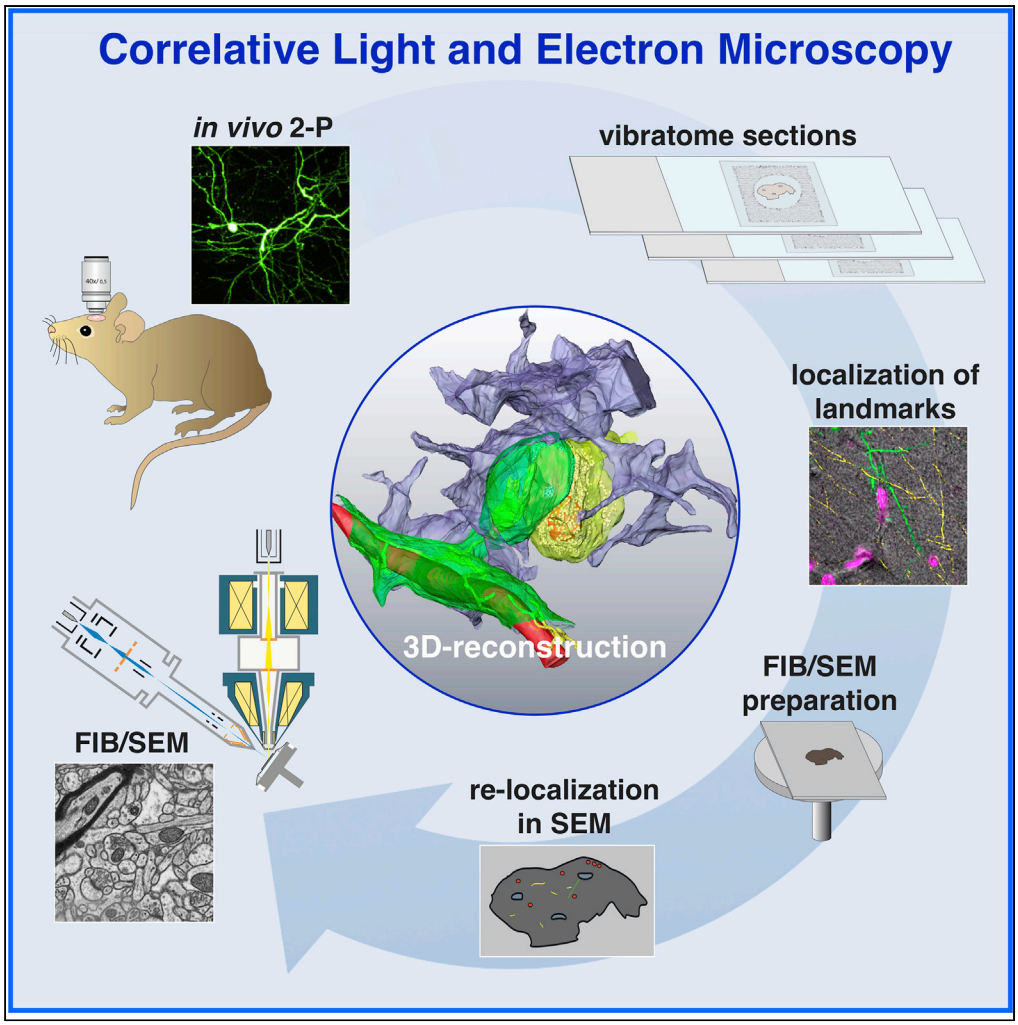

Manja Luckner, Steffen Burgold, Severin Filser, ..., Eric Hummel, Gerhard Wanner, Jochen Herms

jochen.herms@med.uni-muenchen.de

HIGHLIGHTS

Flat embedding of vibratome sections for precise correlation of LM and SEM

Endogenous landmarks are ideal fiducials for CLEM

The glass slide serves as an absolute reference for precise alignment in yz

Correlation of perisynaptic ensheathment and dendritic spine lifetime

Luckner et al., iScience 6, 92–101
August 31, 2018
https://doi.org/10.1016/j.isci.2018.07.012

iScience

CellPress

Article

Label-free 3D-CLEM Using Endogenous Tissue Landmarks

Manja Luckner,[1,2,6] Steffen Burgold,[2,3,4,6,7] Severin Filser,[2,6] Maximilian Scheungrab,[1] Yilmaz Niyaz,[4] Eric Hummel,[4] Gerhard Wanner,[1] and Jochen Herms[1,2,3,5,8,*]

SUMMARY

Emerging 3D correlative light and electron microscopy approaches enable studying neuronal structure-function relations at unprecedented depth and precision. However, established protocols for the correlation of light and electron micrographs rely on the introduction of artificial fiducial markers, such as polymer beads or near-infrared brandings, which might obscure or even damage the structure under investigation. Here, we report a general applicable "flat embedding" preparation, enabling high-precision overlay of light and scanning electron micrographs, using exclusively endogenous landmarks in the brain: blood vessels, nuclei, and myelinated axons. Furthermore, we demonstrate feasibility of the workflow by combining *in vivo* 2-photon microscopy and focused ion beam scanning electron microscopy to dissect the role of astrocytic coverage in the persistence of dendritic spines.

INTRODUCTION

Studying biological key events within complex model systems relies on dynamic and functional imaging at optimum spatial and temporal resolution. Light microscopy (LM) allows visualization of dynamic cellular events in tissues, whereas electron microscopy (EM) remains the only method so far to reveal the complete subcellular architecture at nanometer resolution (Bourne and Harris, 2008). Correlative light and electron microscopy (CLEM) combines the advantages of both imaging modalities, allowing targeting the events of interest in space and time, using LM and subsequently resolving the ultrastructure of the same volume with EM (de Boer et al., 2015; Karreman et al., 2016a; Mironov and Beznoussenko, 2009). In particular, CLEM has greatly advanced our understanding of complex neuronal connectivity matrices by revealing the ultrastructural architecture and dynamics of neurites and synapses (Blazquez-Llorca et al., 2015; Genoud et al., 2006; Maco et al., 2013, 2014). However, a major methodological hurdle remains the correlation of LM and EM datasets by accurately tracking the position of the region of interest (ROI) within the EM specimen. For voluminous specimens such as the mouse brain, ROIs can be retrieved by screening serial thick (50–100 μm) vibratome sections of the tissue (Li et al., 2011). Nevertheless, serial EM imaging of large tissue samples is very cumbersome and results in unnecessarily large datasets. Currently, LM inspection to confine an ROI within the EM specimen is the most common approach for CLEM. For this purpose, fiducials are needed, which are detectable in both LM and EM. The ROIs can be marked by photo-oxidation of fluorophores (Grabenbauer et al., 2005), by affinity labeling with peroxidases (Knott et al., 2009) or by the use of exogenous fiducial markers like polymer beads (Kukulski et al., 2012), quantum dots (Masich et al., 2006), or near-infrared branding (NIRB) (Bishop et al., 2011). Although useful, these approaches require processing of the tissue samples and thereby might obscure the target structure or even deteriorate their ultrastructure. Alternatively, endogenous landmarks, which surround the ROI providing both LM and EM contrast, can be used as a guide to retrace the position of the ROI following EM processing (Karreman et al., 2016b). Unfortunately, resin embedding for EM preparations covers endogenous landmarks, thus prohibiting marker identification by EM. Although there are some protocols to reduce resin embedding, these methods comprise several delicate preparation steps or specialized equipment (Kizilyaprak et al., 2014; Belu et al., 2016; Lucas et al., 2017; Schieber et al., 2017). These issues were addressed by developing a "flat embedding" preparation to enable direct LM visualization of endogenous fiducial markers, present throughout the brain parenchyma. We show that blood vessels, nuclei, and myelinated axons can be used for precise correlation of LM and EM images with micrometer accuracy, allowing retrieval of structures as small as single synapses. A wide range of optical microscopic modalities, including wide-field, differential interference contrast (DIC), and confocal and reflectance microscopies can be used to visualize these endogenous landmarks with minimal labeling effort or even in a completely label-free manner. The feasibility of the protocol was confirmed by revealing the intimate interplay of perisynaptic astrocytic

[1]Department of Biology I, Biocenter Ludwig-Maximilians-University Munich, Planegg-Martinsried 82152, Germany

[2]German Center for Neurodegenerative Diseases (DZNE), Translational Brain Research, Munich 81377, Germany

[3]Center for Neuropathology, Ludwig-Maximilians-University Munich, Munich 81377, Germany

[4]Carl Zeiss Microscopy, Oberkochen 73447, Germany

[5]Munich Cluster of Systems Neurology (SyNergy), Munich 81377, Germany

[6]These authors contributed equally

[7]Present address: Carl Zeiss Microscopy, Oberkochen 73447, Germany

[8]Lead Contact

*Correspondence: jochen.herms@med.uni-muenchen.de

https://doi.org/10.1016/j.isci.2018.07.012

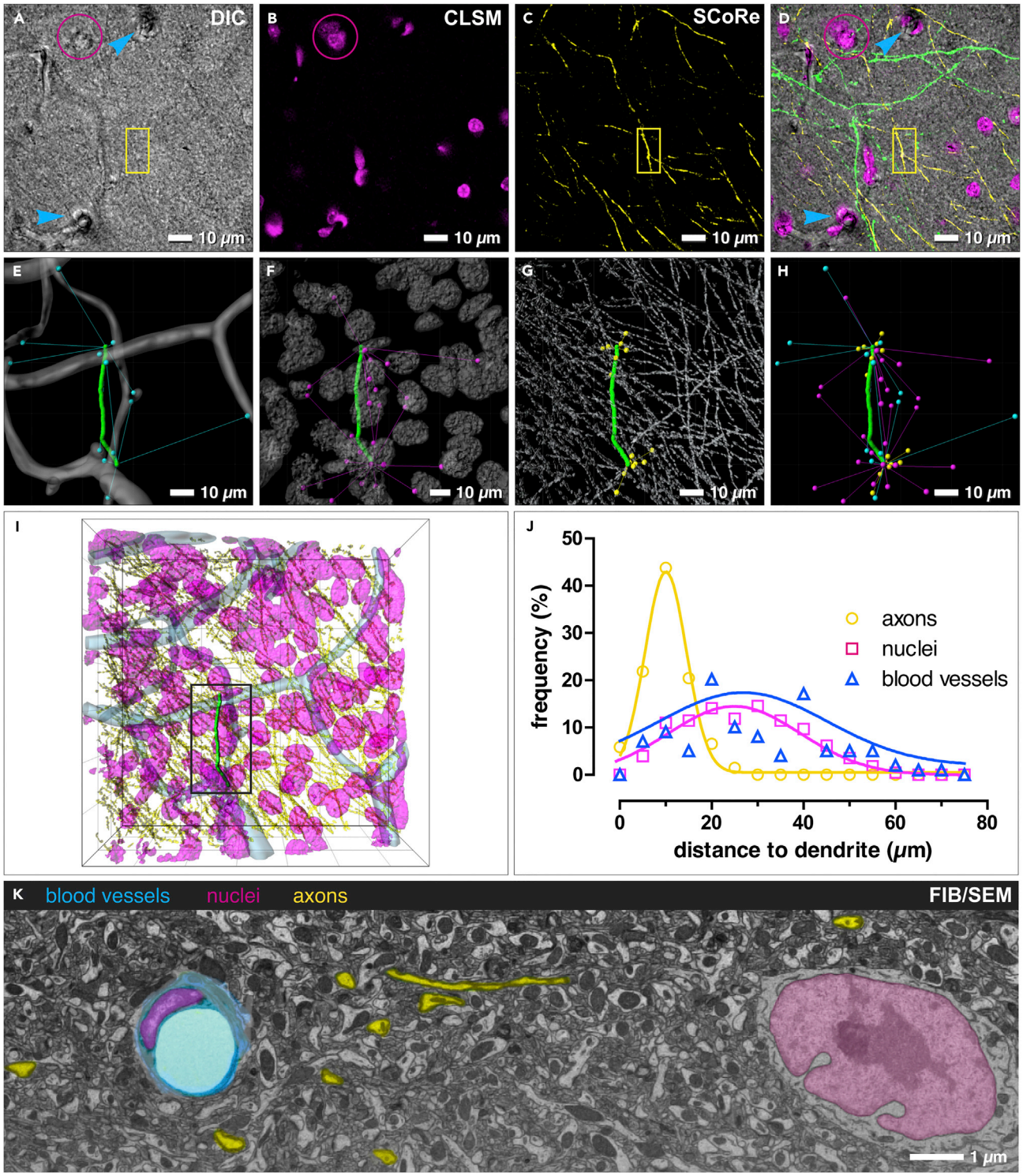

Figure 1. Availability and Precision of Endogenous CLEM Landmarks

(A–C) Blood vessels (arrowheads), nuclei (magenta) and myelinated axons (yellow; boxed area) can be visualized by DIC (A), CLSM (B) and SCoRe (C) microscopy.

(D) Overlay of DIC, CLSM, and SCoRe images. Blood vessels (arrowheads); nuclei (magenta); myelinated axons (yellow; boxed area).

(E–H) 3D reconstructions of blood vessels (E), nuclei (F), and myelinated axons (G) with distance traces between target dendrite and closest landmarks (H).

(I) Overlay of the 3D reconstructions of landmarks and the target dendrite.

Figure 1. *Continued*

(J) Frequency distribution of correlative landmarks, plotted against their respective distance to the target dendrite.

(K) FIB/SEM micrograph of cortical mouse brain tissue clearly represents blood vessels (blue), nuclei (magenta), and myelinated axons (yellow) by their typical shape and contrast.

Related to Figures S1–S3.

processes and dendritic spines, previously imaged by *in vivo* two-photon microscopy and subsequently re-located and imaged by focused ion beam scanning electron microscopy (FIB/SEM) with nanometer resolution.

RESULTS

Natural Landmarks for 3D-CLEM

Blood vessels, nuclei, and myelinated axons are excellent fiducial markers for 3D-CLEM since they fulfill the following criteria: (1) sufficient contrast in LM and EM, (2) distinctive size and shape, and (3) sufficient density to restrict the volume of correlation (Figure 1). They can be readily recognized by DIC (Figure 1A) and FIB/SEM (Figure 1K). The precise 3D position of these landmarks in proximity to the target dendrite can be mapped by various confocal microscopic techniques (Figures 1A–1C). Confocal laser scanning microscopy (CLSM) enables high-resolution imaging of nuclei, stained with the cell-permeant DNA-binding dye DRAQ5 (Figure 1B). Since DRAQ5 is a vital dye, tissue permeabilization can be omitted, which bears the risk of ultrastructural deterioration. In addition, spectral confocal reflectance microscopy (SCoRe) (Schain et al., 2014) can be used for direct, label-free visualization of myelinated axons (Figure 1C). Spatial distances between a randomly selected dendritic segment and its surrounding landmarks in cortical layer I were determined to confirm that landmarks are sufficient for precise CLEM alignment (Figures 1E–1J). The average distance between a dendrite and either blood vessels (Figure 1E) or nuclei (Figure 1F) equaled 25.5 μm or 26.7 μm, respectively (Figure 1J). The distinct morphology of both markers facilitated the identification of ROIs by triangulation of the landmarks. Myelinated axons (Figures 1C and 1G) are present in higher density and subsequently at closer vicinity to the target dendrite, with an average distance of 9 μm (Figure 1J), thus further increasing the precision of ROI retrieval.

"Flat-Embedding" Preparation for CLEM

To demonstrate the applicability and precision of the presented CLEM preparation method, several ROIs with Thy1.2-eGFP-expressing dendritic tufts in the somatosensory cortex of Thy1.2-GFP-M mice (Figures 2A–2C) were imaged by *in vivo* 2-photon microscopy and subsequently relocated in vibratome sections (Figures 2D–2F). Vibratome sections were immobilized on glass slides to maintain specimen orientation during LM and EM preparation. To identify the sections containing the ROI, brain slices were recorded with an epifluorescence microscope to reconstruct the dissected cortex with an imaging software (Adobe Photoshop), based on its unique blood vessel pattern (Figure 2D).

ROI-containing brain sections were further processed for EM (Figure 3A). Excessive resin, covering the brain tissue, was removed by draining and centrifugation to enable direct macroscopic inspection of the tissue surface (Figures 3B and 3C). Superimposition of bright field (Figure 3B) and SEM (Figure 3C) micrographs, based on the characteristic outline of the brain section, was sufficient for an immediate macroscopic correlation. The preparation protocol preserved the integrity of the specimens without major tissue shrinkage or corrugations (Figures 3B and 3C), as could be expected from dehydration. Suitable fiducials for CLEM could be identified in SEM due to the carbon coating of the specimen: since carbon has lower yields of backscattered electrons (BSE) and secondary electrons (SEs), compared with heavy metals, it appears transparent and superficial structures of the tissue become detectable. Structures lying in greater depth become visible by slightly increasing the accelerating voltage (Figure S1). The distinctive sizes and shapes of the apparent natural landmarks (blood vessels appear as channels or large holes, nuclei as dark dots) were used for the subsequent superimposition of light and electron micrographs, to define the target area in x/y direction (Figures 3D–3F).

3D Landmark Correlation of LM and FIB-SEM Datasets

After identification of the target area on the specimen surface, FIB milling was used to gain access into the brain tissue containing the dendrite of interest, which was previously imaged by *in vivo* 2-photon microscopy. Milling time, and consequently costs, were reduced by milling the trench toward the volume of interest with high beam current, which was stepwise decreased, while approaching the final block face of

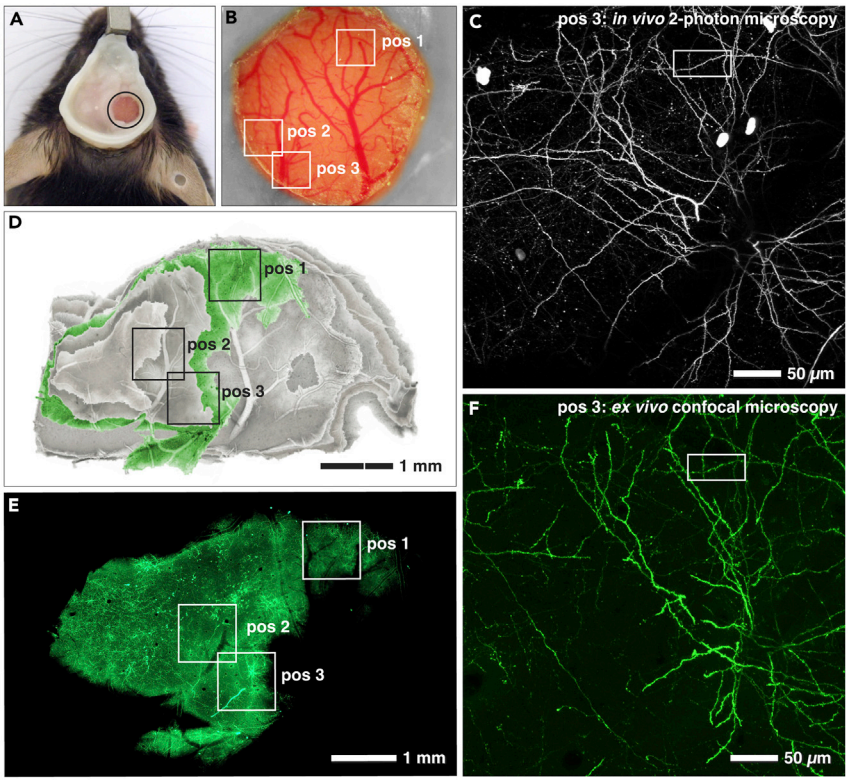

Figure 2. *In vivo* and *Ex Vivo* Light Microscopy for CLEM

(A) Cranial window implantation gives optical access to the cortex of the mouse brain.

(B) Magnified image section of cranial window in (A). The blood vessel pattern enables the retrieval of previously imaged positions (framed areas: pos 1–pos 3).

(C) Maximum intensity projection of *in vivo* 2-photon image stack of pos 3 (framed in B). Framed area designates the target dendrite at the last imaging time point (day 41).

(D and E) Reconstruction of the cortex by alignment of vibratome sections (D), based on the blood vessel pattern, facilitates identification of the brain slice (green) containing the target dendrites of three different positions (pos 1– pos 3) (E).

(F) Maximum intensity projection of *ex vivo* CLSM image stack of pos 3 (D and E). Framed area designates the target dendrite [compare (F) with (C)].

70 × 50 µm (Figures 4A–4C). Since block-face micrographs exhibit sufficient landmarks for correlation, the position of the ROI could be identified by correlating the FIB/SEM 3D reconstructions of nuclei and blood vessels with the corresponding CLSM 3D data in Amira (Figure 4D). A rough 3D reconstruction of the dense axonal network further facilitated the identification of the target dendrite (Figures 3E and 3F; Video S1), thus reducing the ROI to 15 × 15 µm (Figure 4C). The final ROI images were acquired with high resolution (pixel size in x/y: 5 nm) every 15 nm, whereas low-resolution overview images (pixel size in x/y: 27 nm) of the entire block-face area were recorded every 1 µm in z (Figures 4B and 4C) to confirm or eventually adjust the position of the ROI "on the fly."

CLEM of Dendritic Spine Lifetime and Astrocytic Synapse Coverage

The concept of the "tripartite synapse" refers to the functional integration and physical proximity of astrocytic processes with pre- and postsynaptic elements of the chemical synapse (Araque et al., 1999). However, experimental dissection of the morpho-functional relationship between these structures is hampered by the very small size of perisynaptic astrocytic processes (PAPs), which is below the resolution limit of conventional LM (Heller and Rusakov, 2015; Panatier et al., 2014). CLEM in combination with the "flat-embedding" protocol is suitable to study the morpho-functional interactions between PAPs and their corresponding synapses at an ultrastructural level. Hereby, we were able to investigate whether the extent of synaptic PAP coverage correlates with the lifetime of post-synaptic partners. To assess the lifetime of

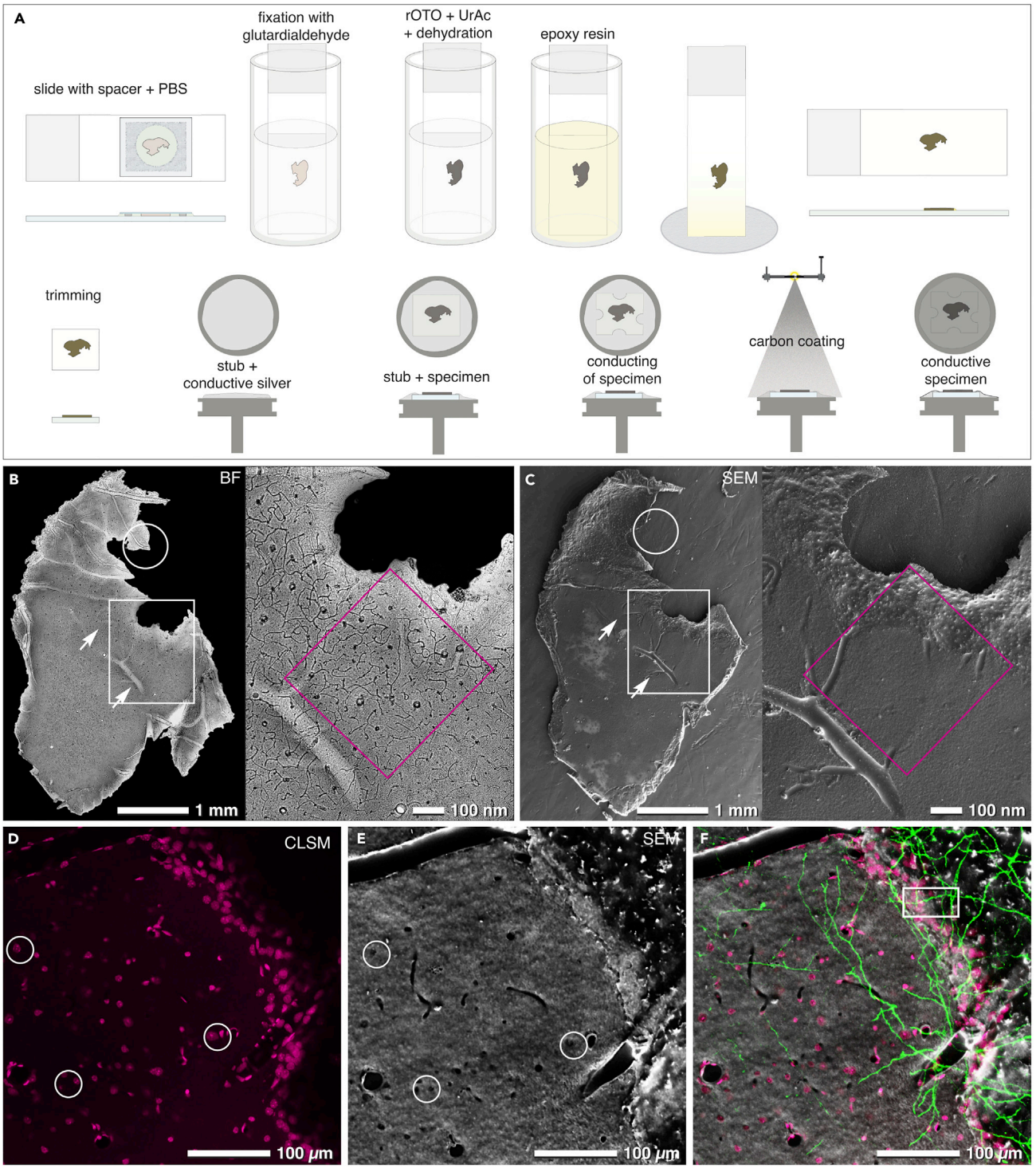

Figure 3. Sample Preparation and Retrieval of Landmarks

(A) Vibratome sections are mounted onto a glass slide with a spacer and sealed by a coverslip. After LM, the coverslip and the spacer are removed. Post-fixation (glutardialdehyde, reduced osmium-ferrocyanide-thiocarbohydrazide-osmium (rOTO), uranyl acetate [UrAC]), dehydration and infiltration with epoxy resin are performed in vials. After removal of excess resin and polymerization, the slide is trimmed to appropriate size. The specimen is mounted with colloidal silver onto an aluminum stub, conducted with bridges of colloidal silver, and coated with carbon (15–20 nm) by evaporation.

(B and C) Comparison of a bright field (BF) micrograph (B) with a scanning electron micrograph (C) of the selected vibratome slice (Figures 2 D and 2E). At low magnification, changes in morphology are easily recognized (B, C, circles). Intersected blood vessels are visible in both images (arrows), serving as the most prominent landmarks.

Figure 3. *Continued*

(D–F) Optical sections of surface near nuclei (D; white circles) can be correlated to intersected nuclei, visible in SEM at higher voltages (20 kV) due to both topographic and material contrast (E; white circles). Superimposition of both signals (DRAQ5: magenta, nuclei; eGFP: green, dendrites) with the SEM image (F) serves as a precise map for localizing the target dendrite in top view (boxed area).

Related to Figures S1–S3.

dendritic spines, chronic *in vivo* 2-photon microscopy in the somatosensory cortex of adult Thy1.2-GFP-M mice (Feng et al., 2000) was performed. The dynamics of eGFP-labeled spines on apical dendritic tufts of layer V pyramidal neurons were monitored before and during enriched environment exposure of mice (Jung and Herms, 2014). As documented by the micrograph time series (Figure 5A), enriched environment substantially and persistently promoted spinogenesis and thus increased the amount of newly formed spines accessible for lifetime analysis. Subsequently, target dendrites were relocated in vibratome sections and respective EM specimen by flat embedding and triangulation of natural landmarks. Correlation of *in vivo* 2-photon microscopy, *ex vivo* CLSM, and FIB/SEM 3D datasets (Figures 5A–5D) demonstrates that structural integrity of the corresponding dendrites and dendritic spines (Figures 2C–2F) was well preserved throughout CLEM preparation. Based on the FIB/SEM tomograms, tripartite synapses were reconstructed in 3D to determine the perimeter of the synaptic cleft and its astrocytic coverage (Figure 5E and Videos S2 and S3). Correlation of these structural parameters with dendritic spine lifetime revealed that the fraction of synaptic perimeter surrounded by PAPs on average amounts to 37% and scales neither with synaptic cleft area nor with spine age (Figures S4A and S4B). The synaptic perimeter of a few old spines (lifetime $\geq$41 days) was even completely devoid of PAPs.

DISCUSSION

Methodological hurdles in CLEM are the re-localization of a rather small target volume within a large tissue volume, changing sample orientation during the transition between different microscopy modalities, and structural distortions or preparation artifacts caused by artificial fiducials (de Boer et al., 2015; Grabenbauer, 2012; Karreman et al., 2016a). Current CLEM approaches, based on artificial fiducials, suffer from several drawbacks (Table 1): (1) labeling with electron-dense precipitate or fluorescent beads/quantum dots can obscure ultrastructural details; (2) fixation and harsh permeabilization conditions, required for antibody labeling, compromise ultrastructure; (3) delivery of tracers to living tissue may induce toxic side effect; and (4) NIRB is mainly used to mark the surface of the sample, as light scattering within the tissue limits the depth of NIRB (Karreman et al., 2014).

To circumvent these technical drawbacks we introduce a "flat-embedding" protocol of vibratome sections, ideal for both SEM and FIB/SEM investigations (Figures 1, 2, S1, S2, and S3). Due to their thickness of approximately 50 μm, vibratome sections can be: (1) adequately fixed, even as large slices (e.g., 20 mm^2), (2) investigated entirely at low and high magnifications with LM and SEM (Figures 3B and 3C), and (3) milled by FIB/SEM in their entire thickness (Figure 4C). Since tissue sections can be permanently immobilized on glass slides, their orientation does not change in the transition from LM to FIB/SEM (Figures 3B and 3C). The complex correlation of LM and SEM data can be achieved by a simple overlay of the LM image, depicting the sample surface, onto the SEM image of the resin-embedded section (Figure 3F), with its characteristic topography (SE image) and material contrast information (BSE image). In addition to the direct surface topography, subsurface information can be gathered at high voltages, as the BSE signal can be detected within a depth of approximately 3 μm at 25 kV (Figures S2 and S3). Thereby, the surface of the specimen becomes transparent and prominent structural features as nuclei and axons become visible with strong contrast (Figure S3). DIC microscopy yields sufficient resolution and depth of field to visualize blood vessels, nuclei, and myelinated axons simultaneously (Figure 1A). Furthermore, SCoRe microscopy can be applied to visualize myelinated axons based on their high refractive index in a label-free manner (Schain et al., 2014) (Figure 1C). Axons are excellent high-resolution fiducials for brain tissue, due to their high density and strong BSE signal in SEM (Figures 1K and S2). As nuclei and blood vessels are abundantly present in all animal tissues, this method can also be used for various organs like kidney, liver, and skin.

A reduction of the laborious FIB/SEM trench milling could be achieved by stepwise adjusting the ion beam current depending on the trench position, thus saving time and costs (Figures 4A and 4B). Monitoring the constantly increasing block face every 0.5–1 μm provides essential information about the position of the relevant landmarks, which can be reconstructed in 3D and compared with the LM stacks for possible corrections or fine adjustments (Figures 4C and 4D). Since the cross-section of the glass slide serves as

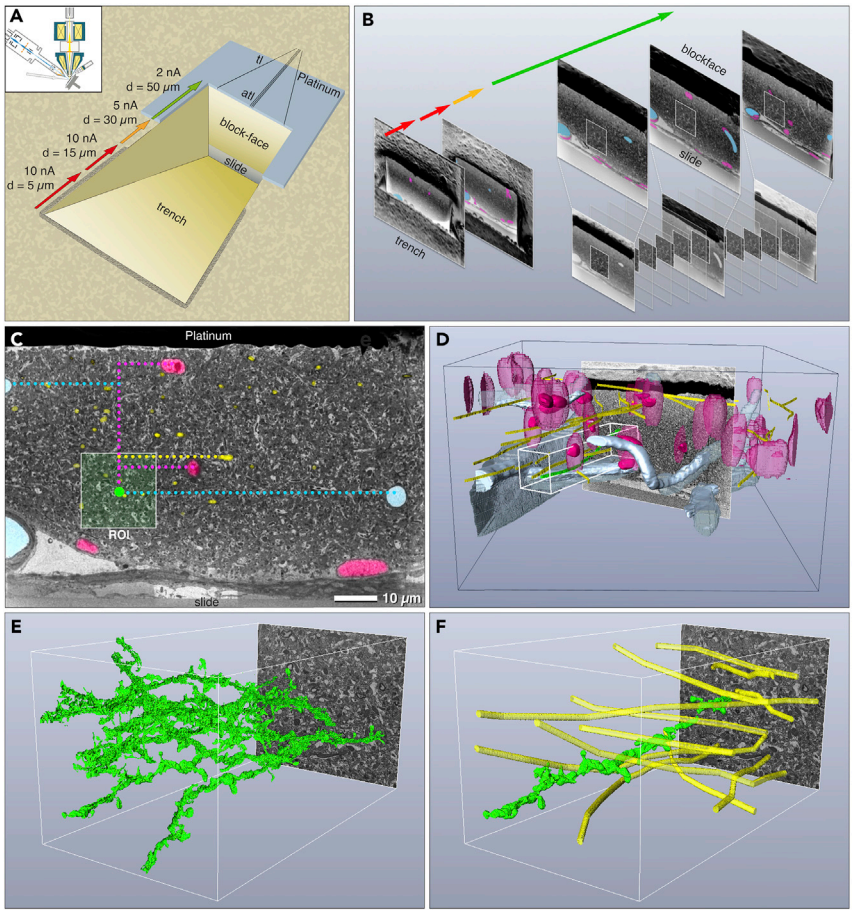

Figure 4. 3D alignment of LM and FIB/SEM Tomograms

(A) Economic trench milling in several steps: successive decrease in ion beam energy with increasing milling depth. FIB/SEM tomography is performed by eucentric tilting of the specimen to 54° into the coincidence point (inset). The target area is coated with approximately 1 µm platinum by ion beam deposition. Thin tracking lines (tl) and autotune lines (atl) serve for controlling the milling/imaging process (section thickness, focus, astigmatism).

(B) High-resolution images (white squares) are taken every 15 nm of milling. In addition, key frames are taken in intervals of 1 µm in z-direction, providing micrographs for fast, "on the fly" 3D correlation of natural landmarks: blood vessels (blue), nuclei (magenta), and myelinated axons (yellow).

(C) When reaching the final block face the region of interest (ROI; white square) with the target dendrite (green spot) is defined in x/y using the coordinates of the landmarks derived from the 3D LM data. Blood vessels (blue); nuclei (magenta); myelinated axons (yellow).

(D) Superimposition of landmarks (blood vessels, nuclei, and axons; transparent) of the LM reconstructions (black box) with the FIB/SEM reconstructions of the corresponding structures (solid).

(E) Preliminary fast reconstructions of several potential dendrites (green) in the target volume (white box) by an automatic labeling algorithm (*Magic Wand*, Amira™).

(F) Usage of myelinated axons (yellow) as correlative marker to identify the target dendrite (green).

Related to Video S1.

absolute reference for precise alignment, an exact correlation is ensured (Figure 4C) (Luckner and Wanner, 2018). These improvements reduce the CLEM workflow and make artificial fiducials and delicate trimming needless (Kolotuev et al., 2012).

The high precision of the presented CLEM method was demonstrated by *in vivo* 2-photon microscopy of single dendritic spines and their subsequent identification within a resin-embedded tissue by FIB/SEM Detailed information could be gathered about dendritic spine lifetime and morphometric measurements of the corresponding tripartite synapse at nanometer resolution (Figure 5). Our data show that astrocytic coverage of the synaptic cleft does not proportionally scale with either the synapse size or the synapse

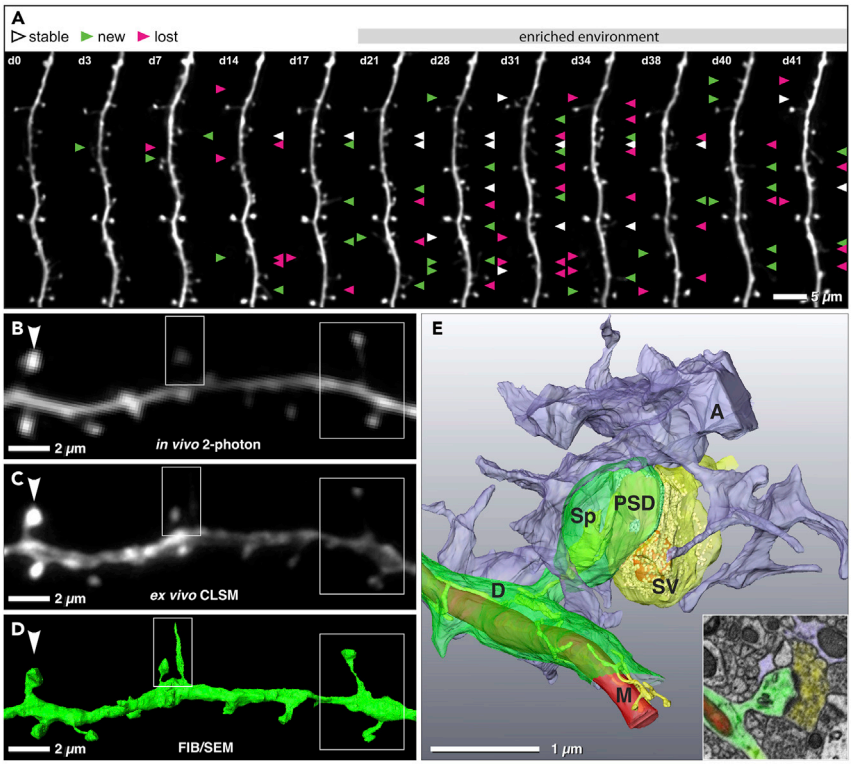

Figure 5. 3D-CLEM of Cortical Tripartite Synapses

(A) *In vivo* 2-photon micrographs of eGFP-labeled apical dendrites of layer V pyramidal neurons in the somatosensory cortex imaged before and during enriched environment. Enriched environment exposure started at day 18 and was continued until end of the imaging period. White arrowheads mark spines that formed newly and remained stable for at least two consecutive imaging time points; gained and lost spines are labeled with green and magenta arrowheads, respectively. Scale bar = 5 µm.

(B–D) Comparative juxtaposition of the same dendritic segment recorded by *in vivo* 2-photon (B), *ex vivo* CLSM (C) and FIB/SEM microscopy (D). White boxes indicate dendritic spines that were detected in high-resolution CLSM microscopy and FIB/SEM; white arrowheads indicate spines that were detected in all imaging modalities. Scale bar = 2 µm.

(E) 3D reconstructed FIB/SEM tomogram of a complete tripartite synapse (A, astrocyte; D, dendrite; M, mitochondrion; PSD, postsynaptic density; Sp, spine; SV, synaptic vesicles). Inset shows a single micrograph of the corresponding FIBS/SEM stack depicting a dendritic spine (green) with associated presynapse (yellow) and astrocyte (purple). Scale bar = 1 µm.

Related to Figure S4.

age (Witcher et al., 2007), indicating that smaller, newly formed spines, as well as established larger spines, have equal access to extracellular glutamate, which is restricted by astroglial ensheathment of the synaptic perimeter. Thus, astrocytes may facilitate integration of synapses by preventing transmitter spillover between neighboring excitatory synapses (Ostroff et al., 2014). Although we did not detect a change of astrocytic coverage during synapse maturation under basal conditions, it has been shown to increase during periods of enhanced neuronal activity to augment glutamate clearance and preserve synaptic response (Genoud et al., 2006). Furthermore, the observation that the synaptic perimeters of some persistent spines are completely devoid of astroglial processes indicates that permanent astrocytic coverage might not be mandatory for the maintenance of excitatory synapse stability (Bernardinelli et al., 2014) (Figure S4).

Summarizing, we introduce a precise and efficient CLEM preparation method, which (1) circumvents the need of artificial fiducials, (2) is compatible with widely accessible optical microscopic techniques, and (3) is suitable for various scientific questions.

METHODS

All methods can be found in the accompanying Transparent Methods supplemental file.

	Pro	Con
"Flat embedding"	Fast Cheap Nondisruptive Suitable for all kind of tissues	Limited in vibratome section thickness of 50 μm
NIRB (Bishop et al., 2011)	Fast Suitable for all kind of tissues	Disruptive Fs-laser needed
DAB (Sonomura et al., 2013)	Direct visualization of the target structure	Masking ultrastructure
QDs (Masich et al., 2006)	Suitable for all kind of tissues	Masking ultrastructure Limited tissue penetration

Table 1. Comparison of Common CLEM Protocols
NIRB, near-infrared branding; DAB, diaminobenzidine; QDs, quantum dots

SUPPLEMENTAL INFORMATION

Supplemental Information includes Transparent Methods, four figures, and three videos and can be found with this article online at https://doi.org/10.1016/j.isci.2018.07.012.

ACKNOWLEDGMENTS

The authors wish to thank Cornelia Niemann and Nadine Lachner for excellent technical assistance. S.B. was supported by the Deutsche Forschungsgemeinschaft (DFG BU 3307/1-1 AOBJ 625759).

AUTHOR CONTRIBUTIONS

J.H. and G.W. designed and led all aspects of the project. M.L., S.B., and S.F. performed most of the experiments. M.L., S.B., S.F., and M.S. analyzed the data. J.H., S.B., and S.F. interpreted data; M.L. and G.W. performed FIB/SEM; S.B., S.F., Y.N., and E.H. performed LM; M.L., M.S., and S.B. reconstructed FIB-SEM datasets; and M.L., S.B., S.F., and G.W. wrote the paper. All authors edited the paper.

DECLARATIONS OF INTERESTS

The authors declare no competing interests.

Received: February 16, 2018
Revised: June 20, 2018
Accepted: July 16, 2018
Published: August 31, 2018

REFERENCES

Araque, A., Parpura, V., Sanzgiri, R.P., and Haydon, P.G. (1999). Tripartite synapses: glia, the unacknowledged partner. Trends Neurosci. *22*, 208–215.

Belu, A., Schnitker, J., Bertazzo, S., Neumann, E., Mayer, D., Offenhäusser, A., and Santoro, F. (2016). Ultra-thin resin embedding method for scanning electron microscopy of individual cells on high and low aspect ratio 3D nanostructures. J. Microsc. *263*, 78–86.

Bernardinelli, Y., Nikonenko, I., and Muller, D. (2014). Structural plasticity: mechanisms and contribution to developmental psychiatric disorders. Front. Neuroanat. https://doi.org/10.3389/fnana.2014.00123.

Bishop, D., Nikić, I., Brinkoetter, M., Knecht, S., Potz, S., Kerschensteiner, M., and Misgeld, T. (2011). Near-infrared branding efficiently correlates light and electron microscopy. Nat. Methods *8*, 568–570.

Blazquez-Llorca, L., Hummel, E., Zimmerman, H., Zou, C., Burgold, S., Rietdorf, J., and Herms, J. (2015). Correlation of two-photon *in vivo* imaging and FIB/SEM microscopy. J. Microsc. *259*, 129–136.

Bourne, J.N., and Harris, K.M. (2008). Balancing structure and function at hippocampal dendritic spines. Annu. Rev. Neurosci. *31*, 47–67.

de Boer, P., Hoogenboom, J.P., and Giepmans, B.N.G. (2015). Correlated light and electron microscopy: ultrastructure lights up! Nat. Methods *12*, 503–513.

Feng, G., Mellor, R.H., Bernstein, M., Keller-Peck, C., Nguyen, Q.T., Wallace, M., Nerbonne, J.M., Lichtman, J.W., and Sanes, J.R. (2000). Imaging neuronal subsets in transgenic mice expressing multiple spectral variants of GFP. Neuron *28*, 41–51.

Genoud, C., Quairiaux, C., Steiner, P., Hirling, H., Welker, E., and Knott, G.W. (2006). Plasticity of astrocytic coverage and glutamate transporter expression in adult mouse cortex. PLoS Biol. *4*, e343.

Grabenbauer, M. (2012). Correlative light and electron microscopy of GFP. Methods Cell Biol. *111*, 117–138.

Grabenbauer, M., Geerts, W.J.C., Fernadez-Rodriguez, J., Hoenger, A., Koster, A.J., and Nilsson, T. (2005). Correlative microscopy and electron tomography of GFP through photooxidation. Nat. Methods *2*, 857–862.

Heller, J.P., and Rusakov, D.A. (2015). Morphological plasticity of astroglia: understanding synaptic microenvironment. Glia *63*, 2133–2151.

Jung, C.K.E., and Herms, J. (2014). Structural dynamics of dendritic spines are influenced by an environmental enrichment: an in vivo imaging study. Cereb. Cortex *24*, 377–384.

Karreman, M.A., Hyenne, V., Schwab, Y., and Goetz, J.G. (2016a). Intravital correlative microscopy: imaging life at the nanoscale. Trends Cell Biol. *26*, 848–863.

Karreman, M.A., Mercier, L., Schieber, N.L., Solecki, G., Allio, G., Winkler, F., Ruthensteiner, B., Goetz, J.G., and Schwab, Y. (2016b). Fast and precise targeting of single tumor cells in vivo by multimodal correlative microscopy. J. Cell Sci. *129*, 444–456.

Karreman, M.A., Mercier, L., Schieber, N.L., Shibue, T., Schwab, Y., and Goetz, J.G. (2014). Correlating intravital multi-photon microscopy to 3D electron microscopy of invading tumor cells using anatomical reference points. PLoS One *9*, e114448.

Kizilyaprak, C., Bittermann, A.G., Daraspe, J., and Humbel, B.M. (2014). FIB-SEM tomography in biology. Methods Mol. Biol. *1117*, 541–558.

Knott, G.W., Holtmaat, A., Trachtenberg, J.T., Svoboda, K., and Welker, E. (2009). A protocol for preparing GFP-labeled neurons previously imaged in vivo and in slice preparations for light and electron microscopic analysis. Nat. Protoc. *4*, 1145–1156.

Kolotuev, I., Bumbarger, D.J., Labouesse, M., and Schwab, Y. (2012). Targeted ultramicrotomy: a valuable tool for correlated light and electron microscopy of small model organisms. Methods Cell Biol. *111*, 203–222.

Kukulski, W., Schorb, M., Welsch, S., Picco, A., Kaksonen, M., and Briggs, J.A.G. (2012). Precise, correlated fluorescence microscopy and electron tomography of lowicryl sections using fluorescent fiducial markers. In Methods in Cell Biology, T. Müller-Reichert and P. Verkade, eds. (Elsevier), pp. 235–257.

Li, J., Erisir, A., and Cline, H. (2011). In vivo time-lapse imaging and serial section electron microscopy reveal developmental synaptic rearrangements. Neuron *69*, 273–286.

Lucas, M.S., Günthert, M., Bittermann, A.G., de Marco, A., and Wepf, R. (2017). Correlation of live-cell imaging with volume scanning electron microscopy. Methods Cell Biol. *140*, 123–148.

Luckner, M., and Wanner, G. (2018). Precise and economic FIB/SEM for CLEM: with 2 nm voxels through mitosis. Histochem. Cell Biol. 1–22.

Maco, B., Holtmaat, A., Cantoni, M., Kreshuk, A., Straehle, C.N., Hamprecht, F.A., and Knott, G.W. (2013). Correlative in vivo 2 photon and focused ion beam scanning electron microscopy of cortical neurons. PLoS One *8*, e57405.

Maco, B., Holtmaat, A., Jorstad, A., Fua, P., and Knott, G.W. (2014). Correlative in vivo 2-photon imaging and focused ion beam scanning electron microscopy. In Methods in Cell Biology, T. Müller-Reichert and P. Verkade, eds. (Elsevier), pp. 339–361.

Masich, S., Östberg, T., Norlén, L., Shupliakov, O., and Daneholt, B. (2006). A procedure to deposit fiducial markers on vitreous cryo-sections for cellular tomography. J. Struct. Biol. *156*, 461–468.

Mironov, A.A., and Beznoussenko, G.V. (2009). Correlative microscopy: a potent tool for the study of rare or unique cellular and tissue events. J. Microsc. *235*, 308–321.

Ostroff, L.E., Manzur, M.K., Cain, C.K., and LeDoux, J.E. (2014). Synapses lacking astrocyte appear in the amygdala during consolidation of Pavlovian threat conditioning. J. Comp. Neurol. *522*, 2152–2163.

Panatier, A., Arizono, M., and Nagerl, U.V. (2014). Dissecting tripartite synapses with STED microscopy. Philos. Trans. R. Soc. Lond. B Biol. Sci. *369*, 20130597.

Schain, A.J., Hill, R.A., and Grutzendler, J. (2014). Label-free in vivo imaging of myelinated axons in health and disease with spectral confocal reflectance microscopy. Nat. Med. *20*, 443–449.

Schieber, N.L., Machado, P., Markert, S.M., Stigloher, C., Schwab, Y., and Steyer, A.M. (2017). Minimal resin embedding of multicellular specimens for targeted FIB-SEM imaging. Methods Cell Biol. *140*, 69–83.

Sonomura, T., Furuta, T., Nakatani, I., Yamamoto, Y., Unzai, T., Matsuda, W., Iwai, H., Yamanaka, A., Uemura, M., and Kaneko, T. (2013). Correlative analysis of immunoreactivity in confocal laser-scanning microscopy and scanning electron microscopy with focused ion beam milling. Front. Neural Circuits *7*, 26.

Witcher, M.R., Kirov, S.A., and Harris, K.M. (2007). Plasticity of perisynaptic astroglia during synaptogenesis in the mature rat hippocampus. Glia *55*, 13–23.

ISCI, Volume *6*

Supplemental Information

Label-free 3D-CLEM

Using Endogenous Tissue Landmarks

Manja Luckner, Steffen Burgold, Severin Filser, Maximilian Scheungrab, Yilmaz Niyaz, Eric Hummel, Gerhard Wanner, and Jochen Herms

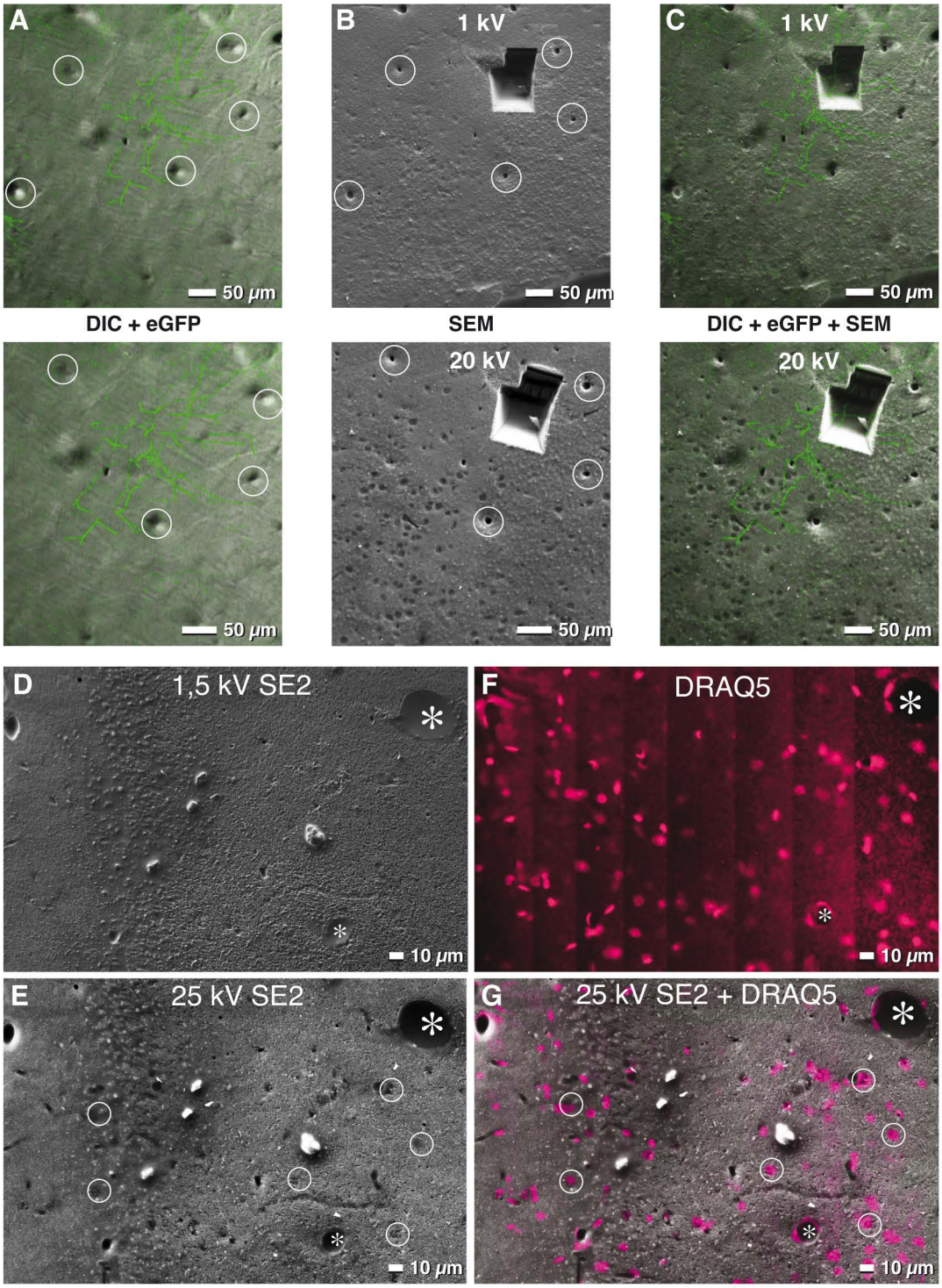

Figure S1. Vibratome sections at different kV, Related to Figure 1

(A) DIC images taken from the surface of the vibratome section and merged with a projection view of the dendrites (green = eGFP).

(B) SEM micrographs at different kV. Topographic and material contrast change are enhanced with increase of the accelerating voltage: Blood vessels are easily recognized as little holes (circles) at low and high kV. Sectioned nuclei with almost no topographic contrast at 1 kV, show a strong material contrast at 20 kV.

(C) Superimpostion of a DIC stack and an eGFP stack allows a precise localization of the target dendrite(s) in a range of a few µm.

(D-E) SEM micrographs at different kV. Different high voltages can be chosen to enhance either the topographic or material contrast of nuclei (circles): 1,5 kV (D) and 25 kV (E).

(F) From the DRAQ5 stack, 7 segments of different height in the stack were combined into a stitched image, representing only surface near nuclei.

(G) Superposition of micrographs enables precise correlation of nuclei (circles) and blood vessels (asterisk) in both, SEM an LSM.

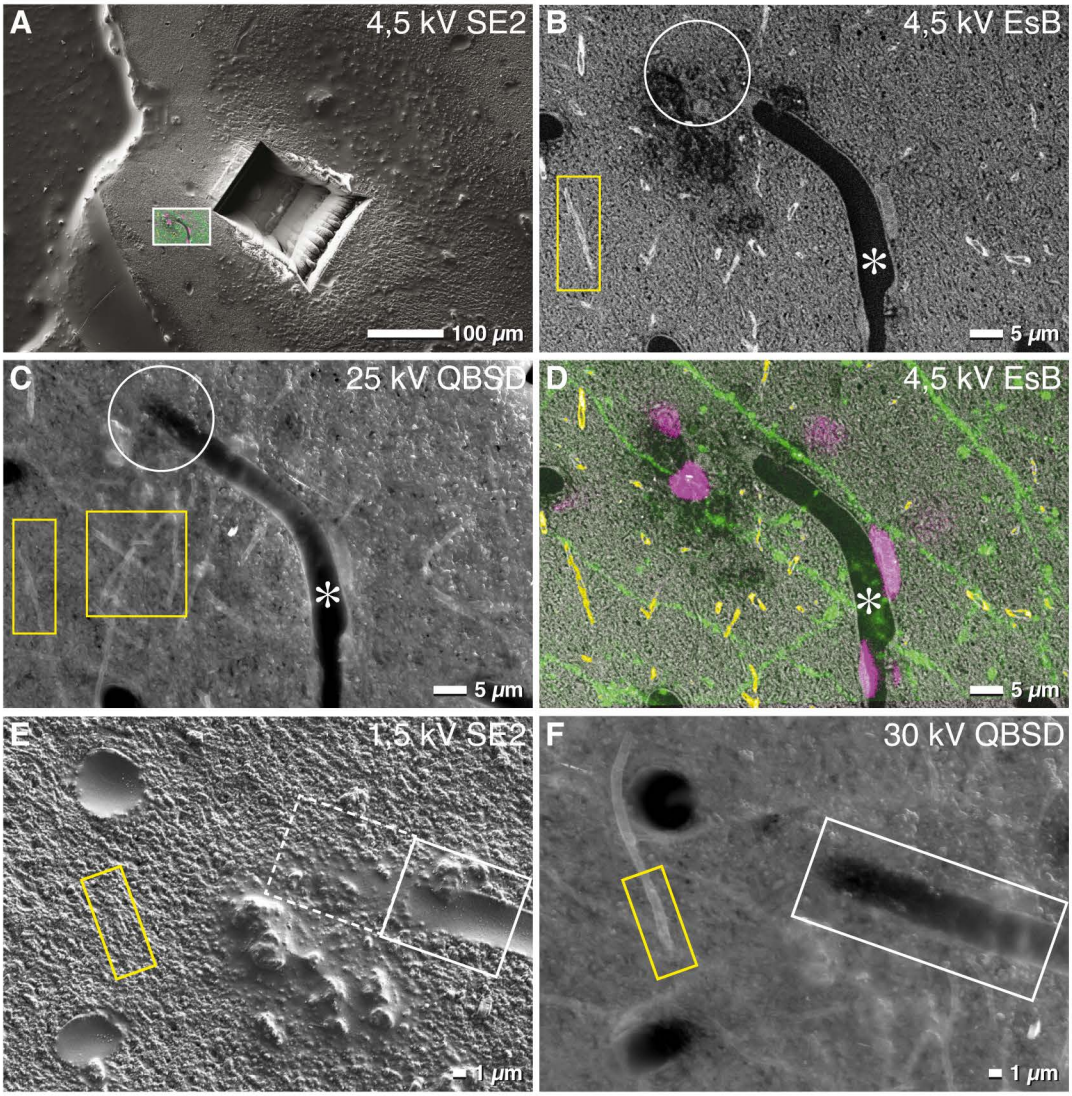

Figure S2. Myelinated axons in SEM, Related to Figure 1 and 2

(A) SEM micrograph of a vibratome slice. The trench indicates a FIB/SEM recorded target volume. Correlation with LM micrograph exhibits the next traget area.

(B-C) Myelinated axons are clearly visible in both, the EsB image at moderate kV (B) or in the QBSD image at high kV (C) due to their strong staining with osmium.

(D) Overlay of myelinated axons (yellow), nuclei (magenta) and dendrites (green) confirm the precision of surface correlation of CLSM and SEM. Blood vessels display at higher voltages a dark contrast (asterisk) or are visible at low kV by topographic contrast of the SE2 image (A).

(E-F) Comparison of 1,5 kV SE2 image (framed areas) with the QBSD image demonstrates the depth information given at high kV. Myelinated axons are clearly visible at high kV (F = yellow frame) and undetectable in the SE2-image (E = yellow frame).

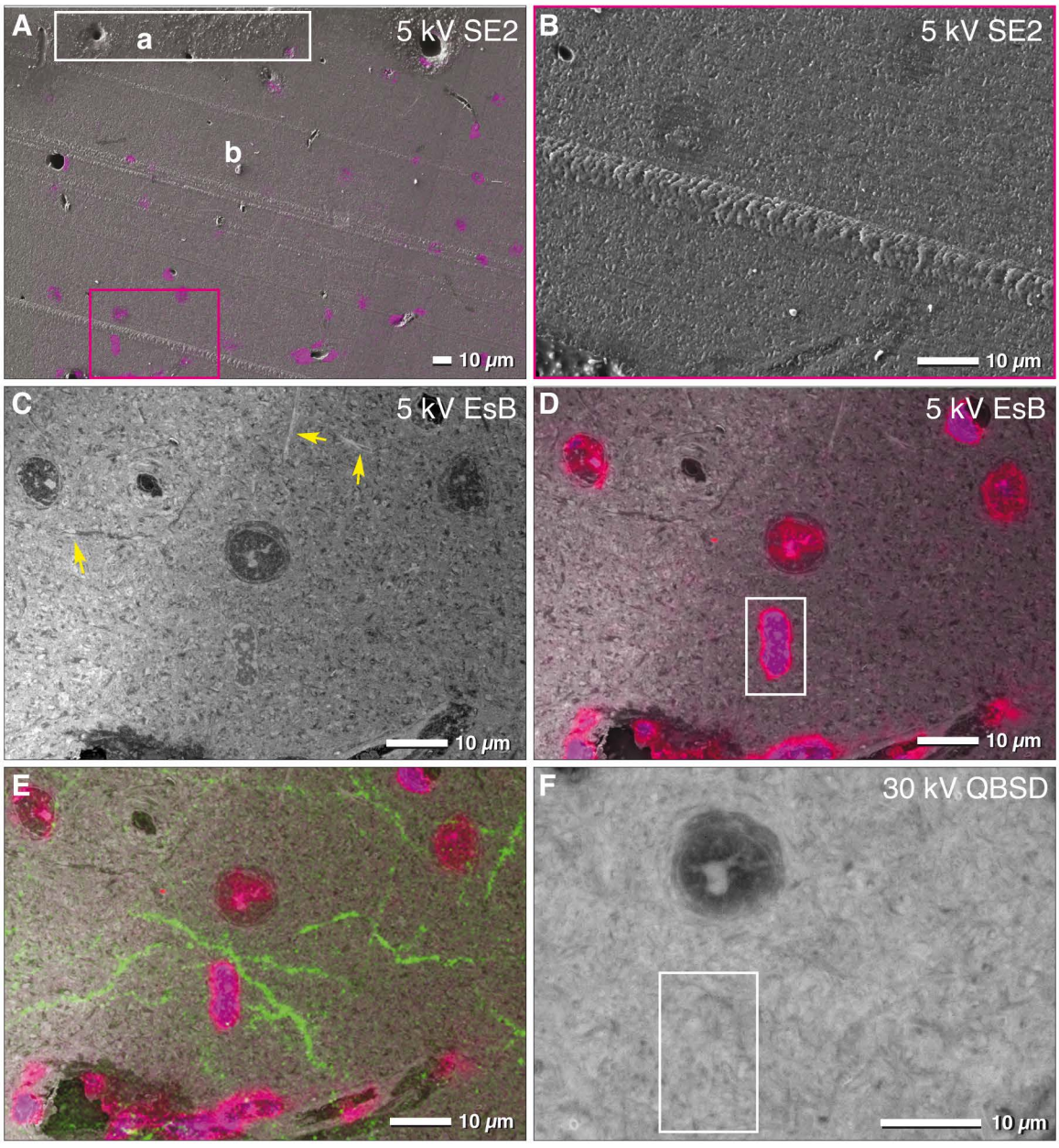

Figure S3. Enhancement of the material contrast after smoothing of vibratome sections, Related to Figure 1 and 2

(A) Correlation of light micrographs of stained nuclei (DRAQ5; LSM) with SEM micrographs of an embedded mouse brain section. For high resolution correlation, the specimen surface was smoothed by removal of few µm with a glass knife equipped ultra microtome. The difference in surface topography can be compared before (a = framed area; white) and after smoothing (b).

(B-E) At high magnification (framed area of A; magenta) nuclear details (nuclear envelope, heterochromatine) can be hardly recognized in the SE2 image (B) but they are clearly visible with the EsB-signal (C and D 5; kV). Axons (arrows) can be identified by their myelin sheets which give a high contrast due to the strong osmium staining. Superposition with the LM image of the nuclei (magenta) and dendrites (green) enable a precise correlation in the sub-micrometer range (E).

(F) The depth information is increased with high accelerating voltage (30 kV). Contrast of tangential sectioned nuclei becomes reduced (framed area; compare with framed area in D).

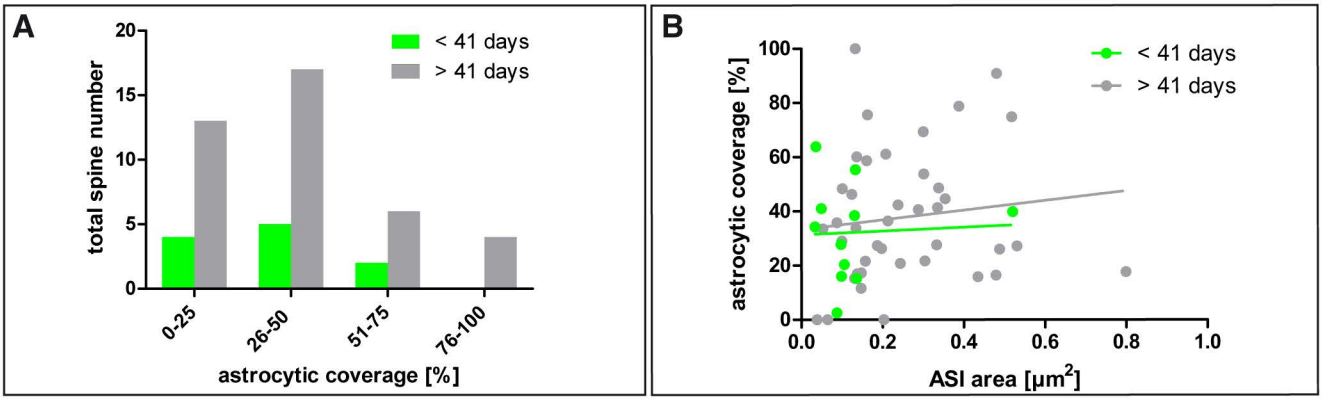

Figure S4. Astrocytes equally cover the synaptic perimeter of young and old spines, Related to Figure 4

(A) Distribution graphs of young (≤ 41 days) and old (≥ 41 days) dendritic spines according to astrocytic coverage of the synaptic perimeter.

(B) Correlation between astrocytic coverage and ASI area of young (≤ 41 days) and old (≥ 41 days) dendritic spines.

Transparent Methods

Animals

Female and male 2-3 months old heterozygous GFP-M mice (Tg(Thy1-EGFP)MJrs from Jackson Laboratory, Bar Harbor, Maine) were used (Feng et al., 2000). Mice were group-housed under pathogen-free conditions and bred in the animal housing facility of the Center of Stroke and Dementia Research, with food and water provided ad libitum (21 ± 1°C, at 12/12 hour light/dark cycle). All experiments were carried out in compliance with the National Guidelines for Animal Protection, Germany with the approval of the regional Animal care committee of the Government of Upper Bavaria, and were overseen by a veterinarian.

Cranial window implantation

Before use, surgical tools were sterilized in a glass-bead sterilizer (FST). Mice were anesthetized by an intra-peritoneal injection of ketamine/xylazine (140/10 mg/kg body weight, WDT, Bayer Health Care). In order to prevent cerebral edema Dexamethasone (6 mg/kg body weight, Sigma Aldrich) was injected intraperitoneally. Subsequently, mice were placed onto a heating blanket (37 °C) and the head was fixed in a stereotactic frame. Eyes were protected from drying by applying eye-ointment (Bepanthen, Bayer). The scalp was washed with swabs soaked with 70 % ethanol. A flap of skin covering the cranium was excised using small scissors. The periosteum was scraped away with a scalpel. The prospective craniotomy location (1.5-2.5 mm AP and 0-4 mm ML relative to bregma) was marked with a biopsy punch (diameter 4 mm, Integra LifeSciences). The exposed skull around the area of interest was covered with a thin layer of dental acrylic (iBond Self Etch, Hereaus Kulzer) and hardened with a LED polymerization lamp (Demi Plus, Kerr). A dental drill (Schick Technikmaster C1, Pluradent) was used to thin the skull around the marked area. After applying a drop of sterile phosphate buffered saline (DPBS, Gibco, Life Technologies) on the craniotomy the detached circular bone flap was removed with forceps. A circular coverslip (4 mm diameter, VWR International) was placed onto the craniotomy and glued to the skull with histoacryl adhesive (Aesculap). The exposed skull was covered with dental acrylic (Tetric Evoflow A1 Fill, Ivoclar Vivadent) and a head-post was attached parallel to the window for head-fixing mice in subsequent imaging sessions. After surgery, mice received a subcutaneous dose of the analgesic Carprophen (7.5 mg/kg body weight, Rimadyl, Pfizer) and antibiotic Cefotaxim (5

mg/kg body weight, Pharmore). Finally, mice were allowed to recover from surgery on a heating blanket.

Chronic *in vivo* two-photon microscopy

In vivo two-photon imaging started 4 weeks after cranial window implantation, using a multiphoton LSM 7 MP microscope (Zeiss) equipped with a fs-laser (Mai Tai DeepSee, Spectra-Physics), a 20x water immersion objective (W Plan-Apochromat 20x/1.0 NA, Zeiss) and a motorized stage. eGFP was excited at 920 nm and the emission was collected after a band pass filter from 470-550 nm by a non-descanned detector (photomultiplier tube GaAsP, Zeiss) directly after the objective. Throughout the imaging sessions, mice were anesthetized with isoflurane (1 % in oxygen, 0.5 l/min) and placed on a heating pad to keep body temperature at 37 °C (Fine Science Tools GmbH). A magnified image of the superficial cerebral blood vessels was acquired by using the camera port of the 7 MP microscope. The same ROIs were repositioned over time by alignment of the field of view based on the vascular pattern. Apical dendritic tufts of layer V pyramidal neurons in the somatosensory cortex were imaged in consecutive sessions at specified time points. For overview images, 3D stacks of 300 µm depth with 3 µm axial resolution and 1024×1024 pixels per image frame (0.4 µm/pixel) were acquired in multiphoton mode of the microscope. To resolve dendritic spines, high-resolution images from single dendrites were taken with 1 µm axial resolution and 512 × 256 pixels per image frame (0.1 µm per pixel). Individual imaging sessions lasted for no longer than 60 min with the laser power kept below 50 mW to avoid phototoxicity. Special care was taken to ensure consistent fluorescence levels both in space and time. After the fourth imaging session mice were placed into an enriched environment accordingly to a recently published protocol to enhance the structural plasticity of dendritic spines (Jung and Herms, 2014).

Preparation of brain sections

Mice were transcardially perfused with a mixture of formaldehyde and glutardialdehyde (Electron Microscopy Sciences, EMS) in PBS. A mixture of 0.5 % glutardialdehyde and 3.5 % formaldehyde was used in order to reduce background fluorescence from glutardialdehyde while preserving eGFP fluorescence and specimen ultrastructure. After 1 h perfusion mice were decapitated and the right

parietal bone with the ipsilateral window was removed. Subsequently, the mouse head was attached via head post to the stage of a vibratome (VT1000S, Leica Biosystems) to cut the brain tissue parallel to the imaging plane. This way, a single brain slice containing all cortical layers and the complete somato-sensory cortex was obtained. The cortical brain slice was incubated in 4% formaldehyde in PBS overnight at 4 °C, washed with PBS at the next day and subsequently stored in PBS at 4 °C. The fixed brain slice was further cut into 50 µm sections on a vibratome. Care was taken to keep the order of all obtained slices from top to bottom as well as not to flip them. Each slice was mounted onto a Cell-Tak™ (Corning®, Thermo Fisher Scientific) coated microscope slide (Superfrost, Menzel) with an adhesive, circular imaging spacer (Secure-Seal™, Grace Bio-Labs). The well of the imaging spacer was filled with 20 µM DRAQ5 (Biostatus) solution, sealed with a coverslip (No. 1.5, Zeiss) and incubated overnight at 4 °C.

LM microscopy

Slides were imaged in “tile scan” mode of an Apotome.2 wide field microscope (Zeiss) equipped with an EC Plan-NEOFLUAR 10x / 0.3 NA objective (Zeiss) to identify brain slices with the desired regions of interest. For bright field microscopy, the illumination aperture (NA 0.1) of the condenser was closed to increase image contrast. Emission of eGFP and DRAQ5 was collected using standard filter sets for green (490-606 nm) and far red (643-752 nm) (Zeiss). Confocal imaging was used (LSM 880 with AiryScan, Zeiss) to map all natural landmarks in 3D. Overview images of the region of interest with 3 µm axial resolution and 1024 × 1024 pixels per image frame (0.4 µm/pixel) were acquired with a Plan-Apochromat 20x / 0.8 NA air objective. High resolution image stacks (135 x 135 x 50 μm^3 with 0.13 µm in xy and 1 µm in z per pixel) of dendrites were acquired with a Plan-Apochromat 63x / 1.4 oil objective (Zeiss). DRAQ5 and eGFP were excited at 633 nm and 488 nm, respectively. Emission was collected from 500-560 nm (eGFP) and 650-700 nm (DRAQ5). Additionally, differential interference contrast images were acquired in the transmitted light channel. Furthermore, spectral confocal reflectance microscopy was used to visualize myelinated axons within the same volume. Axons were imaged with laser lines of 458 nm, 514 nm and 633 nm in a single track. The reflection mode of the microscope was used in combination with a partial mirror (80 % transmission, 20

% reflection) as main beam splitter. Images of all three channels were combined by using the average function of the Zen software (Version 2.3, Zeiss).

EM preparation

After light microscopic inspection mounted vibratome sections were uncovered by removal of the coverslip. Subsequently, samples were washed with cacodylate buffer (75 mM cacodylate 75 mM NaCl, 2 mM $MgCl_2$) and again fixed with 2,5 % glutardialdehyde in cacodylate buffer for 15 min, followed by 3 washing steps in cacodylate buffer. The tissue was post-fixed with 1 % OsO_4 and 1 % $K_4Fe(CN)_6$ in cacodylate buffer for 30 min, washed 3 times in ddH_2O, incubated with 1 % thiocarbohydrazide in ddH_2O for 30 minutes, washed with ddH_2O 3 times, followed by a second post-fixation with 1 % OsO_4 in ddH_2O for 30 min. Samples were further rinsed 3 times with ddH_2O, dehydrated in a graded series of acetone and incubated in 1 % uranyl acetate with 20 % acetone for 30 min. Subsequently, sections were embedded on the glass slide and infiltrated with 1:1 Hard-Plus Resin-812 in acetone for 10 minutes, 2:1 Hard-Plus Resin-812 in acetone for 30 min and finally in 100 % Hard-Plus Resin-812 for 1h at RT. Excessive resin was removed by centrifugation: the slide was placed in a 50 ml falcon tube with a tissue paper at the bottom and centrifuged at 1000 rpm for 2 min. After samples were polymerized for 3 days at 60 °C, the glass was trimmed with a diamond pen and mounted on an aluminum stub with colloidal silver. Finally, the glass was covered with colloidal silver and the entire sample was carbon coated (thickness of 15-20 nm) by evaporation.

FIB/SEM microscopy

Mouse brain tissues were imaged in an Auriga 40 FIB/SEM workstation (Carl Zeiss Microscopy GmbH) operating under SmartSEM (Carl Zeiss Microscopy GmbH) and Atlas3D software (Fibics Inc., Ottawa, Ontario, Canada). To facilitate correlation, the 50 µm thick brain slice was milled down to the surface of the glass slide, which was used as a reference. Subsequently, a 70 µm long ramp was milled by FIB (for vibratome sections with a thickness of 50 µm and a FIB tilt angle of 54°, the length of the milling ramp can be calculated as tan54° = 1.374. In this case, the trapezoid trench has to be approx. 70 µm long). After milling of 20 µm in z-direction milling was stopped, the ion beam current reduced to 10 nA, and the milling depth increased to

10-20 µm. After additional 20 µm of length, the trench was milled with a depth of 30 µm, until the beam reaches the glass slide. While milling the ramp to get access to the target volume, key frames were taken to inspect the correlation landmarks (blood vessels, nuclei and myelinated axons) to determine the position of the target dendrite in all three dimensions. Final milling parameters were set to 1-2 nA milling current of the Ga-emitter. With each cycle 10-15 nm of epoxy resin was removed. SEM images were recorded with an aperture of 60 µm in the high current mode at 1.5 kV of the in-lens EsB detector with the EsB grid set to -800-1200 V. Key frames were imaged with a pixel size of 20-27 nm and the ROI with a pixel size of 5-8 nm. Images series of 3000-4000 sections were recorded. In the synchronous mode of the ATLAS-System, the milling current and depth were adjusted to match milling time with exposure time set to 1 min. Automatic correction of focus (*auto tune*) and astigmatism (*auto stig*) was applied every 30 minutes.

3D reconstruction of LM and FIB/SEM image stacks

LM images of blood vessels, nuclei and myelinated axons were reconstructed in 3D using Imaris (Version 7.7.2, Bitplane). FIB/SEM image stacks were aligned, segmented and 3D reconstructed in Amira (FEI Company). For registration of the LM and FIB/SEM datasets, both 3D reconstructions were fit into each other manually by rotation and translation. FIB/SEM volume was used as a reference to adjust the LM/DIC reconstruction. Registration was performed by successive alignation of blood vessels, nuclei and finally myelinated axons to increase the precision of the correlation.

Image analysis

Amira 3D reconstructions of dendritic spines, corresponding presynapses and perisynaptic astrocytic processes were imported in Blender software for morphometric analysis. Volumes, surfaces and axon spine interfaces (ASI) were quantified with the plugins “NeuroMorph Measurement Tools” and “NeuroMorph Proximity Analysis” (Jorstad, A., Nigro, B., Cali, C. *et al.* 2015 and Barnes *et al.* 2015). Astrocytic coverage was quantified by measuring the total perimeter of the ASI and the proportion that was covered by the astrocyte. To calculate distance distributions of endogenous landmarks in GraphPad Prism 5, distances between 10 randomly chosen dendrites and their closest natural landmarks were measured and

quantified with the 3D measurement tool in Imaris (Version 7.7.2, Bitplane). Dendritic spine lifetime was determined manually off-line by analyzing the corresponding 2-photon micrograph time series. Dendritic spines were defined as stable if their locations did not change along the dendritic shaft between consecutive imaging sessions (acceptable range < 1 µm). Spines, which emerged or disappeared over two consecutive imaging sessions, were assigned as newly gained or lost, respectively. Resolution limitations in the z-plane restricted our analysis to laterally protruding spines. For illustration purpose only, image stacks were deconvolved (AutoQuantX2, Media Cybernetics) and adjusted for contrast and brightness. Figures were created in Adobe Photoshop/Illustrator CS6 and supplementary movies were made in Amira (Thermo Fisher Scientific™).

Key Resource Table

REAGENT or RESOURCE	SOURCE	IDENTIFIER
Chemicals, Peptides, and Recombinant Proteins		
20% Formaldehyde	SCIENCE SERVICES	Cat# E15713
25% Glutardialdehyde	SCIENCE SERVICES	Cat# E16216
Cell-Tak™	Thermo Fisher Scientific	Cat# 10317081
DAPI	Thermo Fisher Scientific	Cat# D1306
DRAQ5	Biostatus	Cat# DR50050
Fetal Bovine Serum (FBS)	GIBCO	Cat# 10270-106
Osmium Tetroxide	SCIENCE SERVICES	Cat# E19130
PBS	GIBCO	Cat# 20012-068
Potassium hexacyanoferrate(II) trihydrate	Sigma-Aldrich	Cat# 455946
Sodium cacodylate trihydrate	MERCK	Cat# 20840-100G-F
Thiocarbohydrazide	Sigma-Aldrich	Cat# 223220
Experimental Models: Organisms/Strains		
Mouse: STOCK Tg(Thy1-EGFP)MJrs/J	The Jackson Laboratory	Stock# 007788
Software and Algorithms		
Adobe Photoshop CC	Adobe Systems Software Ireland Limited	http://www.adobe.com
Altlas3D	Fibics Inc.	
Amira 6.2	Thermo Fisher Scientific	https://www.fei.com/software/amira-3d-for-life-sciences/

Blender Plugin: NeuroMorph Measurement Tools NeuroMorph Proximity Analysis	The Blender Foundation	https://www.blender.org/
GraphPad Prism	GraphPad Software Inc,	http://www.graphpad.com/scientific-software/prism/
ImageJ (1.50, Java 1.8.0_60, 64 bit)	NIH	https://imagej.nih.gov/ij/; RRID:SCR_003070
Imaris 7.7.2	Bitplane	http://www.bitplane.com/
SmartSEM	Carl Zeiss Microscopy GmbH	N/A
Zen 2.3	Carl Zeiss Microscopy GmbH	N/A

10.7 Further Publications

Reinhard Wirth, **Manja Luckner**, Gerhard Wanner. 2018. “Validation of a Hypothesis: Colonization of Black Smokers by Hyperthermophilic Microorganisms.” doi: 10.3389/fmicb.2018.00524

Javier Pascual, Bärbel U. Foesel, Alicia Geppert, Katharina J. Huber, Christian Boedeker, **Manja Luckner**, Gerhard Wanner, Jörg Overmann. 2018. “*Roseisolibacter agri* gen. nov., sp. nov., a novel slow-growing member of the under-represented phylum *Gemmatimonadetes*”. doi: 10.1099/ijsem.0.002619

Vieira S, **Luckner M**, Wanner G, Overmann J. 2017. “Luteitalea pratensis gen. nov., sp. nov. a new member of subdivision 6 Acidobacteria isolated from temperate grassland soil.” doi: 10.1099/ijsem.0.001827

Huber KJ, Geppert AM, Groß U, **Luckner M**, Wanner G, Cooper P, Abakah J, Janssen I, Overmann J. 2017 “*Aridibacter nitratireducens* sp. nov., a member of the family *Blastocatellaceae*, class *Blastocatellia*, isolated from an African soil.” doi: 10.1099/ijsem.0.002318

Artur Wlodarczyka, Thiyagarajan Gnanasekarana, Agnieszka Zygadlo Nielsena, Nodumo Nokolunga Zulub, Silas Busck Mellora, **Manja Luckner**, Jens Frederik Bang Thøfnera, Carl Erik Olsena, Mohammed Saddik Mottawiea, Meike Burowa, Mathias Pribila, Ivo Feussnerb, Birger Lindberg Møllera, Poul Erik. 2017. “Metabolic engineering of light-driven cytochrome P450 dependent pathways into Synechocystis sp. PCC 6803.” doi: 10.1016/j.ymben.2015.10.009

Bärbel U. Foesel, Susanne Mayer, **Manja Luckner**, Gerhard Wanner, Manfred Rohde and Jörg Overmann. 2017. “Occallatibacter riparius gen. nov., sp. nov. and Occallatibacter savannae sp. nov., acidobacteria isolated from Namibian soils, and emended description of the family Acidobacteriaceae.” doi: 10.1099/ijsem.0.000700

Pia K. Wüst, Bärbel U. Foesel, Alicia Geppert, Katharina J. Huber, **Manja Luckner**, Gerhard Wanner and Jörg Overmann. 2016. “Brevitalea aridisoli, B. deliciosa and Arenimicrobium luteum, three novel species of Acidobacteria subdivision 4 (class Blastocatellia) isolated from savanna soil and description of the novel family Pyrinomonadaceae.” doi: 10.1099/ijsem.0.001199

11 Acknowledgments

I wish to thank Prof. Jochen Herms and Prof. Gerhard Wanner for raising the idea of a joint project. I am grateful for the excellent lab environments they provided, inspiring projects, motivating discussions and supportive attitude.

It is Prof. Wanner, who directed my attention to the nano-world of biology and to sense the beauty in the smallest details. I thank him for an outstanding supervision and his deep friendship.

I am very grateful to Silvia Dobler, who shared her entire knowledge with me and taught me everything necessary for any type of preparation and countless tricks. Cornelia Niemann is gratefully acknowledged for her indispensable engagement for the correlative workflows and Jennifer Grünert for her technical support in the daily lab business.

I thank Dr. Eric Hummel who initiated the fruitful cooperation with the LMU and DZNE. I am very grateful that Dr. Renate Burgemeister affiliated me as a member of labs@location and offered me to participate in several workshops and meetings.

PD Dr. Martin Heß is gratefully acknowledged for inspiring discussions and fruitful cooperation concerning 3D. Moreover, I would like to thank Maximilian Scheungrab for his substantial support with 3D reconstructions.